

Uniwersytet Jagielloński

Wydział Chemii



**UNIWERSYTET JAGIELLOŃSKI
W KRAKOWIE**

ROZPRAWA DOKTORSKA

**Badanie wpływu oddziaływań międzycząsteczkowych na
właściwości wybranych jodków i trójjodków**

Mgr Ewelina Właźlak

Promotor: prof. dr hab. Konrad Szaciłowski
Akademickie Centrum Materiałów i Nanotechnologii AGH

Promotor pomocniczy: dr Joanna Kuncewicz
Wydział Chemii Uniwersytetu Jagiellońskiego

Kraków 2019

Składam serdeczne podziękowania mojemu promotorowi prof. dr hab. Koradowi Szaciłowskiemu za opiekę, liczne rozmowy będące inspiracją do badań, niezastąpioną pomoc w planowaniu doświadczeń oraz stworzenie niezwykle przyjaznej atmosfery w pracy.

Dziękuję prof. dr hab. Wojciechowi Macykowi za wsparcie i pomoc udzieloną w trakcie trwania studiów doktoranckich.

Dziękuję dr Joannie Kuncewicz za nieocenioną pomoc udzieloną w trakcie przygotowywania pracy doktorskiej.

Dziękuję Kwadratowi Wiecha za kreatywne podejście do niektórych problemów badawczych.

Dziękuję wszystkim koleżankom i kolegom z ZFKiB oraz ACMiN za przyjazną atmosferę i wsparcie.

Dziękuję współautorom publikacji za ich wkład w wykonanie badań i wspólną interpretację wyników.

Chciałabym również podziękować rodzinie oraz przyjaciołom, za nieustanne wsparcie oraz motywację.

Oświadczenie autora rozprawy:

Oświadczam, świadoma odpowiedzialności karnej za poświadczenie nieprawdy, że niniejszą pracą doktorską wykonałam osobiście i samodzielnie oraz że nie korzystałam ze źródeł innych niż wymienione w pracy.

19 kwietnia 2019

Ewelina Dłoch

Oświadczenie promotora rozprawy:

Niniejsza rozprawa jest gotowa do oceny przez recenzentów.

19 kwietnia 2019



Badania, których wyniki zostały przedstawione w pracy, prowadzone były w ramach grantów Narodowego Centrum Nauki (UMO-2015/18/A/ST4/00058, UMO-2015/18/N/ST5/00533), Ministerstwa Nauki i Szkolnictwa Wyższego (Grant Ideas Plus No. IDP2012000362).

Praca wsparta infrastrukturą badawczą Akademickiego Centrum Materiałów i Nanotechnologii AGH oraz Akademickiego Centrum Komputerowego Cyfronet AGH (w ramach grantu GRAPHENE, GRAPHENE2, IODIDE, IODIDE2).



Ministerstwo Nauki
i Szkolnictwa Wyższego



Spis treści

<i>Streszczenie</i>	1
<i>Abstract</i>	4
<i>Spis rysunków</i>	7
<i>Układ pracy</i>	9
<i>Wprowadzenie, motywacja oraz kontekst pracy</i>	11
<i>Streszczenie artykułów wchodzących w skład rozprawy</i>	22
<i>A1. Heavy pnictogen chalcogenides: the synthesis, structure and properties of these rediscovered semiconductors</i>	22
<i>A2. Influence of π-Iodide Intermolecular Interactions on Electronic Properties of Tin(IV) Iodide Semiconducting Complexes</i>	25
<i>A3. Triiodide Organic Salts: Photochemistry at the Border between Insulators and Semiconductors</i>	30
<i>A4. Memristor in reservoir system – experimental evidence for high level computing and neuromorphic behaviour of PbI_2</i>	34
<i>A5. Molecules, semiconductors, light and information: Towards future sensing and computing paradigms</i>	38
<i>Podsumowanie</i>	41
<i>Bibliografia</i>	43
<i>Dorobek naukowy</i>	46
<i>Załączniki</i>	49

Streszczenie

Dość pobieżnie dotąd scharakteryzowane hybrydowe organiczno-nieorganiczne półprzewodniki są interesującą grupą materiałów o potencjalnym zastosowaniu w elektronice, fotokatalizie, fotowoltaice, optoelektronice i pokrewnych dziedzinach badań. Siła oddziaływań obecnych w strukturze krystalicznej znajduje odzwierciedlenie w strukturze elektronowej, co można zaobserwować analizując dystrybucję gęstości stanów elektronowych poszczególnych materiałów. Silne oddziaływania (kowalencyjne i jonowe) w półprzewodnikach nieorganicznych pozwalają na tworzenie się ciągłych pasm w strukturze elektronowej. Po drugiej stronie stoją półprzewodniki czysto organiczne których, właściwości zależą w głównej mierze od słabych oddziaływań międzycząsteczkowych. Dużo słabsze oddziaływania van der Waalsa, wiązania wodorowe i oddziaływania typu π prowadzą do powstania wąskich pasm energetycznych. W przypadku półprzewodników hybrydowych oba przypadki są możliwe, a przewaga słabych lub silnych oddziaływań w strukturze krystalicznej determinuje właściwości materiału. Półprzewodniki hybrydowe reprezentowane są w niniejszej pracy przez tetrajodkowe kompleksy cyny z ligandami organicznymi ($[\text{SnI}_4\{(\text{C}_6\text{H}_5)_3\text{PO}\}_2]$, $[\text{SnI}_4\{(\text{C}_6\text{H}_5)_2\text{SO}\}_2]$ oraz $[\text{SnI}_4(\text{C}_5\text{H}_5\text{NO})_2]$). Obecny w nich atom jodu charakteryzuje się dużym promieniem oraz polaryzowalnością, co sprzyja tworzeniu się słabszych wiązań i oddziaływań międzycząsteczkowych. W przypadku tych kompleksów główną rolę odgrywają oddziaływania wodorowe z atomami jodu łączące fragmenty organiczne i nieorganiczne sąsiadujących cząsteczek.

Im słabsze oddziaływania międzycząsteczkowe w strukturze krystalicznej tym dyskretniejsza struktura pasmowa i bardziej płaskie pasma w strukturze elektronowej. Jeśli oddziaływania te są odpowiednio słabe może dojść do powstania przypadku granicznego, w którym materiał może zostać sklasyfikowany jako izolator posiadający jednak jeszcze pewne cechy półprzewodnika. Przykładami tego typu materiałów są opisane w rozprawie organiczne sole trójjodkowe o dużych kationach organicznych. W ich strukturze krystalicznej brak silnych oddziaływań międzycząsteczkowych, a liniowo ułożone aniony I_3^- są otoczone przez kationy zawierające liczne podstawniki aromatyczne. Mimo niewielkiej siły oddziaływania pomiędzy anionami trójjodkowymi orbitale atomów jodu budują zarówno krawędzie pasm walencyjnych jak i przewodnictwa. Inne słabe oddziaływania obecne w strukturze to oddziaływania wodorowe $\text{CH}\cdots\text{I}$ (w większości przypadków odległości $\text{H}\cdots\text{I}$ są zbyt duże aby nazywać je wiązaniami). Mimo niewielkiej mobilności nośników ładunku materiały te wydajnie generują fotoprądy w zakresie promieniowania ultrafioletowego, ponieważ zachodzi wówczas

wzbudzenie elektronów do wyższych pasm przewodnictwa, na które składają się orbitale atomów węgla.

Materiałem opierającym się głównie na silnych wiązaniach kowalencyjnych jest jodek ołowiu(II) – półprzewodnik szeroko opisany w literaturze. Głównym aspektem poruszonym w rozprawie jest tworzenie złącza Schottky’ego przez halogenki ołowiu(II) w kontakcie z powierzchnią niektórych metali. Stany powierzchniowe prowadzące do powstania bariery Schottky’ego mogą mieć swoje źródła w chemisorpcji cząsteczek półprzewodnika na powierzchni metalu, co może równocześnie powodować tzw. „pillow effect” przejawiający się redukcją pracy wyjścia metalu. Innym istotnym źródłem stanów powierzchniowych jest nakładanie się funkcji elektronowej metalu na stany obecne w przerwie energetycznej półprzewodnika wynikające ze skończonych rozmiarów kryształów. Niesymetryczne zapelnianie i opróżnianie stanów powierzchniowych obecnych na złączu $\text{PbI}_2|\text{Cu}$ zostało wykorzystane do zbudowania memrystora – elementu, który w wyniku przepływu ładunku zmienia swój opór. W pracy oprócz analizy mechanizmu działania tego urządzenia pokazano podobieństwo zbudowanego memrystora do synapsy oraz zastosowanie memrystora do prostej analizy sygnału.

Opisany w pracy memrystor bazujący na złączu $\text{PbI}_2|\text{Cu}$ został wbudowany w układ rezerwarowy – podtyp sieci neuronowej. Pozwoliło to na wykonanie prostych obliczeń, tj. na klasyfikację sygnałów ze względu na ich amplitudę. Innym zjawiskiem zaobserwowanym w tym układzie jest metaplastyczność. Efekt ten przejawia się jako zmiana podstawowych właściwości urządzenia ze względu na jego historię (tj. dłuższą ekspozycję na dodatni potencjał i związany z nim przepływ ładunku) i jest możliwy dzięki tworzeniu się dodatkowych oddziaływań pomiędzy metalem a półprzewodnikiem, które zmieniają opór takiego złącza. Źródłem tych nowych oddziaływań może być utlenianie atomów miedzi, które następnie mogą utworzyć wiązanie z obecnymi na powierzchni PbI_2 atomami jodu. Działanie całego układu sprowadza się więc do oddziaływań powierzchni halogenku ołowiu(II) z powierzchnią metalu.

W skład rozprawy wchodzi pięć publikacji poświęconych różnym aspektom fizykochemii półprzewodników oraz przetwarzaniu informacji. Trzy z tych publikacji koncentrują się na oddziaływaniach występujących w strukturach krystalicznych związków lub na granicy półprzewodnik/metal. Poddawane analizie związki różnią się znacząco składem i budową: 1) organiczne sole trójjodkowe oprócz anionu I_3^- zawierają duże kationy organiczne zawierające trzy lub sześć pierścieni aromatycznych; 2) jodkowe kompleksy cyny(IV) mają budowę molekularną a atom jodu jest związany jednym wiązaniem kowalencyjnym z atomem

cyny; 3) jodek ołowiu(II) ma budowę warstwową, w której atom jodu ma rolę mostka łączącego sąsiednie atomy ołowiu. Odmienność przedstawionych struktur pozwala na prześledzenie różnorodnych oddziaływań – od silnych wiązań kowalencyjnych, jonowych przez słabsze π - π , wodorowe lub halogenowe, na oddziaływaniach van der Waalsa kończąc. Artykuły opisujące właściwości kompleksów SnI_4 oraz soli trójjodkowych skupiają się na wpływie oddziaływania poszczególnych fragmentów struktury krystalicznej na strukturę elektronową, przewodnictwo, przerwę energetyczną, mobilność i koncentrację nośników ładunku, typ domieszkowania oraz potencjały krawędzi pasm. W publikacjach tych wykazane jest, że słabsze oddziaływania obecne w strukturze w dużych ilościach potrafią mieć dominujący wpływ na strukturę elektronową związku. Wyciągnięte wnioski poparte są między innymi pomiarami spektroskopowymi oraz obliczeniami teoretycznymi. W tych dwóch publikacjach zaprezentowano cztery nowe związki: $[(\text{C}_6\text{H}_5\text{CH}_2)_3\text{NO}]_2\text{H}^+\text{I}_3^-$, $(\text{C}_6\text{H}_5\text{CH}_2)_3\text{NH}^+\text{I}_3^- \cdot \text{C}_6\text{H}_5\text{CH}_3$, $[\text{SnI}_4\{(\text{C}_6\text{H}_5)_2\text{SO}\}_2]$ i $[\text{SnI}_4(\text{C}_5\text{H}_5\text{NO})_2]$ o nieopisanych wcześniej strukturach krystalicznych. Z kolei publikacja skupiająca się na urządzeniu zbudowanym na bazie PbI_2 opisuje oddziaływania tego materiału z powierzchnią różnych metali (Au, Pt, Cu, Ag i Al) oraz wyjaśnia wpływ tego oddziaływania na barierę Schottky'ego, odpowiedzialną za działanie tego urządzenia.

Rozprawę uzupełniają dwie prace przeglądowe, które dopełniają dwa nurty podjęte w pracy: pierwszy dotyczący analizy właściwości konkretnej grupy półprzewodników (chalkohalogenków) oraz drugi związany z budowaniem urządzeń na podstawie materiałów półprzewodnikowych i wykorzystaniem ich w bardziej skomplikowanych układach. W pierwszym przeglądzie nakreślono jak w obrębie jednej grupy związków – chalkohalogenków o stechiometrii MQX (gdzie: M = As, Sb, lub Bi; B = Se, S lub O; X = F, Cl, Br lub I) – zmiany polegające na wymianie atomu fluorowca lub stosunku atomów w cząsteczce wpływa na strukturę związku. W pracy tej zebrano informacje o strukturach różniących się między sobą jedynie atomem M, Q lub X, a także opisano cechy wspólne tych struktur i ich główne różnice. Dla części opisanych struktur możliwe okazało się też powiązanie tych niewielkich zmian strukturalnych ze zmianami w strukturze elektronowej. Drugi przegląd przedstawia między innymi obecny stan wiedzy na temat fotomemrystorów i układów wykazujących właściwości fotomemrystywne, ze szczególnym uwzględnieniem mechanizmu ich działania. W przeglądzie tym poruszono również tematykę obliczeń rezerwuarowych, zasady działania rezerwuarów, a także ich możliwe zastosowanie.

Abstract

Quite briefly characterized hybrid organic-inorganic semiconductors are an interesting group of materials with potential applications in electronics, photocatalysis, photovoltaics, optoelectronics and related fields. The properties of molecular compounds depend profoundly on the weak intermolecular interaction. The strength of the interactions present in the crystal structure is reflected in the band structure and can be observed in the distribution of the density of the electronic states of individual materials. Strong interactions (covalent and ionic) in the inorganic semiconductors allow formation of continuous energy bands. On the other hand, much weaker van der Waals interactions, hydrogen bonds and stacking of the aromatic rings that occur in the purely organic semiconductors lead to narrower energy bands. In the case of hybrid semiconductors, both scenarios are possible and the predominance of weak or strong interactions in the structure determines the properties of the material. The hybrid semiconductors are represented in this dissertation by the tin-iodide complexes with organic ligands ($[\text{SnI}_4\{(\text{C}_6\text{H}_5)_3\text{PO}\}_2]$, $[\text{SnI}_4\{(\text{C}_6\text{H}_5)_2\text{SO}\}_2]$ and $[\text{SnI}_4(\text{C}_5\text{H}_5\text{NO})_2]$). The iodine atoms present in these compounds are characterized by a large radius and polarizability which favors the formation of weaker bonds and intermolecular interactions. In these complexes, hydrogen interactions with iodine atoms combine the organic and inorganic fragments of the adjacent molecules.

The weaker intermolecular interactions in the structure, the more discrete band structure and the more flat bands in the electronic structure. If these interactions are sufficiently weak, a border case may arise in which the material can be classified as an insulator with some of semiconductor features. This scenario in this work is represented by the organic triiodide salts. The crystal structures of these salts lack any strong intermolecular interactions and the linearly arranged I_3^- anions are surrounded by large organic cations. Despite the weak interactions between the triiodide anions, orbitals of iodine atoms build both the edges of the valence and the conduction bands. Other weak interactions present in the structure encompass hydrogen interactions $\text{CH}\cdots\text{I}$ (distances $\text{H}\cdots\text{I}$ are usually too large to be called bonds). Despite their low charge carriers mobility, these materials efficiently generate photocurrents under the ultraviolet radiation due to the excitation of the electrons to the higher conduction bands that consist mostly of orbitals of the carbon atoms.

The material based mainly on strong covalent bonds is lead (II) iodide - a semiconductor well described in the literature. Interestingly, PbI_2 creates a Schottky junction with the surface

of several metals. Surface states that lead to the formation of this barrier may have their sources in the chemisorption of a semiconductor molecules on the surface of the metal which may also cause the so-called "pillow effect" which reduces the work function of the metal. Another important source of surface states is the overlap of the electronic function of the metal with the electronic states (present in the energy gap of the semiconductor) created due to the finite dimensions of the crystals. An asymmetric filling and emptying of the surface states present at PbI_2/Cu junction have been used to build a memristor – an element that changes its resistance as a result of the flow of the charge. In this work the analysis of the mechanism of operation of this device, the similarity of the constructed memristor to synapse and the use of a memristor for simple signal analysis are presented.

The memristor was built into the reservoir system – a sub-type of the neural network – which allowed to perform simple calculations, *e.g.* on the classification of signals due to the amplitude. Another phenomenon observed in this system is metaplasticity. This type of neuromimetic behaviour manifests as the change of the basic properties of the device due to its history (*i.e.* flow of charges under prolonged positive bias). This effect is possible due to the formation of additional interaction between the metal and the semiconductor that changes the resistance of such joint. An example of this is an oxidation of the copper atoms that can subsequently form a bond with the iodine atoms present on the surface of PbI_2 . The operation of this entire system comes down to the interface interactions between the lead(II) halide and metal surface.

This dissertation consists of five publications focusing on the physical chemistry of semiconductors and various aspects of information processing. Presented compounds differ significantly in composition and structure: 1) organic triiodide salts contain – in addition to the anion I_3^- – large organic cations containing three or six aromatic rings; 2) tin(IV) iodide complexes have a molecular structure where the iodine atoms are bound by one covalent bond to a tin atom; 3) lead iodide(II) has a layered structure in which the iodine atom has the role of a bridge connecting neighbouring lead atoms. The diversity of the presented structures allows to investigate various interactions - strong covalent bonds, ionic bonds, weaker π - π interactions, hydrogen or halogen bonds and van der Waals interactions. The article that describes the properties of SnI_4 complexes and triiodide salts focus on the impact of the individual structural elements on the electronic structure, *e.g.* conductivity, energy gap, mobility, type of doping and carrier concentration, and band edge potentials. In these publications it is shown that the weaker interactions present in the structure in large quantities can have a dominant influence on the

electronic structure of the compound. The conclusions drawn are supported, among others, by spectroscopic measurements and theoretical calculations. Four compounds presented in this two articles: $[(C_6H_5CH_2)_3NO]_2H^+I_3^-$, $(C_6H_5CH_2)_3NH^+I_3^- \cdot C_6H_5CH_3$, $[SnI_4\{(C_6H_5)_2SO\}_2]$ and $[SnI_4(C_5H_5NO)_2]$ are new with a structure that has never been described before. The third publication is focused on the device based on PbI_2 and describes the interaction of this material with the surface of various metals (Au, Pt, Cu, Ag and Al). It also explains the effect of this interaction on the Schottky barrier responsible for the operation of this device.

The dissertation is completed by two review papers that expands two topics taken in this work: the systematic analysis of the properties of the chalcogenides and the construction of the devices based on various semiconductors and their use in more complex systems. The first review outlines how in one group of compounds - chalcogenides with the stoichiometry MQX (where: $M = As, Sb, \text{ or } Bi$; $B = Se, S \text{ or } O$; $X = F, Cl, Br \text{ or } I$) - the replacement of a halogen atom or the atomic ratio of atoms in the molecule affects the structure of the compound. In this work it was possible to gather information about structures differing only in M, Q or X atoms, to find the common features of these structures and their main differences. For some of the described structures, it was also possible to link these small structural differences with the changes in the electronic structure. The second review presents, among others, the current state of knowledge on photomemristors and systems exhibiting photomemristic properties, focusing on the mechanism of their operation. The review also touches on the subject of reservoir calculations, the principles of their work and their possible application.

Spis rysunków

Rysunek 1. Najważniejsze niekowalencyjne oddziaływania międzycząsteczkowe.	12
Rysunek 2. Molekularny potencjał elektrostatyczny w Hartree dla CF_3X , gdzie $X = F, Cl, Br, I$ (od lewej do prawej). ⁵	13
Rysunek 3. Wybrane właściwości fizykochemiczne fluorowców.	14
Rysunek 4. Przerwy energetyczne $CH_3NH_3PbX_3$ (a) i $BiOX$ (b), gdzie $X = Cl, Br$ lub I . ¹¹⁻¹²	15
Rysunek 5. Pętla histerezy idealnego memrystora dla różnych częstotliwości zmian potencjału. ²⁷	17
Rysunek 6. Relacje pomiędzy podstawowymi pasywnymi elementami elektronicznymi opisane na planie kwadratu (a) i trójkąta (b). ²⁸	18
Rysunek 7. Polaryzacja elektrod pozwalająca na rozróżnienie impulsów presynaptycznych i postsynaptycznych.	19
Rysunek 8. Graficzna reprezentacja reguły Hebba.	20
Rysunek 9. Schemat klasycznej jednokierunkowej sieci neuronowej (a), sieci rezerwuarowej (b), sieci rezerwuarowej typu “single echo state machine” (c).	21
Rysunek 10. Struktury krystalograficzne związków: $SbTeI$ (widok wzdłuż osi c) (a), $AsSeI$ (widok wzdłuż osi b) (b), $SbSeI$ (widok wzdłuż osi b) (c), $BiSeI$ (widok wzdłuż osi b) (d), $SbSI$ (widok wzdłuż osi c) (e) oraz $BiSI$ (widok wzdłuż osi c) (f).	23
Rysunek 11. Wartości przerw energetycznych wybranych chalkohalogenków wyznaczone metodami obliczeniowymi (a) i eksperymentalnymi (b).	24
Rysunek 12. Dystrybucja gęstości stanów elektronowych kompleksów: $[SnI_4\{(C_6H_5)_3PO\}_2]$ (a), $[SnI_4\{(C_6H_5)_2SO\}_2]$ (b) i $[SnI_4(C_5H_5NO)_2]$ (c). Zaciemnione pola reprezentują całkowitą gęstość stanów elektronowych (TDOS), kolorowe linie reprezentują cząstkowe gęstości stanów elektronowych (PDOS).	27
Rysunek 13. Widma UV-vis badanych kompleksów i SnI_4 zarejestrowane dla związków rozpuszczonych w acetonitrylu (a) i zarejestrowanych w fazie stałej (b).	28
Rysunek 14. Upakowanie komórki (periody $2x2x2$) soli: $[(C_6H_5)_3AsO]_2H^+I_3^-$ (a), $[(C_6H_5CH_2)_3NO]_2H^+I_3^-$ (b), $(C_6H_5CH_2)_3NH^+I_3^- \cdot C_6H_5CH_3$ (c). Widok w kierunku $[001]$ (a) i (c), widok w kierunku $[110]$ (b). Oś a jest oznaczona na czerwono, b na zielono, c na niebiesko.	31
Rysunek 15. Mechanizm generowania fotoprądów katodowych (a) i anodowych (b) w obecności $[(C_6H_5)_3AsO]_2H^+I_3^-$. CB i VB oznaczają odpowiednio pasmo przewodnictwa i	

pasmo walencyjne soli. Na wykresie zamieszczono potencjały par redoksowych obecnych w elektrolicie.	32
Rysunek 16. Typowy przebieg charakterystyki prądowo-napięciowej urządzenia opartego o PbI_2 i metaliczny kontakt oraz układ pomiarowy (a), pomiary chronoamperometryczne urządzenia przełączanego pomiędzy HRS i LRS impulsami o amplitudzie $\pm 1,5$ V (20 s), odczyt stanu odbywał się przy potencjale 0,3 V.	34
Rysunek 17. Schemat systemu ze sprzężeniem zwrotnym i linią opóźniającą (czerwone strzałki pokazują pętlę zawracającą sygnał) (a), graficzna reprezentacja sprzężenia zwrotnego pomiędzy neuronami (b), sygnały zarejestrowane w układzie rezerwuarowym dla sygnału o początkowej amplitudzie 1,7 V _{pp} (c), sygnały zarejestrowane w układzie rezerwuarowym dla sygnału o początkowej amplitudzie 1,9 V _{pp} (d).	36
Rysunek 18. Uproszczony diagram blokowy fotoelektrycznego systemu rezerwuarowego (a). Odpowiedź systemu rezerwuarowego, w którym wykorzystano złotą elektrodę (niebieski sygnał, sygnał odniesienia) oraz tę samą elektrodę pokrytą kwasem liponowym (czerwony sygnał) (b).	38
Rysunek 19. Charakterystyki prądowo-napięciowe złącza grafen/diament podczas naświetlania i w ciemności (a). Charakterystyka prądowo-napięciowa uzyskana dla złącza grafen/diament poprzez oświetlenie materiału przez 5 s w okolicy 10 V i -10 V (b). ³⁹	40

Układ pracy

Na rozprawę składa się pięć artykułów naukowych opublikowanych w renomowanych czasopismach o zasięgu międzynarodowym. Cztery z nich (A1-A4) opisują właściwości fizykochemiczne związków zawierających w swojej strukturze atomy jodu, a dwa (A4 i A5) poświęcone są różnym aspektom przetwarzania informacji na poziomie molekularnym i w nanoskali. Dwie z wymienionych publikacji opisują nowe związki chemiczne nie opisane wcześniej w literaturze (A2, A3). Jeden z wymienionych artykułów opisuje wykorzystanie półprzewodnika do zbudowania memrystora, wyjaśnia mechanizm działania tego urządzenia oraz – w kolejnym etapie – przedstawia wykorzystanie tego memrystora w obliczeniach rezerwuarowych (A4). Rozprawę dopełniają dwie prace przeglądowe: jedna skupiająca się na właściwościach fizykochemicznych grupy półprzewodników zawierających atom fluorowca (A1), druga rozszerza temat fotomemrystorów i obliczeń rezerwuarowych (A5), do których to wykorzystano związek z poprzedniej pracy (A4). Zbiór artykułów uzupełniony został krótkim wprowadzeniem, streszczeniem każdej z prac oraz podsumowaniem najważniejszych wniosków z nich wynikających.

A1. **E. Właźlak**,* A. Blachecki, M. Bisztyga-Szkларz, S. Klejna, T. Mazur, K. Mech,* K. Pilarczyk, D. Przyczyna, M. Suchecki, P. Zawal, K. Szaciłowski*

Heavy pnictogen chalcogenides: the synthesis, structure and properties of these rediscovered semiconductors

Chemical Communications, 2018, 54, 12133-12162

A2. **E. Właźlak**, W. Macyk, W. Nitek, K. Szaciłowski*

Influence of π -Iodide Intermolecular Interactions on Electronic Properties of Tin(IV) Iodide Semiconducting Complexes

Inorganic Chemistry, 2016, 55, 5935-5945

A3. **E. Właźlak**,* J. Kalinowska-Tłuścik, W. Nitek, S. Klejna, K. Mech, W. Macyk, K. Szaciłowski*

Triiodide Organic Salts: Photoelectrochemistry at the Border between Insulators and Semiconductors

ChemElectroChem, 2018, 5, 3486-3497

A4. **E. Właźlak,*** M. Marzec, P. Zawal, K. Szaciłowski*

Memristor in reservoir system – experimental evidence for high level computing and neuromorphic behaviour of PbI_2

ACS Applied Materials & interfaces, 2019, (DOI: 10.1021/acsami.9b01841)

A5. K. Pilarczyk,* **E. Właźlak,*** D. Przyczyna, A. Blachecki, A. Podborska, V. Anathasiou, Z. Konkoli, K. Szaciłowski*

Molecules, semiconductors, light and information: Towards future sensing and computing paradigms

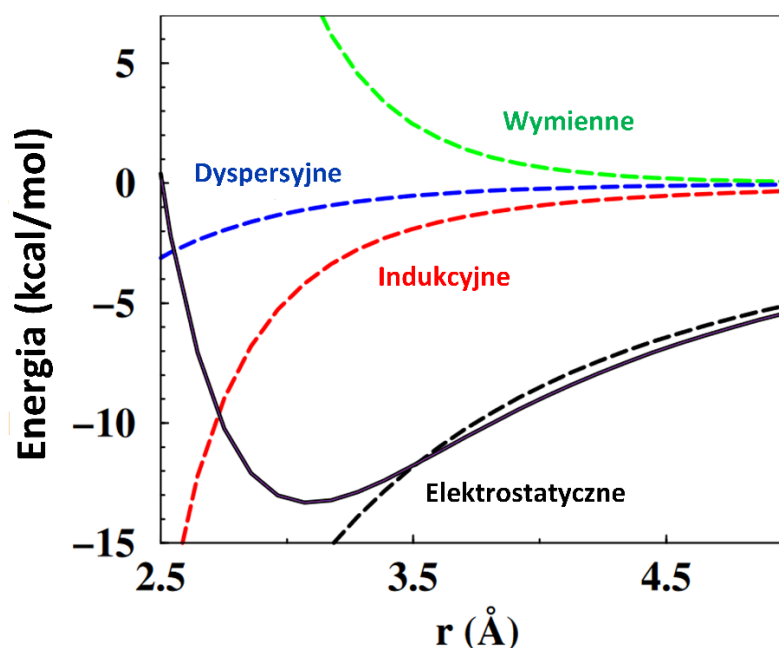
Coordination Chemistry Reviews, 2018, 365, 23-40

Wprowadzenie, motywacja oraz kontekst pracy

Poszukiwanie nowych materiałów o pożądanym, coraz to lepszym właściwościach, niższych kosztach produkcji, łatwo dostępnych i możliwie nietoksycznych jest niekończącym się zadaniem dla badaczy pracujących nad większością rozwijających się dziedzin nauki i przemysłu w tym medycyny, elektroniki, energetyki, katalizy, ekologii, fotowoltaiki i wielu innych. O właściwościach nowych materiałów w pierwszym przybliżeniu decydują występujące w nich oddziaływania międzycząsteczkowe, które to decydują o upakowaniu cząsteczek w komórce krystalograficznej wpływając tym samym na strukturę elektronową i właściwości związku. Oddziaływania te nie są jedynym istotnym czynnikiem, na który należy zwracać uwagę rozważając właściwości nowych materiałów (istotna jest też m.in. morfologia materiału i jego otoczenie tj. oddziaływania na granicach faz) jednak są one elementem niezwykle ważnym. Półprzewodniki wykorzystywane są obecnie w wielu dziedzinach takich jak elektronika (tranzystory, diody), ogniwa fotowoltaiczne, fotokataliza, sztuka (farby i pigmenty), medycyna i kosmetologia (filtry UV). Wszechstronne zastosowanie półprzewodników wynika z różnorodności ich właściwości, z których główną rolę odgrywa struktura elektronowa, a w szczególności przerwa energetyczna, mobilność i koncentracja nośników ładunku, typ domieszkowania, potencjały krawędzi pasm, jak również oddziaływanie z innymi materiałami, a także inne własności, takie jak rozpuszczalność, stabilność, topliwość.

Badanie oddziaływań międzycząsteczkowych jest elementem niezbędnym do zrozumienia właściwości fizykochemicznych materiału. W fazie stałej oddziaływania te odpowiedzialne są za formowanie struktury krystalicznej i elektronowej związku. W półprzewodnikach organicznych oddziaływania niekowalencyjne, determinujące właściwości transportowe, nabierają szczególnego znaczenia. Słabe lub silne sprzężenia międzycząsteczkowe prowadzą odpowiednio do niewielkiej lub dużej mobilności nośników ładunku. Główne niekowalencyjne oddziaływania brane pod uwagę to: oddziaływania wymienne, dyspersyjne, elektrostatyczne i indukcyjne (Rysunek 1).¹⁻² Wynikające z zakazu Pauliego destabilizujące strukturę krystaliczną oddziaływania wymienne muszą zostać zniwelowane przez m.in. siły dyspersyjne – będące bardzo często dominującymi siłami spajającymi kryształy, zwłaszcza w przypadku większych molekuł. Siły dyspersyjne są związane z fluktuacjami gęstości elektronowej, nazywanymi inaczej dipolami indukowanymi. Gdy w cząsteczce obecne są stałe multipole (dipole, kwadrupole) w grę zaczynają wchodzić oddziaływania elektrostatyczne. Przeważnie najmniejszy wkład w strukturę wnoszą

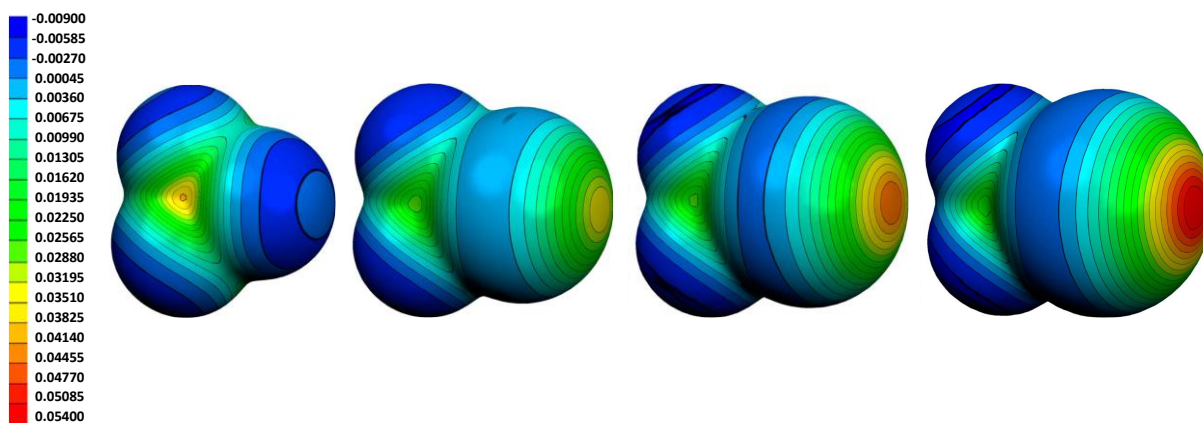
oddziaływania indukcyjne, w których trwały dipol indukuje powstanie dipola w cząsteczce z początkowo równomiernie rozłożonym ładunkiem.



Rysunek 1. Najważniejsze niekowalencyjne oddziaływania międzycząsteczkowe.

W półprzewodnikach nieorganicznych silne sprzężenia wynikające z wiązań kowalencyjnych są odpowiedzialne za dużo lepsze właściwości transportowe. Delokalizacja stanów elektronowych prowadzi do powstania szerokich pasm walencyjnych i przewodnictwa. Z kolei słabe sprzężenia i wąskie pasma energetyczne (10-100 meV) charakterystyczne dla półprzewodników molekularnych oraz stała dielektryczna mieszcząca się w zakresie 2-3 sugeruje słabe ekranowanie i silne efekty kulombowskie.³⁻⁴ Pomiędzy tymi dwiema grupami półprzewodników znajdują się związki hybrydowe: organiczno-nieorganiczne, które w zależności od składu i struktury mogą mieć pośrednie wartości parametrów fizycznych oraz łączyć zalety półprzewodników organicznych i nieorganicznych.

Sporym zainteresowaniem w ostatnich latach cieszą się związki hybrydowe zawierające w swojej strukturze atom fluorowca, a w szczególności jod. Jod jest niemetalem należącym do 17 grupy, 5 okresu układu okresowego. Charakteryzuje się dużym promieniem atomowym, a co za tym idzie dużą polaryzowalnością. W związkach występuje na -I, I, III, V, I VII stopniach utlenienia tworząc często struktury hiperwalencyjne. Z powodu dużej elektroujemności tworzy szereg jodków, w których przyjmuje -I stopień utlenienia.



Rysunek 2. Molekularny potencjał elektrostatyczny w Hartree dla CF_3X , gdzie $X = F, Cl, Br, I$ (od lewej do prawej).⁵

Oprócz wiązań kowalencyjnych i oddziaływań jonowych, jod – jak i inne fluorowce – bierze udział w oddziaływaniach ze strukturami π -elektronowymi, oddziaływaniach van der Waalsa oraz w wiązaniach wodorowych i halogenowych. Obecność tych oddziaływań międzycząsteczkowych ma znaczący wpływ na właściwości związków zawierających w swojej strukturze fluorowce, m.in. na przerwę energetyczną, mobilność nośników ładunku, typ domieszki i koncentrację nośników, potencjały krawędzi pasm, jak również na oddziaływanie z innymi związkami oraz na rozpuszczalność, trwałość i topliwość. Polaryzowalność atomów fluorowca w wiązaniu halogenowym rośnie w szeregu $F < Cl < Br < I$ co przejawia się w rosnącej łatwości w tworzeniu oddziaływań pomiędzy atomami jodu a innymi fragmentami molekuł. Rysunek 2 prezentuje zmianę rozkładu potencjału elektrostatycznego w cząsteczce CF_3X wraz ze wzrostem liczby atomowej atomu fluorowca. Atom fluorowca związany jednym wiązaniem kowalencyjnym ma charakter zarówno nukleofilowy jak i elektrofilowy z powodu aniozotropowego rozkładu gęstości elektronowej. Region o zwiększonej gęstości elektronowej (niebieski obszar na Rysunku 2) tworzy się w kierunku prostopadłym do wiązania kowalencyjnego natomiast region o zmniejszonej gęstości znajduje się na czubku elipsoidy w kierunku równoległym do wiązania kowalencyjnego (czerwony obszar na Rysunku 2). Ten nierównomierny rozkład gęstości elektronowej sprawia, że oddziaływania z kowalencyjnie związanym atomem fluorowca mogą mieć charakter zarówno elektronodonorowy jak i elektronoakceptorowy, w zależności od kierunku, w którym znajduje się atom sąsiedniej cząsteczki. Kiedy kowalencyjnie związany atom fluorowca pełni rolę akceptora elektronów wiązanie to nazywa się wiązaniem halogenowym. Podczas oddziaływania z atomami wodoru, atomy fluorowca pełnią funkcję

nukleofila w tworzeniu wiązania wodorowego. Oba wiązania mają charakter kierunkowy jednak największe odstępstwa od idealnych kątów 90 i 180° (prostopadłe i równoległe wiązanie) napotyka się w przypadku najłatwiej polaryzowalnych atomów jodu.⁶⁻⁷ Te słabe oddziaływania nabierają dużego znaczenia w syntezie związków biologicznie aktywnych. Coraz częściej uwzględnia się podczas projektowania leków oddziaływania wodorowe z jodem obecnym w cząsteczce liganda lub białka.⁸⁻⁹

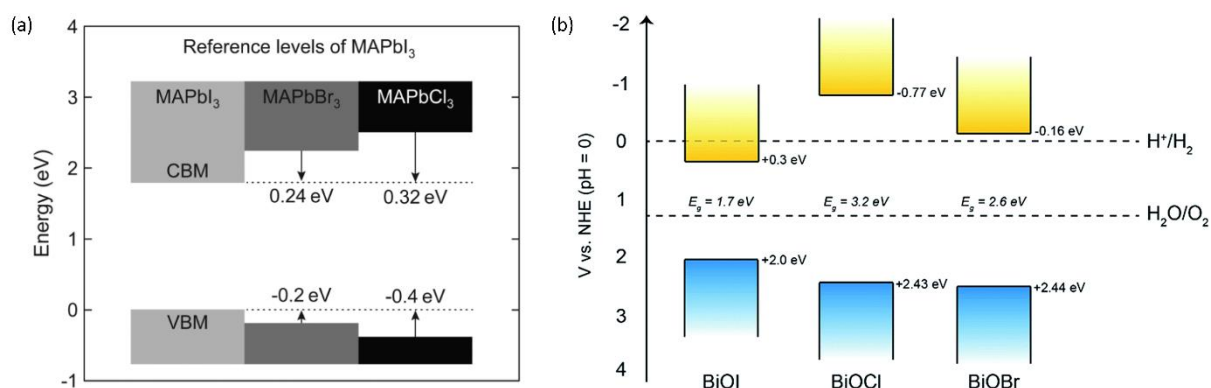
	Masa atomowa	Promień jonowy pm	Temperatura topnienia °C	Temperatura wrzenia °C	Energia jonizacji kJ/mol	Powinowactwo elektronowe kJ/mol	Elektro-ujemność eV
F	18,998	119	-218,6	-188,1	1680,6	332,6	3,9
Cl	35,453	167	-101,0	-34,6	1255,7	348,5	3,0
Br	79,904	182	-7,25	58,78	1142,7	324,7	2,8
I	126,905	206	113,6	184,4	1008,7	295,5	2,5

Rysunek 3. Wybrane właściwości fizykochemiczne fluorowców.

W związkach jodu obserwowane są efekty relatywistyczne znacznie silniejsze niż w przypadku lżejszych fluorowców.¹⁰ Jod posiada także najsilniejszy charakter nukleofilowy. Związki zawierające jod mają przeważnie dużo niższe temperatury topnienia i wrzenia, co znacznie ułatwia i obniża koszty późniejszej obróbki materiału. Zebrane właściwości fluorowców zamieszczone zostały na Rysunku 3.

Systematyczne zmiany struktur krystalograficznych wraz ze zmianą atomu fluorowca w strukturze – a co za tym idzie zmiana struktury elektronowej i właściwości fizykochemicznych – były obserwowane wielokrotnie, zwłaszcza w przypadku związków o charakterze półprzewodnikowym. Pozwala to na modulowanie właściwości półprzewodników na etapie syntezy, co wydaje się naturalnym podejściem w przypadku poszukiwania materiałów o pożądanych właściwościach. Znając wpływ poszczególnych atomów związku na strukturę elektronową można próbować przewidzieć część jego właściwości. W prezentowanej pracy zbadano rolę obecności atomów jodu na właściwości półprzewodnikowe badanych grup materiałów.^{A1-A4} Przerwy energetyczne w półprzewodnikach zawierających jod są mniejsze niż analogiczne struktury zawierające lżejszy atom fluorowca.^{A1} Pozwala to na oddziaływanie

materiału ze światłem z zakresu widzialnego, co jest niezwykle istotne z punktu widzenia fotokatalizy oraz fotowoltaiki. Na Rysunku 4 zaprezentowano ten trend na przykładzie dwóch grup związków: $\text{CH}_3\text{NH}_3\text{PbX}_3$ i BiOX , gdzie X to Cl, Br lub I.



Rysunek 4. Przerwy energetyczne $\text{CH}_3\text{NH}_3\text{PbX}_3$ (a) i BiOX (b), gdzie X = Cl, Br lub I.¹¹⁻¹²

Wyróżniającą się grupą związków zawierających jod są polijodki. Pierwszym opisanym związkiem z tej rodziny jest trójjodek strychniny otrzymany w 1819 roku.¹³ Obecnie I_3^- jest najpowszechniej stosowanym mediatorem redoksywnym w ogniach słonecznych.¹⁴ Tworzenie dużej grupy polijodków o stechiometrii od I_2^- do I_{29}^{3-} jest konsekwencją dużej łatwości tworzenia wiązań hiperwalencyjnych przez ten pierwiastek.

Podstawą niniejszej rozprawy jest pięć publikacji poświęconych różnym grupom półprzewodników zawierających atomy jodu. Jedną z nich stanowią halogenki ołowiu(II) – nieorganiczne półprzewodniki o dość dobrze opisanych właściwościach fizykochemicznych.^{A4} PbX_2 tworzą dwuwymiarowe warstwy o upakowaniu heksagonalnym składające się z atomów jodu i ołowiu połączonych silnymi wiązaniami kowalencyjnymi, natomiast warstwy między sobą spajane są słabymi oddziaływaniami van der Waalsa.¹⁵ Tego rodzaju rozłożenie oddziaływań w materiale skutkuje silną anizotropią właściwości transportowych w kryształach. Związki te badane są od lat 80-tych i ostatnio znów wzbudziły zainteresowanie ponieważ wchodzi w skład perowskitów ołowiowych. Głównym przedstawicielem tej grupy związków jest $\text{CH}_3\text{NH}_3\text{PbI}_3$ o budowie jonowej, w której ładunek kationów organicznych jest kompensowany ujemnym ładunkiem warstwy składającej się z oktaedrow zawierających w centrum atom ołowiu, połączonych atomami jodu znajdującymi się w narożnikach.¹⁶ $\text{CH}_3\text{NH}_3\text{PbI}_3$ jest głównym składnikiem niezwykle wydajnych ogni słonecznych – ich wydajność przekracza obecnie 23%. Interesujące są również właściwości elektryczne elementów elektronicznych zbudowanych na podstawie $\text{CH}_3\text{NH}_3\text{PbI}_3$ (memrystory).¹⁷⁻¹⁹

Sukces $\text{CH}_3\text{NH}_3\text{PbI}_3$ skłonił do badań nad różnymi wariantami możliwymi w tej grupie związków: zsyntezowano struktury zawierające różne kationy między innymi NH_4^+ , $\text{CH}_2(\text{NH}_2)_2^+$, $\text{CH}_3\text{AsH}_3^+$, $\text{CH}_3\text{SbH}_3^+$, kationy metali I grupy (zwłaszcza cezu), inne atomy fluorowca lub mieszane halogenki ($\text{CH}_3\text{NH}_3\text{PbI}_{3-x}\text{Y}_x$ ($\text{Y} = \text{Cl}, \text{Br}, \text{I}$)),²⁰ a także metale inne niż ołów (Sn, Bi, Sb).²¹⁻²⁴ Naturalnym wydaje się być sięgnięcie po związki o zbliżonym składzie lecz innej strukturze. Stało się to motywacją do badań nad tetrajodkowymi kompleksami cyny(IV) o ogólnej stechiometrii $[\text{SnI}_4\text{L}_2]$, stanowiącymi kolejną grupę związków opisanych w niniejszej rozprawie.^{A2}

Wspomniane wyżej halogenki ołowiu(II) w niniejszej rozprawie wykorzystane zostały do zbudowania memrystorów.^{A4} W 2008 roku Dimitri Strukov, Gregory Snider, Dunca Stewart i Stanley Williams opublikowali w *Nature* pracę opisującą działanie dwuelektrodowego urządzenia składającego się z 5 nm warstwy TiO_2 i platynowych kontaktów.²⁵ Autorzy zaproponowali mechanizm powstawania pętli histerezy uzyskiwanych podczas pomiaru charakterystyki prądowo-napięciowej tego układu oraz opisali ją jako dowód na eksperymentalną implementację memrystora, elementu postulowanego jeszcze w 1971 roku przez profesora Leona Chua. Główną cechą charakterystyczną tego urządzenia miała być właśnie pętla histerezy widoczna w przebiegu prądowo-napięciowym. Rysunek 5 pokazuje charakterystykę I - V idealnego memrystora oraz jej zmianę pod wpływem różnych prędkości zmian przykładanego potencjału. Leon Chua wysnuł przypuszczenie o istnieniu tego czwartego pasywnego elementu elektronicznego (obok rezystora, kondensatora i cewki) na podstawie symetrii między pozostałymi trzema elementami (Rysunek 6a).²⁶ Równanie **1** i **2** opisują odpowiednio ładunek (q) i strumień magnetyczny (φ):

$$q(t) = \int_{t_0}^t i(\tau) d\tau \quad (1)$$

$$\varphi(t) = \int_{t_0}^t v(\tau) d\tau \quad (2)$$

Równania te łączą ładunek z natężeniem prądu (i) oraz napięcie ze strumieniem magnetycznym. Pozostałe trzy równania definiują podstawowe pasywne elementy układów elektronicznych: równanie opisujące działanie rezystora (prawo Ohma) to zależność łącząca napięcie z natężeniem (**3**), równanie opisujące działanie kondensatora łączy zmianę ładunku ze zmianą potencjału (**4**), równanie definiujące działanie cewki łączy strumień magnetyczny z natężeniem prądu (**5**):

$$dv = R di \quad (3)$$

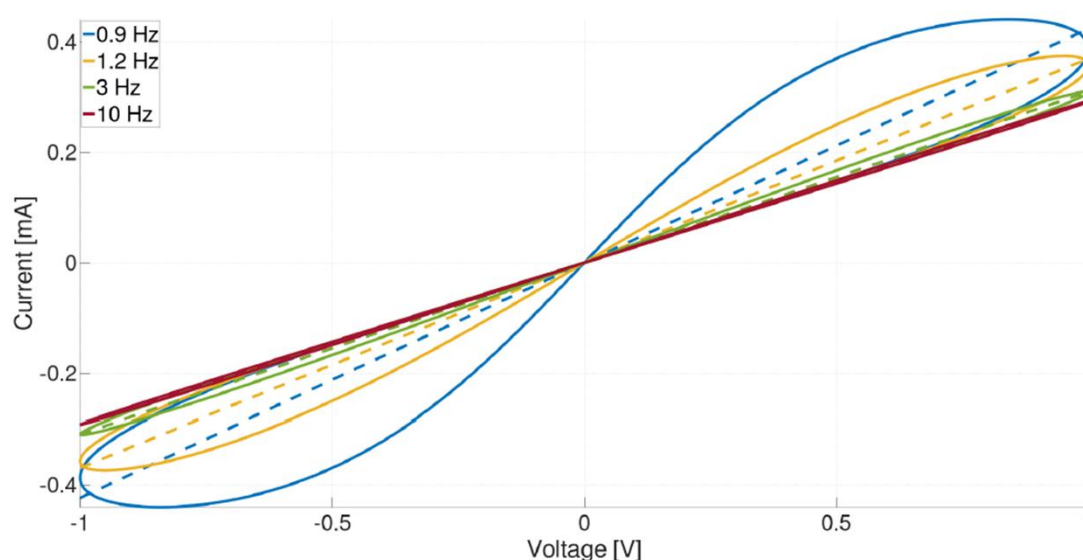
$$dq = Cdv \quad (4)$$

$$d\varphi = Ldi \quad (5)$$

gdzie R oznacza rezystancję, C pojemność kondensatora a L indukcyjność elektromagnetyczną. Profesor Chua zauważył, że jedyną brakującą relacją wydaje się być równanie łączące strumień magnetyczny z ładunkiem. Równanie to powinno mieć postać:

$$d\varphi = Mdq \quad (6)$$

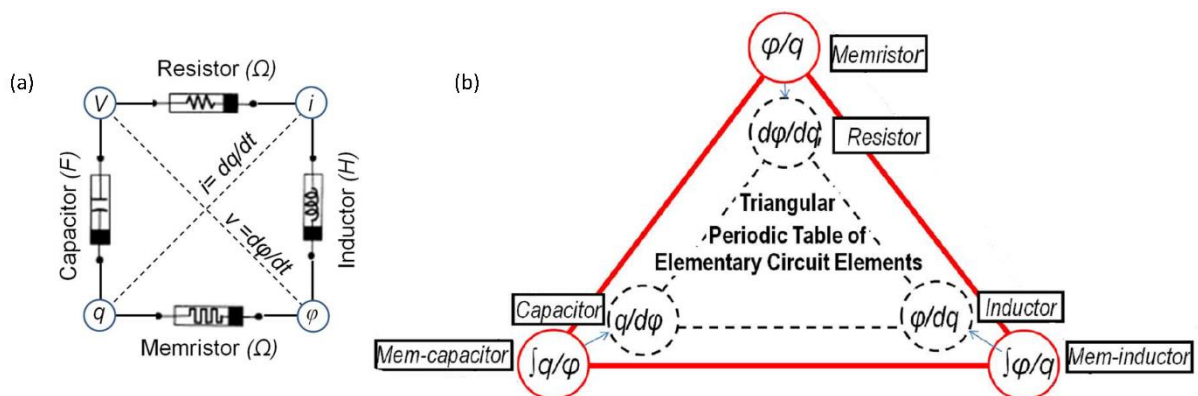
gdzie M oznacza memrystancję. Równanie to definiuje działanie memrystora.



Rysunek 5. Pętla histerezy idealnego memrystora dla różnych częstotliwości zmian potencjału.²⁷

Zasadniczo tego typu nietypowe przebiegi prądowo-napięciowe pojawiały się w literaturze jeszcze przed 2008 rokiem, lecz do tego czasu nikt nie powiązał tej cechy urządzeń z pracami profesora Chua'y.

Wraz z ogromnym zainteresowaniem tematyką memrystorów nadciągnęła jeszcze większa krytyka. Rozgorzała debata na temat tego czy memrystor jest fundamentalnym elementem obwodów elektrycznych, gdyż symetria między fundamentalnymi elementami obwodów może być zachowana na podstawie trzech istniejących już elementów, a memrystor mógłby być traktowany jako rezystor wyższego rzędu (Rysunek 6b).²⁸ Pojawiły się prace, które nie tylko sugerowały, że opisane w 2008 roku urządzenie nie jest memrystorem, lecz również postulowały, że istnienie prawdziwego memrystora jest niemożliwe.²⁹

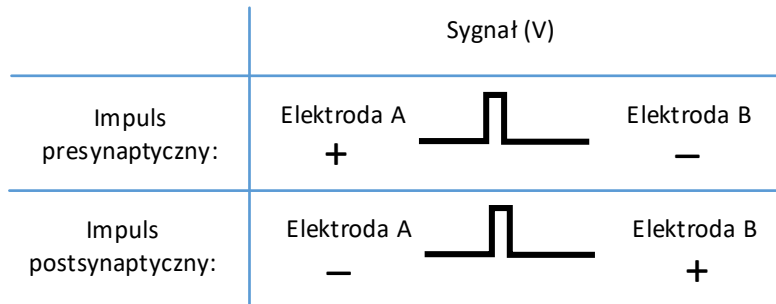


Rysunek 6. Relacje pomiędzy podstawowymi pasywnymi elementami elektronicznymi opisane na planie kwadratu (a) i trójkąta (b).²⁸

Spory wokół nazewnictwa trwają nadal, co nie przeszkodziło wprowadzeniu komercyjnie dostępnego urządzenia na rynek przez firmę Knowm w 2015 roku, a trzy lata później wysłaniu memrystorów w kosmos (MemSat skrót od Memristor Satelite) w celu przetestowania oddziaływania urządzenia z promieniowaniem kosmicznym. W niniejszej pracy memrystory zbudowane zostały w oparciu o halogenki ołowiu(II), jednak nieopublikowane jeszcze wyniki wskazują na analogiczne działanie urządzeń opartych o kompleksy jodku cyny(IV) oraz jodków bizmutu.

Zainteresowanie tematem wynika głównie z możliwości jakie stwarza memrystor. Może być on wykorzystywany jako nośnik pamięci, element programowalnych układów logicznych lub sieci neuronowych.³⁰⁻³¹ Coraz częściej ukazują się prace opisujące podobieństwo między działaniem synaps lub sieci synaps a działaniem memrystorów.^{32, A4} Jednym z tych podobieństw jest wzmocnienie lub osłabienie odpowiedzi w wyniku pobudzenia synapsy/memrystora. Długotrwałe wzmocnienie synaptyczne (LTP, z angielskiego Long-term Potentiation) oraz długotrwałe osłabienie synaptyczne (LTD, z angielskiego Long-term Depression) można zaobserwować gdy przez synapsę memrystor przepływają dwa sygnały: presynaptyczny i postsynaptyczny. Gdy memrystor opisuje się jako synapsę, jedną elektrodę nazywa się odpowiednio presynaptyczną a drugą postsynaptyczną. Sygnał nazywamy presynaptycznym jeżeli impuls o dodatniej polaryzacji został przyłożony do elektrody presynaptycznej, sygnał nazywamy postsynaptycznym jeżeli taki impuls przyłożony został do elektrody postsynaptycznej (Rysunek 7). Alternatywnie, impulsy pre- i postsynaptyczne można

przedstawić jako impulsy o takiej samej wartości bezwzględnej amplitudy i przeciwnej polaryzacji.

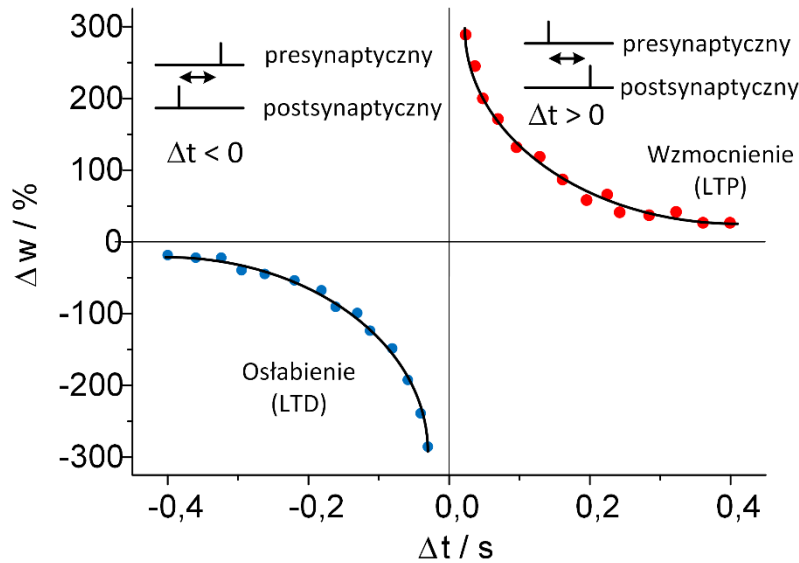


Rysunek 7. Polaryzacja elektrod pozwalająca na rozróżnienie impulsów presynaptycznych i postsynaptycznych.

Pomiar odbywa się poprzez przepuszczenie przez urządzenie pary impulsów. Gdy sygnał presynaptyczny pojawia się później niż sygnał postsynaptyczny (Rysunek 8, $\Delta t < 0$), następuje osłabienie wagi synaptycznej. Gdy sygnał presynaptyczny pojawia się wcześniej niż sygnał postsynaptyczny (Rysunek 8, $\Delta t > 0$) następuje wzmocnienie wagi synaptycznej, którą liczy się ze wzoru:

$$\Delta w = \frac{I_{po} - I_{przed}}{I_{przed}} \times 100\% \quad (7)$$

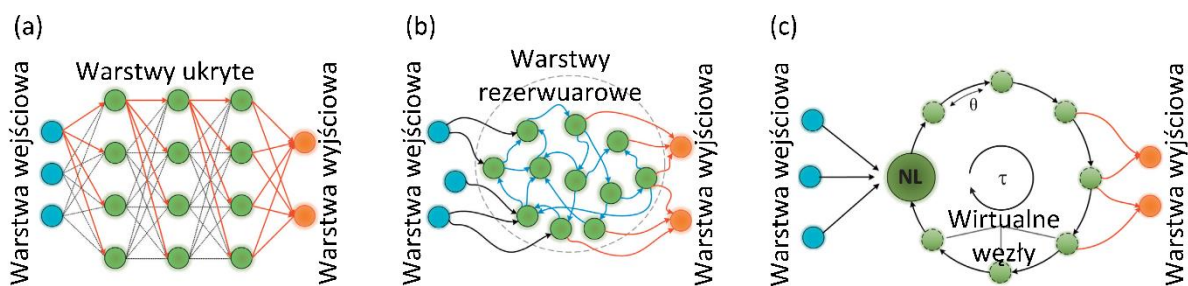
gdzie I_{przed} i I_{po} to prąd mierzony przed i po przepuszczeniu przez synapsę pary impulsów. Zmiana wag synaptycznych następuje w zależności od czasu pomiędzy parą sygnałów – stąd skrót STDP od angielskiego terminu Spike Timing Dependent Plasticity – im ten czas jest krótszy tym większa zmiana wagi synaptycznej, co jest podsumowaniem zasady uczenia się wg. Hebba (Rysunek 8).



Rysunek 8. Graficzna reprezentacja reguły Hebba.

Układy neuromorficzne, między innymi dzięki możliwości uczenia się i mniejszemu zużyciu energii postrzega się jako przyszłość elektroniki.³³ Buduje się obecnie pierwsze procesory neuromorficzne, które naśladują sposób przetwarzania informacji przez mózg.³⁴ Tego typu podejście wykorzystywane jest też w sieciach neuronowych.

Sieci neuronowe składają się zawsze z trzech podstawowych elementów: warstwy wejściowej, warstw ukrytych (jednej lub wielu) i warstwy wyjściowej (Rysunek 9a). Warstwy składają się z elementów nieliniowych, tj. węzłów, które są funkcjonalnymi odpowiednikami neuronów. Połączenia między węzłami opisuje się tzw. wagami. Uczenie się takiej sieci polega na modyfikowaniu wag międzywęzłowych tak, aby w trakcie pracy sieci uzyskiwać pożądany wynik. Systemy rezerwarowe są podtypami sieci neuronowych. Główna różnica pomiędzy układami rezerwarowymi a powszechnie spotykanymi sieciami neuronowymi polega na nieuporządkowanym, przypadkowym połączeniu elementów nieliniowych (węzłów) występującym w systemach rezerwarach (Rysunek 9b). „Single echo state machine” to rodzaj sieci rezerwarowych, w których występują wirtualne węzły, tzn. takie które powstały poprzez opóźnienie i zawrótce sygnału na ten sam węzeł (Rysunek 9c).^{A5, 35} Memrystory mogą z powodzeniem pełnić rolę węzłów w sieciach neuronowych, co zostało potwierdzone eksperymentalnie i teoretycznie.^{A4, 36-38}



Rysunek 9. Schemat klasycznej jednokierunkowej sieci neuronowej (a), sieci rezerwuarowej (b), sieci rezerwuarowej typu “single echo state machine” (c).

Przedstawione powyżej informacje nakreślają kontekst rozprawy, którą można podsumować dwiema tezami badawczymi:

- I) Słabe oddziaływania z atomem jodu w cząsteczce półprzewodnika mogą mieć dominujący wpływ na strukturę elektronową, a w szczególności na skład i położenie krawędzi pasm energetycznych, co można wykorzystać podczas projektowania i syntezy półprzewodników o potencjalnym zastosowaniu w fotokatalizie i optoelektronice.
- II) Półprzewodniki zawierające atomy fluorowców w swojej strukturze nadają się do budowania memrystorów, których działanie oparte jest na oddziaływaniach pomiędzy powierzchniami metalu i półprzewodnika.

Prezentowana rozprawa łączy ze sobą projektowanie, syntezę, charakterystykę i zastosowanie materiałów, których elementem wspólnym jest obecność fluorowców, a w szczególności jodu, w strukturze krystalicznej.

Streszczenie artykułów wchodzących w skład rozprawy

A1. Heavy pnictogen chalcogenides: the synthesis, structure and properties of these rediscovered semiconductors

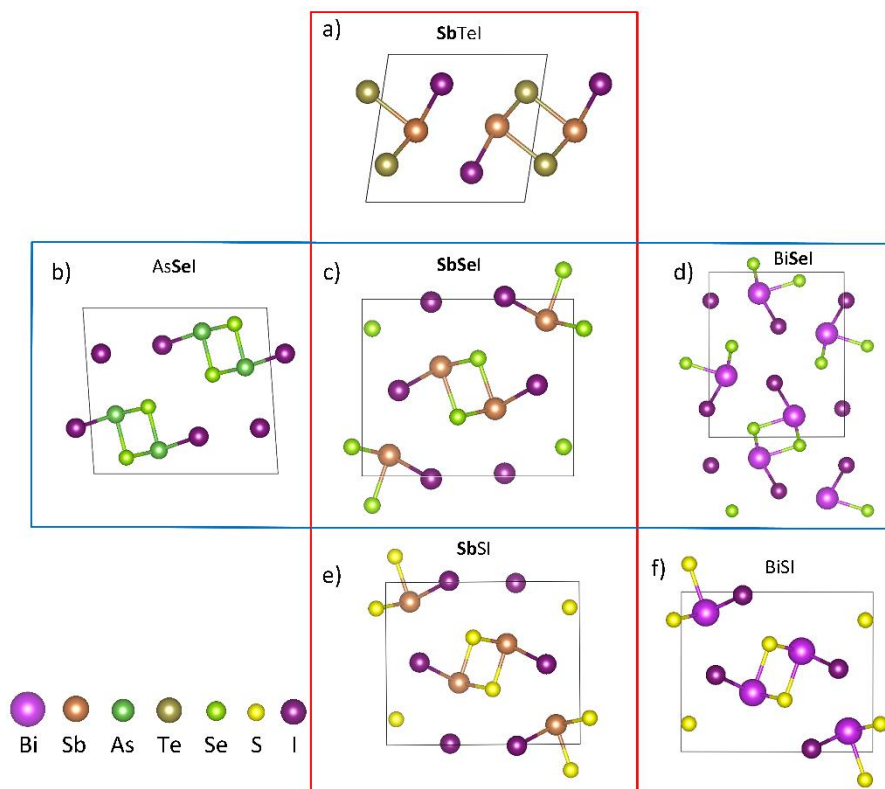
Jest to artykuł przeglądowy będący obszernym wstępem do zagadnień poruszanych w rozprawie. Poszczególne rozdziały skupiają się na osobnym aspekcie właściwości bardzo szerokiej grupy materiałów, jakimi są chalkohalogenki ciężkich azotowców (pniktogenów) o wzorze MQX, gdzie M = As, Sb, Bi; Q = O, S, Se, Te; oraz X = F, Cl, Br lub I. W pracy wymieniono między innymi kilka podgrup chalkohalogenków różniących się między sobą tylko jednym atomem, co w wielu przypadkach skutkuje subtelnymi zmianami strukturalnymi pociągającymi za sobą zmiany we właściwościach fizykochemicznych. Doskonałym przykładem są związki BiOX, gdzie X = F, Cl, Br lub I. Wraz ze wzrostem promienia atomu fluorowca komórka elementarna rośnie w kierunku c od 6,23 Å (BiOF) do 9,15 Å (BiOI), zmniejsza się natomiast przerwa optyczna materiału z 3,6 eV (BiOF) do 1,7 eV (BiOI). Zmiany położenia krawędzi pasm wraz ze zmianą atomu fluorowca są niezwykle istotne w fotokatalizie z użyciem tych materiałów, gdyż skutkują zmianami ich właściwości redoksowych.

Przedstawiony przegląd dotyczy jedynie niewielkiej części chalkohalogenków grupy V układu okresowego, pominięte zostały hybrydowe związki zawierające metale bloku d układu okresowego lub hybrydy zawierające ligandy organiczne, które to wprowadzałyby w strukturę oddziaływania związane z obecnością pierścieni aromatycznych.

W pierwszej części opisane zostały metody syntezy chalkohalogenków, w tym topienie razem substratów w odpowiednich proporcjach i warunkach, kondensacja z par substratów, synteza z roztworów (w tym metody solwo- i hydrotermalne) lub syntezy sonochemiczne.

Kolejny rozdział dotyczy struktur krystalograficznych, które cechują się dużą różnorodnością. Omawiane chalkohalogenki posiadają, obok związków o stechiometrii 1:1:1, wiele struktur o stechiometrii mieszanej. Struktury pojawiające się w bazach i literaturze od lat trzydziestych zostały opisane w podrozdziałach dotyczących kolejno AsQX, SbQX i BiQX. Wśród opisanych grup większość związków o stechiometrii 1:1:1 wykazuje tendencję do tworzenia podstruktury podwójnego łańcucha ciągnącego się wzdłuż jednego z kierunków, co ilustruje Rysunek 10, na którym udało się zgromadzić jodo-chalkogenki różniące się tylko atomem grupy V lub jedynie atomem grupy VI układu okresowego. Dla wybranych przykładów zanalizowano zmiany w długości oddziaływań wiążących (pierwszorzędowych), które

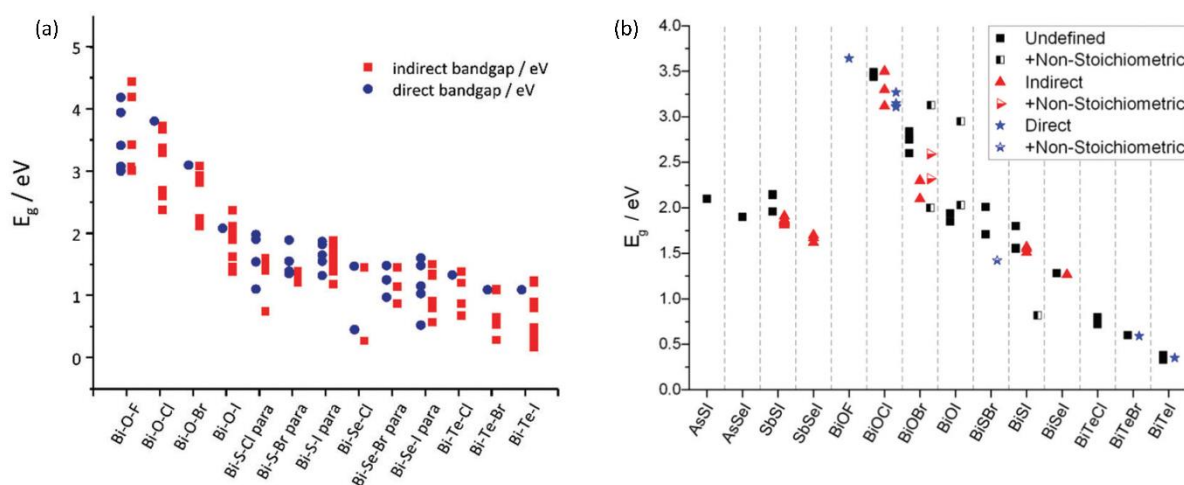
potwierdziły dość intuicyjny trend wzrostu długości wiązań wraz ze wzrostem promienia atomów. Oddziaływania drugorzędowe (słabsze oddziaływania $Q \cdots I$ and $I \cdots I$) nie podążały już ściśle za tym trendem. Co więcej, analiza powierzchni Hirshfelda wykazała, że oddziaływania $M \cdots I$ i $Q \cdots I$ są najsilniejszymi oddziaływaniami międzycząsteczkowymi w tych strukturach.



Rysunek 10. Struktury krystalograficzne związków: *SbTeI* (widok wzdłuż osi *c*) (a), *AsSeI* (widok wzdłuż osi *b*) (b), *SbSeI* (widok wzdłuż osi *b*) (c), *BiSeI* (widok wzdłuż osi *b*) (d), *SbSI* (widok wzdłuż osi *c*) (e) oraz *BiSI* (widok wzdłuż osi *c*) (f).

W publikacji autorzy podjęli się zebraniu doniesień na temat wyznaczonej teoretycznie struktury elektronowej chalkohalogenków. Na szczególną uwagę zasługuje zestawienie obliczonych wartości szerokości przerwy energetycznej, które wskazują na wyraźny trend (w szczególności w przypadku związków zawierających atomy bizmutu), w którym wraz ze wzrostem liczby atomowej atomów składających się na związek maleje szerokość przerwy energetycznej (Rysunek 11a). Wyniki te znajdują potwierdzenie w eksperymentalnie wyznaczonych wartościach przerw (Rysunek 11b). Istnieje wiele eksperymentalnych danych, z których wynika, iż szerokość przerwy energetycznej chalkohalogenku grupy V układu okresowego zmniejsza się wraz ze wzrostem promienia atomu chalkogenku lub fluorowca.

Przykładem może być SbSI i SbSeI o przerwach odpowiednio 1,9 eV i 1,65 eV lub BiOCl, BiOBr i BiOI o przerwach 3,44, 2,76 i 1,85 eV. Podrozdział opisujący właściwości spektroskopowe chalkohalogenków wymienia więcej tego typu przykładów.



Rysunek 11. Wartości przerw energetycznych wybranych chalkohalogenków wyznaczone metodami obliczeniowymi (a) i eksperymentalnymi (b).

Chalkohalogenki piątej grupy układu okresowego charakteryzują się stosunkowo dużym oporem właściwym (10^{10} - 10^{15} $\Omega\cdot\text{cm}$). Mobilność nośników ładunków w związkach arsenu waha się w przedziale 10^{-2} - 10^{-1} $\text{cmV}^{-1}\text{s}^{-1}$, nieco większa jest mobilność nośników ładunku związków antymonu (10^0 - 10^2 $\text{cmV}^{-1}\text{s}^{-1}$), natomiast związki bizmutowe cechują się większymi wartościami mobilności sięgającymi nawet 1450 $\text{cmV}^{-1}\text{s}^{-1}$ w przypadku BiTeBr.

Fotoelektrochemia i fotokataliza przedstawionej grupy związków dotyczy głównie BiOX (X = F, Cl, Br lub I) oraz SbSI. Najszerzej zostały przebadane fotokatalityczne właściwości BiOX, wykazane w przypadku degradacji zanieczyszczeń organicznych z wody, selektywnym utlenianiu alkoholi lub redukcji CO_2 . W badaniach pod uwagę brano zarówno różnice wynikające z różnych przerw energetycznych wynikających z obecności F, Cl, Br lub I w związku, jak i morfologię (nanostruktury 1D i 2D) oraz ekspozycję płaszczyzn krystalograficznych.

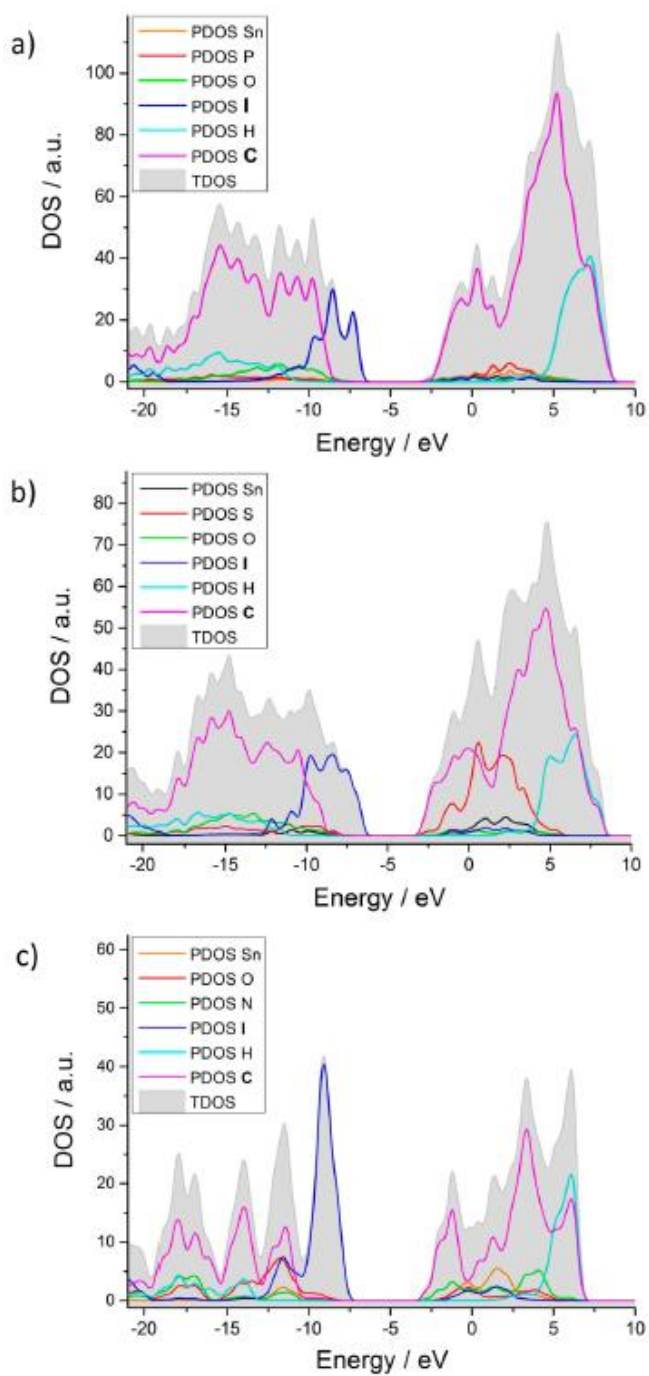
A2. Influence of π -Iodide Intermolecular Interactions on Electronic Properties of Tin(IV) Iodide Semiconducting Complexes

Oddziaływania występujące pomiędzy cząsteczkami półprzewodników mają decydujący wpływ na ich właściwości. Do tej pory niewiele uwagi poświęcono hybrydowym półprzewodnikom molekularnym, których właściwości wynikają ze słabych oddziaływań międzycząsteczkowych. Autorzy omawianego artykułu skupili się na szczegółowej analizie oddziaływań międzycząsteczkowych obecnych w strukturze krystalograficznej trzech molekularnych tetrajodkowych kompleksów cyny(IV): $[\text{SnI}_4\{(\text{C}_6\text{H}_5)_3\text{PO}\}_2]$, $[\text{SnI}_4\{(\text{C}_6\text{H}_5)_2\text{SO}\}_2]$ oraz $[\text{SnI}_4(\text{C}_5\text{H}_5\text{NO})_2]$. Opisany został wpływ obecności ligandów organicznych na strukturę elektronową materiału, a także jej subtelne zmiany wynikające z obecności różniących się między sobą ligandów. Szczególne znaczenie przypisano oddziaływaniom pomiędzy atomami wodoru związanego kowalencyjnie z atomami węgla w pierścieniach aromatycznych, a atomami jodu skoordynowanymi do atomu cyny ($\text{CH}\cdots\text{I}$). Badane materiały zostały zsyntezowane, a następnie została wyznaczona ich struktura krystalograficzna, której to analiza została skorelowana z gęstością stanów elektronowych, elektronowymi widmami absorpcyjnymi, fotonapięciem powierzchniowym, pracą wyjścia i oporem właściwym.

W części poświęconej strukturom krystalograficznym opisano osobno budowę każdego z kompleksów wraz ze szczegółową analizą odległości pomiędzy atomami w cząsteczce i pomiędzy sąsiadującymi cząsteczkami. Wspólną cechą badanych kompleksów jest brak silnych oddziaływań międzycząsteczkowych i obecność sporej ilości oddziaływań wodorowych ($\text{CH}\cdots\text{I}$) oraz oddziaływań typu π - π . W strukturze $[\text{SnI}_4\{(\text{C}_6\text{H}_5)_3\text{PO}\}_2]$ dwa oddziaływania typu $\text{CH}\cdots\text{I}$ spełniają kryteria wymagane by móc nazwać je wiązaniami wodorowymi. Odległości pomiędzy atomami jodu sąsiadujących cząsteczek są duże – ponad 6 Å – co sugeruje brak oddziaływań halogenowych w strukturze. Kompleks $[\text{SnI}_4\{(\text{C}_6\text{H}_5)_2\text{SO}\}_2]$ oprócz oddziaływań wodorowych posiada jedno wiązanie wodorowe, natomiast strukturę tę wyróżnia dystans między atomem siarki a atomem jodu sąsiedniej cząsteczki mniejszy niż suma promieni van der Waalsa tych atomów. Kompleks $[\text{SnI}_4(\text{C}_5\text{H}_5\text{NO})_2]$ ma najmniejszy ligand organiczny i najwięcej oddziaływań wodorowych, w tym trzy wiązania wodorowe. W strukturze kompleksu $[\text{SnI}_4(\text{C}_5\text{H}_5\text{NO})_2]$ można znaleźć wiązanie jodu z heteroatomem, tj. $\text{O}\cdots\text{I}$, oraz kontakt halogenowy typu pierwszego.

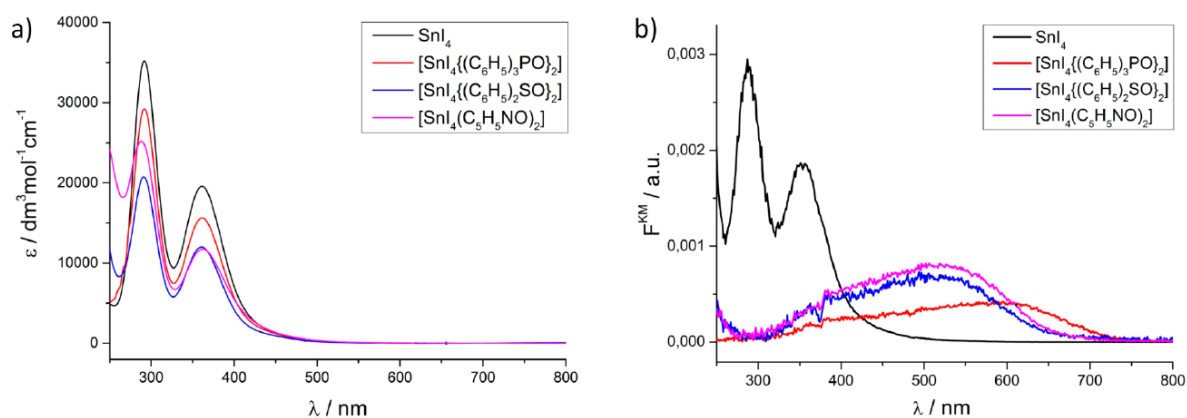
Autorzy wykorzystali spektroskopię magnetycznego rezonansu jądrowego do potwierdzenia hipotezy, iż w rozpuszczalniku organicznym, takim jak np. acetonitryl, kompleks nie ulega dysocjacji. Było to niezbędne do dalszej dyskusji na temat widm elektronowych badanych związków zarejestrowanych dla roztworów i fazy stałej. Przesunięcia sygnałów protonów organicznych w dół pola (wynikające z elektronoakceptorowych właściwości metalu w jodku cyny(IV)) są widoczne w przypadku wszystkich trzech kompleksów, przy czym najsilniejsze przesunięcie jest widoczne w przypadku kompleksu $[\text{SnI}_4(\text{C}_5\text{H}_5\text{NO})_2]$. Wynik ten jest zgodny z analizą rozkładu ładunku wykonaną dla badanych kompleksów, która pokazuje, że największe przeniesienie gęstości elektronowej z ligandów organicznych, będących donorami gęstości elektronowej, na tetrajodek cyny(IV), będący akceptorem, występuje w kompleksie $[\text{SnI}_4(\text{C}_5\text{H}_5\text{NO})_2]$.

Dystrybucja gęstości stanów elektronowych policzona na podstawie uzyskanych struktur krystalograficznych (Rysunek 12) pozwala stwierdzić, że pasma walencyjne badanych związków zbudowane są z orbitali atomów jodu, natomiast orbitale atomów węgla tworzą pasmo przewodnictwa. Podkreśla to istotność oddziaływań wodorowych wymienionych w części artykułu opisujących struktury krystaliczne tych związków. Elektron w wyniku wzbudzenia przeniesiony zostaje z fragmentu nieorganicznej cząsteczki na organiczne fragmenty sąsiadujących cząsteczek, skąd następnie może przemieszczać się w strukturze dzięki obecnym w niej oddziaływaniom typu π . Podobną strukturę elektronową – pasmo walencyjne składające się z orbitali atomów jodu oraz pasmo przewodnictwa uformowane z orbitali cząsteczek organicznych – zaobserwowano dla innych hybrydowych półprzewodników, np. $\text{C}_7\text{H}_7\text{PbI}_3$.



Rysunek 12. Dystrybucja gęstości stanów elektronowych kompleksów: $[\text{SnI}_4\{(\text{C}_6\text{H}_5)_3\text{PO}\}_2]$ (a), $[\text{SnI}_4\{(\text{C}_6\text{H}_5)_2\text{SO}\}_2]$ (b) i $[\text{SnI}_4(\text{C}_5\text{H}_5\text{NO})_2]$ (c). Zaciemnione pola reprezentują całkowitą gęstość stanów elektronowych (TDOS), kolorowe linie reprezentują cząstkowe gęstości stanów elektronowych (PDOS).

Ważnym fragmentem artykułu jest część poświęcona spektroskopii optycznej badanych kompleksów w ciele stałym oraz w rozpuszczalnikach organicznych. Widma UV-vis zarejestrowane w roztworze acetonitrylu (Rysunek 13a) są do siebie niezwykle podobne, za wyjątkiem niewielkiego przesunięcia obserwowanego dla $[\text{SnI}_4(\text{C}_5\text{H}_5\text{NO})_2]$. Jako że widma $^1\text{HNMR}$ potwierdziły trwałość kompleksów w roztworach acetonitrylowych, możliwe było odrzucenie założenia o dysocjacji kompleksów. Wykorzystując TDDFT obliczono skład i rozmieszczenie orbitali HOMO i LUMO dla pojedynczych cząsteczek kompleksów znajdujących się w rozpuszczalniku. Z obliczeń tych wynika, że pasma w widmie absorpcyjnym (w acetonitrylu) są rezultatem przejść pomiędzy orbitalami HOMO zlokalizowanymi na orbitalach p atomów jodu a orbitalami LUMO składającymi się głównie z orbitali antywiążących Sn–I. Orbitale HOMO i LUMO kompleksów w rozpuszczalniku zlokalizowane są więc głównie na nieorganicznych fragmentach kompleksów. Podobieństwa w rozmieszczeniu i składzie orbitali granicznych tłumaczą podobny wygląd widm UV-vis kompleksów w roztworach organicznych.



Rysunek 13. Widma UV-vis badanych kompleksów i SnI_4 zarejestrowane dla związków rozpuszczonych w acetonitrylu (a) i zarejestrowanych w fazie stałej (b).

Widma jodkowych kompleksów cyny(IV) w ciele stałym przedstawiają się zupełnie inaczej: pasma charakterystyczne dla SnI_4 zanikają i pojawiają się nowe, bardzo szerokie pasma w zakresie 300 – 700 nm (Rysunek 13b). Nowe pasma związane są z przeniesieniem ładunku pomiędzy nieorganicznymi a organicznymi fragmentami sąsiadujących cząsteczek kompleksów w strukturze krystalicznej. Założenie to opiera się m.in. na analizie rozkładu gęstości stanów elektronowych, w których pasma walencyjne i przewodnictwa składają się odpowiednio z orbitali atomów jodu i węgla (Rysunek 12). W fazie stałej badanych kompleksów występują oddziaływania $\text{CH}\cdots\text{I}$, które są nieobecne w roztworach. Dlatego też

w roztworach acetonitrylu gdzie nie ma oddziaływań $\text{CH}\cdots\text{I}$ widoczne są jedynie pasma LMCT, charakterystyczne dla tetrajodku cyny.

Autorzy wykorzystali zarejestrowane widma absorpcyjne w fazie stałej do wyznaczenia optycznych przerw energetycznych metodą Tauc'a uzyskując wartości przerw 1,68, 1,90, 1,87 i 2,99 eV odpowiednio dla $[\text{SnI}_4\{(\text{C}_6\text{H}_5)_3\text{PO}\}_2]$, $[\text{SnI}_4\{(\text{C}_6\text{H}_5)_2\text{SO}\}_2]$, $[\text{SnI}_4(\text{C}_5\text{H}_5\text{NO})_2]$ i SnI_4 . Zmniejszenie przerwy energetycznej wraz z koordynacją liganda organicznego jest widoczne nie tylko w wyznaczonych eksperymentalnie wartościach, ale także w wartościach energii przejść elektronowych obliczonych dla pojedynczej, zoptymalizowanej w próżni cząsteczki.

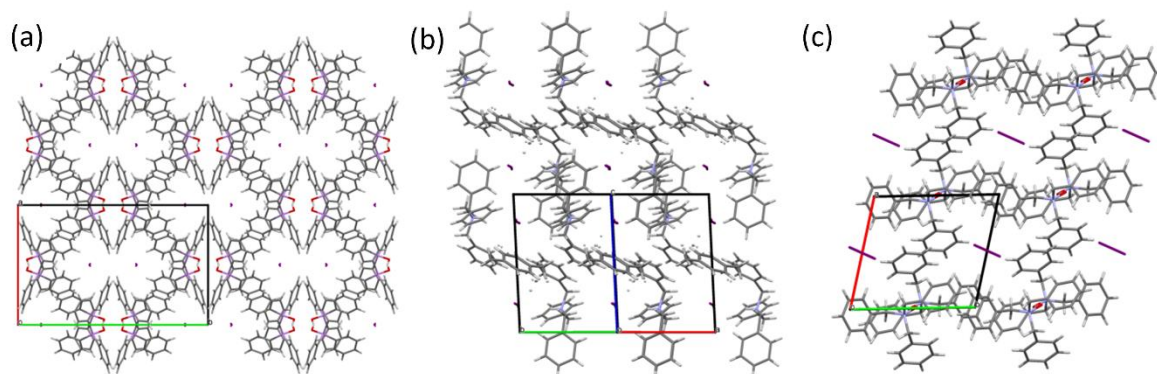
W celu wyznaczenia rodzaju większościowych nośników ładunku badanych półprzewodników wykorzystano widma fotopotencjału powierzchniowego. Zbadane kompleksy oraz SnI_4 wykazują półprzewodnictwo typu *n*. Może to być spowodowane obecnością wakancji Γ^- i częściową redukcją centrów $\text{Sn}(\text{IV})$. Podobne wakancje występują w półprzewodnikach o podobnym składzie (np. $\text{C}_7\text{H}_7\text{PbI}_3$). Ponadto, w przypadku długo przechowywanych próbek obserwuje się sublimację jodu.

Ostatnimi pomiarami wykorzystanymi do scharakteryzowania badanych związków były pomiary pracy wyjścia, które to posłużyły do obliczenia poziomów Fermiego. Wartości te razem z szerokościami przerw energetycznych oraz teoretycznie wyznaczonymi poziomami HOMO i LUMO wykorzystane zostały do stworzenia diagramów energetycznych zbadanych kompleksów i SnI_4 . Diagramy te pokazują, że skoordynowanie organicznego liganda do cząsteczki SnI_4 powoduje zmniejszenie pracy wyjścia materiału, co potwierdza charakter elektronodonorowy ligandów.

A3. Triiodide Organic Salts: Photochemistry at the Border between Insulators and Semiconductors

Polijodki cechują się dużą różnorodną stechiometrii i budowy łańcuchów: od I_2^- do I_{29}^{3-} , natomiast anion I_3^- można odnaleźć w otoczeniu ponad 500 różnych kationów. Szeroki wachlarz procesów redokсовых możliwych dla molekuł jodu jest jednym z głównych powodów rosnącego zainteresowania jego związkami. Aniony trójjodkowe znaleźć można w cieczach jonowych, superkondensatorach, kompleksach z przeniesieniem ładunku, gąbkach protonowych i bateriach litowo-jodowych, znajdują one również zastosowanie jako składnik elektrolitów oraz mediatory redokсовые w ogniwach słonecznych lub domieszki w polimerach. Część soli trójjodkowych ma właściwości metaliczne inne są nadprzewodnikami lub półprzewodnikami. Autorzy artykułu skupiają się na trzech organicznych solach trójjodkowych: $[(C_6H_5)_3AsO]_2H^+I_3^-$, $[(C_6H_5CH_2)_3NO]_2H^+I_3^-$ oraz $(C_6H_5CH_2)_3NH^+I_3^- \cdot C_6H_5CH_3$, których właściwości wynikają głównie z bardzo słabych oddziaływań pomiędzy jonami trójjodkowymi oraz oddziaływań tych jonów z cząsteczkami organicznymi.

Badane sole charakteryzują się obecnością dużych organicznych kationów, których ustawienie pozwala na formowanie się swego rodzaju tuneli zawierających aniony I_3^- (Rysunek 14). Cechą wspólną $[(C_6H_5)_3AsO]_2H^+ I_3^-$ i $[(C_6H_5CH_2)_3NO]_2H^+I_3^-$ jest tworzenie się wiązania wodorowego między dwiema cząsteczkami tlenku trifenyloarsyny lub *N*-tlenku tribenzyloaminy, w wyniku czego ładunek dodatni jest rozdzielony na te dwie cząsteczki. Sól $(C_6H_5CH_2)_3NH^+I_3^- \cdot C_6H_5CH_3$ posiada sprotonowaną tribenzyloaminę i wbudowaną w strukturę cząsteczkę toluenu. W strukturze obecne jest też wiązanie wodorowe pomiędzy atomem jodu ze sprotonowanym atomem azotu tribenzyloaminy. Przerwy pomiędzy anionami trójjodkowymi w tych związkach są większe niż suma promieni van der Waalsa jodu (4,6, 5,16 i 6,82 Å). Oddziaływania typu π - π znaleziono jedynie w strukturze $[(C_6H_5CH_2)_3NO]_2H^+ I_3^-$ natomiast we wszystkich strukturach obecne są oddziaływania $CH \cdots I$. Oddziaływania wodorowe z anionem trójjodkowym zostały zweryfikowane m.in. poprzez wykorzystanie analizy powierzchni Hirshfelda.



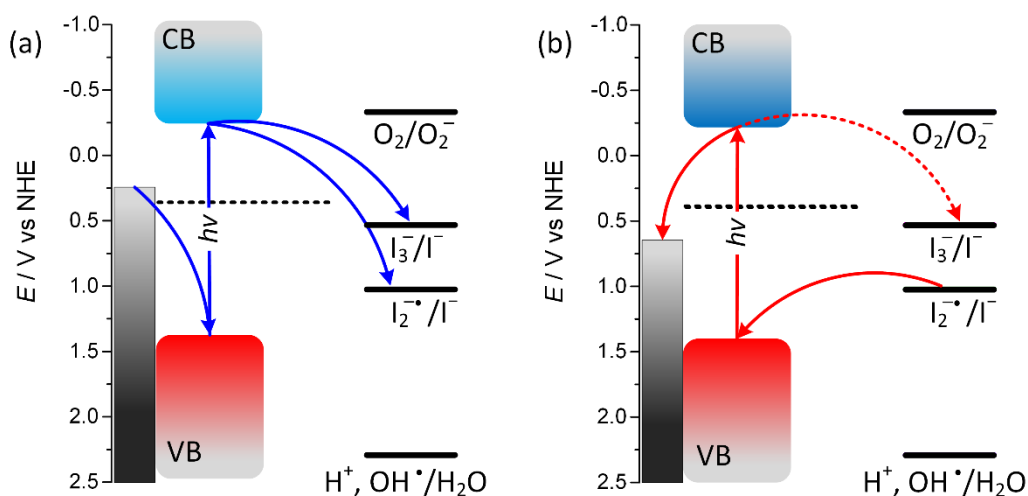
Rysunek 14. Upakowanie komórki (periody $2 \times 2 \times 2$) soli: $[(C_6H_5)_3AsO]_2H^+I_3^-$ (a), $[(C_6H_5CH_2)_3NO]_2H^+I_3^-$ (b), $(C_6H_5CH_2)_3NH^+I_3^- \cdot C_6H_5CH_3$ (c). Widok w kierunku $[001]$ (a) i (c), widok w kierunku $[110]$ (b). Oś a jest oznaczona na czerwono, b na zielono, c na niebiesko.

Separacja anionów trójjodkowych, brak silnych oddziaływań międzycząsteczkowych i obecność słabych oddziaływań $CH \cdots I$ znajduje swoje odzwierciedlenie w strukturze elektronowej badanych soli. Zarówno pasma walencyjne jak i przewodnictwa składają się z orbitali atomów jodu, a w szczególności orbitali 5p z niewielką domieszką stanów pochodzących od orbitali 2p atomów węgla, co pokazuje jak słabe są oddziaływania $CH \cdots I$. W strukturze elektronowej, powyżej wąskiego pasma przewodnictwa znajduje się szerokie pasmo składające się w większości z orbitali atomów węgla (wyższe pasmo przewodnictwa). Można zauważyć niewielką dyspersję bardzo wąskich pasm walencyjnych i przewodnictwa, co wskazuje na niską mobilność nośników i raczej izolatorowy charakter badanych soli.

Widma elektronowe badanych soli w roztworach acetonitrylu są prawie identyczne niezależnie od stowarzyszonego kationu i składają się głównie z dwóch pasm (o maksimach w okolicy 294 i 365 nm) związanych z obecnością jonu trójjodkowego. Dodatkowe pasma wynikające z oddziaływań międzycząsteczkowych (450 i 550 nm) pojawiają się na widmach w fazie stałej na zboczu wyżej energetycznego pasma pochodzącego od przejść w jonach I_3^- . Porównanie widm absorpcyjnych w fazie stałej i w roztworze w połączeniu z analizą obliczonej struktury elektronowej, pozwalają dopatrywać się pochodzenia najniższych energetycznie pasm absorpcyjnych w oddziaływaniach $I_3^- \cdots I_3^-$. Są to bardzo słabe oddziaływania, dlatego szerokość pasm walencyjnych i przewodnictwa z nimi związanych jest niewielka, a pasma widoczne w strukturze elektronowej są dość płaskie.

Słabe oddziaływania wodorowe, które są obecne we wszystkich trzech strukturach nabierają znaczenia podczas wzbudzenia cząsteczki energiami większymi niż przerwa

energetyczna, co potwierdzają profile generowanych przez te materiały fotoprądów. Niewielka wartość fotoprądów w zakresie 500-700 nm wynika z najniższych przejść energetycznych wywodzących się z oddziaływań $I_3^- \cdots I_3^-$ oraz słabej dyspersji pasm walencyjnych i przewodnictwa. W zakresie 300-450 nm wartość fotoprądów jest znacząco większa, co jest rezultatem wzbudzenia elektronów do wspomnianych wcześniej wyższych pasm przewodnictwa, na które składają się stany pochodzące od kationów organicznych. Fotoprądy generowane przez badane związki charakteryzują się przełączeniem fotoelektrochemicznym w okolicy 0,75 V (vs. AgCl/Ag) wynikającym prawdopodobnie z generowania w materiale pary I_2^-/I^- , której potencjał redokсовy (0,83 V vs. AgCl/Ag) jest bardziej zbliżony do potencjału przełączenia niż potencjał pary I_3^-/I^- (0,34 vs. AgCl/Ag). Fotoprądy generowane są też dużo bardziej wydajnie w elektrolicie zawierającym parę I_2 i KI. Charakterystyczne dla tego elektrolitu pary redokсовe są dostosowane energetycznie do zapełniania dziur w paśmie walencyjnym badanych soli, co wizualizuje Rysunek 15, który wyjaśnia również brak wpływu obecności tlenu na wartość fotoprądów. Generowane fotoprądy potwierdzają częściowy charakter półprzewodnikowy badanych materiałów.



Rysunek 15. Mechanizm generowania fotoprądów katodowych (a) i anodowych (b) w obecności $[(C_6H_5)_3AsO]_2H^+I_3^-$. CB i VB oznaczają odpowiednio pasmo przewodnictwa i pasmo walencyjne soli. Na wykresie zamieszczono potencjały par redokсовych obecnych w elektrolicie.

Badane sole, $[(C_6H_5)_3AsO]_2H^+I_3^-$, $[(C_6H_5CH_2)_3NO]_2H^+I_3^-$ i $(C_6H_5CH_2)_3NH^+I_3^- \cdot C_6H_5CH_3$, wykazują przewodnictwo typu n , o potencjałach pasma płaskiego odpowiednio -0,254, -0,483 i -0,441 V vs. AgCl/Ag, co zostało wyznaczone za pomocą analizy wykresów Motta-Schottky’ego. Dodatkowo autorzy określili położenie poziomów Fermiego

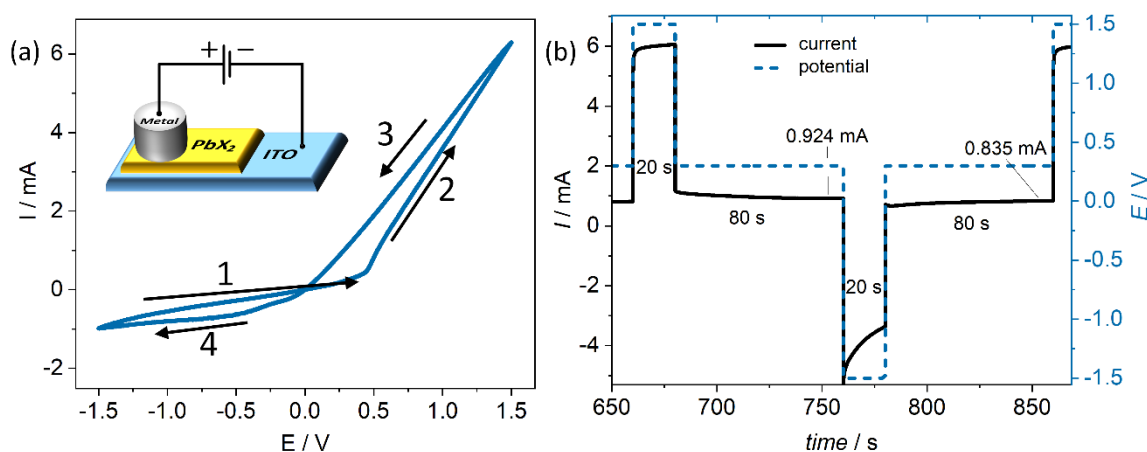
wykorzystując pomiary pracy wyjścia z wykorzystaniem sondy Kelvina oraz wyznaczyli wartości przewodnictwa właściwego badanych soli metodą czteropunktową.

Przedstawione sole posiadają cechy zarówno izolatorów jak i półprzewodników, mają w swojej strukturze anion o złożonych właściwościach fotoelektrochemicznych oraz są rozpuszczalne w rozpuszczalnikach organicznych. Cechy te sprawiają, że materiały te można brać pod uwagę podczas projektowania niekonwencjonalnych układów optoelektronicznych.

A4. Memristor in reservoir system – experimental evidence for high level computing and neuromorphic behaviour of PbI_2

Memrystory swoją unikalną charakterystykę mogą zawdzięczać różnym mechanizmom, takim jak formowanie się przewodzących filamentów, migracji domieszek i jonów lub modulacji wysokości bariery Schottky'ego. W artykule autorzy prezentują prosty memrystor składający się z warstwy halogenku ołowiu(II) umieszczonego między dwiema elektrodami (jedna zbudowana jest z ITO, a drugą stanowi powierzchnia metalu) (Rysunek 16a).

Charakterystykę prądowo-napięciową (I - V) takiego urządzenia można podzielić na cztery części zaznaczone na Rysunku 16a czarnymi strzałkami: strzałka **1** wskazuje zakres potencjału od $-1,5$ V do $0,4$ V, w którym prąd nieznacznie rośnie wraz ze wzrostem potencjału. W okolicy $0,5$ V następuje wyraźna zmiana nachylenia przebiegu prądowo-napięciowego, które nie zmienia się do $1,5$ V (**2**). Prawie liniowy przebieg I - V obserwuje się przykładając potencjał w przeciwnym kierunku tj. od $1,5$ V do $0,1$ V (**3**). Następna drastyczna zmiana w przebiegu charakterystyki I - V występuje w okolicy 0 V gdzie układ przestaje zachowywać się liniowo. Przyrost prądu w ostatnim zakresie od 0 V do $-1,5$ V jest niewielki (**4**). Na wykresie widać więc dwa zakresy, o niskim oporze (**2 i 3**) (LRS, z angielskiego Low Resistive States) oraz o wysokim oporze (**1 i 4**) (HRS, z angielskiego High Resistive States).



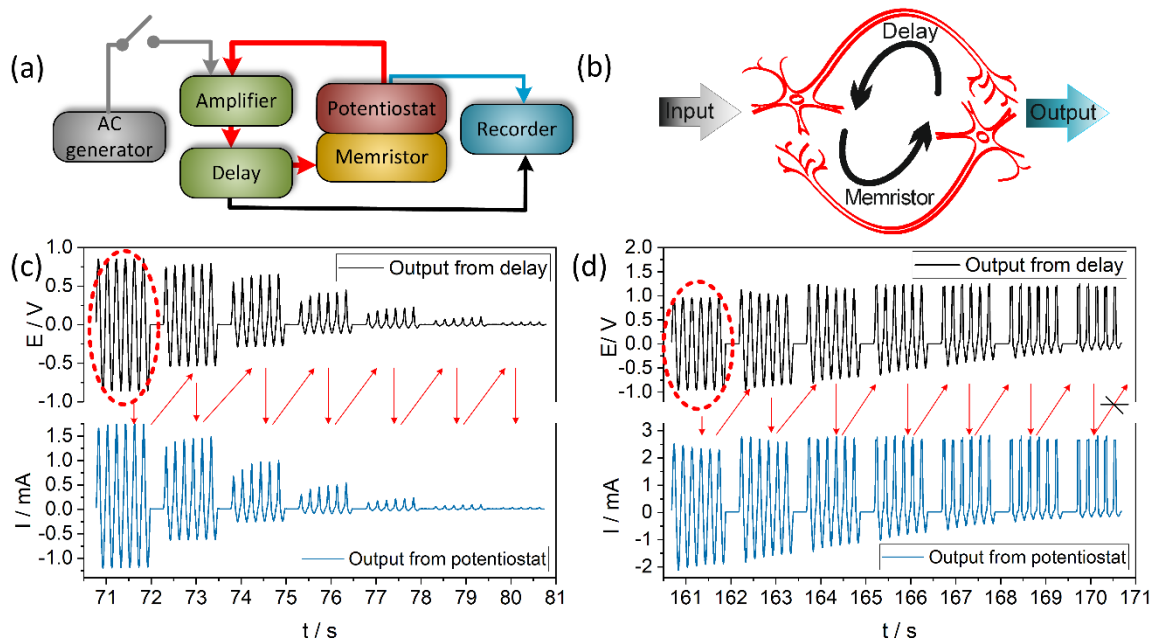
Rysunek 16. Typowy przebieg charakterystyki prądowo-napięciowej urządzenia opartego o PbI_2 i metaliczny kontakt oraz układ pomiarowy (a), pomiary chronoamperometryczne urządzenia przełączanego pomiędzy HRS i LRS impulsami o amplitudzie $\pm 1,5$ V (20 s), odczyt stanu odbywał się przy potencjale $0,3$ V.

Możliwość występowania urządzenia w więcej niż jednym stanie (nisko lub wysokooporowym) jest utożsamiane z posiadaniem przez urządzenie pamięci, co najlepiej ilustruje Rysunek 16b, na którym widać jak urządzenie zostaje przełączone z LRS do HRS impulsami $\pm 1,5$ V. Stan urządzenia odczytano przy 0,3 V, czyli potencjale, przy którym nie zachodzi przełączenie HRS/LRS. Stosunek LRS do HRS wynosi 1,1 (0,924/0,834 mA). W kolejnych eksperymentach, dla zaprezentowanego memrystora pokazano zachowanie zbliżone do synaptycznego (co jest zjawiskiem dość typowym dla memrystorów) co potwierdzają pomiary STDP (z angielskiego Spike-Timing Dependant Plasticity) i SRDP (z angielskiego Spike-Rate Dependant Plasticity).

Pomiary I - V przeprowadzone z różnymi metalami pokazują, że obecność pętli histerezy zależy od użytego materiału złącza i pojawia się w przypadku zastosowania elektrod wytworzonych z Ag, Cu lub Al, natomiast nie pojawia się w przypadku zastosowania Au lub Pt. Analizując charakterystyki prądowo-napięciowe urządzeń zbudowanych z PbI_2 , PbBr_2 i PbCl_2 można zauważyć, że są one bardzo podobne, co sugeruje że ruch jonów nie jest głównym czynnikiem odpowiedzialnym za właściwości memrystyczne materiału. Dodatkowo prędkość zmian przykładanego potencjału w bardzo niewielkim stopniu wpływa na przebiegi I - V , a grubość warstwy półprzewodnika zmienia jedynie całkowity prąd płynący przez materiał. Zaprezentowane wyniki sugerują – razem z niesymetrycznym przebiegiem I - V przypominającym nieco diodę – mechanizm przełączania pomiędzy stanami memrystora, oparty o efekty powierzchniowe pojawiające się na złączu metal| PbX_2 , a w szczególności zmianę wysokości bariery Schottky'ego. Źródłem tej bariery są stany na granicy faz, które tworzą się w wyniku adsorpcji molekuł półprzewodnika na powierzchni metalu lub w wyniku nakładania się funkcji falowej metalu na poziomy energetyczne obecne w przerwie półprzewodnika.

Aby pokazać możliwość wykorzystania tego prostego urządzenia, autorzy zbudowali układ, którego schemat przedstawiony jest na Rysunku 17a. Układ ten posiada sprzężenie zwrotne (czerwone strzałki) osiągnięte poprzez zastosowanie linii opóźniającej. Jest to tzw. układ rezerwuarowy zaliczający się do sieci neuronowych, a w szczególności „single node echo state machine”. W opisanym układzie sygnał napięciowy podany na wejście krąży w pętli i wielokrotnie oddziałuje z memrystorem. Prądowa odpowiedź memrystora jest opóźniana, wzmacniana i zawracana na memrystor w postaci sygnału napięciowego. Sygnał ulega modyfikacji przy kolejnych obiegach. Sygnał rejestrowany jest w dwóch miejscach: przed i po zniekształceniu przez memrystor. Sygnał może ulec z czasem wygaszeniu (Rysunek 17c) lub

krążyć w nieskończoność (Rysunek 17d) w zależności od początkowej amplitudy sygnału. Właściwość tą wykorzystano do zbudowania klasyfikatora amplitud, który dzieli grupę testowanych sygnałów na dwie podgrupy zawierające sygnał poniżej lub powyżej określonego napięcia będącego wartością progową.



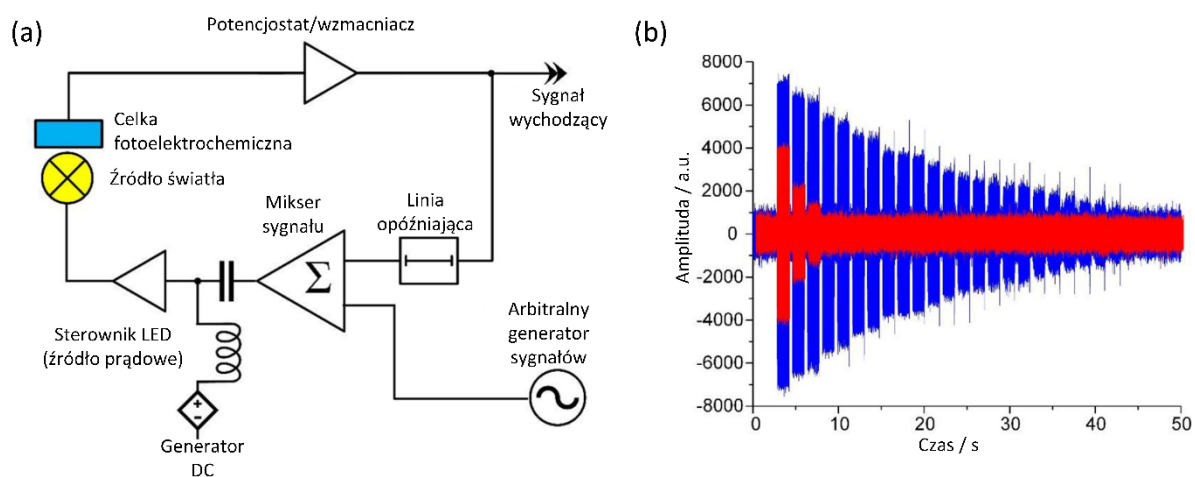
Rysunek 17. Schemat systemu ze sprzężeniem zwrotnym i linią opóźniającą (czerwone strzałki pokazują pętlę zawracającą sygnał) (a), graficzna reprezentacja sprzężenia zwrotnego pomiędzy neuronami (b), sygnały zarejestrowane w układzie rezerwuarowym dla sygnału o początkowej amplitudzie $1,7 V_{pp}$ (c), sygnały zarejestrowane w układzie rezerwuarowym dla sygnału o początkowej amplitudzie $1,9 V_{pp}$ (d).

W zaprezentowanym układzie rezerwuarowym zaobserwowano jeszcze jedną interesującą właściwość badanego materiału, mianowicie metaplastyczność, czyli zmianę plastyczności synapsy w wyniku jej historii. Opisany powyżej proces klasyfikacji charakteryzuje się konkretną wartością progową (amplitudą sygnału wpuszczonego do układu), która na skutek prostujących właściwości złącza ulega przesunięciu do mniejszych wartości. Jeżeli progiem pozwalającym na klasyfikację sygnału było początkowo $1,8 V_{pp}$, w wyniku ewolucji złącza wartość ta zostaje przesunięta do $1,5 V_{pp}$. Co więcej memrystor może zostać zresetowany do stanu początkowego w wyniku przyłożenia ujemnego potencjału. Zjawisko to jest konsekwencją oddziaływań na złączu metal/półprzewodnik. W wyniku niesymetrycznej, prostującej charakterystyki $I-V$ memrystora, sygnał w każdym kolejnym cyklu jest coraz bardziej niesymetryczny i dominuje w nim dodatni potencjał powodujący utlenienie się powierzchni miedzi $Cu^0 \rightarrow Cu^{+2+}$ co prowadzi do zmniejszenia oporu na złączu. Przyłożenie

ujemnego potencjału powoduje redukcję atomów na złączu i powrót układu do stanu początkowego.

A5. Molecules, semiconductors, light and information: Towards future sensing and computing paradigms

Uzupełnieniem rozprawy doktorskiej jest przegląd poruszający różne aspekty przetwarzania informacji w układach chemicznych. Dominującym obecnie podejściem w przetwarzaniu informacji jest algebra Boole'a, w której informacja reprezentowana jest w postaci zer i jedynek. Na pewnym etapie sygnał musi zostać zdigitalizowany aby mógł być dalej przetwarzany. Istnieje jednak inne podejście, w którym to wykorzystanie logiki wielowartościowej lub rozmytej również jest dobrym rozwiązaniem. Przykładem może być wykorzystanie memrystorów o co najmniej trzech stanach lub dostosowanie tablic prawdy logiki wielowartościowej do opisu trójwymiarowej projekcji fotoprądów TiO_2 modyfikowanego antrachinonem. Kolejną gałęzią niekonwencjonalnego przetwarzania danych – obecnie coraz intensywniej rozwijaną – są sieci neuronowe, oraz systemy rezerwarowe będące ich podtypem (Rysunek 18).



Rysunek 18. Uproszczony diagram blokowy fotoelektrycznego systemu rezerwarowego (a). Odpowiedź systemu rezerwarowego, w którym wykorzystano złotą elektrodę (niebieski sygnał, sygnał odniesienia) oraz tę samą elektrodę pokrytą kwasem liponowym (czerwony sygnał) (b).

Przegląd między innymi rozszerza informacje na temat memrystorów, a w szczególności fotomemrystorów. Stan memrystora zależy od zmian pola elektrycznego, temperatury, pola magnetycznego, ale może też zależeć od światła padającego na urządzenie. Tak jak działanie memrystora opierać się może na kilku różnych mechanizmach, tak i w przypadku fotomemrystora sytuacja jest bardzo podobna. Światło oddziałujące z materiałem, z którego zbudowany jest fotomemrystor może powodować generowanie nośników ładunków,

wyłapywanie nośników przez pułapki, opróżnianie wypełnionych pułapek, może indukować zmiany w migracji jonów oraz kombinację tych efektów. W przypadku urządzeń opartych na materiałach tlenkowych (ZnO, CeO/AlO) ZnO/SrTiO₃) mechanizm działania memrystora związany jest z migracją wakancji tlenkowych.

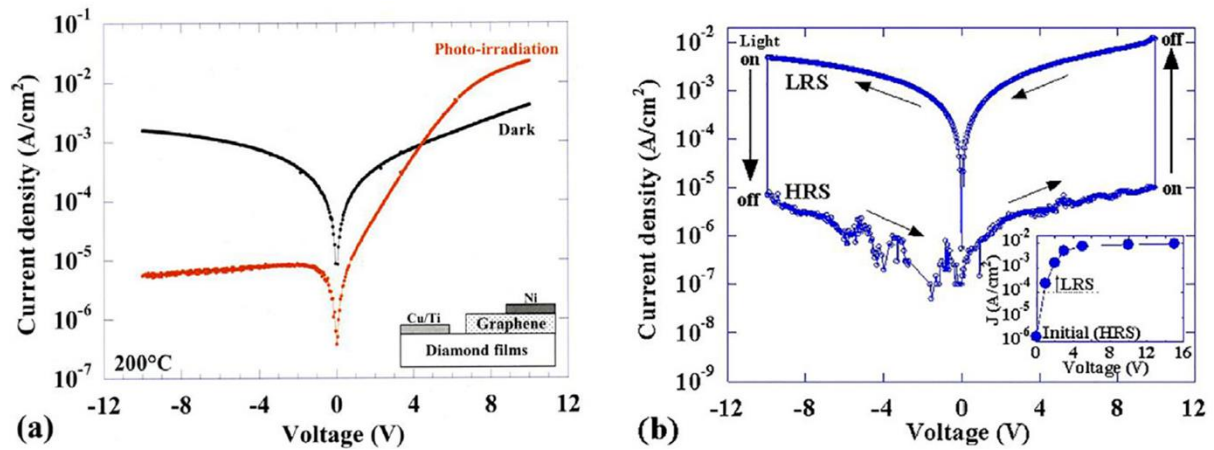
Memrystywne właściwości można znaleźć też w urządzeniu przypominającym w budowie tranzystor, zbudowanym na bazie GaAs/AlGaAs i InAs w postaci kropek kwantowych. Urządzenie w ciemności działa jak typowy memrystor, natomiast można przełączyć je za pomocą promieniowania podczerwonego, które opróżnia kropki kwantowe zmieniając stan urządzenia z HRS do LRS.

Ciekawym rozwiązaniem zastosowanym do budowy fotomemrystora jest wykorzystanie fotoindukowanej izomeryzacji *cis-trans*, która to prowadzi do zmian objętości materiału międzyelektrodowego a tym samym zmian oporu memrystora.

Nieco innym podejściem do użycia światła w przełączaniu stanów memrystora jest wykorzystanie różnych współczynników załamania światła. Nanopręty ZnO pokryte cienką warstwą wody oświetlane pod kątem, w którym następuje całkowite odbicie światła padającego (48°) nie przewodzą, natomiast po przekroczeniu 48° światło dociera do tlenku cynku, indukuje desorpcję tlenu i tworzenie się filamentów z wytworzonych wakancji tlenkowych. Gdy filamenty te połączą obie elektrody następuje wzrost przewodnictwa urządzenia (LRS).

W memrystorach opartych o perowskity ołowiove (np. CH₃NH₃PbI₃) światło nie jest źródłem przełączenia między stanami HRS/LRS ale pozwala na uzyskanie dodatkowych stanów, tzn. że urządzenie posiada przynajmniej dwa różne stany o wysokim oporze. Jest to rezultat zwiększonej ilości nośników ładunku pod wpływem naświetlania półprzewodnika promieniowaniem o energii większej niż przerwa energetyczna tego materiału.

Oryginalnym podejściem do problemu konstrukcji fotomemrystora jest uzyskanie pętli histerezy – cechy charakterystycznej memrystora – przez urządzenie, które w ciemności lub pod wpływem oświetlania, nie zachowuje się jak memrystor. Rysunek 19a przedstawia charakterystyki prądowo-napięciowe złącza grafen/diament. Zarówno w ciemności jak i pod wpływem naświetlania nie obserwuje się efektu pamięci a jedynie dwa różne przebiegi. Poprzez oświetlanie urządzenia przez 5 s w okolicach +10 oraz -10 V można uzyskać przebieg *I-V* z wyraźnymi stanami HRS i LRS (Rysunek 19b).



Rysunek 19. Charakterystyki prądowo-napięciowe złącza grafen/diament podczas naświetlania i w ciemności (a). Charakterystyka prądowo-napięciowa uzyskana dla złącza grafen/diament poprzez oświetlenie materiału przez 5 s w okolicy 10 V i -10 V (b).³⁹

W przeglądzie można znaleźć wyjaśnienie działania układu rezerwarowego, przykład jego konstrukcji oraz pierwsze przykłady jego implementacji. Jednym z możliwych wersji systemu rezerwarowego jest system oparty o sensor – stąd w przeglądzie opisane są również sensory fotoelektrochemiczne – który oprócz wychwytywania bodźców ze środowiska miałyby jednocześnie dokonywać analizy tego bodźca, co jest jednym z założeń algorytmu SWEET. Układ rezerwarowy może być oparty nie tylko o sensory czy też memrystory, ale także sztuczne synapsy, przełączniki molekularne, programowalne tablice bramek logicznych lub układy foniczne.

Podsumowanie

Prezentowana rozprawa opisuje wpływ oddziaływań międzycząsteczkowych na właściwości czterech grup związków: jodkowych kompleksów cyny(IV), organicznych soli trójjodkowych, halogenków ołowiu(II) oraz chalkohalogenków piątej grupy układu okresowego. Praca składa się z dwóch zasadniczych części: pierwszej skupiającej się na półprzewodnikach, oddziaływaniach obecnych w ich strukturze oraz wynikających z nich właściwościach fizykochemicznych, oraz drugiej skupiającej się na wykorzystaniu tych materiałów i ich właściwości do budowy memrystorów, oraz zastosowania ich w niekonwencjonalnych układach obliczeniowych.

W pracy potwierdzono dwie postawione na początku tezy:

- I) W strukturach krystalicznych półprzewodników pozbawionych silnych oddziaływań międzycząsteczkowych, słabe oddziaływania międzycząsteczkowe mają dominujący wpływ na strukturę elektronową. Krawędzie pasm walencyjnego oraz przewodnictwa powstają w wyniku słabych oddziaływań pomiędzy atomami jodu anionów trójjodkowych w cząsteczkach soli organicznych. Wyższe pasma przewodnictwa, na które składają się orbitale atomów węgla wynikają z obecności w strukturze krystalicznej oddziaływań wodorowych, w których atomy jodu pełnią funkcję nukleofila. Podobna zależność pojawia się w grupie jodkowych kompleksów cyny(IV): orbitale atomów jodu budują pasmo walencyjne tych półprzewodników, natomiast pasmo przewodnictwa zbudowane jest głównie z orbitali atomów węgla.

- II) Dwukontaktowe urządzenie jakim jest memrystor można zbudować wykorzystując jako bazowy materiał PbX_2 ($X = Cl, Br, I$). Działanie memrystora na bazie PbX_2 opiera się na modulacji wysokości bariery Schottky'ego. Jako źródło bariery można uważać stany tworzące się na granicy metal/półprzewodnik, w tym stany indukowane metalem oraz stany powstałe w wyniku chemisorpcji na powierzchni metalu. Co więcej, procesy redoksove na powierzchni styku metal/ PbI_2 wydają się być odpowiedzialne za występowanie zjawiska metaplastyczności zaobserwowanego dla układu rezerwarowego opartego o memrystor na bazie PbI_2 .

Projektowanie i synteza półprzewodników jest zadaniem bardzo złożonym. W przypadku serii związków różniących się jedynie atomem fluorowca można przewidzieć

niektóre właściwości (np. szerokość przerwy energetycznej) jak i tendencję ich zmiany, jednak w przypadku całkiem nowych związków pozostaje wiele niewiadomych. Sole organiczne zawierające anion I_3^- posiadają przerwę energetyczną z zakresu światła widzialnego, co może być zaletą podczas konstrukcji ogniw fotowoltaicznych, z drugiej strony najniższe pasma przewodnictwa cechują się niewielką dyspersją, co skutkuje niską mobilnością ładunków i dużym oporem elektrycznym tych soli. Hybrydowe półprzewodniki oparte o SnI_4 posiadają przewodnictwo zbliżone do perowskitów ołowiowych, jednak mimo posiadania dużych ligandów organicznych kompleksy te łatwo ulegają hydrolizie.

Wykorzystanie PbI_2 (i innych związków, takich jak $[SnI_4L_2]$) w budowie memrystorów ma wiele zalet. Szczególnie korzystną wydaje się być prostota i ekonomia wytwarzania tych urządzeń. Nanoszenie warstw związku dobrze rozpuszczalnego w organicznych rozpuszczalnikach (jak np. DMSO) jest rozwiązaniem prostym, niedrogim i możliwym do wykonania bez stosowania specjalnych warunków, jak np. regulacja wilgotności. Ciekawym zastosowaniem tego typu memrystorów może być wykorzystanie ich jako elementów nietypowych układów obliczeniowych jakimi są układy rezerwuarowe.

Bibliografia

1. da Silva Filho, D. A.; Kim, E.-G.; Brédas, J.-L., Transport Properties in the Rubrene Crystal: Electronic Coupling and Vibrational Reorganization Energy. *Advanced Materials* **2005**, *17* (8), 1072-1076.
2. Sutton, C.; Risko, C.; Brédas, J.-L., Noncovalent Intermolecular Interactions in Organic Electronic Materials: Implications for the Molecular Packing vs Electronic Properties of Acenes. *Chemistry of Materials* **2016**, *28* (1), 3-16.
3. Coropceanu, V.; Cornil, J.; da Silva Filho, D. A.; Olivier, Y.; Silbey, R.; Brédas, J.-L., Charge Transport in Organic Semiconductors. *Chemical Reviews* **2007**, *107* (4), 926-952.
4. Bäessler, H., Excitonic Model versus Band Gap Model in Organic Materials. In *Reference Module in Materials Science and Materials Engineering*, Elsevier: 2016.
5. Clark, T.; Hennemann, M.; Murray, J. S.; Politzer, P., Halogen bonding: the σ -hole. *Journal of Molecular Modeling* **2007**, *13* (2), 291-296.
6. Cavallo, G.; Metrangolo, P.; Milani, R.; Pilati, T.; Priimagi, A.; Resnati, G.; Terraneo, G., The Halogen Bond. *Chemical Reviews* **2016**, *116* (4), 2478-2601.
7. Gilday, L. C.; Robinson, S. W.; Barendt, T. A.; Langton, M. J.; Mullaney, B. R.; Beer, P. D., Halogen Bonding in Supramolecular Chemistry. *Chemical Reviews* **2015**, *115* (15), 7118-7195.
8. Lin, F.-Y.; MacKerell, A. D., Do Halogen-Hydrogen Bond Donor Interactions Dominate the Favorable Contribution of Halogens to Ligand-Protein Binding? *The Journal of Physical Chemistry B* **2017**, *121* (28), 6813-6821.
9. Riley, K. E.; Hobza, P., Strength and Character of Halogen Bonds in Protein-Ligand Complexes. *Crystal Growth & Design* **2011**, *11* (10), 4272-4278.
10. Visscher, L.; Dyllal, K. G., Relativistic and correlation effects on molecular properties. I. The dihalogens F₂, Cl₂, Br₂, I₂, and At₂. *The Journal of Chemical Physics* **1996**, *104* (22), 9040-9046.
11. Buin, A.; Comin, R.; Xu, J.; Ip, A. H.; Sargent, E. H., Halide-Dependent Electronic Structure of Organolead Perovskite Materials. *Chemistry of Materials* **2015**, *27* (12), 4405-4412.
12. Bhachu, D. S.; Moniz, S. J. A.; Sathasivam, S.; Scanlon, D. O.; Walsh, A.; Bawaked, S. M.; Mokhtar, M.; Obaid, A. Y.; Parkin, I. P.; Tang, J.; Carmalt, C. J., Bismuth oxyhalides: synthesis, structure and photoelectrochemical activity. *Chemical Science* **2016**, *7* (8), 4832-4841.
13. Pelletier, P. J.; Caventou, J. B., Sur l'asphyxie. *Ann. Chim.* **1819**, *10*, 142-177.
14. Boschloo, G.; Hagfeldt, A., Characteristics of the Iodide/Triiodide Redox Mediator in Dye-Sensitized Solar Cells. *Accounts of Chemical Research* **2009**, *42* (11), 1819-1826.
15. Beckmann, P. A., A review of polytypism in lead iodide. *Crystal Research and Technology* **2010**, *45* (5), 455-460.

16. Liu, X.; Li, P.; Zhang, Y.; Hu, X.; Duan, Y.; Li, F.; Li, D.; Shao, G.; Song, Y., High-efficiency perovskite solar cells based on self-assembly n-doped fullerene derivative with excellent thermal stability. *Journal of Power Sources* **2019**, *413*, 459-466.
17. Hwang, B.; Lee, J.-S., Hybrid Organic-Inorganic Perovskite Memory with Long-Term Stability in Air. *Scientific Reports* **2017**, *7* (1), 673.
18. Yan, K.; Peng, M.; Yu, X.; Cai, X.; Chen, S.; Hu, H.; Chen, B.; Gao, X.; Dong, B.; Zou, D., High-performance perovskite memristor based on methyl ammonium lead halides. *Journal of Materials Chemistry C* **2016**, *4* (7), 1375-1381.
19. Gu, C.; Lee, J.-S., Flexible Hybrid Organic-Inorganic Perovskite Memory. *ACS Nano* **2016**, *10* (5), 5413-5418.
20. Tombe, S.; Adam, G.; Heilbrunner, H.; Apaydin, D. H.; Ulbricht, C.; Sariciftci, N. S.; Arendse, C. J.; Iwuoha, E.; Scharber, M. C., Optical and electronic properties of mixed halide (X = I, Cl, Br) methylammonium lead perovskite solar cells. *Journal of Materials Chemistry C* **2017**, *5* (7), 1714-1723.
21. Leijtens, T.; Eperon, G. E.; Noel, N. K.; Habisreutinger, S. N.; Petrozza, A.; Snaith, H. J., Stability of Metal Halide Perovskite Solar Cells. *Advanced Energy Materials* **2015**, *5* (20), 1500963.
22. Schulz, P.; Edri, E.; Kirmayer, S.; Hodes, G.; Cahen, D.; Kahn, A., Interface energetics in organo-metal halide perovskite-based photovoltaic cells. *Energy & Environmental Science* **2014**, *7* (4), 1377-1381.
23. Filip, M. R.; Eperon, G. E.; Snaith, H. J.; Giustino, F., Steric engineering of metal-halide perovskites with tunable optical band gaps. *Nature Communications* **2014**, *5*, 5757.
24. Adonin, S. A.; Frolova, L. A.; Sokolov, M. N.; Shilov, G. V.; Korchagin, D. V.; Fedin, V. P.; Aldoshin, S. M.; Stevenson, K. J.; Troshin, P. A., Antimony (V) Complex Halides: Lead-Free Perovskite-Like Materials for Hybrid Solar Cells. *Advanced Energy Materials* **2018**, *8* (6), 1701140.
25. Strukov, D. B.; Snider, G. S.; Stewart, D. R.; Williams, R. S., The missing memristor found. *Nature* **2008**, *453*, 80.
26. Chua, L., Memristor-The missing circuit element. *IEEE Transactions on Circuit Theory* **1971**, *18* (5), 507-519.
27. Caravelli, F.; Carbajal, J., *Memristors for the Curious Outsiders*. 2018; Vol. 6, p 118.
28. Wang, F. Z., A Triangular Periodic Table of Elementary Circuit Elements. *IEEE Transactions on Circuits and Systems I: Regular Papers* **2013**, *60* (3), 616-623.
29. Vongehr, S.; Meng, X., The Missing Memristor has Not been Found. *Scientific Reports* **2015**, *5*, 11657.
30. Gao, L.; Alibart, F.; Strukov, D. B., Programmable CMOS/Memristor Threshold Logic. *IEEE Transactions on Nanotechnology* **2013**, *12* (2), 115-119.
31. Prezioso, M.; Merrih-Bayat, F.; Hoskins, B. D.; Adam, G. C.; Likharev, K. K.; Strukov, D. B., Training and operation of an integrated neuromorphic network based on metal-oxide memristors. *Nature* **2015**, *521*, 61.

32. Chang, T.; Jo, S.-H.; Lu, W., Short-Term Memory to Long-Term Memory Transition in a Nanoscale Memristor. *ACS Nano* **2011**, *5* (9), 7669-7676.
33. Burr, G. W.; Shelby, R. M.; Sebastian, A.; Kim, S.; Kim, S.; Sidler, S.; Virwani, K.; Ishii, M.; Narayanan, P.; Fumarola, A.; Sanches, L. L.; Boybat, I.; Le Gallo, M.; Moon, K.; Woo, J.; Hwang, H.; Leblebici, Y., Neuromorphic computing using non-volatile memory. *Advances in Physics: X* **2017**, *2* (1), 89-124.
34. Qiao, N.; Mostafa, H.; Corradi, F.; Osswald, M.; Stefanini, F.; Sumislawska, D.; Indiveri, G., A reconfigurable on-line learning spiking neuromorphic processor comprising 256 neurons and 128K synapses. *Frontiers in Neuroscience* **2015**, *9* (141).
35. Nguimdo, R. M.; Verschaffelt, G.; Danckaert, J.; Van der Sande, G., Reducing the phase sensitivity of laser-based optical reservoir computing systems. *Opt. Express* **2016**, *24* (2), 1238-1252.
36. Du, C.; Cai, F.; Zidan, M. A.; Ma, W.; Lee, S. H.; Lu, W. D., Reservoir computing using dynamic memristors for temporal information processing. *Nature Communications* **2017**, *8* (1), 2204.
37. Kulkarni, M. S.; Teuscher, C., Memristor-based reservoir computing. In *Proceedings of the 2012 IEEE/ACM International Symposium on Nanoscale Architectures*, ACM: Amsterdam, The Netherlands, 2012; pp 226-232.
38. Kudithipudi, D.; Saleh, Q.; Merkel, C.; Thesing, J.; Wysocki, B., Design and Analysis of a Neuromemristive Reservoir Computing Architecture for Biosignal Processing. *Frontiers in Neuroscience* **2016**, *9* (502).
39. Ueda, K.; Aichi, S.; Asano, H., Photo-controllable memristive behavior of graphene/diamond heterojunctions. *Applied Physics Letters* **2016**, *108* (22), 222102.

Dorobek naukowy

Publikacje w czasopismach:

1. M. Buchalska, M. Pacia, M. Kobięłusz, M. Surówka, E. Świętek, **E. Właźlak**, K. Szaciłowski, M. Macyk,
Photocatalytic activity of TiO₂ modified with hexafluorometallates-fine tuning of redox properties by redox-innocent anions,
Journal of Physical Chemistry C, 2018, **118**, 24915-24924
2. **E. Właźlak**,* A. Blachecki, M. Bisztyga-Szklarz, S. Klejna, T. Mazur, K. Mech,* K. Pilarczyk, D. Przyczyna, M. Suchecki, P. Zawal, K. Szaciłowski*
Heavy pnictogen chalcogenides: the synthesis, structure and properties of these rediscovered semiconductors
Chemical Communications, 2018, **54**, 12133-12162
3. **E. Właźlak**, W. Macyk, W. Nitek, K. Szaciłowski*
Influence of π -Iodide Intermolecular Interactions on Electronic Properties of Tin(IV) Iodide Semiconducting Complexes
Inorganic Chemistry, 2016, **55**, 5935–5945
4. **E. Właźlak**,* J. Kalinowska-Tłuścik, W. Nitek, S. Klejna, K. Mech, W. Macyk, K. Szaciłowski*
Triiodide Organic Salts: Photoelectrochemistry at the Border between Insulators and Semiconductors,
ChemElectroChem, 2018, **5**, 3486-3497
5. **E. Właźlak**,* M. Marzec, P. Zawal, K. Szaciłowski*
Memristor in reservoir system – experimental evidence for high level computing and neuromorphic behaviour of PbI₂
ACS Applied Materials and interfaces, 2019, (DOI: 10.1021/acsami.9b01841)

6. K. Pilarczyk,* **E. Właźlak**,* D. Przyczyna, A. Blachecki, A. Podborska, V. Anathasiou, Z. Konkoli, K. Szaciłowski*
Molecules, semiconductors, light and information: Towards future sensing and computing paradigms
Coordination Chemistry Reviews, 2018, **365**, 23-40

7. K. Hnida,* M. Marzec, **E. Właźlak**, D. Chlebda, K. Szaciłowski, D. Gilek, Grzegorz D. Sulka, M. Przybylski
Influence of pulse frequency on physicochemical properties of InSb films obtained via electrodeposition
Electrochimica Acta, 2019, **304**, 396-404

Udział w konferencjach

1. **E. Właźlak**, K. Szaciłowski, W. Macyk, *Tin(IV) Iodide Complexes: A Novel Group of Semiconductors* ELECTROCHEM 2014, ELECTROCHEMICAL HORIZONS, 7-9 Września 2014, poster
2. **E. Właźlak**, K. Szaciłowski, W. Macyk *Modyfikowanie powierzchni tlenku tytanu(IV) za pomocą kompleksów cyny (IV)*, II Sympozjum "Postępy w badaniach i zastosowaniach fotokatalizatorów na bazie ditlenku tytanu (TiO₂ – Szczecin 2014) 8 – 9 lipca, prezentacja
3. **E. Właźlak**, K. Szaciłowski, W. Macyk, *Surface modification of TiO₂ with tin(IV) iodide complexes*, Konferencja PANIC, 27 – 30 kwietnia 2014, prezentacja
4. **E. Właźlak**, W. Macyk, K. Szaciłowski, *Tin Tetraiodide Complexes – Molecular Inorganic Semiconductors*, 21st International Symposium on the Photochemistry and Photophysics of Coordination Compounds, Kraków 5 - 9 lipiec 2015, poster
5. **E. Właźlak**, K. Szaciłowski, W. Macyk, *Photoelectrochemical characterization of tin(IV) iodide complexes*, PhoBiA Annual Nanophotonics International Conference "PANIC", Wrocław 2015, prezentacja
6. **E. Właźlak**, K. Szaciłowski, W. Macyk, W. Nitek, *Molecular tin(IV) complexes as candidates for organic electronics* EMN meeting on organic-electronics and photonics, San Sebastian, Hiszpania, Wrzesień 9–13, 2016, prezentacja na zaproszenie

7. **E. Właźlak**, K. Szaciłowski, *Hybrid Memristor Based on Metal Iodide Complex*, BIT's 3rd Annual World Congress of Smart Materials-2017 Bangkok, prezentacja

Kierowanie projektami naukowymi

- Grant NCN, PRELUDIUM 10, UMO-2015/19/N/ST5/00533

Hybrydowe materiały półprzewodnikowe na bazie związków koordynacyjnych zawierających jod.

Granty obliczeniowe:

- Akademickie Centrum Komputerowe Cyfronet AGH (granty własne: IODIDE, IODIDE2, udział: GRAPHENE, GRAPHENE2, PEROVSKITE).

Dorobek organizacyjny

- Praca w Komitecie organizacyjnym konferencji 21st Symposium on the Photochemistry and Photophysics of Coordination Compounds (ISPPCC), 5–9 lipca 2015, Kraków.

Załączniki

- Artykuły naukowe wchodzące w skład rozprawy
- Oświadczenia współautorów

Artykuły naukowe wchodzące w skład rozprawy



Cite this: *Chem. Commun.*, 2018, 54, 12133

Heavy pnictogen chalcogenides: the synthesis, structure and properties of these rediscovered semiconductors†

Ewelina Właźlak,^{*ab} Andrzej Blachecki,^{ac} Magdalena Bisztyga-Szklarz,^a Sylwia Klejna,^{id a} Tomasz Mazur,^a Krzysztof Mech,^{*a} Kacper Pilarczyk,^a Dawid Przyczyna,^{ad} Maciej Suhecki,^{ad} Piotr Zawal^{ad} and Konrad Szacilowski^{id *a}

Received 27th June 2018,
Accepted 17th September 2018

DOI: 10.1039/c8cc05149f

rsc.li/chemcomm

This review focuses on the synthesis, properties and selected applications of heavy pnictogen chalcogenides, *i.e.* compounds of the MQX stoichiometry, where M = As, Sb, and Bi; Q = O, S, Se, and Te; and X = F, Cl, Br and I. The first section focuses on their synthesis and crystal structures, and the second section discusses the electronic structure on the basis of quantum chemical modelling and selected experimental data. Finally, the third section discusses their electrical, photoelectrochemical and photocatalytic properties and applications. In contrast to perovskites, chalcopyrites and kesterites, chalcogenides have attracted relatively less attention, but their structure and properties are well suited for numerous applications.

Introduction

Wide band gap semiconductors find numerous novel applications in electronics and optoelectronics, photovoltaics, photocatalysis, and biomedical analytics. There are only a few elemental semiconductors among which silicon and germanium are the most commonly used materials. Most of the modern electronic devices are based on these materials. Compound semiconductors are also present in modern technologies: they allow wide band radio frequency communication in the gigahertz range, fabrication of energy efficient light sources and highly efficient solar cells and emerging photocatalytic applications, including self-cleaning and self-sterilizing surfaces, water purification and air deodorization. Titanium dioxide is a leading example of such a successfully applied material. Interestingly, most of the modern semiconductor technologies are dominated by p-block semiconductors: Si, Ge, GaAs and GaN.^{1,2} In contrast, photocatalysis,³ photovoltaics⁴ and emerging electronic technologies^{5–8} usually try to explore binary d-block semiconductors (*e.g.* transition

metal oxides and sulphides, and their alloys and molecular modifications). There is also an interesting group of ternary semiconductors, which were heavily explored in the second half of the 20th century, and have recently been rediscovered, as they exhibit numerous useful properties (Fig. 1).

The rich and versatile chemistry of the elements from the 15th, 16th and 17th main groups of the periodic table of elements yields thousands of possible structures and can be a subject of numerous review papers. In general, if elements other than those indicated in Fig. 1 are included (especially hydrogen, carbon and nitrogen), a manifold of molecular and ionic compounds with the M–Q–X bonding frame can be obtained. These compounds belong, however, to the element–organic species category, whereas purely inorganic species, limited only

B	C	N	O	F
Al	Si	P	S	Cl
Ga	Ge	As	Se	Br
In	Sn	Sb	Te	I
Tl	Pb	Bi	Po	At

Fig. 1 A fragment of the periodic table of elements indicating the most common elemental semiconductors (green), elements forming the most ubiquitous compound semiconductors (blue) and elements forming heavy pnictogen chalcogenides (shaded in yellow and red).

^aAGH University of Science and Technology, Academic Centre for Materials and Nanotechnology, al. A. Mickiewicza 30, 30-059 Krakow, Poland.

E-mail: ewlazlak@agh.edu.pl, kmech@agh.edu.pl, szacilow@agh.edu.pl

^bJagiellonian University, Faculty of Chemistry, ul. Gronostajowa 2, 30-387 Kraków, Poland

^cAGH University of Science and Technology, Faculty of Non-Ferrous Metals, al. A. Mickiewicza 30, 30-059 Krakow, Poland

^dAGH University of Science and Technology, Faculty of Physics and Applied Computer Science, al. A. Mickiewicza 30, 30-059 Krakow, Poland

† Electronic supplementary information (ESI) available. See DOI: 10.1039/c8cc05149f

to selected elements, provide a structurally and stoichiometrically uniform platform on which new materials with tunable properties should be searched for.

A significant drawback of elemental and compound binary semiconductors is the lack of tailorability. These materials have virtually fixed band gaps, band edge potentials, and charge carrier mobilities. Bulk doping is usually used to modulate the charge carrier concentration, whereas surface modification is specifically important in the case of nano- and micromaterials and can be applied to change their band edge potentials and photosensitivity range, parameters essential for photocatalytic and photovoltaic applications. On the other hand, precise band gap engineering of semiconductors and semiconducting nanostructures is essential for tailoring the optical properties of materials, and their integration into functional devices.

Binary semiconductors can be tuned to some extent *via* preparation of semiconductor alloys, but the applicability of this technique is limited by Vegard's law⁹ and band gap bowing. The band gap of alloy semiconductors A and B is usually described by Van Vechten–Bergstresser's rule (eqn (1)):¹⁰

$$E_g = xE_g^A + (1 - x)E_g^B - bx(1 - x) \quad (1)$$

where E_g is the band gap of an alloy, E_g^A and E_g^B are the band gaps of the components, x is the molar fraction of component A and b is the bowing factor. The bowing factor, according to Van Vechten and Bergstresser, describes the deviation from the linear behaviour of Vegard's law resulting from the aperiodic variation of the crystal potential in substitutional alloys; however, other explanations can also be found.¹¹ This short range disorder (at a length scale comparable to the size of the unit cell) is also reflected in anomalous changes in the absorption coefficients of semiconducting alloys due to Anderson's localization, which influences the polaritonic transport phenomenon.¹² The band gap tuning *via* alloying is limited by discontinuous deviations from Vegard's law and Van Vechten–Bergstresser's rule, the strict requirement of the similarity of the atomic radii of the components of substitutional alloys, crystal lattice instabilities and the formation of multiphase materials.

Therefore, new materials have been intensively searched for and a few new families of semiconducting materials have been extensively explored. They include perovskites,¹³ chalcopyrites,¹⁴ kesterites¹⁵ and chalcogenides.¹⁶ Oxide perovskites have been applied as ferroelectric, piezoelectric and high- k materials and high temperature superconductors. Lead and bismuth iodide perovskites are explored mainly as solar cell materials. They offer high energy conversion efficiencies; however, devices based on them suffer from relatively high air and humidity sensitivity and problems with appropriate band alignment at interfaces. Kesterites and chalcopyrites are much more difficult to prepare and therefore tuning of their properties is relatively complex. Furthermore, they show some lattice instabilities and their performance is compromised due to the precipitation of secondary phases. Chalcogenides reported up to now seem to be devoid of all these drawbacks. Their synthesis is relatively simple, and they are stable and their crystal and electronic structures can be easily tuned to provide

very good performance. They are, however, much less extensively studied as compared to other multielement compound semiconductors.

Pnictogen chalcogenides were intensively studied in the 1960s due to their promising glass-forming abilities, and optical properties in the infrared region and ferroelectric properties. The renaissance of pnictogen chalcogenides originates primarily from their prospective applications as solar cell materials. Recently, they demonstrated their potential as materials for nanoelectronics due to their chain-like structure, which facilitates the formation of 1D structures. Interestingly, 1D chalcogenides exhibit much better electrical properties than their bulk counterparts.¹⁷

Chalcogenide semiconductors are well-suited for substitutional tuning due to the possibility of low temperature synthesis, which greatly suppresses halogen volatility, which, in turn, provides good control over materials' stoichiometry. Importantly, they give an opportunity of continuous tunability and phase stability and are based on Earth-abundant materials.¹⁸ Furthermore, due to the presence of high- Z ns^2 levels of $d^{10}s^2p^0$ electron configurations, they exhibit good charge carrier transport properties. Peculiar electronic structures, originating from the anti-bonding character of the top of the valence band (hybridized cation s -orbitals with anion p -orbitals) extended p -states at the bottom of the conduction band, lead to a highly dispersive character of both bands. This in turn favours high charge carrier mobility and defect tolerance. Cross-band gap hybridization gives rise to higher dielectric constants, thus screening the point defects, which is beneficial for transport properties.¹⁹ Therefore the low performance of devices based on these materials should be mainly attributed to band misalignment. Performance improvement requires fine-tuning of semiconductor and contact properties. Therefore, pnictogen chalcogenides can be considered as materials of choice for further studies and numerous emerging applications. This review presents a collection of data on synthesis methodology, crystal and electronic structures, transport properties and some selected applications in photocatalysis and photocurrent generation.

Synthesis

The purpose of this section is to summarize and briefly describe methods used to synthesize V–VI–VII compounds. The most widely described methods are crystallization from melts (sometimes termed the growth from melt and self-flux method) either with or without any temperature gradient, the Bridgman method, chemical and physical vapour transport, growth from vapour (vacuum fusion) and chemical methods, such as sonochemical synthesis, and solvo- and hydrothermal methods.

Growth from melts

The most widely used synthesis method is annealing at high temperatures. This method has been used to synthesize BiSeCl ,²⁰ BiSeI ,^{21–24} BiTeCl ,^{25,26} BiTeI , BiTeCl ,²⁵ BiTeI ,^{27–29} BiTeBr ,²⁸ BiTeBr ,²⁸ AsI ,^{30,31} AsSeI ,^{30–33} AsTeI ,³¹ SbSeI ,³⁴ SbTeI ,³⁵ and AsTeI .³¹

Typically, a mixture of pure elements (or M^V-X^{VII} metal halides with M^V-Q^{VI} type compounds, where $M = As, Sb, Bi$; $Q = S, Se, Te$; $X = Cl, Br, I$) in a stoichiometric ratio with a slight excess of the halide is placed in either a glass or quartz ampoule and sealed at low pressure (of the order of or below 1 Pa). An excessive amount of halide, especially I_2 , due to its volatility, is necessary when the stoichiometric crystal structures are desired.²¹ Such a sealed ampoule is then placed in the furnace and heated above the melting temperature of compounds in the mixture. The temperature is maintained for some period of time, typically ranging from few hours to even weeks. Then, the sample is slowly cooled down. These conditions may differ significantly from one synthesis to another one. Kanchana and Arivuoli heated the mixture to 720–820 K (20 K above the melting temperature) and kept it at this temperature for 4 hours to obtain BiSeI.²¹ Significantly lower temperature was used by Moroz *et al.* (~500 K); however, the crystallization time was extended to 250 hours.²³ Braun and co-workers used a higher temperature (873 K) and crystallization time of 1 week.²² Similar temperature was used by Rosenthal *et al.*, but with a crystallization time of 15 h.²⁴ All of the described syntheses led to crystalline products. It has been shown that reducing the cool down phase duration may lead to amorphous products. Cooling AsSeI melt from 723 K at a rate of 10 K min^{-1} or quenching it with icy water resulted in the formation of amorphous, semiconducting glasses.^{31,32} It has also been shown that with this method one can synthesize non-stoichiometric compounds simply by varying the molar ratio of precursors in the initial mixture.^{21,23,31}

The crystallization from melt method was also used with a temperature gradient to synthesize more complex compounds, such as $Bi_{11}Se_{12}Cl_9$ crystals.³⁶ The ampoule, prepared similarly to that in the regular method, was placed in a temperature gradient of 70 K (1319 K in the hot zone, 1249 K in the cold zone). The crystallization occurs in the colder part of the ampoule. The $Bi_{11}Se_{12}Cl_9$ crystals obtained by this method grew up to 5 mm. The growth from melt method allows obtaining polycrystalline intercalated compounds as well, such as $Cu_xBiTe_{1-y}I_{1+y}$ ³⁷ or $In_2Bi_3Se_7I$ and $InBi_2Se_4I$ phases.²⁴

Gas phase growth

Growth from vapour techniques were also applied to synthesize V–VI–VII compounds. Mainly two distinct types of this technique are distinguished: chemical vapour transport (CVT), which is sometimes termed chemical transport reaction (CTR), and physical vapour transport (PVT). Both methods are widely applicable and allow obtaining high-purity single crystals.

The CVT method, additionally, makes it possible to obtain crystals that cannot be synthesized by Czochralski or Bridgman–Stockbarger techniques, such as compounds decomposing prior to melting or reacting with solutions. Basically, CVT relies on a chemical reaction between the starting compound and the transporting agent in the hotter part of the vessel, resulting in a volatile product, which is then transferred into the colder part of the vessel, where the back reaction occurs. The transporting agent is released and the parent solid grows into a

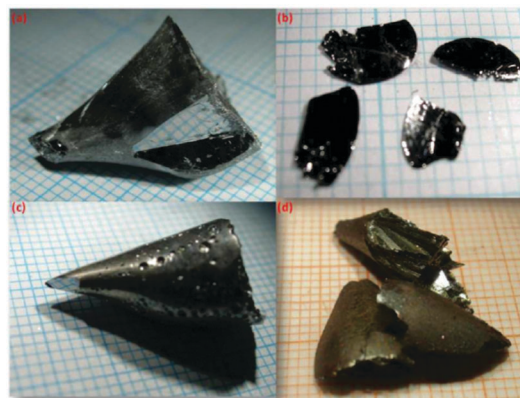


Fig. 2 BiTeI single crystals obtained by the (a) growth from melt, (b) chemical vapour transport and (c) Bridgman methods. Hygroscopic Mn-intercalated BiTeI after 1 day of exposure to air (d). Reproduced from ref. 27 with permission from the Royal Society of Chemistry.

crystalline form.³⁸ This method was used to synthesize BiTeI^{27,39,40} and BiOCl.⁴¹ The disadvantage of CVT is the possibility of a minor contamination of crystals with transporting agent molecules. Sankar *et al.* synthesized BiTeI single crystals with three methods (growth from melt, the Bridgman technique and CVT) and achieved the highest quality crystals with the Bridgman technique approach (Fig. 2).²⁷ The CVT approach was also used to synthesize antimony oxyhalides: SbOF and SbOCl.⁴² $SbCl_3$ in the gaseous state was passed under slow flow and pressure reduced to 0.5 Torr over heated Ag_2O (503 K) and NaF (823 K).²⁷

The PVT method is identical in principle to the CVT; however, it does not utilize the transport agent. The starting crystal is heated to its sublimation temperature and transferred with an inert gas (such as Ar) flow into the cold zone, where the crystal is formed.⁴³ With this technique, BiTeI⁴⁴ and BiSeI⁴⁵ crystals were synthesized.

The growth from vacuum technique is in principle related to the CVT and PVT methods. Here, the mixed precursors of the target compound are subjected to sublimation and react in the gaseous phase, and crystal growth occurs from the vapour.⁴⁶ Various materials, including BiSeI,⁴⁶ BiTeI,⁴⁷ BiSI and SbSI,⁴⁸ were prepared this way from mixtures of pure elements. With this technique, Arivuoli and coworkers observed BiSeI crystallizing into a platelet form for the first time.⁴⁹ The growth from vacuum method allows also obtaining relatively large high purity crystals (e.g. BiSeI of dimensions $2 \times 2 \times 10 \text{ mm}^3$).⁵⁰

Wet chemical methods

V–VI–VII compounds can be synthesized with chemical methods as well. Kunioku *et al.* presented a route to obtain BiSI and BiSeI from BiOI and $BiSeBr_{1-x}I_x$ from $BiOBr_{1-x}I_x$ by low-temperature treatment with diluted H_2S and H_2Se , respectively.¹⁸ This method requires temperatures significantly lower than Bridgman and vacuum transport techniques (423 K compared to ~680 K), takes less time and provides control over the band gap. Hu *et al.* applied an electrochemical method to prepare porous BiOBr thin films on a Bi substrate.⁵¹ The precipitation from solution

method is also used to synthesize bismuth oxyhalides. BiOCl, BiOBr and BiOI exhibiting enhanced photocatalytic properties (in comparison with TiO₂) were obtained by precipitation from Bi(NO₃)₃ solution in water/ethanol solvent with KCl, KBr and KI, respectively.^{52,53} BiOF/B₂O₃ nanoparticles were precipitated from Bi(NO₃)₃ and NaF solution in ethylene glycol.⁵⁴ A BiOI thin film might be obtained through the hydrolysis of HBiI₄, a compound formed when Bi₂O₃ is dissolved in an excess of hydroiodic acid.⁵⁵

Both solvo- and hydrothermal methods are also commonly utilized. Zhu *et al.* obtained micrometer-sized BiSeI and BiSeCl crystals with autoclave synthesis in water/ethanol mixtures.⁵⁶ Varying the pH of the solution in hydrothermal synthesis was shown to affect the stoichiometry of the resulting compound. A Bi₅O₇-Br photocatalyst was obtained in hydrothermal synthesis in alkaline solution at pH = 13, while BiOBr is obtained at neutral pH.⁵⁷ The size and shape of the final product can be controlled by either the reaction conditions or starting reagents. BiTeI hollow microspheres of submicrometer size were obtained from initial Bi₂Te₃ and I₂ solution in a 1 : 6 molar ratio.⁵⁸ Fa *et al.* obtained BiOI nanolamellae and BiSI nanowires by performing competitive growth of these compounds and tuning the growth conditions with the quantity of thiourea in the solution.⁵⁹ With increase of thiourea concentration, the rod-like morphology becomes favoured. Similar shape-tuning with citric acid was shown for BiOCl sub-microcrystals in the precipitation method, exhibiting morphological changes from nanoflakes to hollow microspheres.⁶⁰

Sonochemistry

A sonochemical synthesis is a process using ultrasonic radiation to facilitate the chemical reactions. An acoustic wave is used to create and sustain the cavitation process – a large difference in the pressure created by the acoustic irradiation breaks molecular and van der Waals interactions. Immediate collapse of the bubble leads to the generation of localized hotspots (the theoretical temperatures could reach up to 25 000 K)⁶³ and pressures up to 1700 atm.⁶⁴ Those conditions are favourable for the formation of 1D nanostructures. This method can be successfully applied under ambient temperature and pressure.

The sonochemical method is preferentially used in the synthesis of antimony sulphoiodide (SbSI)⁶⁴ and antimony selenoiodide (SbSeI).⁶⁴ Pure elements in a stoichiometric ratio (antimony, sulfur/selenium and iodine) are placed in a flask. Common solvents used for this process are mostly alcohols (ethanol, methanol, isopropanol), whereas water is rarely used. Subsequently, the flask is immersed in an ultrasonic bath. The required time may be varied depending on the conditions and used reagents. It is usually assumed that the process is finished when the colour stops changing as a function of time (Fig. 3). The synthesis can be carried out at various temperatures but usually takes place at 323 K.⁶⁴

Bridgman technique

The Bridgman method is utilized for the synthesis of mono-crystals. Pure elements in a stoichiometric ratio is placed in a quartz ampoule with a conical tip. Upon sealing in a vacuum,

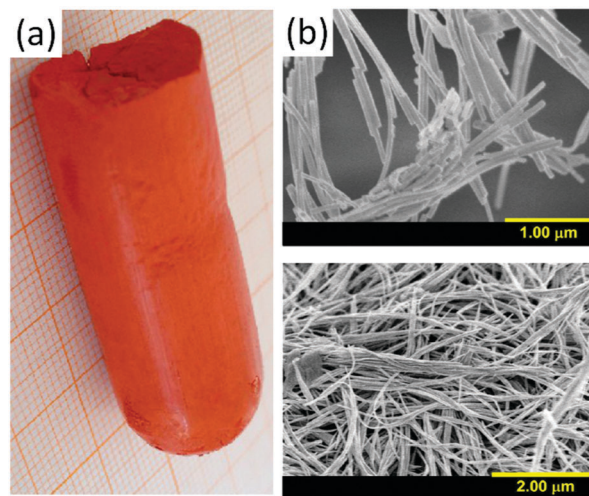


Fig. 3 Sonochemically prepared SbSI aerogel (a) and the SEM images of a sonochemically synthesized SbSI sample (b). Adapted from ref. 61 with the permission of Elsevier and from ref. 62 with the permission of IOP Publishing Ltd.

the sample is put into a furnace with a temperature gradient. Upon melting, the ampoule is moved slowly towards a low temperature zone. Temperatures within the range from 763 K to 873 K are usually sufficient to obtain good quality crystals.

Materials usually obtained with this method after proper adjustment are BiTeBr, BiTeI,⁶⁵ BiTeCl,⁶⁶ SbSI, BiSI, BiSeI and SbSeI.⁶⁷

Crystallography

In this work we focus on the M^V-Q^{VI}-X^{VII} family of compounds, where M is As, Bi, or Sb; Q is O, Se, Te, or S; and X is F, Cl, Br or I. The composition and local and long range structure determine the physical and electronic properties of the materials. The most obvious example is the change in the band gaps of chalcogenides, which decreases in the series F → Cl → Br → I. The orientation of the crystal on the substrate is important in photovoltaics and photocatalysis. The vertical orientation of the BiSI and BiSeI chains on the substrate promotes carrier transport along the covalently bonded fragments and the enforced vertically aligned grain boundaries may occur parallel to the chains and minimize charge carrier recombination.⁶⁸

Crystal structures of AsQX

Ternary chalcogenides containing As, O, S, Se and halogen atoms were mostly investigated in the 70s and 80s. Arsenic chalcogenides tend to form glass structures with short range order and the majority of the works consider the glass phase formation and its properties.³¹ All confirmed that stable crystalline phases are in the monoclinic system and form chain-like motifs. There are known glasses containing Cl or Br atoms; however, no single crystal structure has been obtained so far. Moreover, As-O-X (X – any halide) systems do not form any crystal phases, except for AsOCl₃, which forms dimers in the P2₁/c space group and must be handled at low temperature (–233 K) and in a dry environment

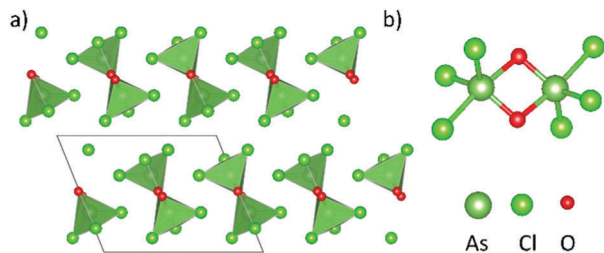


Fig. 4 The crystal structure of AsOCl_3 viewed along the b axis direction (a), and coordination around As atoms in the dimer (b).

due to its facile hydrolysis (Fig. 4).⁶⁹ AsOF_3 was also mentioned in the literature.⁷⁰ As–S–Cl or As–S–Br systems form glasses and their crystal structures have not been obtained so far.^{71–74}

Although systems composed of As, S and I atoms usually form glasses,^{31,73,75–80} a stable crystalline AsSI structure has been determined from X-ray powder data. AsSI crystallizes in the monoclinic space group $P2_1$. The similarity between V–VI–VII type chalcogenides allows assuming a chain-like structure of As–S–As with the iodine atom bonded to the arsenic atoms.^{30,81–83} AsSeCl ternary chalcogenides cannot be found in the literature, even among glasses, whereas AsSeBr can form the glass phase.^{72,77}

Both the glass^{31,32} and crystal^{75,84} phases of AsSeI have been examined. AsSeI exist in two phases: stable α and metastable β .^{84,85} α - AsSeI crystallizes in the monoclinic system and the $P2_1$ space group. β - AsSeI is cubic and belongs to the $F4_132$ space group. The stable α form consists of trigonal pyramids with the arsenic atom located at the apex of the triangle and selenium atoms connecting the triangles (Fig. 5a).

Besides the glass phases,^{72,77,86,87} the As–Te–I system forms four crystal structures: $\text{As}_4\text{Te}_5\text{I}_2$, $\text{As}_5\text{Te}_7\text{I}$, α - AsTeI and β - AsTeI .^{75,81,88} α - AsTeI crystallizes in the monoclinic system and the $P2_1$ space group. It forms a double-chain structure where the tellurium atom bonds three arsenic atoms – similar arrangement can be found in SbSI . The cubic ($Fm\bar{3}m$) β - AsTeI is metastable and transforms into α - AsTeI after annealing. The monoclinic $\text{As}_5\text{Te}_7\text{I}$ crystallizes as grey needle-like crystals in the $C2/m$ space group. The $\text{As}_5\text{Te}_7\text{I}$ structure has two types of As atoms: one is octahedrally coordinated, and the other As atom coordinates seven Se atoms and forms a composite polyhedron – the combination of the tetragonal pyramid and the prism (Fig. 5b).⁸⁸

Crystal structures of SbQX

Antimony oxyhalides were investigated mostly in the 70s and have not attracted much attention since then. SbOF belongs to

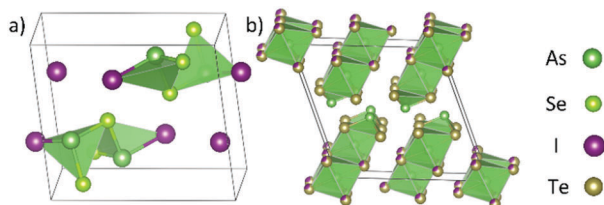


Fig. 5 The crystal structures of AsSeI (a) and $\text{As}_5\text{Te}_7\text{I}$ (b).

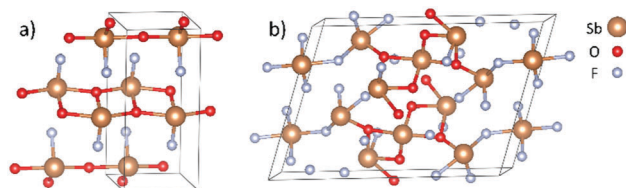


Fig. 6 The crystal structures of SbOF (a) and $\text{Sb}_3\text{O}_2\text{F}_5$ (b).

the $Pnma$ space group and has a ladder-like arrangement of Sb and O atoms (Fig. 6a).⁸⁹

$\text{Sb}_3\text{O}_2\text{F}_5$ crystallizes in the $P2/c$ space group.⁹⁰ Both structures have four coordinated O or F atoms and a stereochemically active lone pair on the Sb(III) centre (Fig. 6). In the Sb–O–F system of hygroscopic compounds SbOF_3 and SbO_2F were also reported.⁷⁰

Antimony oxychlorides SbOCl , $\text{Sb}_4\text{O}_5\text{Cl}_2$ and $\text{Sb}_8\text{O}_{11}\text{Cl}_2$ crystallize in the $P2_1/a$, $P2_1/c$ and $C2/m$ space groups respectively.^{91–93} $\text{Sb}_4\text{O}_5\text{Cl}_2$ has a ladder-like structure, which can be often found in the Sb–O–X family. The structure of $\text{Sb}_8\text{O}_{11}\text{Cl}_2$ is isomorphic with $\text{Sb}_8\text{O}_{11}\text{Br}_2$.⁹¹ Several structures in the Sb–O–I system can be found. $\text{Sb}_5\text{O}_7\text{I}$ exists in two different phases: the ferroelastic monoclinic phase α - $\text{Sb}_5\text{O}_7\text{I}$ ($P2_1/c$) stable and at low temperature and the hexagonal β - $\text{Sb}_5\text{O}_7\text{I}$ ($P6_3/m$) one stable at high temperature (Fig. 7).⁹⁴ $\text{Sb}_3\text{O}_4\text{I}$ undergoes thermal degradation first to $\text{Sb}_8\text{O}_{11}\text{I}_2$ next to $\text{Sb}_5\text{O}_7\text{I}$ then finally to Sb_2O_3 .⁹⁵

The SbSeX family has two 1 : 1 structures (SbSeI and SbSeBr) that both crystallize in the $Pnam$ space group. SbSeI , in which each Sb atom is five coordinated by three Se atoms and two iodine atoms (Fig. 8a), has attracted the most interest.^{96,97} The five atoms (two I, two Se and Sb) form the base of a square pyramid with the third Se atom on the apex. Unusual structures can be found in the Sb–Se–F system. The crystal structures of $\text{Se}_{10}(\text{SbF}_6)_2$, $(\text{Se}_4)_2(\text{Sb}_4\text{F}_{17})(\text{SbF}_6)_3$, and $(\text{Se}_4)(\text{Sb}_2\text{F}_4)(\text{Sb}_2\text{F}_5)(\text{SbF}_6)_5$ contain the square-planar chalcogen cation Se_4^{2+} (or boat-shape Se_{10}^{2+} , Fig. 9).^{98–100}

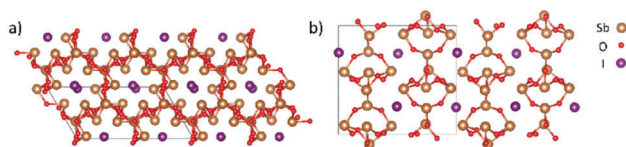


Fig. 7 The crystal structure of α - $\text{Sb}_5\text{O}_7\text{I}$: view along the b axis (a) and view along the a axis (b).

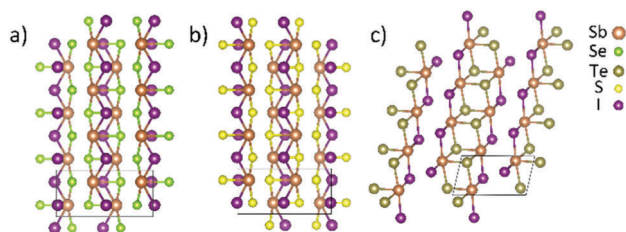


Fig. 8 The crystal structures of SbSeI (view along the a axis) (a), SbSI (view along the b axis) (b), and triclinc SbTeI (view along the b axis) (c).

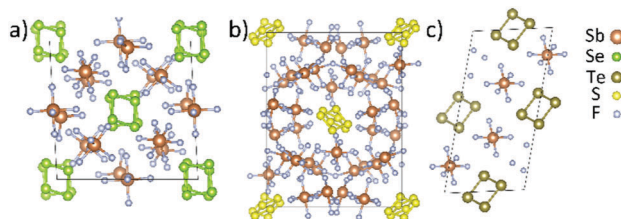


Fig. 9 Crystal structures of $(\text{Se}_4)_2(\text{Sb}_4\text{F}_{17})(\text{SbF}_6)_3$ (view along the *b* axis) (a), $\text{S}_4(\text{Sb}_2\text{F}_4)(\text{Sb}_2\text{F}_5)(\text{SbF}_6)_5$ (view along the *a* axis) (b), and $(\text{Te}_4)(\text{SbF}_6)_2$ (view along the *a* axis) (c).

The compounds SbSBr and SbSI are known for their ferroelectric properties and belong to the *Pnma* and *Pna21* space groups in the ferroelectric and the paraelectric phase respectively.^{16,101,102} These orthorhombic structures consist of pleated double chains arranged along the *c* axis (Fig. 8b). Several other structures in the Sb–S–X system have been obtained. The trigonal pyramids with the Se atom at the apex and connected by the sulfur atom form the structure of $\text{Sb}_4\text{S}_5\text{Cl}_2$.¹⁰³

All three structures of $\text{S}_{19}(\text{SbF}_6)_2$, $\text{S}_8(\text{Sb}_3\text{F}_{14})(\text{SbF}_6)$ and $\text{S}_4(\text{Sb}_2\text{F}_4)(\text{Sb}_2\text{F}_5)(\text{SbF}_6)_5$ contain sulfur cations S_{19}^{2+} , S_8^{2+} or S_4^{2+} (Fig. 9b).¹⁰⁴ The crystal structure of SbTeI is triclinic and belongs to the *P1* space group although the monoclinic structure (*C2/m*) was also determined (Fig. 8c).^{35,97} Similarly to the Sb–S–F family, the Sb–Te–F system has compounds that contain the chalcogen cation M_4^{2+} . The planar-square Te_4^{2+} cations in $(\text{Te}_4)(\text{SbF}_6)_2$ are balanced with SbF_6^- anions (Fig. 9c).¹⁰⁰

Crystal structures of BiQX

Bismuth oxyhalochalcogenides with 1:1:1 BiOX (*X* = F, Cl, Br, I) stoichiometry belong to the tetragonal space group *P4/nmm*.^{55,105,106} All four BiOX share the layered structure in which a positive charge of $[\text{Bi}_2\text{O}_2]^{2+}$ is compensated for with halogen ions (Fig. 10a). Each Bi atom is surrounded by four O atoms and four halogen atoms, forming an asymmetric decahedron connected in the $[\text{X}-\text{Bi}-\text{O}-\text{Bi}-\text{O}-\text{X}]$ motifs, held together by van der Waals forces (Fig. 10).

This decahedral structure distinguishes BiOX from other ABX halochalcogenides with *Q* = S, Se or Te in which the coordination polyhedra are octahedra or 7-coordination polyhedra.¹⁰⁵ In the series $\text{F} \rightarrow \text{Cl} \rightarrow \text{Br} \rightarrow \text{I}$ the lattice

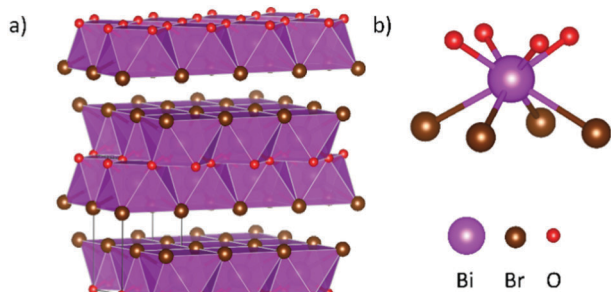


Fig. 10 The crystal structure of BiOBr (a) and the coordination of the Bi atom (b).

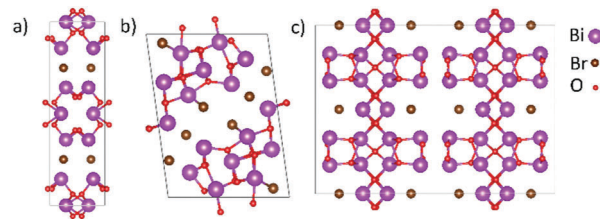


Fig. 11 The crystal structures of $\text{Bi}_5\text{O}_4\text{Br}$ (view along the *b* axis) (a), $\text{Bi}_4\text{O}_5\text{Br}_2$ (view along the *b* axis) (b), and $\text{Bi}_5\text{O}_7\text{Br}$ (view along the *b* axis) (c).

parameter *c* grows from 6.23 Å to 9.15 Å (about 46%) due to the growth of the ionic radius of the halogen atom, while the lattice parameter *a* expands from 3.75 Å to 4.09 Å (only 9%). Besides the well-known BiOX (1:1) compounds, several other compositions in the Bi–O–X system can be found. Usually the thermal decomposition of BiOI leads to the formation of the monoclinic $\text{Bi}_4\text{O}_5\text{I}_2$ (2.5:1 ratio, homologous with $\text{Bi}_4\text{O}_5\text{Br}_2$).^{107,108} In these structures the $[\text{Bi}_4\text{O}_5]^{2-}$ layers are separated from each other by I^- (or Br^-) layers (Fig. 11).

Other closely related structures are $\text{Bi}_{24}\text{O}_{31}\text{Cl}_{10}$ and $\text{Bi}_{24}\text{O}_{31}\text{Br}_{10}$,¹⁰⁹ $\text{Bi}_5\text{O}_7\text{Br}$ and $\alpha\text{-Bi}_5\text{O}_7\text{I}$, and $\text{Bi}_3\text{O}_4\text{Br}$ and $\text{Bi}_3\text{O}_4\text{Br}$ compounds.^{110,111} $\beta\text{-Bi}_5\text{O}_7\text{I}$, $\text{Bi}_7\text{O}_9\text{I}_3$, $\text{Bi}_{12}\text{O}_{17}\text{Cl}_2$, $\text{Bi}_{12}\text{O}_{17}\text{Br}_2$, $\text{Bi}_{12}\text{O}_{16}\text{Cl}_4$, and $\text{Bi}_7\text{O}_9\text{F}_{11}$, which share more irregular (less layered) structures, also belong to the Bi–O–X system.^{110,112,113}

In the family of BiTeX (*X* = Cl, Br, I) halochalcogenides the common feature is the formation of $[\text{BiTe}]^+$ layers (Fig. 12a).²⁸ BiTeCl has a hexagonal structure and the *P6₃mc* space group. The crystal consists of Bi, Te and Cl atom layers and has an almost twice as large *c* parameter as the BiTeBr and BiTeI structures.¹¹⁵ BiTeBr (the *P3₂m1* space group) has a two-layer structure: one layer is made of Bi atoms and the other layer is made of statistically distributed Te and Br atoms.^{28,116} BiTeI

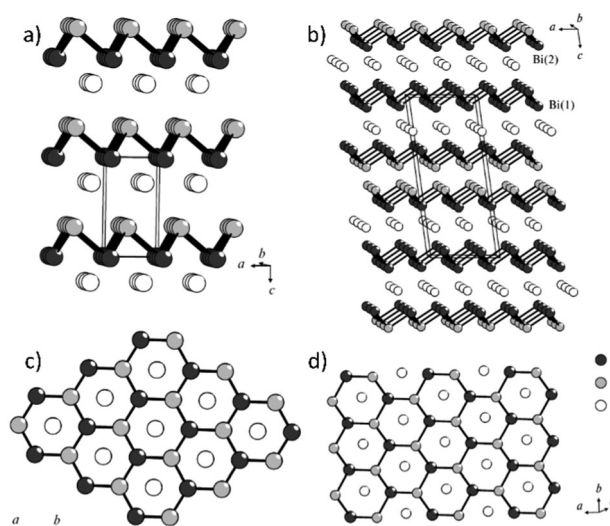


Fig. 12 The crystal structure of BiTeI (an overall view) (a), the crystal structure of Bi_2TeI (an overall view) (b), a projection onto the *ab* plane of BiTeI (c), and corrugated BiTe layers against the background of the planar iodine layers (d). Adapted from ref. 114 with the permission of Springer.

crystallizes in the trigonal space group $P3m1$. Each Bi atom is six-coordinated by three I atoms and three Te atoms in the form of an asymmetric octahedron (Fig. 12c).¹⁰⁵ The Bi–Te–I system, besides the 1:1 structures, contains two other ternary compounds: Bi_2TeI and $\text{Bi}_4\text{TeI}_{1,25}$.^{114,117} Bi_2TeI crystallizes in the monoclinic system (the $C/2m$ space group) and contains a double layer of bismuth stacked between two iodide layers. The arrangement Te–Bi–I–Bi–Bi–I–Bi–Te is presented in Fig. 12b and d.¹¹⁴ Interesting structures with polymeric Te cations can be found in the Bi–Te–Cl system. The structures of $\text{Te}_8[\text{Bi}_4\text{Cl}_{14}]$ and $(\text{Te}_4)(\text{Te}_{10})[\text{BiCl}_{16}]$ belong to the orthorhombic $P2_12_12_1$ and the triclinic $P\bar{1}$ space groups respectively. In these structures the polymeric cations $(\text{Te}_8^{2+})_n$, $(\text{Te}_{10}^{2+})_n$ and $(\text{Te}_4^{2+})_n$ were found.^{118,119}

The Bi–Se–X system with a 1:1:1 ratio includes the BiSeCl , BiSeBr and BiSeI structures.^{20,22,28} BiSeCl and BiSeBr belong to the $Pnam$ space group. BiSeI crystallizes in the $Pbnm$ space group. The common feature of these structures is the formation of chain-like structures in which neighboring Bi atoms are bridged by three Se atoms and two halogen atoms (*vide infra*).^{22,49,120} Outside the 1:1 ratio compounds, in the Bi–Se–Cl system, the compound $\text{Bi}_{11}\text{Se}_{12}\text{Cl}_9$ that belongs to the monoclinic $C2/m$ space group has been found.¹²¹

BiSbI crystallizes in the orthorhombic space group $Pnma$, while the BiSbBr and BiSI structures were solved in the $Pnam$ space group.^{122–124} BiSX systems consist of parallel $[\text{X}(\text{Bi}_2\text{S}_2)\text{X}]$ rods and, similarly to BiSeI , form chain-like structures (*vide infra*). BiSX ternary systems also include the isomorphous $\text{Bi}_{19}\text{S}_{27}\text{Cl}_3$, $\text{Bi}_{19}\text{S}_{27}\text{Br}_3$, and $\text{Bi}_{19}\text{S}_{27}\text{I}_3$ structures belonging to the $P6_3/m$ space group.^{125–129} Recently, the structure with the formula $\text{Bi}_{19}\text{S}_{27}\text{I}_3$ has been redetermined as $\text{Bi}_{13}\text{S}_{18}\text{I}_2$; therefore the other two isomorphous structures are likely to be redetermined in the near future.¹³⁰ The $\text{Bi}_{13}\text{S}_{18}\text{I}_2$ structure has subvalent Bi_2^{4+} dimers and a ribbon-like structure $(\text{Bi}_4\text{S}_6)_\infty$ (Fig. 13).

The common feature among 1:1:1 halochalcogenides is well illustrated in Fig. 14. In the most chalcogenides (excluding oxyhalides) a double chain-like structure forms along one of the axes (Fig. 15). The chain consists of two atoms of A connected with two atoms of B in one rectangle. The rectangles share one edge and are additionally connected

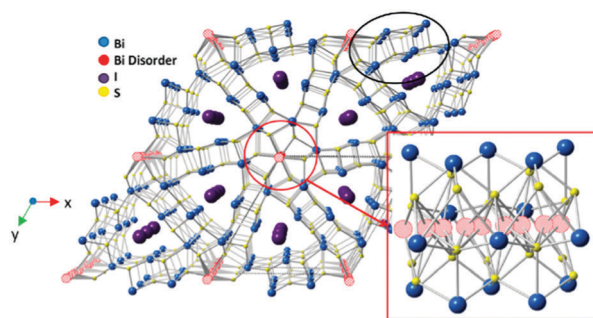


Fig. 13 Averaged cell representation of the $P6_3$ structure of $\text{Bi}_{13}\text{S}_{18}\text{I}_2$ viewed along the c axis. Inset: Normal to the c -axis to highlight bismuth (disordered/averaged dimer) sites, in hatched red. Adapted from ref. 130 with the permission of American Chemical Society.

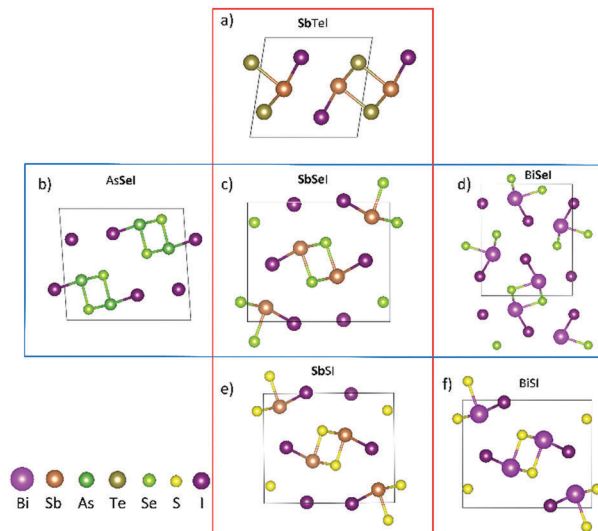


Fig. 14 The crystal structures of SbTeI (view along the c axis) (a), AsSeI (view along the b axis) (b), SbSeI (view along the b axis) (c), BiSeI (view along the b axis) (d), SbSI (view along the c axis) (e), and BiSI (view along the c axis) (f).

via halide atoms. The exception is AsSeI , in which the chain degenerates into a single one, probably due to the smaller radius of the arsenic atom, leading to its weaker Lewis acceptor properties.¹³¹

The closest nonbonding distances between iodide and atom A^{V} or B^{VI} or another iodide atom are collated in Table 1. Interactions inside the crystal structures of these halochalcogenides seem to be complex, but several regularities are noticeable. The first order interactions in the structures (A–B in Table 1) follow an obvious trend in which the bonding distance increases with radii of the atoms involved in the bonding. The second order interactions ($\text{A}\cdots\text{X}$ and $\text{X}\cdots\text{X}$ in Table 1), on the other hand, do not follow this trend that strictly: *e.g.* the smallest distances between $\text{Se}\cdots\text{I}$ and $\text{S}\cdots\text{I}$ are 3.61 Å and 3.62 Å, respectively. The I–I distances are quite large, and after the analysis of Hirshfeld surfaces, I–I is not recognized as an interaction, while $\text{A}\cdots\text{X}$ and $\text{B}\cdots\text{X}$ seem to be the most important intermolecular interactions in the crystal structure (Fig. 16). Table 2 contains combined crystal data for V–VI–VII systems of elements from groups 15, 16 and 17.

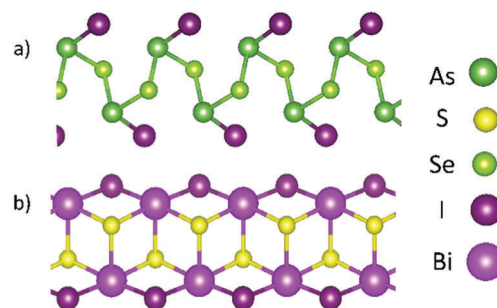


Fig. 15 The chain like structure of AsSeI (a) and the double chain-like structure of BiSI (b).

Table 1 First order interactions (M–Q) and second order interactions (Q···X and X···X) in the crystal structures of chosen V–VI–VII systems

SbTeI	Distance/Å	SbSeI	Distance/Å	SbSI	Distance/Å	AsSeI	Distance/Å	BiSeI	Distance/Å
Sb–Te	2.83, 2.95, 2.95	Sb–Se	2.79, 2.61, 2.79	Sb–S	2.49, 2.73, 2.73	As–Se	2.41, 2.44	Bi–Se	2.71, 2.86, 2.86
Sb–I	3.22, 3.22	Sb–I	3.14, 3.14	Sb–I	3.10, 3.10	As–I	2.67	Bi–I	3.24, 3.24
Sb···I	3.82	Sb···I	3.82	Sb···I	3.81	As···I	3.52, ^a 3.67	Bi···I	3.87, 3.78
Te···I	3.90, 4.01	Se···I	3.61, 3.90	S···I	3.62, 3.82	Se···I	3.87, ^a 3.91	Se···I	3.62, 3.89
I···I	4.19	I···I	4.17	I···I	4.05	I···I	4.19, ^a 3.90	I···I	4.21
						As···Se	3.07 ^a		

^a In the same chain structure.

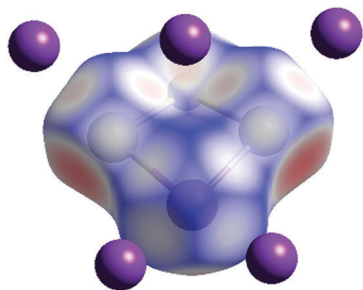


Fig. 16 Hirshfeld surface analysis of a SbSI fragment indicating Sb···I and S···I contacts as the strongest interactions (small red dots) between chains in the crystal structure. Molecular Hirshfeld surface calculations were performed using the CRYSTAL EXPLORER 17 program.¹³²

Electronic structure and optical properties from computations

Parameters that emerge from fundamental electronic structure properties and are taken into account when designing optoelectronic devices include optical band gap energy, the optical absorption coefficient and carrier diffusion lengths, determined by the minority-carrier lifetime (τ) and mobility (μ). Transport related factors, τ and μ , are not easily accessible from experiment nor from first-principles calculations. However, it is possible to gain some information indirectly with well-established computational density functional theory (DFT) methods *via* parameters like the dielectric constant, band bonding character, band dispersion, and effective mass (Table S1, ESI†). High dielectric constants suggest long carrier lifetimes, large diffusion lengths, and effective screening of charged defects. The band bonding character has an implication on the band dispersion relation and on the charge carrier effective masses. Usually, the lower/higher effective mass means higher/lower migration capability and a low/high recombination probability of carriers within semiconductor materials.

The partially oxidized post-transition metal cations Bi³⁺ and Sb³⁺ with ns^2np^0 and chalcogen (O, S, Se, Te) and halogen (X = F, Cl, Br, I) anions with np^6 constitute V–VI–VII type chalcogenide compounds. During the formation of bonds, charge transfer occurs from the cation p to anion p states, resulting in an s lone-pair on the cation. This ns^2 configuration is closely related to the success of these compounds as optoelectronic materials. The valence band (VB) is formed as a result of the overlap of the anion-p with cation-s orbitals with the antibonding maximum (VBM), as depicted in Fig. 17. It is

the relative energy of these orbitals that determines the extent of s contribution to the top of the valence band – energetically closer orbitals result in greater s contribution and thus in a stronger lone pair, resulting in a significant stabilisation effect.^{68,168} As such, the stabilities of these compounds increase up the chalcogen or the halide group, connected with the increasing lone pair effect and ionic character.¹⁶⁹ Hybridization of these antibonding states with cation p states produces an asymmetric electron density responsible for the distortion of the pseudo-octahedra.¹⁷⁰ The antibonding states at the top of the VB also greatly improve defect tolerance¹⁷¹ – it was recently demonstrated that the antibonding character of the valence band maximum (VBM), which leads to shallow intrinsic defects and no surface states.¹⁷² The conduction band (CB) of these compounds is dominated by the spatially extended cation p states with a tendency to cross gap hybridization with the anion p states of the valence band.

The representative electron density of states (DOS), total and projected onto atoms and orbitals, is shown in Fig. 18. The valence band of BiOF¹⁷³ consists of well separated bands. The crystal's upper valence band consists of Bi-6p, O-2p, F-4p and some Bi-6s hybridized orbitals, while the lowest energy band originates mainly from the s orbitals of each atomic component. This is typical for group 15 chalcogenides. DOS have been reported for crystals of SbOX,¹⁶⁹ Sb–S,Se–X,^{173–178} SbTeX,^{177,179} BiOX,^{169,180–186} Bi–S,Se–X^{50,68,169,187–191} and BiTeX.^{156,179,192–194}

The value of the gap can be engineered by a choice of chalcogen or halide: smaller band gaps are found for heavier chalcogenide and halide compositions (Fig. 19 and Table 3).^{50,68,156,169,173–175,177,179,180,182–186,188–190,192–210} It was suggested that despite possessing indirect band gaps, these semiconductors can achieve a fair optoelectronic performance as the differences between the direct and indirect band gaps are small.⁶⁸ The presence of filled ns^2 orbitals have also been associated with the dispersive valence and conduction bands, and therefore low effective masses.¹⁶⁸ Indeed, the calculated effective masses of electrons and holes in these compounds are in many cases lower than or around the rest mass of electrons (m_e).¹⁶⁹ The presence of a heavy cation, and thus large relativistic effects, results in an increase of the conduction band width through a significant lowering of the conduction band minimum (CBM).¹⁷¹ The relativistic renormalisation of the conduction band of BiSI and BiSeI was found to be over 0.6 eV, highlighting the importance of including spin orbit effects in modelling these systems.⁶⁸ The shape of the bands and the electron and hole effective masses are generally insensitive to the level of theory.^{169,211}

Table 2 Crystal data for V–VI–VII systems of elements from groups 15, 16 and 17

Chemical formula	Mol. mass/AMU	Crystal system	Space group	<i>a</i> /Å	<i>b</i> /Å	<i>c</i> /Å	β /deg.	Unit cell volume/Å ³	Z*	Ref.
AsSBr	186.88	Glass	—	—	—	—	—	—	—	71 and 74
AsSI	233.88	Glass	—	—	—	—	—	—	—	78, 79 and 82
AsSeI	280.78	Monoclinic	<i>P2</i> ₁	8.61	4.22	9.95	97.2	358.67	4	81
α -AsSeI		Monoclinic	<i>P2</i> / <i>m</i>	8.839	4.189	9.775	93.87	361.11	4	75 and 133
β -AsSeI ^d		Monoclinic	<i>P2</i> ₁	8.855	4.194	9.792	93.74	362.88	4	81
α -AsTeI	329.42	Monoclinic	<i>F4</i> ₁ 32	11.05				1349.23	16	81
β -AsTeI ^d		Cubic	<i>P2</i> ₁	8.965	4.042	10.341	90.75	374.69	4	81
AsOCl ₃	197.27	Monoclinic	<i>Fm</i> 3 <i>m</i> ^d	5.791				194.21	2	81
As ₄ Te ₅ I ₂	1191.48	Monoclinic	<i>P2</i> ₁ / <i>C</i>	8.043	6.131	10.197	111.99	466.25	2	134
As ₅ Te ₇ I	1394.7	Monoclinic	<i>C2</i> / <i>m</i>	14.58	4.00	12.26	95.0	712.28	2	81
SbOF	156.75	Orthorhombic	<i>C2</i> / <i>m</i>	14.566	14.0353	13.8633	110.53	2644.18	4	75 and 88
SbSBr	233.71	Orthorhombic	<i>Pnam</i>	8.873	4.099	5.483		119.42	4	135
			<i>Pnam</i>	8.2424	9.7556	3.9680		319.07	4	75 and 136
			<i>Pnma</i>	8.20	9.70	3.95		314.18	4	125
			<i>Pnma</i>	8.20	9.70	3.75		298.28		137
SbSI	280.71	Orthorhombic	<i>Pnma</i>	8.49	10.10	4.16		356.72	4	125
				8.527	10.140	4.089		353.55		67
				8.48	10.12	4.16		357.00		138
				8.563	10.15	4.097		356.09		139
				8.58	10.17	4.14		361.25		140
				8.53	10.05	4.10		351.48		141
				8.58	10.17	4.14		361.25		142
				8.587	10.190	4.146		362.78		142
			<i>Pma2</i> ₁	8.473	10.478	4.247		37.70		142
SbSI (321 K)			<i>Pnam</i>	8.522	10.130	4.088		352.91	4	75
SbSI (274.5 K)			<i>Pna2</i> ₁	8.525	10.137	4.097		354.05	4	75
SbSeBr	280.61	Orthorhombic	<i>Pnam</i>	8.30	9.75	3.95		319.65	4	75
			<i>Pnma</i>	8.30	10.20	3.95		334.41	4	125
SbSeI	327.61	Orthorhombic	<i>Pnam</i>	8.6862	10.397	4.145		374.20	4	75 and 96
			<i>Pnma</i>	8.65	10.38	4.12		369.92	4	125
			<i>Pnma</i>	8.698	10.412	4.127		373.76		67
			<i>Pnma</i>	8.698	10.412	4.127		373.76		143
SbTeI	329.42	Monoclinic	<i>C2</i> / <i>m</i>	13.701	4.242	9.201	128.63	417.72	4	35 and 75
			<i>C2</i> / <i>m</i>	14.55	4.23	13.72	81.12	834.30	8	125
		Orthorhombic	<i>Pmmm</i>	9.18	10.8	4.23		419.38	4	125
			<i>Pmmm</i>							
			<i>Pmmm</i>							
Sb ₄ O ₅ Cl ₂	637.9	Monoclinic	<i>P2</i> ₁ / <i>c</i>	6.229	5.107	13.50	97.27	426.00	2	91
Sb ₄ O ₅ Br ₂	726.8	Monoclinic	<i>P2</i> ₁ / <i>c</i>	6.593	5.133	13.43	97.89	450.194	2	91
Sb ₅ O ₇ I	847.65	Monoclinic	<i>P2</i> ₁ / <i>c</i>	6.772	12.726	13.392	120.1	998.50	4	144
Sb ₄ S ₅ Cl ₂	718.2	Orthorhombic	<i>Pnam</i>	10.630	9.489	11.147		1124.38	4	75
			<i>Pnam</i>	10.53	9.38	11.08		1094.39	4	125
Sb ₄ S ₉ Br ₂	935.34	Monoclinic	<i>C2</i>	11.642	12.235	18.546	90.2425	2641.6829		145
BiOF	243.98	Tetragonal	<i>P4</i> / <i>nmm</i>	3.756		6.234		87.9	2	146
BiOCl	260.43	Tetragonal	<i>P4</i> / <i>nmm</i>	3.891		7.369		111.57	2	147
				3.883		7.347		110.78	2	41
				3.89		7.37		111.52		148
				3.894		7.369		111.74		149
				3.928		7.538		116.31		150
BiOBr	304.88	Tetragonal	<i>P4</i> / <i>nmm</i>	3.926		8.103		124.90		151
				3.924		8.101		124.74		149
BiOI	351.88	Tetragonal	<i>P4</i> / <i>nmm</i>	3.992		9.151		145.83		149
				3.99		9.14		145.51		59
BiSCl	276.49	Orthorhombic	<i>Pnam</i>	7.7508	9.9920	3.9955		309.44	4	75 and 152
			<i>Pnma</i>	7.70	9.87	4.00		304.00	4	125
			<i>Pnam</i>	7.7396	9.9824	3.9238		303.15		150
BiSBr	320.94	Orthorhombic	<i>Pnam</i>	8.1666	9.8532	4.0492		325.83	4	75 and 152
			<i>Pnam</i>	8.02	9.70	4.01		311.95	4	137
BiSI	367.94	Orthorhombic	<i>Pnam</i>	8.519	10.177	4.472		387.71	4	75 and 153
			<i>Pnma</i>	8.46	10.15	4.14		355.50	4	125
			<i>Pnam</i>	8.462	10.153	4.145		356.12		67
				8.73	10.54	4.18		284.62		138
				8.5138	10.264	4.1742		364.77		150
			<i>Pnma</i>	8.45	10.05	4.12		349.88		154
			<i>Pnma</i>	8.51	10.26	4.17		364.09		59
BiSeCl	323.39	Orthorhombic	<i>Pnam</i>	8.0787	9.3046	4.2182		317.08	4	20 and 75
			<i>Pmmm</i>	12.37	18.10	4.08		913.50	12	125
BiSeBr	367.84	Orthorhombic	<i>Pnam</i>	8.16	10.47	4.11		351.14	4	75 and 153
			<i>Pnma</i>	8.18	10.47	4.11		352.00	4	125
BiSeI	414.84	Orthorhombic	<i>Pnam</i>	8.71	10.58	4.12		379.67	4	75 and 96

Table 2 (continued)

Chemical formula	Mol. mass/AMU	Crystal system	Space group	<i>a</i> /Å	<i>b</i> /Å	<i>c</i> /Å	β /deg.	Unit cell volume/Å ³	Z*	Ref.
BiTeCl	372.03	Hexagonal	<i>Pnma</i>	8.71	10.45	4.19		381.37	4	125
			<i>Pnam</i>	8.713	10.542	4.193		385.14		67
				8.6899	10.5937	4.221		388.58		56
			<i>Pnma</i>	8.6967	10.574	4.2205		388.1	4	22
			<i>P6₃mc</i>	4.2413		12.4026		193.22	2	25
BiTeBr	416.48	Hexagonal	<i>P6₃mc</i>	4.2426		12.397		193.1	2	28
			<i>P3m</i>	4.22		6.67		102.87	1	75 and 155
			<i>P3m1</i>	4.23		6.47		100.26	1	125
			<i>P3m1</i>	4.266		6.486		102.25		116
			<i>P3m1</i>	4.2662		6.487		102.30	1	28
Monolayer	463.48	Hexagonal		4.27		6.46		102.00		156
				4.37		—		—		156
			<i>P3m1</i>	4.36		6.835		112.52	3	75 and 155
			<i>P3m1</i>	4.31		6.83		109.88	1	125
			<i>P3m1</i>	4.31		6.831		109.89	1	117
				4.3435		6.8547		112.00		27
				4.3421		6.8835		112.39		27
				4.3482		6.8358		111.93		27
				4.30		6.80		108.89		157
				4.344		6.912		112.96		58
				4.3392		6.854		111.8	1	28
			Bi ₇ O ₅ F ₁₁	1751.86	Monoclinic	<i>C2</i>	13.523	5.529	9.189	96.171
Bi ₃ O ₄ Cl	726.39	Monoclinic	<i>I2/a</i>	5.695	5.648	18.573	91.523	597.20	4	159
Bi ₂₄ O ₃₁ Cl ₁₀	5866.02	Monoclinic	<i>P2/c</i>	10.033	7.975	29.552	88.742	2363.8	2	109
Bi ₃ O ₄ Br	770.84	Orthorhombic	<i>Pnan</i>	5.705	5.694	18.949		615.50	4	160
Bi ₄ O ₅ Br ₂	1075.72	Monoclinic	<i>P2₁</i>	14.506	5.614	10.83	97.657	874.049	4	107
Bi ₅ O ₇ Br	1236.8	Orthorhombic	<i>Cmca</i>	16.087	5.297	23.022		1961.50	8	161
Bi ₂₄ O ₃₁ Br ₁₀	6310.62	Monoclinic	<i>A₂/m</i>	10.141	4.005	29.977	90.197	1217.5	1	109
Bi ₄ O ₅ I ₂	817.84	Monoclinic	<i>P2₁</i>	14.944	5.698	11.263	99.81	945.08	4	107
Bi ₅ O ₇ I	1283.8	Orthorhombic	<i>Ibca</i>	16.265	5.344	23.02		2000.86	8	162
Bi ₄ S ₅ Cl ₂	1067.12	Trigonal	<i>R3</i>	19.804		12.359		4197.78	15	163
			<i>R32R3m</i>	19.80		12.4		4210.01	15	125
			<i>R3m</i>							
Bi ₁₉ S ₂₇ Cl ₃	4942.59	Hexagonal	<i>P6₃</i>	15.40		4.02		825.65	2/3	125
Bi ₁₉ S ₂₇ Br ₃	5075.94	Hexagonal	<i>P6₃</i>	15.55		4.02		841.82	2/3	125
			<i>P6₃/m</i>	15.486		4.018		834.49		128
				15.486		4.0182		834.53		150
Bi ₁₃ S ₁₈ I ₂	3547.62	Trigonal	<i>P3</i>	15.612		4.0168		847.8	1	130
			<i>P3</i>	15.63237		4.019707		850.70	1	130
Bi ₁₉ S ₂₇ I ₃	5216.94	Hexagonal	<i>P6₃</i>	15.63		4.02		850.50	2/3	125
Bi ₁₁ Se ₁₂ Cl ₉	3565.35	Monoclinic	<i>C2/m</i>	24.182	8.162	36.368	91.17	7176.6	2	36
Bi ₂ TeI	672.46	Monoclinic	<i>C2/m</i>	7.585	4.381	17.740	98.20	583.47		117
				7.5112	4.3911	7.9025	97.20	258.59		164
Demicheleite-(Cl) ^a	276.11	Orthorhombic	<i>Pnam</i>	7.7933	9.9293	3.9880		308.60	4	165
Demicheleite-(Br) ^b	306.47	Orthorhombic	<i>Pnam</i>	8.0424	9.8511	4.0328		319.50	4	166
Demicheleite-(I) ^c	341.74	Orthorhombic	<i>Pnam</i>	8.4501	10.1470	4.1389		354.88	4	167

^a Bi_{0.97}S_{1.02}(Cl_{0.90}Br_{0.11}) $\Sigma=1.01$. ^b Bi_{0.97}S_{1.02}(Cl_{0.90}Br_{0.11}) $\Sigma=1.01$. ^c Bi_{0.97}S_{1.03}(I_{0.65}Br_{0.25}Cl_{0.10}) $\Sigma=1.00$. ^d The number of molecules in the asymmetric unit.

Recently, Butler *et al.*¹⁹⁸ provided a quantitative electronic structure description within the relativistic quasi-particle GW (QSGW) approximation including spin orbit coupling (SOC) of SbSI, SbSBr, and SbSeI. This truly *ab initio* method showed unusual band dispersion with high degeneracy and several electron and hole basins close to the band extrema. In comparison with the local density approximation (LDA) dispersion relation, the quasi-particle corrections increased the magnitude of the band gap, but did not alter the dispersion. The isotropic electron and hole effective masses were all calculated to be below $0.65m_e$, but larger effective masses were found for higher lying second extrema. The band gaps were consistently overestimated and compared to screened hybrid functional (HSE06) values.

The smallest indirect band gap of 2 eV was calculated for SbSeI. The ionization potentials (IP) and electron affinities (EA)

were also predicted, which are essential for proper band alignment in functional devices (Table 4). In another study, using, however, GGA-DFT, with relativistic effects and SOC included, SbSI was shown to have the smallest effective masses of electrons ($0.07m_e$) and holes ($0.098m_e$) and greater mobility than SbSeI and SbSBr. The p-type nature of all the compounds was suggested.¹⁷³ The bulk-to-1D transition of SbSeI, SbSI, and SbSBr materials was investigated.¹⁷ A quantum confinement results in dramatic changes in band gap, effective masses, and static dielectric constant. Moreover, a small uniaxial strain causes transformation from indirect into direct band gap character.

The cross-gap hybridization indicates covalency in the otherwise ionic materials and a large Born effective charge, leading to strong lattice polarization and anomalously large static dielectric constants.^{168,169,171} Sb-based V–VI–VII materials combine near visible range absorption with polar instabilities.¹⁹⁸

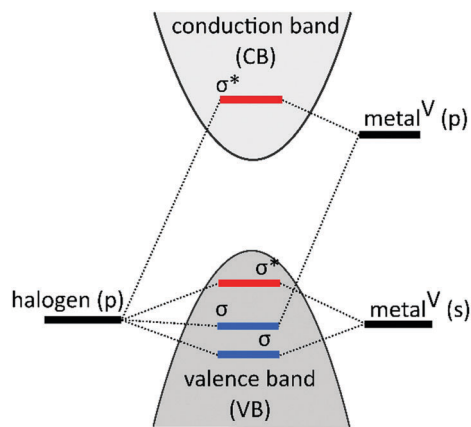


Fig. 17 The schematic orbital interaction in typical bismuth or antimony chalcogenide. The valence band maximum is constituted by the antibonding orbitals (from the s of the metal and the p of the halogen).

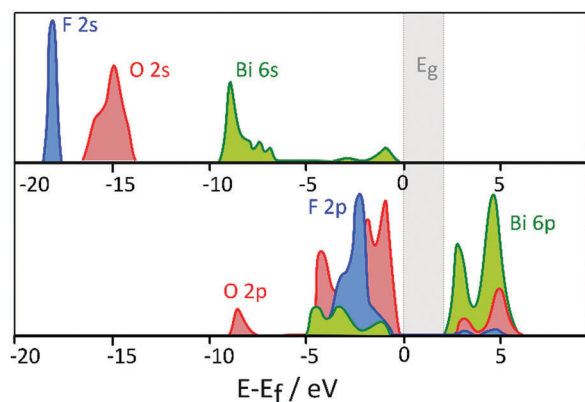


Fig. 18 Representative partial density of states for a V–VI–VII semiconductor (here for BiOF as presented in Khan *et al.*).¹⁷³ The s orbitals are separated (in terms of energy) in the conduction band, whereas the p orbitals interact with each other, enhancing cation–anion bond covalency.

The electronic structures of SbSI, SbSBr, and SbSeI were reviewed in terms of photoferric properties exhibited by these compounds in the non-centrosymmetric phase ($Pna2_1$, C_{2v}).²¹¹ The phase behaviour is associated with the stereochemically active s^2 lone pair electrons on the cation that can exhibit second-order Jahn–Teller instability associated with the change from a symmetric to asymmetric coordination environment.²¹² The small enthalpy difference was calculated between the non-polar and polar phases of SbSI and SbSBr. The Berry phase analysis indicated that all possess significant spontaneous electric dipole moments.²¹¹ A number of theoretical studies have been devoted to the dynamics of a phase transition of (Sb, Bi)–(S, Se)–(Cl, Br, I).^{213–217} It was shown that the Bi atoms are too large and the anharmonicity is too small to induce a ferroelectric phase transition in Bi chalcogenides.^{68,213} The phonon–phonon interaction has been proven to be the origin of the ferroelectric phase transition of SbSI and SbSBr.^{214,218}

The vibrational thermodynamic functions in the harmonic approximation with full potential DFT were studied to show the temperature dependence of the phase stability and to determine

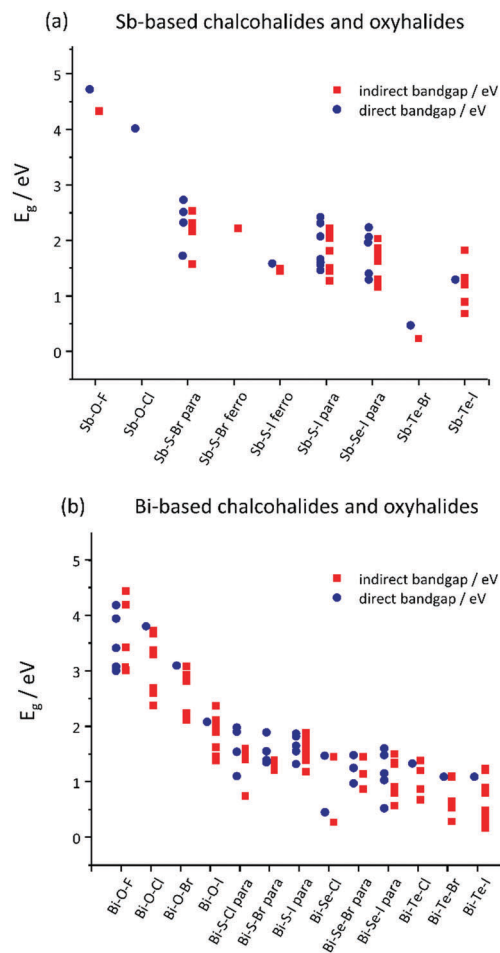


Fig. 19 The comparison between the direct and indirect band gaps of antimony (a) and bismuth (b) chalcogenides.

the theoretical phase transition temperature of SbSI²¹⁹ and SbSBr.¹⁹⁰ The effects of electron–phonon interaction and the characteristics of anomalous behavior in the phase transition region were further addressed for the SbSBr cluster with the Hartree–Fock method.²²⁰ The theoretical calculation revealed that the ferroelectric phase transition changes the bond orders and shift valence bands in SbSI and SbSBr.^{215,221} The averaged total density of states distribution that included the effects of atomic oscillations of both phases of SbSBr was qualitatively compared to the X-ray photoemission spectra (XPS).²¹⁵ In a similar manner, a comparison to XPS was made for SbSI,²²² SbSeI,¹⁷⁶ BiSbCl,¹⁸⁹ BiSbBr,¹⁹¹ BiSI,²²³ BiSeBr¹⁹¹ and BiSeI²²⁴ clusters.

Huang *et al.* demonstrated improvement in the band gap energies by including the first Bi $5d$ ¹⁸³ and later also Bi $5f$ ¹⁸⁴ states while investigating BiOX compounds. The band gap of BiOF is direct according to the generalized gradient approximation (GGA) DFT method¹⁸⁴ but indirect according to the hybrid DFT method.²²⁵ The other species of this family exhibit indirect gaps,^{180,226} with similar transition positions and increasing flatness of the CB bottoms with increase in X atomic number.^{183,184,225} The VB width expands remarkably, while the

Table 3 The computed band gaps of V–VI–VII chalcogenides with various GW (QSGW), DFT (hybrid, GGA and LDA functionals) and semiempirical and empirical methods (EPM, SCPM, ETBT)

	Band gap/eV		Method
	Indirect	Direct	
Sb–O–F	4.33	4.72	HSE + SOC ¹⁶⁹
Sb–O–Cl	—	4.02	HSE + SOC ¹⁶⁹
Sb–S–Br	2.53	—	QSGW + SOC ¹⁹⁸
	2.16	—	PBE + GW ²⁰⁰
	2.31	2.73	HSE06 + SOC ¹⁹⁸
	2.29	2.32	HSE + SOC ¹⁶⁹
	2.21	1.72	EV + SOC ¹⁷³
	2.21	—	EV + SOC ²²⁸
	1.57	—	GGA ²¹¹
	2.18	2.51	EPM ¹⁹⁹
Sb–S–I	2.22	2.42	QSGW + SOC ¹⁹⁸
	2.11	2.31	HSE06 + SOC ¹⁹⁸
	1.82	2.07	HSE + SOC ¹⁶⁹
	1.45	1.60	PBE + SOC ¹⁷¹
	2.05	—	EV + SOC ¹⁷³
	2.05	—	EV + SOC ²²⁸
	1.51	1.66	GGA ²¹¹
	1.45	1.56	LDA ²³⁷
	1.49	1.58	LDA ²³⁸
	1.45	1.58	LDA ¹⁷⁷
2.11	—	EPM ¹⁹⁹	
Sb–Se–Br	0.23	0.47	PBE ²⁰¹
Sb–Se–I	2.03	1.29	QSGW + SOC ¹⁹⁸
	1.65	—	PBE + GW ¹⁷⁵
	1.86	2.23	HSE06 + SOC ¹⁹⁸
	1.75	1.96	HSE + SOC ¹⁶⁹
	1.16	—	PBE + SOC ¹⁷¹
	1.62	1.40	EV + SOC ¹⁷³
	1.62	—	EV + SOC ²²⁸
	1.29	—	GGA ²¹¹
	1.26	—	LDA ¹⁷⁷
	1.67	2.06	EPM ¹⁹⁹
Sb–Te–I	1.20	1.29	HSE + SOC ¹⁶⁹
	0.68	—	PBE + SOC ²⁰³
	0.89	—	PBE ¹⁷⁹
	1.82	—	PBE ²⁰⁴
	0.90	—	LDA ¹⁷⁷
	1.32	—	ETBT ²⁰⁵
Bi–O–F	4.18	—	HSE06 + D3 + SOC ²²⁵
	4.43	3.94	HSE + SOC ¹⁶⁹
	3.07	3.07	PBE + D3 + SOC ²⁰⁶
	4.18	4.18	mBJ + SOC ²⁰⁶
	3.41	3.41	PBE ¹⁸⁴
	3.0	3.0	PBE ¹⁸³
	—	—	—
Bi–O–Cl	3.37	—	HSE06 + D3 + SOC ²²⁵
	3.29	3.80	HSE + SOC ¹⁶⁹
	3.66	—	PBE + vdW + SOC ²⁰⁶
	2.63	—	PBE + D3 + SOC ²⁰⁶
	2.38	—	PBE + SOC ¹⁸²
	3.72	—	mBJ + SOC ²⁰⁶
	2.63	—	PBE + D3 ¹⁸⁰
	2.69	—	PBE ¹⁸⁴
	2.60	—	PBE ¹⁸³
	—	—	—
Bi–O–Br	2.82	—	HSE06 + D3 + SOC ²²⁵
	2.86	3.09	HSE + SOC ¹⁶⁹
	2.11	—	PBE + D3 + SOC ²⁰⁶
	2.93	—	mBJ + SOC ²⁰⁶
	—	—	—

Table 3 (continued)

	Band gap/eV		Method
	Indirect	Direct	
	2.11	—	PBE + D3 ¹⁸⁰
	2.21	—	PBE ¹⁸⁴
	2.24	—	PBE ¹⁸³
Bi–O–I	2.00	—	HSE06 + D3 + SOC ²²⁵
	1.46	—	PBE + D3 + SOC ²⁰⁶
	2.11	—	mBJ + SOC ²⁰⁶
	1.38	1.49	PBE + SOC ¹⁷¹
	1.62	—	PBE ¹⁸⁴
	1.63	—	PBE ¹⁸³
Bi–S–Cl	—	1.98	HSE + SOC ¹⁶⁹
	1.6	1.9	GGA ¹⁹⁰
	1.5	—	GGA ¹⁸⁹
	1.40	1.54	PBE ²⁰¹
	0.74	1.1	SCPM ¹⁹⁷
	—	—	—
Bi–S–Br	—	1.89	HSE + SOC ¹⁶⁹
	1.32	1.35	PBE + SOC ¹⁷¹
	1.21	1.39	PBE ²⁰¹
	1.39	1.55	SCPM ¹⁹⁷
	—	—	—
Bi–S–I	1.66	1.87	HSE + SOC ¹⁶⁹
	1.78	1.82	HSE06 + SOC ⁶⁸
	1.18	1.32	PBE + SOC ¹⁷¹
	1.39	1.55	PBE ²⁰¹
	1.88	—	PBE ¹⁷⁹
	1.57	—	GGA ¹⁸⁸
	1.5	1.65	SCPM ¹⁹⁷
	—	—	—
Bi–Se–Cl	1.45	1.47	HSE + SOC ¹⁶⁹
	0.27	0.45	SCPM ¹⁹⁷
	—	—	—
	—	—	—
Bi–Se–Br	1.45	1.48	HSE + SOC ¹⁶⁹
	1.14	1.25	PBE ²⁰¹
	0.87	0.97	SCPM ¹⁹⁷
	—	—	—
Bi–Se–I	1.32	1.48	HSE + SOC ¹⁶⁹
	1.50	1.60	HSE06 + SOC ⁶⁸
	0.91	1.03	PBE + SOC ¹⁷¹
	0.57	0.52	PBE ²⁰¹
	1.35	—	GGA ⁵⁰
	0.8	1.15	SCPM ¹⁹⁷
Bi–Te–Cl	0.868	—	LDA + GW + SOC ²⁰⁷
	1.20	1.33	HSE + SOC ¹⁶⁹
	0.67	—	PBE + SOC ²⁰⁸
	1.38	—	PBE ¹⁷⁹
	1.20	—	PBE ¹⁹²
	1.38	—	PBE ¹⁷⁹
	—	—	—
	—	—	—
Bi–Te–Br	0.65	—	LDA + GW + SOC ²⁰⁷
	0.28	—	PBE + SOC ¹⁵⁶
	1.09	—	PBE ¹⁷⁹
	1.09	—	PBE ¹⁵⁶
	1.10	—	PBE ¹⁹²
	0.59	—	PBE ²⁰⁸
	1.09	—	PBE ¹⁹⁴
	—	—	—
Bi–Te–I	0.40	—	LDA + GW + SOC ²⁰⁷
	0.90	—	HSE + SOC ¹⁶⁹
	0.21	—	PBE + D2 + SOC ¹⁹³
	0.28	—	PBE + SOC ²⁰²
	0.43	—	PBE + SOC ¹⁹³
	0.17	—	PBEsol + SOC ¹⁹⁵
	0.90	—	GGA + SOC ²⁰³
	0.31	—	mBJ + SOC ²⁰⁹
	1.20	—	PBE ²⁰²
	—	—	—

Table 3 (continued)

Band gap/eV		Method
Indirect	Direct	
1.24	—	PBE ¹⁷⁹
0.80	—	PBE ¹⁹²
0.41	—	PBE ²⁰⁸
0.48	—	PBE ¹⁹⁴

Table 4 Computed electron affinities and ionization potentials of some of the Sb and Bi chalcogenide semiconductors according to the HSE method^{68,198,225}

	Electron affinity/eV	Ionization potential/eV
Sb-S-Br	5.80	3.37
Sb-S-I	5.37	3.15
Sb-Se-I	5.26	3.23
Bi-O-F	8.23	3.87
Bi-O-Cl	7.94	4.35
Bi-O-Br	7.55	4.65
Bi-O-I	7.03	5.03
Bi-S-I	6.4	4.9
Bi-Se-I	6.2	5.0

CB width descends from BiOCl to BiOI.¹⁸⁴ The smallest hole effective masses were found for BiOCl and BiOBr.^{206,225,227} The smallest electron effective masses can be observed in the direction across the [X-Bi-O-Bi-X] sheets in the structure. Ganose *et al.*²²⁵ emphasized that the contribution of the halide p states to the VBM increases, ultimately dominating the VBM in BiOI, and therefore the band gap reduction (as well as the ionization potential) down the halogen family is in line with the binding energy of the halide p orbitals. As such, alloys between these compounds offer the desired band gap, photocatalytic activity¹⁸¹ and electronic band alignment.²²⁵ The Bi-6s lone pair makes only a small contribution to the top of the valence band and is not stereoactive, meaning that the Bi is perfectly octahedral within the BiOX structure.

Bader population analyses reveal that the atomic populations of Bi increase, while those of X decrease from BiOF to BiOI, showing the reduction in oxidative capability.^{183,184} Recent works have shown the effects of compressive and tensile strains on the structural, electronic and optical properties of bulk bismuth oxyhalides.^{182,206,228} Out of the four BiOX systems, the BiOBr bulk phase was found to be one of the best photocatalysts with a moderate band gap, good optical conductivity and favorable separation of photo-excited charge carriers. Various crystal facets of BiOX were also studied in this regard.^{228,229} The (001) BiOI monolayer showed good structural stability, a decreased band gap, a smaller electron effective mass and a red-shift of absorption edges under tensile strain. The one layer of an X terminated (001) facet is superior as a photocatalyst, due to its extremely high thermodynamic stability, proper sunlight absorption, and low electron-hole recombination rate.

Ganose *et al.* demonstrated that BiSI and BiSeI have the electronic characteristics required for solar energy applications, paying attention to the selection of appropriate contact materials due to the large electron affinities of these materials

(>4.9 eV, *cf.* Table 3). The stereoactivity of the cation s anti-bonding states was investigated and the energy band formation mechanism was investigated with the Crystal Orbital Hamilton Population (COHP) analysis. BiSI and BiSeI were found to possess relatively diffused and thus weakly stereoactive lone pairs. It is due to the scalar-relativistic contraction of the Bi-6s shell, which results in a small pseudo-octahedral distortion in the lattice.⁶⁸ Low effective masses have been calculated in the direction along the Bi-(S, Se)-I chains and high dielectric constants were determined.^{68,169}

BiTeX compounds exhibit the ionic nature of the chemical bonds,^{230,231} thus the upper valence band and the lower conduction band are derived from the Bi, Te, and I p orbitals. The valence bands are dominated by Te-5p and X outmost p orbitals, while the conduction bands are predominantly composed of Bi-p orbitals. The inclusion of SOC leads to a huge reduction in the band gap energy.^{29,156,179,195,202,204,232,233} The characteristic feature of the band structure of these compounds is the slight shift of the conduction band minimum and the valence band maximum from the high symmetry points of the Brillouin zone (BZ). The most accurate computations of the band structures and band gaps were performed by Rusinov *et al.*, who employed the GW approximation.²⁰⁷ Due to the non-centrosymmetric crystal structure and strong SOC, this family exhibits a so-called Rashba-type spin splitting. In non-magnetic systems with the inversion symmetry of the bulk crystal potential, the SOC results in a situation where every electron's spin is locked perpendicularly to its momentum. The Rashba spin splitting caused by SOC is manifested as the modification of the energy band structure near the Fermi level by removing the band degeneracy and modifying the band edges depending on their spin states. The effect is inversely proportional to the band gap energy, so the largest effect is observed for BiTeI and the smallest for BiTeCl.²⁰⁹ The origin of the bulk Rashba splitting was discussed by Bahramy *et al.*²⁰² and Zhang *et al.*²³⁴ Many unique quantum phenomena emerge from this effect, *e.g.* exotic inter- and intra-band optical transitions, enhanced magneto-optical response, spin Hall and Edelstein effects, non-centrosymmetric superconductivity, and the formation of topological insulating phases. For a recent review on bulk Rashba semiconductors and their related quantum phenomena and applications, we refer the reader to references 235 and 236 and references therein.

A recent, comprehensive study of the optoelectronic properties of bismuth and antimony-based oxyhalides and chalcogenides provided by Ran *et al.*,¹⁶⁹ who reported the DFT calculations of the thermodynamic stability, electronic structure, effective masses of electrons/holes, and optical absorption. Previously, in a series of publications concerning SbSBr,²⁰⁰ SbSI^{237,238} and SbSeI,¹⁷⁵ Akkus *et al.* computed the linear and non-linear responses to the electric field vector using DFT pseudopotential methods and the SCISSORS approximation²³⁹ to account for the self-energy effects. This study provided detailed optical characteristics of the paraelectric phase, and also the ferroelectric phase in the case of SbSBr and SbSI, including the absorption coefficient, refractive index, energy-loss spectrum,

reflectivity, optical conductivity, effective number of valence electrons, and effective optical dielectric constant.

Similar linear optical characteristics of the bismuth family (BiSeI,⁵⁰ BiSI,¹⁸⁸ BiSbI,¹⁹⁰ BiSBr and BiSeBr²⁴⁰) were reported by Audzijonis *et al.*, who employed GGA-DFT with the full potential linearized augmented plane wave (FLAPW) method. Koc *et al.*¹⁷⁹ used the projected augmented wave (PAW) method and PBE functional to calculate the dielectric functions of SbTeI, BiSI, BiTeCl, BiTeBr, and BiTeI. Secuk *et al.*²⁴¹ investigated the optical properties of BiTeBr using the LDA approximation without SOC. The first principles optical characteristics of Sb–Se, Te–I¹⁷⁸ and BiOX¹⁸⁶ are also available. The optical properties were analysed and the origins of the peaks in the spectra were discussed in terms of the calculated density of states: the intra- and inter-band transitions of theoretical dielectric functions, the role of the p-states in the absorption and reflectivity constants, the energy regions of anisotropy of optical constants, and the energy of the volume plasmon. The density functional perturbation theory (DFPT) based on the linear response regime was used to calculate optically active (Raman and IR active) phonon modes for SbSBr and SbSI crystals.²⁴² The exotic optical properties specific to the Rashba interaction have been investigated on the example of BiTeI.^{243,244} With the help of the first-principles calculations, clear intraband and interband transitions have been identified and the intrinsic character of these excitations have been unveiled, including the Burstein shift, the singular behaviour of the joint density of states and the nature of intraband transitions near the crossing point of Rashba-split bands.

Spectroscopic data

Depending on the system (both the composition of cationic and anionic sublattices), the optical properties of the fifth group chalcogenides vary over a wide range (Table 5 and Fig. 20). There are several representatives of this family which are considered to be suitable candidates for applications in photovoltaics and photocatalysis, and numerous reports may be found on their spectroscopic characteristics (particularly for bismuth-based systems). On the other hand, glasses and amorphous solids (especially those containing arsenic) are underrepresented in this context and only a few authors provide data on their optical properties.

The first articles dealing with arsenic chalcogenides may be traced back to the works by Rodot *et al.*³² (for AsSeI) and Koperles *et al.*⁸⁰ (for AsSeI, AsSI and AsS_{0.5}Se_{0.5}I). It was presented in the latter that the exchange of chalcogenides may lead to a slight shift in the band gap width – from 1.78/1.91 eV for AsSeI to 2.1 eV for AsSI. Some overviews of optical properties collected for various glasses (including arsenic-based ones) were also provided by Sanghera *et al.*⁷² and Fenner *et al.*¹²⁵ Overall, the authors usually focused more on the physical, structural and chemical aspects of arsenic chalcogenides (and there are a significant number of reports on this topic) rather than the optical properties of these systems.

Table 5 Measured values of band gap energies for various pnictogen chalcogenides

Compound	Band gap/eV	Band gap type	Ref.
AsSI	2.1		32
AsSeI	1.9		32
SbSI	1.86	Indirect	280
	1.871	Indirect	247
	1.96	Indirect	67
	1.81	Indirect	248
	1.83, 1.85 ^h	Indirect	142
	1.84	Indirect	249
	2.14		250
	1.91		254
	2.15		255
	SbSeI	1.62	Indirect
1.67		Indirect	67
1.7		Indirect	143
BiOF	3.64	Direct	256
BiOBr	2.76		149
	2.1, ^a 2.3 ^b	Indirect	148
	2.6	Indirect	51
	2.75	Indirect	270
	2.59 ^c		272
	3.13 ^c		57
	2.32 ^c		273
	2.0 ^c		274
	2.84		275
	BiOCl	3.44	
3.46		Indirect	260
3.3, ^a 3.5 ^b		Direct	148
3.11, ^d 3.12, ^b 3.15, ^e 3.27 ^f		Indirect	60
3.46			147
BiOI	3.12		53
	3.49		268
	1.85		149
	1.94		265
	2.03 ^c		273
BiSI	2.95 ^d		275
	1.56		276
	1.8	Indirect	154
BiSBr	1.57	Indirect	277
	1.51	Indirect	279
	1.55, 0.82 ^c		130
	1.55		280
	1.71	Indirect	279
	2.01	Indirect	137
	1.42 ^c	Direct	128
BiSeI	1.28		67
	1.28	Indirect	282
BiTeBr	0.59	Direct	290
	0.6		287
BiTeCl	0.72		290
	0.8		286
BiTeI	0.35–0.6 ^g	Direct	243
	0.33		284
	0.38		285

^a Micro/nanosheets. ^b Nanoplates. ^c Non-stoichiometry. ^d Nanoflakes. ^e Microflowers. ^f Hollow microspheres. ^g Depending on the carrier concentration. ^h Depending on the solvent employed during growth.

With regard to chalcogenide compounds containing antimony, the situation is similar to compounds containing arsenic – less emphasis is put on optical studies in favour of other structural and physicochemical studies, especially in the case of SbTeX (X = Cl, Br, I).

The first work on the optical properties of SbSeI crystals (of the size between 40 and 250 μm, grown by the Bridgman method) was carried out by Žičkus *et al.*,²⁴⁵ where the exponential

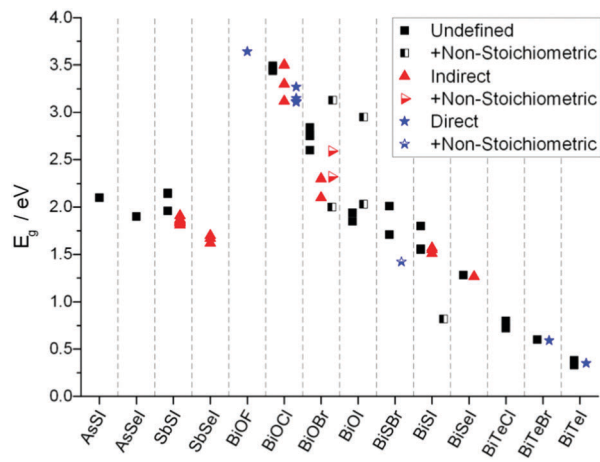


Fig. 20 The summary of band gap values for various pnictogen chalcogenides.

absorption tail was determined from transmission spectra. Li *et al.*²⁴⁶ determined the reflectance and absorption coefficients for SbSI as a function of small temperature modulations (~ 0.02 K) through the null ellipsometry technique with a thermoelectric sample mount. The absorption edge was measured to be around 600 nm (2.07 eV) for crystals grown with the Bridgman technique. Modifications of the SbSI and SbSeI energy band gaps through cationic doping were explored by two groups – Jeon *et al.*²⁴⁷ and Dong-Woon *et al.*⁶⁷ The first group determined the optical band gaps and investigated the effect of cobalt doping on their values. For pure SbSI and SbSeI single crystals, the determined values of the optical band gaps of indirect nature were given as 1.87 eV and 1.62 eV (values estimated from absorption spectra and Tauc plots). Similarly, the second group explored the effect of nickel doping and established the optical band gap width through Tauc plot analysis for single crystal nanoplates (50 nm in length and 10 nm in diameter) to be 1.963 eV for SbSI and 1.674 eV for SbSeI.

An excellent work was done by Nowak *et al.*,²⁴⁸ comparing 12 different techniques for determining the energy gap of SbSI nanowires using optical spectroscopy – the obtained results ranged from 1.76 eV to 2.34 eV. The authors stated that the multiabsorption fitting of the Kubelka–Munk reemission function technique is the best for the determination of the band gap (in the case of indirect, forbidden character, giving 1.81 eV) and other parameters (*e.g.* Urbach energy, which was determined to be 0.571 eV). Starczewska *et al.*¹⁴² explored the substitution of the solvent (methanol instead of ethanol) on the sonochemical growth of SbSI nanowires. The change of the employed solvent influenced the lateral dimensions of crystals, which ranged from 10 to 300 nm for methanol and 10 to 50 nm for ethanol. The technique mentioned above was used to determine the band gaps and Urbach energies of both samples. A slight shift in the energy gap and Urbach energy was observed between two samples (the first prepared in methanol and the second in ethanol) – 1.854 eV to 1.829 eV for band gaps and 0.1470 eV to 0.1031 eV for Urbach energies. Cho and co-authors synthesised one-dimensional SbSI crystals (from ~ 200 nm to 10 μ m thick, from few microns to 0.5 mm long) *via* a hydrothermal route.

The optical band gap value was determined to be 1.84 eV.²⁴⁹ Rod-like crystals (3–4 mm in length, 8–10 mm in diameter) with studded pyramids were obtained by Yang *et al.*²⁵⁰ with a band gap of approximately 2.14 eV. The unusual morphology of crystals may affect their physicochemical properties – hence a slightly different energy gap compared to those of other reports.

Nowak and co-authors were the first to determine the temperature dependence of the optical band gap for pure SbSI nanowires.²⁵¹ Subsequent research was conducted by Jesionek *et al.*²⁵² The authors presented spectral characteristics at different temperatures and the absorption and scattering coefficients at 274 K for SbSI and SbSeI encapsulated in carbon nanotubes (CNT). The temperature dependence of the optical band gap was determined for SbSI@CNT and SbSeI@CNT: at room temperature (293 K) the indirect forbidden optical energy gaps were 1.84 eV and 1.61 eV respectively. Tasviri *et al.*²⁵³ used antimony sulfoiodide nanowires encapsulated in carbon nanotubes as a photocatalyst for organic pollutant degradation. The SbSI@CNT system formed shows better results due to the larger surface area and better electrical conductivity introduced by the CNT, but with no influence on the optical band gap (compared to pure SbSI).

In regard to optical spectroscopy measurements, the optical band gap (1.91 eV) and Urbach energy (0.042 eV) were determined in our work (Kwolek *et al.*)²⁵⁴ for SbSI nanofibers (30 nm long). The authors also recorded photoluminescence spectra in deuterium oxide (for higher luminescence intensities) to determine the emission band for deeper analysis of their electronic structure. Analysis of the mechanism of photocurrent generation along with photocurrent action spectra recorded suggests their potential in the construction of optoelectronic logic gates (PEPS effect).

For photovoltaic applications, Nie *et al.*²⁵⁵ presented a solar cell based on SbSI as a light harvester. The optical band gap was determined to be 2.15 eV for SbSI prepared through several cycles of spin-coating of an SbI_3 solution on an Sb_2S_3 layer followed by thermal annealing. The system exhibited photocurrents around 9 mA under standard illumination conditions with a power conversion efficiency of 3.05%.

Wibowo and co-authors¹⁴³ determined the band gap for SbSeI to be 1.7 eV. The authors employed crystals grown by the Bridgman technique to obtain a single crystal ingot with a needle like morphology. The authors also measured the photoconductivity to determine the mobility–lifetime products for electrons and holes to check the validity of the use of SbSeI as an ionizing radiation detector.

Based on the above reports, it can be noticed that the exchange of chalcogen with the one with a bigger ionic radius decreases the optical band gap of a compound (approximately 1.9 eV for SbSI and 1.65 eV for SbSeI). This reasoning can be supplemented with the theoretical value of the energy gap of SbTeI, which is around 1.256 eV.¹⁷⁷

The situation is completely different for materials containing bismuth. To begin with, bismuth oxyfluoride has been recently rediscovered as a good candidate for applications in photocatalysis. In a report by Su *et al.*²⁵⁶ the authors described the

preparation and presented some spectroscopic data on BiOF with the band gap width determined as 3.64 eV. They also compared the photocatalytic activities of several samples with TiO₂ (P25) in the process of phenol degradation. Recently, similar attempts – of using BiOF-based systems in photocatalysis – have been made by other groups which applied various modifications. Hu *et al.* showed nanocomposites made of BiOF/Bi₂O₃ with the addition of reduced graphene oxide, which exhibited a decrease in the band gap width (to approx. 1.12 eV).⁵⁴ Vadivel *et al.* proved that upon modification with Ag nanoparticles and graphitic carbon nitride BiOF also shows an enhanced photocatalytic activity.²⁵⁷ The freshly published articles have covered also the change in fluoride content^{181,258} and the selection of a preparation method in the context of further improvement of the bismuth oxyfluoride photocatalytic performance.²⁵⁹

The optical and photocatalytic properties of bismuth oxychloride nano- and microstructures have been discussed by several authors. Probably the first systematic report on this material can be attributed to Zhang and co-workers, who investigated the formation of BiOCl micro- and nanoplates, calculated the optical band gap width and compared the photocatalytic activity of this material with that of the TiO₂ (P25) reference against methyl orange.²⁶⁰ The authors determined the E_g value to be 3.46 eV and claimed that the fundamental transition is of indirect nature.

The topic was further investigated by An *et al.*, who reported the optical band gap widths for BiOCl, BiOBr and BiOI microplates – 3.44, 2.76 and 1.85 eV, respectively – and demonstrated that bismuth oxybromide and oxychloride may be efficiently used in photocatalysis (based on the process of rhodamine B degradation and oxygen generation from water). Interestingly, the structures containing iodide did not exhibit any photocatalytic activity.¹⁴⁹

Deng and co-authors compared the optical band gaps for several different morphologies of BiOCl and BiOBr obtaining values between 3.5 and 3.3 eV for the former system and between 2.3 and 2.1 eV for the latter.¹⁴⁸ The same authors also reported the photoluminescence of bismuth oxychloride single-crystal nanoplates. They obtained crystalline structures approximately 20 nm in height and 200–500 nm in diameter with the band gap width equal to 3.40 eV and a strong emission peak centred at 455 nm recorded at room temperature.²⁶¹

There are several other reports on the optical band gap tuning achieved through the changes in morphology. Zhang *et al.* demonstrated how the concentration of citric acid affects the E_g value of BiOCl, getting results in the range between 3.11 and 3.27 eV, discussing also the photocatalytic properties of this system and its photoluminescence. Significantly, they suggested that the transition is of direct nature (contrary to previously mentioned articles).⁶⁰

Finally, there is a recently published paper comparing the optical properties and the photocatalytic activity of nanosheets composed of bismuth oxyhalides by Lv *et al.* The authors provide the band gap width values of 3.22, 2.64 and 1.77 eV for BiOCl, BiOBr and BiOI, respectively (Fig. 21).²²⁷

At the same time, bismuth oxyhalides have been present in various hybrid materials and nonstoichiometric structures.

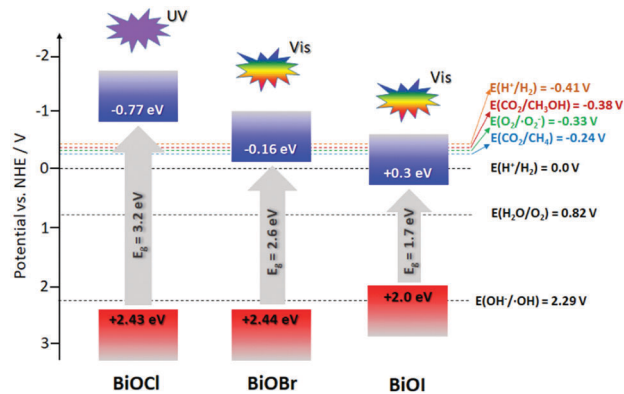


Fig. 21 The schematically presented energy diagrams for bismuth oxyhalides. Adapted from ref. 226 with the permission of Elsevier.

One of the nanocomposites is described by Shamaila and co-workers with tungsten oxide as the modifier. The authors determined the band gap width to be 3.46 eV for unmodified BiOCl, and a significant absorption below that value for samples containing WO₃ was observed. The authors also provided experimental data suggesting that the addition of tungsten oxide to BiOCl enhances the photocatalytic activity towards rhodamine B over the level obtained for pure semiconductors (BiOCl, WO₃ and the reference sample of TiO₂ (P25)).¹⁴⁷

Henle and Kaskel demonstrated the incorporation of BiOCl and BiOI nanoparticles into a polymeric matrix as a convenient way of photochromic composite preparation. The results obtained in the presence of a photoinitiator (Lucirin TPO) were particularly promising for the samples containing bismuth oxyiodide.²⁶² Choi and co-workers showed how CoFe₂O₄ can be used as a photosensitizer for bismuth oxyhalides²⁶³ (with the emphasis put on the photocatalytic performance of the hybrids), Hou *et al.* discussed how the modification with silver nanoparticles enhances the absorption coefficient²⁶⁴ and Chou and co-authors suggested the modification method with the use of graphene oxide for tuning the optical properties of BiO_xI_y-based photocatalysts covering a significantly wide range of band gap widths of 0.21–2.19 eV.²⁶⁵

Another study on hybrid materials dealing with SiO₂/bismuth oxyhalide systems was presented by Shen *et al.*, with band gap widths of 3.20, 2.75 and 1.76 eV for BiOCl, BiOBr and BiOI, respectively.²⁶⁶ Zhou and co-workers showed an interesting case of a core-shell system with Cd_{0.2}Zn_{0.8}S microspheres as a core material and different bismuth oxyhalides as outer layers. The authors determined the energy of indirect transition to be 3.12, 2.58 and 1.92 eV for BiOCl, BiOBr and BiOI, respectively. They also claimed an enhanced stability and photoactivity of such hybrids (Fig. 22).²⁶⁷

An alternative approach towards modification of bismuth oxyhalides is based on the use of various structures containing bismuth. Duo *et al.* presented the optical properties of the BiPO₄/BiOCl composite, which varied depending on the content of bismuth phosphate, yielding a shift in the absorption edge from 3.12 eV for pure BiOCl to 3.23 eV for the 50% content of BiPO₄.⁵³ Similar heterostructures, this time with bismuth

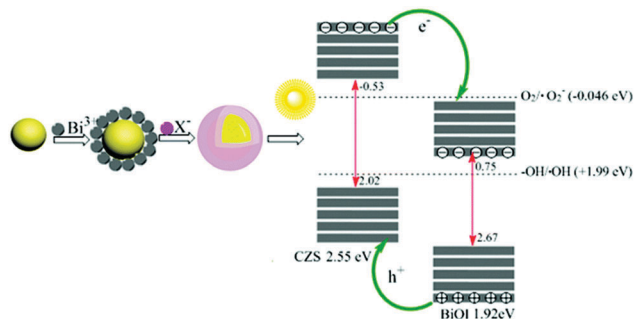


Fig. 22 The structure with the electronic diagram for $\text{BiOX}@\text{Cd}_{0.2}\text{Zn}_{0.8}\text{S}$ core-shell hybrids. Reprinted from ref. 267 with permission of the Royal Society of Chemistry.

sulphide combined with bismuth oxychloride, were discussed by Xu *et al.* In a recently published article the authors demonstrated the impact of the Bi_2S_3 content on the optical properties of the hybrid and its photocatalytic performance. Based on the UV-Vis diffuse reflectance spectroscopy, they managed to calculate E_g values to be 3.49, 1.27 and 2.95 eV for unmodified BiOCl , Bi_2S_3 and Bi_2S_3 - BiOCl composites, respectively.²⁶⁸

Hu *et al.* presented the electrochemical method for the bismuth oxybromide film preparation with the simultaneous formation of Bi nanopowder. The band gap width reported by the authors for BiOBr was 2.60 eV.⁵¹ Jiang and co-workers obtained a composite made of BiOBr and BiOF and observed only a slight change in the optical band gap width but also a significant increase in the photocatalytic efficiency.²⁶⁹

Wang and co-authors proposed a hybrid material composed of bismuth oxybromide grown on bismuth oxide nanocrystals to increase the photocatalytic activity and stability of the system. They also managed to reduce the band gap width from 2.75 eV for pure BiOBr to approximately 2.57 eV for the composite.²⁷⁰ Zuo *et al.* combined BiOCl with bismuth molybdate, observing for the $\text{BiOCl}/\text{Bi}_2\text{MoO}_6$ system a significant decrease in the band gap width.²⁷¹

Peng and co-workers realised the optical band gap tuning through the formation of heterostructures with bromide-deficient $\text{Bi}_{12}\text{O}_{17}\text{Br}_2$ and $\text{Bi}_{24}\text{O}_{31}\text{Br}_{10}$ exhibiting E_g at a level of 2.59 eV for the former one and the indirect transition.²⁷² At the same time, Su *et al.* presented another Br-deficient, hydrothermally prepared nanostructure - $\text{Bi}_5\text{O}_7\text{Br}$ - which showed an increased band gap width of approximately 3.13 eV.⁵⁷ Bai and co-authors demonstrated two bismuth-rich nanosystems - $\text{Bi}_4\text{O}_5\text{Br}_2$ and $\text{Bi}_4\text{O}_5\text{I}_2$ - with increased photocatalytic efficiency towards hydrogen production and the indirect optical transitions with E_g values of 2.32 and 2.03 eV, respectively.²⁷³

A very similar structure (*i.e.* $\text{Bi}_4\text{O}_5\text{Br}_2$) was presented by Mao *et al.* - here the authors claimed that the band gap width was approximately 2.0 eV.²⁷⁴ Also Li and co-workers presented a Bi-rich system with a stoichiometry of $\text{Bi}_5\text{O}_7\text{I}$ combined with $\text{BiOBr}_x\text{I}_{1-x}$. Here, both the photocatalytic activity towards methyl orange and the optical band gap have been successfully tuned and the authors obtained E_g values equal to 2.95, 2.84, 2.15 and 1.98 eV for $\text{Bi}_5\text{O}_7\text{I}$, BiOBr , $\text{BiOBr}_x\text{I}_{1-x}$ and $\text{Bi}_5\text{O}_7\text{I}/\text{BiOBr}_x\text{I}_{1-x}$, respectively.²⁷⁵

The story about the research on the optical properties of bismuth sulfohalides starts with the publication by Xu *et al.*, in which the authors use reflectance ellipsometry in order to measure their differential polarizabilities and determine their refractive indices. They also found the band gap width of BiSI to be 1.56 eV.²⁷⁶ Then, after *ca.* twenty years, a paper by Su *et al.* emerged in which the authors provided a E_g value of 1.8 eV for bismuth sulfoiodide microneedles.¹⁵⁴ Hahn and co-workers presented the preparation method and comprehensive characterisation of BiSI microrods in the context of possible application in photovoltaics. The UV-Vis measurements revealed the indirect transition with a band gap width of 1.57 eV.²⁷⁷

The use of BiSI nanostructures has been also discussed by Aguiar *et al.* for ionizing radiation detection, but little new data on their optical properties were given here.²⁷⁸ A quite convenient synthesis method for BiSI , BiSeI and $\text{BiSBr}_{1-x}\text{I}_x$ solid solutions was proposed by Kunioku *et al.* The authors were able to tune the indirect band gap in the range of 1.71–1.51 eV, lowering the band gap value with increasing content of iodide (the limiting values are 1.71 and 1.51 for BiSBr and BiSI , respectively). This system has been found to obey Vegard's law with a linear dependence of the band gap on the molar fraction of iodine.²⁷⁹ The band gap widths for bismuth sulfoiodides are also given by Groom and co-workers - 1.55 eV for BiSI and 0.82 eV for iodide-deficient $\text{Bi}_{13}\text{S}_{18}\text{I}_2$, which also exhibits significant absorption below that value.¹³⁰ The same group continued the research on BiSI and presented the results of bismuth substitution with antimony. They proved that this method is sufficient to tune the band gap width, with the limiting values of 1.55 eV for pure BiSI and 1.86 eV for pure SbSI .²⁸⁰

Although other halide ions are definitely underrepresented here, there are several reports on the optical properties of bismuth sulfobromide. Jin and co-workers published an article on BiSBr where they calculated the energy gap width associated with the indirect transition to be 2.01 eV.¹³⁷ Later, Deng *et al.* presented $\text{Bi}_{19}\text{S}_{27}\text{Br}_3$ superstructures in which the energy gap was lowered to 1.42 eV and the data analysis shown in the article indicates the direct nature of the transition.¹²⁸

The first reports on bismuth selenohalides may be traced back to 1984 when Zickus and Audzijonis discussed the optical properties of SbSeI and BiSeI . Among others, they calculated the Urbach parameters.²⁸¹ Dong-Woon *et al.* obtained the band gap width value of 1.28 eV for BiSeI single crystals obtained with the use of the Bridgman technique,⁶⁷ and Lee and co-workers confirmed this result, determining the indirect type energy gap width to be 1.28 eV for single crystals prepared with the same method.²⁸²

The literature is also rather rich with theoretical works in which different parameters - including some optical properties - are calculated based on various numerical approaches. Nonetheless, this topic is covered in the preceding section of this review and will be not discussed here.

Due to the fact that BiTeX ($X = \text{Cl}, \text{Br}, \text{I}$) compounds exhibit the Rashba effect, a great deal of research has been done in the characterisation of those systems. Lee *et al.*²⁴³ determined the band gap experimental values ranging from approximately 0.35 eV

to 0.6 eV depending on the carrier concentration of prepared samples of BiTeI. That effect coincides well with the fitted curves based on the Burstein–Moss shift. A Fourier-transform spectrometer and a grating-type spectrometer were used to perform optical measurements. The authors also recorded several intra-band transitions related to the Rashba effect. In two works, Makhnev *et al.*^{283,284} measured optical transitions in BiTeX using the optical ellipsometry method. For each material, the energy band gaps associated with γ -transitions were determined to be 0.72 eV, 0.59 eV and 0.33 eV for BiTeCl, BiTeBr and BiTeI, respectively. These results corroborate the BiTeI (0.38 eV)²⁸⁵ and BiTeCl (0.8 eV)²⁸⁶ band gaps established through the angle resolved photoemission spectroscopy (ARPES) measurement. Additionally, the band gap of BiTeBr was established by Martin *et al.*²⁸⁷ through infrared optical reflectance spectroscopy to be approximately 0.6 eV.

Furthermore, the values obtained for BiTeI and BiTeBr are consistent with the energy gap values obtained through several other measurement methods.²⁸⁸ In their work, Kulbachinskii *et al.* presents collected band gap values ranging from 0.37 eV to 0.48 eV for BiTeI and from 0.472 eV to 0.59 eV for BiTeBr depending on the temperature, the technique used or the character of the transition.

Xi *et al.*²⁸⁶ explored the pressure-induced closing of the band gap in BiTeI. Based on the XRD analysis of the *a/c* ratio (where *a* and *c* are lattice parameters), metallic states were recorded for pressures in the range 2.0–2.9 GPa. Due to the low magnitude of the band gap of BiTeI, infrared spectroscopy was employed to further specify the point of transition, which was found to be 2.2 GPa. Rusinov and co-authors²⁸⁹ determined the absorption and refractive indexes through spectral ellipsometry for BiTeCl and BiTeI compounds. The experimental results coincided well with the theoretical calculations.

Electrical properties

Definitely less attention in comparison to the other physico-chemical properties of pnictogen chalcogenides has been paid to the electrochemical and electrical characterization of this class of compounds. This is mainly due to the difficulties in the Hall effect measurements related to the low carrier mobility and high resistivity of chalcogenide compounds. The electrical characterization of several compounds including mainly studies of the Hall effect (Hall mobility), the thermoelectric effect (the Seebeck coefficient) and the conductivity measurements.

AsSX (X = I, Br) systems

In the literature there are only a few short reports concerning the electrical properties of AsSI and AsSBr. Glasses from the AsSI system are insulators of high resistivity, measured at room temperature, exceeding $10^{13} \Omega \text{ cm}$.²⁹¹ A dozen years later Turyanitsa *et al.* reported that the resistivity in the AsSI system changes from 10^{16} to $10^{12} \Omega \text{ cm}$ with an increase of iodine content.²⁹² Perason *et al.* investigated the electrical properties of glasses containing more than 60 at% of sulphur and 3–9 at%

of bromine. The reported resistivities exceed $3 \times 10^{14} \Omega \text{ cm}$.²⁹³ Sanghera *et al.* reported that the DC electrical conductivity in the AsSBr system measured at 293 K changes from 10^{-15} to $10^{-12} \Omega^{-1} \text{ cm}^{-1}$ and depends on the stoichiometry of the material. Based on the presented data, it is also visible that the conductivity increases with a decrease of the glass transition temperature as well as with halide content. They reported that both the liquid and solid phases exhibit properties typical for the semiconducting state and the melt conductivity ranges from 10^{-5} to $10^{-6} \Omega^{-1} \text{ cm}^{-1}$.⁷²

AsSeX (X = Br) system

In the literature there is very little information concerning the electrical properties of the AsSeBr system. Data presented by Sanghera *et al.* indicate that the conductivities of the compounds in the system range from 10^{-13} to $10^{-11} \Omega^{-1} \text{ cm}^{-1}$ and increase with bromine content.⁷²

AsTeX (X = I, Br, Cl) systems

Arsenic based chalcogenides exist in both the vitreous and crystalline forms.³² The vitreous semiconductors as well as crystalline forms exhibit the Hall effect and photoelectrical and thermoelectric properties. Furthermore, under certain conditions, these kinds of materials show sudden change in their conductivity values.⁸⁶

The Hall effect measurements on chalcogenide glasses were reported for the first time by Nazarova and Kolomiets in 1960. The measurements were performed at room temperature with the alternated current (AC) technique. The observed Hall mobility was independent of the glass composition.²⁹⁴ In 1964 Peck and Dewald reported the Hall effect measurements on the As–Te–Br and As–Te–I systems in the temperature range from 293 to 363 K. They applied the direct current (DC) technique with strong magnetic fields, up to 70 kOe.²⁹⁵ They reported the Hall mobility (μ_{H}) in the As–Te–I system from $0.08 \text{ cm}^2 \text{ V}^{-1} \text{ s}^{-1}$ at room temperature to $0.12 \text{ cm}^2 \text{ V}^{-1} \text{ s}^{-1}$ at 363 K. Similar measurements were performed in the As–Te–Br system and observed μ_{H} values of 0.01 and $0.10 \text{ cm}^2 \text{ V}^{-1} \text{ s}^{-1}$ at room temperature and 363 K, respectively.²⁹⁵ All performed measurements confirm the sign anomaly of the charge carriers. The Hall effect measurements indicate n-type conductivity, while thermoelectric measurements indicate p-type conductivity. Mott,²⁹⁶ Gubanov,²⁹⁷ and Cohen *et al.*²⁹⁸ suppose that the band structures of classical semiconducting materials are well described, but there are some exceptions, especially when the curves of density states form tails inside the forbidden gap.^{298,299} Thus from a theoretical viewpoint the conduction mechanism of chalcogenide compounds is not clear.

The As–Te–I system was investigated for the first time by Eaton.⁸⁶ Eaton observed in this system a conductivity switching effect, which is related to the thermal breakdown of the material, which in turn is related to its semiconducting properties.⁸⁶ In subsequent years this system was investigated with regard to its electrical properties by Prasad and Hilborn⁸⁷ and Pearson *et al.*³⁰⁰ Seager *et al.*³⁰¹ reported results concerning the analysis of electronic transport measurements in $\text{As}_{50}\text{Te}_{50-x}\text{I}_x$

($x = 0, 2, 20$) glasses. The observed Hall mobility changes exponentially with temperature, which indicates that the analyzed compounds exhibit n-type conductivity, whereas the analysis of thermoelectric power indicated opposite p-type similarly to that reported by Dewald and Peck.²⁹⁵ The observed phenomenon was explained by the small polaron hopping model. μ_H observed by the authors ranged from 10^{-2} to $10^{-1} \text{ cm}^2 \text{ V}^{-1} \text{ s}^{-1}$. Peck and Dewald also observed that electronic conduction in this system varies from *ca.* $10^{-3} \Omega^{-1} \text{ cm}^{-1}$ (low iodine content) to $10^{-8} \Omega^{-1} \text{ cm}^{-1}$ (high iodine content).²⁹⁵ Seager *et al.* described observed effects based on the small-polaron hopping motion of holes, resulting from the existence of As_2Te_3 two-dimensional ribbons incorporated into a glassy matrix. The authors believe that carrier transport control in these compounds is mainly related to the presence of the As_2Te_3 moieties.³⁰¹ Analyses of the carrier mobilities of similar chalcogenide glasses performed by Roilos lead to similar conclusions concerning the transport nature in AsTeI compounds.²⁹⁹ Results reported by Seager *et al.*³⁰¹ as well as Johnson and Quinn³⁰² for low iodine compounds show similar conductivity to that observed by Brodsky and Weiser for amorphous arsenic telluride (As_2Te_3) films.³⁰³ It should be underlined that the μ_H values are also in good agreement with values observed by Dewald and Peck at room temperature for $\text{As}_{53}\text{Te}_{43}\text{I}_4$ glass ($\mu \approx 0.08 \text{ cm}^2 \text{ V}^{-1} \text{ s}^{-1}$).^{295,304} All reported AsTeI samples, except for those containing 2% of iodine, exhibit the same carrier activation energy of *ca.* 0.06 eV, which is close to those reported by Roilos (*ca.* 0.05 eV).²⁹⁹ The carrier activation energies were determined by Seager *et al.* using the measured Seebeck coefficient of $0.19 \mu\text{V K}^{-1}$.^{301,304} Bardars *et al.* investigated the influence of annealing on the electrical properties of $\text{As}_{50}\text{Te}_{50-x}\text{I}_x$ ($x = 0, 2, 5, 20$). The authors reported that the conductivity of the surface layer is almost temperature independent and the value of activation energy is *ca.* 10^{-2} eV. An effect of the annealing process resulting in an increase of material conductivity was more visible for compounds with low iodine concentration, *i.e.* $x = 0, 2$.³⁰⁵

SbSX (X = I, Br, Cl) systems

The dielectric properties of SbSI – the first ferroelectric material which is also photoconductive – were investigated by Fatuzzo *et al.* The measured dielectric constant–temperature dependence indicated the ferroelectric character of the material.³⁰⁶ Audzjonis *et al.* reported that SbSI has three phases: ferroelectric ($T < 295$ K), antiferroelectric ($T < 410$ K) and paraelectric ($T > 410$ K).³⁰⁷ The reported conductivities of SbSI glasses depending on their compositions range from 10^{-10} to $10^{-7} \Omega^{-1} \text{ cm}^{-1}$.⁷² The charge carrier mobilities of these materials change from 50 to $100 \text{ cm}^2 \text{ V}^{-1} \text{ s}^{-1}$.³⁰⁸ SbSBr similarly to SbSI exhibits semiconducting ferroelectric properties.³⁰⁹ Depending on the state, the electrical conductivity value was $10^{-7} \Omega^{-1} \text{ cm}^{-1}$ for crystals and $10^{-10} \Omega^{-1} \text{ cm}^{-1}$ for the glass phase. Differences in composition may change the conductivity for few orders of magnitude for both crystal and metallic phases.⁷² Theoretical investigations performed by Kvedaravicius *et al.* indicated that the SbSbCl compound is of non-ferroelectric nature.²¹³

SbSeX (X = I, Br) systems

Wibowo *et al.* analyzed the direct-current (DC) conductivity of SbSeI. The authors determined the Seebeck coefficient at room temperature and the resistivity–temperature dependence starting from room temperature up to 500 K under vacuum conditions. The reported room temperature resistivity value was $10^8 \Omega \text{ cm}^{143}$ and was close to that reported by Chepur *et al.*³¹⁰ The temperature dependence of the Seebeck coefficient indicates an n-type conductivity of the compound.¹⁴³ Audzjonis *et al.* reported that SbSeI depending on temperature can exist as antiferroelectric ($T < 410$ K) and paraelectric ($T > 410$ K) phases.³⁰⁷ The electrical conductivity of SbSeBr reported by Pikka *et al.* is $10^{-7} \Omega^{-1} \text{ cm}^{-1}$ and is very close to that reported for SbSeI.³¹¹ The SbSeCl compound is of non-ferroelectric nature and more complex experimental analyses have not been reported in the literature.²¹³

SbTeX (X = I) system

The electrical properties of SbTeI have been investigated by Bubey *et al.*; however, these data seem to be unreliable.³¹²

BiOX (X = I, Br, Cl) systems

Bismuth oxychloride is a very interesting semiconducting compound mainly due to its photoconductivity³¹³ and possibilities of thermal modulation of the conductivity.⁴⁵ In the literature, however, there are only a few reports concerning the electrical conductivity of BiOCl. The electrical conductivity of the material was studied for the first time by Shilikha *et al.* Measurements were performed in the temperature range 90–300 K. The reported results indicated the insulating character of BiOCl manifested by the negligible electronic component of the heat conductivity and low conductivity ranging from 10^{-10} to $10^{-13} \Omega^{-1} \text{ cm}^{-1}$.³¹⁴ Banerjee *et al.* investigated the electrical conductivity of p-type bismuth oxychloride drop-cast nanosheets. The authors found that the conductivity activation energy in the material was 862 mV in the temperature range from 300 to 420 K. The recorded I–V characteristics also indicated that the conductivity of this p-type semiconducting material decreases with decrease of oxygen partial pressure (Fig. 23).³¹⁵

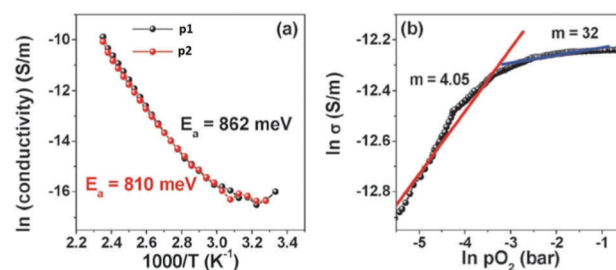


Fig. 23 Arrhenius plots of conductivity versus reciprocal temperature yield the activation energy $E_a = 862$ meV and 810 meV, respectively ($p_1 = 1000$ mbar and $p_2 = 3$ mbar) (a). Plots of conductivity versus oxygen partial pressure (in a logarithmic scale) of the BiOCl nanosheet electrode at 425 K under an applied bias of 30 V (b). Reproduced from ref. 315 with permission from the Royal Society of Chemistry.

Another BiOCl form was characterized by Wang *et al.* The authors analyzed the properties of single-crystalline microplates. They observed that for a sample with a diameter of 10 μm the resistivity initially increases with lowering temperature and drops at temperatures below 8.52 K. Nonlinear behaviour was also observed in the resistivity – excitation current dependences.³¹⁶ Recently, the electrical properties of BiOCl, BiOI and BiOBr single crystals have been studied by Lontyk *et al.* in the temperature range from 2 to 300 K. The Seebeck coefficients were determined to be 115, 97.4 and 63.1 $\mu\text{V K}^{-1}$ for BiOCl, BiOBr and BiOI, respectively. The characterized crystals exhibit relatively high anisotropy in the activation energy, especially in the case of BiOI. Below 250 K the electrical conductivities of these compounds are smaller than $10^{-15} \Omega^{-1} \text{cm}^{-1}$. Based on the experimental values assuming $T = 10$ K and an electron to hole mobility ratio of 0.2, the authors stated that independently of the present halogen BiOX (Cl, Br, I) are p-type semiconductors.³¹⁷ On the other hand, Cai *et al.* reported that in the case of BiOI iodine vacancies appearing at a slightly lower temperature than that corresponding to phase transition may result in a change in the semiconductor behavior from p-type to n-type.³¹⁸ Kwolek *et al.* reported BiOI preparations showing n-type conductivity on the basis of photocurrent and surface photovoltage measurements.^{254,319}

BiSX (X = I, Br, Cl) systems

Needle-like structures of n-type BiSI have been investigated for the first time with regard to their electrical properties by Horak and Cernak. The reported BiSI exhibits high resistivity ranging from 10^8 to $10^9 \Omega \text{cm}$. An increase of temperature up to 200 $^\circ\text{C}$ in an inert atmosphere results in an increase of the electrical conductivity.³²⁰ In 2012, Hahn *et al.* analyzed BiSI and BiSeI with regard to their potential photovoltaic applications, confirming their n-type conductivity.³²¹ BiSBr exhibits semiconducting ferroelectric properties, but no complex investigation concerning its electrical properties has been reported in the literature.³⁰⁹ The electrical resistivity of BiSBr ranging from 10^3 to $10^4 \Omega \text{cm}$ ³⁰⁸ is significantly lower than that reported for BiSI, while BiSCL has been reported to be paraelectric.¹²⁴

BiSeX (X = I) system

BiSeI exhibits piezoelectric, ferroelectric³²² and photoelectric³²³ properties. Additionally, depending on the preparation technique these materials can show n- or p-type conductivity. Genesha *et al.* studied the dielectric properties of BiSeI crystalline platelets. The measurements were carried out perpendicular to the (110) plane in the temperature range from 308 to 426 K (Fig. 24). Through measurement of the capacitance of the crystal placed between Ag electrodes, the authors determined the dielectric permittivities at fixed frequencies of 1, 10 and 100 kHz.^{45,120} Up to now, in the literature, there has been no information concerning the characterization of BiSeBr as well as BiSeCl compounds regarding their electrical properties.

BiTeX (X = I, Br, Cl) systems

BiTeI is a ferroelectric semiconductor with a highly anisotropic layered structure.³²⁴ The thermoelectric properties of both

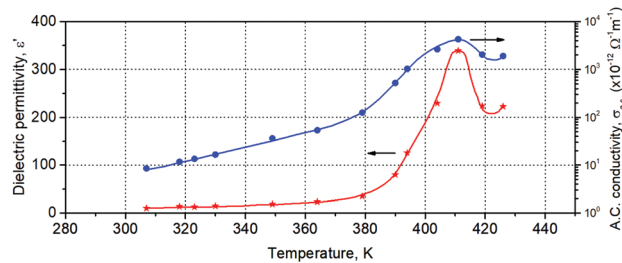


Fig. 24 Variations of the dielectric permittivity and the a.c. conductivity with temperature for 10 kHz. Reproduced from ref. 120 with permission from Springer.

BiTeBr and BiTeI single crystals grown by the Bridgman method were investigated by Kulbachinskii *et al.*²⁸⁸ The temperature dependence of the conductivity as well as the Seebeck coefficient analyzed in the temperature range from 5 K to 300 K indicated that these compounds show n-type conductivity. The electron concentration and mobility were determined at 77 and 300 K. The Hall effect was studied under magnetic field induction of 0.3 T. It was observed that the electron concentration is independent of temperature and is $4.6 \times 10^{19} \text{cm}^{-3}$ for BiTeI and $1.3\text{--}1.4 \times 10^{19} \text{cm}^{-3}$ for BiTeBr, whereas the charge carrier mobility is strongly temperature dependent. An increase of temperature from 77 to 300 K results in a drop of electron mobility in both cases – from 528 to 242 $\text{cm}^2 \text{V}^{-1} \text{s}^{-1}$ for BiTeI and from 1450 to 310 $\text{cm}^2 \text{V}^{-1} \text{s}^{-1}$ for BiTeBr. At room temperature the electron mobility of BiTeBr is 2.7 times higher than that of BiTeI.⁶⁵ Ishizaka *et al.* on the basis of the in-plane electrical resistivity measurements of single crystal BiTeI concluded that this compound exhibits metallic behavior down to 2 K. The authors similarly to Kulbachinskii *et al.* observed that the Hall coefficient is practically temperature independent. The reported electron concentration of $4.54 \times 10^{19} \text{cm}^{-3}$ is very close to the value reported previously.²⁸⁵ Lostak *et al.* on the basis of the optical measurements estimated the concentration of electrons in BiTeI compounds to be $4.7 \times 10^{19} \text{cm}^{-3}$, which is very close to those determined later by Ishizaka and Kulbachinskii *et al.* The values obtained by Lostak *et al.* from the optical measurements are in agreement with those obtained based on the determined Hall constant.³²⁵ BiTeCl has been recently found to be a superconductive material under high pressure conditions. Ying *et al.* reported that the superconductivity in this compound emerges when the charge density wave or the resistivity maximum is suppressed by the applied pressure. The authors investigated the properties of BiTeCl single crystals grown by the self-flux method. The resistivity was analyzed not only at different pressures but also at different values of the magnetic field induction vector (Fig. 25). The resistivities measured at pressures below 4 GPa indicated metallic behavior and are close to that observed under ambient pressure even though this material was thought to be a Rashba semiconductor.³²⁶ Similar behaviors were reported previously for BiTeI by Ideue *et al.*³²⁷ and for BiTeBr and BiTeCl by Akrap *et al.*³²⁸ It should also be underlined that BiTeCl is the first ever observed topological superconductor.¹¹⁶ All the data reported in this section are collated in Table S3 (ESI[†]).

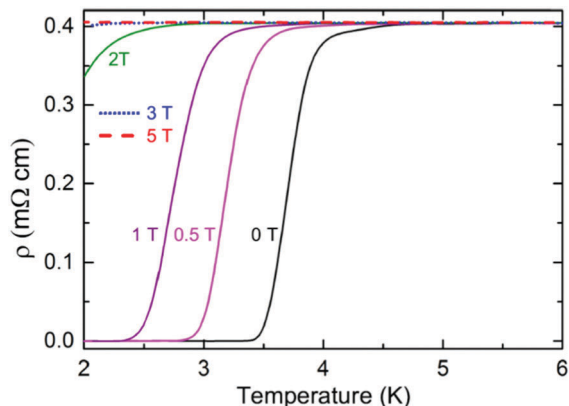


Fig. 25 Temperature dependence of the resistivity of BiTeCl under various magnetic fields and a pressure of 50.8 GPa. Adapted from ref. 326 with the permission of American Physical Society.

Photoelectrochemistry and photocatalysis

The presence of an internal electric field in semiconducting oxo- and chalcogenides makes them ideal candidates for photocatalysis. Despite their application potential, in the literature there are only limited studies about the surface photochemistry and photocatalytic performance of these ferroelectric materials. The most distinctive members of the V–VI–VII group are bismuth oxyhalides. BiOX (X = Cl, Br and I) compounds exhibit promising photocatalytic properties under both UV and visible light irradiation.^{184,226,256,260,329–338} A very good photocatalytic activity is a result of the open and layered crystalline structure with predominately exposed (001) facets (Fig. 26).^{151,260,339}

The reports concerning the photocatalytic performance of BiOX are focused on the decomposition of organic pollutants, CO₂ reduction and selective organic transformations. In 2006 Zhang and co-workers²⁶⁰ reported a notably high catalytic activity

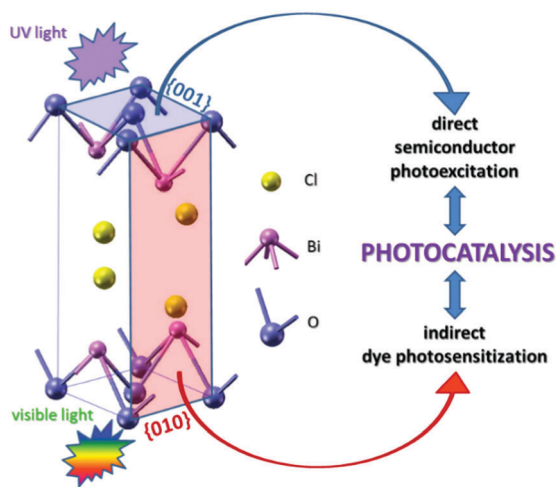


Fig. 26 Schematic picture of the face-dependent photoreactivity of BiOCl single crystalline nanosheets. Reproduced from ref. 366 with permission of American Chemical Society.

of BiOCl in methyl orange degradation under UV irradiation. This activity even exceeds the efficiency of commercially used TiO₂ (P25). Since then, the interests of scientists have focused on BiOX (X = Cl, Br, I) and their photocatalytic performance.^{60,331,337,340–375} Moreover, it is noted that with increasing atomic number of the halogen atom, the band gap of BiOX decreases: BiOF (~3.6 eV²⁵⁶), BiOCl (~3.2 eV³³¹), BiOBr (~2.8 eV³³¹) and BiOI (~1.7 eV³³¹), *vide supra*. This effect allows tuning their redox properties and thus photocatalytic activity.³⁷⁴

It has been proved that dimensionality is a very important factor that affects the photocatalytic properties. Nanomaterials tend to improve the photocatalytic efficiency due to their high surface area to volume ratios and higher concentrations of active sites. 1D nanostructures (nanorods/wires) are objects with thicknesses and widths in the nanoscale range, but their lengths can be several micrometres or even longer.^{374,376} From this viewpoint, 1D semiconductor catalysts are attractive because of the presence of the preferred direction of charge carrier flow (*vide supra*). Due to the highly anisotropic layered crystal structures of BiOX compounds, they tend to grow into two dimensional (2D) nanostructures (nanoplates/sheets). 2D systems due to their lamellar (graphite-like) structures are built with interlamellar van der Waals weak interactions or electrostatic forces, which enhance the photocatalytic activity of BiOX.²⁶⁰ The high surface area to volume ratio for this class of materials facilitates fast separation of the photoinduced electrons and holes, which favours the efficiency of photocatalytic reactions.³⁷⁴

Jiang *et al.*³⁶⁶ synthesized BiOCl single-crystalline nanosheets with exposed (001) and (010) facets *via* a simple hydrothermal route. It is interesting to note that nanosheets with exposed (001) facets show more effective photocatalytic degradation of methyl orange in the UV range, while (010) facets exhibit a higher degradation activity under visible light. It means that the photoactivity of BiOCl nanosheets is highly dependent on the face exposure. The facet effect of BiOX was reported for the first time in 2011.³⁷⁷ Recently, Zhang's group investigated in detail the facet effect of BiOCl.^{340,366,378} The (001) facet-dominant BiOCl nanosheets show efficient photodegradation of pollutants under UV light, which results from the inner electric field, facilitating charge carrier separation. The (010) facet-dominant BiOCl nanosheets exhibit higher activity in methyl orange degradation under visible light because of their larger surface area and open channel characteristics, which contribute to the increased contact between the photocatalyst and dye molecules. Due to this fact, the (010) BiOCl nanosheets enhance the adsorption capacity of methyl orange molecules and thus facilitate interfacial charge transfer, resulting in the oxidation of the dye. Fig. 26 presents a schematic illustration of the face-dependent photoreactivity of BiOCl single crystalline nanosheets.³⁶⁶

Some preliminary data on facet effects for BiOBr³³⁷ and BiOI^{353,368,379} are also available. BiOBr as nanosheets with thicknesses from 9 to 31 nm was synthesized by Zhang *et al.*³³⁷ The visible-light-driven photocatalytic efficiency of BiOBr in rhodamine B degradation improves from *ca.* 83% to 94% when the thickness is decreased. It is worth mentioning that BiOBr

nanosheets show significantly worse capabilities for methyl orange and methylene blue degradation in comparison to rhodamine B degradation. This photocatalytic selectivity in removing the organic pollutants results from the preferential binding of rhodamine B to the oxygen atom that terminates (001) facets.³³⁷

Nevertheless, the most attractive photocatalytic nanostructures are 3D architectures. They are characterized by enhanced light harvesting, shortened diffusion pathways, the presence of numerous reactive sites and fast interfacial charge transfer.³⁷⁴ Moreover, their chemical composition plays an important role considering catalytic features. Zhang and co-workers³³¹ described the photocatalytic degradation of methyl orange solution under visible light. They found that the BiOI architecture exhibits better efficiency towards the photocatalytic degradation of methyl orange than BiOBr and BiOCl. Although BiOI shows higher photocatalytic activity than BiOBr and BiOCl for methyl orange decomposition under visible light,³³¹ BiOBr with a band gap of 2.8 eV shows the best oxidation and reduction properties under full light spectrum irradiation among all bismuth oxohalides.³⁸⁰ The BiOBr properties are a result of the hybridization of O 2p and Bi 6s orbitals, which results in band gap narrowing and enabling efficient conversion of visible light.³³⁴

In summary, BiOX are promising photocatalysts. Numerous papers about BiOX refer to the processes of the degradation of organic pollutants, especially dye pollutants in wastewater. Moreover, BiOX have promising potential applications for photocatalytic indoor-gas purification, water splitting, organic synthesis, and selective oxidation of alcohols.^{338,339,346,381,382} One of them is BiOI, which exhibits high photocatalytic activity under both visible light^{344,345,349,351,360,383} and near-IR,³⁸⁴ whereas BiOBr and BiOCl present very good photocatalytic activity under the full sunlight spectrum.³⁸⁰ Due to this fact, BiOBr and BiOCl are frequently studied as photocatalysts in various systems. BiOBr can remove more types of organic pollutants (including dyes,^{294,342,358,361,364,365,374} phenol,^{342,359} toluene³⁶⁹ and tetrabromobisphenol A³⁵⁵) than other BiOX photocatalysts. Furthermore, BiOBr was used to photo-degrade biological substances. Fang *et al.* demonstrated that BiOBr can degrade microcystin-LR in water under visible light irradiation, while Yu and co-workers demonstrated that hierarchical BiOBr microspheres can be used to remove *Micrococcus lylae* from water under fluorescent light irradiation.³⁵²

The photocatalytic properties of less known BiOF have been reported in 2010.²⁵⁶ BiOF materials show high UV light³⁸⁴ photocatalytic performance in the degradation of many organic pollutants such as phenol, methyl orange, rhodamine B and salicylic acid in aqueous media. This system was able to induce photooxidation of benzene vapour in air.²⁵⁶ A lot of studies have been carried out to investigate the photocatalytic activity of BiOCl nanomaterials. Jin *et al.*³⁸⁵ demonstrated that ultrathin BiOCl nanosheets can be used for photocatalytic reduction of CO₂ to CH₄. However, due to its wide band gap, unmodified BiOCl shows photocatalytic activity only under UV light irradiation.²²⁶ Zhang and co-workers reported the synthesis of flower-like BiOI hierarchical structures, which present higher

(as compared with BiOI nanoplates)³⁴⁹ photocatalytic activity under visible light irradiation towards organic pollutants. The morphology and properties of the obtained product usually depend on the synthesis technique. Detailed data describing the catalytic properties of various BiOX preparations are collated in Table S2 (ESI[†]).

1D structure growth is caused by stacking ribbon-like structures along the atomic chain direction.^{249,386} Additionally, the formation of a lower number of dangling bonds at the surface and cross-band hybridization between the n s² (Sb³⁺) cation and I⁻ ion promote highly efficient degradation of organic pollutants.^{386,387} The literature review indicates the BiOX and SbSI compounds among other chalcogenides with prospective applications in photovoltaics, photocatalysis and optoelectronics. The UV-Vis adsorption edges of BiOCl, BiOBr and BiOI are located at 370 nm, 440 nm and 670 nm, respectively, *i.e.* in the near-UV and visible light regions.^{331,377} Their catalytic efficiencies, however, in the case of sunlight irradiation are still unsatisfactory and limit their practical utility (*cf.* Fig. 21).³⁸⁸

In the case of BiOI we have previously presented the mechanism of photocurrent generation. Bismuth oxyiodide has been extensively studied with regard to the photocatalytic decomposition of organic pollutants from wastewater^{345,389} and photovoltaic applications.^{390,391} The increase of interest in this material is caused by the relatively narrow value of the band gap (the narrowest among the other bismuth oxyhalides),¹⁸³ low toxicity and stability in water.³⁴⁵ Generally, for high performance, a photocatalyst requires a high oxidation potential of the holes in the valence band (VB) and an enough reduction potential of the electrons in the conduction band (CB),³⁹⁰ which could be offered by wide-band-gap semiconductors.³⁹²

Bulk BiOI has a band gap energy in the range of 1.85–1.94 eV, whereas BiOI nanoparticles have a band gap energy of about 2.95 eV and nonstoichiometric phase Bi₄O₅I₂ has a band gap of 2.03 eV (Table 5). BiOI generates anodic photocurrents in a wide potential window (Fig. 27); nevertheless, the intensity of the photocurrent dramatically decreases when the material is exposed to light for a long time due to the irreversible photo-corrosion processes. Moreover, BiOI shows the so-called Photoelectrochemical Photocurrent Switching (PEPS) Effect,^{393–396} as described by Kwolek *et al.*³¹⁹ PEPS is an effect related to the change in the photocurrent polarity (anodic to cathodic transition or *vice versa*) resulting from the changes in the electrode potential or the wavelength of the incident light. Fig. 28 presents the photocurrent profile recorded for the BiOI material. The shape of the photocurrent pulses is a rectangular envelope, which indicates the rapid setting of the steady-state conditions, indicating that photogenerated charge carriers are efficiently collected by the conductive support and the recombination processes as well as other side processes (*e.g.* surface charging due to the high impedance of the semiconductor/conductor interface) are insignificant.³¹⁹ These effects make BiOI a potential candidate for unconventional optoelectronic devices and chemosensors.³⁹⁷

Bulk BiOBr has an optical band gap of 2.84 eV. The edge potentials of the valence (VB) and conduction bands (CB) are

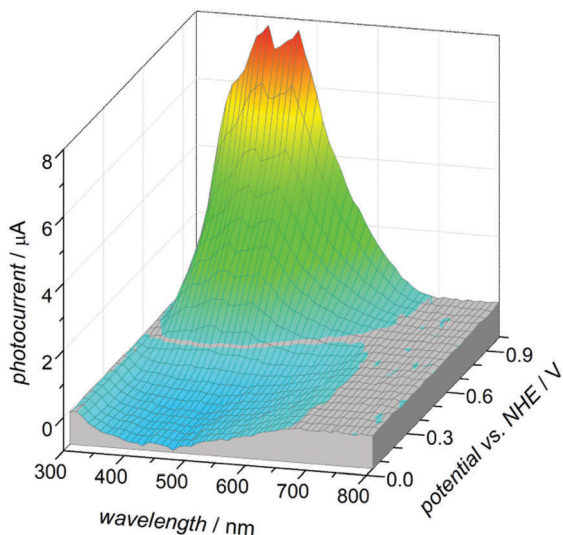


Fig. 27 Photocurrent amplitude of BiOI micro-pellets as a function of the incident light wavelength and photoelectrode potential in oxygenated 0.1 M KNO_3 electrolyte containing 0.01 M KI. Reprinted from ref. 319 with the permission from Elsevier.

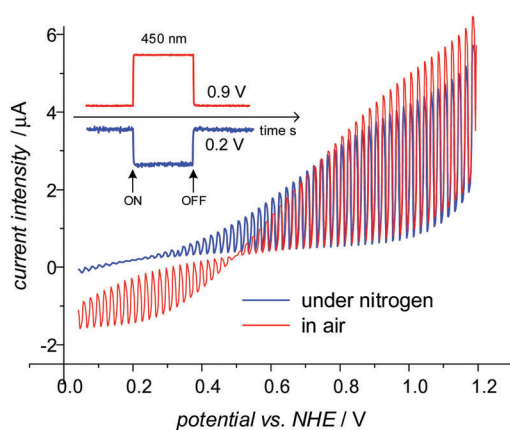


Fig. 28 Linear sweep voltammety of the BiOI electrode under pulsed illumination at 450 nm, 5 mV s^{-1} scan rate, 0.1 M KNO_3 containing 10 mM KI, scan in air and under nitrogen. The inset shows the kinetics of the photocurrent evolution under a constant potential at 450 nm. The red line represents anodic photocurrent at 0.9 V vs. NHE, and the blue line represents cathodic photocurrent at 0.2 V vs. NHE. Reprinted from ref. 319 with permission from Elsevier.

–4.24 eV and –1.4 eV respectively.³⁹⁸ However, the band gap of the BiOCl nanosheets was found to be 3.34 eV with the conduction and valence band edges at –3.63 eV and –6.97 eV with respect to vacuum, respectively.³¹⁵ An oxygen vacancy is formed *in situ* on the (001) facets of BiOCl under UV irradiation. Although the formed oxygen vacancy significantly enhances the absorption of BiOCl in the visible range, it plays a negative role in the dye degradation processes. The oxygen vacancy could effectively trap photoexcited electrons, thus inducing the photocorrosion of the photocatalyst. This results in a decrease of the reaction yields and may also block the degradation pathways involving O_2^- radicals.³⁹⁹

Among the V–VI–VII compounds, antimony sulfide (SbSI) has attracted attention due to its considerable photocatalytic activities.^{253,254,386} SbSI nanowires exhibit promising stable photocatalytic activity under visible light that comes from their one dimensional (1D) structure, large static dielectric constant and high stability in aqueous medium.^{253,254,386} Although SbSI was synthesized earlier than BiOX,^{306,400} its photoelectrochemical properties have not been widely explored yet. From all various synthesis techniques of SbSI (sonochemical method,⁴⁰¹ sol-gel technique,⁴⁰² pulsed laser deposition⁴⁰³ or melt fluctuation growth⁴⁰⁴), the sonochemical method presented by Nowak *et al.*⁴⁰¹ is the most attractive technique due to its simplicity, low cost, high speed and high efficiency. Moreover, this method allows easily synthesizing 1D materials with relatively high surface area-to-volume ratios. Due to SbSI's 1D structure, large static dielectric constant ($\epsilon = \sim 50\,000$)³⁰⁶ and exceptionally high stability in aqueous solutions, this form exhibits appropriate properties for application as visible light photocatalysts.^{253,254,386} Fig. 29 shows the mechanism of the photocurrent generation of antimony sulfide. The anodic photocurrent is generated by the straightforward oxidation reaction of the iodide in the electrolyte with the hole coming from the valence band. The cathodic photocurrent occurs when the conduction band edge of the semiconductor is higher than the reduction potential of molecular oxygen dissolved in the electrolyte (–0.16 V vs. SHE³⁹⁴).²⁵⁴

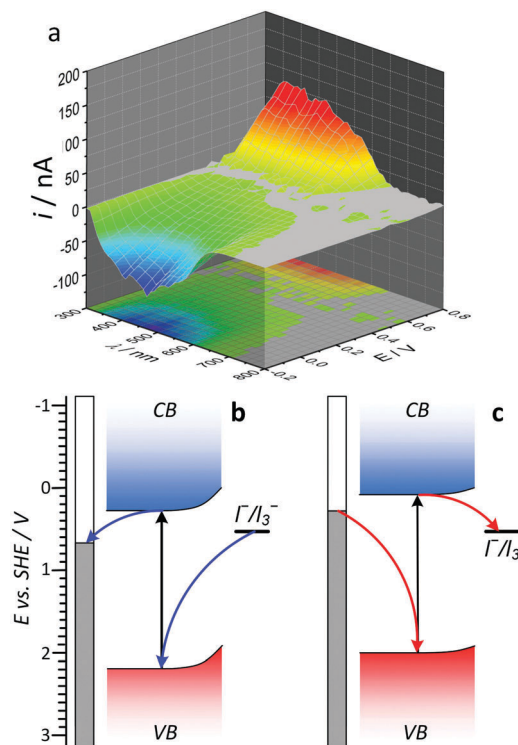


Fig. 29 The potential-dependent photocurrent action spectra recorded for an SbSI nanowire electrode (a), and anodic (b) and cathodic (c) photocurrent generation of SbSI. Adapted from ref. 254 with permission of IOP Publishing Ltd.

The review of the literature revealed that mixed-halogen materials exhibit even higher photocatalytic efficiencies than BiOCl and BiOI individually.⁴⁰⁵ Furthermore, doping is an efficient method to improve photoelectrochemical and photocatalytic performances. BiOCl, BiOBr and BiOI present similar layer structures, atom arrangements and chemical compositions, which allow introducing other halogen atoms into their atomic lattice. Therefore, many bismuth nanomaterials with bismuth oxides, such as BiOCl_xBr_{1-x}, BiOCl_xI_{1-x} and BiOI_xBr_{1-x}, have been successfully synthesized by means of wet chemistry.^{335,405-409} On the other hand, in the case of BiOI doping with atoms of foreign elements is not as effective as it is in the case of halogen atom doping.^{410,411} It is related to the very high symmetry of its layered structure, which leads to a low⁴ thermodynamic solubility of heteroatoms in the bismuth oxyhalide lattice.⁴¹²

Conclusions

Pnictogen chalcogenides constitute a versatile family of compounds. Usually they are wide band gap semiconductors with similar layered or chain-like structures. They are stable and relatively easily prepared. In contrast to other groups of compound semiconductors, their electronic structures as well as electrical and optical properties can be easily tuned *via* halogen or chalcogen exchange and thus their properties can be varied within a large window.

The variety of elemental compositions and crystal structures is characteristic of halochalcogenides presented in this review. Most of the presented structures have a 3D arrangement of chain like or ladder like 1D structures connected in various manners. Bismuth compounds, on the other hand, have a tendency to form 2D planes. Among the very different structures, a few common tendencies can be found. The trend in which the cell parameters change with the size of halogen is observed in BiOX compounds. Due to the arrangement of the halogen atoms on one side of the Bi atom, the BiOX structures change mostly with respect to the *c* parameter of the cell. The isomorphism of Sb₈O₁₁Cl₂ and Sb₈O₁₁Br₂, and Bi₁₉S₂₇Cl₃, Bi₁₉S₂₇Br₃, and Bi₁₉S₂₇I₃ structures is also a direct result of the changes in the halogen atom, which induce small changes in the cell parameters.

As for the spectroscopic properties of the investigated compounds, several trends can be easily noticed. First of all, the arsenic and antimony compounds are not very sensitive to chalcogenide substitution. In the case of bismuth compounds the exchange of either chalcogen or halogen ions with elements from higher periods leads to a significant decrease in the band gap width. Interestingly, this effect is not fully explainable based solely on the changes in the electronegativity values – it is clearly visible in the case of the E_g values for BiOI, BiSI and BiSeI – surely other factors have to be taken into consideration here. Another conclusion may be drawn on the tuning of the E_g value – this may be done over a relatively wide range through the changes in stoichiometry. Taking into account both the abovementioned observations, the discussed family

of semiconductors appears to be a versatile platform for the implementation of interactions with light.

In the undoped state they all are of a very high specific resistivity (10^{10} – 10^{15} Ω cm), which decreases with doping to *ca.* 10^3 – 10^4 Ω cm, irrespective of their composition. The lowest electron mobility is observed in the case of arsenic compounds (10^{-2} – 10^{-1} cm² V⁻¹ s⁻¹), which slightly increases for antimony analogues (10^0 – 10^2 cm² V⁻¹ s⁻¹), whereas in the case of bismuth compounds it is the highest and in the case of BiTeBr (1450 cm² V⁻¹ s⁻¹) slightly outbalances the value recorded for crystalline silicon (1400 cm² V⁻¹ s⁻¹).

These features determine the potential applications of pnictide chalcogenides: bismuth oxyhalides mainly as photocatalysts and heavier bismuth analogues for various emerging semiconducting technologies. Moreover, they are well suited for the fabrication of 1D structures. Due to the collaborative interactions between various anions within their lattice, they exhibit properties not easily available for other materials, *e.g.* high tolerance for defects. Therefore, they seem to be promising materials of choice for future electronic and catalytic applications.

Author contributions

Ewelina Właźlak and Andrzej Blachecki were responsible for the part concerning the crystallography, Magdalena Bisztyga-Szklarz prepared the part on photocatalysis and photoelectrochemistry, Sylwia Klejna and Tomasz Mazur analyzed the electronic structures of the title compounds, and Krzysztof Mech analyzed their electrical properties. Kacper Pilarczyk and Dawid Przychyna prepared the section on optical spectroscopy. Maciej Suchecki and Piotr Zawal described the synthetic strategies. Konrad Szaciłowski, along with Ewelina Właźlak and Krzysztof Mech, was responsible for the introductory part and general concept of the whole manuscript.

Conflicts of interest

There are no conflicts to declare.

Acknowledgements

The authors thank Professor Kapela Pilaka for valuable discussion during the preparation of the manuscript. This work was supported by the Ministry of Science and Higher Education and the National Science Centre (Poland) within the UMO-2015/18/A/ST4/00058 contract. K. Mech gratefully acknowledges the financial support of the Polish National Science Center (Grant No. UMO-2017/26/D/ST8/00508) as well as the Polish Ministry of Science and Higher Education (Grant No. IP2015/049974). K. Pilarczyk would like to acknowledge the financial support of the National Science Centre (Poland) within Grant No. UMO-2016/21/N/ST3/00469.

Notes and references

- 1 S. S. Li, *Semiconductor physical electronics*, Springer Science + Business Media LLC, New York, 2006.

- 2 I. Giangu, V. Buiculescu, F. Bechtold, G. Konstantinidis, K. Szaciłowski, A. Stefanescu, K. Pilarczyk, A. Stavridis, P. Kwolek, G. Stavridis, J. Mech and A. Müller, *Rom. J. Inf. Sci. Technol.*, 2014, **4**, 320–339.
- 3 M. Buchalska, J. Kuncewicz, E. Świętek, P. Łabuz, T. Baran, G. Stochel and W. Macyk, *Coord. Chem. Rev.*, 2013, **257**, 767–775.
- 4 N. D. Kaushika, A. Mishra and A. K. Rai, *Solar Photovoltaics*, Springer International Publishing, Cham, 2018.
- 5 P. Kwolek, M. Oszajca and K. Szaciłowski, *Coord. Chem. Rev.*, 2012, **56**, 1706–1731.
- 6 M. Oszajca, P. Kwolek, J. Mech and K. Szaciłowski, *Curr. Phys. Chem.*, 2011, **1**, 242–260.
- 7 A. Blachecki, J. Mech-Piskorz, M. Gajewska, K. Mech, K. Pilarczyk and K. Szaciłowski, *ChemPhysChem*, 2017, **18**, 1798–1810.
- 8 K. Pilarczyk, A. Podborska, M. Lis, M. Kawa, D. Migdał and K. Szaciłowski, *Adv. Electrode Mater.*, 2016, 1500471.
- 9 L. Vegard, *Z. Phys.*, 1921, **5**, 17–26.
- 10 J. A. Van Vechten and T. K. Bergstresser, *Phys. Rev. B: Solid State*, 1970, **1**, 3351–3358.
- 11 R. Hill, *J. Phys. C: Solid State Phys.*, 1974, **7**, 521–526.
- 12 P. Kwolek, K. Pilarczyk, T. Tokarski, K. Lewandowska and K. Szaciłowski, *Nanoscale*, 2014, **6**, 2244–2254.
- 13 Y. Zhao and K. Zhu, *Chem. Soc. Rev.*, 2016, **45**, 655–689.
- 14 O. Stroyuk, A. Raevskaya and N. Gaponik, *Chem. Soc. Rev.*, 2018, **47**, 5354–5422.
- 15 M. Kumar, A. Dubey, N. Adhikari, S. Venkatesan and Q. Qiao, *Energy Environ. Sci.*, 2015, **8**, 3134–3159.
- 16 J.-R. Xiao, S.-H. Yang, F. Feng, H.-G. Xue and S.-P. Guo, *Coord. Chem. Rev.*, 2017, **347**, 23–47.
- 17 B. Peng, K. Xu, H. Zhang, Z. Ning, H. Shao, G. Ni, J. Li, Y. Zhu, H. Zhu and C. M. Soukoulis, *Adv. Theor. Simul.*, 2018, **1**, 1700005.
- 18 H. Kunioku, M. Higashi and R. Abe, *Sci. Rep.*, 2016, **6**, 32664.
- 19 Z. Ran, X. Wang, Y. Li, D. Yang, X. G. Zhao, K. Biswas, D. J. Singh and L. Zhang, *NJP Comput. Mater.*, 2018, **4**, 14.
- 20 G. Voutsas and P. Rentzeperis, *Z. Kristallogr. – Cryst. Mater.*, 1986, **177**, 117–124.
- 21 G. Kanchana and D. Arivuoli, *Indian J. Eng. Mater. Sci.*, 2001, **8**, 373–376.
- 22 T. P. Braun and F. J. DiSalvo, *Acta Crystallogr., Sect. C: Cryst. Struct. Commun.*, 2000, **56**, e1–e2.
- 23 M. Moroz and M. Prokhorenko, *Inorg. Mater.*, 2016, **52**, 765–769.
- 24 T. Rosenthal, M. Döblinger, P. Wagatha, C. Gold, E. W. Scheidt, W. Scherer and O. Oeckler, *Z. Anorg. Allg. Chem.*, 2011, **637**, 2239–2245.
- 25 J. Jacimovic, X. Mettan, A. Pisoni, R. Gaal, S. Katrych, L. Demko, A. Akrap, L. Forro, H. Berger, P. Bugnon and A. Magrez, *Scr. Mater.*, 2014, **76**, 69–72.
- 26 C. Martin, A. Suslov, S. Buvaev, A. Hebard, P. Bugnon, H. Berger, A. Magrez and D. Tanner, *Phys. Rev. B: Condens. Matter Mater. Phys.*, 2014, **90**, 201204.
- 27 R. Sankar, I. Panneer Muthuselvam, C. J. Butler, S. C. Liou, B. H. Chen, M. W. Chu, W. L. Lee, M.-T. Lin, R. Jayavel and F. C. Chou, *CrystEngComm*, 2014, **16**, 8678–8683.
- 28 A. Shevelkov, E. Dikarev, R. Shpanchenko and B. Popovkin, *J. Solid State Chem.*, 1995, **114**, 379–384.
- 29 L. Wu, J. Yang, S. Wang, P. Wei, J. Yang, W. Zhang and L. Chen, *Phys. Rev. B: Condens. Matter Mater. Phys.*, 2014, **90**, 195210.
- 30 E. V. Bryukhova, A. P. Chernov, S. A. Dembovskii and G. K. Semin, *J. Struct. Chem.*, 1972, **13**, 493–494.
- 31 P. P. Seregin, V. P. Sivkov, F. S. Nasredinov, L. N. Vasilev, Y. V. Krylnikov and Y. P. Kostikov, *Phys. Status Solidi A*, 1977, **39**, 437–444.
- 32 H. Rodot, A. Hrubý and J. Horák, *Czech. J. Phys.*, 1971, **21**, 1213–1221.
- 33 D. Arivuoli, F. D. Gnanam and P. Ramasamy, *J. Cryst. Growth*, 1988, **88**, 353–357.
- 34 Z. S. Aliev, S. S. Musaeva, D. M. Babanly, A. V. Shevelkov and M. B. Babanly, *J. Alloys Compd.*, 2010, **505**, 450–455.
- 35 A. G. Papazoglou and P. J. Rentzeperis, *Z. Kristallogr. – Cryst. Mater.*, 1983, **165**, 159–168.
- 36 U. Eggenweiler, E. Keller, V. Krämer, U. Petasch and H. Oppermann, *Z. Kristallogr.*, 1999, **214**, 264–270.
- 37 L. Wu, J. Yang, M. Chi, S. Wang, P. Wei, W. Zhang, L. Chen and J. Yang, *Sci. Rep.*, 2015, **5**, 14319.
- 38 B. Michael, G. Robert, S. Marcus and S. Peer, *Z. Anorg. Allg. Chem.*, 2013, **639**, 219–229.
- 39 A. Crepaldi, L. Moreschini, G. Autès, C. Tournier-Colletta, S. Moser, N. Virk, H. Berger, P. Bugnon, Y. J. Chang, K. Kern, A. Bostwick, E. Rotenberg, O. V. Yazyev and M. Grioni, *Phys. Rev. Lett.*, 2012, **109**, 096803.
- 40 G. A. H. Schober, H. Murakawa, M. S. Bahramy, R. Arita, Y. Kaneko, Y. Tokura and N. Nagaosa, *Phys. Rev. Lett.*, 2012, **108**, 247208.
- 41 H. Peng, C. K. Chan, S. Meister, X. F. Zhang and Y. Cui, *Chem. Mater.*, 2009, **21**, 247–252.
- 42 A. W. Allaf and Z. Aji, *Spectrochim. Acta, Part A*, 2000, **56**, 1971–1977.
- 43 C. Reese and Z. Bao, *Mater. Today*, 2007, **10**, 20–27.
- 44 I. Y. Sklyadneva, R. Heid, K. P. Bohnen, V. Chis, V. A. Volodin, K. A. Kokh, O. E. Tereshchenko, P. M. Echenique and E. V. Chulkov, *Phys. Rev. B: Condens. Matter Mater. Phys.*, 2012, **86**, 094302.
- 45 R. Ganesha, D. Arivuoli and P. Ramasamy, *J. Cryst. Growth*, 1993, **128**, 1081–1085.
- 46 E. Kaldis, R. Cadoret and E. Schönherr, in *Fluid Sciences and Materials Science in Space: A European Perspective*, ed. H. U. Walter, Springer Berlin Heidelberg, Berlin, Heidelberg, 1987, pp. 355–404, DOI: 10.1007/978-3-642-46613-7_11.
- 47 J. Hobák, P. Lošťák, L. Jansa and P. Matoušek, *Phys. Status Solidi A*, 1985, **89**, 493–498.
- 48 D. Arivuoli, F. D. Gnanam and P. Ramasamy, *J. Phys. D: Appl. Phys.*, 1988, **21**, 1019.
- 49 D. Arivuoli, F. D. Gnanam and P. Ramasamy, *J. Mater. Sci. Lett.*, 1986, **5**, 597–598.
- 50 A. Audzijonis, G. Gaigalas, L. Žigas, R. Sereika, R. Žaltauskas, D. Balnionis and A. Rėza, *Phys. Status Solidi B*, 2009, **246**, 1702–1708.
- 51 Y. Hu, R. Li, C. Fan and X. Mao, *Mater. Lett.*, 2015, **161**, 41–44.
- 52 I. D. Sharma, G. K. Tripathi, V. K. Sharma, S. N. Tripathi, R. Kurchania, C. Kant, A. K. Sharma and K. K. Saini, *Cogent Chem.*, 2015, **1**, 1076371.
- 53 F. Duo, Y. Wang, X. Mao, X. Zhang, Y. Wang and C. Fan, *Appl. Surf. Sci.*, 2015, **340**, 35–42.
- 54 L. Hu, S. Dong, Q. Li, J. Feng, Y. Pi, M. Liu, J. Sun and J. Sun, *J. Alloys Compd.*, 2015, **633**, 256–264.
- 55 F. A. Bannister and M. H. Hey, *Mineral. Mag.*, 1935, **24**, 49–58.
- 56 L. Zhu, X. Zheng, X. Yin, X. Liu, Y. Jia and Y. Xie, *Chem. Lett.*, 2003, **32**, 350–351.
- 57 Y. Su, C. Ding, Y. Dang, H. Wang, L. Ye, X. Jin, H. Xie and C. Liu, *Appl. Surf. Sci.*, 2015, **346**, 311–316.
- 58 C. Wang, K. Tang, Q. Yang, J. Hu and Y. Qian, *J. Mater. Chem.*, 2002, **12**, 2426–2429.
- 59 W. J. Fa, P. J. Li, Y. G. Zhang, L. L. Guo, J. F. Guo and F. L. Yang, *Adv. Mater. Res.*, 2011, **236–238**, 1919–1922.
- 60 K. Zhang, J. Liang, S. Wang, J. Liu, K. Ren, X. Zheng, H. Luo, Y. Peng, X. Zou, X. Bo, J. Li and X. Yu, *Cryst. Growth Des.*, 2012, **12**, 793–803.
- 61 A. Starczewska, M. Nowak, P. Szperlich, B. Toroń, K. Mistewicz, D. Stróż and J. Szala, *Sens. Actuators, A*, 2012, **183**, 34–42.
- 62 K. Przemysław, P. Kacper, T. Tomasz, M. Justyna, I. Jakub and S. Konrad, *Nanotechnology*, 2015, **26**, 105710.
- 63 A. Gedanken, *Ultrason. Sonochem.*, 2004, **11**, 47–55.
- 64 M. Nowak, *Nanowires science and technology*, InTech, 2010.
- 65 V. A. Kulbachinskii, V. G. Kytin, A. A. Kudryashov and A. V. Shevelkov, *AIP Conf. Proc.*, 2012, **1449**, 358–361.
- 66 G. Landolt, S. V. Eremeev, O. E. Tereshchenko, S. Muff, B. Slomski, K. A. Kokh, M. Kobayashi, T. Schmitt, V. N. Strocov, J. Osterwalder, E. V. Chulkov and J. H. Dil, *New J. Phys.*, 2013, **15**, 085022.
- 67 S. Dong-Woon, H. Seung-Cheol, P. Sang-an, K. Yoeng-Geun, K. Chang-dae and K. Wha-Tek, *J. Phys. Chem. Solids*, 1994, **55**, 825–830.
- 68 A. M. Ganose, K. T. Butler, A. Walsh and D. O. Scanlon, *J. Mater. Chem. A*, 2016, **4**, 2060–2068.
- 69 H. Silvia and S. Konrad, *Z. Anorg. Allg. Chem.*, 2000, **626**, 1778–1782.
- 70 K. Dehnicke and J. Weidlein, *Z. Anorg. Allg. Chem.*, 1966, **342**, 225–232.
- 71 K. Abe, T. Usuki, O. Uemura, Y. Kameda and M. Sakurai, *J. Non-Cryst. Solids*, 2001, **293–295**, 464–470.
- 72 J. S. Sanghera, J. Heo and J. D. Mackenzie, *J. Non-Cryst. Solids*, 1988, **103**, 155–178.
- 73 J. Heo, J. S. Sanghera and J. D. Mackenzie, *Opt. Eng.*, 1991, **30**, 470–479.
- 74 L. Koudelka and M. Pisárčik, *Mater. Chem. Phys.*, 1983, **9**, 571–582.
- 75 P. Rentzeperis, *Prog. Cryst. Growth Charact. Mater.*, 1991, **21**, 113–138.
- 76 M. V. Kurushkin, V. A. Markov, A. V. Semencha, M. D. Mikhailov, A. S. Tverjanovich, A. L. Shakhmin, T. V. Larionova and V. D. Andreeva, *Int. J. Appl. Glass Sci.*, 2018, **9**, 85–89.

- 77 M. Mitkova and P. Boolchand, *J. Non-Cryst. Solids*, 1998, **240**, 1–21.
- 78 L. Koudelka and M. Pisárčik, *J. Non-Cryst. Solids*, 1984, **64**, 87–94.
- 79 S. L. Kuznetsov, M. D. Mikhailov, I. M. Pecheritsyn and E. Y. Turkina, *J. Non-Cryst. Solids*, 1997, **213–214**, 68–71.
- 80 B. M. Koperles, P. P. Puga, I. D. Turyanitsa, A. N. Borets and D. V. Chepur, *Sov. Phys.*, 1973, **16**, 1421–1424.
- 81 R. Kniep and H. D. Reski, *Angew. Chem., Int. Ed. Engl.*, 1981, **20**, 212–214.
- 82 Y. Kameda, Y. Sugawara and O. Uemura, *J. Non-Cryst. Solids*, 1993, **156–158**, 725–727.
- 83 A. A. Lavrentiev, B. V. Gabrel'yan, I. Y. Nikiforov and V. B. Vorzhev, *J. Struct. Chem.*, 2005, **46**, 805–812.
- 84 D. Arivuoli, F. D. Gnanam and P. Ramasamy, *J. Cryst. Growth*, 1988, **88**, 353–357.
- 85 K. Rüdiger and R. H. Dieter, *Angew. Chem., Int. Ed. Engl.*, 1981, **20**, 212–214.
- 86 D. L. Eaton, *J. Am. Ceram. Soc.*, 1964, **47**, 554–558.
- 87 R. B. Hilborn and K. Prasad, *J. Vac. Sci. Technol.*, 1969, **6**, 632–634.
- 88 A. Stergiou and P. J. Rentzeperis, *Z. Kristallogr. – Cryst. Mater.*, 1985, **172**, 111–119.
- 89 A. Åström and S. Andersson, *J. Solid State Chem.*, 1973, **6**, 191–194.
- 90 K. Holz and R. Mattes, *Z. Anorg. Allg. Chem.*, 1989, **578**, 133–142.
- 91 M. Edstrand, *Acta Chem. Scand.*, 1947, **1**, 178–203.
- 92 S. Menchetti, C. Sabelli and R. Trosti-Ferroni, *Acta Crystallogr., Sect. C: Cryst. Struct. Commun.*, 1984, **40**, 1506–1510.
- 93 M. Edstrand, *Ark. kemi*, 1953, **6**, 89–112.
- 94 V. Kramer, *Acta Crystallogr., Sect. B: Struct. Crystallogr. Cryst. Chem.*, 1975, **31**, 234–237.
- 95 V. Krämer, M. Schuhmacher and R. Nitsche, *Mater. Res. Bull.*, 1973, **8**, 65–74.
- 96 G. P. Voutsas and P. J. Rentzeperis, *Z. Kristallogr. – Cryst. Mater.*, 1982, **161**, 345–347.
- 97 A. Ibanez, J.-C. Jumas, J. Olivier-Fourcade, E. Philippot and M. Maurin, *J. Solid State Chem.*, 1983, **48**, 272–283.
- 98 R. C. Burns, W.-L. Chan, R. J. Gillespie, W.-C. Luk, J. F. Sawyer and D. R. Slim, *Inorg. Chem.*, 1980, **19**, 1432–1439.
- 99 R. Minkwitz, H. Borrmann and J. Nowicki, *Z. Naturforsch., B: J. Chem. Sci.*, 1991, **46**, 629.
- 100 G. Cardinal, R. J. Gillespie, J. F. Sawyer and J. E. Vekris, *J. Chem. Soc., Dalton Trans.*, 1982, 765–779, DOI: 10.1039/DT9820000765.
- 101 A. Kikuchi, Y. Oka and E. Sawaguchi, *J. Phys. Soc. Jpn.*, 1967, **23**, 337–354.
- 102 G. D. Christofferson and J. D. McCullough, *Acta Crystallogr.*, 1959, **12**, 14–16.
- 103 M. Schulte-Kellinghaus and V. Krämer, *Z. Kristallogr. – Cryst. Mater.*, 1980, **152**, 47.
- 104 R. Faggiani, R. J. Gillespie, J. F. Sawyer and J. E. Vekris, *Acta Crystallogr., Sect. C: Cryst. Struct. Commun.*, 1989, **45**, 1847–1853.
- 105 K. G. Keramidas, G. Voutsas and P. I. Rentzeperis, *Z. Kristallogr.*, 1993, **205**, 35–40.
- 106 J. L. Soubeyroux, S. F. Matar, J. M. Reau and P. Hagenmuller, *Solid State Ion.*, 1984, **14**, 337–345.
- 107 E. Keller, V. Krämer, M. Schmidt and H. Oppermann, *Z. Kristallogr. – Cryst. Mater.*, 2002, **217**, 256.
- 108 E. Keller, J. Ketterer and V. Krämer, *Z. Kristallogr. – Cryst. Mater.*, 2001, **216**, 595.
- 109 U. Eggenweiler, E. Keller and V. Kramer, *Acta Crystallogr., Sect. B: Struct. Sci.*, 2000, **56**, 431–437.
- 110 B. Aurivillius, *Chem. Scr.*, 1984, **24**, 125–129.
- 111 E. Keller and V. Krämer, *Acta Crystallogr., Sect. C: Struct. Chem.*, 2007, **63**, i109–i111.
- 112 J. Laval, J. C. Champarnaud-Mesjard, B. Frit, A. Britel and A. Mikou, *ChemInform Abstract: Bi7F11O5: A New Ordered Anion-Excess Fluorite-Related Structure with Columnar Clusters*, 2010.
- 113 J. Ketterer, E. Keller and V. Krämer, *Crystal structure of bismuth oxide iodide, β -Bi₅O₇I*, 1985.
- 114 S. Savilov, V. Khrustalev, A. Kuznetsov, B. A. Popovkin and M. Yu. Antipin, *Russ. Chem. Bull.*, 2005, **54**, 87–92.
- 115 K. Pal, S. Anand and U. V. Waghmare, *J. Mater. Chem. C*, 2015, **3**, 12130–12139.
- 116 J. A. Sans, F. J. Manjón, A. L. J. Pereira, R. Vilaplana, O. Gomis, A. Segura, A. Muñoz, P. Rodríguez-Hernández, C. Popescu, C. Drasar and P. Ruleova, *Phys. Rev. B*, 2016, **93**, 024110.
- 117 Z. S. Aliev and M. B. Babanly, *Inorg. Mater.*, 2008, **44**, 1076–1080.
- 118 J. Beck and A. Stankowski, *Z. Naturforsch., B: J. Chem. Sci.*, 2001, **56**, 453.
- 119 B. Johannes, F. Andreas and S. Alexander, *Z. Anorg. Allg. Chem.*, 2002, **628**, 2542–2548.
- 120 R. Ganesha, D. Arivuoli and P. Ramasamy, *J. Mater. Sci. Lett.*, 1992, **11**, 1608–1610.
- 121 U. Eggenweiler, E. Keller, V. Krämer, U. Petasch and H. Oppermann, *Z. Kristallogr. – Cryst. Mater.*, 1999, **214**, 264.
- 122 E. Keller and V. Krämer, *Acta Crystallogr., Sect. B: Struct. Sci.*, 2006, **62**, 417–423.
- 123 G. P. Voutsas and P. J. Rentzeperis, *Z. Kristallogr. – Cryst. Mater.*, 1984, **166**, 153.
- 124 G. P. Voutsas and P. J. Rentzeperis, *Z. Kristallogr. – Cryst. Mater.*, 1980, **152**, 109.
- 125 J. Fenner, A. Rabenau and G. Trageser, in *Advances in Inorganic Chemistry and Radiochemistry*, ed. H. J. Emeléus and A. G. Sharpe, Academic Press, 1980, vol. 23, pp. 329–425.
- 126 Y. Yan, Y. Xu, S. Lei, X. Ou, L. Chen, J. Xiong, Y. Xiao and B. Cheng, *Dalton Trans.*, 2018, **47**, 3408–3416.
- 127 Z. S. Aliev, S. S. Musayeva, F. Y. Jafarli, I. R. Amiraslanov, A. V. Shevelkov and M. B. Babanly, *J. Alloys Compd.*, 2014, **610**, 522–528.
- 128 C. Deng, H. Guan and X. Tian, *Mater. Lett.*, 2013, **108**, 17–20.
- 129 V. Krämer, *Z. Naturforsch., B: Anorg. Chem., Org. Chem.*, 1974, **29**, 688.
- 130 R. Groom, A. Jacobs, M. Cepeda, R. Drummey and S. E. Latturmer, *Chem. Mater.*, 2017, **29**, 3314–3323.
- 131 P. M. R. Alasdair, A. G. Paul and B. Neil, *Angew. Chem., Int. Ed.*, 2014, **53**, 6050–6069.
- 132 M. J. Turner, J. J. McKinnon, S. K. Wolff, D. J. Grimwood, P. R. Spackman, D. Jayatilaka and M. A. Spackman, *CrystalExplorer17*, University of Western Australia, 2017, <http://hirshfeldsurface.net>.
- 133 A. S. Kanishcheva, Yu. N. Mikhailov and A. P. Chernov, *Dokl. Akad. Nauk SSSR*, 1980, **251**, 1396–1398.
- 134 S. Haupt and K. Seppelt, *Z. Anorg. Allg. Chem.*, 2000, **626**, 1778–1782.
- 135 A. Astrom and S. Andersson, *J. Solid State Chem.*, 1973, **6**, 191–194.
- 136 D. Siapakas, A. Bartzokas, G. P. Voutsas and P. J. Rentzeperis, *Z. Kristallogr. – Cryst. Mater.*, 1986, **175**, 305–315.
- 137 M. S. Jin, K. H. Park, H. G. Kim, S. H. Choe, B. S. Park, S. C. Hyun and W. T. Kim, *Semicond. Sci. Technol.*, 1995, **10**, 1167–1171.
- 138 D. Arivuoli, F. D. Gnanam and P. Ramasamy, *Mater. Chem. Phys.*, 1987, **16**, 181–188.
- 139 S. Narayanan and R. Pandey, *Proceedings of 1994 IEEE International Symposium on Applications of Ferroelectrics*, 1991, pp. 309–311.
- 140 M. Nowak, P. Mroczek, P. Duka, A. Kidawa, P. Szperlich, A. Grabowski, J. Szala and G. Moskal, *Sens. Actuators, A*, 2009, **150**, 251–256.
- 141 L. Palaniappan, F. Gnanam and P. Ramasamy, *Semicond. Sci. Technol.*, 1987, **2**, 790.
- 142 A. Starczewska, R. Wrzalik, M. Nowak, P. Szperlich, M. Jesionek, G. Moskal, T. Rzychoń, J. Szala, D. Stróż and P. Maślanka, *Ultrason. Sonochem.*, 2009, **16**, 537–545.
- 143 A. C. Wibowo, C. D. Malliakas, Z. Liu, J. A. Peters, M. Sebastian, D. Y. Chung, B. W. Wessels and M. G. Kanatzidis, *Inorg. Chem.*, 2013, **52**, 7045–7050.
- 144 V. Krämer, *Acta Crystallogr., Sect. B: Struct. Crystallogr. Cryst. Chem.*, 1975, **31**, 234–237.
- 145 S. G. Bhat and S. Dharmaprasanth, *Mater. Lett.*, 1997, **30**, 19–22.
- 146 J. L. Soubeyroux, S. F. Matar, J. M. Reau and P. Hagenmuller, *Solid State Ionics*, 1984, **14**, 337–345.
- 147 S. Shamailla, A. K. L. Sajjad, F. Chen and J. Zhang, *J. Colloid Interface Sci.*, 2011, **356**, 465–472.
- 148 Z. Deng, D. Chen, B. Peng and F. Tang, *Cryst. Growth Des.*, 2008, **8**, 2995–3003.
- 149 H. An, Y. Du, T. Wang, C. Wang, W. Hao and J. Zhang, *Rare Met.*, 2008, **27**, 243–250.
- 150 L. Zhu, Y. Xie, X. Zheng, X. Yin and X. Tian, *Inorg. Chem.*, 2002, **41**, 4560–4566.
- 151 L. Ye, L. Wang, H. Xie, Y. Su, X. Jin and C. Zhang, *Energy Technol.*, 2015, **3**, 1115–1120.
- 152 G. P. Voutsas and P. J. Rentzeperis, *Z. Kristallogr. – New Cryst. Struct.*, 1980, **152**, 109–118.
- 153 E. Dönges, *Z. Anorg. Allg. Chem.*, 1950, **263**, 280–291.
- 154 X. Su, G. Zhang, T. Liu, Y. Liu, J. Qin and C. Chen, *Russ. J. Inorg. Chem.*, 2006, **51**, 1864–1868.

- 155 E. Dönges, *Z. Anorg. Allg. Chem.*, 1951, **265**, 56–61.
- 156 S.-D. Guo and H.-C. Li, *Comput. Mater. Sci.*, 2017, **139**, 361–367.
- 157 N. T. Dich, P. Lošák and J. Horák, *Czech. J. Phys.*, 1978, **28**, 1297–1303.
- 158 J.-P. Laval, J.-C. Champarnaud-Mesjard, B. Frit, A. Britel and A. Mikou, *Eur. J. Solid State Inorg. Chem.*, 1994, **31**, 943–956.
- 159 U. Eggenweiler, E. Keller, V. Krämer, C. A. Meyer and J. Ketterer, *Z. Kristallogr. - New Cryst. Struct.*, 1998, **213**, 695.
- 160 B. Aurivillius, *Chem. Scr.*, 1984, **24**, 125–129.
- 161 U. Eggenweiler, J. Ketterer, E. Keller and V. Krämer, *Z. Kristallogr. - Cryst. Mater.*, 2001, **216**, 230–233.
- 162 E. Keller and V. Krämer, *Acta Crystallogr., Sect. C: Cryst. Struct. Commun.*, 2007, **63**, 109–111.
- 163 V. Krämer, *Acta Crystallogr., Sect. B: Struct. Crystallogr. Cryst. Chem.*, 1979, **35**, 139–140.
- 164 G. Ryu, K. Son and G. Schütz, *J. Cryst. Growth*, 2016, **440**, 26–30.
- 165 F. Demartin, C. M. Gramaccioli and I. Campostrini, *Am. Mineral.*, 2009, **94**, 1045–1048.
- 166 F. Demartin, C. M. Gramaccioli, I. Campostrini and P. Orlandi, *Am. Mineral.*, 2008, **93**, 1603–1607.
- 167 F. Demartin, C. M. Gramaccioli and I. Campostrini, *Mineral. Mag.*, 2010, **74**, 141–145.
- 168 H. Shi, W. Ming and M.-H. Du, *Phys. Rev. B*, 2016, **93**, 104108.
- 169 Z. Ran, X. Wang, Y. Li, D. Yang, X.-G. Zhao, K. Biswas, D. J. Singh and L. Zhang, *NJP Comput. Mater.*, 2018, **4**, 14.
- 170 A. Walsh and G. W. Watson, *J. Phys. Chem. B*, 2005, **109**, 18868–18875.
- 171 R. E. Brandt, V. Stevanović, D. S. Ginley and T. Buonassisi, *MRS Commun.*, 2015, **5**, 265–275.
- 172 A. Zakutayev, C. M. Caskey, A. N. Fioretti, D. S. Ginley, J. Vidal, V. Stevanovic, E. Tea and S. Lany, *J. Phys. Chem. Lett.*, 2014, **5**, 1117–1125.
- 173 W. Khan, S. Hussain, J. Minar and S. Azam, *J. Electron. Mater.*, 2018, **47**, 1131–1139.
- 174 H. Akkus and A. M. Mamedov, *J. Phys.: Condens. Matter*, 2007, **19**, 116207.
- 175 H. Akkus, A. Kazempour, H. Akbarzadeh and A. M. Mamedov, *Phys. Status Solidi B*, 2007, **244**, 3673–3683.
- 176 A. Audzijonis, L. Žigas, J. Siroic, A. Pauliukas, R. Žaltauskas, A. Čerškus and J. Narušis, *Phys. Status Solidi B*, 2006, **243**, 610–617.
- 177 T. Ozer and S. Cabuk, *J. Mol. Model.*, 2018, **24**, 66.
- 178 C. Tablero, *J. Alloys Compd.*, 2016, **678**, 18–22.
- 179 H. Koc, S. Palaz, A. M. Mamedov and E. Ozbay, *Ferroelectrics*, 2017, **511**, 22–34.
- 180 G. Wang, X. Luo, Y. Huang, A. Kuang, H. Yuan and H. Chen, *RSC Adv.*, 2016, **6**, 91508–91516.
- 181 M. Ren, F. Teng, Y. Yang, Y. Zhai, W. Gu, Z. Liu, Z. Liu and Y. Teng, *Mater. Des.*, 2017, **131**, 402–409.
- 182 J. Zhao, L. Xu, Y. Liu, Z. Yu, C. Li, Y. Wang and Z. Liu, *J. Phys. Chem. C*, 2015, **119**, 27657–27665.
- 183 W. L. Huang and Q. Zhu, *Comput. Mater. Sci.*, 2008, **43**, 1101–1108.
- 184 W. L. Huang and Q. Zhu, *Comput. Mater. Sci.*, 2009, **46**, 1076–1084.
- 185 Z. Yang, Y. Pei, S. Tan, X. Wang, L. Liu and X. Su, *Comput. Mater. Sci.*, 2013, **74**, 50–54.
- 186 L. Zhao, X. Zhang, C. Fan, Z. Liang and P. Han, *Physica B*, 2012, **407**, 3364–3370.
- 187 A. Audzijonis and R. Sereika, *Int. J. Mod. Phys. B*, 2013, **27**, 1350122.
- 188 A. Audzijonis, R. Žaltauskas, R. Sereika, L. Žigas and A. Rėza, *J. Phys. Chem. Solids*, 2010, **71**, 884–891.
- 189 A. Audzijonis, L. Žigas, G. Gaigalas, R. Sereika and B. Žygaitienė, *J. Cluster Sci.*, 2010, **21**, 577–589.
- 190 A. Audzijonis, R. Sereika, R. Žaltauskas and L. Žigas, *Phys. Status Solidi B*, 2010, **247**, 176–181.
- 191 A. Audzijonis, G. Gaigalas, L. Žigas, A. Pauliukas, R. Žaltauskas, A. Kvedaravičius and A. Čerškus, *J. Electron Spectrosc. Relat. Phenom.*, 2008, **162**, 13–18.
- 192 S. Zhou, J. Long and W. Huang, *Mater. Sci. Semicond. Process.*, 2014, **27**, 605–610.
- 193 S. Güler-Kılıç and Ç. Kılıç, *Phys. Rev. B: Condens. Matter Mater. Phys.*, 2015, **91**, 245204.
- 194 V. A. Kulbachinskii, V. G. Kytin, A. A. Kudryashov, A. N. Kuznetsov and A. V. Shevelkov, *J. Solid State Chem.*, 2012, **193**, 154–160.
- 195 S. Güler-Kılıç and Ç. Kılıç, *Phys. Rev. B*, 2016, **94**, 165203.
- 196 C. Fong and F. Wooten, *Experimental and Theoretical Study of the Feasibility of the Gunn Effect in BiSbCl, BiSbBr, BiSi, BiSeI, BiSeBr and BiSeCl*, California Univ. Davis Dept of Applied Science, 1981.
- 197 C. Fong, C. Perlov and F. Wooten, *J. Phys. C: Solid State Phys.*, 1982, **15**, 2605.
- 198 K. T. Butler, S. McKechnie, P. Azarhoosh, M. Van Schilfgaarde, D. O. Scanlon and A. Walsh, *Appl. Phys. Lett.*, 2016, **108**, 112103.
- 199 J. Alward, C. Fong, M. El-Batanouny and F. Wooten, *Solid State Commun.*, 1978, **25**, 307–310.
- 200 H. Akkus, A. M. Mamedov, A. Kazempour and H. Akbarzadeh, *Cent. Eur. J. Phys.*, 2008, **6**, 64–75.
- 201 H. Akkus, *Int. J. Mod. Phys. B*, 2009, **23**, 97–104.
- 202 M. S. Bahramy, R. Arita and N. Nagaosa, *Phys. Rev. B: Condens. Matter Mater. Phys.*, 2011, **84**, 041202.
- 203 G. San-Dong, Z. Ai-Xia and L. Hui-Chao, *Nanotechnology*, 2017, **28**, 445702.
- 204 H. L. Zhuang, V. R. Cooper, H. Xu, P. Ganesh, R. G. Hennig and P. R. C. Kent, *Phys. Rev. B: Condens. Matter Mater. Phys.*, 2015, **92**, 115302.
- 205 I. Lefebvre, M. Lannoo, G. Allan, A. Ibanez, J. Fourcade, J. Jumas and E. Beaupaire, *Phys. Rev. Lett.*, 1987, **59**, 2471.
- 206 S. Dutta, T. Das and S. Datta, *Phys. Chem. Chem. Phys.*, 2018, **20**, 103–111.
- 207 I. P. Rusinov, I. A. Nechaev, S. V. Ereemeev, C. Friedrich, S. Blügel and E. V. Chulkov, *Phys. Rev. B: Condens. Matter Mater. Phys.*, 2013, **87**, 205103.
- 208 I. Rusinov, T. Menshchikova, I. Y. Sklyadneva, R. Heid, K. Bohnen and E. Chulkov, *New J. Phys.*, 2016, **18**, 113003.
- 209 W. Lihua, Y. Jiong, Z. Tiansong, W. Shanyu, W. Ping, Z. Wenqing, C. Lidong and Y. Jihui, *J. Phys.: Condens. Matter*, 2016, **28**, 085801.
- 210 L. Moreschini, G. Autès, A. Crepaldi, S. Moser, J. C. Johannsen, K. S. Kim, H. Berger, P. Bugnon, A. Magrez, J. Denlinger, E. Rotenberg, A. Bostwick, O. V. Yazyev and M. Grioni, *J. Electron Spectrosc. Relat. Phenom.*, 2015, **201**, 115–120.
- 211 K. T. Butler, J. M. Frost and A. Walsh, *Energy Environ. Sci.*, 2015, **8**, 838–848.
- 212 A. Walsh, D. J. Payne, R. G. Egdell and G. W. Watson, *Chem. Soc. Rev.*, 2011, **40**, 4455–4463.
- 213 S. Kvedaravičius, A. Audzijonis, N. Mykolaitienė and A. Jcancerevičius, *Phase Transitions*, 1996, **58**, 235–246.
- 214 S. Kvedaravičius, A. Audzijonis and N. Mykolaitienė, *Ferroelectrics*, 1993, **150**, 381–385.
- 215 A. Audzijonis, L. Žigas, R. Žaltauskas, J. Narušis, A. Pauliukas and A. Čerškus, *Ferroelectrics*, 2006, **330**, 25–35.
- 216 Y. Ota, T. Abe and T. Inushima, *Ferroelectrics*, 2011, **414**, 113–120.
- 217 K. Rao and S. Chaplot, *Phys. Status Solidi B*, 1985, **129**, 471–482.
- 218 A. Audzijonis, S. Kvedaravičius, V. Paulikas, J. Siroicas, N. Mykolaitienė and R. Šadžius, *Ferroelectrics*, 1998, **215**, 221–231.
- 219 A. Audzijonis and R. Sereika, *Phase Transitions*, 2014, **87**, 509–514.
- 220 A. Audzijonis, G. Gaigalas, L. Žigas, V. Lazauskas, J. Narušis, N. Mykolaitienė and A. Pauliukas, *Phase Transitions*, 2004, **77**, 941–954.
- 221 A. Audzijonis, R. Žaltauskas, L. Žigas, I. V. Vinokurova, O. V. Farberovich, A. Pauliukas and A. Kvedaravičius, *Physica B*, 2006, **371**, 68–73.
- 222 J. Grigas, E. Talik and V. Lazauskas, *Ferroelectrics*, 2003, **284**, 147–160.
- 223 A. Audzijonis, G. Gaigalas, L. Žigas, A. Pauliukas, R. Žaltauskas, A. Čerškus, J. Narušis and A. Kvedaravičius, *Physica B*, 2007, **391**, 22–27.
- 224 A. Audzijonis, G. Gaigalas, L. Žigas, A. Pauliukas, R. Žaltauskas, A. Čerškus, D. Balnionis and A. Kvedaravičius, *J. Electron Spectrosc. Relat. Phenom.*, 2008, **164**, 19–23.
- 225 A. M. Ganose, M. Cuff, K. T. Butler, A. Walsh and D. O. Scanlon, *Chem. Mater.*, 2016, **28**, 1980–1984.
- 226 Y. Yang, C. Zhang, C. Lai, G. Zeng, D. Huang, M. Cheng, J. Wang, F. Chen, C. Zhou and W. Xiong, *Adv. Colloid Interface Sci.*, 2018, **254**, 76–93.
- 227 J. Lv, Q. Hu, C. Cao and Y. Zhao, *Chemosphere*, 2018, **191**, 427–437.
- 228 T. Kong, X. Wei, G. Zhu and Y. Huang, *J. Mater. Sci.*, 2018, **53**, 708–715.
- 229 H. Zhang, L. Liu and Z. Zhou, *RSC Adv.*, 2012, **2**, 9224–9229.
- 230 S. Fiedler, T. Bathon, S. V. Ereemeev, O. E. Tereshchenko, K. A. Kokh, E. V. Chulkov, P. Sessi, H. Bentmann, M. Bode and F. Reinert, *Phys. Rev. B: Condens. Matter Mater. Phys.*, 2015, **92**, 235430.

- 231 Y. Qi, W. Shi, P. G. Naumov, N. Kumar, R. Sankar, W. Schnelle, C. Shekhar, F. C. Chou, C. Felser, B. Yan and S. A. Medvedev, *Adv. Mater.*, 2017, **29**, 1605965.
- 232 J. Park, K.-H. Jin, Y. J. Jo, E. S. Choi, W. Kang, E. Kampert, J. S. Rhyee, S.-H. Jhi and J. S. Kim, *Sci. Rep.*, 2015, **5**, 15973.
- 233 Z. Zhiyong, C. Yingchun and S. Udo, *New J. Phys.*, 2013, **15**, 023010.
- 234 X. Zhang, Q. Liu, J.-W. Luo, A. J. Freeman and A. Zunger, *Nat. Phys.*, 2014, **10**, 387.
- 235 M. S. Bahramy and N. Ogawa, *Adv. Mater.*, 2017, **29**, 1605911.
- 236 A. Manchon, H. C. Koo, J. Nitta, S. M. Frolov and R. A. Duine, *Nat. Mater.*, 2015, **14**, 871.
- 237 A. Harun and M. N. Amirullah, *J. Phys.: Condens. Matter*, 2007, **19**, 116207.
- 238 H. Akkus and A. M. Mamedov, *Cent. Eur. J. Phys.*, 2007, **5**, 25–34.
- 239 I. S. Haque and V. S. Pande, *J. Chem. Inf. Model.*, 2010, **50**, 1075–1088.
- 240 A. Audzijonis, R. Sereika, R. Žaltauskas and A. Rėza, *J. Phys. Chem. Solids*, 2011, **72**, 1501–1505.
- 241 M. N. Secuk and H. Akkus, *J. Phys.: Conf. Ser.*, 2016, **707**, 012017.
- 242 E. K. Dogan, M. Aycibin, S. E. Gulebaglan, M. Secuk, B. Erdinc and H. Akkus, *J. Korean Phys. Soc.*, 2013, **63**, 2133–2137.
- 243 J. S. Lee, G. A. H. Schober, M. S. Bahramy, H. Murakawa, Y. Onose, R. Arita, N. Nagaosa and Y. Tokura, *Phys. Rev. Lett.*, 2011, **107**, 117401.
- 244 L. Demkó, G. A. H. Schober, V. Kocsis, M. S. Bahramy, H. Murakawa, J. S. Lee, I. Kézsmárki, R. Arita, N. Nagaosa and Y. Tokura, *Phys. Rev. Lett.*, 2012, **109**, 167401.
- 245 K. Žiček and A. Audzijonis, *Phys. Status Solidi B*, 1996, **565**, 1–11.
- 246 J. Li, A. Bhalla and L. Cross, *Ferroelectr., Lett. Sect.*, 1990, **12**, 1–7.
- 247 S. Jeon, G. Cho, W. T. Kim and S. I. Kwun, *Solid State Commun.*, 1988, **68**, 1043–1046.
- 248 M. Nowak, B. Kauch and P. Szperlich, *Rev. Sci. Instrum.*, 2009, **80**, 046107.
- 249 I. Cho, B.-K. Min, S. W. Joo and Y. Sohn, *Mater. Lett.*, 2012, **86**, 132–135.
- 250 Q. Yang, K. Tang, C. Wang, B. Hai, G. Shen, C. An, C. Zhang and Y. Qian, *J. Cryst. Growth*, 2001, **233**, 774–778.
- 251 M. Nowak and P. Szperlich, *Opt. Mater.*, 2013, **35**, 1200–1206.
- 252 M. Jesionek, M. Nowak, K. Mistewicz, M. Kępińska, D. Stróż, I. Bednarczyk and R. Paszkiewicz, *Ultrasonics*, 2018, **83**, 179–187.
- 253 M. Tasvirri and Z. Sajadi-Hezave, *Mol. Catal.*, 2017, **436**, 174–181.
- 254 P. Kwolek, K. Pilarczyk, T. Tokarski, J. Mech, J. Irzmański and K. Szaciłowski, *Nanotechnology*, 2015, **26**, 105710.
- 255 R. Nie, H. s. Yun, M. J. Paik, A. Mehta, B. w. Park, C. Choi Yong and I. Seok Sang, *Adv. Energy Mater.*, 2017, **8**, 1701901.
- 256 W. Su, J. Wang, Y. Huang, W. Wang, L. Wu, X. Wang and P. Liu, *Scr. Mater.*, 2010, **62**, 345–348.
- 257 S. Vadivel, V. P. Kamalakannan, N. P. Kavitha, T. Santhoshini Priya and N. Balasubramanian, *Mater. Sci. Semicond. Process.*, 2016, **41**, 59–66.
- 258 W. Gu, G. Zhang, F. Teng, Y. Teng, Z. Zhao and W. Fan, *Chem. Phys. Lett.*, 2016, **659**, 221–224.
- 259 M. Yang, Q. Yang, J. Zhong, J. Li, S. Huang and X. Li, *Mater. Lett.*, 2017, **201**, 35–38.
- 260 K.-L. Zhang, C.-M. Liu, F.-Q. Huang, C. Zheng and W.-D. Wang, *Appl. Catal., B*, 2006, **68**, 125–129.
- 261 D. Zhengtao, T. Fangqiong and J. M. Anthony, *Nanotechnology*, 2008, **19**, 295705.
- 262 J. Henle and S. Kaskel, *J. Mater. Chem.*, 2007, **17**, 4964–4971.
- 263 Y. I. Choi, Y.-I. Kim, D. W. Cho, J.-S. Kang, K. T. Leung and Y. Sohn, *RSC Adv.*, 2015, **5**, 79624–79634.
- 264 R. Hou, Y. Gao, H. Zhu, G. Yang, W. Liu, Y. Huo, Z. Xie and H. Li, *Chem. Eng. J.*, 2017, **317**, 386–393.
- 265 S.-Y. Chou, W.-H. Chung, L.-W. Chen, Y.-M. Dai, W.-Y. Lin, J.-H. Lin and C.-C. Chen, *RSC Adv.*, 2016, **6**, 82743–82758.
- 266 F. Shen, L. Zhou, J. Shi, M. Xing and J. Zhang, *RSC Adv.*, 2015, **5**, 4918–4925.
- 267 Y. Zhou, T. Wen, B. Chang, B. Yang and Y. Wang, *Dalton Trans.*, 2016, **45**, 13709–13716.
- 268 J.-j. Xu, J.-w. Yang, P. Zhang, Q. Yuan, Y.-h. Zhu, Y. Wang, M.-m. Wu, Z.-m. Wang and M.-d. Chen, *Water Sci. Eng.*, 2017, **10**, 334–339.
- 269 T. Jiang, J. Li, Y. Gao, L. Li, T. Lu and L. Pan, *J. Colloid Interface Sci.*, 2017, **490**, 812–818.
- 270 Q. Wang, D. Jiao, J. Lian, Q. Ma, J. Yu, H. Huang, J. Zhong and J. Li, *J. Alloys Compd.*, 2015, **649**, 474–482.
- 271 Y. Zuo, C. Wang, Y. Sun and J. Cheng, *Mater. Lett.*, 2015, **139**, 149–152.
- 272 Y. Peng, P.-P. Yu, Q.-G. Chen, H.-Y. Zhou and A.-W. Xu, *J. Phys. Chem. C*, 2015, **119**, 13032–13040.
- 273 Y. Bai, T. Chen, P. Wang, L. Wang and L. Ye, *Chem. Eng. J.*, 2016, **304**, 454–460.
- 274 X. Mao, F. Xie and M. Li, *Mater. Lett.*, 2016, **166**, 296–299.
- 275 X. Li, T. Chen, H. Lin, J. Cao, H. Huang and S. Chen, *Sci. Bull.*, 2018, **63**, 219–227.
- 276 Z. C. Xu, C. Y. Fong, F. Wooten and Y. Yehs, *Ferroelectrics*, 1984, **56**, 187–202.
- 277 N. T. Hahn, J. L. Self and C. B. Mullins, *J. Phys. Chem. Lett.*, 2012, **3**, 1571–1576.
- 278 I. Aguiar, M. Momburú, M. P. Barthaburu, H. B. Pereira and L. Fornaro, *Mater. Res. Express*, 2016, **3**.
- 279 H. Kunioku, M. Higashi and R. Abe, *Sci. Rep.*, 2016, **6**, 32664.
- 280 R. A. Groom, A. Jacobs, M. Cepeda, R. Drummey and S. E. Lattur, *Inorg. Chem.*, 2017, **56**, 12362–12368.
- 281 K. Žiček and A. Audzijonis, *Phys. Status Solidi B*, 1984, **121**, K51–K53.
- 282 Y.-L. Lee, H.-J. Song, S.-A. Park, S.-H. Choe, M.-S. Jin and W.-T. Kim, *Ferroelectrics*, 1995, **165**, 255–261.
- 283 A. A. Makhnev, L. V. Nomerovannaya, T. V. Kuznetsova, O. E. Tereshchenko and K. A. Kokh, *Opt. Spectrosc.*, 2016, **121**, 364–370.
- 284 A. A. Makhnev, L. V. Nomerovannaya, T. V. Kuznetsova, O. E. Tereshchenko and K. A. Kokh, *Opt. Spectrosc.*, 2014, **117**, 764–768.
- 285 K. Ishizaka, M. S. Bahramy, H. Murakawa, M. Sakano, T. Shimojima, T. Sonobe, K. Koizumi, S. Shin, H. Miyahara, A. Kimura, K. Miyamoto, T. Okuda, H. Namatame, M. Taniguchi, R. Arita, N. Nagaosa, K. Kobayashi, Y. Murakami, R. Kumai, Y. Kaneko, Y. Onose and Y. Tokura, *Nat. Mater.*, 2011, **10**, 521.
- 286 X. Xi, C. Ma, Z. Liu, Z. Chen, W. Ku, H. Berger, C. Martin, D. B. Tanner and G. L. Carr, *Phys. Rev. Lett.*, 2013, **111**, 155701.
- 287 C. Martin, A. V. Suslov, S. Buvaev, A. F. Hebard, P. Bugnon, H. Berger, A. Magrez and D. B. Tanner, *Europhys. Lett.*, 2016, **116**, 57003.
- 288 V. A. Kulbachinskii, V. G. Kytin, Z. V. Lazrukina, A. N. Kuznetsov and A. V. Shevelkov, *Semiconductors*, 2010, **44**, 1548–1553.
- 289 I. P. Rusinov, O. E. Tereshchenko, K. A. Kokh, A. R. Shakhmametova, I. A. Azarov and E. V. Chulkov, *JETP Lett.*, 2015, **101**, 507–512.
- 290 A. Makhnev, L. Nomerovannaya, T. Kuznetsova, O. Tereshchenko and K. Kokh, *Opt. Spectrosc.*, 2016, **121**, 364–370.
- 291 S. S. Flaschen, A. D. Pearson and W. R. Northover, *J. Appl. Phys.*, 1960, **31**, 219–220.
- 292 I. D. Turyanitsa, V. V. Khiminets and O. V. Khiminets, *Fiz. Khim. Stekla*, 1975, **1**, 170.
- 293 A. D. Pearson, W. R. Northover, J. F. Dewald and W. F. Peck, *Advances in Glass Technology*, Plenum Press, New York, 1962.
- 294 B. T. Kolomiets and T. F. Nazarova, *Phys. Solid State*, 1960, **2**, 369.
- 295 W. F. Peck and J. F. Dewald, *J. Electrochem. Soc.*, 1964, **111**, 561–563.
- 296 N. F. Mott, *Philos. Mag. A*, 1969, **19**, 835–852.
- 297 A. I. Gubanov, *Quantum Electron Theory of Amorphous Conductors*, Consultants Bureau, New York, 1965.
- 298 M. H. Cohen, H. Fritzsche and S. R. Ovshinsky, *Phys. Rev. Lett.*, 1969, **22**, 1065–1068.
- 299 M. Roilos, *J. Non-Cryst. Solids*, 1971, **6**, 5–12.
- 300 A. D. Pearson, *J. Non-Cryst. Solids*, 1970, **2**, 1–15.
- 301 C. H. Seager, D. Emin and R. K. Quinn, *J. Non-Cryst. Solids*, 1972, **8–10**, 341–346.
- 302 R. T. Johnson and R. K. Quinn, *Solid State Commun.*, 1971, **9**, 393–396.
- 303 K. Weiser and M. H. Brodsky, *Phys. Rev. B: Solid State*, 1970, **1**, 791–799.
- 304 C. H. Seager, D. Emin and R. K. Quinn, *Phys. Rev. B: Solid State*, 1973, **8**, 4746–4760.
- 305 R. T. Johnson, R. K. Quinn and J. A. Borders, *J. Non-Cryst. Solids*, 1974, **15**, 289–309.
- 306 E. Fatuzzo, G. Harbeke, W. J. Merz, R. Nitsche, H. Roetschi and W. Ruppel, *Phys. Rev.*, 1962, **127**, 2036–2037.
- 307 A. Audzijonis, R. Sereika and R. Žaltauskas, *Solid State Commun.*, 2008, **147**, 88–89.
- 308 O. Madelung, in *Semiconductors: Other than Group IV Elements and III–V Compounds*, ed. O. Madelung, Springer Berlin Heidelberg, Berlin, Heidelberg, 1992, pp. 53–80, DOI: 10.1007/978-3-662-00464-7_4.

- 309 F. M. Fridkin, E. I. Gerzanich, I. I. Groshik and V. A. Lyakhovitskaya, *JETP Lett.*, 1966, **4**, 139.
- 310 D. V. Chepur, D. M. Bercha, I. D. Turyanitsa and V. Yu. Slivka, *Phys. Status Solidi B*, 1968, **30**, 461–468.
- 311 T. A. Pikka and V. M. Fridkin, *Phys. Solid State*, 1969, **140**, 2668.
- 312 H. K. Dubey, L. P. Deshmukh, D. E. Kshirsagar, M. Sharon and M. Sharon, *Adv. Phys. Chem.*, 2014, **6**.
- 313 R. Nitsche and W. J. Merz, *J. Phys. Chem. Solids*, 1960, **13**, 154–155.
- 314 M. V. Shtilikha and D. V. Chepur, *Phys. Solid State*, 1972, **14**, 1354.
- 315 Y. Myung, F. Wu, S. Banerjee, J. Park and P. Banerjee, *Chem. Commun.*, 2015, **51**, 2629–2632.
- 316 Z. Yangwei, X. Xianghan, X. Ying, W. Huichao, F. Hailong, L. Xi and W. Jian, *Adv. Mater. Interfaces*, 2015, **2**, 1500194.
- 317 D. Lotnyk, V. Komanický, A. Feher and V. Bunda, *Appl. Phys. Lett.*, 2016, **109**, 242106.
- 318 M. Long, P. Hu, H. Wu, Y. Chen, B. Tan and W. Cai, *J. Mater. Chem. A*, 2015, **3**, 5592–5598.
- 319 P. Kwolek and K. Szaciłowski, *Electrochim. Acta*, 2013, **104**, 448–453.
- 320 J. Horák and K. Čermák, *Czechoslovakij fiziceskij zurnal B*, 1965, **15**, 536–538.
- 321 N. T. Hahn, A. J. E. Rettie, S. K. Beal, R. R. Fullon and C. B. Mullins, *J. Phys. Chem. C*, 2012, **116**, 24878–24886.
- 322 T. A. Pikka, *Kristallografiya*, 1967, **12**, 1075.
- 323 J. Horák, I. D. Turyanitsa and K. Nejezchleb, *Krist. Tech.*, 1968, **3**, 2231.
- 324 V. V. Sobolev, E. V. Pesterev and V. V. Sobolev, *Inorg. Mater.*, 2004, **40**, 128–129.
- 325 P. Lostak, J. Horak, A. Vasko and T. D. Nguyen, *Phys. Status Solidi A*, 1980, **59**, 311–316.
- 326 J.-J. Ying, V. V. Struzhkin, Z.-Y. Cao, A. F. Goncharov, H.-K. Mao, F. Chen, X.-H. Chen, A. G. Gavriliuk and X.-J. Chen, *Phys. Rev. B*, 2016, **93**, 100504.
- 327 T. Ideue, J. G. Checkelsky, M. S. Bahramy, H. Murakawa, Y. Kaneko, N. Nagaosa and Y. Tokura, *Phys. Rev. B: Condens. Matter Mater. Phys.*, 2014, **90**, 161107.
- 328 A. Akrap, J. Teyssier, A. Magrez, P. Bugnon, H. Berger, A. B. Kuzmenko and D. van der Marel, *Phys. Rev. B: Condens. Matter Mater. Phys.*, 2014, **90**, 035201.
- 329 J. C. Ahern, R. Fairchild, J. S. Thomas, J. Carr and H. H. Patterson, *Appl. Catal., B*, 2015, **179**, 229–238.
- 330 H. Park, A. Bak, Y. Y. Ahn, J. Choi and M. R. Hoffmann, *J. Hazard. Mater.*, 2012, **211–212**, 47–54.
- 331 X. Zhang, Z. Ai, F. Jia and L. Zhang, *J. Phys. Chem. C*, 2008, **112**, 747–753.
- 332 X. Chang, J. Huang, C. Cheng, Q. Sui, W. Sha, G. Ji, S. Deng and G. Yu, *Catal. Commun.*, 2010, **11**, 460–464.
- 333 P. Wang, P. Yang, Y. Bai, T. Chen, X. Shi, L. Ye and X. Zhang, *J. Taiwan Inst. Chem. Eng.*, 2016, **68**, 295–300.
- 334 L.-w. Shan, L.-q. He, J. Suriyaprakash and L.-x. Yang, *J. Alloys Compd.*, 2016, **665**, 158–164.
- 335 J. Cao, B. Xu, B. Luo, H. Lin and S. Chen, *Catal. Commun.*, 2011, **13**, 63–68.
- 336 H. Li, Q. Jia, Y. Cui and S. Fan, *Mater. Lett.*, 2013, **107**, 262–264.
- 337 D. Zhang, J. Li, Q. Wang and Q. Wu, *J. Mater. Chem. A*, 2013, **1**, 8622–8629.
- 338 N. Kijima, K. Matano, M. Saito, T. Oikawa, T. Konishi, H. Yasuda, T. Sato and Y. Yoshimura, *Appl. Catal., A*, 2001, **206**, 237–244.
- 339 M. Guan, C. Xiao, J. Zhang, S. Fan, R. An, Q. Cheng, J. Xie, M. Zhou, B. Ye and Y. Xie, *J. Am. Chem. Soc.*, 2013, **135**, 10411–10417.
- 340 L. Ye, L. Zan, L. Tian, T. Peng and J. Zhang, *Chem. Commun.*, 2011, **47**, 6951–6953.
- 341 J. Xia, J. Zhang, S. Yin, H. Li, H. Xu, L. Xu and Q. Zhang, *J. Phys. Chem. Solids*, 2013, **74**, 298–304.
- 342 L. Zhang, X.-F. Cao, X.-T. Chen and Z.-L. Xue, *J. Colloid Interface Sci.*, 2011, **354**, 630–636.
- 343 S. Peng, L. Li, P. Zhu, Y. Wu, M. Srinivasan, S. G. Mhaisalkar, S. Ramakrishna and Q. Yan, *Chem. – Asian J.*, 2013, **8**, 258–268.
- 344 R. Hao, X. Xiao, X. Zuo, J. Nan and W. Zhang, *J. Hazard. Mater.*, 2012, **209**, 137–145.
- 345 Y. Li, J. Wang, H. Yao, L. Dang and Z. Li, *J. Mol. Catal. A: Chem.*, 2011, **334**, 116–122.
- 346 Z. Ai, W. Ho, S. Lee and L. Zhang, *Environ. Sci. Technol.*, 2009, **43**, 4143–4150.
- 347 J. Xiong, Z. Jiao, G. Lu, W. Ren, J. Ye and Y. Bi, *Chem. – Eur. J.*, 2013, **19**, 9472–9475.
- 348 L. Chen, S.-F. Yin, R. Huang, Y. Zhou, S.-L. Luo and C.-T. Au, *Catal. Commun.*, 2012, **23**, 54–57.
- 349 X. Xiao and W.-D. Zhang, *J. Mater. Chem.*, 2010, **20**, 5866–5870.
- 350 J.-M. Song, C.-J. Mao, H.-L. Niu, Y.-H. Shen and S.-Y. Zhang, *CrystEngComm*, 2010, **12**, 3875–3881.
- 351 J. Xia, S. Yin, H. Li, H. Xu, L. Xu and Y. Xu, *Dalton Trans.*, 2011, **40**, 5249–5258.
- 352 D. Zhang, M. Wen, B. Jiang, G. Li and C. Y. Jimmy, *J. Hazard. Mater.*, 2012, **211**, 104–111.
- 353 D.-H. Wang, G.-Q. Gao, Y.-W. Zhang, L.-S. Zhou, A.-W. Xu and W. Chen, *Nanoscale*, 2012, **4**, 7780–7785.
- 354 H. Cheng, B. Huang, Z. Wang, X. Qin, X. Zhang and Y. Dai, *Chem. – Eur. J.*, 2011, **17**, 8039–8043.
- 355 J. Xu, W. Meng, Y. Zhang, L. Li and C. Guo, *Appl. Catal., B*, 2011, **107**, 355–362.
- 356 C. Wang, C. Shao, Y. Liu and L. Zhang, *Scr. Mater.*, 2008, **59**, 332–335.
- 357 X. Chang, M. Gondal, A. Al-Saadi, M. Ali, H. Shen, Q. Zhou, J. Zhang, M. Du, Y. Liu and G. Ji, *J. Colloid Interface Sci.*, 2012, **377**, 291–298.
- 358 M. Shang, W. Wang and L. Zhang, *J. Hazard. Mater.*, 2009, **167**, 803–809.
- 359 H. Tian, J. Li, M. Ge, Y. Zhao and L. Liu, *Catal. Sci. Technol.*, 2012, **2**, 2351–2355.
- 360 Y. Lei, G. Wang, S. Song, W. Fan, M. Pang, J. Tang and H. Zhang, *Dalton Trans.*, 2010, **39**, 3273–3278.
- 361 J. Zhang, F. Shi, J. Lin, D. Chen, J. Gao, Z. Huang, X. Ding and C. Tang, *Chem. Mater.*, 2008, **20**, 2937–2941.
- 362 L.-P. Zhu, G.-H. Liao, N.-C. Bing, L.-L. Wang, Y. Yang and H.-Y. Xie, *CrystEngComm*, 2010, **12**, 3791–3796.
- 363 J. Xia, S. Yin, H. Li, H. Xu, Y. Yan and Q. Zhang, *Langmuir*, 2010, **27**, 1200–1206.
- 364 Y. Huo, J. Zhang, M. Miao and Y. Jin, *Appl. Catal., B*, 2012, **111**, 334–341.
- 365 Y. Chen, M. Wen and Q. Wu, *CrystEngComm*, 2011, **13**, 3035–3039.
- 366 J. Jiang, K. Zhao, X. Xiao and L. Zhang, *J. Am. Chem. Soc.*, 2012, **134**, 4473–4476.
- 367 S. Wu, C. Wang, Y. Cui, T. Wang, B. Huang, X. Zhang, X. Qin and P. Brault, *Mater. Lett.*, 2010, **64**, 115–118.
- 368 L. Ye, L. Tian, T. Peng and L. Zan, *J. Mater. Chem.*, 2011, **21**, 12479–12484.
- 369 Y. Feng, L. Li, J. Li, J. Wang and L. Liu, *J. Hazard. Mater.*, 2011, **192**, 538–544.
- 370 R. Yuan, C. Lin, B. Wu and X. Fu, *Eur. J. Inorg. Chem.*, 2009, 3537–3540.
- 371 Y. Lei, G. Wang, S. Song, W. Fan and H. Zhang, *CrystEngComm*, 2009, **11**, 1857–1862.
- 372 X. Qin, H. Cheng, W. Wang, B. Huang, X. Zhang and Y. Dai, *Mater. Lett.*, 2013, **100**, 285–288.
- 373 J. Xiong, G. Cheng, G. Li, F. Qin and R. Chen, *RSC Adv.*, 2011, **1**, 1542–1553.
- 374 H. Cheng, B. Huang and Y. Dai, *Nanoscale*, 2014, **6**, 2009–2026.
- 375 B. Zhang, G. Ji, M. A. Gondal, Y. Liu, X. Zhang, X. Chang and N. Li, *J. Nanopart. Res.*, 2013, **15**, 1773.
- 376 Y. Xia, P. Yang, Y. Sun, Y. Wu, B. Mayers, B. Gates, Y. Yin, F. Kim and H. Yan, *Adv. Mater.*, 2003, **15**, 353–389.
- 377 L. Ye, Y. Su, X. Jin, H. Xie and C. Zhang, *Environ. Sci.: Nano*, 2014, **1**, 90–112.
- 378 C. Wang, X. Zhang, B. Yuan, C. Shao and Y. Liu, *IET Micro Nano Lett.*, 2012, **7**, 152–154.
- 379 L. Ye, J. Chen, L. Tian, J. Liu, T. Peng, K. Deng and L. Zan, *Appl. Catal., B*, 2013, **130**, 1–7.
- 380 L. Ye, in *Semiconductor Photocatalysis – Materials, Mechanisms and Applications*, ed. W. Cao, InTech, Rijeka, 2016, ch. 10, DOI: 10.5772/62626.
- 381 R. Yuan, S. Fan, H. Zhou, Z. Ding, S. Lin, Z. Li, Z. Zhang, C. Xu, L. Wu and X. Wang, *Angew. Chem., Int. Ed.*, 2013, **52**, 1035–1039.
- 382 H. Li, F. Qin, Z. Yang, X. Cui, J. Wang and L. Zhang, *J. Am. Chem. Soc.*, 2017, **139**, 3513–3521.
- 383 B. Zhang, G. Ji, M. Gondal, Y. Liu, X. Zhang, X. Chang and N. Li, *J. Nanopart. Res.*, 2013, **15**, 1773.
- 384 X. Meng and Z. Zhang, *J. Mol. Catal. A: Chem.*, 2016, **423**, 533–549.
- 385 J. Jin, Y. Wang and T. He, *RSC Adv.*, 2015, **5**, 100244.
- 386 M. Tamilselvan and A. J. Bhattacharyya, *RSC Adv.*, 2016, **6**, 105980.

- 387 Y. Zhou, L. Wang, S. Chen, S. Qin, X. Liu, J. Chen, D.-J. Xue, M. Luo, Y. Cao, Y. Cheng, E. H. Sargent and J. Tang, *Nat. Photonics*, 2015, **9**, 409–415.
- 388 Y. Yang, C. Zhang, C. Lai, G. Zeng, D. Huang, M. Cheng, J. Wang, F. Chen, C. Zhou and W. Xiong, *Adv. Colloid Interface Sci.*, 2018, **254**, 76–93.
- 389 Y. Wang, K. Deng and L. Zhang, *J. Phys. Chem. C*, 2011, **115**, 14300–14308.
- 390 K. Zhao, X. Zhang and L. Zhang, *Electrochem. Commun.*, 2009, **11**, 612–615.
- 391 K. Wang, F. Jia, Z. Zheng and L. Zhang, *Electrochem. Commun.*, 2010, **12**, 1764–1767.
- 392 J. Jiang, L. Zhang, H. Li, W. He and J. J. Yin, *Nanoscale*, 2013, **5**, 10573–10581.
- 393 K. Szaciłowski and W. Macyk, *C. R. Chim*, 2006, **9**, 315–324.
- 394 K. Szaciłowski, W. Macyk, M. Hebda and G. Stochel, *Chem-PhysChem*, 2006, **7**, 2384–2391.
- 395 K. Szaciłowski, W. Macyk and G. Stochel, *J. Mater. Chem.*, 2006, **16**, 4603–4611.
- 396 M. Hebda, G. Stochel, K. Szaciłowski and W. Macyk, *J. Phys. Chem. B*, 2006, **110**, 15275–15283.
- 397 K. Pilarczyk, E. Wlazłak, D. Przyczyna, A. Blachecki, A. Podborska, V. Anathasiou, Z. Konkoli and K. Szaciłowski, *Coord. Chem. Rev.*, 2018, **365**, 23–40.
- 398 Z. Jiang, F. Yang, G. Yang, L. Kong, M. O. Jones, T. Xiao and P. P. Edwards, *J. Photochem. Photobiol., A*, 2010, **212**, 8–13.
- 399 M. Chen, S. Yu, X. Zhang, F. Wang, Y. Lin and Y. Zhou, *Superlattices Microstruct.*, 2016, **89**, 275–281.
- 400 D. Berlincourt, H. Jaffe, W. Merz and R. Nitsche, *Appl. Phys. Lett.*, 1964, **4**, 61–63.
- 401 M. Nowak, P. Szperlich, J. Szala, G. Moskal and D. Stróż, *Ultrason. Sonochem.*, 2008, **15**, 709–716.
- 402 Y. Xu, F. D. Monte, J. Mackenzie, K. Namjoshi, P. Muggli and C. Joshi, *Ferroelectrics*, 1999, **230**, 11–20.
- 403 S. Surthi, S. Kotru and R. Pandey, *Integr. Ferroelectr.*, 2002, **48**, 263–269.
- 404 L. Palaniappan, F. Gnanam and P. Ramasamy, *J. Mater. Sci. Lett.*, 1986, **5**, 1007–1008.
- 405 T. B. Li, G. Chen, C. Zhou, Z. Y. Shen, R. C. Jin and J. X. Sun, *Dalton Trans.*, 2011, **40**, 6751–6758.
- 406 Z. Jia, F. Wang, F. Xin and B. Zhang, *Ind. Eng. Chem. Res.*, 2011, **50**, 6688–6694.
- 407 F. Dong, Y. Sun, M. Fu, Z. Wu and S. Lee, *J. Hazard. Mater.*, 2012, **219**, 26–34.
- 408 S. Shenawi-Khalil, V. Uvarov, Y. Kritsman, E. Menes, I. Popov and Y. Sasson, *Catal. Commun.*, 2011, **12**, 1136–1141.
- 409 H. Gnayem and Y. Sasson, *ACS Catal.*, 2013, **3**, 186–191.
- 410 B. Pare, B. Sarwan and S. Jonnalagadda, *Appl. Surf. Sci.*, 2011, **258**, 247–253.
- 411 J. Yu, B. Wei, L. Zhu, H. Gao, W. Sun and L. Xu, *Appl. Surf. Sci.*, 2013, **284**, 497–502.
- 412 J. Li, Y. Yu and L. Zhang, *Nanoscale*, 2014, **6**, 8473–8488.

Heavy pnictogen chalcogenides: synthesis, structure and properties of rediscovered semiconductors

Ewelina Właźlak,^{a,b,*} Andrzej Blachecki,^{a,c} Magdalena Bisztyga-Szklarz,^a Sylwia Klejna,^a Tomasz Mazur,^a Krzysztof Mech,^{a*} Kacper Pilarczyk,^a Dawid Przychyna,^{a,d} Maciej Suchecki,^{a,d} Piotr Zawal,^{a,d} Konrad Szaciłowski^{a,*}

Electronic supplementary information

Table S1. Computed with various methods band gaps, electron and hole effective masses, ionization potentials, electron affinities and static dielectric constants for bulk 15 group oxyhalides and chalcogenides.

	Space Group (International S. G. number)	E_g [eV]	E_g direct [eV]	$m_{\text{eff}}(e)$ [me]	$m_{\text{eff}}(h)$ [me]	IP	EA	Ionic Dielectric constant ϵ_r	Method
Sb-O-F	<i>Pnma</i>	4.33	4.72	1.94	1.23	20.49			HSE+SOC ¹⁶⁹
Sb-O-Cl	<i>P2₁/C</i>		4.02	1	2.66	19.68			HSE+SOC ¹⁶⁹
Sb-S-Cl	<i>Pnam</i> (62)	2.18	2.51						EPM ¹⁹⁹
		2.31	2.73	0.51	0.64	5.80	3.37		HSE06-SOC ¹⁹⁸
		2.53		0.10	0.32				QSGW-SOC ¹⁹⁸
Sb-S-Br		2.21	1.72	0.26	0.57				EV-SOC ¹⁷³
		1.57							SR-GGA ²¹¹
		2.16		0.52	3.6				NCPP-PBE-GW ²⁰⁰
		2.29	2.32					105.15	HSE+SOC ¹⁶⁹
	<i>Pna2₁</i> (33)	2.21							(GGA)E-V + SOC ²²⁸
Sb-S-I	<i>Pnam</i> (62)	2.11							EPM ¹⁹⁹
		1.82	2.07	0.53	1.39			37.28	HSE+SOC ¹⁶⁹
		2.05							(GGA)E-V + SOC ²²⁸
		1.445							LDA + PAW ¹⁷⁷
		1.28							PAW-PBE-SOC ¹⁷¹
	<i>P2₁2₁2₁</i> (19)	1.45	1.46	0.91	2.84			31.59	PAW-PBE-SOC ¹⁷¹
	<i>Pna2₁</i> (33)	1.45	1.60	1.31	2.06			69.72	PAW-PBE-SOC ¹⁷¹
		2.11	1.60	1.25	2.06			69.38	HSE06-SOC ¹⁹⁸
		2.22	2.31			5.37	3.15		QSGW-SOC ¹⁹⁸
		2.05	2.42	0.43	0.57				EV-SOC ¹⁷³
		1.51		0.07	0.098				SR-GGA ²¹¹
		1.45	1.66	0.21	0.27				NCPP-LDA ²³⁷
	<i>Pna2₁</i> (33)	1.49	1.56						NCPP-LDA ⁴¹³
		1.446	1.58						LDA+PAW ¹⁷⁷
Sb-Se-Br		0.23	0.47						NCPP-PBE ²⁰¹
Sb-Se-I		1.67	2.06						EPM ¹⁹⁹
		1.86	2.23	0.54	0.58	5.26	3.23		HSE06-SOC ¹⁹⁸
	<i>Pnma</i> (62)	2.03	1.29	0.59	4.37			43.94	QSGW-SOC ¹⁹⁸
		1.16		0.082	0.164				PAW-PBE-SOC ¹⁷¹
		1.62	1.40	0.52	0.24				EV-SOC ¹⁷³
		1.29							SR-GGA ²¹¹
		1.65		0.35	1.83				NCPP-PBE&GW ¹⁷⁵
		1.75	1.96					57.18	HSE+SOC ¹⁶⁹
		1.62							(GGA)E-V + SOC ²²⁸
		1.26							LDA + PAW ¹⁷⁷
Sb-Te-I		0.89							PAW-PBE ¹⁷⁹
	<i>C2/m</i>	1.20	1.29	0.31	1.59			44.69	HSE+SOC ¹⁶⁹
		0.90							LDA + PAW ¹⁷⁷

		0.68							GGA-PBE + SOC ²⁰³	
		0.89							PBE ¹⁷⁹	
		1.82							PBE ²⁰⁴	
		1.32							Empirical methods ²⁰⁵	
Bi-O-F	<i>P4/nmmS</i> (129)	3.41	3.41						SR-PBE ¹⁸⁴	
			3.0	3.0						PBE ¹⁸³
			3.07	3.07	0.31	0.90				PBE-D3-SOC ²⁰⁶
			4.18	4.18						mBJ-SOC ²⁰⁶
			4.18		0.5	12.5	8.23	3.87		SR-PAW-HSE06-D3-SOC ²²⁵
		4.43	3.94	0.52	2.35			102.1	HSE+SOC ¹⁶⁹	
			3.07						PBE-GGA + vdW + SO ₂₀₆	
Bi-O-Cl	<i>P4/nmmS</i> (129)	2.69							SR-PBE ¹⁸⁴	
			2.60							PBE ¹⁸³
			2.63		0.46	0.27				PBE-D3-SOC ²⁰⁶
			3.72							mBJ-SOC ²⁰⁶
			3.37		0.3	0.8	7.94	4.35		SR-PAW-HSE06-D3-SOC ²²⁵
	<i>P4/nmm</i>	3.29	3.80	$m_e=0.39, m_h=1.33$				51.74 ¹⁶⁹	HSE+SOC ¹⁶⁹	
		2.63							PBE-GGA + D3, HSE ¹⁸⁰	
		3.66							PBE-GGA + vdW + SO ₂₀₆	
		2.38							PBE + PAW + SO ¹⁸²	
Bi-O-Br	<i>P4/nmmS</i> (129)	2.21							SR-PBE ¹⁸⁴	
			2.24							PBE ¹⁸³
			2.11		5.68	0.2				PBE-D3-SOC ²⁰⁶
			2.93							mBJ-SOC ²⁰⁶
			2.82		0.3	0.7	7.55	4.65		SR-PAW-HSE06-D3-SOC ²²⁵
	<i>P4/nmm</i>	2.86	3.09	$m_e=0.36, m_h=1.72$				44.62	HSE+SOC ¹⁶⁹	
		2.11							PBE-GGA + D3, HSE ¹⁸⁰	
		3.08							PBE-GGA + vdW + SO ₂₀₆	
Bi-O-I	<i>P4/nmmS</i> (129)	1.38		0.37	3.75				PAW-PBE-SOC ¹⁷¹	
			1.62							SR-PBE ¹⁸⁴
			1.63							PBE ¹⁸³
			1.46	1.49	6.34	0.54			46.32	PBE-D3-SOC ²⁰⁶
			2.11							mBJ-SOC ²⁰⁶
		2.00			1.9	7.03	5.03		SR-PAW-HSE06-D3-SOC ²²⁵	
Bi-S-Cl		0.74	1.1						SCPM ¹⁹⁷	
		1.40	1.54						NCPP-PBE ²⁰¹	
		1.6	1.9						FLAPW-GGA ¹⁹⁰	
		1.5							FLAPW-GGA ¹⁸⁹	
Bi-S-Cl		0.74	1.1						SCPM ¹⁹⁷	
		1.40	1.54						NCPP-PBE ²⁰¹	
		1.6	1.9						FLAPW-GGA ¹⁹⁰	
		1.5							FLAPW-GGA ¹⁸⁹	
	<i>Pnma</i>		1.98 ¹⁶⁹	0.51	2.91			37.53		
Bi-S-Br	<i>Pnma</i> (62)	1.39	1.55						SCPM ¹⁹⁷	
		1.32	1.35	0.24	6.21			30.10	PAW-PBE-SOC ¹⁷¹	
		1.21	1.39						NCPP-PBE ²⁰¹	
	<i>Pnma</i>		1.89 ¹⁶⁹	$m_e=0.52, m_h=3.73$				35.75		
Bi-S-I		1.5	1.65						SCPM ¹⁹⁷	
	<i>Pnam</i> (62)	1.18	1.32	0.53	4.79			29.59	PAW-PBE-SOC ¹⁷¹	
	<i>Pnma</i> (62)	1.78	1.82	0.68	0.36	6.4	4.9	36.8	HSE06-SOC ⁶⁸	
		1.88							PAW-PBE ¹⁷⁹	

		1.39	1.55						NCP-PBE ²⁰¹
		1.57							FLAPW-GGA ¹⁸⁸
	<i>Pnma</i>	1.66	1.87	$m_c=0.45, m_h=1.72$				37.81	HSE+SOC ¹⁶⁹
		1.88							PBE ¹⁷⁹
Bi-Se-Cl		0.27	0.45						SCPM ¹⁹⁷
	<i>Pnma</i>	1.45	1.47	$m_c=0.46, m_h=2.65$				20.38	HSE+SOC ¹⁶⁹
Bi-Se-Br		0.87	0.97						SCPM ¹⁹⁷
		1.14	1.25						NCP-PBE ²⁰¹
	<i>Pnma</i>	1.45	1.48	$m_c=0.44, m_h=2.25$				34.59	HSE+SOC ¹⁶⁹
Bi-Se-I		0.8	1.15						SCPM ¹⁹⁷
	<i>Pnma</i> (62)	0.91	1.03	0.25	5.89			26.83	PAW-PBE-SOC ¹⁷¹
	<i>Pnma</i> (62)	1.50	1.60	0.51	0.28	6.2	5.0	35.8	HSE06-SOC ⁶⁸
		0.57	0.52						NCP-PBE ²⁰¹
		1.35							FLAPW-GGA ⁵⁰
	<i>Pnma</i>	1.32	1.48	$m_c=0.42, m_h=2.39$				35.05	HSE+SOC ¹⁶⁹
Bi-Te-Cl		1.38							PAW-PBE ¹⁷⁹
		0.868							FLAPW-LDA-GW-SOC ²⁰⁷
	P3m1	1.20	1.33						HSE+SOC ¹⁶⁹
		1.20							PBE + UPPW ¹⁹²
		0.67							PBE + SOC ²⁰⁸
	P63mc	1.38							PBE ¹⁷⁹
Bi-Te-Br		1.09							PAW-PBE ¹⁷⁹
		1.09							FLAPW-PBE ¹⁵⁶
		0.28							FLAPW-PBE-SOC ¹⁵⁶
		0.65							FLAPW-LDA-GW-SOC ²⁰⁷
	P3m1	1.10							PBE + UPPW ¹⁹²
		0.53							PBE ¹⁷⁹
		0.59							PBE ²⁰⁸
		1.09							PBE ¹⁹⁴
Bi-Te-I		1.24							PAW-PBE ¹⁷⁹
		0.43							PAW-PBE-SOC ¹⁹³
		0.21							PAW-PBE-D2-SOC ¹⁹³
		0.17							PAW-PBESol-SOC ¹⁹⁵
		1.2							FLAPW-PBE ²⁰²
		0.28							FLAPW-PBE-SOC ²⁰²
		0.4							FLAPW-LDA-GW-SOC ²⁰⁷
	P3m1	0.90							HSE+SOC ¹⁶⁹
		0.80							PBE + UPPW ¹⁹²
		0.90							GGA+SOC ²⁰³
		0.41							PBE ²⁰⁸
		0.48							PBE ¹⁹⁴
		0.31							LDA + mBJ + SOC ²⁰⁹
		1.24							PBE ¹⁷⁹

Table S2. BiOX (X = Cl, Br, I) and their photocatalytic applications.

	Samples	Photocatalytic applications	Range irradiation	Synthetic procedures	Ref.
1D template Nanowire	BiOCl nanofibers	Completely RhB degraded within 60 min	UV	electro-spinning	356
	BiOCl fibers	75% MO mineralization in 110 min	UV	solvothermal synthesis (ethanol)	370
	BiOCl nanowire arrays	Almost 100% RhB degradation within 130 min	UV	sol-gel	367
2D intrinsic nanostructures	BiOCl plates	Completely MO degradation within 10 min	UV	hydrolysis	260
	BiOCl nanosheets	About 2 times higher RhB photodegradation rate than that on P25	UV	hydrolysis	340
		About 99% MO degradation within 45 min	UV	hydrothermal synthesis	366
	BiOCl nanoplates	Completely RhB disappearance within 8 min	Visible light	mannitol-assisted hydrothermal synthesis	373
	BiOCl lamellae	Good catalytic activity and selectivity in the oxidative coupling of the methane (OCM) reaction	ultrasonic irradiation	sonochemical method	414
	BiOBr lamellas	Completely RhB degraded within 30 min	Visible light	hydrolysis	337
		96% MO degraded within 120 min	Visible light	hydrothermal synthesis	358
	BiOI nanosheets	7 times higher photoactivity than that on irregular BiOI	Visible light	thermal annealing	368
BiOX (X = Cl, Br, I) nanosheets	95.9% sodium pentachlorophenate (Na-PCP) degradation on BiOI within 1 h following BiOI > BiOBr > BiOCl	Xe-lamp	hydrolysis	332	
3D assembled hierarchical architectures	BiOX (X = Cl, Br, I) nanoplate microspheres	80% MO degraded on BiOI within 3 h with the order BiOI > BiOBr > BiOCl	Visible light	solvothermal synthesis (ethylene glycol)	331
	BiOX (X = Cl, Br, I) hierarchical architectures	Completely MO degradation on BiOI within 60 min	UV-Vis	solvothermal synthesis (2-methoxyethanol, ethylene glycol)	372
	BiOCl porous nanospheres	Almost 100% RhB degraded within 2 h	Visible light	solvothermal synthesis (ethylene glycol)	341
	BiOCl nano-flowers	Completely MO degradation within 10 min	UV	solvothermal synthesis (pirydyne)	350
	BiOCl hierarchical architectures	Completely degrade RhB within 60 min	UV	solvothermal synthesis (ethylene glycol)	362
	BiOCl hierarchical self-assemblies	90.2% RhB degraded within 50 min	UV	hydrothermal synthesis	343
	BiOCl micro-flowers	99.3% RhB degraded within 15 min	Visible light	hydrothermal synthesis (glycerol + H ₂ O)	353
	BiOCl hierarchical flowers	90% MO degraded after 1 h	simulated sunlight	sonochemical route	360
	BiOCl 3D desert roses	Completely RhB degraded within 20 min	Visible light	Refluxing method	415
	BiOCl nano-flowers	Completely RhB degradation within 50 min	Visible light	hydrolysis	348
	BiOCl 3D flowers	100% RhB degraded within 80 min	Visible light	solution oxidation process	347
	BiOCl sub-microcrystals	99.5% RhB decomposed within 75 min	UV	hydrolysis	60
	BiOBr nanoplate microspheres	Nearly 30% NO removal within 10 min	Visible light	solvothermal synthesis (ethylene glycol)	346
	BiOBr	100% tetrabromobisphenol A decomposed within 15 min	simulated	solvothermal	355

microspheres		sunlight	synthesis (ethylene glycol)	
	99% phenol decomposed within 80 min	UV	microwave-assisted solvothermal synthesis (DEG)	342
	90% <i>Micrococcus lylae</i> inactivated after 6 h	fluorescent light	solvothermal synthesis (TEG)	352
	95% RhB degraded within 40 min	Visible light	solvothermal synthesis (isopropanol + ethylene glycol)	364
	Higher MO degradation than that on BiOBr bulk plates	Visible light	solvothermal synthesis (ethylene glycol)	361
BiOBr 3D microspheres	Toluene conversion rate 2-fold larger than that on P25	simulated sunlight	solvothermal synthesis (ethanol)	369
BiOBr mesoporous microspheres	Nearly 100% bisphenol A degradation within 90 min	simulated sunlight	solvothermal synthesis (ethanol)	359
BiOBr porous nanospheres	RhB completely degraded within 105 min	Visible light	solvothermal synthesis (ethylene glycol)	363
BiOBr hollow microspheres	100% RhB degraded in 15 min and 90% Cr(VI) reduced in 20 min	Visible light	solvothermal synthesis (2-methoxyethanol)	354
BiOBr micro-flowers	92.5% methylene blue (MB) degraded for 4.5 h	Visible light	solvothermal synthesis (ethylene glycol)	365
BiOBr fullerene-like eggshells	Over 95% RhB degraded within 25 min	Visible light	ultrasound reaction and heating synthesis	416
BiOI hierarchical structures	MO completely degraded within 50 min	Visible light	hydrothermal synthesis	345
BiOI hollow microspheres	92% MO degraded within 3 h	Visible light	solvothermal synthesis (ethylene glycol)	351
BiOI microspheres	94% tetracycline hydrochloride decomposed within 2 h	Visible light	direct precipitation	344
	97% phenol decomposed within 4 h	Visible light	chemical bath	349
BiOI micro-flowers	80% RhB degraded within 4 h	Visible light	solvothermal synthesis (ethylene glycol)	383
	100% RhB degraded within 2 h	Visible light	direct precipitation	360

Table S3. Electrical properties of pnictide chalcogenides

Compound	Specific resistivity, $\Omega\text{-cm}$	Charge carrier mobility, $\text{cm}^2\text{V}^{-1}\text{sec}^{-1}$	Ref
AsSI	$>10^{13}$ (at room temperature)		291
	10^{16} to 10^{12} (decreases with iodine concentration increase)		292
AsSBr	$>3\cdot 10^{14}$ (for 60 at. % of sulphur and 3-9 at % of bromine)		293
	10^{15} to 10^{12} (at 20 °C)		72
AsSeBr	10^{13} to 10^{11} (decreases with Br concentration increase)		72
AsTeI	10^3 (low iodine content) to 10^8 (high iodine content)	0.08 (at room temperature)	295
		0.12 (at 90°C)	295
		10^{-2} to 10^{-1} ($\text{As}_{50}\text{Te}_{50-x}\text{I}_x$ ($x = 0, 2, 20$) glasses)	301
		0.08 ($\text{As}_{53}\text{Te}_{43}\text{I}_4$ glass)	295, 304
AsTeBr		0.01 (at room temperature)	295
		0.10 (at 90°C)	295
SbSI	10^{10} to 10^7 (glasses)		72
		50 to 100	308
SbSBr	10^7 (crystal phase) 10^{10} (glass phase)		309
SbSeI	10^8 (at room temperature)		143
SbSeBr	10^7		311
SbTeI		1.01	312
BiOCl	10^{10} to 10^{13} $>10^{15}$ (<200K)		314
			317
BiOI	$>10^{15}$ (<200K)		317
BiOBr	$>10^{15}$ (<200K)		317
BiSI	10^8 to 10^9 (Needle-like structures)		320
BiSBr	10^3 to 10^4		308
BiSeI	$\sim 10^{10}$ to 10^6 (decreases with temperature increase)		45
BiTeI		528 (at 77K)	65
		242 (at 300K)	
BiTeBr		1450 (at 77K)	65
		310 (at 300K)	

Additional references for Tables S1 and S2.

413. H. Akkus and A. Mamedov, *Open Physics*, 2007, **5**, 25.
414. J. Geng, W.-H. Hou, Y.-N. Lv, J.-J. Zhu and H.-Y. Chen, *Inorg. Chem.*, 2005, **44**, 8503-8509.
415. G. Cheng, J. Xiong and F. J. Stadler, *New J. Chem.*, 2013, **37**, 3207-3213.
416. C. Deng and H. Guan, *Mater. Lett.*, 2013, **107**, 119-122.

Influence of π -Iodide Intermolecular Interactions on Electronic Properties of Tin(IV) Iodide Semiconducting Complexes

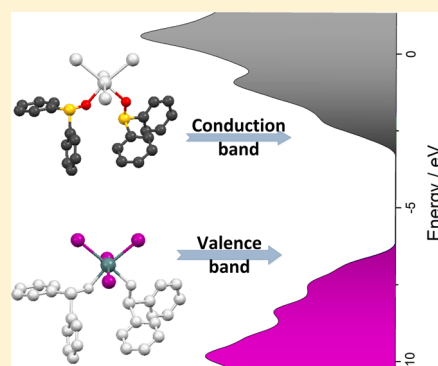
Ewelina Właźlak,^{†,‡} Wojciech Macyk,[†] Wojciech Nitek,[†] and Konrad Szaciłowski^{*,‡}

[†]Faculty of Chemistry, Jagiellonian University, ul. R. Ingardena 3, 30-060 Kraków, Poland

[‡]AGH University of Science and Technology, Academic Centre for Materials and Nanotechnology, al. A. Mickiewicza 30, 30-059 Kraków, Poland

Supporting Information

ABSTRACT: Coordination compounds with a tin center surrounded by both organic and inorganic ligands ($[\text{SnI}_4\{(\text{C}_6\text{H}_5)_3\text{PO}\}_2]$, $[\text{SnI}_4\{(\text{C}_6\text{H}_5)_2\text{SO}\}_2]$, and $[\text{SnI}_4(\text{C}_5\text{H}_5\text{NO})_2]$) acting as molecular semiconductors are in the spotlight of this article. This is a new class of hybrid semiconducting materials where optoelectronic properties of inorganic core (SnI_4) were tuned by organic ligands. The valence band is located at the inorganic portion of the molecule while the conduction band is made of carbon-based orbitals. This suggests the great importance of hydrogen bonds where iodine atoms play the role of an acceptor. Weak intermolecular interactions between iodine atoms and aromatic rings are essential in a band structure formation. These materials form orange-red crystals soluble in most of organic solvents. Their semiconducting properties are addressed experimentally via photovoltage measurements, as well as theoretically, using DFT and semiempirical approaches.



INTRODUCTION

Further development of photovoltaics and optoelectronics requires easily processable materials with tunable electronic and optical properties. Their application may result in devices with higher efficiencies and better parameters. To date, hybrid semiconducting materials in which molecules of metal compounds interact with each other only by weak forces have been studied only scarcely. This group of materials has interesting electronic properties; therefore, more detailed studies are required. Semiconductors can be divided into two main groups: inorganic and organic materials (Figure 1). These classes of materials not only differ at the chemical level but also, more importantly, possess completely different electronic properties due to the differences in their atomic and electronic structures. In inorganic semiconductors, atoms are held together by strong covalent and ionic interactions whereas weak van der Waals and hydrogen interactions determine properties of organic semiconductors. Differences in intramolecular interactions are the most important factor that determines delocalization of electrons and their wave functions over the crystal lattice and thus the electronic properties of a semiconducting material.

Strong bonds (covalent, ionic) induce formation of band structure where allowed energy states form continuous conduction and valence bands, with a broad bandwidth (inorganic semiconductors, such as Si or ZnS). On the other hand, weak van der Waals and hydrogen bonds dominate in organic crystals. The strength of the intermolecular interactions is reflected in their band structure and density of states.¹ The weaker the intermolecular interactions are, the thinner and the

SEMICONDUCTORS

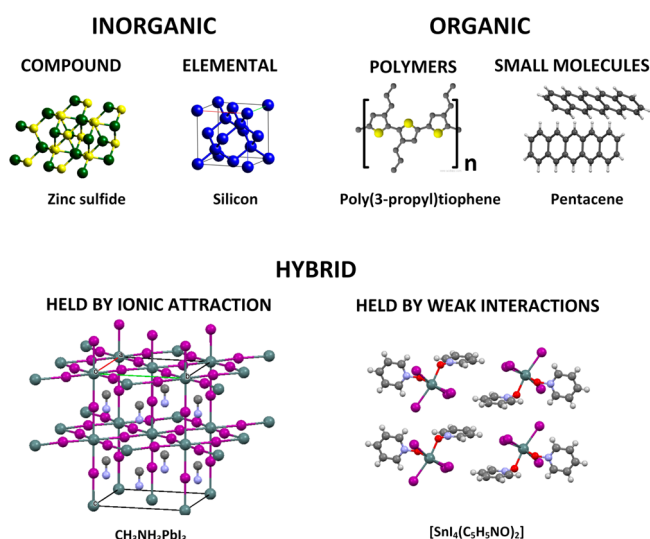


Figure 1. A general classification of semiconductors on the basis of their chemical characteristics.

less continuous the bands are that are formed.² Organic semiconductors (polymers and small molecules) have in common a π -electron system formed by the p_z orbitals of sp^2

Received: February 11, 2016

hybridized carbon atoms.³ In organic semiconductors, weak van der Waals and hydrogen interactions govern the formation of crystal structures. In hybrid materials both scenarios are possible. Covalently bonded metal halides and charged layers held together by ionic interactions make perovskites more similar to inorganic semiconductors, in which the layered structure provides a suitable arrangement for a high charge carrier mobility.⁴ Hybrid materials combine properties of organic and inorganic semiconductors. Perovskites have the corner sharing metal halide octahedra that form an anionic lattice, and organic cations form a network for the inorganic structure. The observed properties in this group of materials have their origin in the connectivity of the inorganic sublattice—organic cations are used to tune the electronic properties by structural templating.^{5,6} There are also materials which cannot be classified as perovskites, but are based on similar building blocks.^{7–9} For example, the anionic metal halide octahedra lattice was found in a hybrid material where the negative charge of the inorganic sheets is compensated by a noninnocent tropylium cation, involved in a charge transfer interaction within the lattice of $(C_7H_7PbI_3)$.¹⁰ In this compound the electrostatic interactions between organic and inorganic components held the structure together.

In neutral SnI_4L_2 complexes described in this paper, in contrast to the inorganic and the majority of hybrid semiconductors, the weak interactions are responsible for formation of the band structure. These materials are hybrid semiconductors with tin(IV) iodide complexed by two organic ligands. Organic and inorganic molecules are connected by coordination bonds between oxygen and tin atoms unlike the other hybrid materials, where molecules of these materials are held together by weak van der Waals interactions and hydrogen bonds.

The crystal structure of tin tetraiodide was reported in literature for the first time in 1923.¹¹ Since then the topic of SnI_4 properties has been discussed in several papers, mostly during the 1960–1980s. $[SnI_4\{(C_6H_5)_3PO\}_2]$ and $[SnI_4\{(C_6H_5)_2SO\}_2]$ were mentioned in literature but mostly in the context of the Mössbauer spectroscopy, whereas their electronic properties were not investigated.^{12–14} In this paper $[SnI_4\{(C_6H_5)_3PO\}_2]$, $[SnI_4\{(C_6H_5)_2SO\}_2]$, and $[SnI_4(C_5H_5NO)_2]$ complexes were studied. The influence of different ligands on electronic properties and correlation between intermolecular interactions and the electronic structure have been described on the basis of theoretical calculations, experimental studies, and a crystal structure analysis. Particular attention was paid to the $CH\cdots I$ interaction which influences the properties of these complexes.

EXPERIMENTAL SECTION

Syntheses. SnI_4 . Tin powder (1 g) and iodine (3 g) were heated at 40 °C in anhydrous dichloromethane (100 mL), under reflux, until the reaction mixture turned dark orange. The solution was then filtered to remove unreacted tin, concentrated to 50 mL and cooled in an ice bath. Precipitated orange solid was filtered, dried and recrystallized from chloroform, yielding orange crystals of SnI_4 (2.7 g). Yield: 51%.

$[SnI_4\{(C_6H_5)_3PO\}_2]$. Triphenylphosphine oxide (2.1 mmol) and tin tetraiodide (1 mmol) were dissolved in 15 mL of anhydrous dichloromethane and stirred for 1 h at room temperature. The solution was concentrated to 7 mL and cooled. The dark red participate was filtered off, washed with anhydrous dichloromethane, and dried. The final product was recrystallized from a mixture of cyclohexane and isobutanol. Elemental analysis: C, 36.48%; H, 2.59%. Calculated for $C_{36}H_{30}P_2O_2SnI_4$: C, 36.55%; H, 2.55%. Yield: 60%.

$[SnI_4\{(C_6H_5)_2SO\}_2]$. Diphenyl sulfoxide (2.1 mmol) and tin tetraiodide (1 mmol) were dissolved in 15 mL of anhydrous dichloromethane and stirred for 1 h at room temperature. Subsequently dichloromethane was evaporated under reduced pressure. As a result, a dark red solid was obtained. The final product was isolated by crystallization from acetonitrile as fine, red crystals with an orange shine. Elemental analysis: C, 27.91%; H, 1.96%; S, 6.21%. Calculated for $C_{24}H_{20}S_2O_2SnI_4$: C, 27.96%; H, 1.96%; S, 6.22%. Yield: 27%.

$[SnI_4(C_5H_5NO)_2]$. Pyridine-*N*-oxide (2.1 mmol) and tin tetraiodide (1 mmol) were dissolved in 15 mL of anhydrous dichloromethane and stirred for 1 h at room temperature. The solution was concentrated to 7 mL and cooled. The red-orange participate was filtered off, washed with anhydrous dichloromethane, and dried. The final product was recrystallized from acetonitrile. Elemental analysis: C, 14.74%; H, 1.23%; N, 3.51%. Calculated for $C_{10}H_{10}N_2O_2SnI_4$: C, 14.71%; H, 1.23%; N, 3.43%. Yield: 18%.

Caution! These syntheses are potentially hazardous due to the toxic, irritating, and lachrymatory properties of iodine. Appropriate means of personal protection should be applied. All waste should be properly disposed due to high toxicity toward aquatic organisms.

X-ray Crystallography. Data collection and reduction: Diffraction data for single crystal were collected at 120 K using the Oxford Diffraction SuperNova four circle diffractometer, equipped with the Mo (0.71069 Å) $K\alpha$ radiation source, graphite monochromator, and Oxford CryoJet system for measurements at low temperature. Cell refinement and data reduction were performed using the firmware.¹⁵ Structure solution and refinement: The positions of all non-hydrogen atoms were determined by direct methods using SIR-97.¹⁶ All non-hydrogen atoms were refined anisotropically using weighted full-matrix least-squares on F². Refinement and further calculations were carried out using SHELXL-97.¹⁷ Graphics were created by MERCURY.¹⁸ Whole used software is a component of the WINGX.¹⁹ Hydrogen atoms treatment: All hydrogen atoms joined to carbon atoms were positioned with an idealized geometry and refined using a riding model with Uiso(H) fixed at 1.2 Ueq of C.

Computational Details. Optimized molecular structures of the studied complexes were obtained from experimental crystal structures. First, structures were optimized in vacuum (UFF) using the Avogadro software package²⁰ and then optimized again with the Polarizable Continuum Model (PCM, acetonitrile) using the Gaussian 09 software package²¹ at the HF level of theory with the 6-31+G(d,p)²² basis set for C, O, and P atoms and the DGDZVP²³ basis set for Sn and I atoms. Mixed basis sets were used to shorten the initial calculation time. Based on the optimized structures of the complexes, UV–vis simulations and charge decomposition analysis were performed.

Simulation of UV–vis absorption spectra was performed with Time Dependent Density Functional Theory (TDDFT) using Gaussian 09, the PCM solvation model (acetonitrile), the DGDZVP²³ basis set for all atoms, and RB3LYP^{24,25} (hybrid density functional model). GaussSum software²⁶ was used to calculate the lowest 50 transitions. The obtained results were used to prepare electrostatic visualizations of frontier orbitals of single molecules with GaussView 5 software.²⁷ From these calculations also frontier orbital diagrams and theoretical band gap values were obtained. Visualizations of frontier orbitals of dimers were prepared for two neighboring molecules in crystal, without any optimization, by applying TDDFT calculations, Gaussian 09, and GaussView 5 software. Density of states distributions were calculated for clusters consisting of 12 molecules, using MOPAC2012²⁸ with the PM7 method and postprocessed with the AOMix package.^{29,30} Charge decomposition analysis was performed using AOMix program and population analysis performed by the Gaussian 09 program at the DFT level of theory with the DGDZVP basis set.

Kelvin Probe Measurements. Surface photovoltage (SPV) measurements were performed using a Kelvin probe-based surface photovoltage spectrometer (Instytut Fotonowy, Poland, and Besocke Delta Phi, Germany) using a 150 W xenon arc lamp with a monochromator. The work function (WF) and Fermi level (FL) were

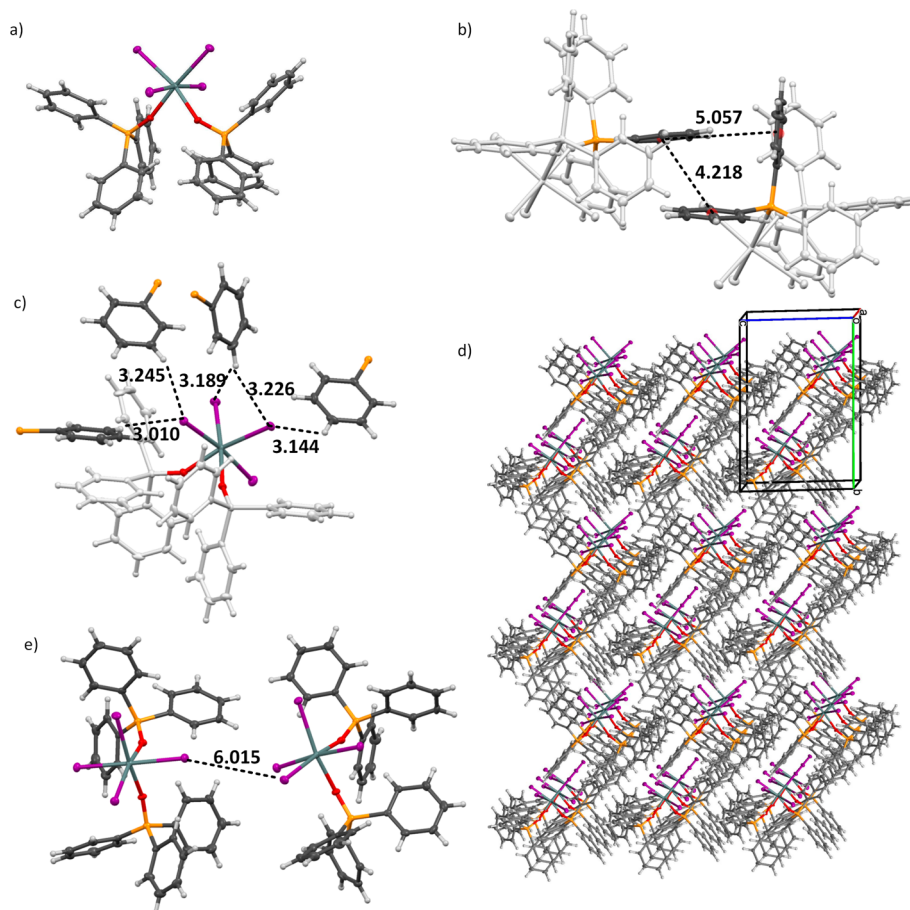


Figure 2. Crystal structures of single $[\text{SnI}_4\{(\text{C}_6\text{H}_5)_3\text{PO}\}_2]$ molecule (a), intermolecular stacking of phenyl rings arranged in parallel (offset) or perpendicular fashion (black dashed lines indicate distances between centroids) (b), distances (black dashed lines) and aromatic rings arrangement in $\text{H}\cdots\text{I}$ interaction (only intermolecular aromatic rings are highlighted) (c), packing $3 \times 3 \times 3$ and monoclinic cell (d), and $\text{I}\cdots\text{I}$ distance (black dashed line) (e). Ellipsoids represent 50% probability.

Table 1. Intermolecular Nonbonded Contact Distances and Angles for Phenyl Rings and Various Atom Pairs

Interaction	$[\text{SnI}_4\{(\text{C}_6\text{H}_5)_3\text{PO}\}_2]$	$[\text{SnI}_4\{(\text{C}_6\text{H}_5)_2\text{SO}\}_2]$	$[\text{SnI}_4(\text{C}_5\text{H}_5\text{NO})_2]$
$\pi\cdots\pi$, ^a $\angle\pi-\pi$ ^b	π_{II} 4.218 Å, 4.2° π_{I} 5.057 Å, 67.4°	π_{II} 4.068 Å, 11.7° π_{I} 4.856 Å, 87.5°	π_{II} 4.199 Å, 0°
A \cdots I	—	S1\cdotsI2 3.651 Å ^c	O1\cdotsI1 3.463 Å ^c
I \cdots I	I2 \cdots I3 6.015 Å	I1 \cdots I4 4.033 Å	I2 \cdots I2 3.837 Å ^c
H \cdots I, $\angle\text{Sn}-\text{I}\cdots\text{H}$	H37\cdotsI1 3.010 Å, ^c 134.89° H20\cdotsI4 , 3.144 Å, ^c 106.74° H19 \cdots I1 3.245 Å H45 \cdots I2 3.189 Å H45 \cdots I4 3.226 Å	H32\cdotsI4 3.105 Å, ^c 91.92° H21 \cdots I3 3.268 Å H26 \cdots I4 3.234 Å	H9\cdots I3 3.085 Å, ^c 151.99° H10\cdots I3 3.180 Å, ^c 93.08° H6\cdots I4 3.122 Å, ^c 107.38° H3 \cdots I2 3.269 Å H11 \cdots I3 3.269 Å H8 \cdots I4 3.240 Å H10 \cdots I4 3.280 Å

^aCentroid–centroid distance. ^bAngle between ring planes. ^c**Bold:** distance shorter than the sum of van der Waals radii.

measured with the Kelvin probe. Samples before measurements were deposited on ITO foil.

Resistivity Measurements. Room temperature resistivity measurements were performed with Keithley 4200 SCS. Thin layers of dissolved compound were spin coated on glass substrate and measured with a four-point probe technique. Film thicknesses were measured using Bruker's DektakXT Stylus Profiler.

UV–vis Spectroscopy, ¹H NMR, and Elemental Analysis. Diffuse reflectance spectra were recorded on the Lambda 950 (PerkinElmer, USA) spectrophotometer. The Kubelka–Munk function was used to convert the diffuse reflectance spectra into absorption spectra. Absorption spectra were recorded with HP 8453. ¹H NMR

spectra were recorded with Bruker Avance III 600 MHz. Elemental analyses were undertaken with the elemental microanalyzer CHNS Vario Micro Cube.

RESULTS AND DISCUSSION

Crystal Structure and Interactions. Crystal structures of $[\text{SnI}_4\{(\text{C}_6\text{H}_5)_3\text{PO}\}_2]$, $[\text{SnI}_4\{(\text{C}_6\text{H}_5)_2\text{SO}\}_2]$, and $[\text{SnI}_4(\text{C}_5\text{H}_5\text{NO})_2]$ obtained by a single crystal X-ray diffraction enable a detailed analysis of inter- and intramolecular interactions. As a result of steric intramolecular interactions, SnI_4 forms *cis* adducts with triphenylphosphine oxide, diphenyl

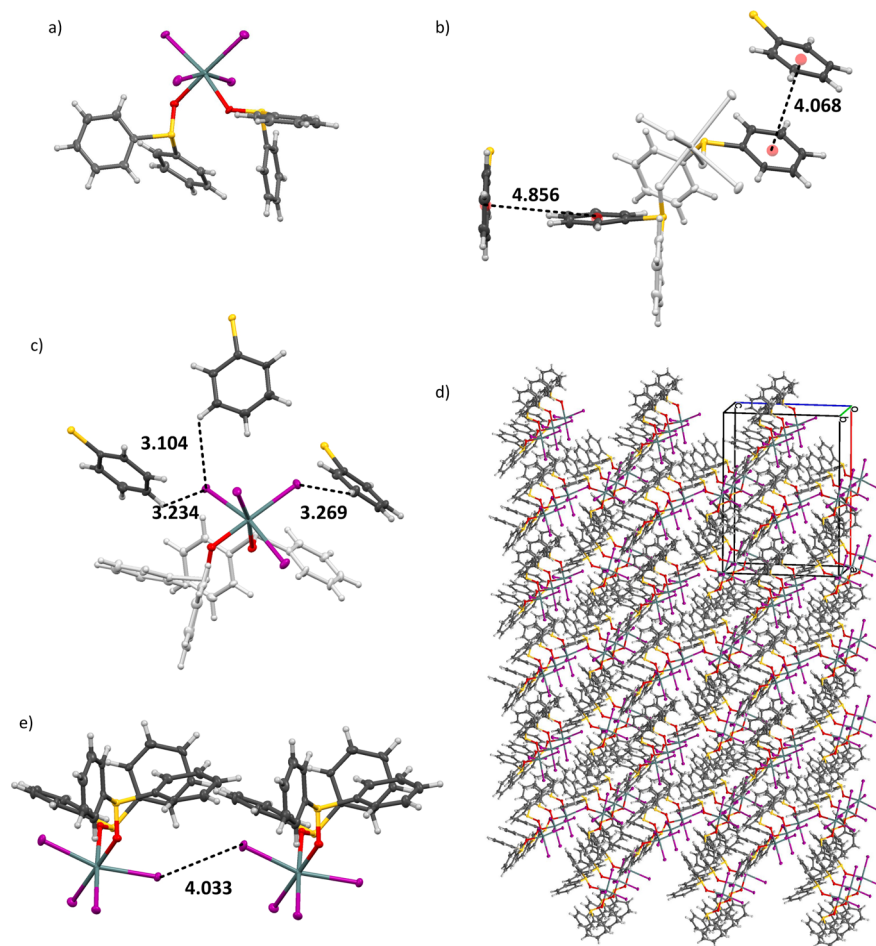


Figure 3. Crystal structures of single [SnI₄{(C₆H₅)₂SO}₂] molecule (a), intermolecular stacking of phenyl rings arranged in parallel (offset) or perpendicular fashion (black dashed line indicates distances between centroids) (b), distances (black dashed lines) and aromatic rings arrangement in H...I interaction (only intermolecular aromatic rings are highlighted) (c), packing 3 × 3 × 3 and orthorhombic cell (d), I...I distance (black dashed lines) (e). Ellipsoids represent 50% probability.

sulfoxide, and pyridine *n*-oxide. Crystal structures of these complexes are present in Figures 2–4. Hydrogen bonding with iodide acceptors (Table 1) seem to play an important role in this group of complexes. The distance (*d*) and angle (α) of H...I–Sn interaction have been used to determine whether they are consistent with a hydrogen bond description (preferable $d < 3.14$ Å, $90^\circ < \alpha < 180^\circ$; see Brammer et al.).³¹ Stacking distances and selected interatomic distances of iodide are collected in Table 1.

Crystal Structure of the [SnI₄{(C₆H₅)₃PO}₂] Complex.

[SnI₄{(C₆H₅)₃PO}₂] (Figure 2a) crystallizes in the monoclinic space group *P*2₁. There are one Sn⁴⁺ cation, four coordinated I[−] anions, and two coordinated triphenylphosphine oxide ligands in the asymmetric unit. The Sn cation is in a distorted octahedral configuration where it is coordinated by four I[−] anions as well as by O1 and O2 atoms from triphenylphosphine oxide molecules. The Sn–O bond distances (2.142 and 2.128 Å) are the shortest among other complexes, with an O1–Sn–O2 angle of 78.25°. Unlike perovskite, the presented structure lacks strong interactions within the crystal lattice. The role of stacking in semiconductors is well-known (in molecular semiconductors the coupling between conjugated systems allows charge to travel through the crystal lattice), but there is only a little information about the role of a weak I...H hydrogen bond on the band structure formation. These weak

interactions are often found in crystal structures. In the [SnI₄{(C₆H₅)₃PO}₂] complex two intermolecular I...H bonds, which meet the above-mentioned criteria for the hydrogen bond, were found: H37...I1, $d = 3.010$ Å, $\alpha = 134.89^\circ$ and H20...I4–Sn, $d = 3.144$ Å, $\alpha = 106.74^\circ$. In Table 1 and Figure 2c also I...H interactions with slightly larger distances are listed. These hydrogen bonds with halogen acceptors obviously contribute to crystal formation, but as we explained further, I...H bonds also have an impact on the electronic properties of this material. Also π – π interactions are present in this structure (Figure 2b). Angles between stacked rings seem to be influenced by steric hindrances. Distances between centroids of phenyl rings arranged in parallel (offset) or perpendicular fashion are 4.218 and 5.057 Å, respectively. Listed close contacts are responsible for formation of a zigzag pattern present in the crystal structure (Figure 2d). The last interesting factor that may influence electronic properties of this material is the distance between the two closest iodine atoms (Figure 2e). In contrast to the [SnI₄{(C₆H₅)₂SO}₂] and [SnI₄(C₅H₅NO)₂] complexes, the distance I...I in [SnI₄{(C₆H₅)₃PO}₂] is quite large, namely 6.015 Å.

Crystal Structure of the [SnI₄{(C₆H₅)₂SO}₂] Complex.

The [SnI₄{(C₆H₅)₂SO}₂] complex crystallizes in the orthorhombic space group *Pna*2₁. The Sn⁴⁺ cation coordinates four iodide anions and two oxygen atoms from diphenyl sulfoxide

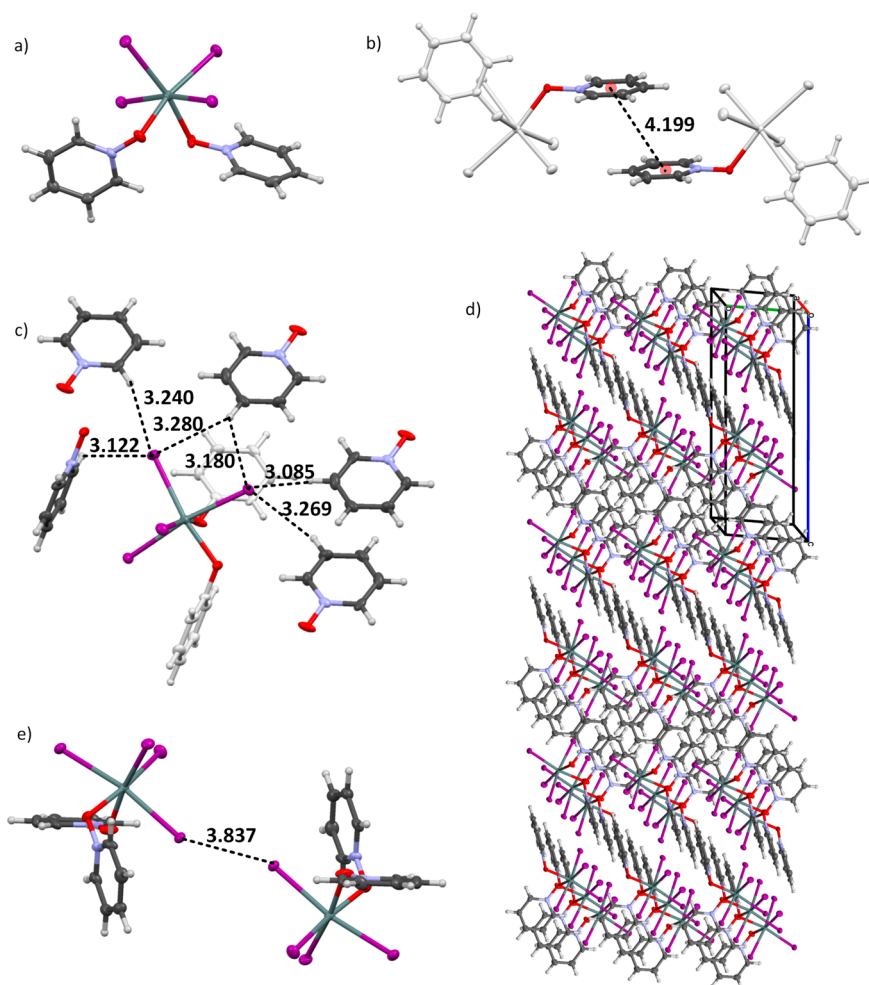


Figure 4. Crystal structures of single $[\text{SnI}_4(\text{C}_5\text{H}_5\text{NO})_2]$ molecule (a), intermolecular stacking of pyridine rings arranged in parallel (offset), (black dashed line indicates the distance between centroids) (b), distances (black dashed lines) and aromatic rings arrangement in $\text{H}\cdots\text{I}$ interaction (only intermolecular aromatic rings are highlighted) (c), packing $3 \times 3 \times 3$ and triclinic cell (d), and $\text{I}\cdots\text{I}$ distance (black dashed line) (e). Ellipsoids represent 50% probability.

ligands (Figure 3a). $\text{Sn}-\text{O}1$ and $\text{Sn}-\text{O}2$ lengths are 2.167 and 2.207 Å, respectively, with an $\text{O}1-\text{Sn}1-\text{O}2$ angle of 86.17° . In the crystal structure, $\pi-\pi$ interactions have been found (Figure 3b). Offset parallel stacking with a distance between centroids of 4.068 Å shows a slight slope (11.7°). Second, π interaction is formed by two almost perpendicular phenyl rings (4.856 Å, 87.5°). As mentioned above, the $\text{I}\cdots\text{H}$ bonding seems to be very important in this material. One strong intermolecular hydrogen bond was found ($\text{H}32\cdots\text{I}4$, $d = 3.105$ Å, $\alpha = 91.92^\circ$), but in a short distance (less than the sum of van der Waals radii +0.1 Å). Two other $\text{I}\cdots\text{H}$ interactions are present (Figure 3c, Table 1). Interestingly, a close $\text{S}1\cdots\text{I}2$ distance, 3.651 Å, points at a halogen bond. Crystal packing of complex $[\text{SnI}_4\{(\text{C}_6\text{H}_5)_2\text{SO}\}_2]$ is presented in Figure 3d. The distance between iodine atoms is 4.033 Å (Figure 3e).

Crystal Structure of the $[\text{SnI}_4(\text{C}_5\text{H}_5\text{NO})_2]$ Complex. The $[\text{SnI}_4(\text{C}_5\text{H}_5\text{NO})_2]$ complex (Figure 4a) crystallizes in the triclinic space group $P\bar{1}$. It consists of a Sn^{4+} cation coordinated with four iodide anions and two pyridine *N*-oxides where the $\text{Sn}1-\text{O}1$ distance is 2.162, $\text{Sn}1-\text{O}2$ is 2.168 Å, and the $\text{O}1-\text{Sn}1-\text{O}2$ angle is 82.79° . The crystal packing is presented in Figure 4d. The pyridine rings of neighboring molecules lay in the same planes. The presence of the N^+O^- group induces formation of intramolecular hydrogen bond $\text{O}2\cdots\text{H}6$, 2.686 Å.

The coordination of a strongly polarized ligand is probably responsible for deviations in the electrochemical behavior of this compound in solution. As in previous structures, hydrogen bonds with a halogen acceptor, suspected to contribute strongly to the band structure, are formed: $\text{H}6\cdots\text{I}4$, $d = 3.122$ Å, $\alpha = 107.38^\circ$; $\text{H}9\cdots\text{I}3$, $d = 3.085$ Å, $\alpha = 151.99^\circ$; and $\text{H}10\cdots\text{I}3$, $d = 3.180$ Å, $\alpha = 93.08^\circ$. The arrangement of iodide-rings contacts is presented in Figure 4c. In this structure also an intermolecular halogen bond between the $\text{I}1$ atom and $\text{O}2$ atom is observed. The π interaction is represented by an offset parallel arrangement of two pyridine rings. The type I halogen contact was found with the 3.837 Å $\text{I}\cdots\text{I}$ distance (Figure 4e).^{32,33} This and other contact distances are listed in Table 1.

^1H NMR Spectroscopy. The ^1H NMR spectra of ligands and complexes dissolved in acetonitrile prove that SnI_4L_2 complexes are present in the solution. The spectra of $[\text{SnI}_4(\text{C}_5\text{H}_5\text{NO})_2]$ are strongly influenced by coordination of tin tetraiodide, which is reflected in the shift of the pyridine ring signal, even by 0.9 ppm. Moreover, the impact of an electron-withdrawing substituent is noticeable: the triplet belonging to the *meta* position in the ring exhibits the biggest shift in the complex (by ca. 0.9 ppm) while signals from protons in *ortho* and *para* positions show a smaller shift, by ca. 0.6 ppm. In $[\text{SnI}_4\{(\text{C}_6\text{H}_5)_3\text{PO}\}_2]$ and $[\text{SnI}_4\{(\text{C}_6\text{H}_5)_2\text{SO}\}_2]$ the shift is

smaller (0.04 and 0.01 ppm, respectively Figure 5). The shift toward a lower field means that the electron density is slightly

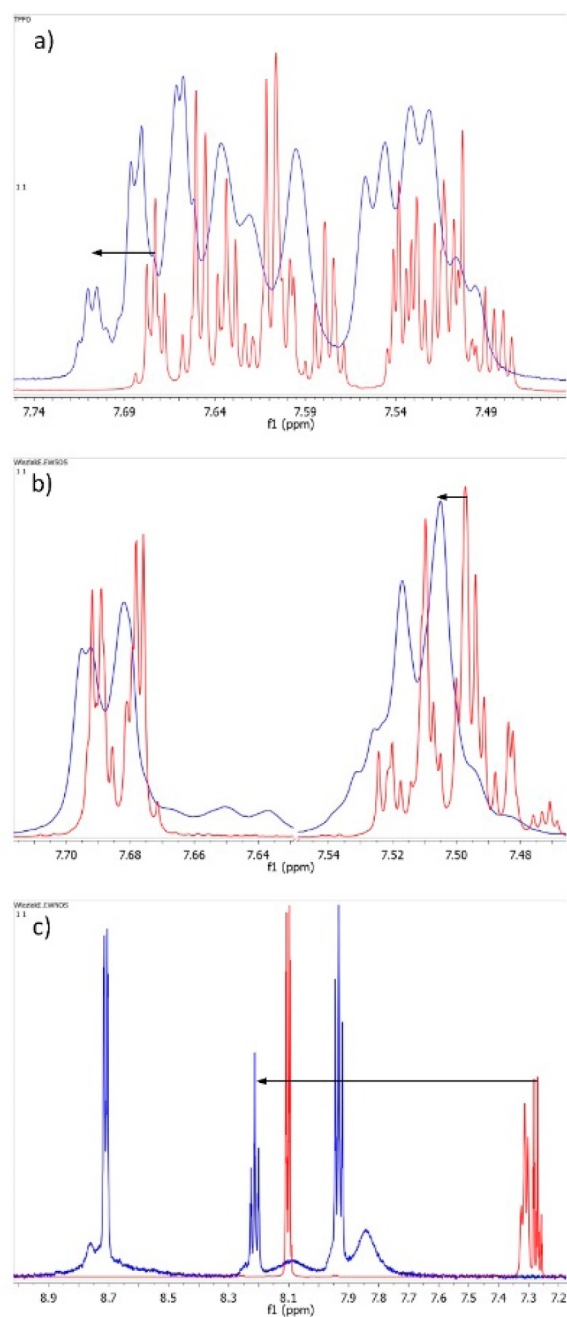


Figure 5. ^1H NMR spectra of $[\text{SnI}_4\{(\text{C}_6\text{H}_5)_3\text{PO}\}_2]$ (a), $[\text{SnI}_4\{(\text{C}_6\text{H}_5)_2\text{SO}\}_2]$ (b), and $[\text{SnI}_4(\text{C}_5\text{H}_5\text{NO})_2]$ (c) in deuterated acetonitrile. Spectra of the complexes are marked in blue, whereas spectra of free ligands are marked in red.

withdrawn from rings. Neat charge transfer values obtained from Charge Transfer Analysis (*vide infra*) correlate with the shifts observed in NMR spectra (Table 2). The charge transfer

for $[\text{SnI}_4(\text{C}_5\text{H}_5\text{NO})_2]$ is the biggest, and for $[\text{SnI}_4\{(\text{C}_6\text{H}_5)_2\text{SO}\}_2]$ it is the smallest. This explains the different values of ^1H NMR shifts.

Density of States (DOS) and Resistivity Measurements. DOS distribution analysis is useful for determining the contribution of individual atomic orbitals in conduction and valence bands. DOS distribution (Figure 6) was calculated for clusters made of 12 molecules, with the crystal structure arrangement. The PM7 method (implemented within the MOPAC software) including the LCAO-MO approximation was used to calculate the contribution of atomic orbitals to molecular orbitals while AOMix software was used to calculate the DOS and PDOS distributions. A qualitative analysis of DOS distribution reveals that valence bands of studied materials consist of iodine orbitals, while conduction bands are composed of carbon orbitals. This indicates the importance of short distances between iodine atoms of one molecule and conjugated rings of another one (*vide infra*). These interactions, listed in Table 1, provide a significant orbital overlap and hence an efficient electron transfer upon excitation. After excitation, the electron is transferred from the iodine atom to aromatic rings. Subsequently, it can travel through the crystal structure due to the π -stacked assembly of the rings. One can notice in Figure 6 that the appearance of the valence band of $[\text{SnI}_4(\text{C}_5\text{H}_5\text{NO})_2]$ differs from the appearance of the other two complexes: the PDOS distribution of iodine-related states at the top of the valence band is narrower and more intense. This is the result of the short contact between iodine atoms in the crystal structure. In the $[\text{SnI}_4(\text{C}_5\text{H}_5\text{NO})_2]$ complex the I2–I2 distance is only 3.837 Å (Table 1), and the van der Waals spheres of these iodide atoms intersect. In the $[\text{SnI}_4\{(\text{C}_6\text{H}_5)_3\text{PO}\}_2]$ complex and $[\text{SnI}_4\{(\text{C}_6\text{H}_5)_2\text{SO}\}_2]$ complex the distances are larger and the van der Waals spheres of the closest iodide atoms do not cross, which suggests a much smaller influence of these interactions on the DOS distribution.

Similar results were found in a hybrid $\text{C}_7\text{H}_7\text{PbI}_3$ inorganic–organic material,¹⁰ the valence and conduction bands consist of iodine and carbon orbitals, respectively. Although $\text{C}_7\text{H}_7\text{PbI}_3$ exhibits a strong organic–inorganic coupling, this compound has an ionic structure (organic cation and inorganic anion). Measured with a four point method, the values of the sheet resistance of thin layers of the studied complexes are very large with 1.3 $\text{M}\Omega/\square$, 0.4 $\text{M}\Omega/\square$, and 21 $\text{M}\Omega/\square$ for $[\text{SnI}_4\{(\text{C}_6\text{H}_5)_3\text{PO}\}_2]$, $[\text{SnI}_4\{(\text{C}_6\text{H}_5)_2\text{SO}\}_2]$, and $[\text{SnI}_4(\text{C}_5\text{H}_5\text{NO})_2]$ polycrystalline thin films of 35, 63, and 45 nm thicknesses, respectively. These values correspond to specific resistivities of 0.46, 0.24, and 9.45 Ωm at room temperature, which are not worse than those for lead iodide perovskites.³⁴

UV–vis Absorption Spectra. Prepared complexes are soluble in most organic solvents. The UV–vis absorption spectra of all studied complexes (including SnI_4) in acetonitrile are very similar (Figure 7a). The only difference is observed for a slightly shifted spectrum of $[\text{SnI}_4(\text{C}_5\text{H}_5\text{NO})_2]$. It is worth noting that the ^1H NMR spectra in acetonitrile confirm formation of the complexes in solution; therefore, the

Table 2. Neat Charge Transfer Values and Chemical Shifts

	$[\text{SnI}_4\{(\text{C}_6\text{H}_5)_3\text{PO}\}_2]$	$[\text{SnI}_4\{(\text{C}_6\text{H}_5)_2\text{SO}\}_2]$	$[\text{SnI}_4(\text{C}_5\text{H}_5\text{NO})_2]$
Neat charge transfer	0.483 e^-	0.419 e^-	0.587 e^-
Chemical shift	0.04 ppm	0.01 ppm	0.9 – 0.6 ppm

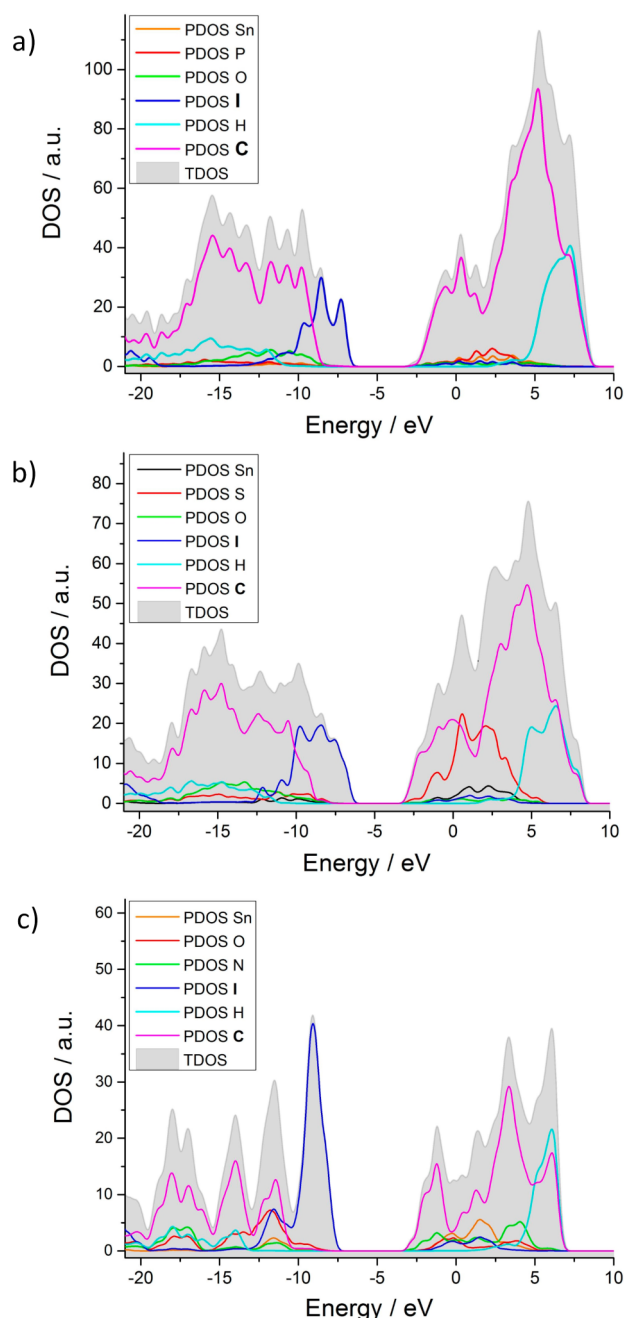


Figure 6. Density of states distribution of $[\text{SnI}_4\{(\text{C}_6\text{H}_5)_3\text{PO}\}_2]$ (a), $[\text{SnI}_4\{(\text{C}_6\text{H}_5)_2\text{SO}\}_2]$ (b), and $[\text{SnI}_4(\text{C}_3\text{H}_5\text{NO})_2]$ (c). Gray area represents the total density of states; color lines represent partial densities of states.

presented UV–vis absorption spectra are the results of neither dissociation of organic ligands from SnI_4 nor solvation of the complexes. TDDFT calculations were applied to explain this observation. Results suggest that the absorption bands of SnI_4 in acetonitrile consist of transitions from HOMO (H-1, H-2, H-3, H-4) localized on iodine p orbitals to LUMO which is a Sn–I antibonding orbital. Calculations show also that transition between the same orbitals dominates in the absorption spectra of $[\text{SnI}_4\{(\text{C}_6\text{H}_5)_3\text{PO}\}_2]$, $[\text{SnI}_4\{(\text{C}_6\text{H}_5)_2\text{SO}\}_2]$, and $[\text{SnI}_4(\text{C}_3\text{H}_5\text{NO})_2]$. Moreover, the HOMO and LUMO of isolated complexes in acetonitrile are localized on inorganic fragments (see Figures S1–S3, Supporting Information),

making all spectra very similar (Figure 7a). Therefore, organic ligands have almost no influence on the absorption spectra of these complexes studied in solutions.

Solid state absorption spectra are strikingly different from absorption spectra in solution. Diffuse reflectance spectroscopy allowed new bands in the red part of the spectrum to be observed. Owing to their relatively high intensity they can be assigned to a charge transfer character. When an organic ligand is coordinated to tin(IV) iodide, a new, very broad absorption band appears, while two characteristic maxima (289 and 354 nm) disappear (Figure 7b). The difference between solid and solution absorption spectra is a result of the presence of intermolecular interactions between complex molecules, especially via the $\text{I}\cdots\text{HC}$ contacts. This interaction is too weak to reveal itself in the UV–vis absorption spectra in solution, but in the solid crystal structure numerous $\text{I}\cdots\text{HC}$ contacts were encountered (Table 1). Under the influence of the $\text{I}\cdots\text{HC}$ interactions, the electronic structure of the complex changed: maxima (289 and 354 nm) vanished, whereas a new broad band extending to the visible range (ca. 300–700 nm) appeared. This new spectral feature may be attributed to the charge transfer process involving iodide ligands (donor) and aromatic rings (acceptor) belonging to adjacent molecules. This assumption is supported by the DOS distribution, where the conduction band is made of carbon atom orbitals and the valence band of the iodine atom orbitals. Therefore, for the isolated molecule of the complex without any $\text{I}\cdots\text{HC}$ interactions, HOMO–LUMO transitions appear on the inorganic (SnI_4) moiety. Conversely, spectral properties of the solid phase are determined by the intermolecular interactions within the lattice. The main structural features involved are close $\text{I}\cdots\text{HC}$ contacts.

In order to better explain how the presence of neighboring molecules influences the localization of the frontier orbitals, DFT and TDDFT calculations were performed on molecular dimers with initial geometries extracted from the crystal structures. This computational approach is commonly used in the determination of electrical/optical properties of molecular semiconductors.^{35–37} More accurate calculations for solids, where three-dimensional clusters are made of 12 molecules, are present in the DOS section (*vide supra*). The significance of intermolecular interactions of adjacent molecules appear in the solid state arrangement. As the HOMO of the single molecule in solution and dimer in crystal arrangement are alike, the important changes appear in the LUMO: for the molecule of the complex in solution, the HOMO is composed of p orbitals of iodide, while the LUMO shows the I–Sn antibonding character. The arrangement of atoms in the crystal phase and the presence of the neighboring molecule result in the HOMO still being localized mostly on iodine atoms (Figure 8a, c, and e) of one molecule within a dimer, whereas the LUMO possesses a significant contribution from the phenyl (or pyridine) rings of the second molecule of the dimer (Figure 8 b, d, and f). These iodine–aromatic ring are characterized by a smaller energy and appear in the visible part of the absorption spectra. It is consistent with the results of semiempirical calculations where conduction and valence bands are made of carbon and iodine atom orbitals, respectively.

Diffuse reflectance spectroscopy was employed to determine the band gap energies. By plotting $(F^{KM} * hv)^{1/n}$ vs hv (Tauc plot) the optical band gap can be obtained. In the case of typical inorganic semiconductors, $n = 1/2$ for direct and $n = 2$ for indirect allowed transitions. In organic and molecular

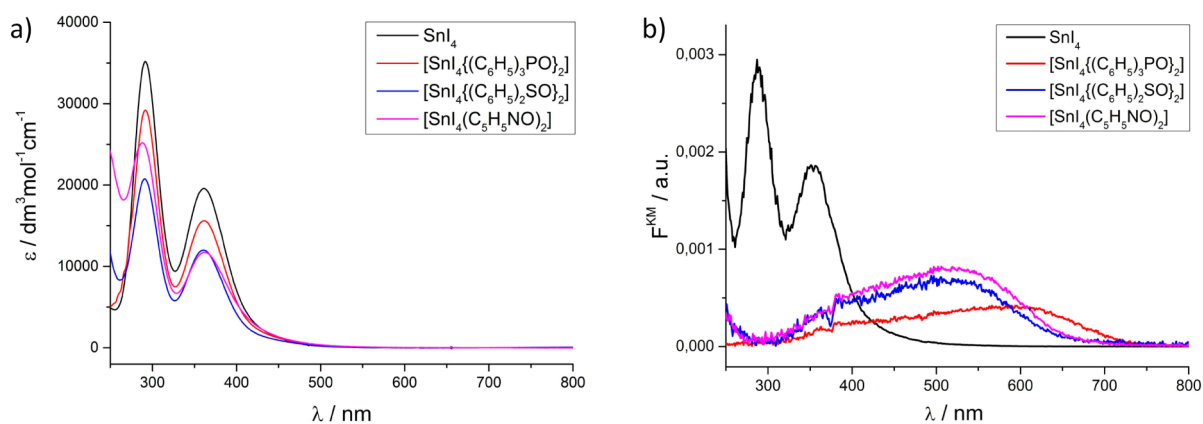


Figure 7. UV-vis absorption spectra of tin tetraiodide complexes in acetonitrile (a) and solid state absorption spectra of tin tetraiodide and complexes (b). F^{KM} is the Kubelka–Munk function.

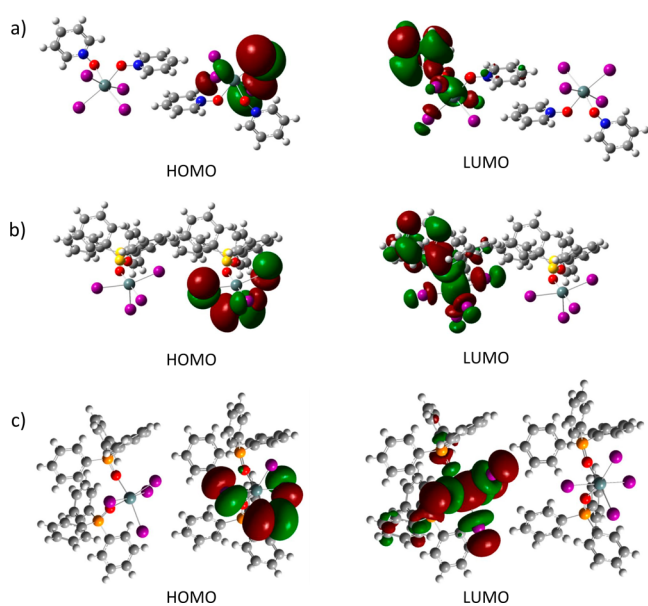


Figure 8. Visualization of frontier molecular orbitals of the dimers of $[\text{SnI}_4(\text{C}_5\text{H}_5\text{NO})_2]$ (a), $[\text{SnI}_4\{(\text{C}_6\text{H}_5)_2\text{SO}\}_2]$ (b), and $[\text{SnI}_4\{(\text{C}_6\text{H}_5)_3\text{PO}\}_2]$ (c). HOMO orbitals are localized on *p* iodine orbitals, whereas LUMO orbitals are localized mainly on aromatic carbon rings. HOMO and LUMO are on the opposite sides of the dimer.

semiconductors, in which weak van der Waals interactions play an important role in band formation, the *n* factor is often equal to unity (as used in Figure 9). The analysis of crystallographic structures of the compounds reveals the presence of those weak interactions between individual molecules in the crystals of studied materials. Therefore, it seems reasonable to use $n = 1$ for the studied compounds.³⁸ Optical band gaps and calculated TDDFT lowest transitions (for isolated, optimized molecule in vacuum) are collected in Table 3. Coordination of organic ligands causes a reduction in optical band gap energy by about 1 eV. The lowest transition calculated by TDDFT reflects the excitation of a molecule. Changes in calculated transition energy values (for allowed transitions) show the same trend as changes in experimentally obtained band gap energies.

Charge Decomposition Analysis. Bonding in the complex is considered as an interaction of fragment molecular orbitals of two closed-shell fragments. Charge decomposition analysis (CDA) distinguishes three interactions between the

metal center and ligands: (i) mixing of occupied orbitals of ligand with unoccupied orbitals of metal—the electron donation, charge transfer from ligand to metal (LMCT); (ii) mixing of unoccupied orbitals of ligand with occupied orbitals of metal—the electron back-donation, charge transfer from metal to ligand (MLCT); (iii) repulsive interaction of occupied orbitals of ligand and metal—repulsive polarization.³⁹ When SnI_4 (1) and organic ligand (2) combine to form a complex, two types of electronic interactions appear: polarization (PL) of one fragment in the presence of another and a charge transfer (CT) from a donor to an acceptor. Electronic polarizations do not move electron density from the donor fragment to the acceptor, but cause the electron redistribution within the fragment, in contrast to the CT process.⁴⁰ Using quantum-chemical calculations at the DFT level of theory and charge decomposition analysis, the CT and PL interactions were separated (Figure 10). The CT(2 → 1)–CT(1 → 2) difference confirms the supposition that SnI_4 is an acceptor of electron density and the organic ligand is a donor in the complexes, but more striking are the differences in ΔCT between these three complexes. $[\text{SnI}_4(\text{C}_5\text{H}_5\text{NO})_2]$ stands out with the highest ΔCT and, hence, the biggest net charge transfer value. It means that in the $[\text{SnI}_4(\text{C}_5\text{H}_5\text{NO})_2]$ complex bonding between tin and oxygen is the strongest. The higher ΔCT value influences the properties of the complex both in solution and in the solid phase. It correlates with the biggest changes in ^1H NMR spectra for this complex. Furthermore, it is related to the lowest specific conductivity due to the depletion of π -electron density. ΔPL values for $[\text{SnI}_4\{(\text{C}_6\text{H}_5)_3\text{PO}\}_2]$ and $[\text{SnI}_4\{(\text{C}_6\text{H}_5)_2\text{SO}\}_2]$ are basically the same, while for $[\text{SnI}_4(\text{C}_5\text{H}_5\text{NO})_2]$ Δp is the smallest which indicates the smallest repulsion between pyridine *n*-oxide and tin tetraiodide.

Surface Photovoltage (SPV) Measurements. Surface photovoltage measurements were used to determine the majority current type. It is a widely used noncontact method, based on changes of surface and near surface potential distribution under illumination. Band bending (upward for *n*-type, downward for *p*-type semiconductors) is a result of many factors, including surface dipole, termination of crystal structure, doping, surface states, crystal structure defects, and many others. Under illumination of the semiconductor surface, minority current carriers travel to the surface causing flattening of bands. The measurements of ΔCPD allow determination of the type of conductivity. In general:

$$e\Delta\text{CPD} = -e\Delta\text{SPV}$$

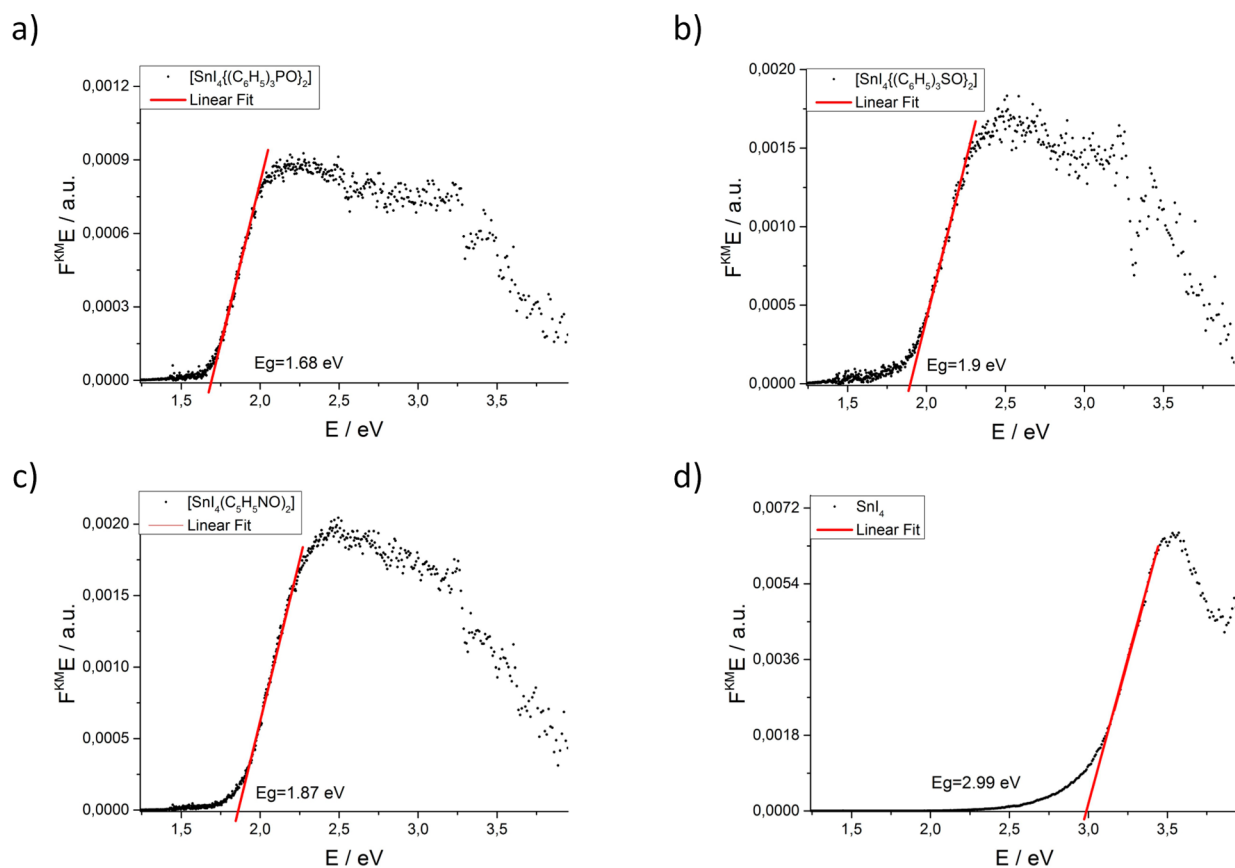


Figure 9. Tauc plots for $[\text{SnI}_4\{(\text{C}_6\text{H}_5)_3\text{PO}\}_2]$ (a), $[\text{SnI}_4\{(\text{C}_6\text{H}_5)_2\text{SO}\}_2]$ (b), $[\text{SnI}_4(\text{C}_5\text{H}_5\text{NO})_2]$ (c), and SnI_4 (d).

Table 3. Optical Energy Gaps and the Lowest Calculated Transitions

Compound	Optical band gap/eV	Calculated transitions/eV
$[\text{SnI}_4\{(\text{C}_6\text{H}_5)_3\text{PO}\}_2]$	1.68	2.31
$[\text{SnI}_4\{(\text{C}_6\text{H}_5)_2\text{SO}\}_2]$	1.90	2.48, ^a 2.50
$[\text{SnI}_4(\text{C}_5\text{H}_5\text{NO})_2]$	1.87	2.29, ^a 2.34
SnI_4	2.99	3.04

^aThe first transition with oscillator strength equal to zero.

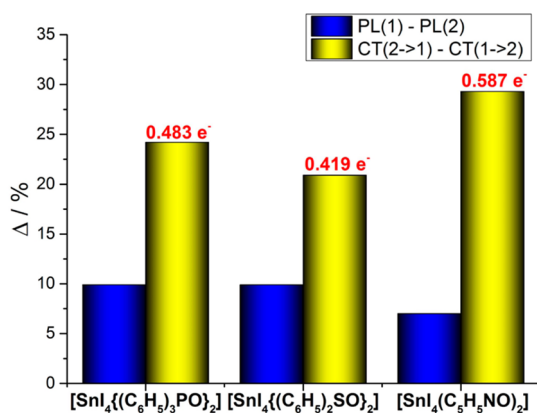


Figure 10. Differences between polarizations (ΔPL , blue), charge transfer processes (ΔCT , yellow) and the neat charge transfer (red) in tin(IV) complexes.

where e is the electric charge, ΔCPD is the contact potential difference, and SPV is the surface photovoltage.⁴¹ The differential surface photovoltage spectra of examined com-

pounds (Figure 11) point to the n -type of tin tetraiodide complexes (negative ΔCPD) with a small excess of majority

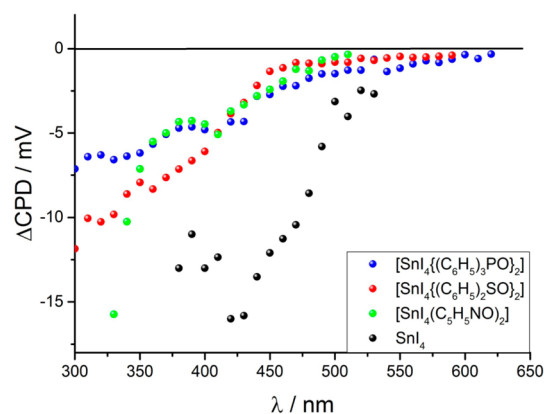


Figure 11. Differential surface photovoltage spectra of tin tetraiodide complexes deposited on the surface of ITO foil. Negative ΔCPD indicates the n -type conductivity.

current carriers (a small absolute value of ΔCPD). N -type conductivity might be caused by I^- vacancies, associated with a partial reduction of Sn(IV) centers. The n -type conductivity may be caused by a partial reduction of Sn(IV) centers (and hence iodide depletion).^{42,43} Iodide vacancies in similarly composed perovskites were described in literature as the primary source of charge carriers;⁴⁴ this statement also supports the observation of iodine sublimation from long-time stored

materials. The spectral range of SPV response (UV and vis) is consistent with solid state absorption spectra.

Work Function (WF) and Fermi Level (FL). Measurement of the work function (WF) allows determination of one of the most basic parameters in semiconductor studies, the potential of the Fermi level (FL). The work function is the energy required to remove one electron from the Fermi level. Using a Kelvin probe technique, the WF and FL have been determined (Table 4). Tin(IV) iodide in the studied complexes acts as an

Table 4. Work Function and Fermi Levels of Tin Tetraiodide Complexes

compound	work function/eV	Fermi level/mV vs NHE (−4.4 + WF)
[SnI ₄ {(C ₆ H ₅) ₃ PO} ₂]	4.704	304
[SnI ₄ {(C ₆ H ₅) ₂ SO} ₂]	4.815	415
[SnI ₄ (C ₅ H ₅ NO) ₂]	4.825	425
SnI ₄	5.084	684

acceptor of electron density while the ligand acts as a donor. Upon coordination of an organic ligand to SnI₄, WF decreases, due to a higher electron density on the SnI₄ fragment of the complex. The energies of frontier orbitals were obtained from TDDFT calculations made for molecules with vacuum-optimized geometries. The HOMO and LUMO of complexes are shifted with respect to the corresponding orbitals for tin tetraiodide, which is consistent with decreasing values of the work function observed upon coordination of the organic ligands to SnI₄ (Figure 12). Due to a significant discrepancy

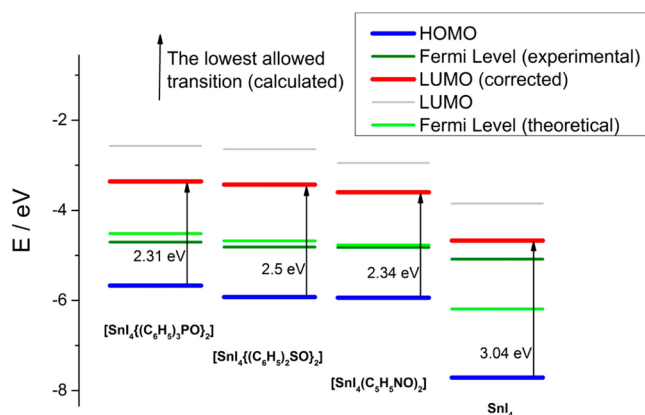


Figure 12. Energies of frontier orbitals (HOMO – blue, LUMO – gray) of examined complexes and SnI₄. The values of the first allowed transition (next to arrow) were used to correct the LUMO position (red). Fermi levels are depicted in green.

between predicted and observed electron affinities (LUMO energy), which is a well-known problem of the DFT method,⁴⁵ the values of the original LUMO energies were corrected by adding to the HOMO energies the value of the lowest allowed transitions (Table 3) to obtain a more reasonable energy diagram. This correction is often used to calculate LUMO energy levels.⁴⁶ The theoretical values of the Fermi level energies were estimated on the basis of DFT calculations and Janak's theorem as follows:⁴⁷

$$E_F = \frac{E_{\text{HOMO}} + E_{\text{LUMO}}}{2}$$

where E_F is the Fermi level energy and E_{HOMO} and E_{LUMO} are energies of the HOMO and LUMO orbitals. The results of these calculations show that theoretical and measured Fermi levels of complexes are consistent and localized around the middle of the energy gap. For SnI₄ the measured Fermi level is located close to the LUMO level and significantly differs from the theoretical Fermi level energy, which indicates more defects in SnI₄.

CONCLUSIONS AND OUTLOOK

The current study can be summarized in four points indicating the main findings regarding the chemistry and physics of classical tin(IV) complexes.

The analysis of crystal structures of the synthesized tin(IV) tetraiodide complexes shows the presence of π interactions along with hydrogen bonds (H \cdots I). Due to the presence of only weak intermolecular interactions, SnI₄ complexes are unique among the hybrid materials. Moreover, the composition of band structure highlights the importance of weak interactions in the solid state: it causes the formation of the valence band mainly from the orbitals belonging to the inorganic core and the conduction band from the organic-ligand-centered orbitals. Also short I \cdots I contacts were found to contribute significantly to the band structure of [SnI₄(C₅H₅NO)₂]. Their distances are smaller than those in the SnI₄ crystal structure (4.206 Å).

Solid state and solution absorption spectra are completely different for the studied complexes. A new, very broad charge transfer band appears in the solid state spectra. TDDFT analysis of complexes in solution and in a solid shows that the transitions in the visible part of the spectra (solid absorption) are between organic and inorganic fragments of neighboring molecules. In solution, due to a lack of weak intermolecular interaction, both HOMO and LUMO are localized at SnI₄.

Charge Decomposition Analysis explains differences between measured properties of complexes under conditions where intermolecular interactions are absent, i.e. in acetonitrile solution. Therefore, proton signals in ¹H NMR spectra exhibit the smallest shift for the complex with the smallest charge transfer ([SnI₄{(C₆H₅)₂SO}₂]) and the biggest shift for the complex with the biggest charge transfer ([SnI₄(C₅H₅NO)₂]).

Work function measurements show how coordination of the organic ligand decreases the Fermi level potential. Measured Fermi levels are localized close to the center of calculated energy gaps of complexes, which is characteristic for molecular semiconductors. Surface photovoltage measurements revealed that these complexes are *n*-type semiconductors with a small excess of majority charge current carriers.

The detailed studies presented above indicate the crucial role of intermolecular interactions in the design of novel semiconducting materials. Structural and physicochemical analysis helped to reveal a new and exciting family of molecular semiconductors based on main group elements. The main features of these materials are good solubility in common solvents (what enables, e.g., application of printing technologies to produce SnI₄L₂-based devices) and the possible tunability of properties. Tin iodide offers an easily accessible platform for numerous semiconducting materials, as the variety of ligands it can accept is almost unlimited.

■ ASSOCIATED CONTENT

● Supporting Information

The Supporting Information is available free of charge on the ACS Publications website at DOI: 10.1021/acs.inorgchem.6b00336.

HOMO and LUMO of isolated complexes in acetonitrile (Figures S1–S3) (PDF)

Crystallographic data of studied compounds obtained by single crystal diffraction (CIF, CIF, CIF)

■ AUTHOR INFORMATION

Corresponding Author

*E-mail: szacilow@agh.edu.pl.

Notes

The authors declare no competing financial interest.

■ ACKNOWLEDGMENTS

Authors acknowledge the support of Polish Ministry of Science and Higher Education (Grant Ideas Plus No. IDP2012000362), National Science Centre (Poland) within the MAESTRO project (Grant No. UMO-2015/18/A/ST4/00058), and European Union (RECORD-IT within the H2020-FETOPEN-1-2014 project, Grant No. 664786).

■ REFERENCES

- (1) Klauk, H. *Organic electronics: materials, manufacturing and applications*; Wiley-VCH: Weinheim, 2006.
- (2) Brütting, W. *Physics of organic semiconductors*; Wiley-VCH: Weinheim, 2005.
- (3) Schwoerer, M.; Wolf, H. C. *Organic molecular solids*; Wiley-VCH: Weinheim, 2007.
- (4) Kagan, C. R.; Mitzi, D. B. *Science* **1999**, *286*, 945–947.
- (5) Knutson, J. L.; Martin, J. D.; Mitzi, D. B. *Inorg. Chem.* **2005**, *44*, 4699–4705.
- (6) Mitzi, D. B. *Inorg. Chem.* **2000**, *39*, 6107–6113.
- (7) Yu, T. L.; Zhang, L.; Shen, J. J.; Fu, Y. B.; Fu, Y. L. *Dalton Transactions* **2014**, *43*, 13115–13121.
- (8) She, Y. J.; Zhao, S. P.; Tian, Z. F.; Ren, X. M. *Inorg. Chem. Commun.* **2014**, *46*, 29–32.
- (9) Zhu, X. H.; Mercier, N.; Frere, P.; Blanchard, P.; Roncali, J.; Allain, M.; Pasquier, C.; Riou, A. *Inorg. Chem.* **2003**, *42*, 5330–5339.
- (10) Maughan, A. E.; Kurzman, J. A.; Neilson, J. R. *Inorg. Chem.* **2015**, *54*, 370–378.
- (11) Dickinson, R. G. *J. Am. Chem. Soc.* **1923**, *45*, 958–962.
- (12) Jatsenko, A. V.; Medvedev, S. V.; Paseshnitchenko, K. A.; Aslanov, L. A. *J. Organomet. Chem.* **1985**, *284*, 181–188.
- (13) Tudela, D.; J. Sanchez-Herencia, A.; Diaz, M.; Fernandez-Ruiz, R.; Menendez, N.; D. Tornero, J. *J. Chem. Soc., Dalton Trans.* **1999**, 4019–4023.
- (14) Tursina, A. I.; Aslanov, L. A.; Chernyshev, V. V.; Medvedev, S. V.; Yatsenko, A. V. *Koord. Khim.* **1986**, *12*, 420–424.
- (15) *CrysAlis PRO*; Oxford Diffraction Ltd.: Yarnton, U.K., 2010.
- (16) Altomare, A.; Burla, M. C.; Camalli, M.; Cascarano, G. L.; Giacovazzo, C.; Guagliardi, A.; Moliterni, A. G. G.; Polidori, G.; Spagna, R. *J. Appl. Crystallogr.* **1999**, *32*, 115–119.
- (17) Sheldrick, G. M. *Acta Crystallogr., Sect. A: Found. Crystallogr.* **2008**, *64*, 112–122.
- (18) Macrae, C. F.; Edgington, P. R.; McCabe, P.; Pidcock, E.; Shields, G. P.; Taylor, R.; Towler, M.; Van de Streek, J. *J. Appl. Crystallogr.* **2006**, *39*, 453–457.
- (19) Farrugia, L. J. *J. Appl. Crystallogr.* **1999**, *32*, 837–838.
- (20) Hanwell, M. D.; Curtis, D. E.; Lonie, D. C.; Vandermeersch, T.; Zurek, E.; Hutchison, G. R. *J. Cheminf.* **2012**, *4*, 17.
- (21) Frisch, M. J.; Trucks, G. W.; Schlegel, H. B.; Scuseria, G. E.; Robb, M. A.; Cheeseman, J. R.; Scalmani, G.; Barone, V.; Petersson, G. A.; Nakatsuji, H.; Caricato, M.; Li, X.; Hratchian, H. P.; Izmaylov, A. F.; Bloino, J.; Zheng, G.; Sonnenberg, J. L.; Hada, M.; Ehara, M.; Toyota, K.; Fukuda, R.; Hasegawa, J.; Ishida, M.; Nakajima, T.; Honda, Y.; Kitao, O.; Nakai, H.; Vreven, T.; Montgomery, J. A., Jr.; Peralta, P. E.; Ogliaro, F.; Bearpark, M.; Heyd, J. J.; Brothers, E.; Kudin, K. N.; Staroverov, V. N.; Kobayashi, R.; Normand, J.; Raghavachari, K.; Rendell, A.; Burant, J. C.; Iyengar, S. S.; Tomasi, J.; Cossi, M.; Rega, N.; Millam, N. J.; Klene, M.; Knox, J. E.; Cross, J. B.; Bakken, V.; Adamo, C.; Jaramillo, J.; Gomperts, R.; Stratmann, R. E.; Yazyev, O.; Austin, A. J.; Cammi, R.; Pomelli, C.; Ochterski, J. W.; Martin, R. L.; Morokuma, K.; Zakrzewski, V. G.; Voth, G. A.; Salvador, P.; Dannenberg, J. J.; Dapprich, S.; Daniels, A. D.; Farkas, Ö.; Ortiz, J. V.; Cioslowski, J.; Fox, D. J. *Gaussian 09*, revision D.01; Gaussian, Inc.: Wallingford, CT, 2013.
- (22) Petersson, G. A.; Al-Laham, M. A. *J. Chem. Phys.* **1991**, *94*, 6081–6090.
- (23) Godbout, N.; Salahub, D. R.; Andzelm, J.; Wimmer, E. *Can. J. Chem.* **1992**, *70*, 560–571.
- (24) Kim, K.; Jordan, K. D. *J. Phys. Chem.* **1994**, *98*, 10089–10094.
- (25) Stephens, P. J.; Devlin, F. J.; Chabalowski, C. F.; Frisch, M. J. *J. Phys. Chem.* **1994**, *98*, 11623–11627.
- (26) O’Boyle, N. M.; Tenderholt, A. L.; Langner, K. M. *J. Comput. Chem.* **2008**, *29*, 839–45.
- (27) Dennington, R.; Keith, T.; Millam, J. *GaussView 5*; Semichem Inc.: Shawnee Mission, KS, 2009.
- (28) Stewart, J. J. P. *MOPAC2012*, Stewart Computational Chemistry; Colorado Springs: CO, USA, <http://OpenMOPAC.net>, 2012.
- (29) Gorelsky, S. I.; Lever, A. B. P. *J. Organomet. Chem.* **2001**, *635*, 187–196.
- (30) Gorelsky, S. I. *AOMix: Program for Molecular Orbital Analysis*; University of Ottawa: Ottawa, Canada, 2007; <http://www.sg-chem.net>.
- (31) Brammer, L.; Bruton, E. A.; Sherwood, P. *Cryst. Growth Des.* **2001**, *1*, 277–290.
- (32) Gilday, L. C.; Robinson, S. W.; Barendt, T. A.; Langton, M. J.; Mullaney, B. R.; Beer, P. D. *Chem. Rev.* **2015**, *115*, 7118–7195.
- (33) Cavallo, G.; Metrangolo, P.; Milani, R.; Pilati, T.; Priimagi, A.; Resnati, G.; Terraneo, G. *Chem. Rev.* **2016**, *116*, 2478–2601.
- (34) Stoumpos, C. C.; Kanatzidis, M. G. *Acc. Chem. Res.* **2015**, *48*, 2791–2802.
- (35) Nouri, H.; Cadiou, C.; Lawson-Daku, L. M.; Hauser, A.; Chevreux, S.; Dechamps-Olivier, I.; Lachaud, F.; Ternane, R.; Trabelsi-Ayadi, M.; Chuburu, F.; Lemerrier, G. *Dalton Trans.* **2013**, *42*, 12157–12164.
- (36) Baumeier, B.; Kirkpatrick, J.; Andrienko, D. *Phys. Chem. Chem. Phys.* **2010**, *12*, 11103–11113.
- (37) Brédas, J. L.; Calbert, J. P.; da Silva Filho, D. A.; Cornil, J. *Proc. Natl. Acad. Sci. U. S. A.* **2002**, *99*, 5804–5809.
- (38) Singh, J.; Shimakawa, K. *Advances in amorphous semiconductors/ Jai Singh and Koichi Shimakawa*; Taylor & Francis: London, 2003.
- (39) Frenking, G.; Pidun, U. *J. Chem. Soc., Dalton Trans.* **1997**, 1653–1662.
- (40) Gorelsky, S. I.; Ghosh, S.; Solomon, E. I. *J. Am. Chem. Soc.* **2006**, *128*, 278–90.
- (41) Kronik, L.; Shapira, Y. *Surf. Sci. Rep.* **1999**, *37*, 1–206.
- (42) Frolova, L. A.; Dremova, N. N.; Troshin, P. A. *Chem. Commun.* **2015**, *51*, 14917–14920.
- (43) Eames, C.; Frost, J. M.; Barnes, P. R. F.; O’Regan, B. C.; Walsh, A.; Islam, M. S. *Nat. Commun.* **2015**, *6*, 7497.
- (44) Zheng, F.; Saldana-Greco, D.; Liu, S.; Rappe, A. M. *J. Phys. Chem. Lett.* **2015**, *6*, 4862–4872.
- (45) Zhang, G.; Musgrave, C. B. *J. Phys. Chem. A* **2007**, *111*, 1554–1561.
- (46) Zhang, L.; Shen, W.; He, R.; Liu, X.; Tang, X.; Yang, Y.; Li, M. *Org. Electron.* **2016**, *32*, 134–144.
- (47) Janak, J. F. *Phys. Rev. B: Condens. Matter Mater. Phys.* **1978**, *18*, 7165–7168.

Influence of π – iodide intermolecular interactions on electronic properties of tin(IV) iodide semiconducting complexes

Supporting Information

Ewelina Wlaźlak,^{a,b} Wojciech Macyk,^a Wojciech Nitek,^a Konrad Szaciłowski^{b,}*

^aFaculty of Chemistry, Jagiellonian University, ul. R. Ingardena 3, 30-060 Kraków, Poland

^bAGH University of Science and Technology, Academic Centre for Materials and
Nanotechnology, al. A. Mickiewicza 30, 30-059 Kraków, Poland

*corresponding author: szacilow@agh.edu.pl

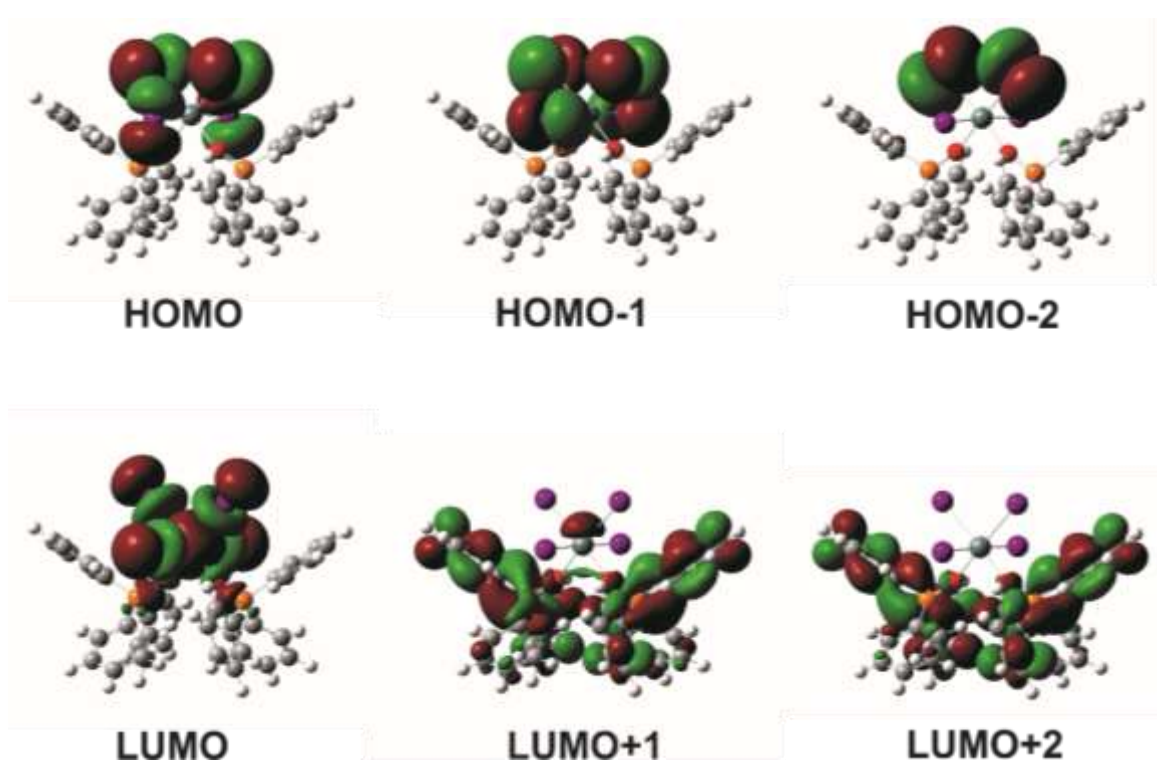


Fig. S1 Visualisation of frontier molecular orbitals of $[(C_6H_5)_3PO]_2SnI_4$

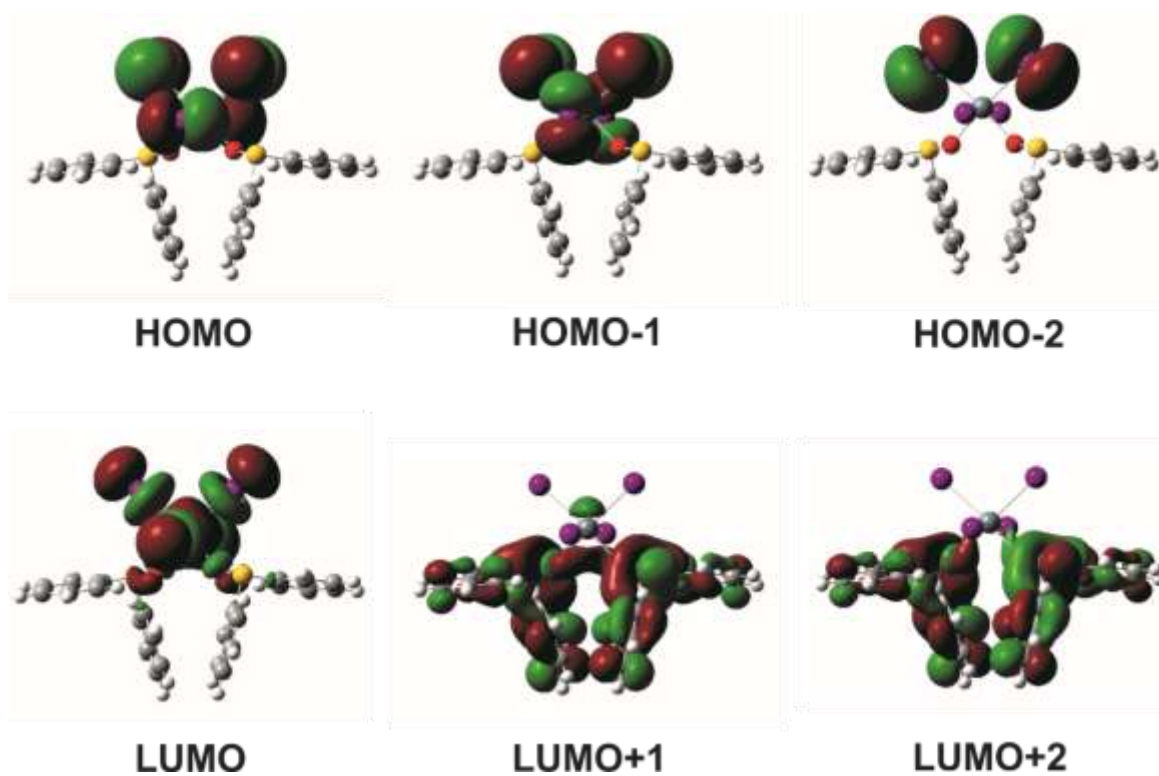


Fig. S2 Visualisation of frontier molecular orbitals of $[(C_6H_5)_2SO]_2SnI_4$

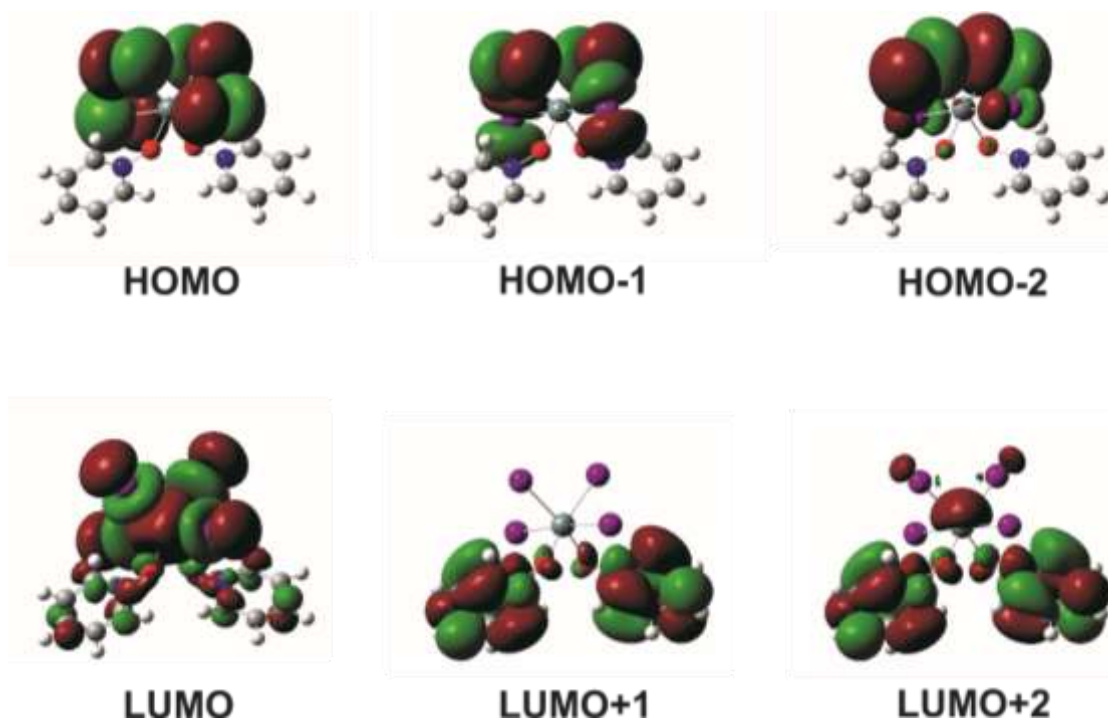
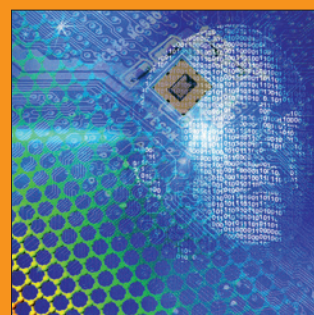
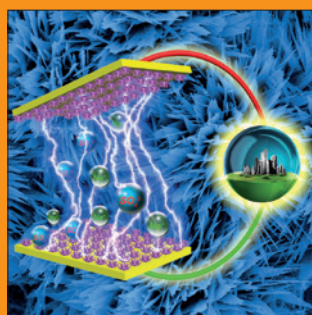
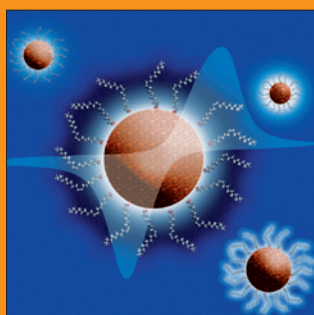
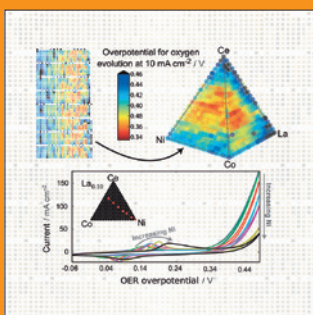
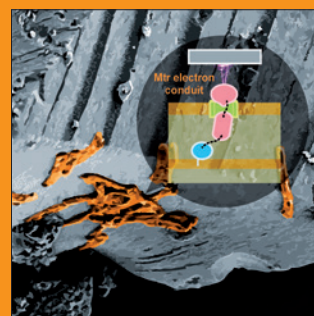
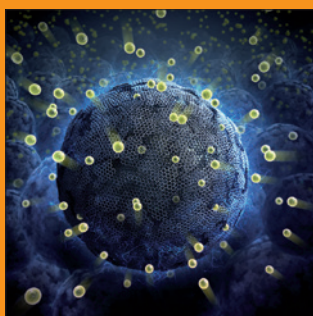
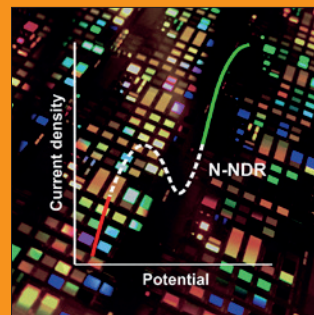
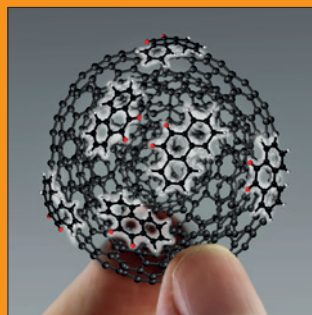
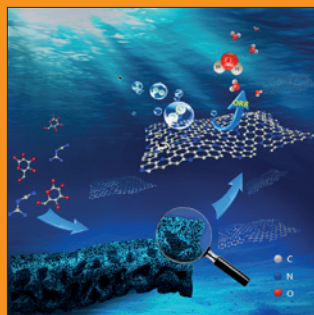
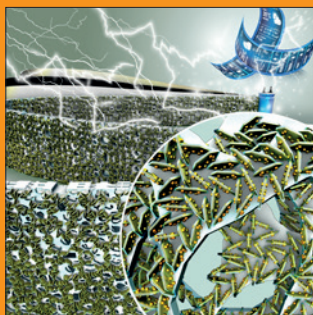


Fig. S3 Visualisation of frontier molecular orbitals of $[C_5H_5NO]_2SnI_4$

FUNDAMENTALS & APPLICATIONS

CHEMELECTROCHEM

ANALYSIS & CATALYSIS, BIO & NANO, ENERGY & MORE



Reprint

WILEY-VCH

www.chemelectrochem.org

A Journal of



Triiodide Organic Salts: Photoelectrochemistry at the Border between Insulators and Semiconductors

Ewelina Wlazlak,^{*,[a, b]} Justyna Kalinowska-Tluscik,^[a] Wojciech Nitek,^[a] Sylwia Klejna,^[b] Krzysztof Mech,^[b] Wojciech Macyk,^[a] and Konrad Szacilowski^{*,[b]}

The intriguing properties of triiodide organic salts ($[(C_6H_5)_3AsO]_2H^+I_3^-$, $(C_6H_5CH_2)_3NH^+I_3^- \cdot C_6H_5CH_3$, and $[(C_6H_5CH_2)_3NO]_2H^+I_3^-$) have been analyzed in detail using experimental and theoretical techniques. The analysis of crystal structures, density of states distribution and photocurrent generation of this purely ionic materials indicates insulating character of the ground state, whereas semiconducting character in higher excited states is observed. These peculiar properties of the studied compounds are the consequence of a specific electronic structure: very flat dispersion diagrams of the valence and conduction band and

highly dispersive character on the higher conduction band. Weak triiodide-triiodide interactions play the key role in the visible absorption range of these salts, while the charge transfer involving high energy carbon-centered states is responsible for photocurrent generation. The complexity of the electrochemical reactions and the interactions of the I_3^- anion with light, solubility in organic solvents and the simplicity of preparation make these materials interesting candidates for application in unconventional optoelectronic devices.

1. Introduction

Polyiodides have attracted a lot of interest owing to their fascinating chemistry and structural diversity.^[1] The family of polyiodides encompasses structures of various dimensionalities and stoichiometries ranging from I_2^- to I_{29}^{3-} , whereas the triiodide (I_3^-), with approximately 500 different cations and structures, is the most common one.^[1] Recently the interest in polyiodide chemistry was revitalized by their redox properties. Due to the versatility of redox reactions of iodine species the organic iodide salts are used as electrolytes and redox mediators for dye sensitized solar cells,^[2] anions of ionic liquids,^[3] energy storage agents (light-induced formation of I–I bonds),^[4] proton sponges,^[5] in electrocatalytic reduction of triiodide,^[6] lithium-iodide batteries,^[7] lithium-sulfur batteries,^[8] supercapacitors,^[9] charge-transfer and mixed-valence salts.^[10] Iodine species were also considered as dopants of polymers and graphene.^[11] Some triiodide salts exhibited metallic,^[12] semiconducting or superconducting properties, but they are attributed to formation of cationic stacks,^[13] whereas the role of triiodide was reduced to the counterion stabilizing the radical salt structure. In this work we present our studies on three

semiconducting salts with triiodide anion. We demonstrate that the semiconducting character of these compounds is the result of the electronic interactions between triiodide anions.

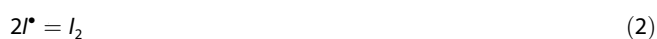
In our previous report^[14] we have demonstrated that combination of weak interactions between aromatic substituents and iodide ligands is the series of $[SnI_4L_2]$ complexes (L = diphenylsulfoxide, triphenylphosphine oxide, pyridine N-oxide) results in semiconducting character despite the lack of strong intermolecular interaction. Therefore, we were searching for compounds with analogous structural features: pnictogen or pnictogen oxide center with three aromatic substituents. Due to the facility of crystal growth and stability of obtained compounds we have selected three bulky compounds: tribenzylamine, tribenzylamine N-oxide and triphenylarsine oxide and used them, upon protonation, as counterions for triiodide. Application of these bulky organic cations brings about two benefits: they are insoluble in water and resistant towards hydrolysis, and their stability is expected to be much higher than small-cation triiodides.^[1,15] In this paper, triiodide organic salts ($[(C_6H_5)_3AsO]_2H^+I_3^-$, $(C_6H_5CH_2)_3NH^+I_3^- \cdot C_6H_5CH_3$, and $[(C_6H_5CH_2)_3NO]_2H^+I_3^-$) are proven to be semiconductors in which I_3^- ions are placed in specific organic scaffolds. These anions are placed in the channels, in which movement of these entities might be possible. In contrary to the previous research, due to the specific crystal structure and the presence of tunnels, the Grothuss^[16]-type transport in one dimension is possible. The same mechanism was already suggested to contribute to the high electrical conductivity of molten polyiodides,^[17] ion-conducting polymers^[18] and ionic liquids.^[19] The main photoelectrochemical properties of these materials result from the interactions between iodine species, as well as the triiodide interactions with light and organic molecules. A simple synthesis, inertness towards air and humidity, as well as a good solubility in common solvents (combined with a very

[a] E. Wlazlak, Dr. J. Kalinowska-Tluscik, Dr. W. Nitek, Prof. Dr. W. Macyk
Faculty of Chemistry
Jagiellonian University
ul. Gronostajowa 2, 30-387 Kraków, Poland
E-mail: ewelina.wlazlak@doctoral.uj.edu.pl

[b] E. Wlazlak, Dr. S. Klejna, Dr. K. Mech, Prof. Dr. K. Szacilowski
AGH University of Science and Technology
Academic Centre for Materials and Nanotechnology
al. A. Mickiewicza 30, 30-059 Kraków, Poland
E-mails;
E-mail: szacilow@agh.edu.pl
ewlazlak@agh.edu.pl

Supporting information for this article is available on the WWW under <https://doi.org/10.1002/celc.201800975>

low solubility in water) make them good candidates for prospective applications in photovoltaics and disposable screen-printed electronics. Taking into consideration the large scope of possible applications of these compounds arising from the specific crystal structure and presence of the photoelectrochemically active moiety (I_3^-) in the structure, the detailed studies of their properties are required. A wide application of polyiodides-based electrolytes in solar cells is a consequence of their diversity of chemical equilibria and redox processes, which are well-tuned to the redox properties of dyes and titanium dioxide [e.g., Eq (1)–(12)]. Iodine binds with iodide in solution forming triiodide ion, however, also formation of polyiodide species like I_5^- or I_7^- is possible, if concentration of iodine in the solution is sufficiently high.^[21]



According to voltammetric measurements in the systems with iodide and triiodide ions, the following reactions take place:^[20]



Several other reactions are also possible:



Light induced reactions, involving a direct excitation and photodissociation, should be also considered.^[4,20b,21]



Various organic triiodide salts have been synthesized so far. Derivatives of tetrathiafulvalenes with triiodide anion have attracted attention since the eighties, as the organic radical cation salts,^[22] or organic superconductors.^[23] Salts with protonated tertiary amines and metal triiodide complexes are often reported in the literature.^[5,24] Also a quite rare example of protonated arsine oxide has been found.^[25] A few simple salts were used to explain the mechanism of polyiodide formation. Iodine species have a tendency to catenate through donor acceptor interactions. By changing the molar ratio of reactants (I^- and I_2) in solution salts with various polymerization degrees

can be obtained, although some of them are stable only in solutions.^[26]

In this paper we present synthesis, crystal structures and studies on semiconducting properties of three triiodide salts with bulky cations. A detailed structural analysis followed by electronic structure calculations, Kelvin probe measurements, UV-vis spectroscopy and photocurrent measurements enabled elucidation of the mechanism of photocurrent generation by these materials.

2. Results and Discussion

2.1 Crystal structure

Presented structures of $[(C_6H_5)_3AsO]_2H^+I_3^-$, $(C_6H_5CH_2)_3NH^+I_3^- \cdot C_6H_5CH_3$ and $[(C_6H_5CH_2)_3NO]_2H^+I_3^-$ were determined by single crystal X-Ray diffractometry. In the packing of presented compounds there are channels occupied by I_3^- . The channels are situated in the [001] direction for $[(C_6H_5)_3AsO]_2H^+I_3^-$ and $[(C_6H_5CH_2)_3NO]_2H^+I_3^-$ and [110] for $(C_6H_5CH_2)_3NH^+I_3^- \cdot C_6H_5CH_3$. As shown in Figure 1, linear anions are positioned along the dual channels in parallel directions for $[(C_6H_5)_3AsO]_2H^+I_3^-$ and $(C_6H_5CH_2)_3NH^+I_3^- \cdot C_6H_5CH_3$. In the case of the $[(C_6H_5CH_2)_3NO]_2H^+I_3^-$ structure there is an angular arrangement of the anion in respect to the direction of the single but expanded channel. Detailed crystal data and structure refinement results for $[(C_6H_5)_3AsO]_2H^+I_3^-$, $(C_6H_5CH_2)_3NH^+I_3^- \cdot C_6H_5CH_3$ and $[(C_6H_5CH_2)_3NO]_2H^+I_3^-$ are listed in Table S1 in the Supplementary Information.

$[(C_6H_5)_3AsO]_2HI_3$ crystallizes in the monoclinic space group C 2/c. The asymmetric unit consists of one organic molecule and half of the triiodide anion. The I1 atom is located in a special position on the 2-fold axis. The positive charge is displaced between two organic molecules by sharing proton between triphenylarsine oxides (Figure 2a). The two organic molecules are in relation of the two-fold axis in [010] direction with proton located in the special position. The As–O19 distance is 1.682(2) Å, O···H 1.22(1) Å, forming the hydrogen bond. The As–O19–H19 angle is 122(3)° and O19–H19···O19#1 (#1: $-x + 1, y, -z + 0.5$) is 162(6)°. Additionally, the aromatic moieties of organic compounds are arranged in a T-shape like motives in distances confirming the van der Waals interactions. The crystal packing is stabilized by several $C_{ar} \cdots H \cdots I$ interactions, where C_{ar} is the carbon atom of the aromatic system (see Figure 2b and Table 1 for geometrical parameters of mentioned interactions).

Table 1. The most important C–H, H···I, C···I distances and C–H···I angle observed in the crystal structure of $[(C_6H_5)_3AsO]_2HI_3$.

	C–H [Å]	H···I [Å]	C···I [Å]	<(CHI) [°]
C17–H17...I2	0.93	3.393	4.012(1)	126.15(1)
C18–H18...I2	0.93	3.354	3.995(1)	128.04(1)
C5–H5...I1 #1	0.93	3.416	3.967(1)	120.26(1)
C15–H15...I1 #2	0.93	3.428	4.264(1)	106.73(1)
#1 $x + 1/2, y + 1/2, z, \#2 x + 1/2, -y + 1/2, z - 1/2$				

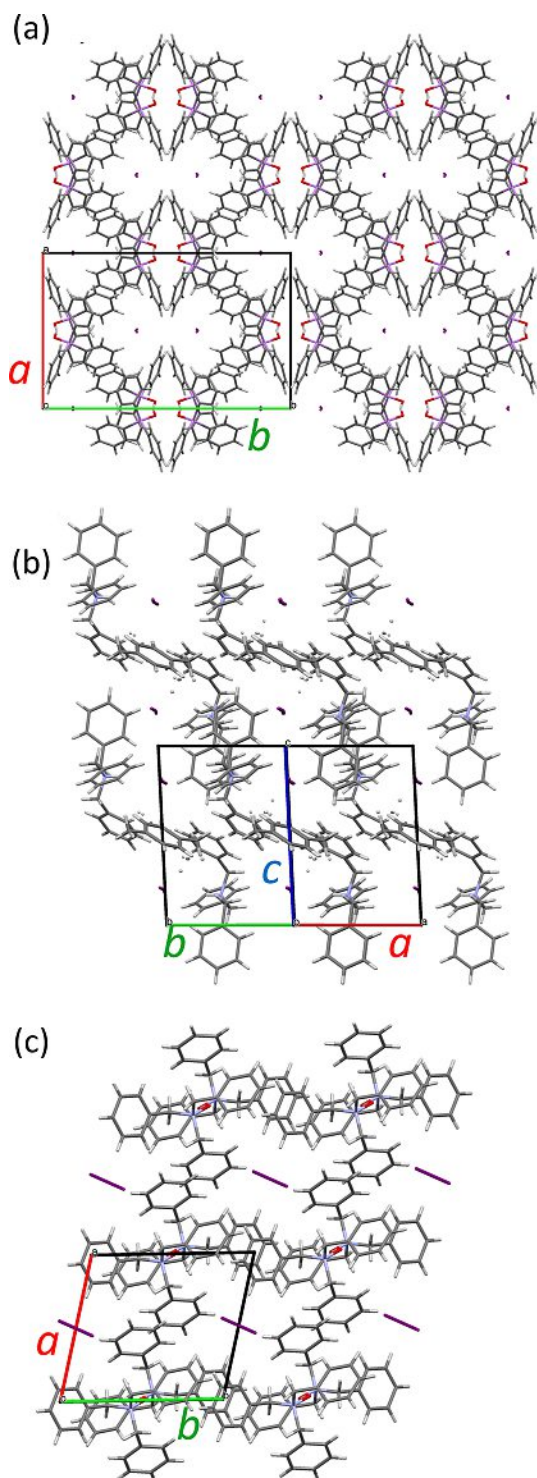


Figure 1. Scheme The crystal packing of $2 \times 2 \times 2$ periods of $[(C_6H_5)_3AsO]_2H^+I_3^-$ (a), $(C_6H_5CH_2)_3NH^+I_3^- \cdot C_6H_5CH_3$ (b) and $[(C_6H_5CH_2)_3NO]_2H^+I_3^-$ (c), presenting channels filled with the I_3^- anions. Views along [001] for $[(C_6H_5)_3AsO]_2H^+I_3^-$ and $[(C_6H_5CH_2)_3NO]_2H^+I_3^-$, and [110] for $(C_6H_5CH_2)_3NH^+I_3^- \cdot C_6H_5CH_3$.

The triiodide anions are nearly linear with the I2–I1–I2#2 (#2: $-x+1, y, -z-0.5$) angle of $176.49(1)^\circ$ and I–I distance of $2.914(1)$ Å. Two triiodide anions occupy the double-like channel (Figure 1a). Distances between neighboring anions occupying

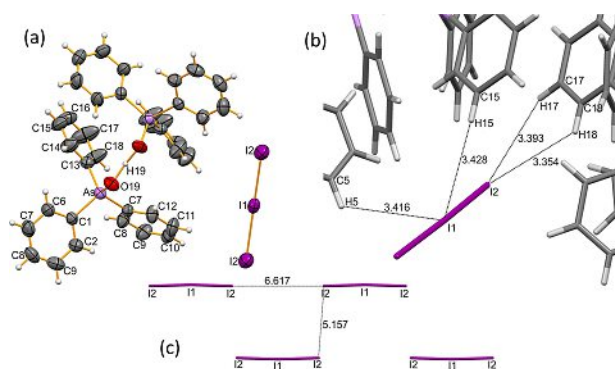


Figure 2. The molecular structure of $[(C_6H_5)_3AsO]_2H^+I_3^-$ with labelled atoms of the asymmetric unit (a), short contacts Car–H...I observed in the crystal structure of $[(C_6H_5)_3AsO]_2H^+I_3^-$ (b), and the triiodide ions arrangement in the double channel (c).

the same stream of the dual channel are $6.617(1)$ Å and $5.157(1)$ Å between I_3^- in two parallel parts of the channel (Figure 2c).

$(C_6H_5CH_2)_3NH_3^+ \cdot C_6H_5CH_3$ crystallizes in a salt form in the triclinic $P\bar{1}$ space group. The positive charge is located on the protonated amine group of the tribenzylamine and it is balanced by the triiodide anion. This compound co-crystallizes with the toluene solvent, which is disordered in this structure (Figure 3a). The strongest noncovalent interaction observed in

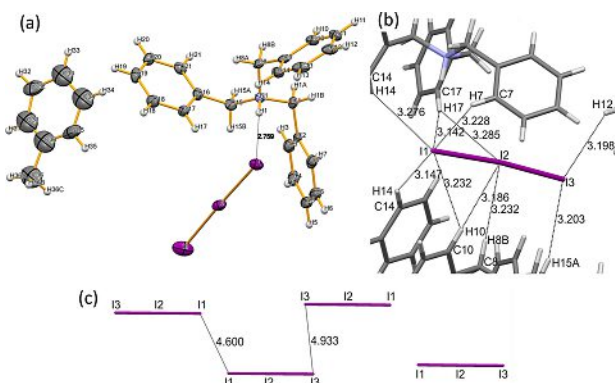


Figure 3. The asymmetric unit of $(C_6H_5CH_2)_3NH_3^+ \cdot C_6H_5CH_3$; the charge assisted hydrogen bond is shown with dashed lines (a); weak C–H...I hydrogen bonds and short contacts to I1, I2 and I3 (b) and the triiodide anions arrangement in the double channels (c).

this crystal structure is a hydrogen bond N1–H1...I1, with N1...I1 distance $3.642(3)$ Å, H...I distance $2.76(4)$ Å and N1–H1...I1 angle $175(4)^\circ$ (Figure 3a). In the crystal of $(C_6H_5CH_2)_3NH_3^+ \cdot C_6H_5CH_3$ there are several weak hydrogen bonds and short contacts of C–H...I type, which additionally stabilize the structure (see Figure 3b and Table 2 for the geometrical parameters of mentioned interactions). Despite of the parallel arrangement of the aromatic rings, the π ... π interactions are not observed. The triiodide anion is nearly linear with the I1–I2–I3 angle $175.34(1)^\circ$. Distances I1–I2 and I2–I3 are $2.984(1)$ Å and $2.869(1)$ Å, respectively. As observed in the case of the $[(C_6H_5)_3AsO]_2H^+I_3^-$

Table 2. The most important C–H, H...I, C...I distances and C–H...I angle observed in the crystal structure of $(C_6H_5CH_2)_3NHl_3 \cdot C_6H_5CH_3$.

	C–H [Å]	H...I [Å]	C...I [Å]	<(CHI) [°]
C14–H14...I1 #1	0.95	3.147	3.968(1)	145.72(1)
C17–H17...I1	0.95	3.142	4.026(1)	155.42(1)
C10–H10...I1 #2	0.95	3.223	3.899(1)	129.61(1)
C7–H7...I1	0.95	3.228	3.651(1)	109.06(1)
C14–H14...I1	0.95	3.276	3.831(1)	119.22(1)
C10–H10...I2 #2	0.95	3.186	4.080(1)	157.32(1)
C17–H17...I2	0.95	3.285	4.061(1)	140.32(1)
C8–H8...I2 #2	0.99	3.232	4.184(1)	161.76(1)
C15–H15...I3	0.99	3.203	4.149(1)	160.56(1)
C12–H12...I3 #3	0.95	3.188	3.958(1)	138.32(1)

#1 $-x+1, -y, -z$, #2 $x+1, y, z$, #3 $x-1, y+1, z$

structure, the two triiodide anions occupy the double-like channel along the [110] direction (Figure 1b)). The distance between neighboring anions in one part of the channel is 7.360(1) Å. In comparison to the structure of $[(C_6H_5)_3AsO]_2HI_3$, two parallel triiodide anions occupying the dual channel are closer to each other with the distance of 4.933(1) Å for overlapping atoms I3...I3#1 (#1: $-x, -y, -z$) and 4.600(1) Å for I1...I1#2 (#2: $1-x, 1-y, -z$) (Figure 3c, Table 2).

$[(C_6H_5CH_2)_3NO]_2HI_3$ crystallizes in the triclinic $P\bar{1}$ space group. The asymmetric unit consists of one organic molecule and half of the triiodide anion, with I2 atom placed in the special position of the inversion centre. Two tribenzylamine oxides bridged by hydrogen bond O1...H1...O1#1 (#1: $-x, -y, -z$) form a dimer with H1 in the special position (Figure 4a).

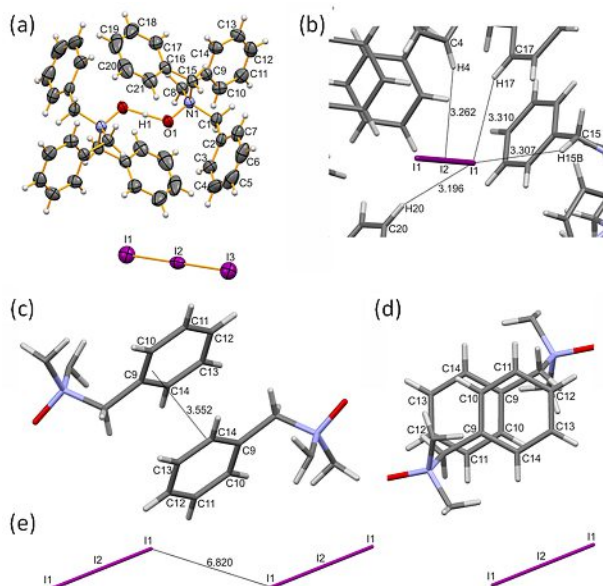


Figure 4. The crystal structure of the dimer $[(C_6H_5CH_2)_3NO]_2HI_3$ with labelled atoms of the asymmetric unit (a), weak hydrogen bonds and close contacts of the C–H...I type (b), the intermolecular $\pi\cdots\pi$ interaction (c–d) and the triiodide anions arrangement (e).

The mentioned hydrogen atom is displaced between two oxygen atoms, inducing the positive charge which is compen-

sated by the triiodide anion. In comparison to both previous structures, here there is only one weak hydrogen bond and few close contacts of C–H...I type (see Figure 4b and the Table 3 for

Table 3. The most important C–H, H...I, C...I distances and C–H...I angle observed in the crystal structure of $[(C_6H_5CH_2)_3NO]_2HI_3$.

	C–H [Å]	H...I [Å]	C...I [Å]	<(CHI) [°]
C17–H17...I2	0.93	3.310	4.045(1)	137.53(1)
C15–H15B...I1 #1	0.969	3.307	4.135(1)	144.55(1)
C20–H20...I1 #2	0.93	3.199	4.067(1)	156.71(1)
C4–H4...I2 #3	0.93	3.262	4.145(1)	159.25(1)

#1 $-x+1, -y+1, -z+1$; #2 $x, y+1, z$; #3 $-x, -y+1, -z+1$

geometrical parameters of the mentioned interactions). In this structure a $\pi\cdots\pi$ interaction is observed between two molecules related *via* inversion center (Figure 4c). In the $[(C_6H_5CH_2)_3NO]_2HI_3$ structure there is a single channel in the [001] direction, occupied by linear triiodide anions, but this time this ion is in the angular orientation to the channel path. The I1–I2 distance is 2.921(1) Å and the distance between neighboring anions I1...I1#2 (#2: $1-x, 2-y, 1-z$) is 6.820(1) Å (Figure 4d).

2.2 Electronic Structure

The band structure along with the projected atomic and angular momentum decomposed electronic density of states for investigated iodide salts are displayed in Figures 5, S1 and

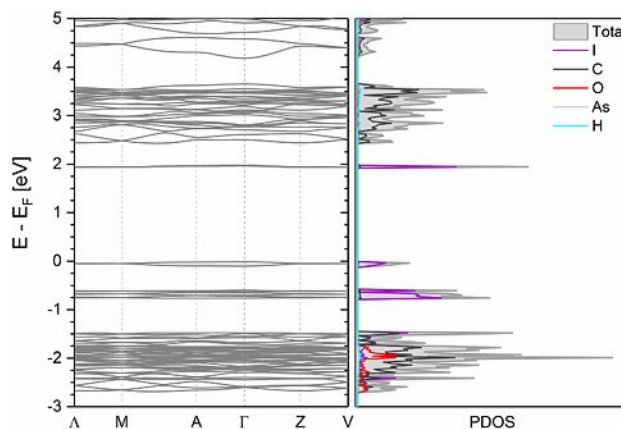


Figure 5. The band structure and projected density of states of $[(C_6H_5)_3AsO]_2HI_3$ from DFT–D3–SOC. The Fermi level is set to zero.

S3. The labeled Brillouin zone points for the monoclinic space group $C2/c$ are: $\Lambda = (-1/2, 0, 1/2)$, $M = (-1/2, 1/2, 1/2)$, $A = (-1/2, 0, 0)$, $\Gamma = (0, 0, 0)$, $Z = (0, -1/2, 1/2)$, $V = (0, 0, 1/2)$ and for the triclinic $P\bar{1}$ space group: $F = (0, 1/2, 0)$, $Q = (0, 1/2, 1/2)$, $Y = (0, 0, 1/2)$. For all studied materials, the valence band (VB) and the conduction band (CB) states show rather a sharp peak structure indicating presence of localized states resulting from the flat energy bands. A negligible dispersion of the VB and the CB suggests a direct character of the fundamental excitation in all three

semiconductors. $[(C_6H_5)_3AsO]_2HI_3$ has a computed electronic band gap of 1.95 eV. The top of the VB as well as the bottom of the CB are composed predominantly of the I 5p states with a minor, but notable contribution of the C 2p states and H, showing very weak $C_{ar}-H\cdots I$ interactions. The valence band maximum (VBM) is assigned mainly to I 5p_{xy} states and the conduction band minimum (CBM) to I 5p_z which is visualized in Figure 6a–b. The C 2p states dominate 2.4 eV above the Fermi

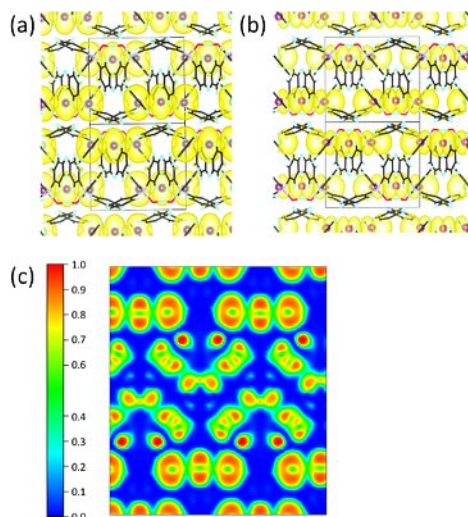


Figure 6. The partial charge density plots of the valence band maximum (VBM) (a) and the conduction band minimum (CBM) (b) and electron localization function (ELF) plots of $[(C_6H_5)_3AsO]_2HI_3$ on the (1 1 0) plane (c).

level and have increased band dispersion, while a strong hybridization of the I, C and O states occurs below -1.5 eV. The electronic structure of $(C_6H_5CH_2)_3NHI_3 \cdot C_6H_5CH_3$ reveals the band gap energy of 1.84 eV. The VB and CB are of mixed I 5p orbital character with some C 2p contribution, represented Figure S2a–b. Interestingly, the two polyiodide sites in the cell are not electronically equivalent, which is reflected in the partial density plots (Figures S2a–b). A further analysis shows domination of the C 2p states above 3 eV for this structure. States below -0.5 eV are derived from a mixture of I 5p and C 2p orbitals. The band gap of 1.83 eV opens up for $[(C_6H_5CH_2)_3NO]_2HI_3$. Similarly, to $[(C_6H_5)_3AsO]_2HI_3$, the majority of the VB states are derived from I 5p_{xy} orbitals with a little contribution of I 5p_z and even smaller contribution of C 2p states. The CB consists mainly of I 5p_z states with a small admixture of I 5p_{xy} and also C 2p states (Figure S4a–b). Around -0.7 eV a sharp peak consisting of mixed 5p I states arises, again with a minor C orbitals contribution. This time, pure C states stand up 2.9 eV above the VB edge while mixing of the I, C and O states occurs already below -1.0 eV.

Figure 6c, S2c and S4c show ELF plotted on different lattice planes of regarded structures and quantifies the probability of finding an electron pair in the region of molecular space,^[27] which is helpful in characterizing the chemical bonding. Planes are chosen to visualize channels of the triiodide anions. Large values of ELF between the iodine atoms within the I₃[−] anions

indicate a strong covalent bonding nature within these moieties. An indication of lone electron pairs can be seen as the non-spherical charge localization on the central atom of the anion. This indicates a relatively weak ground state electronic coupling between the triiodide anions at the PBE–D3 level of theory. The details of computational results are presented in Tables S2–S4 and animations S1–S6 in the Supplementary Information.

The results of calculations in the case of all three materials reveal negligible dispersion of the valence and conduction bands. As a consequence, one should expect very high effective mass of charge carrier, and therefore very low charge carrier mobility. Therefore, these materials can be considered as insulators.

2.3 Electronic Spectra

The electronic spectra of acetonitrile solutions of studied compounds are almost identical, irrespectively on the cation nature. The UV-vis solid absorption spectra are dominated by the presence of the triiodide anion: the positions of main peaks at ca. 294 and 365 nm are fully consistent with previous reports (Figure 7a).^[11] In the solid-state spectra (Figure 7b) at least two

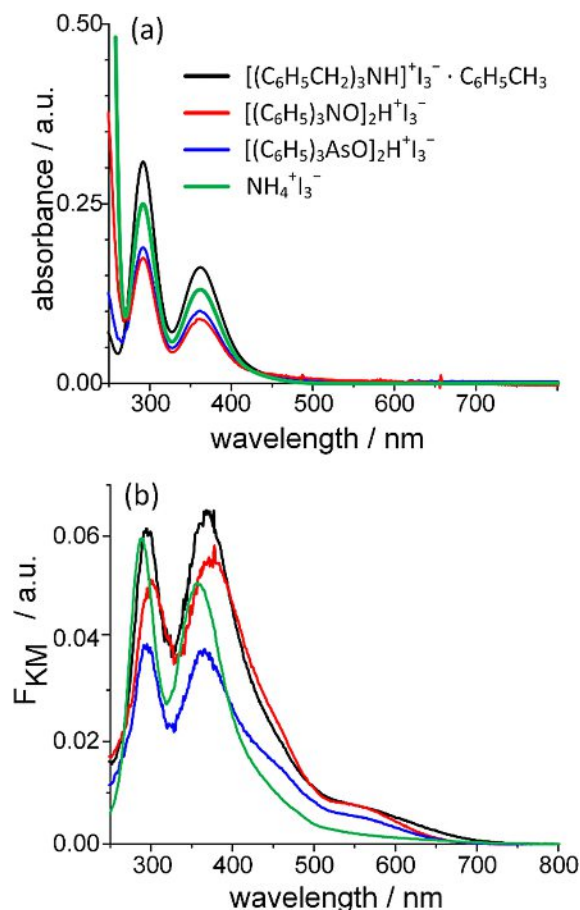


Figure 7. Solution (a) and solid state (b) electronic spectra of three studied organic triiodides. Ammonium triiodide spectra are shown as a reference.

additional absorption bands are present, they are localized at ca. 450 nm and 550 nm. They differ in shape and intensity and can be observed as shoulders on the low energy side of the triiodide band. Therefore, it can be concluded that those additional bands originate from some intermolecular interactions present in the solid state. The comparison of solid and solution spectra (Figure 7) allows to extract the contribution of

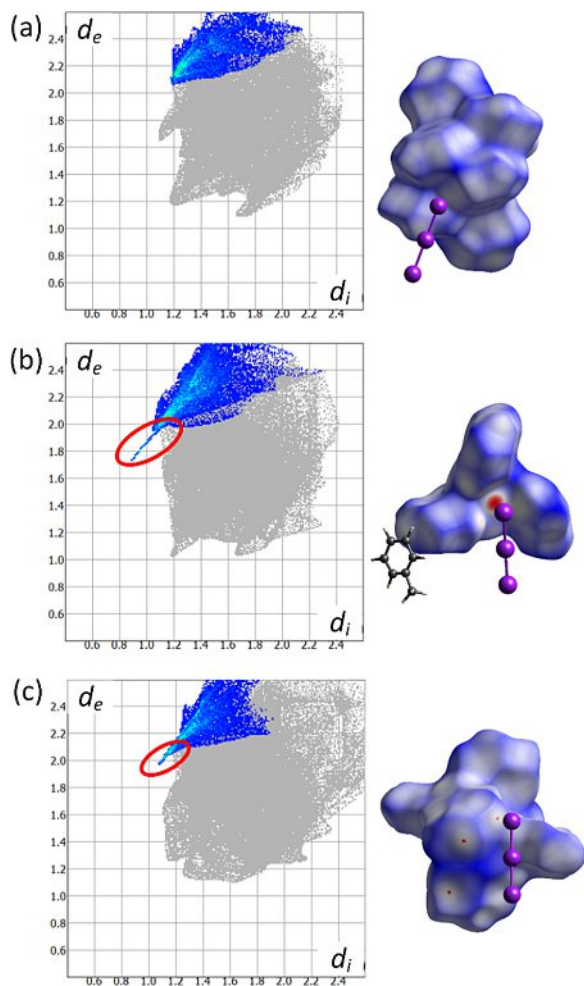


Figure 8. Fingerprint of H...I interaction (left) and 3D_{norm} Hirshfeld surface (right) of [(C₆H₅)₃AsO]₂H⁺I₃⁻ (a), (C₆H₅CH₂)₃NH⁺I₃⁻·C₆H₅CH₃ (b), [(C₆H₅CH₂)₃NO]₂H⁺I₃⁻ (c). Red ellipses indicate iodide – hydrogen interaction, red dots shows overlapping of vdW spheres.

the triiodide anion from the solid absorption spectra and identify the absorption range where the intermolecular interactions promote lower energy transitions. Interestingly, in the case of ammonium triiodide these bands show a much lower intensity. Gaussian deconvolution of these spectra reveals their complex structure and again indicates their similarities (Figure 9). In all studied cases the shoulder is composed from two transitions at ca. 2.2 eV and 2.8 eV for all organic salts. Ammonium triiodide, in turn, shows a similar structure of the spectrum, but with transitions localized at 2.48 and 2.86 eV. Similar spectral features were observed in various organic hydrotriiodides.^[28] The band at 550 nm is responsible for the

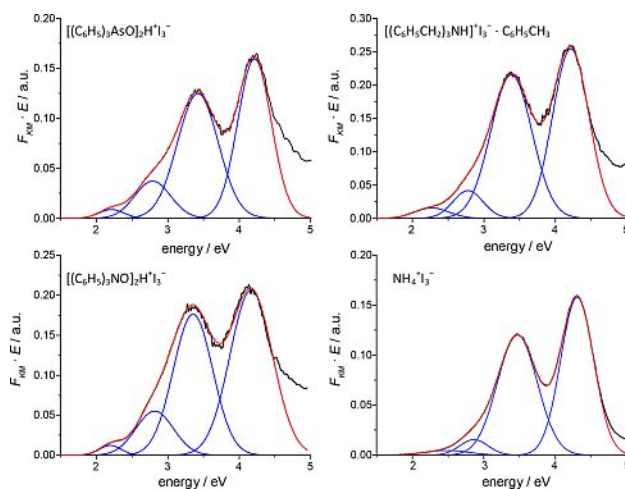


Figure 9. Deconvolution of the solid-state UV-Vis diffuse reflectance spectra (in the form of Kubelka-Munk function) into Gaussian components. Experimental spectra are shown in black, fitted spectra in red, whereas individual components in blue.

photocurrent generation in the wide range of the visible part of spectra (*vide infra*). As predicted by the calculated partial charge density plots (Figure 6, S1, and S3, *vide supra*), the interactions between the triiodide anions are responsible for the two lowest energy transitions from the top of the valence band to the bottom of the conduction band. The distribution of the density of states within these bands is narrow, as the consequence of their separation, and therefore weak electronic interactions between different triiodide moieties within the lattice (*vide supra*). The electronic interactions between the triiodide anions and the aromatic moieties within cations are excluded on the basis of calculated density of states for the lowest energy transitions. The I₃⁻ – I₃⁻ interactions in these structures are therefore stronger than organic – organic or I₃⁻ – organic interactions which were reported previously.^[29] There is a large energy separation between iodide-centered orbitals and carbon centered ones, despite of some weak hydrogen bonds and close contacts of the C–H...I type. These interactions gain the importance when the compounds are illuminated within higher energy transitions (*vide infra*). In order to investigate closer the I₃⁻ – organic interactions the Hirshfeld surface analysis has been used. Hirshfeld surfaces allows to recognize the important contact area and the red spots represents the intersections within the vdW radii. The fingerprint plots and Hirshfeld surfaces (Figure 8a, b, c) have been used to compare intermolecular interactions within crystal structures. As it was mentioned above, a hydrogen bond has been found in the structure of (C₆H₅CH₂)₃NH⁺I₃⁻·C₆H₅CH₃. This bond is well presented at Figure 8b by the relatively large red dot on the Hirshfeld surface and the characteristic feature in the fingerprint plot (red ellipsoid, Figure 8b). Similar, although much weaker interaction was found in the structure of [(C₆H₅CH₂)₃NO]₂H⁺I₃⁻, whereas the structure of [(C₆H₅)₃AsO]₂H⁺I₃⁻ lacks any strong C–H...I interactions. All fingerprint plots are presented in the Supplementary information (Figures S8–S10) Although these interactions exist in the two of three studied structures they do not influence

strongly the electronic spectra but can be source (among others) of subtle shifts of the respective bands. Hydrogen bonds, depending on their nature, are known to cause either bathochromic or hypsochromic shifts in the electronic spectra, however in some cases they exert no visible spectral effects.^[30] Stronger influence of the C–H...I type interaction has been shown in previous studied case on tin iodide complexes, in which interactions between iodide ligands and aromatic moieties were responsible for semiconducting properties.^[14]

Optical band gaps for studied materials were determined using the Tauc plots.^[31] The diffuse reflectance spectra were converted using Kubelka-Munk function.^[32] By plotting the $(F_{KM} * E)^n$ function versus energy (where F_{KM} is Kubelka-Munk function, E is energy) the optical band gap can be obtained, if an appropriate exponent is taken. In a typical inorganic semiconductors $n=1/2$ for indirect and $n=2$ for direct transitions, but for organic, molecular and amorphous semiconductors usually $n=1$.^[33] With the assumption of $n=1$ the optical band gaps of studied samples were determined as follows: $[(C_6H_5)_3AsO]_2HI_3 = 1.87$ eV, $[(C_6H_5CH_2)_3NO]_2HI_3 = 1.89$ eV, $(C_6H_5CH_2)_3NHI_3 \cdot C_6H_5CH_3 = 1.78$ eV. Described method and fitting parameters are presented in Figure S5 in the Supplementary Information. These values are comparable with other iodide-containing semiconductors, like lead halide perovskites^[34] and organotin complexes.^[14]

2.4 Photocurrents

The working electrodes for all three compounds were prepared by drop-casting the solutions (in organic solvents) of particular triiodide salts on the transparent indium tin oxide coated poly (terephthalate) foil. Upon pulsed illumination, in the closed three electrode system, the thin films of examined salts produce photocurrents in a broad spectral range. The ability to generate current upon illumination with the appropriate photon energy is a characteristic feature of semiconductors. Examined triiodide salts are insoluble in water, which allows to measure the photocurrents as a function of the incident photon energy and the applied potential in the aqueous solution of different electrolytes. Each compound was measured under four different conditions: (i) in deoxygenated water solution of 0.1 M KNO_3 , (ii) in solution of 0.1 M KNO_3 and dissolved oxygen, (iii) deoxygenated solution containing 0.1 M KI and 0.01 M I_2 , and (iv) solution containing 0.1 M KI and 0.01 M I_2 and dissolved oxygen (Figures 10, S6, S7). This approach allows to validate the mechanism of generated photocurrents. As triiodide anion itself is electrochemically active species, the potential range applied during these measurements has been adjusted to prevent triiodide salts to undergo electrochemical reactions.

As mentioned above, the valence and the lowest levels of the conduction band consist of the p orbitals of the triiodide anions. It is reflected in the absorption spectra and the band structures: relatively small amplitude of the photocurrents in the 500–700 nm range and shoulders on absorption bands at 420–500 nm originate from triiodide – triiodide interactions.

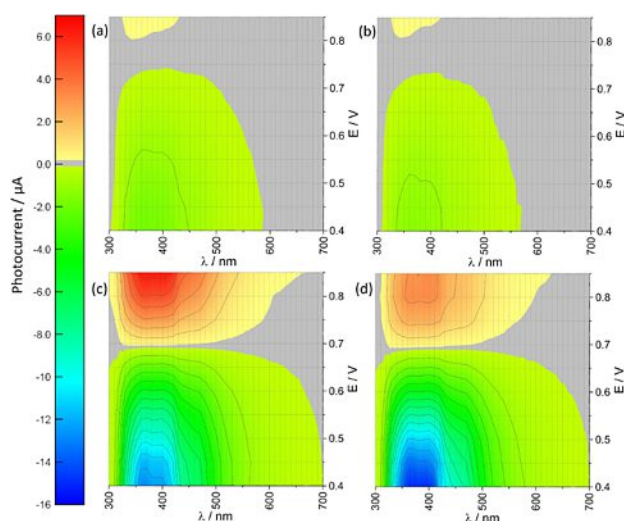


Figure 10. The photocurrent amplitude of $[(C_6H_5)_3AsO]_2HI_3$ as a function of wavelength of incident light and the photoelectrode potential in deoxygenated electrolyte containing 0.1 M KNO_3 (a), oxygenated electrolyte containing 0.1 M KNO_3 (b), deoxygenated electrolyte containing 0.1 M KI and 0.01 M I_2 (c) and oxygenated electrolyte containing 0.1 M KI and 0.01 M I_2 (d). Contour lines are distributed every 1 μA .

What is important, the small amplitude of photocurrent at 500–700 nm is the consequence of low dispersion of electronic bands originating from iodine atoms (Figures 5, S1, S3). In the range of 300–420 nm compounds exhibit stronger absorption and higher photocurrents amplitude (Figures 10, S6, S7) as a consequence of excitation to higher conduction bands. These bands originate from the organic fragments of molecules and exhibit more dispersive character (cf. Figures 5, S1, S3). In all three I_3^- salts the photoelectrochemical photocurrent switching effect (PEPS)^[35] appears around 0.75 V vs. AgCl/Ag. This effect is not associated with the presence of any redox couple in the electrolyte. It appears in both iodine free electrolyte and with I_2 and KI in solution, where the potential of oxygen reduction (2.1 V vs AgCl/Ag) is much lower than 0.75 V. Therefore, the PEPS effect is associated with photoelectrochemical processes that occur in the semiconductors themselves. Surprisingly, the switching potential is closer to the redox potential of $I_2^{*•}/I^-$ (0.83 V vs AgCl/Ag) than I_3^-/I^- (0.34 V vs AgCl/Ag).^[36] It suggests that the $I_2^{*•}$ ion radical is involved in secondary photophysical processes following the excitation. This means that the regeneration of holes (electron deficiency in the band made of I_3^- orbitals) might undergo the Grotthus-like mechanism.

The main factor that must be taken into account is the regeneration of the I_3^- . Without a proper redox couple all I_3^- anions of the working electrode will photodissociate making the working electrode photoinactive. If the I_3^-/I^- redox couple is not present in the solution (Figures 14, S6, S7 a, b), the generated photocurrents are of a much lower intensity. There is no striking influence of dissolved oxygen, which is an alternative electron acceptor (Figures 14, S6, S7 b, d). The redox potential of the redox couple I_3^-/I^- is higher than the potential of oxygen reduction, which is the reason of the efficient photocurrent generation. Small photocurrent amplitude that

appear in the presence of iodide – free electrolyte result from the presence of triiodide ions in the crystal structure of the electrode material. These anions are consumed during the experiment, what leads to a partial bleaching of the electrode as a consequence of photodissociation of I_3^- . When triiodide/iodide redox system is present in the solution, degradation of the electrode is not observed. Similar photocurrent pattern is observed for all three organic triiodide salts due to structural similarities – I_3^- surrounded by the phenyl rings. The spectral range of generated current is consistent with the solid state absorption spectra. $[(C_6H_5)_3AsO]_2HI_3$ and $(C_6H_5CH_2)_3NH_3 \cdot C_6H_5CH_3$ are more soluble than $[(C_6H_5CH_2)_3NO]_2HI_3$ and working electrodes prepared with them show a more compact surface. The working electrode made of $[(C_6H_5CH_2)_3NO]_2HI_3$ generates definitely smaller photocurrents (around $0.5 \mu A$ anodic and $-0.8 \mu A$ cathodic photocurrents) and presents an inhomogeneous surface due to instant crystal aggregates formation at the surface of ITO. It might result from the lack of strong π interactions in the crystal structure of this material, which appear in other two materials (Figure S7 in the Supplementary Information).

2.5 Electrical Properties

Mott-Schottky measurements allow to determine the potential of the conduction band minimum and the type of semiconductors, whereas the measurement of the work function informs about the Fermi level position. These measurements are, however, not fully compatible, as electrochemical impedance spectroscopy is performed for samples contacted with the electrolyte, whereas the contact potentials are measured in air (or under vacuum) in a contactless fashion. The flat-band potential (E_{FB}) value was determined from the Mott-Schottky plot presented in Figure 11. The flat band potential is a fundamental factor that gives an information that allows estimation of the conduction band edge potential at the surface of an n -type semiconductor. The impedance spectra were fitted using a basic equivalent circuit composed of a resistor (R) and a constant phase element (CPE) in series. Standard capacitance was replaced with CPE to eliminate any influence of non-homogeneity of the surface (differences in composition, stoichiometry and morphology, presence of defects, accompanying adsorption processes) on determined locations of E_{FB} . The impedance of the CPE is expressed by Equation (13).

$$Z_{CPE} = \frac{1}{Q(j\omega)^\alpha} \quad (13)$$

where Q stands for charge, j is the imaginary unit, ω depicts the angular frequency and α is a constant ($0 < \alpha < 1$, for capacitor $\alpha = 1$). The general relation between electrode capacitance (C) and applied voltage value (E) for n - and p -type semiconductors is described by the following form of the Mott-Schottky Equation (14):

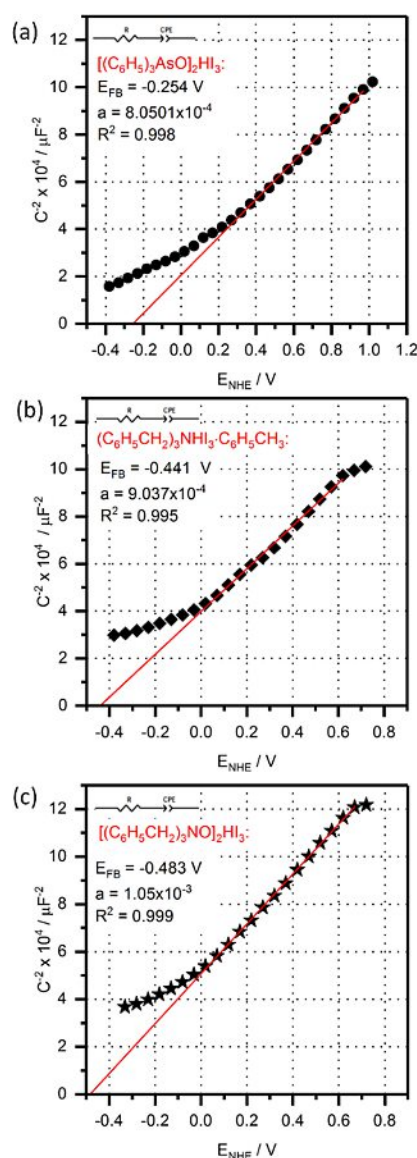


Figure 11. Mott-Schottky plot and estimated flat band potentials of $[(C_6H_5)_3AsO]_2H^+I_3^-$ (a), $(C_6H_5CH_2)_3NH^+I_3^- \cdot C_6H_5CH_3$ (b), $[(C_6H_5CH_2)_3NO]_2H^+I_3^-$ (c).

$$\frac{1}{C^2} = \frac{2}{\epsilon \epsilon_0 A^2 q N_q} \left(-E + E_{FB} + \frac{k_B T}{q} \right) \quad (14)$$

where ϵ is the dielectric constant of layer, ϵ_0 is the vacuum permittivity, A is the electrode surface area, q is the elementary charge ($-e$ for electron, $+e$ for holes), N_q is the doping density which represents the acceptor N_a or the donor N_d density for p - and n -type semiconductors, respectively, e is the electron charge, k_B is Boltzmann's constant, T stands for the absolute temperature, and $\frac{k_B T}{q}$ is a temperature dependent correction term amounting 25 mV at room temperature. Mott-Schottky dependences presented in Figure 11 indicate that all analyzed materials are n -type semiconductors. In each case the estimated value of flat band potential is negative characterized by values of -0.254 V, -0.483 V and -0.441 V vs NHE for $[(C_6H_5)_3AsO]_2HI_3$, $[(C_6H_5CH_2)_3NO]_2HI_3$ and $(C_6H_5CH_2)_3NH_3 \cdot C_6H_5CH_3$, respectively.

The slopes of Mott-Schottky relations ($a = \frac{2}{\epsilon\epsilon_0 A^2 q N_d}$) indicate that analyzed materials possess similar charge carrier densities.

The work function values were calculated from the contact potential measurements using an ambient Kelvin probe technique. The contact potential was measured with respect to stainless steel electrode and the absolute work function values were obtained using a gold reference ($WF_{Au} = 5.100$ eV) as follows [Eq. (15) and (16)]:

$$WF_{\text{steel}} = WF_{\text{Au}} - CPD_{\text{steel/Au}} \quad (15)$$

$$WF_{\text{sample}} = WF_{\text{steel}} - CPD_{\text{steel/sample}} \quad (16)$$

Obtained work function values and corresponding Fermi level potentials (electrochemical potential corresponding to the work function, referred to normal hydrogen electrode) are collated in Table 4.

Table 4. Collective physical information obtained from electrical and optical measurements.			
	$[(C_6H_5)_3AsO]_2HI_3$	$(C_6H_5CH_2)_3NHI_3 \cdot C_6H_5CH_3$	$[(C_6H_5CH_2)_3NO]_2HI_3$
WF [eV] ^[a]	4.706	4.799	4.740
E_F [V] ^[b]	0.306	0.399	0.340
E_{fb} [V] ^[c]	-0.254	-0.441	-0.483
E_g [eV] ^[d]	1.87	1.78	1.89
ρ [Ωm] ^[e]	3.93×10^4	2.08×10^3	1.64×10^2

* referenced to NHE, [a] work function, [b] Fermi level potential, [c] flat band potential, [d] optical band gap, [e] specific resistivity

A four-point probe has been used to determine the sheet resistance of thin layer of the studied materials. The sheet resistance were $130 \text{ G}\Omega/\square$, $7.81 \text{ G}\Omega/\square$ and $51.9 \text{ G}\Omega/\square$ for $[(C_6H_5)_3AsO]_2HI_3$, $[(C_6H_5CH_2)_3NO]_2HI_3$ and $(C_6H_5CH_2)_3NHI_3 \cdot C_6H_5CH_3$ with thicknesses of measured layers: 302, 21 and 40 nm, respectively. These values correspond to resistivities of 3.93×10^4 , 1.64×10^2 and $2.08 \times 10^3 \text{ }\Omega m$ at room temperature in the dark conditions. Those high resistivities originate from grain boundaries and weak intermolecular interactions within the lattice, which is also reflected in narrow distributions of DOS in the highest part of the valence band and the lowest part of the conduction band.

The collective diagram (Figure 12) presents the anodic and cathodic photocurrents and the role of particular redox mediators. As mentioned above the presence of oxygen in the electrolyte does not induce any significant changes in photocurrent spectra due to a more negative potential of the O_2/O_2^- couple compared to I_3^-/I^- one. Also $H^+, HO^+/H_2O$ redox couple has too positive value to participate in the oxidation counterpart reaction. This results in the low photocurrent values in the aqueous solutions lacking any additional redox mediator. In the electrolyte containing I_2 and KI at least two important redox couples: I_3^-/I^- and I_2^-/I^- should be taken into account. Photocurrent spectra show that both I_3^-/I^- and I_2^-/I^- can be used in the anodic photocurrent generation, while the potential of

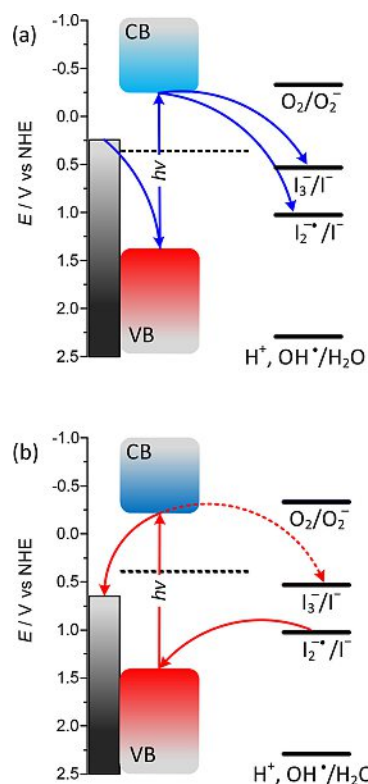


Figure 12. Mechanism of cathodic (a) and anodic (b) photocurrent generation. The black solid lines represent potential levels of redox-active moieties present in the electrolyte. Black dotted lines show the position of the Fermi level in the band gap. CB and VB stand for conduction and valence band respectively. The dark rectangles represent the potential of the ITO electrode. Blue and red arrows represent processes involving electron transfer during anodic and cathodic photocurrent generation respectively (i. e., excitation across the band gap, oxidation and reduction of the redox species, the exchange of electron between ITO electrode and triiodide salt). The simplified diagram is based on experimentally obtained data (Mott-Schottky measurements, the optical band gap and Fermi level from Kelvin probe measurement).

switching to the cathodic photocurrent, $0.7\text{--}0.65$ V vs. NHE, suggests the involvement of I_2^-/I^- ($E_0 = +1.03$ V).^[36]

3. Conclusions

The three studied triiodide salts appear to be the very first examples of purely ionic compounds with some semiconductor-like properties. There are numerous compounds which appear ionic (or are based on ionic scaffolds), but their electric properties result from the π -electron overlap of aromatic moieties. These materials, usually referred to as 'radical salts', possess a semiconducting, metallic or superconducting character. Materials described in this paper are classical, easily soluble ionic compounds with a weak anion-anion, cation-cation and cation-anion electronic coupling. Their synthesis is extremely simple, they are solution processed and are air and water resistant. They crystallize as highly pure samples, with a low level of an n -type doping, which is substantiated by the Fermi level potential close to the center of the band gap. Their optical properties (absorption range) is comparable with lead halide

perovskites, however, their absorptivity appears to be much lower. All of them show a significant photoelectrochemical photocurrent switching effect and two of them, $[(C_6H_5)_3AsO]_2HI_3$ and especially $(C_6H_5CH_2)_3NH_3 \cdot C_6H_5CH_3$, generate high intensity photocurrents, which makes them interesting potential candidates for novel optoelectronic devices.

Experimental Section

Synthetic Procedures

Caution! These syntheses are potentially hazardous due to toxicity of triphenylarsine oxide and toxic, irritating and lachrymatory properties of iodine. Appropriate means of personal protection should be applied. All wastes should be properly disposed due to high toxicity towards aquatic organisms.

$[(C_6H_5)_3AsO]_2HI_3$: Triphenylarsine oxide (2 mmol), potassium iodide (1 mmol) and iodine (1 mmol) were dissolved in acetonitrile. Hydrochloric acid (1 mmol diluted with a few ml of acetonitrile) was added. The brown solution was condensed to 1/5 of the volume, then the white precipitate was filtered off and discarded. The brown filtrate was evaporated and the dark brown solid was recrystallized from the mixture of ethyl acetate and dichloromethane (1:1) twice. The final product is black, crystalline solid in the form of cubes.

$[(C_6H_5CH_2)_3NO]_2H^+I_3^-$: Tribenzylamine oxide (2 mmol), potassium iodide (1 mmol) and iodine (1 mmol) were dissolved in acetonitrile. Hydrochloric acid (1 mmol diluted with a few ml of acetonitrile) was added. The brown solution was condensed to 1/5 of the volume, then the white precipitate was filtered off and discarded. The brown filtrate was evaporated and the dark brown solid was recrystallized from the mixture of toluene and chloroform (1:1) twice. The final product is brown, shiny crystalline solid in the form of needle.

$(C_6H_5CH_2)_3NH_3 \cdot C_6H_5CH_3$: Tribenzylamine (1 mmol), potassium iodide (1 mmol) and iodine (1 mmol) were dissolved in acetonitrile. Hydrochloric acid (1 mmol diluted with a few ml of acetonitrile) was added. The brown solution was condensed to 1/5 of the volume, then the white precipitate was filtered off and discarded. The brown filtrate was evaporated and the dark brown solid was recrystallized from toluene (twice). The final product is brown crystalline solid.

Prepared compounds were stable over a year when stored in a closed container in the dark conditions

X-Ray Crystallography. Data collection and reduction: Diffraction data for single crystal were collected at 120(2) K using the Oxford Diffraction SuperNova four circle diffractometer, equipped with the Mo (0.71069 Å) $K\alpha$ radiation source, graphite monochromator and Oxford CryoJet system for measurements at low temperature. Cell refinement and data reduction were performed using the CrysAlis PRO.^[37] The phase problem was solved by direct methods using SIR-97.^[38] All non-hydrogen atoms were refined anisotropically using weighted full-matrix least-squares on F^2 . Refinement and further calculations were carried out using SHELXL-97.^[39] All hydrogen atoms bound to carbon atoms were positioned with an idealized geometry and refined using a riding model with Uiso(H) fixed at 1.2 or 1.5 (methyl groups) Ueq of C. Hydrogen attached to N or O atoms were found on the difference Fourier maps and refined with no restraints on the isotropic displacement parameter. Used software is a component of the WINGX.^[40] Graphics were

created by MERCURY.^[41] Crystallographic data for structures presented in this paper have been deposited with the Cambridge Crystallographic Data Centre as supplementary publication nos. CCDC 1838550 (I), CCDC 1838548 (II), CCDC 1838551 (III). Copies of the data can be obtained, free of charge, on application to CCDC, 12 Union Road, Cambridge CB2 1EZ, UK, (fax: +44-(0)1223-336033 or e-mail: deposit@ccdc.cam.ac.uk).

Spectroscopy. Diffuse reflectance spectra were recorded on Lambda 950 (Perkin Elmer, USA) spectrophotometer. Absorption spectra were recorded on Agilent 8453 spectrophotometer in 1 cm quartz cells.

Computational Details. To study the electronic structure of the crystalline materials we employed the periodic density functional theory (DFT), as implemented in the VASP package.^[42] We used the generalized gradient approximation (GGA) of Perdew-Burke-Ernzerhof (PBE)^[43] for the exchange-correlation energy. To describe core-valence interaction we used a Bloch's projector augmented wave (PAW) method^[44] and a plane-wave basis with a kinetic energy cutoff of 500 eV. H 1 s^1 , C 2 $s^2 2p^2$, N 2 $s^2 2p^3$, O 2 $s^2 2p^4$, As 4 $s^2 4p^3$, I 5 $s^2 5p^5$ valence electron potentials were employed. The long-range van der Waals interaction was accounted by the DFT-D3 method of Grimme.^[45] We also considered a spin-orbit coupling (SOC) due to the presence of heavy elements. We found an improvement in the band gap energies that were overestimated by GGA, therefore discussion was based on PBE-D3+SOC results. The comparison of the electronic structures obtained from GGA and GGA+SOC is presented in the Supplementary Information.

The geometry optimization of atomic position within fixed experimental lattice parameters was carried out with the Γ -centered k -point sampling of the reciprocal space. For structural relaxation and for the electronic properties study, converged meshes of $4 \times 4 \times 4$, corresponding to 36 irreducible k -points for $[(C_6H_5)_3AsO]_2HI_3$ and 64 for $(C_6H_5CH_2)_3NH_3 \cdot C_6H_5CH_3$ and $[(C_6H_5CH_2)_3NO]_2HI_3$, were sufficient. A conjugate-gradient algorithm was used for ionic relaxation with all ions relaxed until the forces on the ions were smaller than 0.02 eV/Å and the total energy change in the electronic self-consistent loop was smaller than 10^{-4} eV. In addition to the ionic relaxation with the PBE-D3 method, we also tested applicability of another GGA functionals as well as hybrid functionals within plane wave formalism as well as local basis set scheme for cell shape optimization which can be found in the Supplementary Information.

Tetrahedron method with Blöchl corrections was used, giving accurate total energy and the density of states (DOS). Orbital and site projected wavefunction character of each band was calculated with the PAW projection scheme implemented in VASP. The PAW projection scheme did not include interstitial contributions to the total DOS, therefore the sum of atomic projected DOSs does not reproduce the total DOS. The band dispersion relations were calculated with the Methfessel-Paxton approach for Fermi level smearing, with $\sigma=0.1$ eV and with 10 k -points between high-symmetry Brillouin zone points. VESTA software^[46] was used for visualization of charge density and electron localization function (ELF) plots. Molecular Hirshfeld surfaces calculations were performed using the CRYSTALEXPLORER17 program.^[47]

Photoelectrochemical Measurements. Working electrode was made of an ITO substrate covered with the studied salt. AgCl/Ag and platinum wire were used as reference and auxiliary electrodes, respectively. Used electrolytes contained 0.1 M KNO_3 or 0.1 M KI and 0.01 M I_2 and were purged with argon to remove dissolved oxygen when necessary. To minimise the influence of the material thickness the working electrodes were illuminated through ITO foil. A high pressure 150 W xenon lamp with computer controlled

shutter and monochromator (Instytut Fotonowy, Poland) was used as the source of light. Electrochemical measurements were performed on SP-300 potentiostat (Biologic, France).

Kelvin Probe Measurements. Work function (WF) and Fermi level (FL) were measured with Kelvin probe (KP1, KP Technology, UK). Samples before measurements were deposited on the ITO foil.

Electrochemistry. Electrodes for the Mott-Schottky analysis were prepared by spin coating of the particular triiodide salt (dissolved in acetone) on the surface of ITO. Measurements were performed in a three-electrode setup where ITO covered with triiodide salt was the working electrode, Ag/AgCl (3.5 M KCl) served as a reference electrode and Pt wire was used as a counter electrode. 0.1 M KNO₃ was used as a supporting electrolyte. Electroactive surface area (EAS) of particular samples was 0.0525 cm². The electrode was conditioned at corresponding potential for 5 s before each measurement. Several potentials spectra were recorded starting from 1 MHz to 0.1 Hz (with 10 points per decade) for potential amplitude of 0.02 V in the dark with the potential step of 50 mV. EIS analysis was performed in 0.1 mol/dm³ KNO₃. Measurements were performed with the use of Biologic SP-300 potentiostat.

Resistivity Measurements. Resistivity measurements at room temperature were performed with Keithley 4200 SCS. Thin layers were prepared by spin coating of dissolved compound on a glass substrate and measured with the four-point probe method. Film thicknesses were measured with Bruker's DektakXT Stylus Profiler.

Acknowledgements

This work has received funding from the European Union's Horizon 2020 research and innovation programme under grant agreement No. 664786. Authors acknowledge the support of Polish Ministry of Science and Higher Education (Grant Ideas Plus No. IDP2012000362 and statutory funds), National Science Centre (Poland) within the MAESTRO project (grant agreement No. UMO-2015/18/A/ST4/00058), PRELUDIUM (grant agreement No. UMO-2015/19/N/ST5/00533). The X-ray diffraction experiments were carried out with the equipment purchased thanks to the financial support of the European Regional Development Fund in the framework of the Polish Innovation Economy Operational Program (contract no. POIG.02.01.00-12-023/08). We gratefully acknowledge Poland's high-performance computing infrastructure PL-Grid and CYFRONET AGH for providing computer facilities and support within computational grants IODIDE and GRAPHENE3.

Conflict of Interest

The authors declare no conflict of interest.

Keywords: I₃⁻ spectroscopy • molecular electronics • photocurrents • semiconductors • triiodide organic salts

[1] P. H. Svensson, L. Kloo, *Chem. Rev.* **2003**, *103*, 1649–1684.

[2] a) W. C. J. , M. C. A. , G. E. A. , *ChemElectroChem* **2016**, *3*, 1827–1836; b) O. O. Ogunsolu, J. C. Wang, K. Hanson, *Inorg. Chem.* **2017**, *56*, 11168–11175; c) A. Midya, Z. Xie, J. X. Yang, Z. K. Chen, D. J. Blackwood, J.

- Wang, S. Adams, K. P. Loh, *Chem. Commun. (Camb.)* **2010**, *46*, 2091–2093; d) Y. Huang, X. Zhou, S. Fang, Y. Lin, *RSC Adv.* **2012**, *2*, 5550–5553; e) G. Boschloo, E. A. Gibson, A. Hagfeldt, *J. Phys. Chem. Lett.* **2011**, *2*, 3016–3020; f) B. H. Farnum, W. M. Ward, G. J. Meyer, *Inorg. Chem.* **2013**, *52*, 840–847; g) T. Jayaraman, S. A. Raja, M. Jagannathan, M. Thandavarayan, *ChemElectroChem* **2015**, *2*, 928–945; h) J. W. Ondersma, T. W. Hamann, *Coord. Chem. Rev.* **2013**, *257*, 1533–1543; i) G. Boschloo, A. Hagfeldt, *Acc. Chem. Res.* **2009**, *42*, 1819–1826; j) K. Kusama, *J. Photochem. Photobiol. A* **2018**, *365*, 110–118; k) S. Huang, J. Zai, D. Ma, Z. Hu, Q. He, M. Wu, D. Chen, Z. Chen, X. Qian, *Electrochim. Acta* **2017**, *241*, 89–97.
- [3] a) R. Thapa, N. Park, *J. Phys. Chem. Lett.* **2012**, *3*, 3065–3069; b) Z. Fei, F. D. Bobbink, E. Păunescu, R. Scopelliti, P. J. Dyson, *Inorg. Chem.* **2015**, *54*, 10504–10512; c) W. Zhang, C. Willa, J.-K. Sun, R. Guterman, A. Taubert, J. Yuan, *Polymer* **2017**, *124*, 246–251; d) P. Wang, S. M. Zakeeruddin, R. Humphry-Baker, M. Grätzel, *Chem. Mater.* **2004**, *16*, 2694–2696; e) M. Bidikoudi, T. Stergiopoulos, V. Likodimos, G. E. Romanos, M. Francisco, B. Iliev, G. Adamova, T. J. S. Schubert, P. Falaras, *J. Mater. Chem. A* **2013**, *1*, 10474–10486.
- [4] J. M. Gardner, M. Abrahamsson, B. H. Farnum, G. J. Meyer, *J. Am. Chem. Soc.* **2009**, *131*, 16206–16214.
- [5] H. Zachová, S. Man, J. Taraba, M. Potáček, *Tetrahedron* **2009**, *65*, 792–797.
- [6] a) S. A. Patil, D. V. Shinde, I. Lim, K. Cho, S. S. Bhande, R. S. Mane, N. K. Shrestha, J. K. Lee, T. H. Yoon, S.-H. Han, *J. Mater. Chem. A* **2015**, *3*, 7900–7909; b) H. Yuan, J. Liu, H. Li, Y. Li, X. Liu, D. Shi, Q. Wu, Q. Jiao, *J. Mater. Chem. A* **2018**, *6*, 5603–5607; c) W. Yang, X. Xu, L. Hou, X. Ma, F. Yang, Y. Wang, Y. Li, *J. Mater. Chem. A* **2017**, *5*, 5952–5960.
- [7] a) W. Zhao, T. Lin, S. Sun, H. Bi, P. Chen, D. Wan, F. Huang, *J. Mater. Chem. A* **2013**, *1*, 194–198; b) P. Seong-Hyo, K. H. Jin, J. Joomi, C. Yongsu, C. Jeong-Ju, L. Hochun, *ChemElectroChem* **2016**, *3*, 1915–1921; c) G.-M. Weng, G. C. Zhejun Li, Y. Zhou, Y.-C. Lu, *Energy Environ. Sci.* **2017**, *10*, 735–741.
- [8] Y. X. Ren, T. S. Zhao, M. Liu, Y. K. Zeng, H. R. Jiang, *J. Power Sources* **2017**, *361*, 203–210.
- [9] X. Gao, L. Zu, X. Cai, C. Li, H. Lian, Y. Liu, X. Wang, X. Cui, *Nanomaterials* **2018**, *8*, 335.
- [10] a) C. D. Bryan, A. W. Cordes, N. A. George, R. C. Haddon, C. D. Mackinnon, R. T. Oakley, T. T. M. Palstra, A. S. Perel, *Chem. Mater.* **1996**, *8*, 762–768; b) P. Lunkenheimer, B. Hartmann, M. Lang, J. Müller, D. Schweitzer, S. Krohns, A. Loidl, *Phys. Rev. B* **2015**, *91*, 245132; c) T. Kawamoto, T. Mori, T. Konoike, K. Enomoto, Y. Rashima, S. Uji, H. Kitagawa, K. Takimiya, T. Otsubo, *Phys. Rev. B* **2006**, *73*, 094513; d) C. D. Bryan, A. W. Cordes, R. C. Haddon, R. G. Hicks, R. T. Oakley, T. T. M. Palstra, A. S. Perel, S. R. Scott, *Chem. Mater.* **1994**, *6*, 508–515; e) V. Lebedev, E. Laukhina, E. Moreno-Calvo, C. Rovira, V. Laukhin, I. Ivanov, S. M. Dolotov, V. F. Traven, V. V. Chernyshev, J. Veciana, *J. Mater. Chem. C* **2014**, *2*, 139–146; f) S. Rabaça, S. Oliveira, I. C. Santos, V. Gama, D. Belo, E. B. Lopes, E. Canadell, M. Almeida, *Inorg. Chem.* **2016**, *55*, 10343–10350.
- [11] a) P. H. Ling, P. Martin, *ChemElectroChem* **2015**, *2*, 190–199; b) J. Morgado, I. C. Santos, R. T. Henriques, M. Fourmigue, P. Matias, L. F. Veiros, M. J. Calhorda, M. T. Duarte, L. Alcacer, M. Almeida, *Chem. Mater.* **1994**, *6*, 2309–2316; c) B. C. Sherman, B. K. Schmitz, W. B. Euler, *Chem. Mater.* **1995**, *7*, 806–812; d) W. B. Euler, *Chem. Mater.* **1996**, *8*, 554–557; e) M. Forsyth, D. F. Shriver, M. A. Ratner, D. C. DeGroot, C. R. Kannewurf, *Chem. Mater.* **1993**, *5*, 1073–1077.
- [12] J. Janczak, R. Kubiak, *Inorg. Chem.* **1999**, *38*, 2429–2433.
- [13] H. Kobayashi, H. B. Cui, A. Kobayashi, *Chem. Rev.* **2004**, *104*, 5265–5288.
- [14] E. Wlazlak, W. Macyk, W. Nitek, K. Szacilowski, *Inorg. Chem.* **2016**, *55*, 5935–5945.
- [15] L. E. Topol, *Inorg. Chem.* **1971**, *10*, 736–740.
- [16] a) N. Agmon, *Chem. Phys. Lett.* **1995**, *244*, 456–462; b) V. K. Thorsmølle, G. Rothenberger, D. Topgaard, J. C. Brauer, D. B. Kuang, S. M. Zakeeruddin, B. Lindman, M. Grätzel, J. E. Moser, *ChemPhysChem* **2011**, *12*, 145–149.
- [17] a) H. Stegemann, A. Rohde, A. Reiche, A. Schnitke, H. Füllbier, *Electrochim. Acta* **1992**, *37*, 379–383; b) M. Zistler, P. Wachter, P. Wasserscheid, D. Gerhard, A. Hinsch, R. Sastrawan, H. J. Gores, *Electrochim. Acta* **2006**, *52*, 161–169.
- [18] M. M. Lerner, L. J. Lyons, J. S. Tonge, D. F. Shriver, *Chem. Mater.* **1989**, *1*, 601–606.
- [19] R. Kawano, M. Watanabe, *Chem. Commun.* **2005**, 2107–2109.
- [20] a) C. L. Bentley, A. M. Bond, A. F. Hollenkamp, P. J. Mahon, J. Zhang, *Anal. Chem.* **2016**, *88*, 1915–1921; b) J. G. Rowley, B. H. Farnum, S. Ardo, G. J. Meyer, *J. Phys. Chem. Lett.* **2010**, *1*, 3132–3140.

- [21] R. Xian, G. Corthey, D. M. Rogers, C. A. Morrison, V. I. Prokhorenko, S. A. Hayes, R. J. D. Miller, *Nat. Chem.* **2017**, *9*, 516–522.
- [22] a) R. C. Teitelbaum, T. J. Marks, C. K. Johnson, *J. Am. Chem. Soc.* **1980**, *102*, 2986–2989; b) H. Veith, F. Gross, C. P. Heidmann, K. Andres, H. Fuchs, E. Amberger, *Physica B + C* **1986**, *143*, 360–362; c) L. Martin, S. Yang, A. C. Brooks, P. N. Horton, L. Male, O. Moulfi, L. Harmand, P. Day, W. Clegg, R. W. Harrington, J. D. Wallis, *CrystEngComm* **2015**, *17*, 7354–7362.
- [23] T. Kawamoto, T. Mori, T. Konoike, K. Enomoto, T. Terashima, S. Uji, H. Kitagawa, K. Takimiya, T. Otsubo, *Phys. Rev. B* **2006**, *73*, 094513.
- [24] a) G. J. Reiss, P. B. Leske, *Acta Crystallogr. Sect. A* **2013**, *69*, o1060–o1061; b) A. N. Chernyshev, D. Morozov, J. Mutanen, V. Y. Kukushkin, G. Groenhof, M. Haukka, *J. Mater. Chem. C* **2014**, *2*, 8285–8294; c) M. S. Chernov'yants, Z. A. Starikova, A. O. Karginova, T. S. Kolesnikova, A. Y. Tereznikov, *Spectrochim. Acta Part A* **2013**, *115*, 861–865; d) J. He, P. Cao, C. Wu, J. Huang, J. Huang, Y. He, L. Yu, M. Zeller, A. D. Hunter, Z. Xu, *Inorg. Chem.* **2015**, *54*, 6087–6089; e) A. Y. Rogachev, R. Hoffmann, *Inorg. Chem.* **2013**, *52*, 7161–7171.
- [25] B. Beagley, O. El-Sayrafi, G. A. Gott, D. G. Kelly, C. A. McAuliffe, A. G. Mackie, P. P. MacRory, R. G. Pritchard, *J. Chem. Soc. Dalton Trans.* **1988**, 1095–1097.
- [26] Y. Wang, Y. Xue, X. Wang, Z. Cui, L. Wang, *J. Mol. Struct.* **2014**, *1074*, 231–239.
- [27] B. Silvi, A. Savin, *Nature* **1994**, *371*, 683–686.
- [28] M. Mizuno, J. Tanaka, I. Harada, *J. Phys. Chem.* **1981**, *85*, 1789–1794.
- [29] S. Lee, B. Chen, D. C. Fredrickson, F. J. DiSalvo, E. Lobkovsky, J. A. Adams, *Chem. Mater.* **2003**, *15*, 1420–1433.
- [30] J. Joseph, E. D. Jemmis, *J. Am. Chem. Soc.* **2007**, *129*, 4620–4632.
- [31] J. Tauc, R. Grigorovici, A. Vancu, *Phys. Status Solidi B* **1966**, *15*, 627–637.
- [32] P. Kubelka, F. Munk, *Z. Tech. Phys.* **1931**, *12*, 593–601.
- [33] J. Singh, *Advances in amorphous semiconductors / Jai Singh and Koichi Shimakawa*, Taylor & Francis, London, **2003**.
- [34] C. C. Stoumpos, M. G. Kanatzidis, *Acc. Chem. Res.* **2015**, *48*, 2791–2802.
- [35] W. Macyk, G. Stochel, K. Szaciłowski, *Chem. Eur. J.* **2007**, *13*, 5676–5687.
- [36] G. Boschloo, A. Hagfeldt, *Acc. Chem. Res.* **2009**, *42*, 1819–1826.
- [37] *Crysalis PRO. Oxford Diffraction Ltd Yarnton, England 2010*.
- [38] A. Altomare, M. C. Burla, M. Camalli, G. L. Cascarano, C. Giacovazzo, A. Guagliardi, A. G. G. Moliterni, G. Polidori, R. Spagna, *J. Appl. Crystallogr.* **1999**, *32*, 115–119.
- [39] G. M. Sheldrick, *Acta Crystallogr.* **2008**, *A64*, 112–122.
- [40] L. J. Farrugia, *J. Appl. Crystallogr.* **1999**, *32*, 837–838.
- [41] C. F. Macrae, P. R. Edgington, P. McCabe, E. Pidcock, G. P. Shields, R. Taylor, M. Towler, J. Van de Streek, *J. Appl. Crystallogr.* **2006**, *39*, 453–457.
- [42] G. Kresse, J. Furthmüller, *Phys. Rev. B* **1996**, *54*, 11169–11186.
- [43] J. P. Perdew, K. Burke, M. Ernzerhof, *Phys. Rev. Lett.* **1996**, *77*, 3865.
- [44] a) P. E. Blöchl, *Phys. Rev. B* **1994**, *50*, 17953–17979; b) G. Kresse, D. Joubert, *Phys. Rev. B* **1999**, *59*, 1758–1775.
- [45] S. Grimme, J. Antony, S. Ehrlich, H. Krieg, *J. Chem. Phys.* **2010**, *132*, 154104.
- [46] K. Momma, F. Izumi, *J. Appl. Crystallogr.* **2011**, *44*, 1272–1276.
- [47] M. J. Turner, J. J. McKinnon, S. K. Wolff, D. J. Grimwood, P. R. Spackman, D. Jayatilaka, M. A. Spackman, *CrystalExplorer17*, University of Western Australia, <http://hirshfeldsurface.net>, **2017**.

Manuscript received: July 18, 2018

Accepted Article published: August 28, 2018

Version of record online: September 11, 2018

Supporting Information

© Copyright Wiley-VCH Verlag GmbH & Co. KGaA, 69451 Weinheim, 2018

Triiodide Organic Salts: Photoelectrochemistry at the Border between Insulators and Semiconductors

Ewelina Właźlak,* Justyna Kalinowska-Tłuścik, Wojciech Nitek, Sylwia Klejna, Krzysztof Mech, Wojciech Macyk, and Konrad Szaciłowski*

Crystallographic information

Table S1. Crystal data and structure refinement results for compounds $[(C_6H_5)_3AsO]_2H^+ I_3^-$, $[(C_7H_7)_3NH]^+ I_3^- \cdot C_7H_8$ and $[(C_7H_7)_3NO]_2H^+ I_3^-$

Empirical moiety formula	$[(C_6H_5)_3AsO]_2H^+ I_3^-$	$2x\{[(C_7H_7)_3NH]^+ I_3^-\} \cdot C_7H_8$	$[(C_7H_7)_3NO]_2H^+ I_3^-$
Formula weight [g/mol]	1026.15	1430.32	988.48
Crystal system	Monoclinic	Triclinic	Triclinic
Space group	C2/c	$P\bar{1}$	$P\bar{1}$
Unit cell dimensions	a = 14.152(5) Å b = 21.269(5) Å c = 12.432(5) Å $\alpha = 90^\circ$ $\beta = 108.810(5)^\circ$ $\gamma = 90^\circ$	a = 9.3485(4) Å b = 12.0173(6) Å c = 13.3054(8) Å $\alpha = 109.236(5)^\circ$ $\beta = 105.395(4)^\circ$ $\gamma = 104.973(4)^\circ$	a = 9.802(5) Å b = 10.030(5) Å c = 11.916(5) Å $\alpha = 75.107(5)^\circ$ $\beta = 65.785(5)^\circ$ $\gamma = 72.287(5)^\circ$
Volume [Å ³]	3542(2)	1458.66(12)	1005.9(8)
Z	4	1	1
D _{calc} [Mg/m ³]	1.924	1.887	1.632
μ [mm ⁻¹]	4.532	3.735	2.366
F(000)	1952	678	484
Crystal size [mm ³]	0.340 x 0.196 x 0.177	0.2 x 0.1 x 0.1	0.505 x 0.304 x 0.141
Θ range	3.041 to 28.703°	2.97 to 28.74°	3.081 to 28.584°
Index ranges	-17 ≤ h ≤ 18, -26 ≤ k ≤ 28, -16 ≤ l ≤ 16	-11 ≤ h ≤ 12, -16 ≤ k ≤ 16, -17 ≤ l ≤ 16	-12 ≤ h ≤ 13, -13 ≤ k ≤ 13, -15 ≤ l ≤ 15
Refl. collected	23984	16995	13756
Independent reflections	4257 [R(int) = 0.0409]	5949 [R(int) = 0.0547]	4716 [R(int) = 0.0330]
Completeness [%] to Θ	99.8	99.8 (Θ 25.2°)	99.8
Absorption correction	Gaussian	Multi-scan	Gaussian
Tmin. and Tmax.	0.387 and 0.561	0.610 and 1.000	0.491 and 0.732
Data/restraints/parameters	4257 / 0 / 198	5949 / 15 / 270	4716 / 0 / 224
GooF on F2	1.068	1.040	1.064
Final R indices [I > 2σ(I)]	R1 = 0.0277, wR2 = 0.0608	R1 = 0.0379, wR2 = 0.0772	R1 = 0.0367, wR2 = 0.0664
R indices (all data)	R1 = 0.0405, wR2 = 0.0688	R1 = 0.0610, wR2 = 0.0928	R1 = 0.0643, wR2 = 0.0818
$\Delta\rho_{max}, \Delta\rho_{min}$ [e·Å ⁻³]	0.573 and -0.641	0.979 and -1.960	0.943 and -1.147

Computational method

To test applicability of different DFT functionals and different DFT approaches we performed cell shape relaxation and ionic relaxation of iodide salts. We use local basis scheme implemented in CRYSTAL14 code¹ and plane-wave formalism as proposed in VASP package.² In the CRYSTAL14 calculations all-

electron Gaussian basis sets (Gaussian type orbitals, GTO) were used. For As, C, H, N and O, we tested Peintinger-Oliveira-Bredow (POB) triple- ζ valence + polarization basis set for solid state systems.³ An effective core pseudopotential basis set was used for I⁴ with valence electrons described as in⁵. We examine generalized gradient approximation (GGA) where exchange correlation functionals were: PW91⁶, PBE⁷, PBEsol⁸ and hybrid functionals: B3LYP⁹ and HSE06¹⁰. The five tolerances setting the accuracy of the Coulomb and exchange series were set to 10^{-7} , 10^{-7} , 10^{-7} , 10^{-14} and SCF convergence on the total energy was set to 10^{-6} Ha for geometry optimization. The Monkhorst-Pack k -point sampling scheme was applied, with 24 irreducible k -points for $[(C_6H_5)_3AsO]_2HI_3$ and 36 k -points for $(C_6H_5CH_2)_3NH_3 \cdot C_6H_5CH_3$ and $[(C_6H_5CH_2)_3NO]_2HI_3$. We present obtained results from all-electron calculations in comparison to plane-wave/pseudopotential basis based calculations. For these, we employ Perdew–Burke–Ernzerhof (PBE)⁷ exchange-correlation functional and Blöchl’s projector augmented wave (PAW) method^{11, 12}. Energy cutoff for valence electron was 500 eV, convergence threshold for forces on the ions 0.02 eV/Å and SCF convergence of the total energy 10^{-4} eV. For structural relaxation converged meshes of Γ -centered k -point sampling $4 \times 4 \times 4$, corresponding to 36 irreducible k -points for $[(C_6H_5)_3AsO]_2HI_3$ and 64 for $(C_6H_5CH_2)_3NH_3 \cdot C_6H_5CH_3$ and $[(C_6H_5CH_2)_3NO]_2HI_3$, were sufficient. Tetrahedron method with Blöchl corrections was used, giving accurate total energy and density of states (DOS). Orbital and site projected wavefunction character of each band is calculated with PAW projection scheme implemented in VASP. The PAW projection scheme does not include interstitial contributions to the total DOS, therefore the sum of atomic projected DOSs does not reproduce the total DOS. The band dispersion relations were calculated with the Methfessel-Paxton approach for Fermi level smearing, with $\sigma = 0.1$ eV and with 10 k -points between high-symmetry Brillouin zone points. The labeled Brillouin zone points for the monoclinic space group $C 2/c$ are: $\Gamma = (-\frac{1}{2}, 0, \frac{1}{2})$, $M = (-\frac{1}{2}, \frac{1}{2}, \frac{1}{2})$, $A = (-\frac{1}{2}, 0, 0)$, $\Gamma = (0, 0, 0)$, $Z = (0, -\frac{1}{2}, \frac{1}{2})$, $V = (0, 0, \frac{1}{2})$ and for the triclinic $P\bar{1}$ space group: $F = (0, \frac{1}{2}, 0)$, $Q = (0, \frac{1}{2}, \frac{1}{2})$, $Y = (0, 0, \frac{1}{2})$.

DFT lattice relaxation

Table S2 presents relaxed lattice constants and calculated band gaps obtained from full relaxation of cell and atomic positions. In general, we were not able to reach sufficient agreement with experimental constants given in Table S2 with all-electron approach with chosen GTO basis sets. The best agreement was achieved for $[(C_6H_5CH_2)_3NO]_2HI_3$ complex with the use of PW91, PBE and B3LYP functionals with the deviation of less than 2%. Scanning through different GGA as well as hybrid functionals, we find no functional dependent trend in prediction of cell constants. The inclusion of long range van der Waals forces¹³ resulted in underestimation of lattice parameters. We find that GGA functionals underestimate band gaps, while hybrid functionals overestimate band gaps. Inclusion of dispersion correction resulted in increased energy band gap in comparison to the functional without correction. Moving to the plane-wave PAW calculations, we note that PBE functional is known to overestimate lattice parameters and band gaps, which is the case here. The addition of D3 dispersion correction¹⁴ improves the fit of the constants to the experimental ones and the best agreement is achieved with deviations of less than 1 % for all investigated complexes. Based on this, for electronic structure calculations we employ PBE-D3-PAW method.

Table S2. Experimental and computed lattice parameters and band gaps for $[(C_6H_5)_3AsO]_2HI_3$, $(C_6H_5CH_2)_3NH_3 \cdot C_6H_5CH_3$ and $[(C_6H_5CH_2)_3NO]_2HI_3$.

$[(C_6H_5)_3AsO]_2HI_3$							
	a [Å]	b [Å]	c [Å]	β [°]	γ [°]	δ [°]	Band gap [eV]
experimental	14.15	21.27	12.43	90.00	108.81	90.00	1.72
PBE-GTO	14.52	20.88	12.12	90.00	109.34	90.00	1.44
B3LYP-GTO	14.76	21.97	11.60	90.00	97.67	90.00	2.55

PBE-PAW	14.43	22.04	12.69	90.00	108.95	90.00	2.15
PBE-D3-PAW	14.13	21.11	12.44	90.00	109.04	90.00	2.14
$(\text{C}_6\text{H}_5\text{CH}_2)_3\text{NH}_3 \cdot \text{C}_6\text{H}_5\text{CH}_3$							
	a [Å]	b [Å]	c [Å]	α [°]	β [°]	γ [°]	Band gap [eV]
experimental	9.35	12.02	13.31	109.24	105.40	104.97	1.63
PBE-GTO	9.89	12.59	13.87	109.89	107.69	108.79	1.33
PBE-D2-GTO	9.17	11.73	12.71	109.04	106.40	106.23	1.38
PBEsol-GTO	9.66	11.77	12.78	109.47	107.74	107.10	1.21
B3LYP-GTO	10.16	12.75	13.98	109.76	107.98	108.66	2.40
HSE06-GTO	9.87	12.49	13.81	109.83	107.94	108.75	2.01
PBE-PAW	9.67	12.41	13.72	109.47	105.02	105.38	2.10
PBE-D3-PAW	9.32	12.04	13.41	109.37	105.52	104.64	2.10
$[(\text{C}_6\text{H}_5\text{CH}_2)_3\text{NO}]_2\text{HI}_3$							
	a [Å]	b [Å]	c [Å]	α [°]	β [°]	γ [°]	Band gap [eV]
experimental	9.80	10.03	11.92	75.11	65.79	72.29	1.75
PW91-GTO	9.85	9.89	11.77	74.11	65.86	70.56	1.57
PBE-GTO	9.86	9.89	11.78	74.03	65.88	70.49	1.57
PBE-D2-GTO	9.44	9.64	11.46	75.84	64.20	70.54	1.74
PBEsol-GTO	9.61	9.64	11.55	73.79	65.77	69.81	1.63
PBEsol-D2-GTO	9.01	9.30	11.08	75.29	63.32	68.79	1.83
B3LYP-GTO	9.98	9.97	11.87	74.17	65.94	70.75	2.76
B3LYP-D2-GTO	9.41	9.54	11.45	73.38	64.97	68.97	2.88
PBE-PAW	10.08	10.16	12.13	75.27	65.25	72.40	2.12
PBE-D3-PAW	9.75	9.98	11.85	75.09	66.03	71.88	2.14

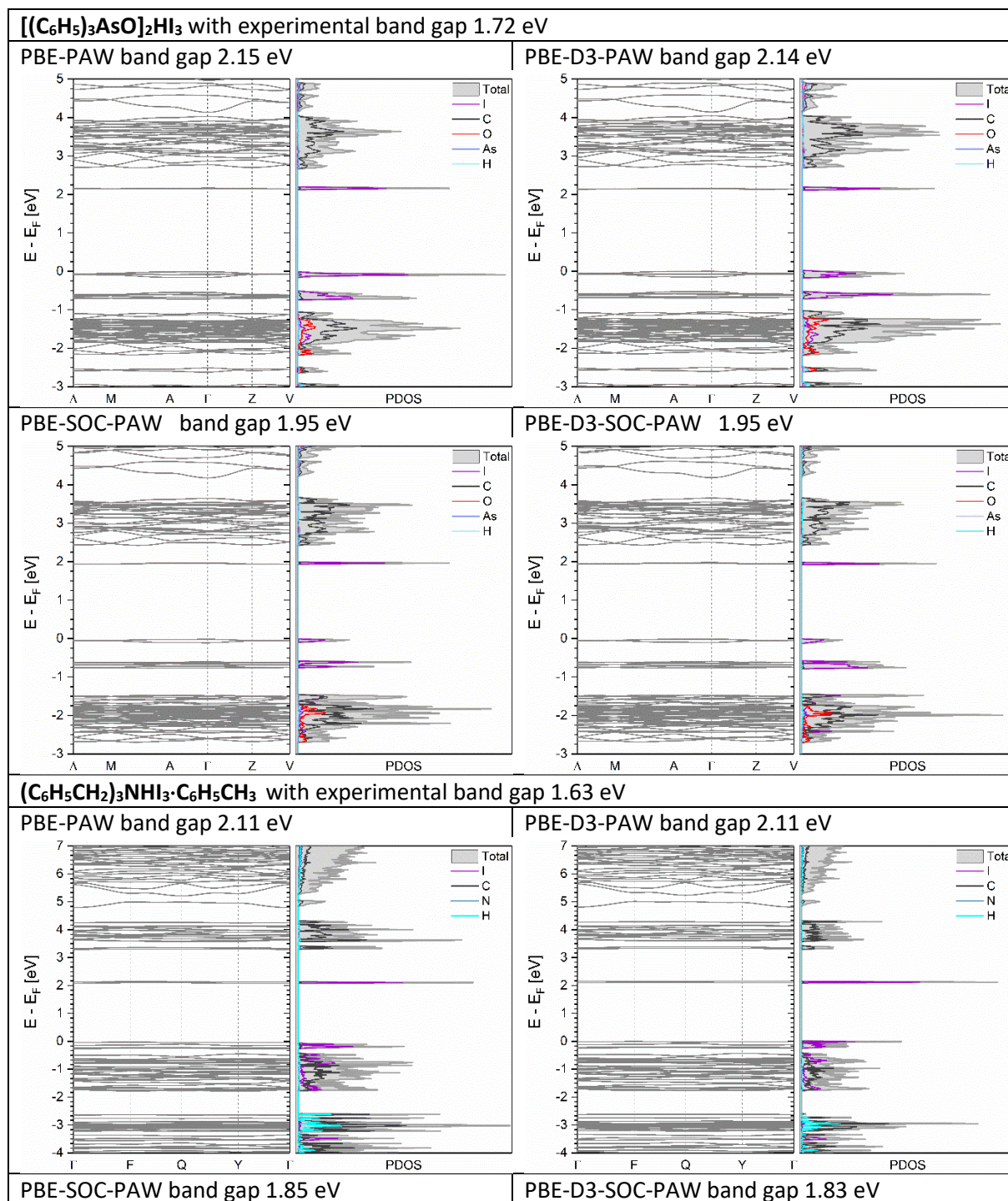
DFT structural and electronic properties

To be able to include spin orbit coupling (SOC) effect, further computations were performed using fixed lattice parameters at experimental values. We relaxed atomic positions with PBE, PBE-D3, PBE-SOC and PBE-D3-SOC so the influence of D3 and SOC on the electronic structure can be examined (Table S3).

Comparison of selected geometrical parameters obtained experimentally and from only ionic relaxation in GGA computations is presented in Table S3. The PBE-D3 ionic relaxation method provide excellent description of the structural properties of the investigated complexes as determined parameters agree well with the experimental ones. We can also compare band gaps calculated with cell shape relaxation (Table S2) and ionic relaxation (Table S4) methods and conclude that the results presented in this paper show no significant dependence on the choice between those two methods.

The inclusion of D3 dispersion correction shows almost no influence on the electronic structure and band gaps. The SOC effect reduces the energy level in the conduction band for I atom, improving the band gaps. SOC also lowers the energy of C unoccupied states as well as strongly hybridized occupied bands. In addition, the GGA + SOC suggests presence of localized states seen as the decreased C contribution in the valence band as well as separation of I 5p states from hybridized bands at -0.7 eV for the $[(\text{C}_6\text{H}_5\text{CH}_2)_3\text{NO}]_2\text{HI}_3$ case. Therefore, the results indicate existence of spin orbit effect in these compounds, so the accurate electronic structures can be obtained by considering SOC.

Table S3. Comparison of electronic structures of iodide complexes obtained from ionic relaxation with PBE-PAW, PBE-D3-PAW, PBE-SOC-PAW and PBE-D3-SOC-PAW.



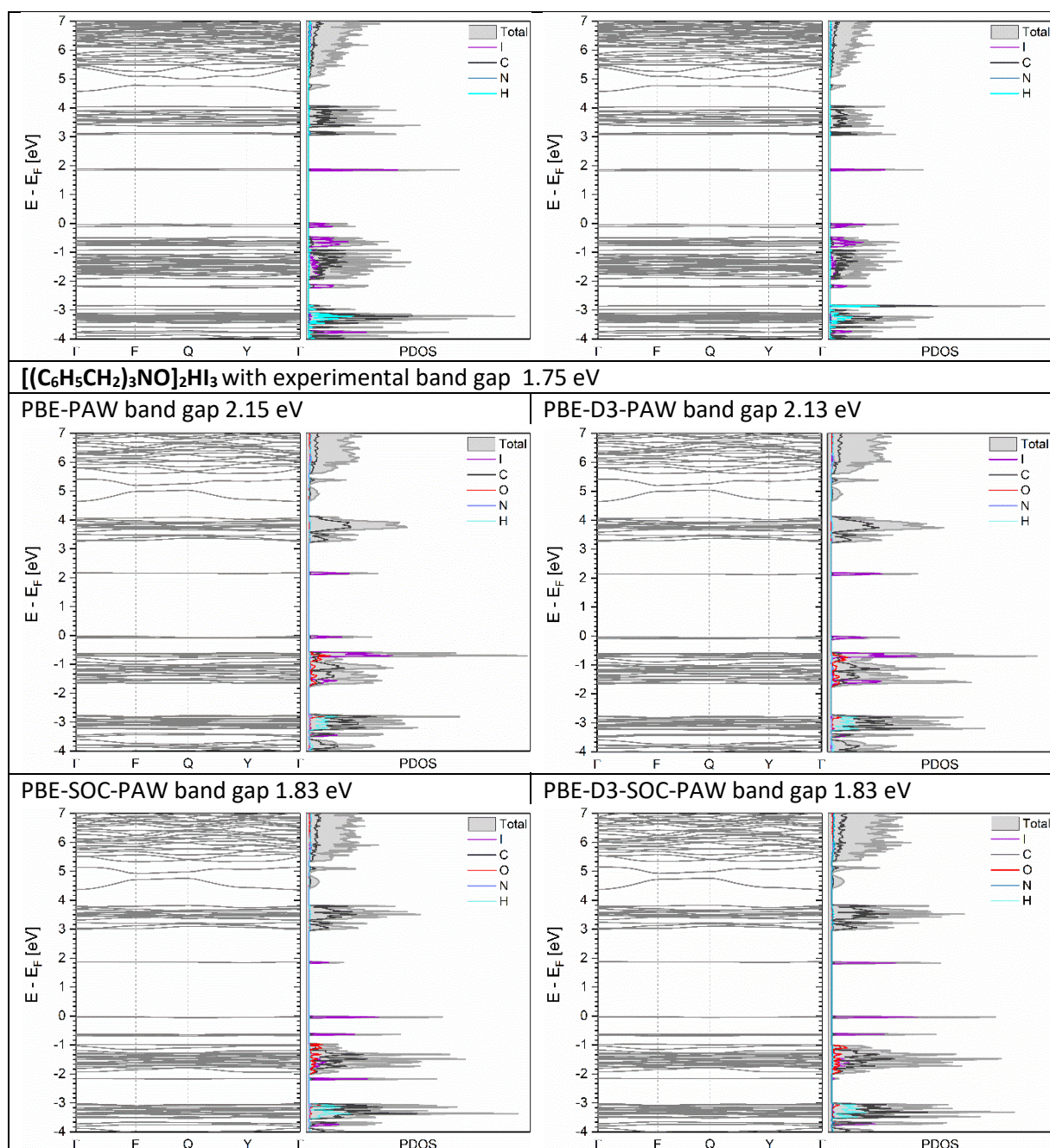


Table S4. Experimental and calculated with ionic relaxation method, selected geometrical parameters for [(C₆H₅)₃AsO]₂HI₃, C₆H₅CH₂)₃NHI₃·C₆H₅CH₃ and [(C₆H₅CH₂)₃NO]₂HI₃ salts. Bond distances are in Å.

Geometrical parameters	Experimental	Calc. PBE-D3
[(C₆H₅)₃AsO]₂HI₃		
As–O19	1.682(2)	1.72
O...H	1.22(1)	1.21
As–O19–H19	122(3)°	122°
O19–H19...O19#1	162(6)°	166°
I2–I1–I2#2	176.49(1)°	175°
I–I	2.914(1)	2.95
I ₃ ⁻ ... I ₃ ⁻ parallel channel	5.157(1)	5.12

$I_3^- \dots I_3^-$ same channel	6.617(1)	6.55
$(C_6H_5CH_2)_3NHI_3 \cdot C_6H_5CH_3$		
N1...I1	3.642(3)	3.67
H...I	2.76(4)	2.63
N1-H1...I1	175(4) $^\circ$	173 $^\circ$
I1-I2-I3	175.34(1) $^\circ$	175 $^\circ$
I1-I2	2.984(1)	3.00
I2-I3	2.869(1)	2.93
$I_3^- \dots I_3^-$ parallel channel	4.933(1)	5.15
I3...I3#1 parallel channel	4.600(1)	4.58
$I_3^- \dots I_3^-$ same channel	7.360(1)	7.29
$[(C_6H_5CH_2)_3NO]_2HI_3$		
C20-H20...I1	3.199	3.19
I1-I2	2.921(1)	2.96
$I_3^- \dots I_3^-$	6.820(1)	6.83

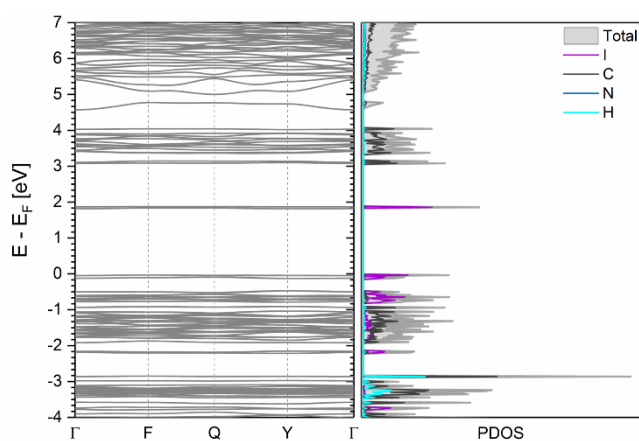


Figure S1. Band structure and projected density of states of $(C_6H_5CH_2)_3NHI_3 \cdot C_6H_5CH_3$ from DFT-D3-SOC. The Fermi level is set to zero.

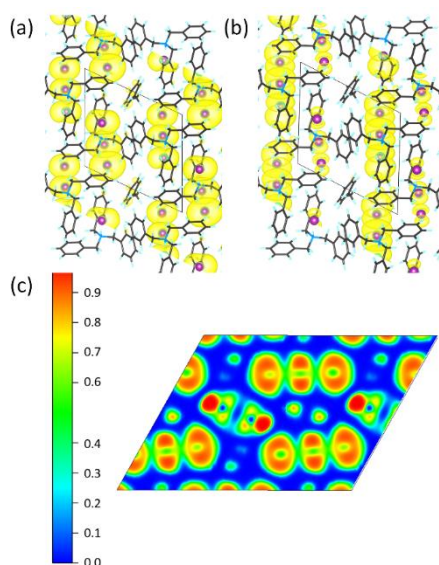


Figure S2. Partial charge density plots of a) valence band maximum (VBM) and b) conduction band minimum (CBM) and c) electron localization function (ELF) plots of $(\text{C}_6\text{H}_5\text{CH}_2)_3\text{NHI}_3 \cdot \text{C}_6\text{H}_5\text{CH}_3$ on the $(-1\ 1\ 0)$ plane.

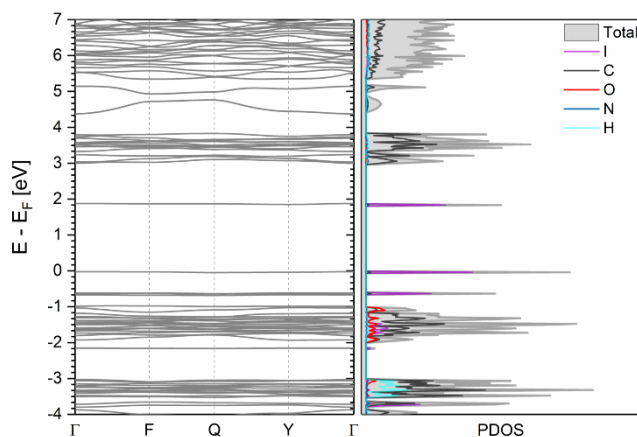


Figure S3. Band structure and projected density of states of $[(\text{C}_6\text{H}_5\text{CH}_2)_3\text{NO}]_2\text{HI}_3$ from DFT-D3-SOC. The Fermi level is set to zero.

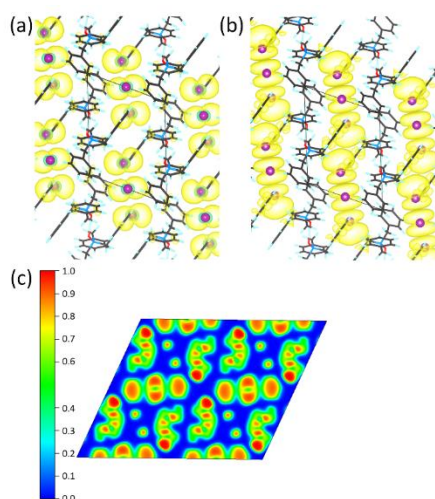


Figure S4. Partial charge density plots of a) valence band maximum (VBM) and b) conduction band minimum (CBM) and c) electron localization function (ELF) plots of $[(\text{C}_6\text{H}_5\text{CH}_2)_3\text{NO}]_2\text{HI}_3$ on the $(0\ 1\ 0)$ plane.

Animations present 3D views of the partial electron density plots of the top of the valence band and the bottom of the conduction band:

S1: conduction band of $[(\text{C}_6\text{H}_5)_3\text{AsO}]_2\text{HI}_3$

S2: valence band of $[(\text{C}_6\text{H}_5)_3\text{AsO}]_2\text{HI}_3$

S3: conduction band of $[(\text{C}_6\text{H}_5\text{CH}_2)_3\text{NO}]_2\text{HI}_3$

S4: valence band of $[(\text{C}_6\text{H}_5\text{CH}_2)_3\text{NO}]_2\text{HI}_3$

S5: conduction band of $(\text{C}_6\text{H}_5\text{CH}_2)_3\text{NHI}_3 \cdot \text{C}_6\text{H}_5\text{CH}_3$

S6: valence band of $(\text{C}_6\text{H}_5\text{CH}_2)_3\text{NHI}_3 \cdot \text{C}_6\text{H}_5\text{CH}_3$

Band gap determination

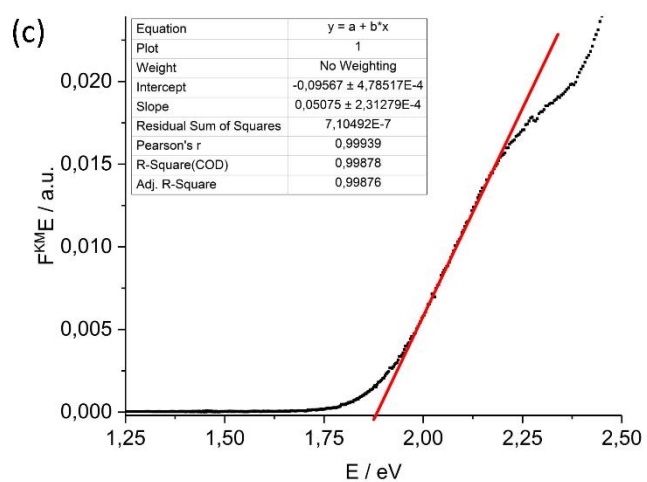
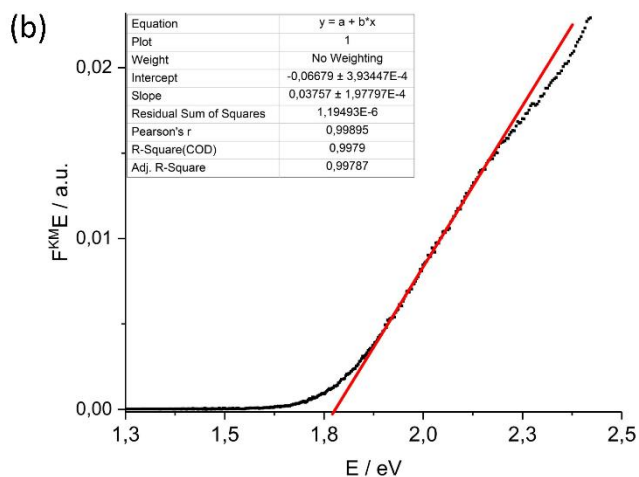
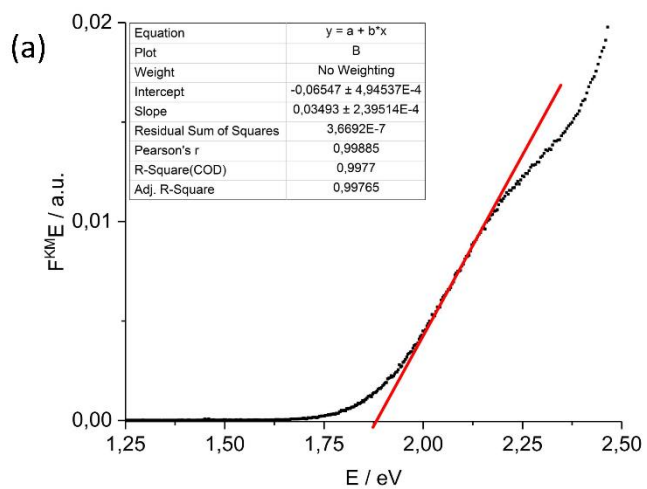


Figure S5. Optical band gap determination with Tauc plots and fitting parameters of (a) $[(C_6H_5)_3AsO]_2HI_3$, (b) $C_6H_5CH_2)_3NH_3 \cdot C_6H_5CH_3$ and (c) $[(C_6H_5CH_2)_3NO]_2HI_3$ salts.

Photocurrents

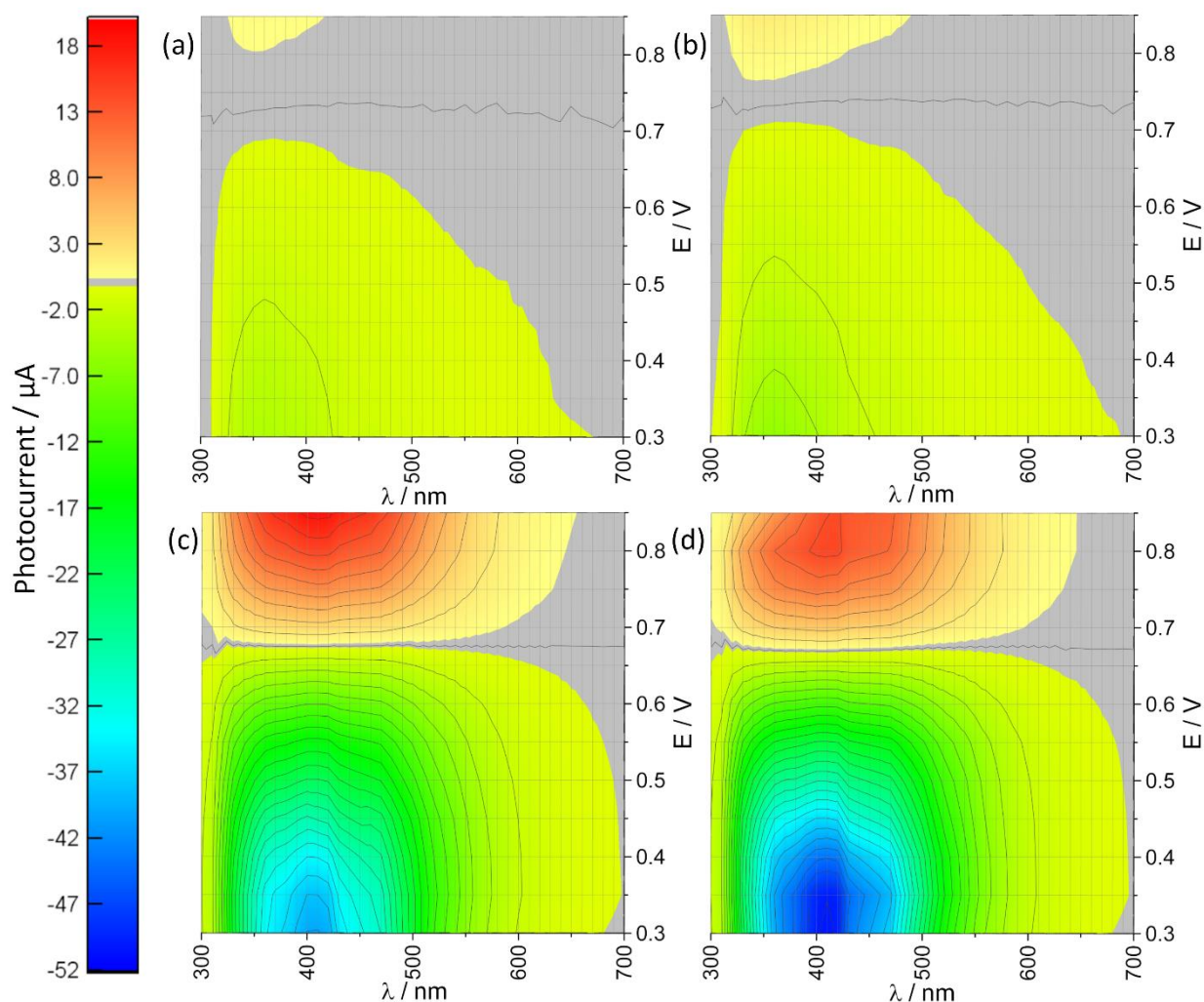


Figure S6. Photocurrent amplitude as a function of incident light wavelength and photoelectrode potential in a) deoxygenated electrolyte containing 0.1 M KNO_3 , b) oxygenated electrolyte containing 0.1 M KNO_3 , c) deoxygenated electrolyte containing 0.1 M KI and 0.01 M I_2 , d) oxygenated electrolyte containing 0.1 M KI and 0.01 M I_2 of $(\text{C}_6\text{H}_5\text{CH}_2)_3\text{NH}_3 \cdot \text{C}_6\text{H}_5\text{CH}_3$. Contour lines are distributed every 2 μA .

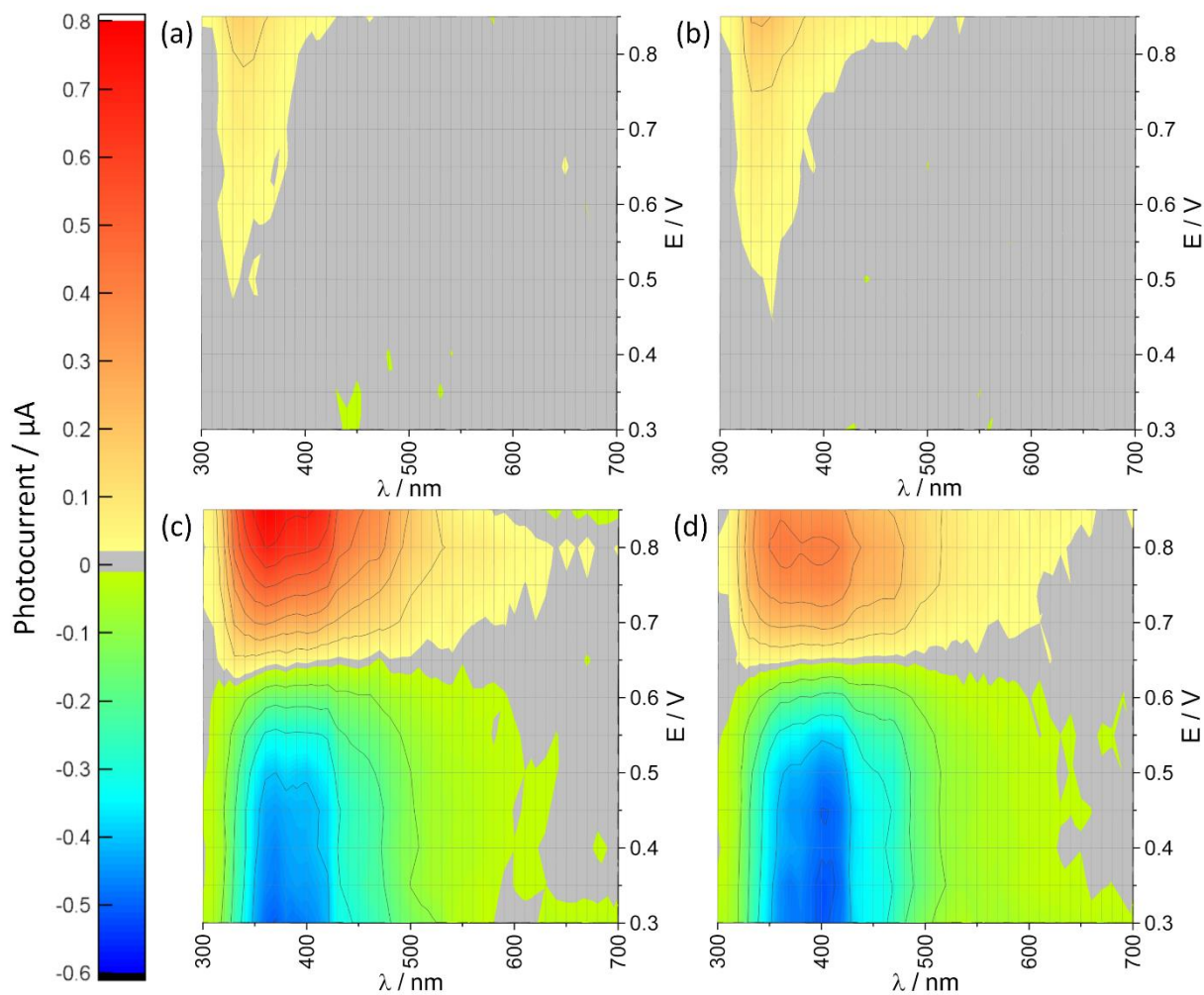


Figure S7. Photocurrent amplitude as a function of incident light wavelength and photoelectrode potential in a) deoxygenated electrolyte containing 0.1 M KNO₃, b) oxygenated electrolyte containing 0.1 M KNO₃, c) deoxygenated electrolyte containing 0.1 M KI and 0.01 M I₂, d) oxygenated electrolyte containing 0.1 M KI and 0.01 M I₂ of [(C₆H₅CH₂)₃NO]₂HI₃. Contour lines are distributed every 0.1 μA.

Hirshfeld surface analysis

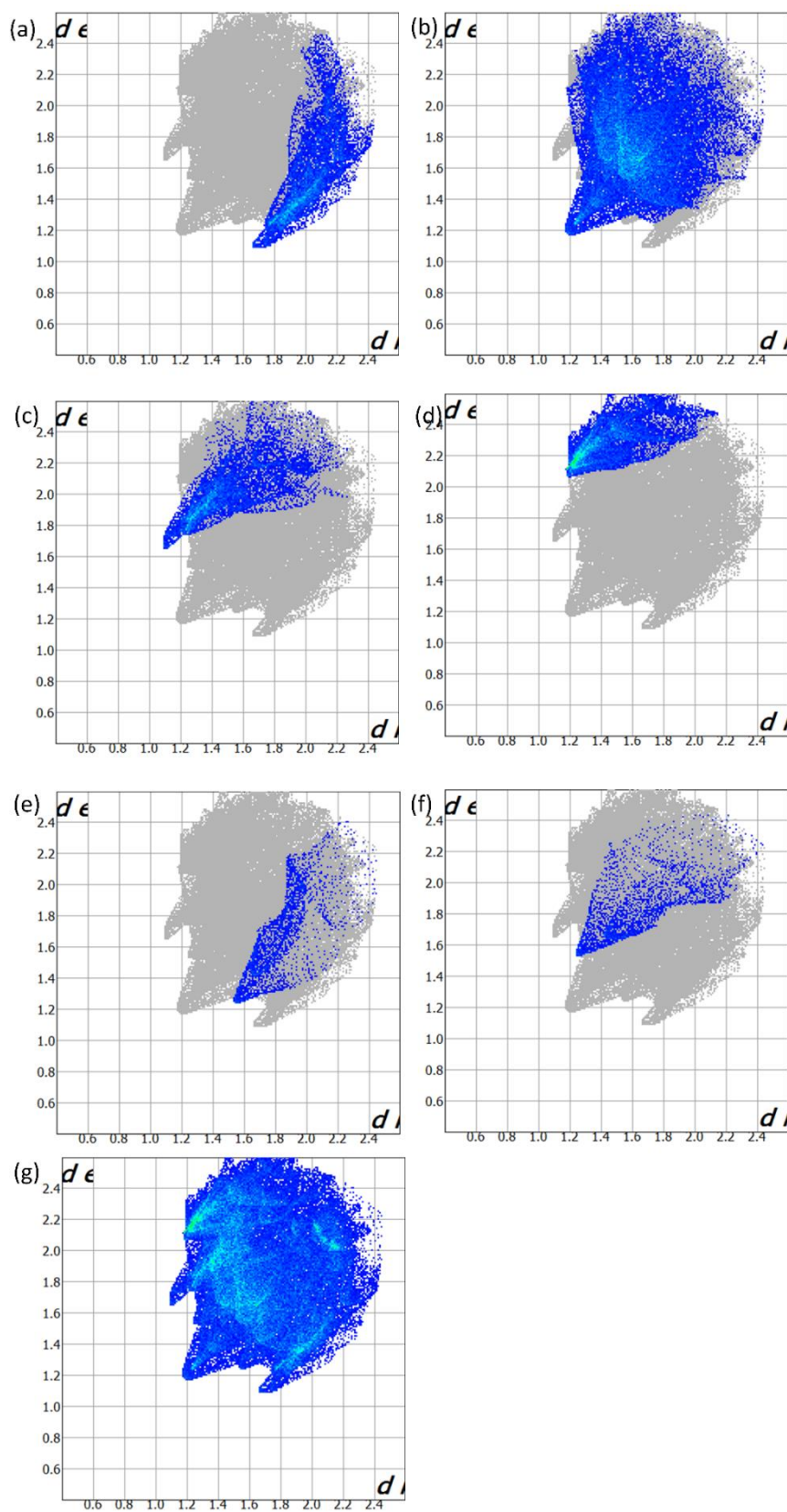


Figure S8. Fingerprints of intermolecular C...H(a), H...H (b), H...C (c), H...I (d), O...OH (e), H...O (f), all (g) contacts of $[(C_6H_5)_3AsO]_2H^+I_3^-$ crystal structure.

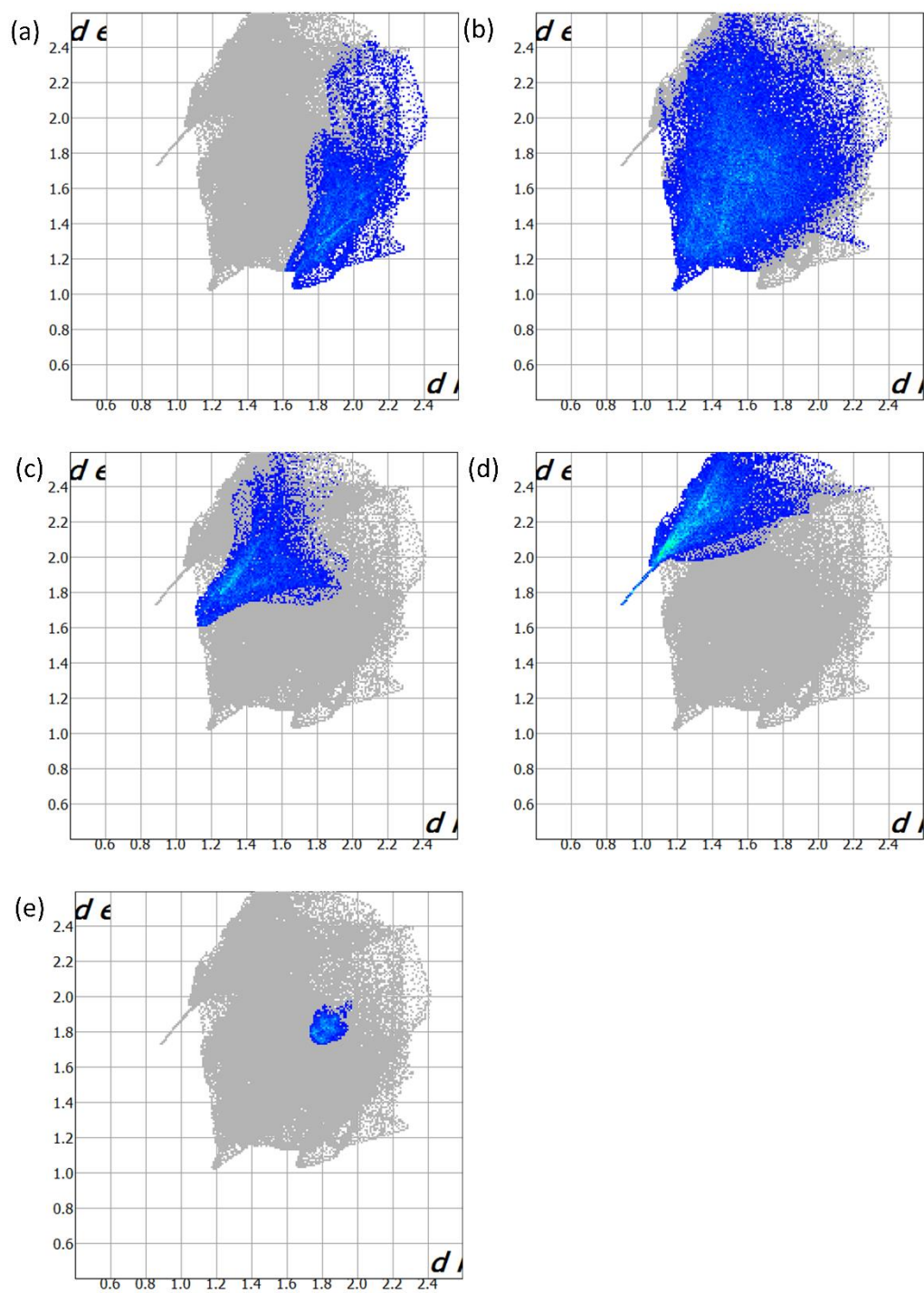


Figure S9. Fingerprints of intermolecular $\text{C}\dots\text{H}$ (a), $\text{H}\dots\text{H}$ (b), $\text{H}\dots\text{C}$ (c), $\text{H}\dots\text{I}$ (d), $\text{C}\dots\text{C}$ (e), contacts of $(\text{C}_6\text{H}_5\text{CH}_2)_3\text{NH}^+\text{I}_3^- \cdot \text{C}_6\text{H}_5\text{CH}_3$ crystal structure.

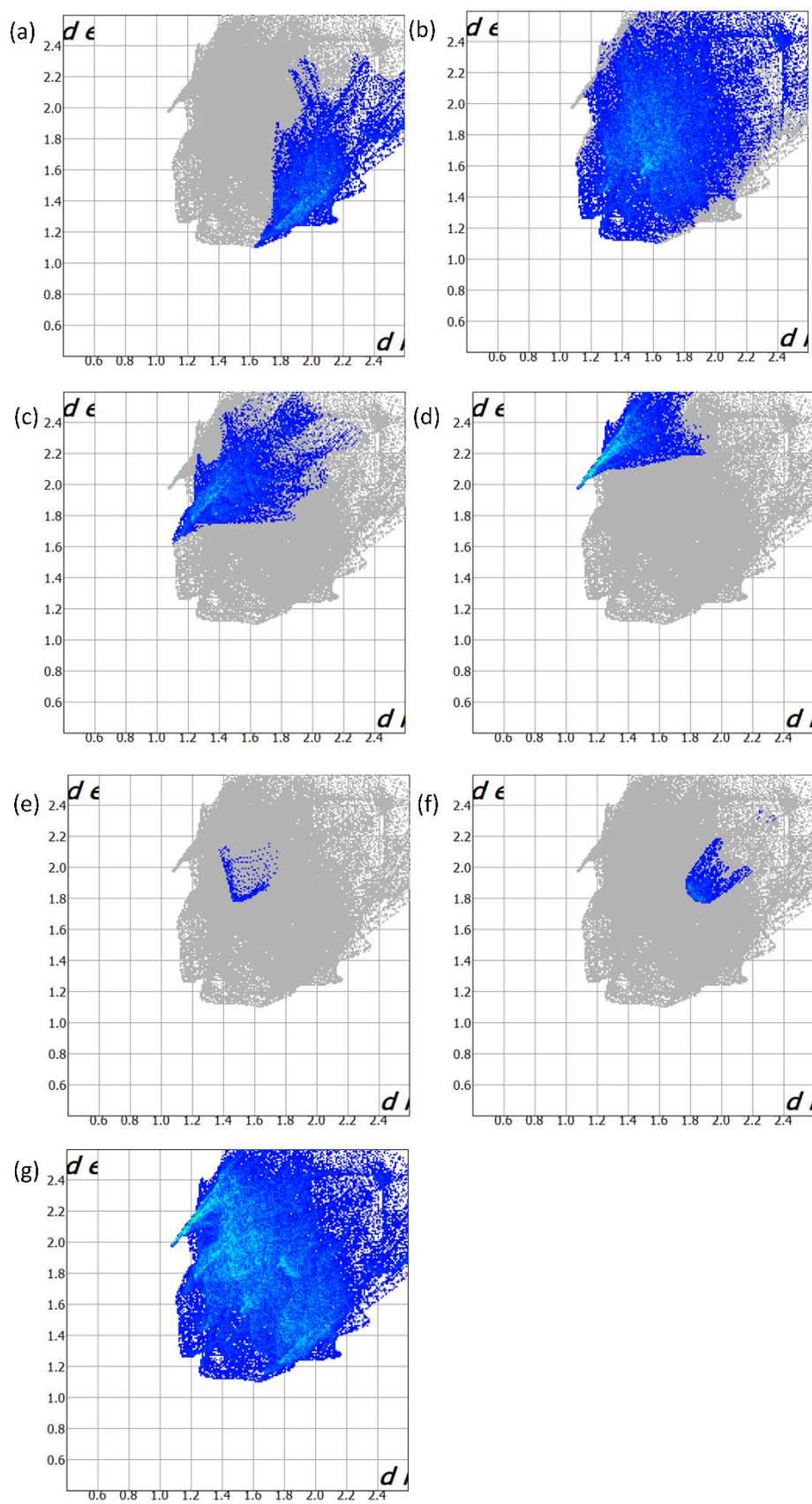


Figure S10. Fingerprints of intermolecular C...H(a), H...H (b), H...C (c), H...I (d), O...H (e), C...C (f), all (g) contacts of $[(C_6H_5CH_2)_3NO]_2H^+I_3^-$ crystal structure.

References

1. R. Dovesi, R. Orlando, A. Erba, C. M. Zicovich-Wilson, B. Civalleri, S. Casassa, L. Maschio, M. Ferrabone, M. De La Pierre, P. D'Arco, Y. Noël, M. Causà, M. Rérat and B. Kirtman, *Int. J. Quantum Chem*, 2014, **114**, 1287-1317.
2. G. Kresse and J. Furthmüller, *Phys. Rev. B*, 1996, **54**, 11169.
3. M. F. Peintinger, D. V. Oliveira and T. Bredow, *J. Comput. Chem.*, 2013, **34**, 451-459.
4. W. R. Wadt and P. J. Hay, *J. Chem. Phys.*, 1985, **82**, 284-298.
5. K. Doll and H. Stoll, *Phys. Rev. B*, 1998, **57**, 4327-4331.
6. J. P. Perdew, J. A. Chevary, S. H. Vosko, K. A. Jackson, M. R. Pederson, D. J. Singh and C. Fiolhais, *Phys. Rev. B*, 1992, **46**, 6671.
7. J. P. Perdew, K. Burke and M. Ernzerhof, *Phys. Rev. Lett.*, 1996, **77**, 3865.
8. J. P. Perdew, A. Ruzsinszky, G. I. Csonka, O. A. Vydrov, G. E. Scuseria, L. A. Constantin, X. Zhou and K. Burke, *Phys. Rev. Lett.*, 2008, **100**, 136406.
9. A. D. Becke, *J. Chem. Phys.*, 1993, **98**, 5648-5652.
10. A. V. Krukau, O. A. Vydrov, A. F. Izmaylov and G. E. Scuseria, *J. Chem. Phys.*, 2006, **125**, 224106.
11. P. E. Blöchl, *Phys. Rev. B*, 1994, **50**, 17953-17979.
12. G. Kresse and D. Joubert, *Phys. Rev. B*, 1999, **59**, 1758-1775.
13. S. Grimme, *J. Comput. Chem.*, 2006, **27**, 1787-1799.
14. S. Grimme, J. Antony, S. Ehrlich and H. Krieg, *J. Chem. Phys.*, 2010, **132**, 154104.

Memristor in a Reservoir System—Experimental Evidence for High-Level Computing and Neuromorphic Behavior of PbI_2

E. Właźlak,^{*,†,‡} M. Marzec,[†] P. Zawal,^{†,§} and K. Szaciłowski^{*,†}

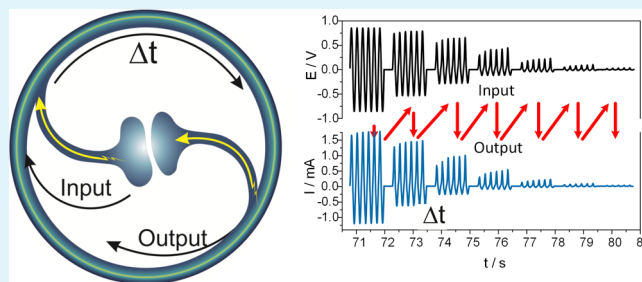
[†]Academic Centre for Materials and Nanotechnology and [§]Faculty of Physics and Applied Computer Science, AGH University of Science and Technology, al. A. Mickiewicza 30, 30-059 Kraków, Poland

[‡]Faculty of Chemistry, Jagiellonian University, ul. Gronostajowa 2, 30-060 Kraków, Poland

Supporting Information

ABSTRACT: Lead halides in an asymmetric layered structure form memristive devices which are controlled by the electronic structure of the PbX_2 /metal interface. In this paper, we explain the mechanism that stands behind the I – V pinched hysteresis loop of the device and shortly present its synaptic-like plasticity (spike-timing-dependent plasticity and spike-rate-dependent plasticity) and nonvolatile memory effects. This memristive element was incorporated into a reservoir system, in particular, the echo-state network with delayed feedback, which exhibits brain-like recurrent behavior and demonstrates metaplasticity as one of the available learning mechanisms. It can serve as a classification system that classifies input signals according to their amplitude.

KEYWORDS: memristor, Schottky barrier, reservoir computing, neuromorphic systems, metaplasticity



INTRODUCTION

Memristors are considered as the holy grail of future electronics and unconventional computing owing to their unique electrical characteristics analogous to synapses.^{1–6} Neuromimetic electronics, cognitive computing, and other bioinspired approaches^{7–10} are seriously considered as a future IT technology, especially in the coming era of big data¹¹ and Internet of Things.^{12,13} These two-terminal, passive devices show a characteristic switching pattern in their current–voltage characteristics: the pinched hysteresis loop¹⁴ resulting from charge-dependent resistance of the device. It is a result of various processes, both bulk and interfacial, which modulate the conductivity of the device as a function of electric charge. More generally, other features, such as capacitance or inductance of an element, may also vary as a function of electric charge passing through the device: these features are usually referred to as memcapacitance¹⁵ and meminductance,¹⁵ respectively. These terms can be further generalized as memfractance.¹⁶ The memristive properties of various solid-state devices are a consequence of several processes: formation of conductive filaments,^{17–23} migration of vacancies and dopants,^{24–28} charge trapping on quantum dots,²⁹ or modulation of Schottky barrier height (SBH).^{30,31}

The brain—probably the most complicated complex dynamic system—uses the feedback loops in different ways, at many levels, and for different purposes. The internal feedback loop appears in the subcortical regions in classical eyeblink conditioning. Learning processes are improved by the feedback loops in a brain.³² In that specific case, the loop leads to stronger inhibition of specific cells which results in an

enhanced conditioning. Another example is the generation of rhythmic activity in the cortex and thalamus, which strongly influences sensory processing and is influenced by the interaction of a positive feedback loop with negative feedback control.³³ The functional magnetic resonance imaging experiments show that conscious sensations appear only when the specific brain areas are involved in recurrent interactions, enabling the long-lasting exchange of information between brain regions.³⁴ Biologically inspired systems that mimic biological mechanisms,^{35–39} theoretically and experimentally implemented reservoir computing using the memristor array or delay line can be found in the literature.^{40–44} The combination of an experimentally implemented memristor in a single-node echo-state machine^{45,46} that exhibits neuromorphic properties is still a novelty; however, the theoretical approach toward such constructs has been already reported.⁴⁷

The main technical limitations in studies and applications of memristive elements are their rather complex fabrication protocols and low stability. Most of them (oxide- and chalcogenide-based) require high vacuum processing; polyaniline and other polymers are hardly soluble and perovskites (which on the other hand are solution-processed semiconductors of versatile and tunable properties)^{48,49} are usually extremely sensitive to humidity. In this paper, we present a simple memristive device based on lead halides PbX_2 ($X = \text{Cl}, \text{Br}, \text{I}$) prepared by contacting nanometer-thin layers of PbX_2 on

Received: January 28, 2019

Accepted: April 15, 2019

Published: April 15, 2019

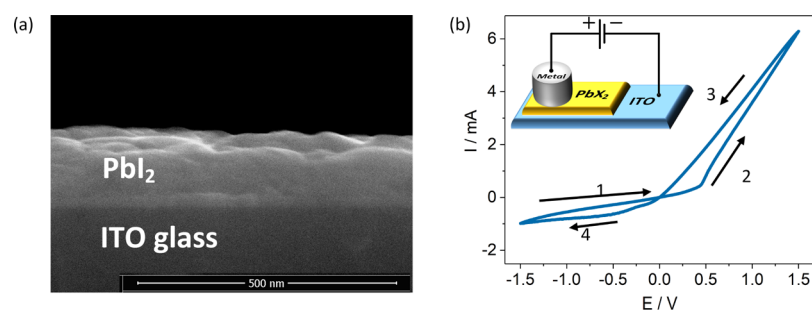


Figure 1. Cross section of the PbI_2 layer deposited on the ITO/glass substrate (a). Typical current–voltage characteristic of the PbI_2 -based memristive device with metallic electrode (b); the inset presents the measurement setup.

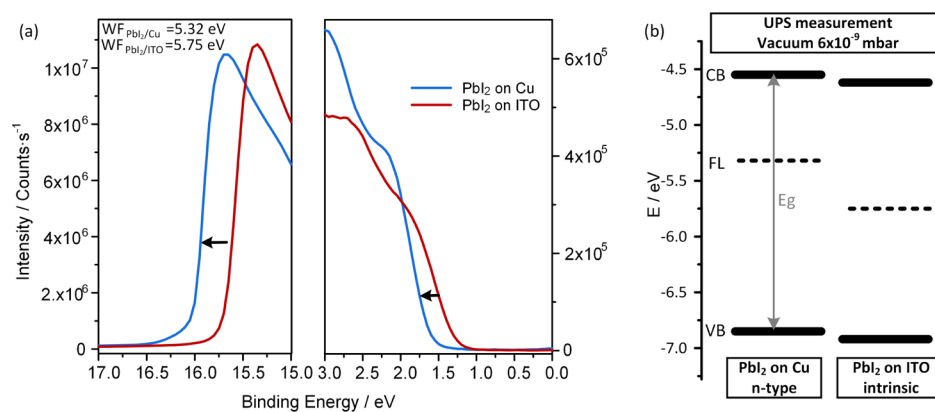


Figure 2. UPS spectra of PbI_2 on the surface of the ITO glass and polycrystalline Cu taken after sputtering with Ar-GCIB. Black arrows indicate the shifts of HOMO and Fermi levels toward higher binding energy (a), energy band diagram of PbI_2 deposited on the Cu and ITO surface, Fermi levels and valence bands obtained via UPS measurements; conduction bands were calculated with $E_{\text{VB}} + E_{\text{g}}$, where E_{VB} is the valence band energy level and E_{g} is the optical energy gap (b).

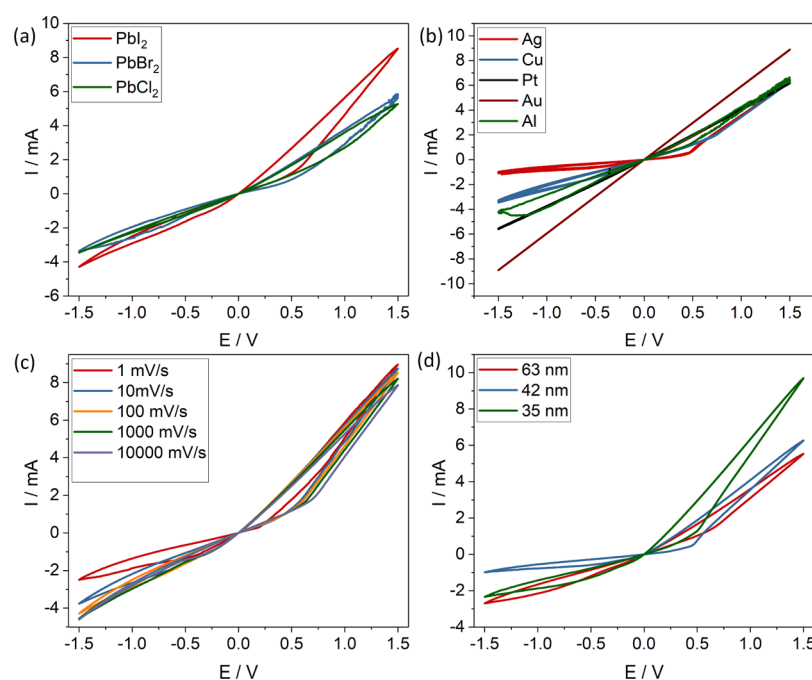


Figure 3. Current–voltage characteristics of different lead(II) halide memristors measured with an Ag second electrode and 100 mV/s scan rate (a), the same PbI_2 layer measured with different metal as a second electrodes with 100 mV/s scan rate (b), the same PbI_2 layer measured with different scan rates with a Cu second electrode (c), three layers with different thicknesses measured with an Ag as a second electrode and 100 mV/s scan rate (d). Single scans only. Examples of characteristics with a higher number of recorded cycles are presented in Figure S8.

indium tin oxide (ITO) glass with various metal contacts. Experimental data are explained in terms of interfacial

interactions and modulation of SBH. Moreover, we present nonvolatile memory of the device, synapse-like plasticity,

reservoir system mimicking the recurrent brain processes, and metaplasticity.

RESULTS AND DISCUSSION

Device Overview. The cross section of the device under test is shown in Figure 1a. Current–voltage characteristics are measured in the setup shown in Figure 1b. A typical I – V plot consist of four parts: arrow 1 indicates the potential scan from -1.5 to 0.4 V where the current intensity slightly increases with increasing potential. Around the potential of 0.5 V a definite change in the slope of current appears and it is constant till 1.5 V (2). When scanned from 1.5 to 0.1 V, a different but still constant slope is observed (3). The second drastic change in the current amplitude occurs at around 0 V where significant nonlinear behavior is observed. Arrows labeled 1 and 4 indicate the low current area and can be thus related to the high resistive state (HRS), whereas arrows 2 and 3 to the low resistive state (LRS). One can divide that characteristic into the left side where currents are of low intensity and the right side with current intensity ca. six times higher. The I – V characteristic is, with some approximation, similar to a Schottky-barrier diode one, but with two current onset points instead of one. The modified diode-like behavior is typical for memristors with resistive switching based on the surface effects.^{31,50,51} The pinched hysteresis loop is observed in the I – V characteristic with the intersection point at 0 V and the persistence of HRS and LRS lasts for a period of at least 1 h when readout voltage is applied (Figure S1, see the Supporting Information). These features indicate that the device can be regarded as a memristor.⁵²

The n-type conductivity of PbI_2 prepared on the Cu surface presented in Figure 2 is confirmed by the X-ray photoelectron spectroscopy (XPS) and ultraviolet photoelectron spectroscopy (UPS). The XPS spectra of the surface of the PbI_2 layer on Cu and ITO surfaces were measured before and after sputtering with an argon gas cluster ion beam (Ar-GCIB, Figures S2–S5, see the Supporting Information). These spectra indicate that the main signals originate from Pb and I content only. The UPS spectra of PbI_2 on the ITO surface reveal the almost intrinsic character of PbI_2 as the optical band gap is 2.3 eV and the valence band lay 1.17 eV below the Fermi level of the material. Lead(II) iodide changes its character in contact with the copper surface. Both Fermi secondary electron cut-off (SE cut-off) and Fermi edge region shift toward higher energies (Figure 2a). As a consequence, PbI_2 on Cu surface has lower work function by 0.43 eV and the valence band is closer to the Fermi level by 0.36 eV (Figure 2b).

Mechanism Determination. The memristive hysteresis loops recorded for perovskite-based devices have a very similar shape to those presented here. It can be argued, however, that despite the similarity the mechanism must be different in currently studied case. Figure 3b shows hysteresis loops recorded for different metal contacts and the shape of their I – V characteristics strongly depends on the contact material. In the case of bulk switching processes (such as ion migration, filament formation from atoms of core material) the I – V characteristics should be contact-independent. Therefore, in the case of PbX_2 memristors we postulate an interfacial switching mechanism (*vide infra*). Furthermore, assuming from different radii of halide atoms, various lead halides would have different ionic mobilities but the pinched hysteresis loops for PbCl_2 , PbBr_2 , and PbI_2 are very similar (only PbI_2 shows slightly higher current intensities, Figure 3a). Our thin-layer

devices show very strong dependence on contact materials: very prominent hysteresis loops are observed for Ag, Cu, and Al contacts, whereas with Au and Pt contacts only linear Ohmic characteristics can be recorded. This implies barrierless transport through these contacts and the absence of the metal-induced gap states (MIGS).

Another mechanism, the contribution of which can be definitely excluded, is the migration of metal cations from the electrode into the layer. The electrode made of electrochemically active metals as Cu or Ag could work as a cation source.⁵³ It would happen for different metals at different potential values, but devices with aluminum ($E_{1/2} = -1.66$ V), silver ($E_{1/2} = 0.80$ V), and copper ($E_{1/2} = 0.37$ V) electrodes have the first threshold in the same range of potential. This observation excludes the possibility of the filamentary switching mechanism, at least involving electrode materials. Measurements with aluminum electrodes are usually less stable and noisy owing to the oxide layer on the surface, but apart from this difference the hysteresis curves are qualitatively very similar. It should be also noticed that the scan rates (Figure 3c) affect the shape of the hysteresis loop in a limited manner: the lower the scan rate the lower the potential of the first threshold, and the faster the scan the more the linear I – V characteristics, whereas the areas of the lobes are comparable (at least in the positive potential range). To complete the investigation, devices with the same material (PbI_2), the same metal electrode (Ag), and the same scan rate (100 mV) have been measured. The only difference was the thickness of the lead halide layer. It can be noticed (Figure 3d) that with decreasing thickness of the PbI_2 layer the overall resistivity decreases, which is fully consistent with Ohmic behaviors of the bulk material (eq 1)

$$\rho = R(l/A) \quad (1)$$

where R is the electrical resistance characteristic for the material, l is the thickness, and A is the cross-section area. Therefore, it can be concluded that only interfacial processes associated with the metal–lead halide interface are responsible for the memristive character of devices under test and the bulk of the film shows purely Ohmic behavior, at least in the case of forward bias of the Schottky junction. Under the reverse bias the maximum of cathodic current of the layer of 35 nm thickness lies between currents of 63 and 42 nm layers, which suggests an additional process that does not follow a simple linear relation. Figure 3b shows two linear I – V characteristics for golden and platinum electrodes. This behavior is attributed to the absence of the Schottky barrier (SB) at the interface and formation of an Ohmic contact instead. Symmetrical devices with two ITO contacts also exhibit linear behavior. These results suggest that electronic structure alignment at the metal–lead halide junction and electron trapping processes at this interface result in history-dependent modulation of the SBH. To estimate the value of the SBH we employed the Richardson–Laue–Dushman equation (eq 2)

$$J_0 = A^* \cdot T^2 \exp\left(\frac{q_e \Phi_B}{kT}\right) \quad (2)$$

where J_0 is the reverse saturation current, T is the temperature, q_e is the elementary charge, Φ_B is the SBH, k is the Boltzmann constant, and A^* is the effective Richardson constant defined as follows (3)

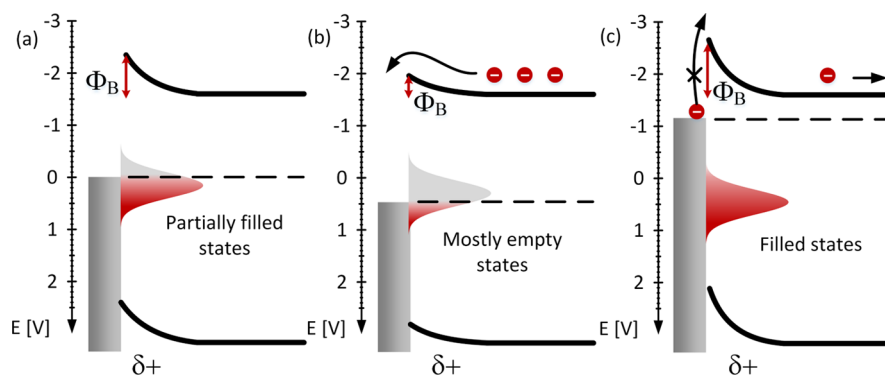


Figure 4. Idealistic presentation of current flow through the device at various polarizations: no bias applied (a), forward bias (b), and reversed bias (c). These polarizations result in intermediate SBH (a), small SBH (b), and large SBH (c) as a consequence of filling of the interfacial states (shaded in red).

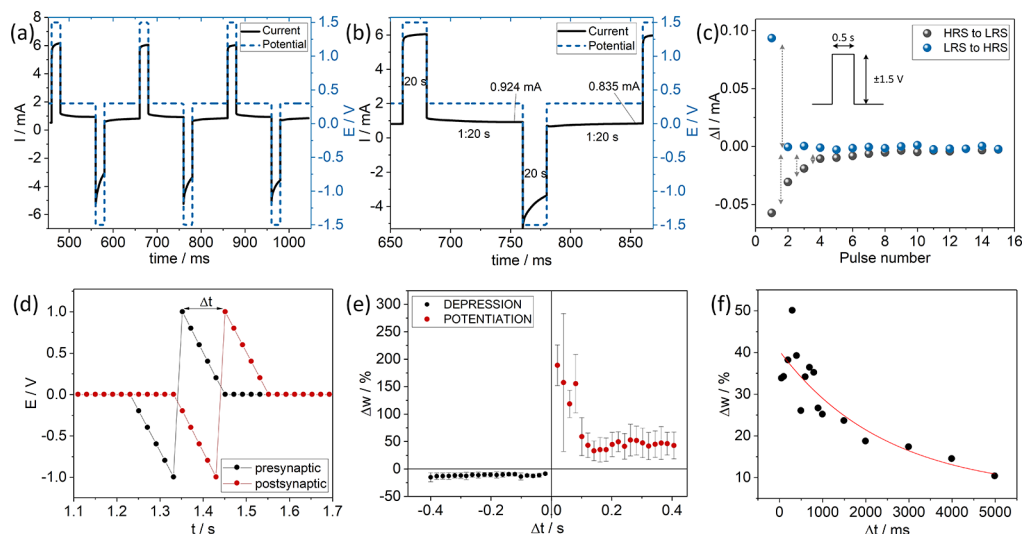


Figure 5. Chronoamperometry of an ITO|PbI₂|Ag device. The readout potential is equal to 0.3 V (120 s); 1.5 V (20 s) and −1.5 V (20 s) are the potentials that switch the device to LRS and HRS, respectively: several pulses (a) and a zoom into two pulses (b). Differential current ΔI measured at 0.1 V (60 s) between fifteen 0.5 s pulses of 1.5 V (black) and −1.5 V (blue) illustrating a gradual change from HRS to LRS and abrupt change from LRS to HRS (c). Voltage pattern in STDP measurement (d), antisymmetric Hebbian learning rule (e), and SRDP pattern with exponential fit (for parameters see Table S1) (f).

$$A^* = 4\pi q m_e k^2 h^{-3} \quad (3)$$

where m_e is the electron effective mass and h is the Planck constant. Electron effective mass has been calculated elsewhere and is equal to $0.55 m_0$.⁵⁴ The calculated height of SB at the PbI₂|Cu interface is therefore equal to 0.63 eV. The equivalent circuit and fitting procedure to linear fragments of the hysteresis loop (Figure S6) is described in the Supporting Information.

As the modulation of the SB is independent of the surface area, a larger surface of the metal electrode results in larger currents flowing through the device. An additional measurement concerning two different areas of the metal electrode surface is presented in Figure S7 in the Supporting Information.

Figure 4a–c presents a tentative visualization of the processes during scanning from a positive to a negative potential. When the metal electrode is positively polarized with a potential higher than the first threshold (e.g. 1.0 V), there is only a small (or even negligible) SB. Under these conditions the device is in the LRS and electrons flow between the electrodes almost freely. When the potential is around 0.4 V,

the SB is still present but low enough to sustain some current. This is the reason why the current intensity increases gradually, unlike in the case of the filamentary mechanism, which shows a rather abrupt change in the current intensity. When the potential is low enough, the SB is high enough to reduce the current intensity. The variation of the potential across the device changes the occupancy of the interfacial states, which is another factor that affects the height of the SB. The surface dipole, which is a direct source of the SBH Φ (Figure 4a–c),⁵⁵ is responsible for the memristive properties of the presented devices and is a result of the surface states that can originate from several processes. The most important one involves formation of MIGS. MIGS are sometimes called intrinsic states and represent intrinsic properties of a semiconductor.

Depending on the charge neutrality level, MIGS can exhibit both donor- or acceptor-like properties.^{56–58} Moreover, additional gap states may result from chemisorption involving gas molecules.^{59,60} Chemisorption is also known to change the work function of materials.⁶¹ Furthermore, the work function of the metal surface can be also reduced by adsorbed molecules owing to the pillow effect.^{62,63} Therefore, it is hard to describe the process of SB formation and its height unequivocally,

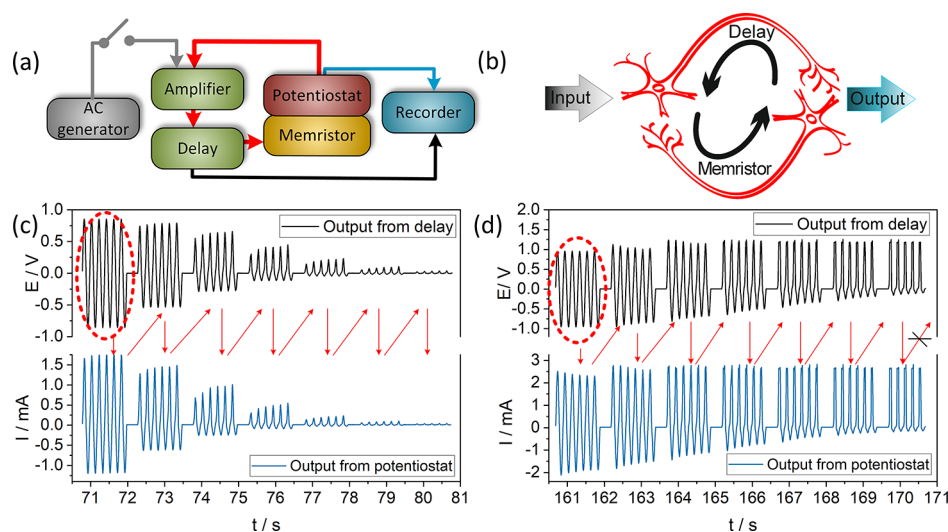


Figure 6. Scheme of a recurrent system based on a single memristor, red arrows indicate the feedback loop (a). Simplified representation of the recurrent feedback loop between neurons in the nervous system (b). Recorded signals from closed loop experiments for 1.7 V_{pp} of initial amplitude: amplitudes vs time (c). Recorded signals from closed loop experiments for 1.9 V_{pp} of initial amplitude: amplitudes vs time (d). The red dashed ellipse indicates the initial input signal.

especially for material that is prepared and held under ambient atmosphere. Despite these facts it is possible to observe its rectifying and memristive behavior in I – V measurements. On this basis, it can be postulated that modulation of the SBH by the variation of the potential across the device is the main factor responsible for memristive effects in PbX₂-based devices.

On the basis of all the experimental data presented above the ITO/PbI₂/M (M = Cu, Ag, Al) can be classified as a bipolar memristor. The device is driven by the electric field, but in contrast to the majority of bipolar memristors the main mechanism of resistive switching involves the modulation of the SBH. This in turn can be attributed to chemical changes at the interface.^{64–66} If one considers the polycrystalline and disordered structure of these devices, it becomes evident that its electrical behavior is close to a fractional device (observed as an unsymmetrical pinched hysteresis loop) owing to the complexity of the charge carrier transport in polycrystalline material.^{67–70} These disordered structures are much closer to memristive networks⁷¹ (or memfractors)^{16,72} than to ideal memristors.⁷³

Brain-like Learning. In chronoamperometric measurements (Figure 5a–c) potentials of +1.5 and –1.5 V were applied to turn the device to LRS and to HRS, respectively. A potential range of 0.1–0.3 V has been chosen to detect the current state of the device. These values are smaller than the first threshold potential (i.e., 0.5 V) and thus does not affect the state of the memristive device. The $I_{\text{LRS}}/I_{\text{HRS}}$ ratio amounts to ca. 1.1 under static mode after 80 s and 3.24 in the dynamic mode for the same device. It can be also noticed that switching from HRS to LRS is faster than the change from HRS to LRS (Figure 5c). This difference is a consequence of different resistivities of the device under forward and reverse polarizations, whereas the electrical capacitance associated with the trap states is the same. It obviously leads to different time constants of charging and discharging. The gradual change from HRS to LRS and abrupt change from LRS to HRS affects the spike-timing-dependent plasticity (STDP) characteristics and is crucial in the metaplasticity induced in the reservoir system (*vide infra*).

In STDP (Figure 5d,e) measurement, the plasticity depends on the relative time interval between two action potentials of neighboring neurons as well as the order of the pre- and postsynaptic stimulation. Here, the metal and ITO electrodes act as pre- and postsynaptic neurons, respectively. If the presynaptic neuron fires its action potential before the postsynaptic neuron, the synaptic weight increases and the synapse is potentiated. PbI₂-based memristors exhibit such strengthening of the synapse if the presynaptic spikes preceded the postsynaptic spikes by no more than 0.15 s. Contrary to that, when the postsynaptic neuron fires before the presynaptic one, the synaptic weight decreases and the synaptic connection efficacy is lowered. The presented memristor does not exhibit gradual synaptic depression, which is fully consistent with abrupt switching from LRS to HRS (Figure 5c). Instead, along with the STDP plasticity, the PbI₂ memristors also present the spike-rate-dependent plasticity (SRDP). Increased pulse frequency results in amplified response; this process is well fitted with a monoexponential function (Figure 5f), which indicates a single charge trapping event at the interface as the main reason for this effect. These two learning modes can be realized within the same device and under the same experimental conditions, which makes the lead halide memristors a universal platform for neuromimetic research.

Reservoir Computing and Neuromorphism. The versatile switching dynamics (STDP + SRDP) of lead halide memristors along with their known electronic structure and simplicity of fabrication makes them perfect devices for construction of more advanced neuromimetic circuits. We have chosen reservoir computing, which is a nontrivial approach toward information processing. The device studied here is especially well suited for application in a single-node echo state machine, a computing device that requires a moderate complexity of the computing node and a delayed feedback loop.^{45,46,74} Figure 6a describes how the PbI₂-based memristor was implemented in the reservoir computing circuit. The system consists of an arbitrary function generator (ac source) that generates the input signal initiating the sequence (gray arrow). The signal is passed to the delay line and then to the potentiostat. The waveform imposes the modulated

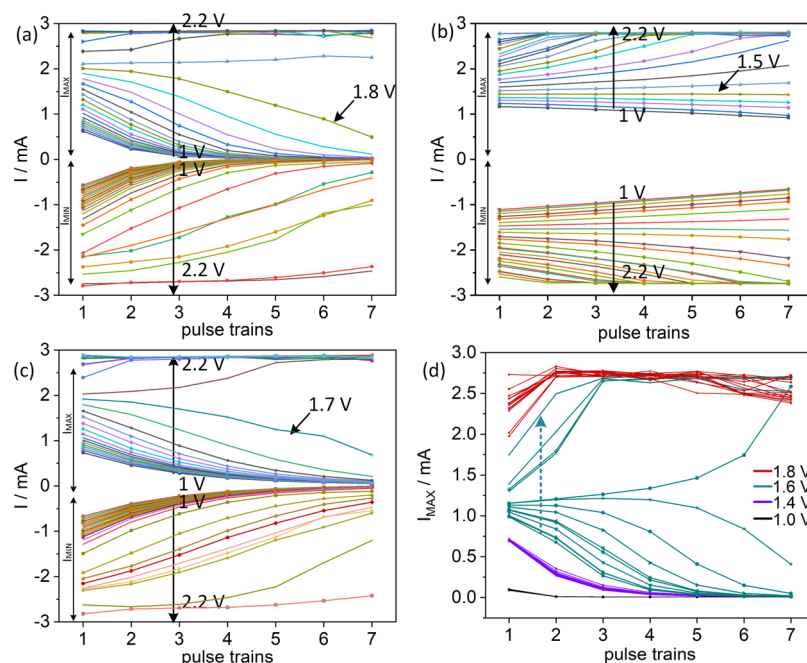


Figure 7. Maximum and minimum of the current amplitude of each pulse train of a 1–2.2 V_{pp} range initial amplitude of an untrained system (a), trained system (b), and system after reset with reversed bias (c). Maximum of the current amplitude of the untrained system, in response to 1, 1.4, 1.6, 1.8 V_{pp} amplitude when the initial signal was repeated 14 times (100 times measured for 1 and 1.4 V_{pp} Figure S9, see the [Supporting Information](#)) (d). Input amplitudes of 1 and 1.4 V_{pp} do not induce any metaplastic behavior, whereas signals of 1.6 V_{pp} amplitude induce metaplastic evolution of the device, as indicated by the cyan arrow.

potential between the electrodes of the memristor. A current signal measured by the potentiostat is then amplified, delayed, and transferred back to the potentiostat as a second-generation input. In this loop (red arrow) the signal is measured as the output from the potentiostat (blue arrow) and the output from delay (black arrow)—before and after the PbI_2 -based device. The memristor is the only nonlinear element in this system. Every time the signal with sufficiently high amplitude is getting through the memristor, it evolves according to the state of the device, as in recurrent neural networks, which is schematically depicted in [Figure 6b](#).⁷⁵ The rectifying character of the Cu– PbI_2 junction leads to the reduction of the current amplitude under reverse bias; therefore, in every cycle the signal gets more and more asymmetric as the negative part of the voltage pattern decreases. As a consequence, only the positive part of the signal survives till the end of all cycles. Depending on the state of the memristor and the initial amplitude of the ac signal, there are two possible scenarios of signal evolution. In the case of low input amplitude the signal is gradually attenuated ([Figure 6c](#)). If the input amplitude is sufficiently high the signal is gradually amplified till it reaches the compliance limit ([Figure 6d](#)). This behavior should lead to a neuromimetic classification device, discriminating various input waveforms according to their initial amplitude. Furthermore, the dynamic change in the output can emulate specific learning processes.

In our system the success of learning depends on the amplitude of the stimulus (initial amplitude) and the state of the memristor (metaplasticity, *vide infra*). It is in close analogy to cortical excitatory and inhibitory neurons that can be excited depending on the amplitude of a recurrent excitatory signal.^{33,76} As long as the stimulus has the amplitude lower than a certain threshold level, the signal vanishes after several cycles ([Figure 6c](#)). When the threshold amplitude is reached, every subsequent cycle yields signals of higher amplitude—

without termination the signal would circulate indefinitely ([Figure 6d](#)). In this experiment the stimulus with the amplitude of 1.9 V_{pp} was sufficient enough to induce long-term response, whereas the signal with the 1.7 V_{pp} amplitude disappeared in time—stimulus got forgotten.

On this basis a simple classification of initial signal amplitudes can be performed: signals with amplitudes lower than 1.85 V_{pp} vanish completely, whereas those of amplitudes equal to 1.85 V_{pp} or higher persist in the feedback loop ([Figure 7a](#)). An amplification of strong and attenuation of weak signals closely resemble processes like natural selection, evolutionary computing, and the so-called St. Matthew algorithm.⁷⁷

Interestingly, these threshold values also undergo gradual evolution owing to the rectifying character of the junction and its memristive properties, and converges to the new equilibrium threshold value of 1.50 V_{pp} ([Figure 7b](#)). Furthermore, this process is fully reversible and application of reverse bias resets the device to its initial condition ([Figure 7c](#)). Therefore, it can be considered as a simple form of synaptic metaplasticity, as this behavior conforms to the definition given by Abraham and Bear, which describes metaplasticity as the ability to modulate the subsequent plasticity (potentiation or depression).⁷⁸ This effect can be attributed to the $Cu^0 \rightarrow Cu^{+2+}$ oxidation, which in turn leads to attenuated SB and thus decreased resistance of the junction. This metaplastic modulation can be induced either by sufficiently high positive bias or by multiple application of the subthreshold input signal, each time followed by its evolution within the feedback loop ([Figure 7d](#)).

CONCLUSIONS

Commercially available lead(II) halides serve as the core material of a memristor that can be easily prepared without humidity control, vacuum, or thermal processing. Memristive

properties of the lead halide-based devices arise from the interface states and the SBH modulation and therefore strongly depend on the nature of the metallic contact. This device offers higher robustness as compared with other memristors and can sustain relatively high currents (up to 10 mA) without degradation of the device. Furthermore, this allows higher operation frequency as compared with filament-based or ionic drift-based memristors. The simplicity of the memristive device and its complex plastic behavior (concomitant STDP, SRDP, and metaplasticity) and presented integration with the reservoir echo state machine system are the most significant advantages of the described system. Electrical simplicity of the ITO|PbI₂|Cu memristors and the input–output compatibility create the possibility of facile concatenation of elements and thus construction of devices with much higher complexity.^{79,80} These assemblies can be used either as more complex neuromimetic nodes⁸¹ or a platform for synthesis of logic functions.⁸² Future development of these devices may encompass both large integration scale leading toward computing systems with distributed memory^{83,84} and discrete devices with increased functionality, for example, in the field of data security.^{85–87} Our system offers learning phenomena at several levels. First, the PbI₂-based memristor has a nonvolatile memory embodied as LRS/HRS. Second, the memristor incorporated in the reservoir system imitates feedback loop-based learning processes like motor-learning. Finally, the metaplasticity of the device enables two additional general states of the device. Moreover, supplemented with an additional linear read-out layer the echo state machine may serve as a signal amplitude classifier, leading to amplification of strong and attenuation of weak signals, according to the so-called St. Matthew algorithm.

EXPERIMENTAL SECTION

Commercially available, analytically pure PbI₂, PbBr₂, and PbCl₂ (Sigma-Aldrich) have been recrystallized for further experiments. ITO-coated glass (Sigma-Aldrich) was washed with detergent, deionized water, isopropanol, and treated with oxygen plasma before spin-coating solutions of PbI₂ (from dimethylformamide) and PbBr₂ and PbCl₂ (from dimethyl sulfoxide). The thicknesses of spin-coated layers were measured with a Bruker DektakXT profiler. Metal contacts are obtained by pressing freshly polished surfaces of silver, gold, platinum, copper, or aluminum wires (cross-sectional area of 3.14 mm²) against the lead halide layer. In order to secure the reproducibility of the contact quality, the electrodes were mounted on standard test needles and a constant force of 0.7 N was applied throughout all experiments.

Electrical measurements were taken in a two-electrode setup where a solid polished piece of metal was the working (+) electrode and the ITO glass substrate served as the counter electrode (–). All measurements were taken under ambient atmosphere at room temperature. Samples after measurements and during the ageing process were kept in humidity-free atmosphere. Current–voltage characteristics were recorded on a Bio-Logic SP150 potentiostat.

The UPS/XPS experiments were performed with a VersaProbeII system (ULVAC-PHI, Chigasaki, Japan) at a base pressure of 3×10^{-7} Pa. The energy resolutions for UPS (He–I, 21.22 eV) and XPS (Al K α , 1486.6 eV) are 100 and 700 meV, respectively. For both methods the experimental error (reproducibility) is estimated to be 50 meV. Ion sputtering was done using Ar-GCIB with the cluster size set to 4000 atoms/cluster, energy of 20 keV, sputtered area of 7 mm \times 7 mm, additionally with Zalar rotation. For UPS, the sample is set to an acceleration potential of –5 V, leading to a much more pronounced SE cut-off. For each depth at a given interval during sputtering, the work function (measured as the difference between photon energy and SE cut-off position) and hole injection barrier

[given by the difference of the substrate Fermi level to the highest occupied molecular orbital (HOMO) onset of the material] are measured by UPS. For each UPS spectrum, the emission features because of the secondary line excitations of the He–I gas discharge are subtracted. As the actual relative intensities of the satellite excitations depend on the He discharge pressure, the secondary line subspectra were adjusted slightly in intensity to the measured UPS spectrum and subtracted incrementally starting with the highest photon energy satellite. The measurement times were kept as short as possible to avoid UV degradation damage of the examined materials. The XPS survey scan spectra were taken at the beginning and at the end of measurement.

The STDP measurements were conducted on Keithley 4200-SCS with the two-electrode setup. The bipolar, triangular shape of the voltage pattern was chosen to induce an anti-Hebbian learning response. The chosen amplitude was ± 1 V and was based on previous experiments. The duration time of the single pulse was 220 ms. Here, the metal and ITO electrodes act as pre- and postsynaptic neurons, respectively. The time interval was decreased from 400 to 20 ms and the synaptic weight was calculated with eq 4

$$\Delta w = \frac{I_{\text{after}} - I_{\text{before}}}{I_{\text{before}}} \times 100\% \quad (4)$$

where I_{before} and I_{after} are the currents measured before and after the stimulation, respectively. The current was measured at +0.2 V before and after applying the voltage pattern. After the stimulation, the device was set either to HRS or LRS with ± 1 V for 10 s.

The SRDP measurements were conducted on an Autolab PGSTAT302N potentiostat with the two-electrode setup, where the working electrode was the Cu electrode, whereas ITO served as the counter electrode. In SRDP, the synaptic weight is solely dependent on the frequency of the spikes applied to the presynaptic electrode. Thirty unipolar spikes of amplitude of +0.5 V and duration of 200 ms were utilized. After each voltage pattern the device was reset to the HRS state with –1 V bias applied for 10 s. The time interval was changed from 5000 to 50 ms. The synaptic weight was measured and calculated as in the STDP measurements.

The reservoir system consists of a Baltazar-01 analog potentiostat (Instytut Fotonowy, Poland); the delay line was obtained via a signal processor DP-02 (Zakład Elektroniki i Automatyki CHIP, Poland), ac source Aim-TTi TGP3152, Aim-TTi WA301 waveform amplifier. Two analog channels of Bio-Logic SP-150 were used to record the outputs from the analog potentiostat and the delay line.

Neuromorphic Simulation. The delay time was 1.5 s and the width of the signal from the ac source 1 s (2.5 Hz, sinusoidal signal) and the initial amplitudes were for 1.7 and 1.9 V_{pp} .

Metaplasticity. The initial signals have the amplitude that changed by 50 mV in the 1–2.2 V_{pp} range. Three cycles $1 V_{\text{pp}} \rightarrow 2.2 V_{\text{pp}} \rightarrow 1 V_{\text{pp}}$ have been recorded one after another and the most positive and most negative current response in each pulse train was determined (Figure S10a–f, see the Supporting Information). Subsequently, the reverse potential of –1 V (120 s) was applied and the sequence cycles $1 V_{\text{pp}} \rightarrow 2.2 V_{\text{pp}} \rightarrow 1 V_{\text{pp}}$ have been recorded. This bias-induced reset was performed twice (Figure S11a–d, see the Supporting Information). The delay time was 1.5 s and the width of the signal from the ac source 1 s (5 Hz, sinusoidal signal).

ASSOCIATED CONTENT

Supporting Information

The Supporting Information is available free of charge on the ACS Publications website at DOI: 10.1021/acsami.9b01841.

Retention data for HRS and LRS; XPS spectra of the surface of the PbI₂ layer on Cu and ITO surfaces were measured before and after sputtering with Ar-GCIB; estimation of the SB volume; SRDP fitting parameters; I – V characteristics with different surface areas of metal electrodes; I – V characteristics of different devices—11, 21, or 101 cycles; metaplasticity in the reservoir system:

the current amplitudes of the untrained system, in response to 1 and 1.4 V_{pp} , repeated 100 times; amplitudes in three cycles $1 V_{pp} \rightarrow 2.2 V_{pp} \rightarrow 1 V_{pp}$ repeated twice; and amplitudes after reset at a $-1 V$ bias (PDF)

AUTHOR INFORMATION

Corresponding Authors

*E-mail: ewlazlak@agh.edu.pl (E.W.).

*E-mail: szacilow@agh.edu.pl (K.S.).

ORCID

E. Wlazlak: 0000-0003-4614-8193

M. Marzec: 0000-0001-9834-3930

Notes

The authors declare no competing financial interest.

ACKNOWLEDGMENTS

The authors acknowledge the support of the National Science Centre (Poland) within the MAESTRO (grant agreement no. UMO-2015/18/A/ST4/00058) and PRELUDIUM (grant agreement no. UMO-2015/19/N/ST5/00533) projects. P.Z. has been partly supported by the EU Project POWR.03.02.00-00-I004/16. The authors thank Dr. Katarzyna Berent for SEM images of the studied layers and Prof. Kapela Pilaka for extremely friendly support.

REFERENCES

- (1) Chang, T.; Jo, S.-H.; Lu, W. Short-Term Memory to Long-Term Memory Transition in a Nanoscale Memristor. *ACS Nano* **2011**, *5*, 7669–7676.
- (2) Yoong, H. Y.; Wu, H.; Zhao, J.; Wang, H.; Guo, R.; Xiao, J.; Zhang, B.; Yang, P.; Pennycook, S. J.; Deng, N.; Yan, X.; Chen, J. Epitaxial Ferroelectric $Hf_{0.5}Zr_{0.5}O_2$ Thin Films and Their Implementations in Memristors for Brain-Inspired Computing. *Adv. Funct. Mater.* **2018**, *28*, 1806037.
- (3) Chua, L. Memristor, Hodgkin-Huxley, and edge of chaos. *Nanotechnology* **2013**, *24*, 383001.
- (4) Chua, L.; Sbitnev, V.; Kim, H. Hodgkin-Huxley axon is made of memristors. *Int. J. Bifurcation Chaos Appl. Sci. Eng.* **2012**, *22*, 1230011.
- (5) Tetzlaff, R. *Memristors and Memristive Systems*; Springer: New York, 2014.
- (6) Adamatzky, A.; Chua, L. *Memristor Networks*; Springer: New York, 2014.
- (7) Huang, W.; Fang, Y.-W.; Yin, Y.; Tian, B.; Zhao, W.; Hou, C.; Ma, C.; Li, Q.; Tsybal, E. Y.; Duan, C.-G.; Li, X. Solid-State Synapse Based on MagnetoElectrically Coupled Memristor. *ACS Appl. Mater. Interfaces* **2018**, *10*, 5649–5656.
- (8) Zhang, A.; Lieber, C. M. Nano-bioelectronics. *Chem. Rev.* **2016**, *116*, 215–257.
- (9) Raes-Hosseini, N.; Park, Y.; Lee, J.-S. Flexible Artificial Synaptic Devices Based on Collagen from Fish Protein with Spike-Timing-Dependent Plasticity. *Adv. Funct. Mater.* **2018**, *28*, 1800553.
- (10) Xing, Y.; Shi, C.; Zhao, J.; Qiu, W.; Lin, N.; Wang, J.; Yan, X. B.; Yu, W. D.; Liu, X. Y. Mesoscopic-Functionalization of Silk Fibroin with Gold Nanoclusters Mediated by Keratin and Bioinspired Silk Synapse. *Small* **2017**, *13*, 1702390.
- (11) Lee, H. E.; Park, J. H.; Kim, T. J.; Im, D.; Shin, J. H.; Kim, D. H.; Mohammad, B.; Kang, I.-S.; Lee, K. J. Novel Electronics for Flexible and Neuromorphic Computing. *Adv. Funct. Mater.* **2018**, *28*, 1801690.
- (12) Singh, R.; Singh, E.; Nalwa, H. S. Inkjet printed nanomaterial based flexible radio frequency identification (RFID) tag sensors for the internet of nano things. *RSC Adv.* **2017**, *7*, 48597–48630.
- (13) Zhang, R.; Jiang, H.; Wang, Z. R.; Lin, P.; Zhuo, Y.; Holcomb, D.; Zhang, D. H.; Yang, J. J.; Xia, Q. Nanoscale diffusive memristor

crossbars as physical unclonable functions. *Nanoscale* **2018**, *10*, 2721–2726.

(14) Chua, L. If it's pinched it's a memristor. *Semicond. Sci. Technol.* **2014**, *29*, 104001.

(15) Di Ventra, M.; Pershin, Y. V.; Chua, L. O. Circuit Elements With Memory: Memristors, Memcapacitors, and Meminductors. *Proc. IEEE* **2009**, *97*, 1717–1724.

(16) Abdelouhab, M.-S.; Lozi, R.; Chua, L. Memfractance: A mathematical paradigm for circuit elements with memory. *Int. J. Bifurcation Chaos Appl. Sci. Eng.* **2014**, *24*, 1430023.

(17) Dirkmann, S.; Kaiser, J.; Wenger, C.; Mussenbrock, T. Filament Growth and Resistive Switching in Hafnium Oxide Memristive Devices. *ACS Appl. Mater. Interfaces* **2018**, *10*, 14857–14868.

(18) Yildirim, H.; Pachter, R. Mechanistic Analysis of Oxygen Vacancy-Driven Conductive Filament Formation in Resistive Random Access Memory Metal/NiO/Metal Structures. *ACS Appl. Mater. Interfaces* **2018**, *10*, 9802–9816.

(19) Kim, S.; Kim, H.; Hwang, S.; Kim, M.-H.; Chang, Y.-F.; Park, B.-G. Analog Synaptic Behavior of a Silicon Nitride Memristor. *ACS Appl. Mater. Interfaces* **2017**, *9*, 40420–40427.

(20) Kim, S.; Choi, S.; Lu, W. Comprehensive Physical Model of Dynamic Resistive Switching in an Oxide Memristor. *ACS Nano* **2014**, *8*, 2369–2376.

(21) Younis, A.; Chu, D.; Li, S. Evidence of Filamentary Switching in Oxide-based Memory Devices via Weak Programming and Retention Failure Analysis. *Sci. Rep.* **2015**, *5*, 13599.

(22) Yang, Y.; Gao, P.; Gaba, S.; Chang, T.; Pan, X.; Lu, W. Observation of conducting filament growth in nanoscale resistive memories. *Nat. Commun.* **2012**, *3*, 732.

(23) Yang, Y.; Lu, W. Nanoscale resistive switching devices: mechanisms and modeling. *Nanoscale* **2013**, *5*, 10076–10092.

(24) Lee, T.-H.; Hwang, H.-G.; Woo, J.-U.; Kim, D.-H.; Kim, T.-W.; Nahm, S. Synaptic Plasticity and Metaplasticity of Biological Synapse Realized in a $KNbO_3$ Memristor for Application to Artificial Synapse. *ACS Appl. Mater. Interfaces* **2018**, *10*, 25673–25682.

(25) Schmitt, R.; Spring, J.; Korobko, R.; Rupp, J. L. M. Design of Oxygen Vacancy Configuration for Memristive Systems. *ACS Nano* **2017**, *11*, 8881–8891.

(26) Hwang, B.; Lee, J.-S. Hybrid Organic-Inorganic Perovskite Memory with Long-Term Stability in Air. *Sci. Rep.* **2017**, *7*, 673.

(27) Bae, Y. C.; Lee, A. R.; Lee, J. B.; Koo, J. H.; Kwon, K. C.; Park, J. G.; Im, H. S.; Hong, J. P. Oxygen Ion Drift-Induced Complementary Resistive Switching in Homo $TiO_x/TiO_y/TiO_x$ and Hetero $TiO_x/TiON/TiO_x$ Triple Multilayer Frameworks. *Adv. Funct. Mater.* **2012**, *22*, 709–716.

(28) Xu, Z.-T.; Jin, K.-J.; Gu, L.; Jin, Y.-L.; Ge, C.; Wang, C.; Guo, H.-Z.; Lu, H.-B.; Zhao, R.-Q.; Yang, G.-Z. Evidence for a Crucial Role Played by Oxygen Vacancies in $LaMnO_3$ Resistive Switching Memories. *Small* **2012**, *8*, 1279–1284.

(29) Younis, A.; Chu, D.; Lin, X.; Yi, J.; Dang, F.; Li, S. High-Performance Nanocomposite Based Memristor with Controlled Quantum Dots as Charge Traps. *ACS Appl. Mater. Interfaces* **2013**, *5*, 2249–2254.

(30) Sawa, A. Resistive switching in transition metal oxides. *Mater. Today* **2008**, *11*, 28–36.

(31) Baeumer, C.; Schmitz, C.; Marchewka, A.; Mueller, D. N.; Valenta, R.; Hackl, J.; Raab, N.; Rogers, S. P.; Khan, M. I.; Nemsak, S.; Shim, M.; Menzel, S.; Schneider, C. M.; Waser, R.; Dittmann, R. Quantifying redox-induced Schottky barrier variations in memristive devices via in operando spectromicroscopy with graphene electrodes. *Nat. Commun.* **2016**, *7*, 12398.

(32) Gao, Z.; Proietti-Onori, M.; Lin, Z.; ten Brinke, M. M.; Boele, H.-J.; Potters, J.-W.; Ruigrok, T. J. H.; Hoebeek, F. E.; De Zeeuw, C. I.; Chris, I. Excitatory Cerebellar Nucleocortical Circuit Provides Internal Amplification during Associative Conditioning. *Neuron* **2016**, *89*, 645–657.

(33) McCormick, D. A.; McGinley, M. J.; Salkoff, D. B. Brain state dependent activity in the cortex and thalamus. *Curr. Opin. Neurobiol.* **2015**, *31*, 133–140.

- (34) van Gaal, S.; Lamme, V. A. F. Unconscious High-Level Information Processing: Implication for Neurobiological Theories of Consciousness. *Neuroscientist* **2012**, *18*, 287–301.
- (35) Indiveri, G.; Linares-Barranco, B.; Legenstein, R.; Deligeorgis, G.; Prodromakis, T. Integration of nanoscale memristor synapses in neuromorphic computing architectures. *Nanotechnology* **2013**, *24*, 384010.
- (36) Liu, B.; Liu, Z.; Chiu, I.-S.; Di, M.; Wu, Y.; Wang, J.-C.; Hou, T.-H.; Lai, C.-S. Programmable Synaptic Metaplasticity and below Femtojoule Spiking Energy Realized in Graphene-Based Neuromorphic Memristor. *ACS Appl. Mater. Interfaces* **2018**, *10*, 20237–20243.
- (37) Lv, Z.; Zhou, Y.; Han, S.-T.; Roy, V. A. L. From biomaterial-based data storage to bio-inspired artificial synapse. *Mater. Today* **2018**, *21*, 537–552.
- (38) Ielmini, D. Brain-inspired computing with resistive switching memory (RRAM): Devices, synapses and neural networks. *Microelectron. Eng.* **2018**, *190*, 44–53.
- (39) Walter, F.; Röhrbein, F.; Knoll, A. Neuromorphic implementations of neurobiological learning algorithms for spiking neural networks. *Neural Network* **2015**, *72*, 152–167.
- (40) Athanasiou, V.; Konkoli, Z. On using reservoir computing for sensing applications: exploring environment-sensitive memristor networks. *Int. J. Parallel, Emergent Distributed Syst.* **2018**, *33*, 367–386.
- (41) Sillin, H. O.; Aguilera, R.; Shieh, H.-H.; Avizienis, A. V.; Aono, M.; Stieg, A. Z.; Gimzewski, J. K. A theoretical and experimental study of neuromorphic atomic switch networks for reservoir computing. *Nanotechnology* **2013**, *24*, 384004.
- (42) Du, C.; Cai, F.; Zidan, M. A.; Ma, W.; Lee, S. H.; Lu, W. D. Reservoir computing using dynamic memristors for temporal information processing. *Nat. Commun.* **2017**, *8*, 2204.
- (43) Larger, L.; Baylón-Fuentes, A.; Martinenghi, R.; Udaltsov, V. S.; Chembo, Y. K.; Jacquot, M. High-Speed Photonic Reservoir Computing Using a Time-Delay-Based Architecture: Million Words per Second Classification. *Phys. Rev. X* **2017**, *7*, 011015.
- (44) Yi, Y.; Liao, Y.; Wang, B.; Fu, X.; Shen, F.; Hou, H.; Liu, L. FPGA based spike-time dependent encoder and reservoir design in neuromorphic computing processors. *Microprocess. Microsyst.* **2016**, *46*, 175–183.
- (45) Jaeger, H. *The “Echo State” Approach To Analysing and Training Recurrent Neural Networks-with an Erratum Note*; GMD Report 148; German National Research Center for Information Technology, 2001.
- (46) Jaeger, H.; Haas, H. Harnessing Nonlinearity: Predicting Chaotic Systems and Saving Energy in Wireless Communication. *Science* **2004**, *304*, 78–80.
- (47) Tanaka, G.; Nakane, R.; Yamane, T.; Takeda, S.; Nakano, D.; Nakagawa, S.; Hirose, A. Waveform Classification by Memristive Reservoir Computing. In *Neural Information Processing*; Liu, D., Xie, S., Li, Y., Zhao, D., El-Alfy, E. M., Eds.; Springer: Cham, Switzerland, 2017; Vol. 4.
- (48) Saparov, B.; Mitzi, D. B. Organic-inorganic perovskites: Structural versatility for functional materials design. *Chem. Rev.* **2016**, *116*, 4558–4596.
- (49) Mitzi, D. B. Solution-processed inorganic semiconductors. *J. Mater. Chem.* **2004**, *14*, 2355–2365.
- (50) Mei, F.; Shen, H.; Li, Y.; Li, L.; Zang, G.; Zhou, M.; Ti, R.; Yang, D.; Huang, F.; Lu, X.; Zhu, J. Combination of conductive filaments and Schottky behavior in multifunctional $\text{Sn}_{1-x}\text{Cu}_x\text{O}_{2-\delta}$ memristor. *Appl. Phys. Lett.* **2017**, *111*, 143503.
- (51) Wang, J.; Pan, R.; Cao, H.; Wang, Y.; Liang, L.; Zhang, H.; Gao, J.; Zhuge, F. Anomalous rectification in a purely electronic memristor. *Appl. Phys. Lett.* **2016**, *109*, 143505.
- (52) Adhikari, S. P.; Sah, M. P.; Kim, H.; Chua, L. O. Three Fingerprints of Memristor. *IEEE Trans. Circuits Syst.* **2013**, *60*, 3008–3021.
- (53) Han, U.-B.; Lee, J.-S. Bottom-up synthesis of ordered metal/oxide/metal nanodots on substrates for nanoscale resistive switching memory. *Sci. Rep.* **2016**, *6*, 25537.
- (54) Bloch, P. D.; Hodby, J. W.; Jenkins, T. E.; Stacey, D. W.; Lang, G.; Levy, F.; Schwab, C. Electronic transport and cyclotron resonance in 2H-PbI₂. *J. Phys. C: Solid State Phys.* **1978**, *11*, 4997–5003.
- (55) Tung, R. T. Recent advances in Schottky barrier concepts. *Mater. Sci. Eng., R* **2001**, *35*, 1–138.
- (56) Mönch, W. Barrier heights of real Schottky contacts explained by metal-induced gap states and lateral inhomogeneities. *J. Vac. Sci. Technol., B: Microelectron. Nanometer Struct.–Process., Meas., Phenom.* **1999**, *17*, 1867–1876.
- (57) Nishimura, T.; Kita, K.; Toriumi, A. Evidence for strong Fermi-level pinning due to metal-induced gap states at metal/germanium interface. *Appl. Phys. Lett.* **2007**, *91*, 123123.
- (58) Vázquez, H.; Gao, W.; Flores, F.; Kahn, A. Energy level alignment at organic heterojunctions: Role of the charge neutrality level. *Phys. Rev. B: Condens. Matter Mater. Phys.* **2005**, *71*, 041306.
- (59) Preobrajenski, A.; Krasnikov, S.; Vinogradov, A.; Ng, M. L.; Käämbre, T.; Cafolla, A.; Mårtensson, N. Adsorption-induced gap states of h-B N on metal surfaces. *Phys. Rev. B: Condens. Matter Mater. Phys.* **2008**, *77*, 085421.
- (60) Sopiha, K. V.; Malyi, O. I.; Persson, C.; Wu, P. Band gap modulation of SrTiO₃ upon CO₂ adsorption. *Phys. Chem. Chem. Phys.* **2017**, *19*, 16629–16637.
- (61) Gu, C.; Lee, J.-S. Flexible Hybrid Organic–Inorganic Perovskite Memory. *ACS Nano* **2016**, *10*, 5413–5418.
- (62) Crispin, X.; Geskin, V.; Crispin, A.; Cornil, J.; Lazzaroni, R.; Salaneck, W. R.; Brédas, J.-L. Characterization of the Interface Dipole at Organic/Metal Interfaces. *J. Am. Chem. Soc.* **2002**, *124*, 8131–8141.
- (63) Vázquez, H.; Dappe, Y. J.; Ortega, J.; Flores, F. Energy level alignment at metal/organic semiconductor interfaces: “Pillow” effect, induced density of interface states, and charge neutrality level. *J. Chem. Phys.* **2007**, *126*, 144703.
- (64) Joshua Yang, J.; Strukov, D. B.; Stewart, D. R. Memristive devices for computing. *Nat. Nanotechnol.* **2013**, *8*, 13.
- (65) Li, Y.; Wang, Z.; Midya, R.; Xia, Q.; Yang, J. J. Review of memristor devices in neuromorphic computing: materials sciences and device challenges. *J. Phys. D: Appl. Phys.* **2018**, *51*, 503002.
- (66) Caravelli, F.; Carbajal, J. Memristors for the Curious Outsiders. *Technologies* **2018**, *6*, 118.
- (67) Uchaikin, V. V.; Sibatov, R. T. Fractional theory for transport in disordered semiconductors. *Commun. Nonlinear Sci. Numer. Simul.* **2008**, *13*, 715–727.
- (68) Choo, K. Y.; Muniandy, S. V.; Woon, K. L.; Gan, M. T.; Ong, D. S. Modeling anomalous charge carrier transport in disordered organic semiconductors using the fractional drift-diffusion equation. *Org. Electron.* **2017**, *41*, 157–165.
- (69) Sibatov, R. T.; Uchaikin, V. V. Fractional differential approach to dispersive transport in semiconductors (in Russian). *Usp. Fiz. Nauk* **2009**, *179*, 1079–1104.
- (70) Choo, K. Y.; Muniandy, S. V. Fractional dispersive transport in inhomogeneous organic semiconductors. *Int. J. Mod. Phys.: Conf. Ser.* **2015**, *36*, 1560008.
- (71) Pu, Y.-F.; Yuan, X. Fracmemristor: Fractional-order memristor. *IEEE Access* **2016**, *4*, 1872–1888.
- (72) Tenreiro Machado, J. Fractional generalization of memristor and higher order elements. *Commun. Nonlinear Sci. Numer. Simul.* **2013**, *18*, 264–275.
- (73) Chua, L. Memristor-The missing circuit element. *IEEE Trans. Circuit Theory* **1971**, *18*, 507–519.
- (74) Konkoli, Z.; Nichele, S.; Dale, M.; Stepney, S. Reservoir computing with computational matter. In *Computational Matter*; Stepney, S., Rasmussen, S., Amos, M., Eds.; Springer: Cham, Switzerland, 2018.
- (75) Yuste, R. From the neuron doctrine to neural networks. *Nat. Rev. Neurosci.* **2015**, *16*, 1–11.
- (76) Haider, B.; Duque, A.; Hasenstaub, A. R.; McCormick, D. A. Neocortical Network Activity In Vivo Is Generated through a Dynamic Balance of Excitation and Inhibition. *J. Neurosci.* **2006**, *26*, 4535–4545.

- (77) Holy Bible, New International Version, Matthew 25, 29-30: "For whoever has will be given more, and they will have an abundance. Whoever does not have, even what they have will be taken from them. And throw that worthless servant outside, into the darkness, where there will be weeping and gnashing of teeth", 1973.
- (78) Abraham, W. C.; Bear, M. F. Metaplasticity: the plasticity of synaptic plasticity. *Trends Neurosci.* **1996**, *19*, 126–130.
- (79) Kasai, S.; Aono, M.; Naruse, M. Amoeba-inspired computing architecture implemented using charge dynamics in parallel capacitance network. *Appl. Phys. Lett.* **2013**, *103*, 163703.
- (80) Saito, K.; Suefuji, N.; Kasai, S. Amoeba-inspired electronic solution-searching system and its application to finding walking maneuver of a multi-legged robot. *Proceedings 48th International Symposium on Multiple-Valued Logic*, 2019; pp 127–131.
- (81) Athanasiou, V.; Konkoli, Z. On using reservoir computing for sensing applications: exploring environment-sensitive memristor networks. *Int. J. Parallel, Emergent Distributed Syst.* **2017**, *33*, 367–386.
- (82) Gharpinde, R.; Thangkhiew, P. L.; Datta, K.; Sengupta, I. A Scalable In-Memory Logic Synthesis Approach Using Memristor Crossbar. *IEEE Trans. Very Large Scale Integr. Syst.* **2018**, *26*, 355–366.
- (83) Li, C.; Hu, M.; Li, Y.; Jiang, H.; Ge, N.; Montgomery, E.; Zhang, J.; Song, W.; Dávila, N.; Graves, C. E.; Li, Z.; Strachan, J. P.; Lin, P.; Wang, Z.; Barnell, M.; Wu, Q.; Williams, R. S.; Yang, J. J.; Xia, Q. Analogue signal and image processing with large memristor crossbars. *Nat. Electron.* **2018**, *1*, 52–59.
- (84) Xia, Q.; Yang, J. J. Memristive crossbar arrays for brain-inspired computing. *Nat. Mater.* **2019**, *18*, 309–323.
- (85) Jiang, H.; Belkin, D.; Savel'ev, S. E.; Lin, S.; Wang, Z.; Li, Y.; Joshi, S.; Midya, R.; Li, C.; Rao, M.; Barnell, M.; Wu, Q.; Yang, J. J.; Xia, Q. A novel true random number generator based on a stochastic diffusive memristor. *Nat. Commun.* **2017**, *8*, 882.
- (86) Rai, V. K.; Tripathy, S.; Mathew, J. Memristor based Random Number Generator: Architectures and Evaluation. *Procedia Comput. Sci.* **2018**, *125*, 576–583.
- (87) Yang, C.; Hu, Q.; Yu, Y.; Zhang, R.; Yao, Y.; Cai, J. Memristor-Based Chaotic Circuit for Text/Image Encryption and Decryption, 2015 8th International Symposium on Computational Intelligence and Design (ISCID), Dec 12–13, 2015; pp 447–450.

Supporting Information

Memristor in a Reservoir System – Experimental Evidence for High Level Computing and Neuromorphic Behavior of PbI_2

E. Wlazlak,^{a,b} M. Marzec,^a P. Zawal,^{ac} and K. Szacilowski^{a*}*

^aAGH University of Science and Technology, Academic Centre for Materials and Nanotechnology, al. A. Mickiewicza 30, 30-059 Kraków, Poland

^bFaculty of Chemistry, Jagiellonian University, ul. Gronostajowa 2, 30-060 Kraków, Poland

^cFaculty of Physics and Applied Computer Science AGH University of Science and Technology al. A. Mickiewicza 30, 30-059 Kraków, Poland

[*ewlazlak@agh.edu.pl](mailto:ewlazlak@agh.edu.pl), szacilow@agh.edu.pl

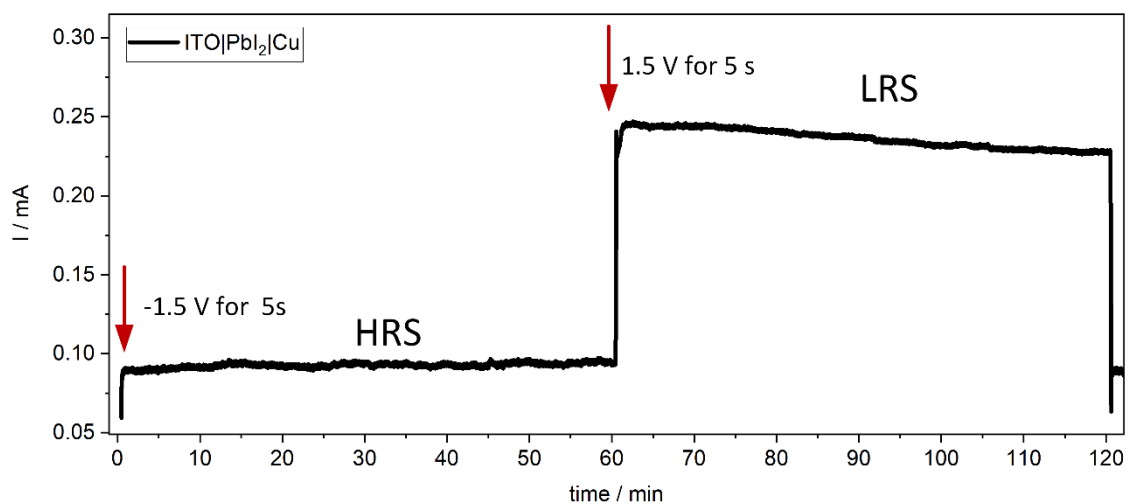


Figure S1. Current vs time measured for 60 min of the device in HRS and LRS at 0.15 V. The state of the device was changed with pulses ± 1.5 V (5 s)

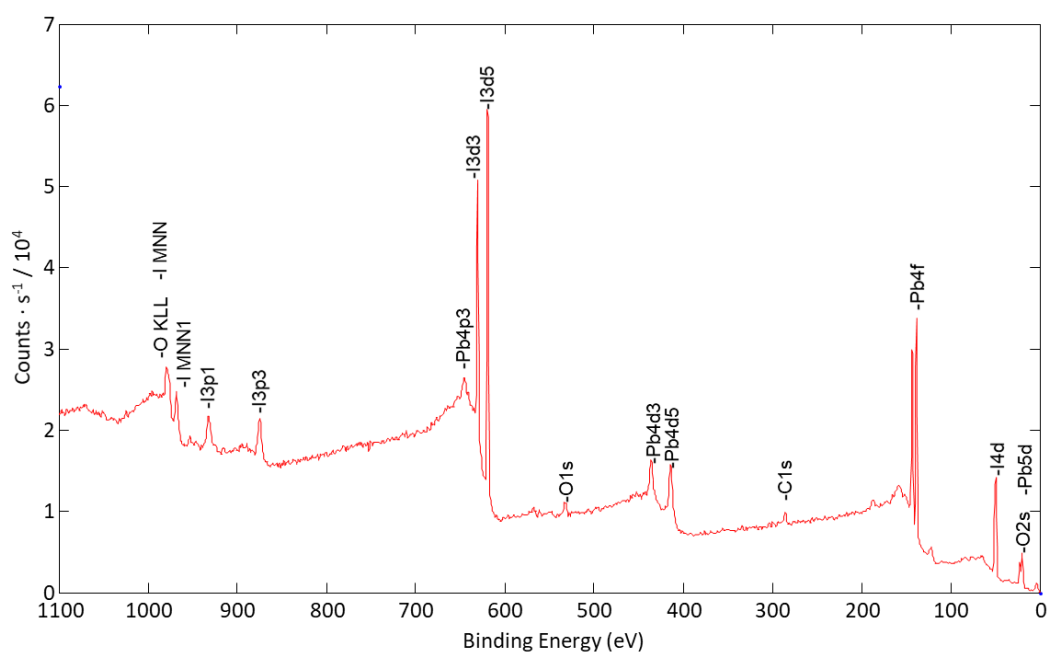


Figure S2. XPS survey scan of as-received surface of PbI_2 sample deposited on polycrystalline Cu surface. Main signals originate from Pb, I, C and O content.

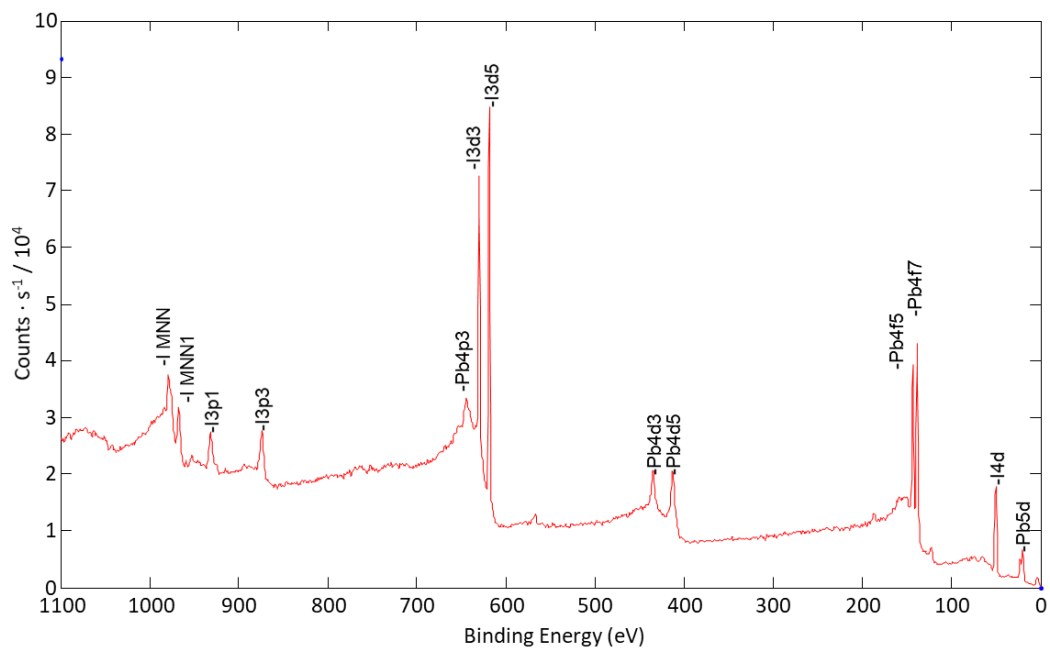


Figure S3. XPS survey scan of sputtered surface of PbI₂ sample deposited on polycrystalline Cu surface after sputtering with Argon Gas Cluster Ion Beam. Main signals originate from Pb and I content only.

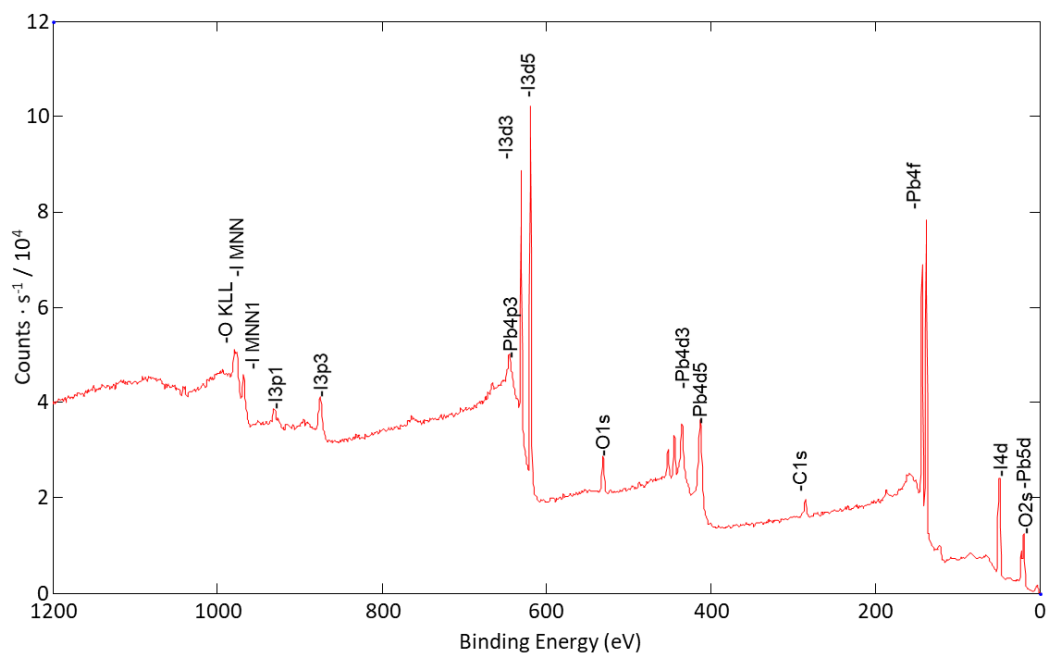


Figure S4. XPS survey scan of as-received surface of PbI₂ on ITO sample. Main signals originate from Pb, I, C and O content.

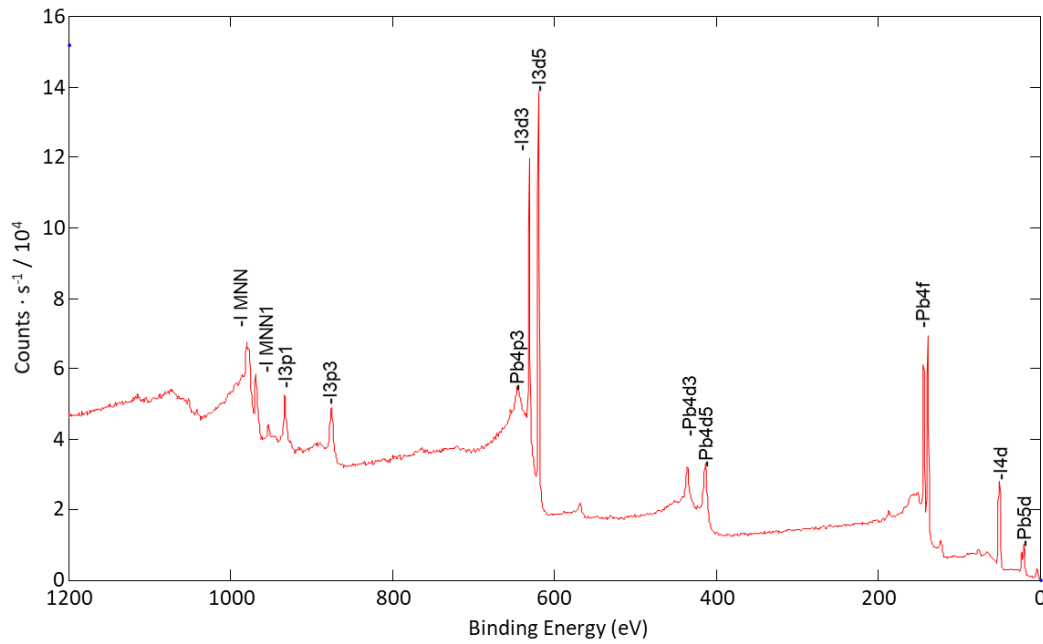


Figure S5. XPS survey scan of sputtered surface of PbI₂ on ITO sample after sputtering with Argon Gas Cluster Ion Beam. Main signals originate from Pb and I content only.

The estimation of the Schottky barrier volume: To investigate the Schottky behaviour at PbI₂|Cu interface we assumed the following equivalent circuit presented in Figure S6, a. This choice is motivated by the shape of the hysteresis loop observed in the *I-V* scan. In the 0 V → 1.5 V direction scan, at around 0.5 V a gradual switch from HRS to LRS occurs. This process can be modeled with the serial connection of the Schottky diode and resistor R₁. Above this potential and in the reverse direction scan from 1.5 V → -1.5 V the current response is Ohmic and can be attributed to serial connection of R₁ and R₂ resistors.

To extract the resistance values we have plotted the Schottky-like part of the hysteresis loop and fitted linear functions to both regimes of the memristor's resistance presented in Figure S6, b. The calculated resistance values are: R₁+R₂ = 414 Ω (HRS regime), R₁ = 131 Ω (LRS regime) and R₂ = 283 Ω. To calculate the reverse current of the diode we have subtracted the ohmic

component in the HRS regime (i.e. in the potential range from ~ 0.3 V to -1.5 V). The obtained value of the reverse current was estimated to be $3.98 \mu\text{A}$.

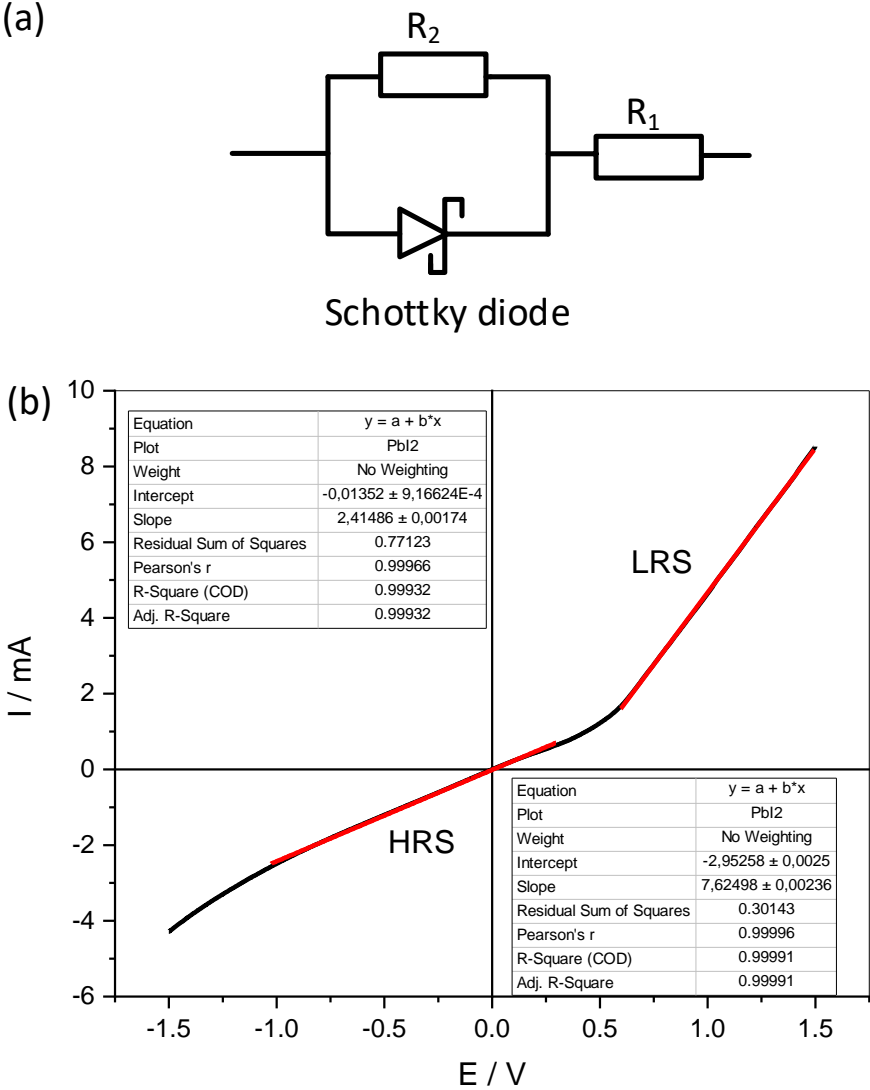


Figure S6. The equivalent circuit used to estimation of the Schottky barrier value (a), the fitting regimes and parameters to Schottky-like fragments of the hysteresis loop.

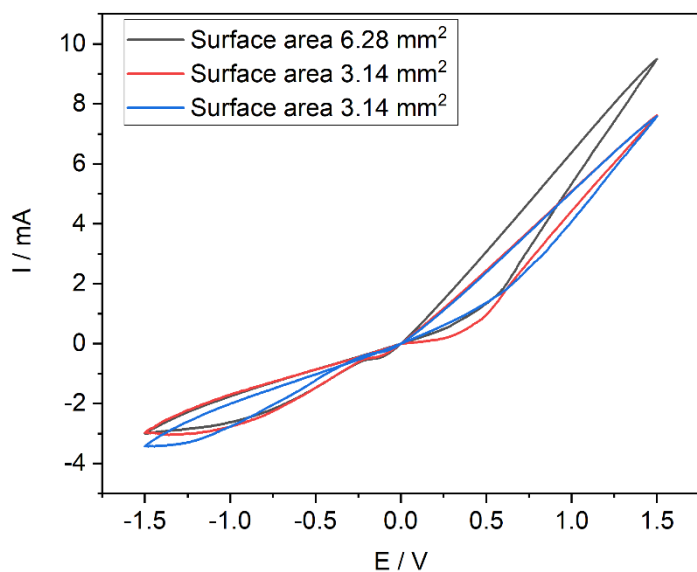


Figure S7. Current-voltage characteristics of different PbI_2/Cu memristors measured with two different metal surface areas.

Table S1. Parameters of exponential fit for presented SRDP pattern.

Model	ExpDec1
Equation	$y = A1 \cdot \exp(-x/t1) + y0$
Plot	B
y0	6.29001 ± 10.95033
A1	34.07961 ± 9.64261
t1	2459.5288 ± 1697.8695
Reduced Chi-Sqr	30.99935
R-Square (COD)	0.99999
Adj. R-Square	0.99999

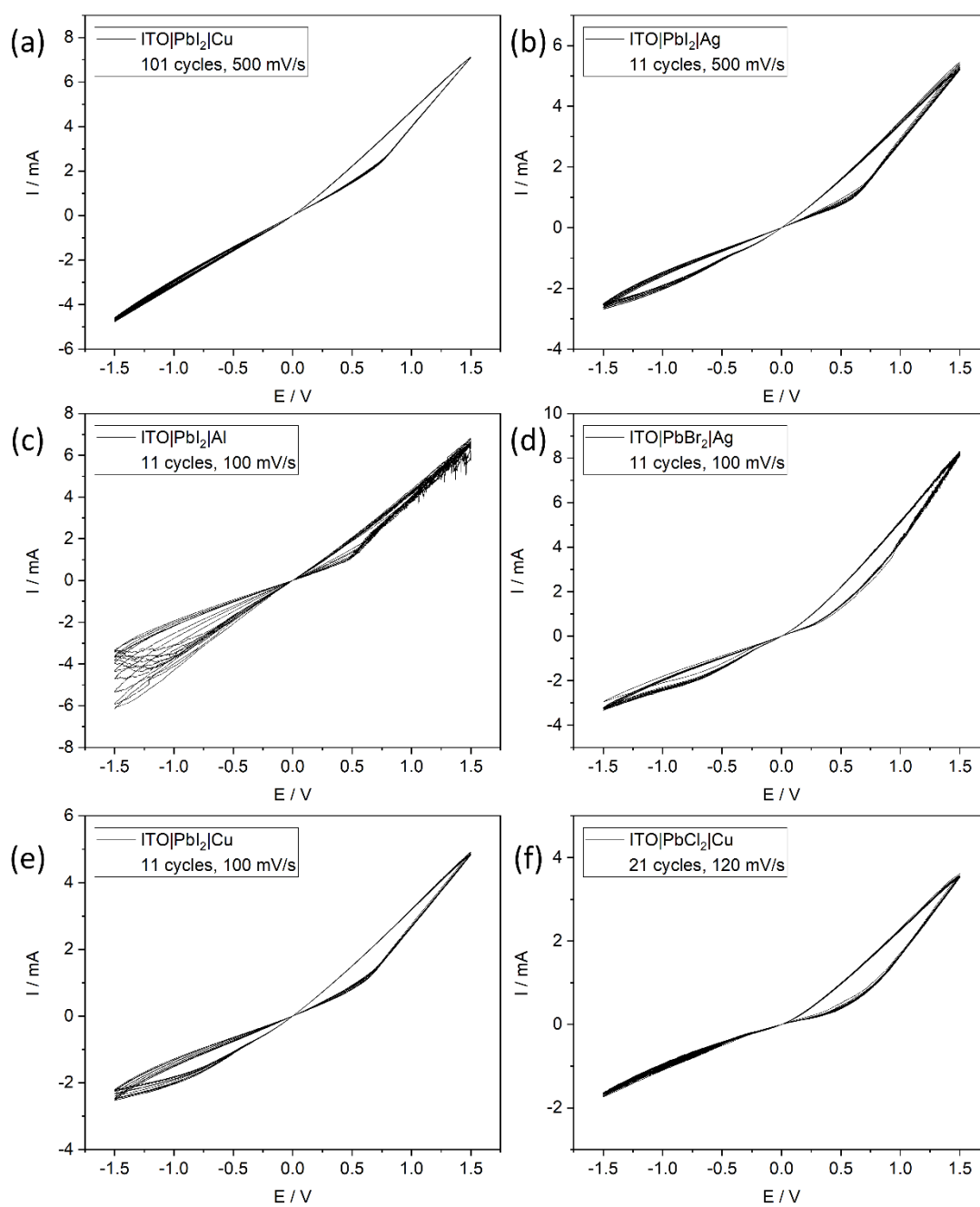


Figure S8. Current-voltage characteristics of different lead(II) halide memristors measured with different metal electrodes at scan rates – several cycles.

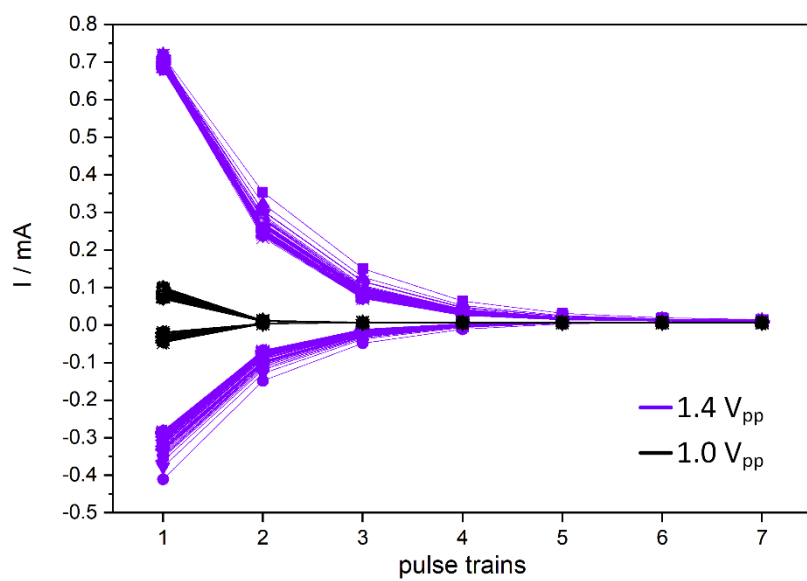


Figure S9. Maximum and the minimum of the current amplitude of untrained system, in the response to $1 V_{pp}$, $1.4 V_{pp}$, amplitude when the initial signal repeated 100 times.

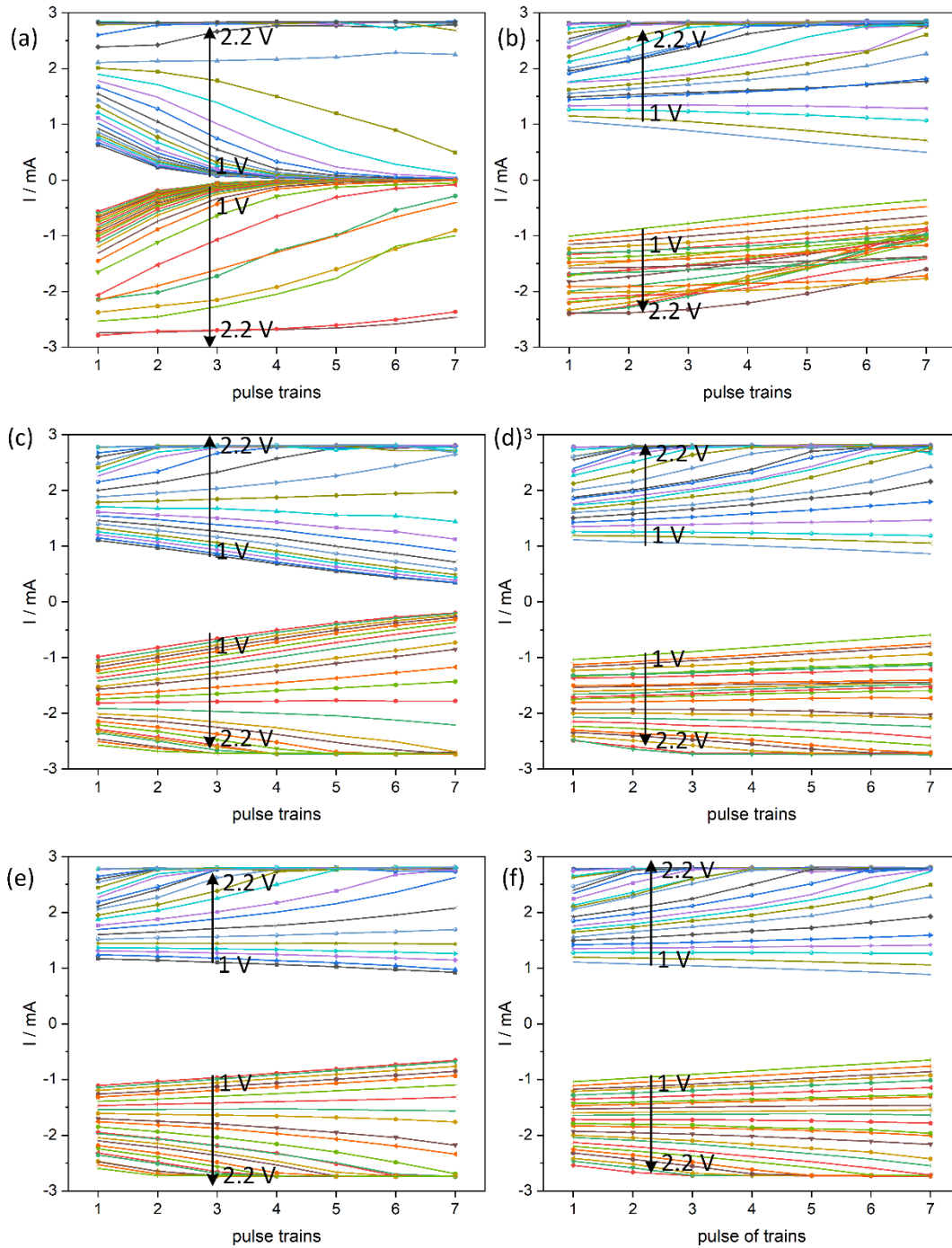


Figure S10. Maximum and minimum of the current amplitude of each pulse trains of $1\text{--}2.2 V_{pp}$ range. Three cycles in $1 V_{pp} \rightarrow 2.2 V_{pp} \rightarrow 1 V_{pp}$ range recorded one after another. The initial amplitude of untrained system at $1 V_{pp} \rightarrow 2.2 V_{pp}$ range (a), trained system at $2.2 V_{pp} \rightarrow 1 V_{pp}$ range (b), trained system at $1 V_{pp} \rightarrow 2.2 V_{pp}$ range (c), trained system at $2.2 V_{pp} \rightarrow 1 V_{pp}$ (d), trained system at $1 V_{pp} \rightarrow 2.2 V_{pp}$ range (e), trained system at $2.2 V_{pp} \rightarrow 1 V_{pp}$ range (f).

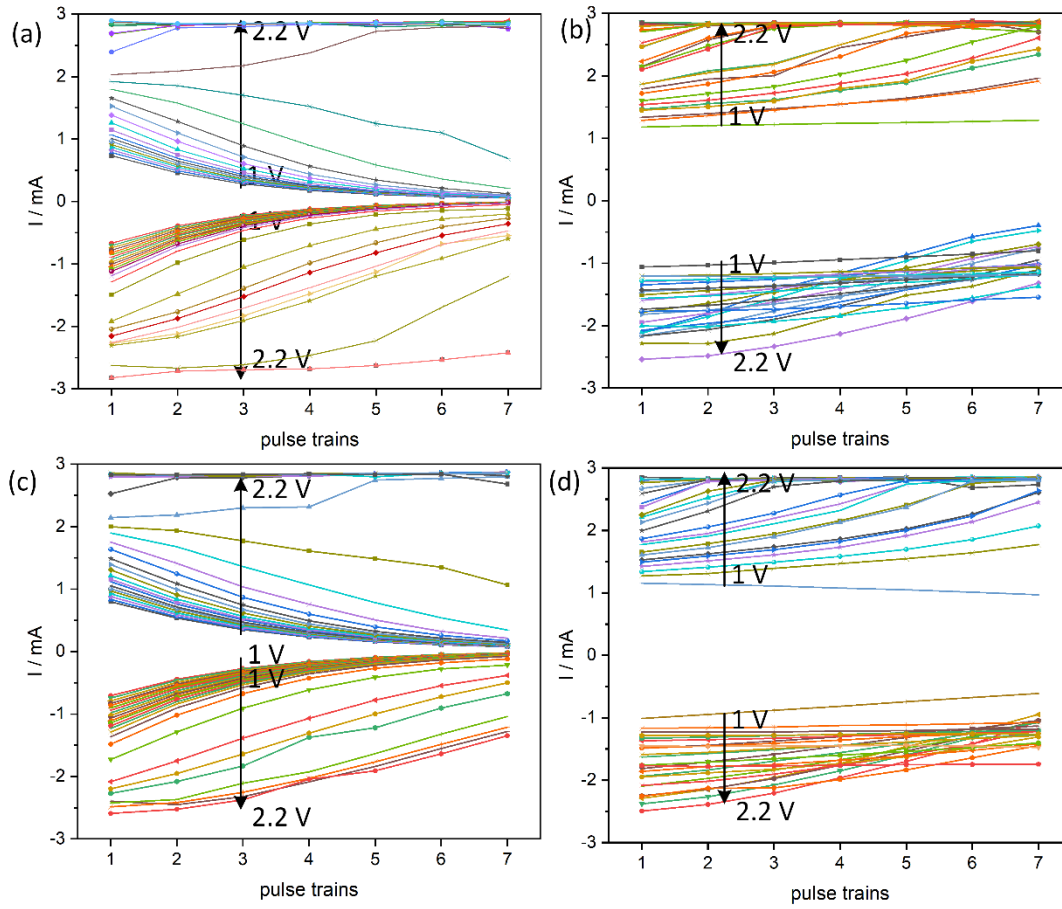
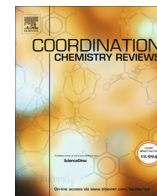


Figure S11. Maximum and minimum of the current amplitude of each pulse trains of 1–2.2 V_{pp} range. The trained system after first reset by -1 V bias (120 s): the initial amplitude of system at 1 V_{pp} → 2.2 V_{pp} range (a) and at 2.2 V_{pp} → 1 V_{pp} range (b). The trained system after second reset by -1 V bias (120 s): the initial amplitude of system at 1 V_{pp} → 2.2 V_{pp} range (c) and at 2.2 V_{pp} → 1 V_{pp} range (d).



Review

Molecules, semiconductors, light and information: Towards future sensing and computing paradigms



Kacper Pilarczyk^{a,*}, Ewelina Właźlak^{a,b,*}, Dawid Przychyna^{a,c}, Andrzej Blachecki^{a,d}, Agnieszka Podborska^a, Vasileios Anathasiou^e, Zoran Konkoli^e, Konrad Szaciłowski^{a,*}

^aAGH University of Science and Technology, Academic Centre for Materials and Nanotechnology, al. Mickiewicza 30, 30-059 Kraków, Poland

^bJagiellonian University, Faculty of Chemistry, ul. Gronostajowa 2, 30-387 Kraków, Poland

^cAGH University of Science and Technology, Faculty of Physics and Applied Computer Science, al. Mickiewicza 30, 30-059 Kraków, Poland

^dAGH University of Science and Technology, Faculty of Non-Ferrous Metals, al. Mickiewicza 30, 30-059 Kraków, Poland

^eChalmers University of Technology, Department of Microtechnology and Nanoscience, SE-412 96 Gothenburg, Sweden

ARTICLE INFO

Article history:

Received 14 February 2018

Received in revised form 12 March 2018

Accepted 14 March 2018

Keywords:

Molecular logic devices
Chemical sensing
Memristive systems
Photoelectrochemistry
Reservoir computing

ABSTRACT

Over the last few years we have witnessed a great progress in the research devoted to unconventional computing – an unorthodox approach to information handling. It includes both novel algorithms and computing paradigms as well as completely new elements of circuitry: whole organisms (e.g., *Physarum* species), DNA, enzymes, various biomolecules, molecular and nanoparticulate materials. One of the biggest challenges in this field is the realisation of *in-materio* computing – i.e., the utilisation of properties of pristine materials, instead of high-tech structures – for advanced information processing. In this review we present recent achievements in the design of logic devices (binary, ternary and fuzzy) implemented in molecular and nanoscale components, photoelectrochemical chemosensing, photoactive memristive devices and reservoir computing systems. A common denominator for all these devices is the involvement of molecular species, semiconducting nanoparticles and light in information processing.

© 2018 Elsevier B.V. All rights reserved.

Contents

1. Introduction	23
2. Photoelectrochemical sensors	24
3. Photoelectrochemical logic gates – The Boolean algebra and more	25
4. Photomemristive and neuromimetic devices	30
5. Reservoir computing and its sensing applications	34
6. Signal analysis and other applications	36
7. Conclusions	37
Acknowledgements	37
References	38

1. Introduction

In the 21st century information is one of the most valued goods. It is being collected, transmitted, stored, and encrypted using the

most sophisticated techniques. Information is a notion that defies simple definitions. In the most general terms it was described by Norbert Wiener “Information is information, not matter or energy” [1]. It has been agreed, however, that information cannot exist without a carrier (matter or energy) [2]. In this review we will focus on various information carriers in the nano-world: ions, molecules, nanostructures, and their participation in simple acts of information processing, which utilise energy in the form of light and electric potential. This field, at least in the area of the binary

* Corresponding authors at: AGH University of Science and Technology, Academic Centre for Materials and Nanotechnology, al. Mickiewicza 30, 30-059 Kraków, Poland.

E-mail addresses: kpilarcz@agh.edu.pl (K. Pilarczyk), ewlzlak@agh.edu.pl (E. Właźlak), szacilow@agh.edu.pl (K. Szaciłowski).

logic, is highly advanced [3–7], however other logical systems are underrepresented in at molecular scale [8–14]. Information can be processed at different abstraction levels: syntactic, semantic and pragmatic. The syntactic level describes the formal relations between elements of the language and is necessary for automated information processing (e.g., as a stream of zeros and ones). At this level of complexity any meaning of transmitted or processed information is neglected. At the semantic level the stream of symbols becomes a message. Still, it can be handled and stored without any context and irrespectively of its pragmatic value. At the pragmatic level the context is introduced, which gives information its practical value (of economical, psychological or political character) that depends also on time. Usually delayed information is less valuable and correct predictions of near future are of the high value [15].

The classical approach to information processing is based on the Boolean logic [16]. All information to be transmitted, stored or processed is encoded as a stream of '0' and '1' characters. Due to its simplicity the technology is very efficient and noise resistant. At the same time its use poses severe conceptual problems and requires additional steps of conversion into a digital signal. In many cases it is seamless, but there are numerous problems that can be easily solved with the use of multi-valued logic systems. One of the examples is the SQL (structural query language) which uses the ternary logic for processing of incomplete sets of data [17].

The fuzzy logic may be perceived as a generalisation of any discrete logic system. The principal objective of the fuzzy logic is the formalisation of typical human information processing capabilities: (i) reasoning in imprecise environment on the basis of incomplete or uncertain information and (ii) performing complex physical and mental tasks (walking, driving, playing musical instruments and writing review papers) without any numerical measurements and computation [18]. This is beneficial for any systems which include a user/machine interface.

The neuromorphic computation has emerged as a relatively well-defined paradigm for the type of computation described above. A natural candidate for the realisation of the neuromorphic computation is an artificial neural network. The reservoir computing branched off from these developments, and matured into a subset of techniques for neuromorphic computation [19–23]. A reservoir computer consists of two components, a dynamical system that serves as a reservoir of states, and a readout layer. In very simplistic terms, the reservoir computer can be seen as a finite state automaton that accepts time series data as an input, and makes transitions between the internal states of the reservoir, accordingly. The readout layer is used only to access the results of computation. The key idea behind this construct is that one never tries to carefully engineer the reservoir part, only the readout layer. The reservoir computing technique has been used for plethora of applications in health [24], bridge monitoring [25], optical pattern recognition [26], or other types of control systems that exploit machine learning techniques [26–28]. The method has also found an extensive use in the area of sensing [29–39], as will be discussed later. A generic theory of using reservoir computing for sensing, the SWEET sensing algorithm, has been recently developed [40].

2. Photoelectrochemical sensors

The first phase of the sensing process gives us merely syntactic knowledge about the sensor response to the state of environment, without any significance (semantics) or value (pragmatics). In order to determine the value of the information obtained, it is necessary to place it in the previously established semantic frame – in the case of photoelectrochemical (PEC) sensor devices our

framework takes the form of a calibration curve with specified precision of obtained photocurrent amplitudes in regard to analyte concentrations [41,42].

In most cases, PEC sensors are implemented in a three-electrode system, and the mechanism of operation is based on the internal photoelectric effect of a semiconductor-based working electrode (assembled on a conducting substrate), coupled with a reference electrode (e.g., saturated silver chloride or saturated calomel electrodes) and a counter electrode (e.g., platinum wire), all in the presence of electrolyte containing donor D/D^+ and acceptor A/A^- species. Photogenerated charge carriers from the semiconductor can move to the conducting substrate or to the counter electrode (with corresponding oxidation/reduction of donor (D/D^+)/ acceptor (A/A^-) species in the electrolyte), resulting in anodic or cathodic photocurrents, respectively. By controlling the applied potential, the photoelectrochemical photocurrent switching (PEPS) effect can be observed [43–45].

In general, the PEC sensing strategy can be classified as dependent on: electron transfer, energy transfer, ion exchange or reactant determinant mechanisms (Fig. 1) [46]. *Electron transfer* strategies can be regulated through the applied potential [47,48], the promotion of competitive electron processes [47,49,50] or the use of hybrid systems with energy levels matched to enhance the photocurrent response [51,52]. The latter approach provides an important advantages such as possible photosensitization and higher energy conversion efficiency due to more efficient charge separation [53]. *Energy transfer* strategies can be divided into three types: surface plasmon resonance (SPR), resonant energy transfer and chemiluminescence-based energy transfer. The SPR phenomenon is based on collective surface oscillations of electrons induced by incident light. Surface plasmons which undergo dumping may induce excitation within adjacent semiconductor, which, in the presence of a proper electron donor, results in the signal amplification [54]. In the case of resonant energy transfer, competitive processes of interparticle interactions in the form of non-radiative or radiative electron-hole recombination take place. It allows either the exciton energy transfer from semiconductor

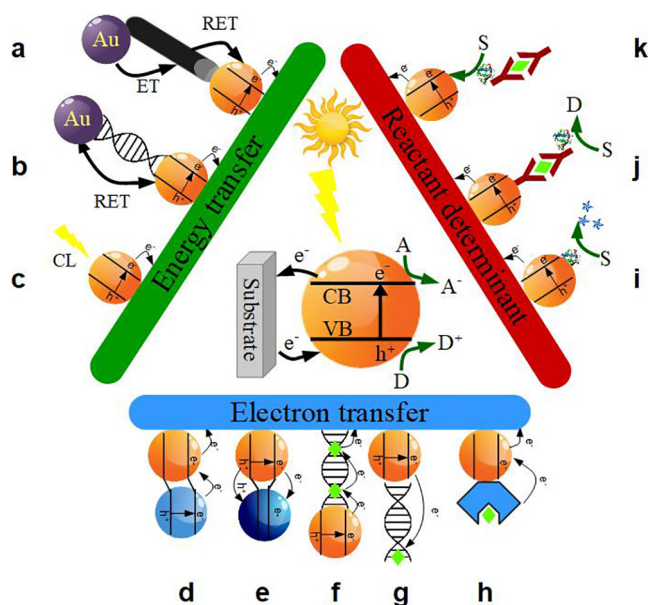


Fig. 1. A schematic illustration of various strategies for creating PEC sensors: surface plasmon resonance (a), resonant energy transfer (b), chemiluminescence-based energy transfer (c), charge separation (d), electron trapping (e), competitive electron transfer (f, g), conditional, analyte-induced photosensitization (h), introduction/release of photoactive species (i), consumption/generation of electron donor/acceptor (j) and effect of steric hindrance (k). Adapted from Ref. [46].

quantum dots (QD) to noble metal nanoparticles, or surface plasmon generation induced by excitonic emission from the semiconductor QD within noble metal nanoparticle [55]. In the third approach, chemiluminescence is used as a replacement for external light source [56]. *Ion exchange* mechanism involves the exchange of ions of the same charge between an insoluble solid and solution that the solid is in contact with. It occurs when the resulting solid compound is less soluble than initial structure. *Reactant determinant* mechanisms are based on the introduction/release of photoactive species in response to analyte [57], the consumption/generation of an electron donor/acceptor present in the electrolyte, or through the steric hindrance arising from the specific molecular recognition reaction of antibodies–antigens, biotin–avidin or DNA–analyte.

Based on the applied materials, the PEC sensors for metal ions recognition can be divided into inorganic, organic, and bio-functionalized ones. Inorganic PEC sensors made of sulphides like CdS or ZnS operate based on the ion-exchange mechanism for the detection of Cu^{2+} and Hg^{2+} . Copper cations exchange Cd^{2+} on the materials surface and form copper sulphide domains. It is due to lower solubility of Cu_{2-x}S than CdS or ZnS. Photocurrents generated by the sensor decrease as more inclusions of Cu_{2-x}S begin to form. These domains act as recombination centres for photogenerated electrons and holes. To increase initial photocurrents intensity, and as a result the sensitivity of a device, authors do not use pure sulphides. They add gold nanoparticles [58,59], tin [60], zinc [61], and iron oxides [62], reduced graphene oxide (r-GO) [63] or carbon nitride (C_3N_4) nanosheets [64]. These sensors have very good or good (in the case of sensors with r-GO and C_3N_4) selectivity and sensitivity for Cu^{2+} . Only Ag^+ was reported as a significant interference due to much lower solubility of silver sulphide compared to copper sulphide.

For the detection of Hg^{2+} Wen et al. made a sensor from meso-2,3-dimercaptosuccinic acid (DMSA) capped CdTe quantum dots [65]. Mercury ions react with DMSA and this process induces a partial decomposition of QDs. This in turn results in the formation of mercury telluride at the surface of QDs. Such modification decreases the photocurrent intensity similarly to copper sulphide on CdS. From examined metal ions: Zn^{2+} , Cd^{2+} , Pb^{2+} , Fe^{2+} , Co^{2+} , Mn^{2+} , Mg^{2+} , Ca^{2+} , Ba^{2+} , Ni^{2+} , and Ag^+ only silver can interfere with the detection of mercury. Another sensor for Hg^{2+} is made from zinc sulphide quantum dots [66]. Similarly as before, a layer of HgS is formed, but the increasing concentration of mercury ions results in the increasing photocurrents. It is caused by the used light source – blue LED with maximum intensity at 470 nm. ZnS is characterised by the band gap of about 3.6 eV, so it generates very low photocurrents (<10 nA) upon irradiation with the blue LED. Mercury sulphide on the other hand, have much narrower band gap, and can generate photocurrents at the used wavelength. But even with the highest concentration of mercury photocurrents intensities are below 100 nA. This sensor exhibits very good selectivity for mercury. Only Cu^{2+} have a significant influence on its operation.

Sensors made from graphitic carbon nitride [67–69] and Bi_2MoO_6 /graphitic carbon nitride composite [70] are also used in the detection of Cu^{2+} . In these systems, copper ions are complexed by nitrogen atoms of C_3N_4 . The photocurrents intensities are increasing with an increasing concentration of Cu^{2+} due to the charge transfer process between metal ions and C_3N_4 semiconductor. These materials are selective for copper ions. It was reported however, that Ag^+ ions may interfere with the copper determination [69].

Apart from the aforementioned inorganic systems, more complex, bio-functionalised semiconductor-based sensors have been intensively studied in recent years [46,71,72]. The operation of biosensors is based on the transformation of recognition event into

detectable signal (optical, electrical or magnetic). These systems comprise of components responsible for the target recognition and the signal transduction [73]. The most desirable recognition element is characterised by robustness, high sensitivity and selectivity, and fast response towards analytes. The units that best match the above description and have been the most commonly used in recent years are binding proteins (e.g., antibodies–antigens and biotin–avidin) and DNA-related molecules (of which aptamers are a hot-topic) [74].

The effect of recognition reactions may manifest itself as a steric hindrance, which suppresses the diffusion of D/D^+ or A/A^- species present in the electrolyte to the photoactive species resulting in a decrease of photocurrents intensities [75–78]. Conversely, biocomplexing realised by aptamers may as well bring the enhancement of photocurrents. As shown by Okoth et al. [79], Mo-doped BiVO_4 /graphene/streptomycin–aptamer system (without the analyte) presents the steric hindrance toward the diffusion of acceptor species, which is explained on the basis of electrostatic repulsion between the negatively charged phosphate backbone of aptamers and $[\text{Fe}(\text{CN})_6]^{3-/4-}$ anion. Additionally, the authors suggest the possibility of π – π bonds formation between aptamers and graphene. When the system is illuminated in the presence of streptomycin, photogenerated holes oxidise the complexed analyte, resulting in the enhancement of observed photocurrents. Similar results were presented by Yan et al. [80], where aptamers molecules hindered contact between acceptor species and the photoactive system. During the operation, the recognition reaction (the complexation of analyte by aptamer) causes the release of aptamers bonded to the surface of thiophene–sulphur-doped graphene/ZnO system (tSG/ZnO) It results in a decreased potential barrier for the electron transfer between ZnO nanoparticles and tSG, thus enhancing photocurrents intensities.

A common strategy is the use of DNA aptamers as a complexing agent for K^+ [81], Pb^{2+} [82], or Hg^{2+} ions [42,83–85], resulting in conformational changes of considered biomolecules. As a result of the formation of DNA–metal ion complexes, a decrease of photocurrents intensities is observed due to the aforementioned mechanisms: impediment of reactions involving electron donor/acceptor species in electrolyte through the introduction of an insulating layer (reactant determinant steric hindrance) [81,82,85], the detachment of a portion of the sensing system to the electrolyte (reactant determinant release of photoactive species) [42,84] or through the hindrance of energy transfer between sensor elements caused by DNA hybridisation [83].

3. Photoelectrochemical logic gates – The Boolean algebra and more

Professor de Silva is considered the inventor of molecular logic gates. 25 years ago he presented the revolutionary concept of the Boolean logic implementation in molecular systems [86–88]. The first molecular AND logic gate was built from anthracene derivative with tertiary amine and benzocrown ether receptors and its operation was based on the fluorescence detection. In this logic device as input channels the hydrogen and sodium ions were used and the fluorescence signal was interpreted as an output [86,87]. The successful operation of this molecule as the AND logic gate is based on the photoinduced electron transfer (PET) which is the basic process in photoluminescent sensors and logic devices [10,89,90].

The same PET process is crucial in logic gates based on wide band gap semiconductors, such as titanium dioxide (TiO_2) or cadmium sulphide (CdS) [4,10,44,45]. This is an alternative to molecular systems based mainly on organic compounds. In the case of semiconducting materials light and/or photoelectrode potential

are used as inputs and the changes in the photocurrent intensity are usually considered as an output [4]. This closely relates photoelectrochemical logic gates to photoelectrochemical sensors. The first photoelectrochemical logic devices were based on the nanocrystalline titanium dioxide (TiO_2) photoelectrode modified with cyanoferrate [91,92]. The photoelectrode was illuminated with pulsed LEDs light (400 and 460 nm), whereas various photoelectrode potentials (400, 250, -200 mV) were applied to program devices behaviour. The changes in the incident light wavelength or applied photoelectrode potential result in variations of the photocurrent intensity and polarity. In order to analyse the output in terms of the Boolean logic it is necessary to assign logic values to the input and the output signals. The following convention can be applied: (i) two different wavelengths correspond to two different input channels; (ii) the state of Boolean “0” is assigned to the LED in its off state, whereas the Boolean “1” to the LED ON state; (iii) the null net photocurrent intensity at the output is assigned “0” whereas Boolean “1” to any non-zero photocurrent intensity irrespectively of its polarisation. This example shows that even very simple chemical system can convert information in different ways (YES, OR, XOR gate) depending on the combination of input signals and the conditions applied to the output signal.

Over the last few decades, molecular logic gates have become increasingly popular, challenging the conventional systems and materials in terms of superior control over molecular structure and reproducibility of operations at the nanoscale. From simple logic gates one can create more logic systems of higher complexity which have sophisticated functions, like a binary half-adder, a half-subtractor, a digital comparator, a full adder, a full subtractor, multiplexers or decoders [4,93,94]. What is more, the different chemical (pH, redox agents concentrations, ions, etc.) and physical (light, potential, temperature, etc.) signals are being used as inputs and outputs of these devices. All these factors allow the construction of a variety of molecular computing systems.

Nowadays we can observe two main paths of the molecular devices development: sensors and nanoelectronic systems. The most important problem in both areas is the concatenation of logic gates or, in more general terms, the integration of simple molecular components into larger systems of improved functionality. The lab-on-a-molecule is one of the approaches towards functional integration. In contrary to classical electronics, molecular components cannot be easily wired together, their integration requires advanced synthetic approach [3,5,95]. Therefore, so much attention is paid to an appropriate design of molecular structures and a careful design of the electronic properties of each individual building block. This approach is illustrated by the example of a complex molecular sensor/logic device based on the receptor₂-spacer₁-receptor₁-spacer₂-fluorophore-spacer₃-electron-donor architecture (Fig. 2) [96].

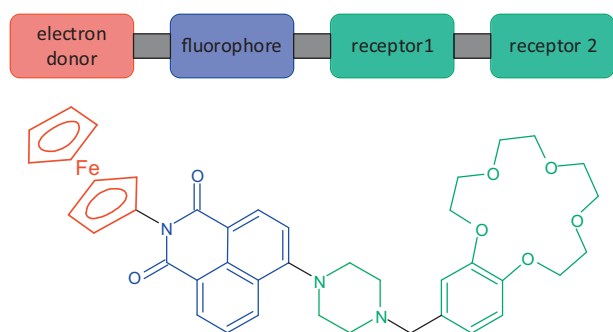


Fig. 2. The colour-coded design concept (top) and a corresponding molecular structure (bottom) of the tree-input logic gate. Adapted from Ref. [96].

This system is an example of a three-input AND, a three-input INHIBIT, or two-input OR combinatorial logic gate array. The data inputs are Fe^{3+} (electron-donor in Fig. 2) and H^+ (receptor 1 in Fig. 2), the control data input is Na^+ (receptor 2 in Fig. 2). The emission spectra were measured for eight different input combinations with low or high concentrations of each ion. For six input combinations, corresponding to low H^+ and/or Fe^{3+} concentrations no emission signal was observed. Only when the concentrations of both H^+ and Fe^{3+} are high the output signal is observed. The fluorescence intensity increases after the addition of Na^+ to the solution. It is a result of a photo-initiated charge transfer process from tertiary amine or ferrocene to the excited state of naphthalimide fluorophore, which easily quenches the emission of the fluorophore [96].

Carbon nanomaterials (fullerenes, carbon nanotubes or graphene oxide) have been reported to improve the performance of photoelectrochemical switching devices due to their good conductivity and/or stability of charge-trapping states. The use of these materials also includes the synthesis of hybrid systems with dinuclear ruthenium complexes as reported by Haga and co-workers [97]. The protonation and deprotonation of these complexes is a convenient external stimuli for controlling their optical and electrochemical properties. The latest report presents a monolayer composite film of a dinuclear Ru^{2+} complex with graphene oxide (Fig. 3a). The changes of pH of the electrolyte results in the protonation/deprotonation processes and are responsible for switching of the photocurrent polarity. In acidic solutions (pH 1–7) the cathodic photocurrent is observed, but for higher pH values only the anodic photocurrent is recorded (Fig. 3b).

The changes in the photocurrent response of materials are associated with shifts in energy levels of the ruthenium complex as a function of their protonation state. The electron donation from the LUMO of the photoexcited Ru^{4+} to O_2 in the electrolyte and a subsequent hole transfer from the HOMO of the oxidised Ru^{5+} to the Fermi level of GO and then to the conduction band of ITO results in the cathodic photocurrent generation (Fig. 3c). However, an increase in the HOMO level energy of Ru^{4+} induced by the increasing pH of the solution renders the hole transfer from the HOMO level of Ru^{4+} to the GO Fermi level much less favourable as compared with the situation at pH = 1. Whereas a sequential electron flow from the LUMO level of Ru^{4+} to the GO and then to the conduction band of ITO becomes dominant and oxidised Ru^{6+} could be regenerated by the reduction with superoxide anion radical, resulting in the anodic photocurrent (Fig. 3d). The photocurrent polarity could also be changed through the electrode polarisation. The Boolean analysis of this system (assuming that as the input signals the pH and the potential were used and the photocurrent intensity was interpreted as the output signal) allows the construction of a half-subtractor.

Although the majority of information processing devices (including those implemented in molecular systems) [3,4] operate based on the two-valued logic system there are several features of the binary approach which make it ineffective or even obsolete in certain applications. One of the most important drawbacks results from its inability to deal with the uncertainty – the limitation which is significant for example when the behaviour of biological [98] or biomimetic structures is taken into consideration – the states of a system that neither true nor false logic values may be assigned to. This disadvantage may also be analysed from a more fundamental point of view, i.e., statements which have no logical meaning within the bivalent framework but could be appropriately interpreted if additional logic values are taken into account. This kind of reasoning led to the formulation of the multi-valued approach at the beginning of the 20th century by logicians such as Łukasiewicz [99] and Peirce [100].

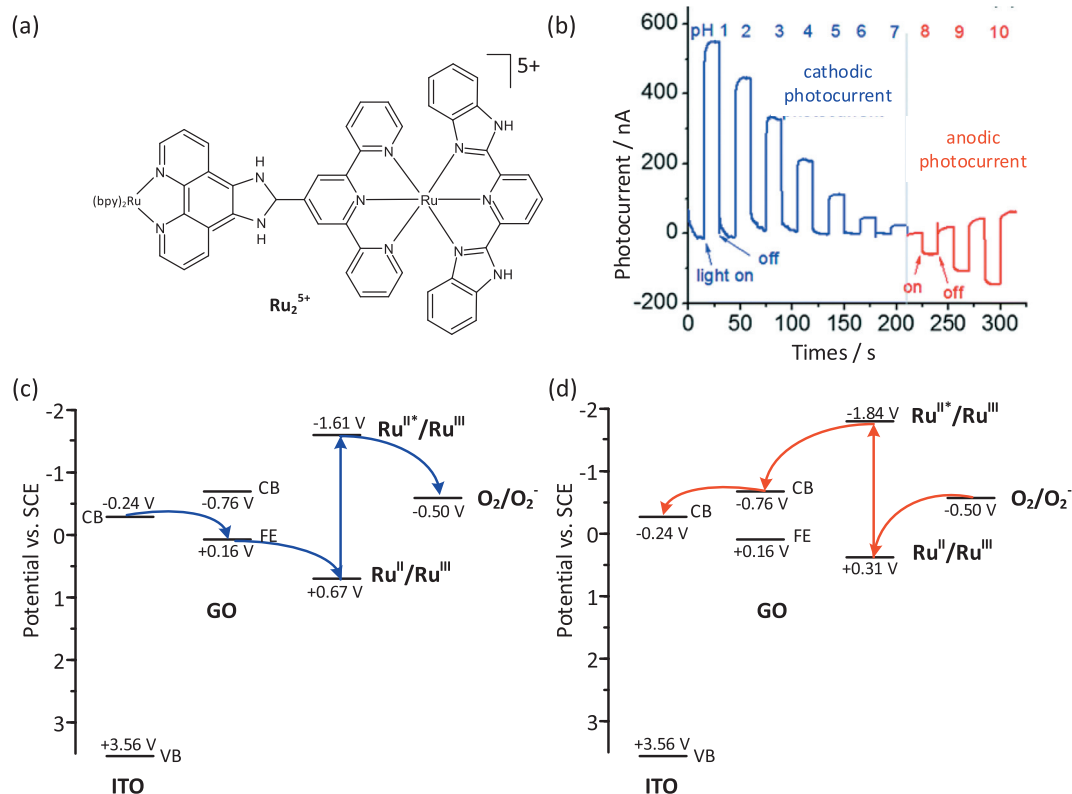


Fig. 3. The structure of Ru₂ complex (a), the pH dependence of the photocurrent polarity within 0–10 range recorded for GO/Ru₂ thin film electrodes biased at 0.1 V vs. SCE (b), the mechanism of cathodic photocurrent generation at pH = 1 (c) and the mechanism of anodic photocurrent generation at pH = 10 (d). Adapted from Ref. [97].

The simplest extension of the binary logic is achieved through the introduction of the third state, the step which can be realised in several different ways depending on the chosen formalism – we usually end up with the set defined as $\{-1, 0, 1\}$ (the balanced variant), $\{0, \frac{1}{2}, 1\}$ (which corresponds to the Łukasiewicz logic) or $\{0, 1, 2\}$ (the unbalanced version). A straightforward comparison of the approaches based on binary and ternary systems exposes another advantage associated with the use of the latter – the higher density of information storage and transmission which scales with the factor of $(3/2)^n$, where n stands for the number of bits. This could translate into more efficient architectures of information processing circuits with reduced number of chips and interconnections. A more detailed analysis of the problem reveals also the possibility of three-valued algorithms implementation which efficiency may be superior compared to the solutions founded on the binary system [101].

In our recent review [10] we discussed the philosophical background and ideas behind the three-valued logic system along with some examples of its implementation within devices made of molecular or hybrid materials. Noteworthy, in the last two years numerous works in the field of unconventional information processing systems which behaviour can be interpreted in terms of the multi-valued logic have emerged. These may be divided into two distinctive categories – in the first one biological structures such as DNA, enzymes and proteins are harnessed as the backbone of devices and the second one comprises of all systems which are made of “synthetic” materials (organic, inorganic and hybrid).

Moreover, we may also distinguish various input/output types, hence the media available as information carriers. In the majority of cases electrical signals are used either to sustain operation of a device or as a stimuli affecting its state. Particularly, ternary circuits composed of memristors are typically fully dependant on the electrical stimulation as their behaviour is modified through

an appropriate change in the applied potential and/or current flow. One of the recent contributions is based on the use of a multistate resistive switching device which heart is made of tantalum oxide and appropriately selected voltage pulses may be used to program or read its state in a manner which resembles multi-valued logic operations [102]. There are also articles describing a combination of memristors with other unconventional electronic elements – such as carbon nanotube field-effect transistors (CNTFETs) – in which authors indicate the possibility of ternary logic implementation [103].

Furthermore, several authors reported the construction of multilevel resistive memory devices characterised by different architectures, operation of which involved three logic values. Two similar sandwich-like structures with poly(methyl methacrylate) interleaved with either graphene quantum dots [104] or CdSe/ZnS core-shell quantum dots [105] and comparable principle of operation have been presented. Quite similar results have been achieved through the use of a purely molecular material – i.e., modified porphyrins – which is additionally processible from solutions [106]. In all these cases the device is capable of storing ternary information and could be coupled with three-valued logic gates through an appropriately designed readout layer.

The systems capable of processing information encoded in signals other than electrical are also considered in the literature. A good example is given by Balynsky et al., who proposed a spintronic device (magnonic interferometric switch) based on Y₃Fe₂(FeO₄)₃. The output signal phase carries here an additional piece of information [107] – a concept similar to the one characteristic to light-controlled ternary logic gates where two available polarisations of either incident or emitted light may be interpreted as two independent logic states. Another example is presented by Shim et al. The authors demonstrate a three-state device containing a phosphorene/rhenium disulfide junction which exhibits

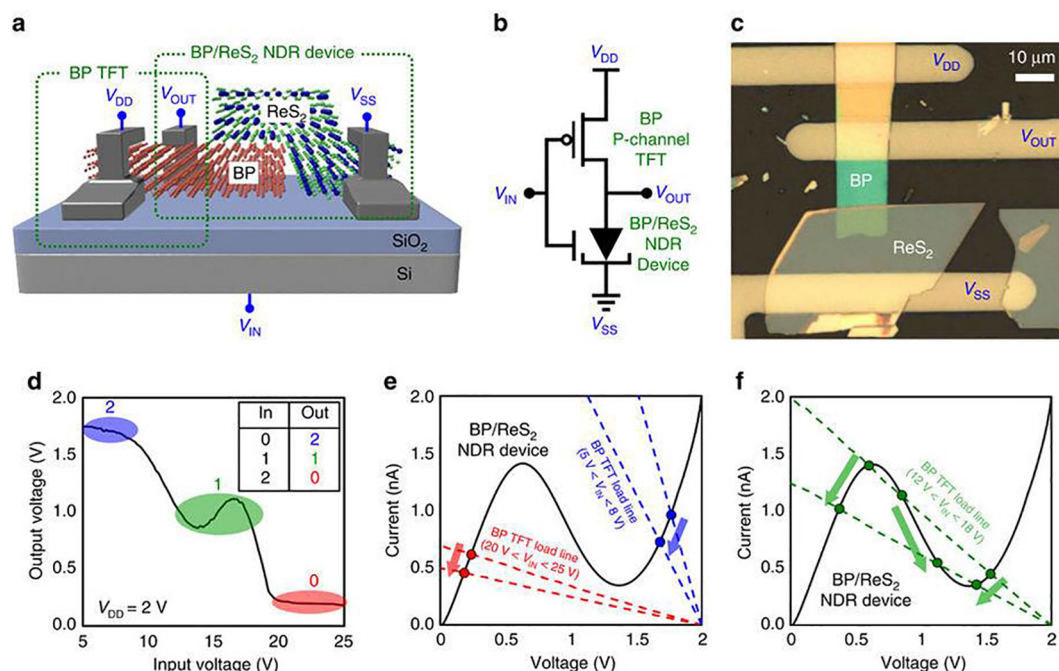


Fig. 4. Ternary inverter with three logical states. (a) Schematic illustration of the ternary inverter. (b) Equivalent circuit configuration of the ternary inverter. (c) Optical image of the ternary inverter. (d) V_{IN} versus V_{OUT} characteristic of the ternary inverter. The inset shows an input–output table of the ternary inverter. (e, f) Load-line analysis of the ternary inverter circuit under three bias conditions: (e) $5\text{ V} < V_{IN} < 8\text{ V}$, $20\text{ V} < V_{IN} < 25\text{ V}$ and (f) $12\text{ V} < V_{IN} < 18\text{ V}$. The I–V characteristics of the phosphorene (BP)/ ReS_2 NDR device (driver) and the BP TFT (load resistor) are represented by solid and dashed lines, respectively. Reprinted from Ref. [108] with permission.

negative differential resistance region and is capable of mimicking the function of a ternary inverter (Fig. 4) [108]. A similar design was presented by the same group, this time employing a graphene/tungsten diselenide junction which exhibited light-induced negative differential transconductance that allowed for a construction of a three-valued light-controlled inverter [109].

A different approach, which is particularly interesting for the authors of this review, bases on interactions with small molecules, ions and light. Several purely molecular platforms have been reported recently. Li et al. analysed the electrochemistry of a polyallylamine/graphene oxide hybrid in different solutions varying the oxidation state of GO, pH of electrolytes and the concentration of redox-active species (in this case hexacyanoferrate(III) ions). Eventually, they recreated the operation of a ternary INHIBIT gate based on the analysis of cyclic voltammetry data [110]. Meantime, a similar way of data interpretation – in this case the analysis of CV oxidation peak current dependence recorded for P(NIPAM-co-APBA) polymer on pH, temperature and the addition of biologically active molecules (particularly NADH) – led Liang et al. to the electrochemical implementation of a ternary *consensus* gate [111]. Another similar system was proposed by Lian et al. in which electrochemiluminescence response of molecularly imprinted polypyrrole/polyluminol to the addition of glucose oxidase/glucose, ampicillin and ferrocenedicarboxylic acid was interpreted as a realisation of an AND gate ternary equivalent [112].

Another article which also focuses on the pH-controlled system is presented by Spiteri et al. – here a fluorophore–spacer₁–receptor₁–spacer₂–receptor₂ system, sensitive to Na^+ and H^+ concentration changes is described also in the context of the three-valued logic implementation. This time the discussion focuses on the emission intensities which depend strongly on pH (here, some similarities with entirely electric sandwich-like three-state systems discussed in previous paragraphs may be noticed) [113].

An alternative method of programming devices behaviour to resemble the ternary logic gate operation is to tune its photocurrent response. It is particularly interesting and effective, since

two available photocurrent polarities may be readily interpreted (in a similar fashion as two independent polarisations of absorbed, transmitted or emitted light) as two additional logic states (with no net photocurrent interpreted as the third one). Such approach is proposed by Bouree et al., who use iron(III) oxide combined with copper(I)iron(III)oxide for which the photocurrent generation pattern depends on the Cu:Fe ratio, the applied potential and the incident light wavelength [114]. We also have presented recently a system based on the titanium dioxide modified with cyanocarbons which behaviour could be interpreted as an implementation of ternary *accept anything* and *consensus* gates [11].

We explored this subject further in another work devoted to core-shell systems with anthraquinone derivatives adsorbed at or encapsulated inside TiO_2 nanocrystals. This time we came up with a more complex ternary logic circuit that consisted of an *accept anything* gate with modified inputs (Fig. 5). The device was controlled independently through the change in the incident light wavelength and the applied potential and utilised the photoelectrochemical photocurrent switching (PEPS) effect. Such design allows the concatenation of similar units (with an appropriately selected buffer) into more sophisticated information processing circuits with simultaneous simplification of elementary components as their operation resembles three already linked three-valued logic gates (it resembles so called cascade logic gates designs) [8].

As it was mentioned at the beginning of this section, some of unconventional devices implementing the multi-valued logic exploit biological structures as an active part of the system. One of the most popular approach is based on the use of modified nucleic acids. We mentioned in our previous review works by Zade-gan et al. in the context of fuzzy logic system implementation [115]. The interpretation of information processing realised by the discussed device was based mainly on the fluorescence response of the system and the changes associated with energy transfer mechanisms. Remarkably, new findings are also established on this concept. Zhou et al. demonstrated a graphene

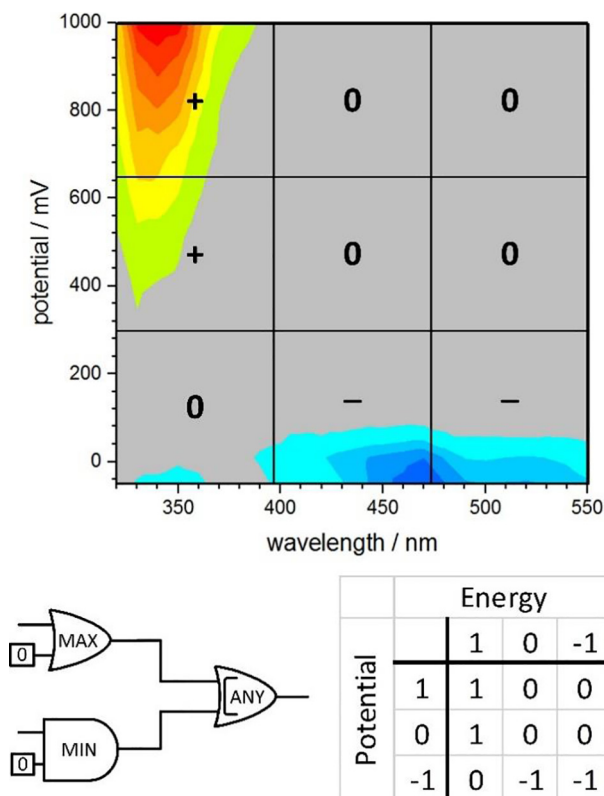


Fig. 5. A projection of the selected photocurrent action spectrum with ternary logic values assigned and the interpretation of the obtained result in terms of three-valued logic circuit operation. Adapted from Ref. [8].

oxide/DNA-based platform with the use of which ternary equivalents of INHIBIT and OR logic gates have been realised [116]. Fan et al. reproduced the functionality of ternary OR, INHIBIT, NOR and IMPLICATION gates owing to the use of DNA strands with additional reporters in the form of Cu nanoparticles which fluorescence intensity was analysed as an output of the system [117].

Although the three-valued logic offers new possibilities for efficient computation some tasks might be optimised if no crisp logic values are used but instead a more human-like information processing is involved. This kind of approach has been considered by Zadeh and the fuzzy logic (FL) was introduced in 1965 [99,118,119] – it was later developed by Mamdani [120], Takagi and Sugeno [121] and others. The proposed idea seemed suitable for the use in control systems and interfaces in which instructions expressed in the terms of natural language by a user can be processed into a form comprehensible for electronic systems. It was later proposed that this formalism may be applied in a wider context – namely to describe some of the fundamental biological processes which involve some degree of uncertainty (for example signals provided by our sensory system) [12].

Together with a rising interest in the molecular logic and information processing realised in chemical systems the concept of the fuzzy logic implementation in this context also found its advocates. One of the most influential works are credited to Pier Luigi Gentili who proposed several different molecular platforms based on both inorganic and organic compounds for the fuzzy logic application and discussed the possibility of using this kind of formalism in the development of artificial intelligent systems [12,122,123]. This line of work is currently evolving as two biologically inspired FL implementations, which could be used for UV radiation type recognition and mimicking of selected features of the human nervous system, have been recently presented [124,125].

At the same time, other platforms which could be adopted for the implementation of the fuzzy logic formalism are suggested. For example, the aforementioned group who discussed the possibility of using tantalum oxide memristive device for the ternary logic gates realisation [102] proposed a quite similar system for the fuzzy logic implementation [126]. Karmakar et al. constructed a FL system utilising changes in ruthenium complex photoluminescence response and extinction coefficients upon the addition of selected ions (Fe^{2+} , Zn^{2+} , F^-) [127]. Xu and Yan employed europium functionalised metal–organic frameworks to construct device capable of molecular events detection (e.g., simultaneous presence of two analytes) based on the analysis facilitated by chosen elements of the FL formalism [128].

The authors of this review also contributed to the available pallet of devices implementing the fuzzy logic. We proposed the use of the aforementioned system containing anthraquinone-modified titanium dioxide and its photocurrent generation pattern as suitable for designing the FL system (Fig. 6). It is noteworthy that the presented platform can be controlled by either electrode potential changes or incident light wavelengths alterations, thus may be linked with several other systems described in this review [8].

Some of the already discussed ideas paved the way for more sophisticated applications of molecular logic gates. One of the most interesting possibilities of exercising this class of devices is to hide, encode or – in other way – secure the information. This goal may be achieved with the use of cryptography (encrypt the message, so your adversary knows about it but cannot read it), steganography (hide the message, so your adversary does not know about it) or password protection (lock the message, so your adversary knows about it but cannot reach it) – obviously some combinations may be beneficial in certain situations. These techniques can be adapted within molecular-based systems, as discussed by Lustgarten et al. in a recently published review [129].

Numerous attempts to harness molecules to secure information transfer and storage can be traced back to the ancient times in a form of invisible inks [130] and simple ciphers. The means of information protection have developed tremendously throughout the centuries and reached state-of-the-art level with knowingly designed devices working at the nanoscale and molecular level. Similarly to the aforementioned multi-valued and fuzzy logic systems also here DNA-based solutions are quite popular among researchers and several successful implementations of cryptographic and steganographic approaches have been demonstrated [131–138]. It is important to note, that although the use of DNA-based devices may be beneficial in some aspects [139] the technological requirements to implement it efficiently are still relatively high.

That is one of the reasons several groups have engaged the topic using simpler molecules. One of significant examples was presented by Margulies et al. in 2006 – the first realisation of a molecular keypad operation of which was based on the interplay between several fluorescence patterns recorded for fluorescein–linker–pyrene system [140]. Noteworthy, that is just the tip of the iceberg – similar concepts have been developed and many new devices have emerged including: keypad locks in various configurations [141–148], a platform which could allow efficient combination of cryptographic and steganographic information protection [149], the two-factor authentication (2FA) implementation at the molecular level [150], a rewritable phosphorescent paper for secure information handling [151] and many more encoding/decoding molecular systems [152–154]. To sum up, the growing interest in the application of molecules for sophisticated information processing can be observed, which may lead to commercially available solutions within few next years.

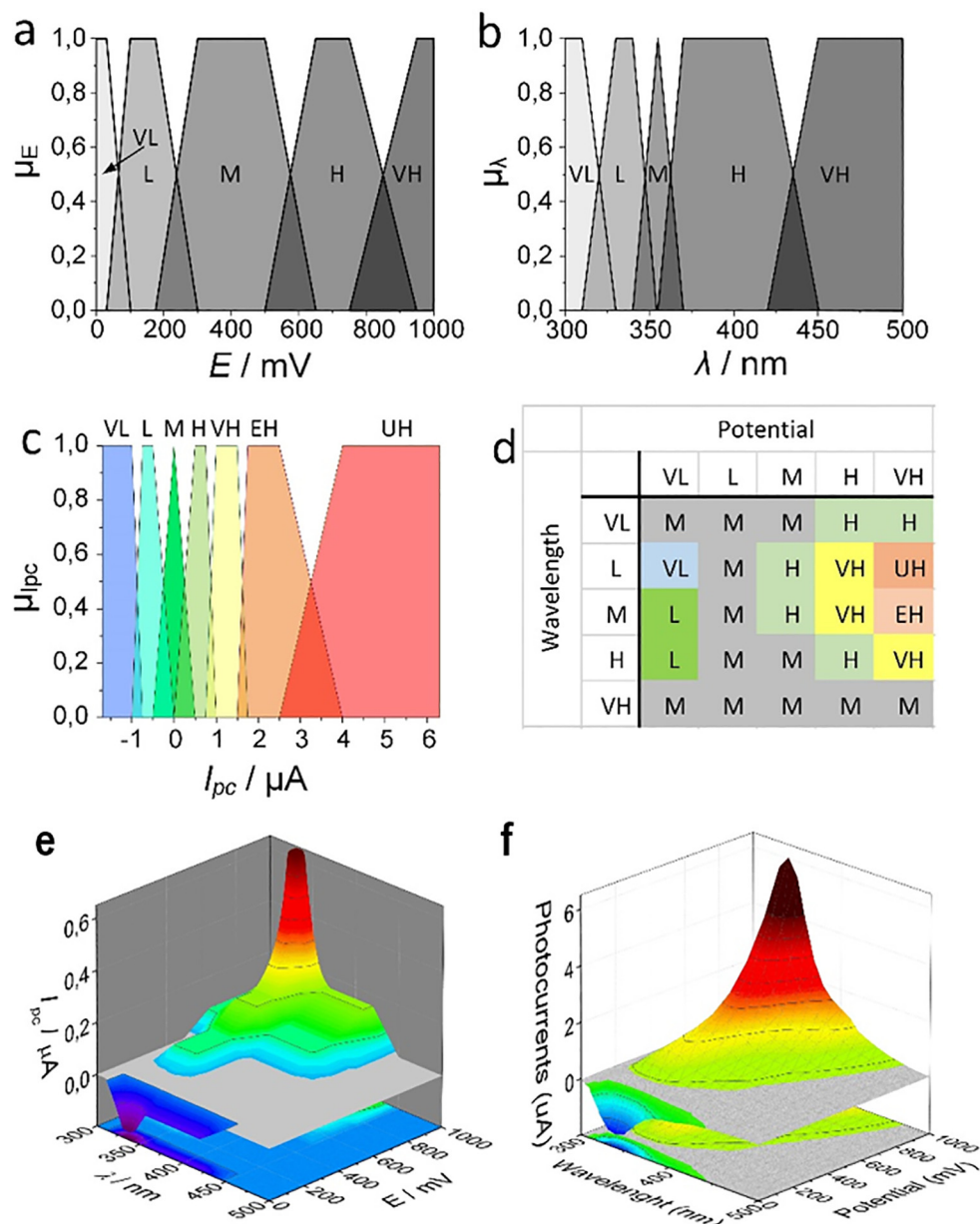


Fig. 6. The effect of fuzzification for both inputs (a and b) and output (c) presented with the rules base for the inference engine (d). The result of the defuzzification step (e) with the photocurrent map used for the construction of the fuzzy logic system (f). Adapted from Ref. [8].

4. Photomemristive and neuromimetic devices

Memristors and memristive devices depend usually on electrical field changes but the modulation of temperature, magnetic field and incident light can also be the source of the resistive switching. A photomemristor, although it does not have a strict definition, is an attractive concept due to its broad prospective applications in unconventional information processing. There are several mechanisms responsible for the memristive behaviour, starting with a very common conductive filament formation, ionic movements, Schottky barrier at interfaces, tunnelling effects, conducting paths formation and probably many others, depending on the chemical compounds and the device architecture [155–157]. Therefore, light can be involved in the operation of memristive devices in numerous ways, including charge carriers generation and trapping [158] light-induced changes in defect migration [159], and others.

The movement of oxygen vacancies and their interplay with the Schottky barrier could be found in devices based on metal oxides [160–162] but also in graphene, graphene oxide, and diamond junctions [163,164]. A similar role play ions in metal halide perovskites [165]. Another mechanism which is often brought up involves the formation of conductive filaments from ions that can penetrate the compound layer between two electrodes [166–170] or in a nanogap [171–173]. Those filaments can be made of electrochemically active metals [168,169,173], silica [167,171], iodide vacancies [174], oxygen species [166], or metal-organic complexes [172]. Sometimes less obvious mechanisms take place. *cis-trans* photoisomerisation can lead to the contraction/expansion of a bulk material and a subsequent change in the resistivity of memristor due to the change of its thickness [175]. Unusual arrangement of quantum dots between two gate electrodes enables the charging and discharging of QDs via trapping/detrapping of

holes and electrons [176,177]. Not all of the presented devices can be considered memristors and most of the authors do not try to prove that their systems exhibit convincing memristive properties. Usually only the current–voltage characteristics are analysed and other important features of memristors behaviour – such as non-volatile memory, multiple resistive states and the frequency dependence – are neglected. Nevertheless, the quoted works deserve attention since only a fraction of articles about memristors mention the light induced/tuned memristive behaviours.

The clearest and most convincing demonstration of a light-controlled memristor would be a device which exhibits a memristive hysteresis loop (the fingerprint of a memristor) only upon irradiation. Such a device, made of superhydrophobic ZnO nanorods covered with a thin layer of water, acts as a memristor or a resistor under illumination or in the dark respectively [166]. The water layer allows to choose resistive or memristive properties upon constant irradiation by simple manipulation of a light incident angle due to different refractive indexes of air and water. After exceeding the angle of incidence critical value of $\theta = 48^\circ$, the device loses its memristive properties because the light does not reach the ZnO layer anymore. In the device there is also an air pocket located beneath the water layer. It acts as an oxygen source for the ZnO nanorods surface. The illumination induces desorption of the chemisorbed oxygen. That allows oxygen vacancies movement and the formation of conductive filaments between top and bottom electrodes. Without the irradiation the adsorbed oxygen prevents diffusion of oxygen vacancies and the device remains in the high resistive state.

Another family of devices works as memristors in the dark but under illumination different changes in hysteresis pattern appear. The most common result of irradiation is an increase in overall current that flows through the device [161–163,165,170,175,178]. Depending on the material used, it results in higher a ON/OFF ratio [178], changes the HRS/LRS switching time [169], tunes short-term or long-term memory features and the retention time of stored information [175] or gives additional distinguishable states for the logic implementation [161,165,178]. The OR logic gate with both electrical and optical inputs has been realised with Cu/CH₃NH₃PbI₃/PEDOT:PSS/ITO memristor (Fig. 7a) [165]. In this device a high resistive state (HRS) is obtained by the application of positive potential, whereas the low resistive state is obtained through the application of negative potential. The conductance of this memristor in the HRS increases upon illumination by at least three orders of magnitude, meanwhile the conductance of the device in the LRS remains constant under pulsed irradiation (Fig. 7b c). The photo and electro-responsive performance of the device has been used to design the logic OR gate. As presented in Fig. 7d, two input signals have been assigned to the gate: electric (input A) and optical (input B). The positive potential corresponds to the logical 0 while the negative potential to the logical 1. The optical input has been described as 0 without light and 1 under illumination. When at least one of the input signals had the value 1 (negative voltage or irradiation), the logic gate returned high current level realising logical disjunction.

An interesting concept of reconfigurable OR and AND logic gates have been realised with ITO/CeO_{2-x}/AlO_y/Al memristor [161]. For

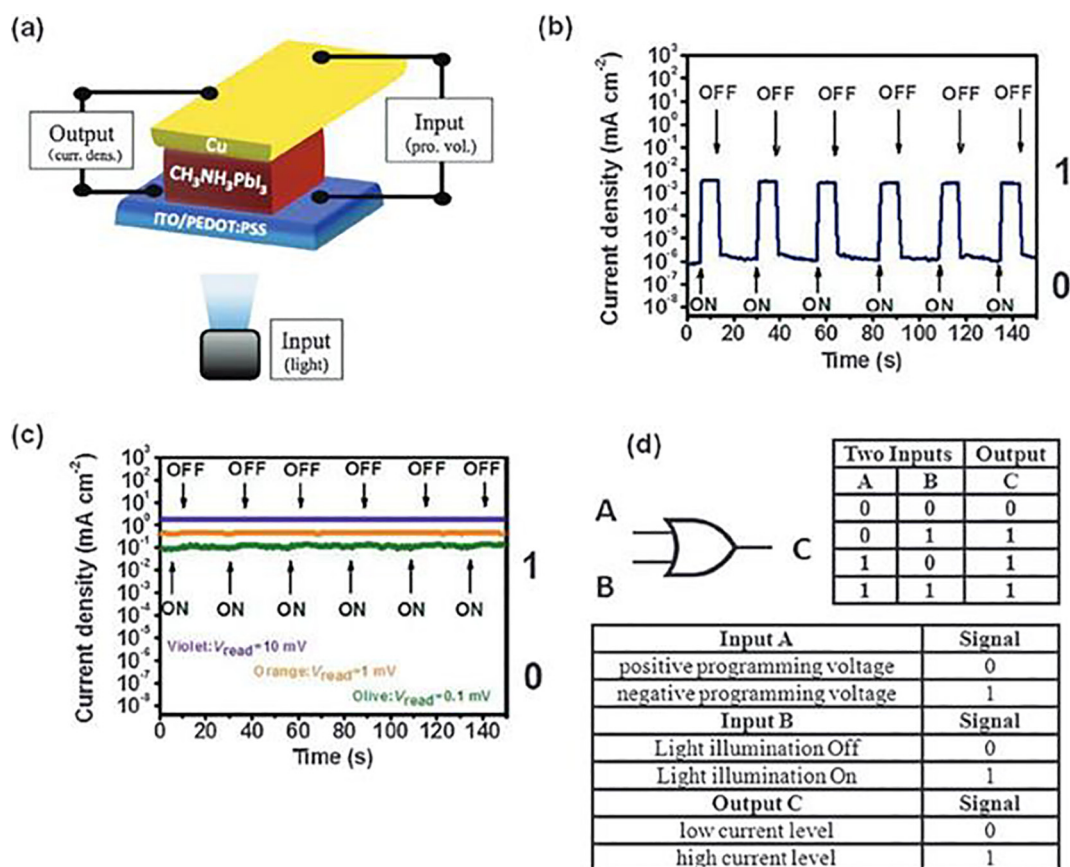


Fig. 7. The photo-induced logic OR gate based on Cu/CH₃NH₃PbI₃/PEDOT:PSS/ITO memristor (a). The current–time response of the device at the initial high resistive state (HRS) upon pulsed illumination at read potential of 10 mV (b), the current–time response of the device at the initial low resistive state (LRS) upon pulsed illumination at read potential of 10 mV (c), the two (optical and electrical) input OR truth table (d). Adapted from Ref. [165] with permission from The Royal Society of Chemistry.

this device the hysteresis loop upon illumination exhibits higher overall current than the device in the dark, and even short optical pulses can cause higher conductance. The irradiation of the sample have been assigned as the logical 1 and the lack of irradiation as the logical 0 for the optical input. Analogically the higher conductive state can be also achieved through the positive potential sweeping, therefore the positive potential (10 V) has been assigned as the logical 1 for the electric input and the logical 0 is the operation without the applied potential. The crucial element that enables the reconfiguration of the device between OR and AND gates functionalities is the initial state of the device (Fig. 8). If the device has been reset to the high resistive state by applying -2 V for 0.1 s the photomemristor will realise the AND function: when the positive potential (electrical input value 1) and light (optical input value 1) will be applied the resulting current will be high enough to exceed the threshold voltage. If the device has been set by the illumination with halogen lamp at $60 \text{ pW}/\mu\text{m}^2$ for 4 s the memristor will realise the OR operation because the setting operation increases the initial current level (the device is not in the highest resistance state anymore) and the application of positive potential or illumination alone will be enough to exceed the same threshold potential. Therefore, ITO/CeO_{2-x}/AlO_y/Al memristor can be used to reduce circuit complexity by a selective switching between different operation modes. The authors also proposed the configuration with additional, second electrical input (-2 V for 0.1 s) with value 1 in ON and 0 in OFF states. The application of the second electrical input always results in the logical 0 as an output but this condition is fulfilled only when the second electrical input is applied after the optical and the first electrical inputs. As the negative potential resets the memristor to the highest resistive state so this type of modulation is just another reset operation. The same ITO/CeO_{2-x}/AlO_y/Al memristor has been used to demonstrate the realisation of computing functions due to the linear relationship between identical light pulses and current intensity [162].

Examples of devices with the memristive behaviour in the dark and an additional modulation option upon illumination (ON or OFF) can be found. A memristive device composed of GaAs/AlGaAs

heterostructure with InAs quantum dots (QDs) positioned along source-drain path (Fig. 9a) is turned ON and OFF by the electric field and exhibits typical bidirectional hysteresis loop (Fig. 9b). The lateral gates are tuning the amount of charge on the QDs. The quantum dots can trap both electrons and holes. Analogically, discharging appears when more holes than electrons have been trapped. Charging of the quantum dots causes a decrease of conductance while discharging is responsible for the increase of conductance. The illumination of the device with the red light induces interband excitation (Fig. 9c d). The total number of holes and electrons that populate the QDs depends on their drift, diffusion and the band profile which is modulated by the applied potential. Moreover, the infrared illumination is postulated to discharge QDs via intraband absorption (Fig. 9d) [176,177]. This device requires low (4.2 K) temperature to operate, therefore it would be hard to implement it in everyday applications.

The memristive behaviour of the device made of ZnO nanorods grown on SrTiO₃ perovskite can be also modulated with the UV light [160]. ZnO nanorods create Schottky junction with SrTiO₃. Under reverse bias conditions the oxygen vacancies migrate towards the ZnO/SrTiO₃ interface. Trapping of these vacancies effectively reduces the interfacial barrier. Photogenerated holes can also migrate to the interface and recombine with trapped electrons. Moreover, electrons trapped at the interface in oxygen vacancies can be photo-excited to the conduction band leaving additional ionised vacancy. Because of the long lifetimes of holes captured within the interface and ionised oxygen vacancies the change at the interface is persistent. It takes around one day in dark or 5 min at 300 °C for the device to restore previous properties.

An interesting alteration of memristive properties and the current-voltage characteristic can be observed in graphene/graphene oxide and MoS₂ based devices [163,170]. Although different mechanisms are responsible for the memristive properties of these two systems, in both cases the set and reset operations in the dark and upon illumination occur at the potential values of opposite polarity i.e., set/reset voltage is about 3.3/−3.8 V in the dark and −3.5/4 V

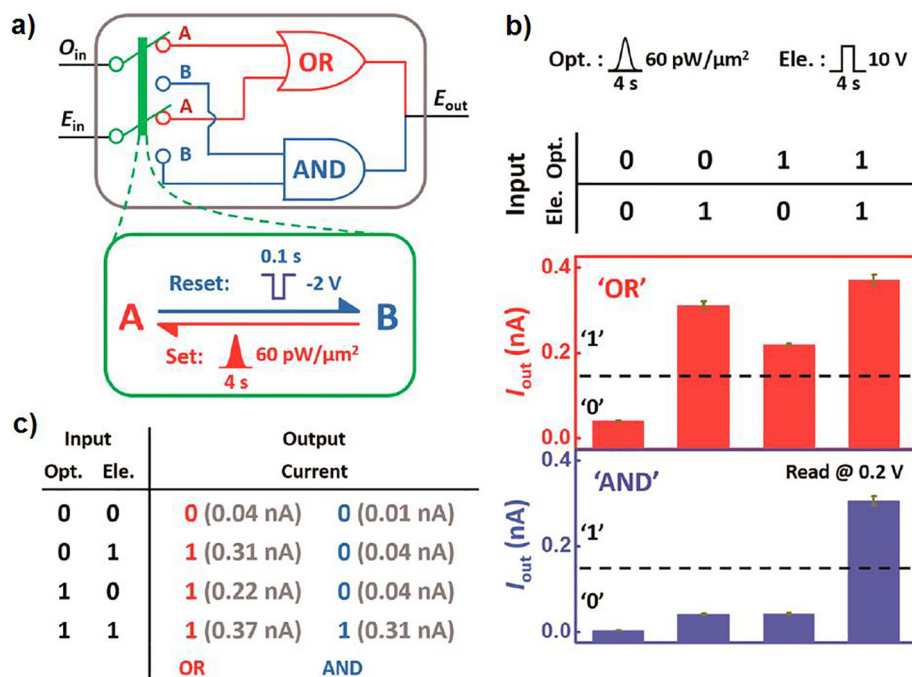


Fig. 8. The implementation of ITO/CeO_{2-x}/AlO_y/Al memristor as reconfigurable AND and OR logic gates. (a) Schematic diagram of OR and AND logic operations, in the green frame the optical-set and electrical-reset operations are shown, (b) an electrical outputs (red and blue) with the corresponding electrical and optical inputs (black), (c) the truth table with output current values for the AND and OR logic operations. The read voltage was 0.2 V. Reprinted from Ref. [161] with permission.

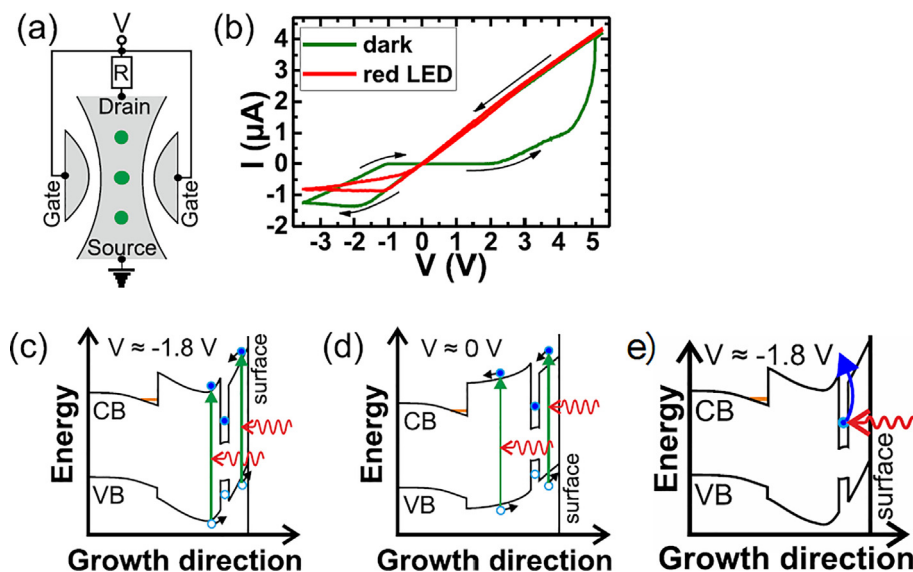


Fig. 9. The schematic representation of memristive device (a), the bidirectional hysteresis loop (b), the conduction and valence band profiles, interband absorption and electron/holes dynamics at -1.8 V (c) and 0 V (d). Intraband absorption at -1.8 V (e). Reprinted from Ref. [177] with permission of AIP Publishing.

under illumination for the graphene/graphene oxide photomemristive heterojunction. The same effect of inverted set/reset voltages exhibit the MoS_2 -based memristor in the potential range of ± 6 V but additionally, at smaller potential window of about ± 3 V only a typical increase in the current intensity has been recorded (Fig. 10).

The pinched hysteresis loop is called the fingerprint of a memristor [179]. The photo-memristive behaviour can be achieved not only under static optical conditions like the constant illumination or in the dark but also by changing the light intensity in appropriate moments. An excellent example is given by a photocontrollable graphene/diamond heterojunction [164]. For the measurement taken at 150 °C the ohmic behaviour has been observed in the dark but under illumination with the blue light the rectifying behaviour appears. Separately, those characteristics are not memristive (Fig. 11a). The pulsed irradiation with the blue light (5 s) during the potential sweep at 10 V changes the state of the device from the initial HRS to the low resistive state (LRS). An another pulsed irradiation at -10 V (5 s) changes the state of the device from LRS to HRS. This two steps resulting in the memristive

hysteresis loop are presented in Fig. 11b. A similar approach has been suggested for the device based on nanowire arrays of a copper complex: Cu:7,7,8,8-tetracyanoquinodimethane [172]. This nanowires form during the potential sweep. The device upon irradiation yields higher currents, therefore by an appropriate manipulation with the optical conditions one can mimic the memristive behaviour (similar as in the case of the graphene/diamond junction). The major advantage for the future applications of systems based on Cu complexes is the operation at the room temperature in contrast to the diamond/graphene device.

Although the control over conductance by an additional light stimulation is an obvious advantage, the light can also probe the current state of the device (e.g., distinguish between HRS and LRS). A planar graphene/ SiO_2 device has a strong electroluminescence related to its resistance states [171]. For the HRS and LRS the maxima of the electroluminescence are around 550 nm and 770 nm respectively. A strong emission of light was observed especially during switching device from the LRS to the HRS. This kind of surplus optical output can be useful to create optical communication path with other photonic devices. A light emitting cell

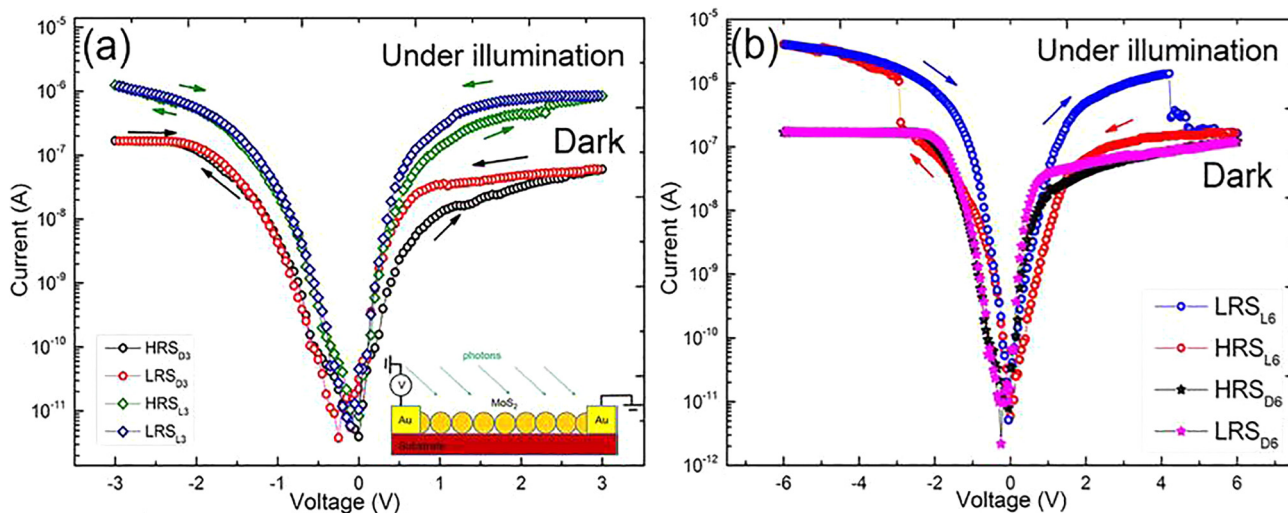


Fig. 10. The current–voltage characteristics of Au/ MoS_2 nanospheres/Au memristor in the dark or under illumination recorded with the scan rate of 50 mV/s in (a) ± 3 V and (b) ± 6 V sweeping voltage range. The arrows indicate the direction of current changes. Reprinted from [170] with permission of Springer-Nature.

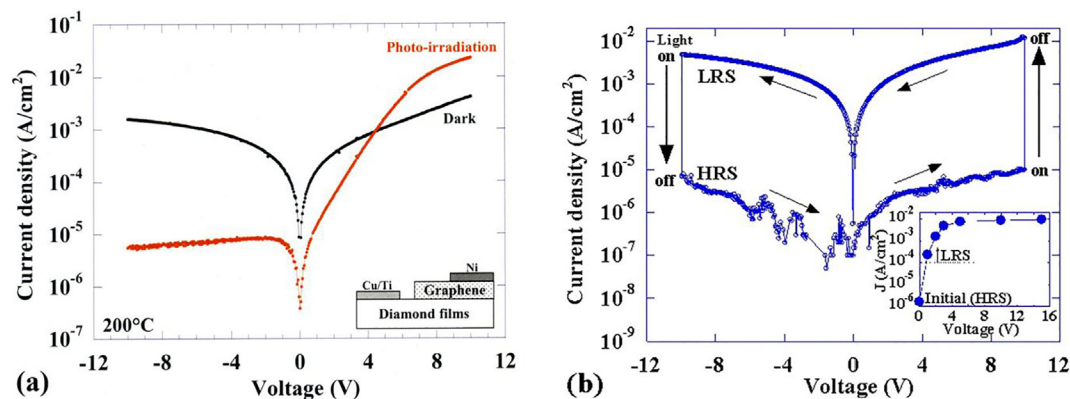


Fig. 11. The current–voltage characteristics of the graphene/diamond memristive device at 200 °C with (red) and without white light illumination (a), the current–voltage characteristics of the memristive junction at 150 °C (b). The resistive states were changed to HRS or LRS by the illumination at +10 V and –10 V for 5 s. Reproduced from Ref. [164] with permission of AIP Publishing.

(MEH-PPV)₂₀(MHPI)_{x-y}) with distinguishable resistive states has also been presented but unfortunately that device does not have the reset option [180]. A different approach to obtaining information with the assistance of light can be applied in the plasmonic memristors/optical switches. The electromagnetic field interacts with conducting filaments responsible for the changes of the resistivity in the devices e.g., Ag/a-Si/p-Si or Ag/a-Si/Pt [167,168,173]. Those plasmonic devices are based on the formation of nanoscale conducting Ag filaments. The light can propagate through a-Si layer and in the presence of Ag filaments (partial barrier for light) the optical transmission is low for the LRS or high for the device in the HRS (the lack of the filaments) giving the information about the current state of the device.

Similar behaviour has been observed for a multilayer device of the structure Pd/Al₂O₃/SiO₂/p-Si. In the dark it exhibits extremely low conductivity and the discrimination between the HRS and LRS is difficult [181]. Upon illumination with either 390 or 950 nm (2.5 mW/cm²) light the conductivity of the system increases by four orders of magnitude. Moreover, the irradiation results in the electron injection into the Al₂O₃ barrier layer, which affects the current intensity. Authors postulate, that due to a long information retention time (up to one year) and the dependence of current on light intensity, the device can be used for secure storage of information. More complex structures involving coupled Ni/In₂O₃/Ni light sensor and Ni/Al₂O₃/Au memristor have been reported to store low resolution visual information for ca. 1 week [182]. Similar performance has been observed in hybrid organic–inorganic devices based on fullerene–thiophene photodiodes coupled with Al/Alq₃/Ag memristors (q = 8-hydroxyquinolate) [183].

5. Reservoir computing and its sensing applications

The development of modern civilisation requires progressively more efficient processing of increasing amount of information. Emerging concepts of the Internet of Things, due to predicted enormous growth within coming years [184], will require the integration of elementary functions of obtaining information (sensors), processing (e.g., neural networks), transmission and memory. What is more, the processing of huge collections of incomplete data of variable and irregular structure (the so-called Big Data) is a great challenge at the moment. Although classical semiconductor technologies will dominate the IT market for a long time, one cannot neglect the development of alternative ways of information processing for niche applications and using non-standard material technologies and computational paradigms.

One of the emerging concepts which could provide high speed, non-linear, time-varying data recognition, prediction and classifi-

cation is Reservoir Computing (RC). RC belongs to the field of machine learning, to the group of recurrent neural networks, including within its framework Liquid State Machine (LSM) [185] and Echo State Network (ESN) [186] algorithms. The architecture of a functional RC consists of three layers: input layer, reservoir layer and readout layer. The main concept of operation is based on feeding time-dependent signal into a non-linear dynamical system (reservoir). This external signal drives the dynamical system towards a specific region of the configuration space, which serves as a reservoir of states. In such a way, the introduced information is translated into the state occupied by the device. This transformation constitutes the act of computation performed by the device. Its result can be obtained by identifying which reservoir state has been occupied [185,186].

Major advantage of the RC over classical recurrent neural networks (RNN) is that all connections between network nodes (neurons) within reservoir layer are fixed – all training is performed at the readout layer, which is computationally more efficient (Fig. 12). The readout layer is used to access or decode internal states of reservoir – assuming that the reservoir is sufficiently complex, even linear readout may be sufficient. For the reservoir to work efficiently, two conditions must be met: (i) point-wise separation property – different inputs need to be mapped to different reservoir states and (ii) approximation property of current state of the reservoir by the read-out with required accuracy [185,186].

At the same time, it is important to note, that in most cases data fed to the reservoir needs to be pre-processed for higher performance – by normalisation, Fourier transformation or by masking [187]. The pre-processing by masking consists in modification of the input signal, which functions as diversification of the reservoir response, thus increasing its dimensionality in the state-space. The applied mask can take a form of digital binary values [188] or simple sinusoidal wave. It has been shown by Nakayama et al. that analogue mask with chaotic values is also efficient (Fig. 13) [189].

These ideas are based on a rigorous mathematical foundation. A detailed discussion that explains how these rigorous mathematical aspects of RC are implemented in practice can be found in [190]. The RC can be exploited for numerous purposes, exceeding the originally intended scope of RC as a theory to explain some intriguing properties of the learning process of artificial neural networks. Namely, RC is a genuine theory of computation with generic dynamical systems, and we argue that applications of RC in this broader “out of the box” context still need to be defined. In particular, there is a significant novelty in exploring reservoirs made of chemical systems and the community yet needs to discover the possibilities associated with this approach. For example, we have

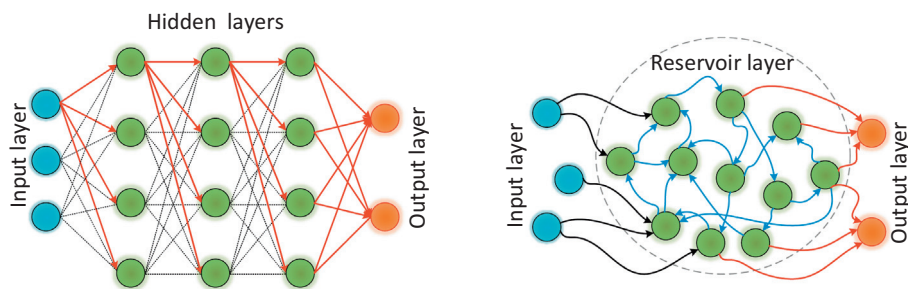


Fig. 12. A schematic representation of a classical feed-forward neural network (left) and a reservoir (right). In the case of the neural network all connections have to be tuned, in the case of the reservoir only those to the output layer (marked in red).

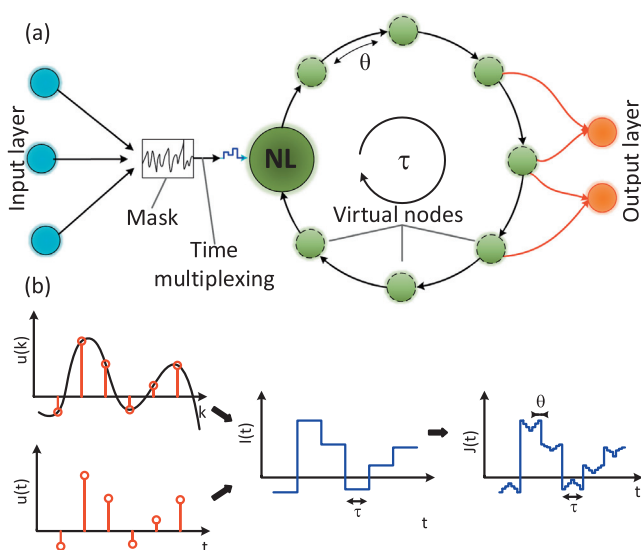


Fig. 13. A schematic structure of delay-based reservoir computer with feedback loop. Input data undergoes sampling and hold functions for the duration of the delay line (represented by τ). The procedure of masking and time-multiplexing enables division of duration of delay line to create temporally separated virtual nodes (distances between virtual nodes are marked by θ , (a). A schematic representation of input data pre-processing and masking procedures. Time-continuous or time-discrete signal is sampled and held for the duration of the delay line. By time-multiplexing, duration of delay line is divided, so that masking function can attribute different states for each virtual neuron (b). Adapted from Ref. [191].

presented a way of using RC in this “out of the box” mode for sensing applications [40].

The flexibility and the ease of use make the reservoir computing paradigm the method *par preference* for many sensing applications, when there is a need to analyse the output of the sensor and classify it in the pattern recognition sense [29–38]. Typically, in the traditional setup, the flow of information is linear; the object one wishes to study interacts with the sensor, which transduces this information into some sort of signal that can be manipulated with the ordinary engineering techniques (cf. the section on photoelectrochemical sensing). At the end of the chain is an Artificial Intelligence unit that analyses the information. Another, more profound approach has been suggested recently that genuinely exploits internal features of RC. The key idea of the state weaving environment echo tracker (SWEET) sensing algorithm [40] is to merge the sensing and the analysis parts into one component, the Echo State Weaver (ESW). The reservoir “feels” the environment over time, and the state of the environment can be inferred by studying the response of the reservoir towards external perturbation. Although the flow of information in the SWEET setup may seem more complex, the SWEET setup is more flexible from the engineering point

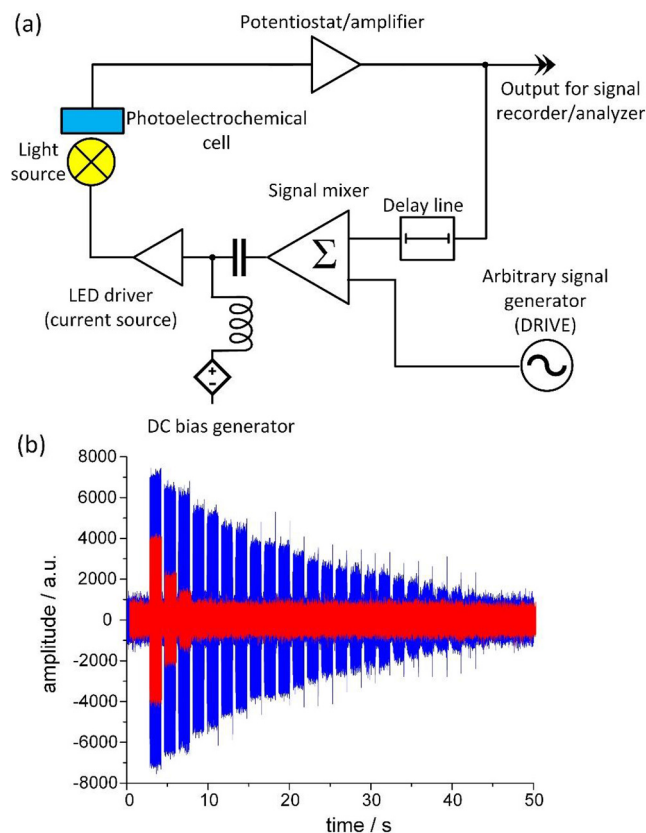


Fig. 14. A simplified block diagram of the photoelectrochemical reservoir computing sensory system. Any perturbation in the electrolyte composition, which may influence the dynamics or quantum yield of the photocurrent generation (a). The reservoir response recorded for a simplified device (signal mixer was coupled with control input of potentiostat) recorded for bare gold electrode (blue) and gold covered with lipoic acid (red, b).

of view. The Fig. 14a shows an example of how the algorithm can be realised using photoelectrochemical components along with some preliminary results (Fig. 14b).

The SWEET setup has been tested extensively through theoretical studies, where memristor networks have been used as the model for the reservoir [192,193]. The memristive element is very attractive since it has a relatively simple response, and it is an element that “remembers” its past: the present state of the device depends on the voltage signal that was used to drive it in the past. The simulation of memristor networks can be performed relatively fast, e.g., using the algorithm presented in Ref. [194]. We briefly summarise some important concepts for building chemical sensors based on the SWEET algorithm in further parts of this review.

A new approach towards extraction and amplification of weak analytical signals, with coined name ‘heterodyne sensing’ is also closely related to sensing with the reservoir computing. In heterodyne sensors an analyte modifies dynamic properties of a semiconducting nanodevice based on graphene [195–197] or conducting polymers [198]. The increased sensitivity of these devices results from frequency-mixing properties of semiconducting nanostructures which may be applied not only in a new generation of sensors [199] but also in other signal-processing devices [200]. The significant difference between these systems and the reservoir computing-based solutions is the lack of the feedback and formal differences in terms of the theory of information.

The key feature of a good reservoir is the separability condition. For any two inputs that are different, one should be able to engineer a readout layer that will produce different outputs when the system is exposed to these inputs [190]. However, this condition is hard to meet in practice. It is impossible to expose the system to all possible pairs of distinct inputs, and test whether a readout layer that separates them can be found, as the number of possible input signals is infinite. Instead, we have found a way to validate this separability condition by analysing the structure of the configuration space of the device directly [193]. In general, the question of the reservoir quality has received some attention, but there is still plenty of work to do.

Generic measures for describing the structure of the phase space are important: a good sensing performance can be achieved if the phase space is driven to different regions under different inputs (different environmental conditions but the same drive signal). A large separation implies simpler readout layers, and accordingly large intrinsic computational capacity of the device. In contrast, a relatively poor state space separation means that a more complex readout layer would be needed. The main drawbacks of a complex readout layer are related to higher requirements in terms of resources such as memory, software engineering or energy consumption (Fig. 15).

To quantify the state space separation, we have introduced a real number, which we refer to as the separability index. The advantage of having a single number is that different sensor designs can be easily compared. The key idea we exploit is that under optimal sensing conditions the system should be driven to distinct regions of the configuration space for different states of the environment [40,193]. The index quantifies how well the trajectories separate in the configuration space. The separability index is useful since it describes the sensing capacity of the system. The large separability index corresponds to a good sensor and vice versa. Note that by default, a random drive u will likely result in poor separability (cf. Fig. 15b, the left panel). Thus, to achieve good separability, the drive needs to be carefully optimised. To do this, we have formulated a generic optimisation problem, which, when solved, results in the optimal drive.

To investigate the performance of the SWEET sensing setup, we studied theoretically reservoirs made of memristor elements in two studies [192,193]. Due to the properties discussed earlier, these components are suitable for this kind of tests (two-point electronic components with a memory). In [192] we constructed a simple model of an environment sensitive memristor that is simple to simulate and yet plausible. Using that model, we showed that a simple pattern recognition problem for distinguishing between two specific environmental conditions can be solved with the use of a one-memristor network [192]. Later, we studied how larger memristor networks (i.e., with the increased size of the phase space) could be exploited for solving more complex pattern recognition problems [193]. Both studies were theoretical and were useful to understand concepts regarding sensing.

Further, in [193] the impact of collaborative effects on the sensing capacity was addressed. The idea is that the sensing capacity

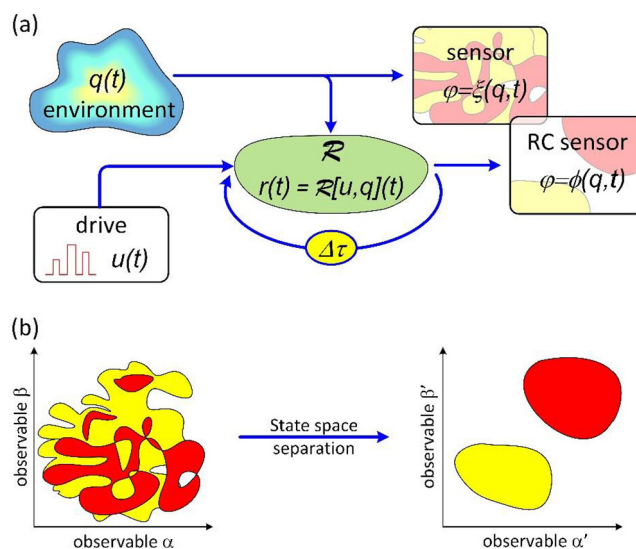


Fig. 15. The overview of the SWEET sensing setup. The environment-sensitive reservoir is used to obtain information about the environment. This is done through indirect sensing by studying the response of the reservoir to user-provided queries – the drive signal $u(t)$. The delayed feedback $\Delta\tau$ (a) is added to increase the complexity of the configuration space and achieve better reservoir computing properties. (b) On the left, the case of a low phase space separation is illustrated. The trajectories mix under different environmental conditions. To build a sensor with such a system a complex readout layer is required, which implies overhead costs in the terms of engineering effort, computational complexity or energy. On the right the case of a high phase space separation is shown. Different colours correspond to the regions that the system visits under different environmental conditions. In this scenario, a relatively simple readout layer can be used to infer the state of the environment. Most of the computation is performed by the device, and not the readout layer. Adapted from Ref. [40].

can be increased if memristor elements do not share the identical tasks, which would be a waste of resources, but each memristor processes a piece of information about the environment. We tested these ideas by computing the separability index for a series of memristor networks with an increasing order of complexity with both the increasing topological complexity and additional delayed feedback mechanisms. We found immediately that the latter approach improved the sensing performance. This finding is in line with earlier reports on using a single photonic system for reservoir computing. The most significant improvement was observed when the delayed feedback mechanisms were heterogeneous in terms of delay times. This indicates that heterogeneity and appropriate coupling between components can lead to a genuine collaboration between elements, and more efficient information processing. It is tempting to speculate about the possibilities of using chemical systems, which contain astronomical numbers of interacting units, to implement such a behaviour.

These findings have severe consequences for the practical implementation of the reservoir computing concept in (photo)electrochemical systems. Photoelectrochemical cells containing hybrid semiconducting materials (e.g., CdS + carbon nanotubes) exhibit memristive-like properties due to the efficient charge trapping at nanotubes [9]. Therefore, systems composed of photoelectrodes equipped with an appropriate delay can be considered as hardware optoelectronic implementations of reservoirs. It can be demonstrated that cycling of a simple drive results in the amplification of analytical signals or may facilitate the extraction of more complex information from simple experiments (cf. Fig. 14b).

6. Signal analysis and other applications

There is a great deal of research in the topic of RC focused mostly on software implementations. Of course, it is important

to develop software solutions or theoretical models that can outline new development paths (e.g., Nakane et al. provided theoretical a model for the RC based on spin waves propagated in epitaxial garnet films) [201]. In the 21st century a great emphasis is put on weight, size and energy efficient operation of information processing devices, therefore the research and development of hardware systems and *in materio* computation attains progressively more attention.

The RC can be physically realised based on memristors [202,203], artificial synapses [204,205], field programmable gate arrays [206,207], atomic switches [208] or in photonic systems [209–212]. Du et al. showed memristor-based reservoir composed of WO_x semiconductor [203]. Applied memristors exhibited short-term memory effect with a synaptic-like response to short voltage pulses (500 μs –50 ms) that can be described by the ion-diffusion mechanism. In an experimental setup, an array of 88 memristors has been used for the handwritten image recognition (handwritten numbers converted to spatially distributed black and white pixels) with the accuracy of 88.1%. The authors state, that the system accuracy can be raised to 91.5% for 112 memristors (based on ideal model simulation). In addition, it has been shown that the system can be used to solve a second-order nonlinear dynamic problem. For the uniform random signals, the RC reconstructed output with normalised mean squared error (NMSE) of 3.61×10^{-3} with training and 3.13×10^{-3} without training (for independently generated random sequence).

Dale et al. have reported an interesting way for hardware implementation of the RC through the computer controlled evolution *in materio* of carbon nanotubes [213]. The authors stated that some systems classified as weak RC can be improved by a deliberate reconfiguration of materials properties to produce effective computational results. In this case, a static voltage was used to adapt the samples for signal processing. Their experimental system consisted of single-wall carbon nanotubes mixed with polymer (poly-butyl-methacrylate or poly-methyl methacrylate), deposited on a glass slide with 12 chromium/gold-contact microelectrodes in circle or a square array. The system showed good results in the Non-linear Auto Regressive Moving Average (NARMA) benchmark test.

For further efficiency improvement and system simplification, the research is carried out on systems based on a single node operating in the delayed feedback loop. In the delay-based RC, the masking of input through time-multiplexing can increase the computational capabilities of the reservoir by the introduction of virtual nodes. The time interval of the input signal (which is equal to operation duration of a delay line) is divided in the masking step, and each separate element distributed within the duration of delay line operation creates a virtual neuron (cf. Fig. 13) [191,212]. When compared to a linearly operating RC, the delayed systems may have supreme computational potential, but they work several times slower, therefore to compensate this drawback, such systems are mainly implemented in fast photonic systems [212]. State-of-the-art results were shown by Larger et al. with the RC realised based on the transient motion of an electro-optically modulated phase of a laser beam [210]. The delay feedback loop was constructed using optical fibre pigtailed providing 63.33 ns delay time. The time separation between each virtual node was set to 56.8 ps thus giving total number of 1115 virtual neurons. Further improvements to the system led to an outstanding performance with the capability of classification at the level of 1 million words per second with a very low word error rate.

Photoelectrochemical reservoir systems, based on wide band gap semiconductors (neat or modified with simple coordination compounds) cannot compete with photonic devices in terms of speed or efficiency. They operate, however, in a frequency domain corresponding to the audible range. There is a plethora of different data sets within this range that require advanced processing

techniques, including ECG and EEG signals, automated speech analysis or the classification of music. At the same time, the combination of reservoirs with logic devices (Boolean or fuzzy) may lead to a substantial increase of complexity and computing efficiency. The first reports on practical combinations of the Boolean logic and the reservoir computing are already available [214,215].

7. Conclusions

The first step towards implementation of signal/information processing within molecular systems has been made in middle 70ties by Aviram and Ratner [216]. They predicted that a molecule with electron donor and electron acceptor moieties separated by a saturated bridge of an appropriate length should behave like a diode (rectifier). This *Ansatz* was based on a structure of rectifying *p*–*n* junction, where electron rich (*n*-type) and electron deficient (*p*-type) semiconductors are separated by a depletion layer and supported by the analogy to the electron transfer mechanism between donor and acceptor sites. As it was argued by Aviram and Ratner, any chemical system capable of unidirectional electron transfer should behave like a diode. Such a system should be capable of sequential electron transfer from the cathode to the electron acceptor (or from the donor site to the anode), while the electron transfer in the opposite direction should be thermodynamically unfavoured. Moreover, donor and acceptor sites should be effectively decoupled preventing a direct reaction between these moieties [216,217].

After over four decades the picture is much more complex. There are thousands of molecular-scale binary logic gates, various molecular sensors (from very simple ones to the systems capable of differentiating sugars, proteins and antibiotics) and other sophisticated information processing systems. Moreover, the molecular (or nanoparticle-based) devices can perform complex operations based on the ternary or fuzzy logic, neuromimetic computing and reservoir computing paradigms. Finally, cryptographic and steganographic applications of molecular systems have emerged recently. The development and the introduction of new commercially available products seems much slower than in the case of semiconductor-based electronics. It partially results from the unmatched performance of analogue and digital silicon devices and overall maturity of this technology. Anyway, there are some niche applications, in which molecular signal/information processing could be successfully applied. Medical analysis is one of the most visible examples – numerous medical tests are based on the molecular recognition, enzymatic logic gates or the combination of both.

The unconventional computing devices discussed in this review might also pave the way for a faster development of complex systems capable of more human-like reasoning which could be enhanced by the addition of sophisticated bio-inspired sensing mechanisms. This step may not only lead to the evolution of artificial intelligences and artificial life forms but could help people affected with various disabilities (especially these affecting the sensory system) to recover or even surpass the ordinary human abilities. A similar thought may be found more and more often outside science-fiction books but rather in scientific articles covering a wide spectrum of topics (*vide Ref. [118]*). There is still a long way for a wider application of devices and concepts presented in this review, but the power of *in materio* information processing and unconventional computing surely cannot be underestimated.

Acknowledgements

The authors wish to acknowledge a series of discussions with all the partners of the RECORD-IT consortium. This work has received

funding from the European Union's Horizon 2020 research and innovation programme under grant agreement No. 664786. AP, KS, KP and EW acknowledge partial funding from National Science Centre (Poland) under grant agreements Nos. UMO-2013/11/D/ST5/03010, UMO-2015/18/A/ST4/00058, UMO-2016/21/N/ST3/00469, UMO-2015/17/B/ST8/01783, respectively, and Polish Ministry of Science and Higher Education.

References

- [1] N. Wiener, *Cybernetics: Or Control and Communication in the Animal and the Machine*, MIT Press, 1985.
- [2] J.G. Roederer, *Information and Its Role in Nature*, Springer-Verlag, Berlin, 2005.
- [3] K. Szaciłowski, *Infochemistry. Information Processing at the Nanoscale*, John Wiley & Sons, Chichester, 2012.
- [4] K. Szaciłowski, *Chem. Rev.* 108 (2008) 3481–3548.
- [5] A.P. de Silva, *Molecular Logic-based Computation*, The Royal Society of Chemistry, Cambridge, 2012.
- [6] E. Katz, *Biomolecular Information Processing*, Wiley-VCH, Weinheim, 2012.
- [7] E. Katz, *Molecular and Supramolecular Information Processing*, Wiley-VCH, Weinheim, 2012.
- [8] A. Blachecki, J. Mech-Piskorz, M. Gajewska, K. Mech, K. Pilarczyk, K. Szaciłowski, *ChemPhysChem* 18 (2017) 1798–1810.
- [9] K. Pilarczyk, A. Podborska, M. Lis, M. Kawa, D. Migdal, K. Szaciłowski, *Adv. Electron. Mater.* (2016) 1500471.
- [10] K. Pilarczyk, B. Daly, A. Podborska, P. Kwolek, V.A.D. Silvester, A.P. de Silva, K. Szaciłowski, *Coord. Chem. Rev.* 325 (2016) 135–160.
- [11] M. Warzecha, M. Oszejka, K. Pilarczyk, K. Szaciłowski, *Chem. Commun.* 51 (2015) 3559–3561.
- [12] P.L. Gentili, *Int. J. Intell. Fuzzy Syst.* 27 (2014) 2137–2151.
- [13] P.L. Gentili, *RSC Adv.* 3 (2013) 25523–25549.
- [14] P.L. Gentili, *Chem. Phys.* 336 (2007) 64–73.
- [15] R. Waser, *Nanoelectronics and Information Technology*, Wiley-VCH, Weinheim, 2003.
- [16] G. Boole, *An Investigation of the Laws of Thought of which are Founded the Mathematical Theories of Logic and Probabilities*, Walton and Maberley, London, 1854.
- [17] J. Chomiccki, G. Saake, *Logics for Databases and Information Systems*, Springer Science+Business Media, New York, 1998.
- [18] L.A. Zadeh, *Fuzzy logic*, in: R.A. Meyers (Ed.), *Encyclopedia of Complexity*, Springer Science+Business Media, New York, 2009.
- [19] D.V. Benjamin Schrauwen, Jan Van Campenhout, in: 15th European Symposium on Artificial Neural Networks (ESANN2007-15), Bruges, Belgium, 2007, pp. ES2007-2008.
- [20] M. Lukoševičius, H. Jaeger, *Comp. Sci. Rev.* 3 (2009) 127–149.
- [21] ORGANIC-EU-FP7, *Reservoir Computing: Shaping Dynamics into Information*, <http://reservoir-computing.org>, 2009, accessed: Feb 2th, 2018.
- [22] M.S. Kulkarni, C. Teuscher, in: 2012 IEEE/ACM International Symposium on Nanoscale Architectures (NANOARCH), Amsterdam, 2012, pp. 226–232.
- [23] M. Lukoševičius, H. Jaeger, B. Schrauwen, *Künstliche Intelligenz* 26 (2012) 365–371.
- [24] M.A. Escalona-Moran, M.C. Soriano, I. Fischer, C.R. Mirasso, *IEEE J. Biomed. Health Inform.* 19 (2015) 892–898.
- [25] A.J. Wootton, C.R. Day, P.W. Haycock, *An echo state network approach to structural health monitoring*, 2015 International Joint Conference on Neural Networks, IEEE, New York, 2015.
- [26] C. Mesaritikakis, A. Bogris, A. Kapsalis, D. Syvridis, *Opt. Lett.* 40 (2015) 3416–3419.
- [27] Y. Paquot, J. Dambre, B. Schrauwen, M. Haelterman, S. Massar, 2010, pp. 77280B-77212.
- [28] J.P. Carbajal, J. Dambre, M. Hermans, B. Schrauwen, *Neural Comp.* 27 (2015) 725–747.
- [29] K. Caluwaerts, M. D'Haene, D. Verstraeten, B. Schrauwen, *Artif. Life* 19 (2012) 35–66.
- [30] H. Hauser, A.J. Ijspeert, R.M. Fuchsli, R. Pfeifer, W. Maass, *Biol. Cybern.* 106 (2012) 595–613.
- [31] T. Li, K. Nakajima, M. Cianchetti, C. Laschi, R.S. Pfeifer, 2012 IEEE International Conference on Robotics and Automation (ICRA) (2012) 4918–4924.
- [32] F. Palumbo, P. Barsocchi, C. Gallicchio, S. Chessa, A. Micheli, *Multisensor data fusion for activity recognition based on reservoir computing*, in: J.A. Botia, J.A. Álvarez-García, K. Fujinami, P. Barsocchi, T. Riedel (Eds.), *Evaluating AAL Systems Through Competitive Benchmarking: International Competitions and Final Workshop, EVAAL 2013*, July and September 2013. Proceedings, Springer, Berlin Heidelberg, 2013, pp. 24–35.
- [33] D. Bacciu, P. Barsocchi, S. Chessa, C. Gallicchio, A. Micheli, *Neur. Comp. Appl.* 24 (2014) 1451–1464.
- [34] H. Hauser, R.M. Fuchsli, K. Nakajima, *Morphological computation – the physical body as a computational resource*, in: R.M.F. Hauser Helmut, R. Pfeifer (Eds.), *Opinions and Outlooks on Morphological Computation*, Self-published, 2014, pp. 226–244.
- [35] S. Sheik, S. Marco, R. Huerta, J. Fonollosa, in: *EUROSENSORS 2014, the 28th European Conference on Solid-State Transducers*, Procedia Engineering, Brescia, Italy, 2014, pp. 843–846.
- [36] C. Feng, S. Dai, L. Wang, *Biosens. Bioelectron.* 59 (2014) 64–74.
- [37] J. Fonollosa, S. Sheik, R. Huerta, S. Marco, *Sens. Actuators, B Chem.* 215 (2015) 618–629.
- [38] C. Mesaritikakis, A. Kapsalis, D. Syvridis, in: *Quantum Sensing and Nanophotonic Devices XII*, Spie-Int Soc Optical Engineering, San Francisco, California, United States, 2015, p. 937033.
- [39] B. Wang, J.C. Cancilla, J.S. Torrecilla, H. Haick, *Nano Lett.* 14 (2014) 933–938.
- [40] Z. Konkoli, *Int. J. Parallel Emergent Distrib. Syst.* (2016), <https://doi.org/10.1080/17445760.17442016.11241880>.
- [41] L. Zhou, D. Jiang, X. Du, D. Chen, J. Qian, Q. Liu, N. Hao, K. Wang, *J. Mater. Chem. B* 4 (2016) 6249–6257.
- [42] H. Li, Y. Xue, W. Wang, *Biosens. Bioelectron.* 54 (2014) 317–322.
- [43] K. Szaciłowski, W. Macyk, *Chimia* 61 (2007) 831–834.
- [44] S. Gawęda, R. Kowalik, P. Kwolek, W. Macyk, J. Mech, M. Oszejka, A. Podborska, K. Szaciłowski, *Isr. J. Chem.* 51 (2011) 36–55.
- [45] S. Gawęda, A. Podborska, W. Macyk, K. Szaciłowski, *Nanoscale* 1 (2009) 299–316.
- [46] Y. Zang, J. Lei, H. Ju, *Biosens. Bioelectron.* 96 (2017) 8–16.
- [47] A. Efrati, O. Yehezkeili, R. Tel-Vered, D. Michaeli, R. Nechushtai, I. Willner, *ACS nano* 6 (2012) 9258–9266.
- [48] R. Gill, F. Patolsky, E. Katz, I. Willner, *Angew. Chem. Int. Ed.* 44 (2005) 4554–4557.
- [49] R. Tel-Vered, O. Yehezkeili, H.B. Yildiz, O.I. Wilner, I. Willner, *Angew. Chem. Int. Ed.* 47 (2008) 8272–8276.
- [50] Q. Hao, X. Shan, J. Lei, Y. Zang, Q. Yang, H. Ju, *Chem. Sci.* 7 (2016) 774–780.
- [51] X. Pang, J. Pan, L. Wang, W. Ren, P. Gao, Q. Wei, B. Du, *Biosens. Bioelectron.* 71 (2015) 88–97.
- [52] G.C. Fan, L. Han, J.R. Zhang, J.J. Zhu, *Anal. Chem.* 86 (2014) 10877–10884.
- [53] P. Zhou, J. Yu, M. Jaronec, *Adv. Mater. (Weinheim, Ger.)* 26 (2014) 4920–4935.
- [54] Z. Kang, X. Yan, Y. Wang, Y. Zhao, Z. Bai, Y. Liu, K. Zhao, S. Cao, Y. Zhang, *Nano Res.* 9 (2015) 344–352.
- [55] W.W. Zhao, J. Wang, J.J. Xu, H.Y. Chen, *Chem. Commun.* 47 (2011) 10990–10992.
- [56] C. Ding, H. Li, X. Li, S. Zhang, *Chem. Commun.* 46 (2010) 7990–7992.
- [57] H. Cao, S. Liu, W. Tu, J. Bao, Z. Dai, *Chem. Commun.* 50 (2014) 13315–13318.
- [58] H. Xu, D. Huang, Y. Wu, J. Di, *Sens. Actuators, B* 235 (2016) 432–438.
- [59] I. Ibrahim, H.N. Lim, O.K. Abou-Zied, N.M. Huang, P. Estrela, A. Pandikumar, *J. Phys. Chem. C* 120 (2016) 22202–22214.
- [60] F. Huang, F. Pu, X. Lu, H. Zhang, Y. Xia, W. Huang, Z. Li, *Sens. Actuators, B* 183 (2013) 601–607.
- [61] Q. Shen, X. Zhao, S. Zhou, W. Hou, J.-J. Zhu, *J. Phys. Chem. C* 115 (2011) 17958–17964.
- [62] J. Tang, J. Li, Y. Zhang, B. Kong, Yiliguma, Y. Wang, Y. Quan, H. Cheng, A.M. Al-Enizi, G. Gong, G. Zheng, *Anal. Chem.* 87 (2015) 6703–6708.
- [63] I. Ibrahim, H.N. Lim, N.M. Huang, A. Pandikumar, *PLoS One* 11 (2016) 1–18.
- [64] Q. Hao, J. Lei, Q. Wang, Y. Zang, H. Ju, *J. Electroanal. Chem.* 759 (2015) 8–13.
- [65] G. Wen, X. Wen, M.M.F. Choi, S. Shuang, *Sens. Actuators, B* 221 (2015) 1449–1454.
- [66] Y. Wang, P. Wang, Y. Wu, J. Di, *Sens. Actuators, B* 254 (2018) 910–915.
- [67] X. She, H. Xu, Y. Xu, J. Yan, J. Xia, L. Xu, Y. Song, Y. Jiang, Q. Zhang, H. Li, *J. Mater. Chem. A* 2 (2014) 2563–2570.
- [68] H. Xu, J. Yan, X. She, L. Xu, J. Xia, Y. Xu, Y. Song, L. Huang, H. Li, *Nanoscale* 6 (2014) 1406–1415.
- [69] L. Xu, J. Xia, L. Wang, H. Ji, J. Qian, H. Xu, K. Wang, H. Li, *Eur. J. Inorg. Chem.* 2014 (2014) 3665–3673.
- [70] S. Chen, N. Hao, D. Jiang, X. Zhang, Z. Zhou, Y. Zhang, K. Wang, *J. Electroanal. Chem.* 787 (2017) 66–71.
- [71] W.W. Zhao, J.J. Xu, H.Y. Chen, *Chem. Soc. Rev.* 44 (2015) 729–741.
- [72] W.-W. Zhao, M. Xiong, X.-R. Li, J.-J. Xu, H.-Y. Chen, *Electrochem. Commun.* 38 (2014) 40–43.
- [73] A. Devadoss, P. Sudhagar, C. Terashima, K. Nakata, A. Fujishima, *J. Photochem. Photobiol., C* 24 (2015) 43–63.
- [74] W.-W. Zhao, J.-J. Xu, H.-Y. Chen, *TrAC, Trends Anal. Chem.* 82 (2016) 307–315.
- [75] D. Jin, A. Gong, H. Zhou, *RSC Adv.* 7 (2017) 17489–17496.
- [76] J. Feng, Y. Li, Z. Gao, H. Lv, X. Zhang, D. Fan, Q. Wei, *Biosens. Bioelectron.* 99 (2018) 14–20.
- [77] Y. Liu, Y. Zhang, D. Wu, D. Fan, X. Pang, Y. Zhang, H. Ma, X. Sun, Q. Wei, *Biosens. Bioelectron.* 86 (2016) 301–307.
- [78] A. Liu, H. Shan, M. Ma, L. Shanguan, K. Jiang, M. Shi, Y. Zhao, S. Liu, S. Li, *J. Electroanal. Chem.* 803 (2017) 1–10.
- [79] O.K. Okoth, K. Yan, J. Zhang, *Carbon* 120 (2017) 194–202.
- [80] Y. Yan, H. Li, Q. Liu, N. Hao, H. Mao, K. Wang, *Sens. Actuators, B* 251 (2017) 99–107.
- [81] J. Li, Z. Dai, H. Li, *Analyst* 142 (2017) 2177–2184.
- [82] D.-M. Han, Z.-Y. Ma, W.-W. Zhao, J.-J. Xu, H.-Y. Chen, *Electrochem. Commun.* 35 (2013) 38–41.
- [83] D.-M. Han, L.-Y. Jiang, W.-Y. Tang, J.-J. Xu, H.-Y. Chen, *Electrochem. Commun.* 51 (2015) 72–75.
- [84] Y. Shi, G. Zhang, J. Li, Y. Zhang, Y. Yu, Q. Wei, *Microchim. Acta* 184 (2017) 1379–1387.
- [85] W. Zhang, B. Shan, D. Liang, Y. Shi, D. Han, C. Huang, *Anal. Methods* 8 (2016) 7762–7766.

- [86] A.P. de Silva, H.Q.N. Gunaratne, C.P. McCoy, *Nature* 364 (1993) 42–44.
- [87] A.P. de Silva, K.R.A.S. Sandanayake, *Angew. Chem. Int. Ed.* 29 (1990) 1173.
- [88] A.P. de Silva, H.Q.N. Gunaratne, C.P. McCoy, *J. Am. Chem. Soc.* 119 (1997) 7891–7892.
- [89] B. Daly, J. Ling, A.P. de Silva, *Chem. Soc. Rev.* 44 (2015) 4203–4211.
- [90] A.P. de Silva, N.D. McClenaghan, *J. Am. Chem. Soc.* 122 (2000) 3965–3966.
- [91] K. Szaciłowski, W. Macyk, *Solid State Electron.* 50 (2006) 1649–1655.
- [92] K. Szaciłowski, W. Macyk, G. Stochel, *J. Am. Chem. Soc.* 128 (2006) 4550–4551.
- [93] D. Margulies, G. Melman, A. Shanzer, *J. Am. Chem. Soc.* 128 (2006) 4865–4871.
- [94] A. Podborska, K. Szaciłowski, *Aust. J. Chem.* 63 (2010) 165–168.
- [95] J. Andréasson, U. Pischel, S.D. Straight, T.A. Moore, A.L. Moore, D. Gust, *J. Am. Chem. Soc.* 133 (2011) 11641–11648.
- [96] D.C. Magri, *Org. Biomol. Chem.* 15 (2017) 6706–6709.
- [97] T.T. Meng, L.X. Xue, H. Wang, K.Z. Wang, M. Haga, *J. Mater. Chem. C* 5 (2017) 3390–3396.
- [98] M. Elati, P. Neuvial, M. Bolotin-Fukuhara, E. Barillot, F. Radvanyi, *C. Rouveiro, Bioinformatics* 23 (2007) 2407–2414.
- [99] J. Łukasiewicz, *Selected Works, North-Holland, Amsterdam, 1970.*
- [100] M. Fisch, A. Turquette, *TCS Peirce Soc.* 2 (1966) 71–85.
- [101] P.C. Balla, A. Antoniou, *IEEE J. Solid-State Circ.* 19 (1984) 739–749.
- [102] W. Kim, A. Chattopadhyay, A. Siemon, E. Linn, R. Waser, V. Rana, *Sci. Rep.* 6 (2016) 36652.
- [103] N.S. Soliman, M.E. Fouda, A.G. Radwan, *Microelectron. J.* 72 (2018) 74–85.
- [104] P.C. Ooi, J. Lin, T.W. Kim, F. Li, *Org. Electron.* 38 (2016) 379–383.
- [105] Z. Ma, C. Wu, D.U. Lee, F. Li, T.W. Kim, *Org. Electron.* 28 (2016) 20–24.
- [106] H. Chan, S.-H. Lee, C.-T. Poon, M. Ng, V.W.-W. Yam, *ChemNanoMat* 3 (2017) 164–167.
- [107] M. Balynsky, A. Kozhevnikov, Y. Khivintsev, T. Bhowmick, D. Gutierrez, H. Chiang, G. Dudko, Y. Filimonov, G. Liu, C. Jiang, A.A. Balandin, R. Lake, A. Khitun, *J. Appl. Phys.* 121 (2017) 024504.
- [108] J. Shim, S. Oh, D.-H. Kang, S.-H. Jo, M.H. Ali, W.-Y. Choi, K. Heo, J. Jeon, S. Lee, M. Kim, Y.J. Song, J.-H. Park, *Nat. Commun.* 7 (2016) 13413.
- [109] J. Shim, S.-H. Jo, M. Kim, Y.J. Song, J. Kim, J.-H. Park, *ACS Nano* 11 (2017) 6319–6327.
- [110] M.L. Li, X. Yu, H.Y. Liu, *Electrochim. Acta* 220 (2016) 562–572.
- [111] J. Liang, X. Yu, T. Yang, M. Li, L. Shen, Y. Jin, H. Liu, *PCCP* 19 (2017) 22472–22481.
- [112] W. Lian, J. Liang, L. Shen, Y. Jin, H. Liu, *Biosens. Bioelectron.* 100 (2018) 326–332.
- [113] J.M.A. Spiteri, C.J. Mallia, G.J. Scerri, D.C. Magri, *Org. Biomol. Chem.* 15 (2017) 10116–10121.
- [114] W.S. Bourée, M.S. Prévot, X.A. Jeanbouquin, N. Guijarro, M. Johnson, F. Le Formal, K. Sivila, *Adv. Mater.* 28 (2016) 9313–9319.
- [115] R.M. Zadeh, M.D.E. Jepsen, L.L. Hildebrandt, V. Birkedal, J. Kjems, *Small* 11 (2015) 1811–1817.
- [116] C. Zhou, D. Liu, C. Wu, S. Dong, E. Wang, *ACS Appl. Mater. Interfaces* 8 (2016) 30287–30293.
- [117] D. Fan, E. Wang, S. Dong, *Nano Res.* 10 (2017) 2560–2569.
- [118] L.A. Zadeh, *Inform. Control* 8 (1965) 338–353.
- [119] M. Bergmann, *An Introduction to Many-Valued and Fuzzy Logic: Semantics, Algebras, and Derivation Systems*, Cambridge University Press, Cambridge, 2008.
- [120] E.H. Mamdani, S. Assilian, *Int. J. Human-Comput. Stud.* 51 (1999) 135–147.
- [121] M. Sugeno, T. Takagi, *Fuzzy Sets Syst.* 9 (1983) 313–325.
- [122] P.L. Gentili, *Dyes Pigm.* 110 (2014) 235–248.
- [123] P.L. Gentili, V. Horvath, V.K. Vanag, I.R. Epstein, *Int. J. Uncov. Comput.* 8 (2012) 177–192.
- [124] P.L. Gentili, A.L. Rightler, B.M. Heron, C.D. Gabbutt, *Chem. Commun.* 52 (2016) 1474–1477.
- [125] P.L. Gentili, A.L. Rightler, B.M. Heron, C.D. Gabbutt, *Dyes Pigm.* 135 (2016) 169–176.
- [126] D. Bhattacharjee, W. Kim, A. Chattopadhyay, R. Waser, V. Rana, *Sci. Rep.* 8 (2018) 8.
- [127] S. Karmakar, M. Nandi, S. Mukherjee, S. Baitalik, *Inorg. Chim. Acta* 454 (2017) 76–88.
- [128] X.-Y. Xu, B. Yan, *Adv. Funct. Mater.* 27 (2017), 1700247–n/a.
- [129] O. Lustgarten, L. Motiei, D. Margulies, *ChemPhysChem* 18 (2017) 1678–1687.
- [130] J.F. Dooley, *Cryptologia* 40 (2016) 107–112.
- [131] C.T. Clelland, V. Risca, C. Bancroft, *Nature* 399 (1999) 533–534.
- [132] A. Leier, C. Richter, W. Banzhaf, H. Rauhe, *Biosystems* 57 (2000) 13–22.
- [133] K. Tanaka, A. Okamoto, I. Saito, *Biosystems* 81 (2005) 25–29.
- [134] S. Shoshani, R. Piran, Y. Arava, E. Keinan, *Angew. Chem., Int. Ed.* 51 (2012) 2883–2887.
- [135] J. Chen, S. Zhou, J. Wen, *Angew. Chem.* 127 (2015) 456–460.
- [136] G. Hamed, M. Marey, S.A. El-Sayed, M.F. Tolba, in: 2016 11th International Conference on Computer Engineering & Systems (ICCES), 2016, pp. 220–225.
- [137] S. Marwan, A. Shawish, K. Nagaty, *Biosystems* 150 (2016) 110–118.
- [138] C. Mao, T.H. LaBean, J.H. Reif, N.C. Seeman, *Nature* 407 (2000) 493–496.
- [139] L.M. Adleman, *Science* 266 (1994) 1021–1024.
- [140] D. Margulies, C.E. Felder, G. Melman, A. Shanzer, *J. Am. Chem. Soc.* 129 (2007) 347–354.
- [141] J. Andréasson, S.D. Straight, T.A. Moore, A.L. Moore, D. Gust, *Chem. Eur. J.* 15 (2009) 3936–3939.
- [142] M. Kumar, R. Kumar, V. Bhalla, *Chem. Commun.* (2009) 7384–7386.
- [143] W. Jiang, M. Han, Z. Heng-Yi, Z. Zhi-Jun, Y. Liu, *Chem. Eur. J.* 15 (2009) 9938–9945.
- [144] J. Wang, C.S. Ha, *Analyst* 135 (2010) 1214–1218.
- [145] B. Rout, P. Milko, M.A. Iron, L. Motiei, D. Margulies, *J. Am. Chem. Soc.* 135 (2013) 15330–15333.
- [146] S. Chen, Z. Guo, S. Zhu, W.E. Shi, W. Zhu, *ACS Appl. Mater. Interfaces* 5 (2013) 5623–5629.
- [147] C.P. Carvalho, Z. Domínguez, J.P. Da Silva, U. Pischel, *Chem. Commun.* 51 (2015) 2698–2701.
- [148] T. Majumdar, B. Haldar, A. Mallick, *Sci. Rep.* 7 (2017) 42811.
- [149] T. Sarkar, K. Selvakumar, L. Motiei, D. Margulies, *Nat. Commun.* 7 (2016) 11374.
- [150] G. Naren, S. Li, J. Andréasson, *ChemPhysChem* 18 (2017) 1726–1729.
- [151] A. Kishimura, T. Yamashita, K. Yamaguchi, T. Aida, *Nat. Mater.* 4 (2005) 546–549.
- [152] T. Ratner, O. Reany, E. Keinan, *ChemPhysChem* 10 (2009) 3303–3309.
- [153] I.B. Burgess, L. Mishchenko, B.D. Hatton, M. Kolle, M. Lončar, J. Aizenberg, *J. Am. Chem. Soc.* 133 (2011) 12430–12432.
- [154] H. Sun, S. Liu, W. Lin, K.Y. Zhang, W. Lv, X. Huang, F. Huo, H. Yang, G. Jenkins, Q. Zhao, W. Huang, *Nat. Commun.* 5 (2014) 3601.
- [155] K. Szot, M. Rogala, W. Speier, Z. Klusek, A. Besmehn, R. Waser, *Nanotechnology* 22 (2011) 254001.
- [156] R. Waser, R. Dittmann, G. Staikov, K. Szot, *Adv. Mater.* 21 (2009) 2632–2663.
- [157] F. Pan, S. Gao, C. Chen, C. Song, F. Zeng, *Mater. Sci. Eng. R* 83 (2014) 1–59.
- [158] M. Dragoman, M. Batiri, A. Dinescu, V. Ciobanu, E. Rusu, D. Dragoman, I. Tiginyanu, *J. Appl. Phys.* 123 (2018) 024506.
- [159] Y. Li, Y. Lei, B.G. Chen, *J.R. Sun, Sci. Rep.* 5 (2015) 14576.
- [160] A. Bera, H. Peng, J. Lourembam, Y. Shen, X.W. Sun, T. Wu, *Adv. Funct. Mater.* 23 (2013) 4977–4984.
- [161] H. Tan, G. Liu, H. Yang, X. Yi, L. Pan, J. Shang, S. Long, M. Liu, Y. Wu, R.-W. Li, *ACS Nano* 11 (2017) 11298–11305.
- [162] H. Tan, G. Liu, X. Zhu, H. Yang, B. Chen, X. Chen, J. Shang, W.D. Lu, Y. Wu, R.-W. Li, *Adv. Mater.* 27 (2015) 2797–2803.
- [163] O.K. Olesya, N.P. Gennady, C. Hak Dong, N.B. Andrey, K. Tae Won, *Nanotechnology* 28 (2017) 204005.
- [164] K. Ueda, S. Aichi, H. Asano, *Appl. Phys. Lett.* 108 (2016) 222102.
- [165] G. Lin, Y. Lin, R. Cui, H. Huang, X. Guo, C. Li, J. Dong, X. Guo, B. Sun, *J. Mater. Chem. C* 3 (2015) 10793–10798.
- [166] J. Park, S. Lee, J. Lee, K. Yong, *Adv. Mater.* 25 (2013) 6423–6429.
- [167] C. Hoessbacher, Y. Fedoryshyn, A. Emboras, A. Melikyan, M. Kohl, D. Hillerkuss, C. Hafner, J. Leuthold, *Optica* 1 (2014) 198–202.
- [168] A. Emboras, I. Goykman, B. Desiatov, N. Mazurski, L. Stern, J. Shappir, U. Levy, *Nano Lett.* 13 (2013) 6151–6155.
- [169] N.I. Mou, M. Tabib-Azar, *Appl. Surf. Sci.* 340 (2015) 138–142.
- [170] W. Wang, G.N. Panin, X. Fu, L. Zhang, P. Ilanchezhiyan, V.O. Pelenovich, D. Fu, *T.W. Kang, Sci. Rep.* 6 (2016) 31224.
- [171] C. He, J. Li, X. Wu, P. Chen, J. Zhao, K. Yin, M. Cheng, W. Yang, G. Xie, D. Wang, D. Liu, R. Yang, D. Shi, Z. Li, L. Sun, G. Zhang, *Adv. Mater.* 25 (2013) 5593–5598.
- [172] R. Basori, K. Das, P. Kumar, K.S. Narayan, A.K. Raychaudhuri, *Appl. Phys. Lett.* 102 (2013) 061111.
- [173] A. Emboras, J. Niegemann, P. Ma, C. Haffner, A. Pedersen, M. Luisier, C. Hafner, T. Schimmel, J. Leuthold, *Nano Lett.* 16 (2016) 709–714.
- [174] X. Zhu, W.D. Lu, *ACS Nano* 12 (2018) 1242–1249.
- [175] A.H. Jaafar, R.J. Gray, E. Verrelli, M. O'Neill, S.M. Kelly, N.T. Kemp, *Nanoscale* 9 (2017) 17091–17098.
- [176] P. Maier, F. Hartmann, M. Emmerling, C. Schneider, M. Kamp, S. Höfling, L. Worschech, *Phys. Rev. Appl.* 5 (2016) 054011.
- [177] P. Maier, F. Hartmann, M.R.S. Dias, M. Emmerling, C. Schneider, L.K. Castellano, M. Kamp, G.E. Marques, V. Lopez-Richard, L. Worschech, S. Höfling, *Appl. Phys. Lett.* 109 (2016) 023501.
- [178] N.M. Samardžić, B. Bajac, J. Bajić, E. Đurđić, B. Miljević, V.V. Srdić, G.M. Stojanović, *Microelectron. Eng.* 187–188 (2018) 139–143.
- [179] L. Chua, If it's pinched it's a memristor, in: R. Tetzlaff (Ed.), *Memristors and Memristive Systems*, Springer, New York, NY, 2014, pp. 17–90.
- [180] C.-C. Shih, C.-W. Huang, M. Gao, C.-C. Chueh, W.-C. Chen, *J. Mater. Chem. C* 5 (2017) 11421–11428.
- [181] M. Ungureanu, R. Zazpe, F. Golmar, P. Stoliar, R. Llopis, F. Casanova, L.E. Hueso, *Adv. Mater.* 24 (2012) 2496–2500.
- [182] S. Chen, Z. Lou, D. Chen, G. Shen, *Adv. Mater.* 30 (2018) 1705400.
- [183] S. Nau, C. Wolf, S. Sax, E.J.W. List-Kratochvil, *Adv. Mater.* 27 (2015) 1048–1052.
- [184] A. Nordrum, *Popular Internet of Things Forecast of 50 Billion Devices by 2020 Is Outdated*, <https://spectrum.ieee.org/tech-talk/telecom/internet/popular-internet-of-things-forecast-of-50-billion-devices-by-2020-is-outdated>, 2016, accessed: Feb 6th, 2018.
- [185] W. Maass, T. Natschläger, H. Markram, *Neur. Comput.* 14 (2002) 2531–2560.
- [186] H. Jaeger, H. Haas, *Science* 304 (2004) 78–80.
- [187] Y. Liao, L. Hongmei, *Global J. Res. Eng.: F: Electr. Electron. Eng.* 17 (2017) 45–50.
- [188] B. Schneider, J. Dambre, P. Bienstman, *IEEE Trans. Neural Netw. Learn. Syst.* 27 (2016) 2748–2753.
- [189] J. Nakayama, K. Kanno, A. Uchida, *Opt. Express* 24 (2016) 8679–8692.
- [190] Z. Konkoli, On reservoir computing: from mathematical foundations to unconventional applications, in: A. Adamatzky (Ed.), *Advances in Unconventional Computing*, Springer, 2016.

- [191] L. Appellant, M.C. Soriano, G. Van der Sande, J. Danckaert, S. Massar, J. Dambre, B. Schrauwen, C.R. Mirasso, I. Fischer, *Nat. Commun.* 2 (2011) 468.
- [192] V. Athanasiou, Z. Konkoli, *Int. J. Parallel Emergent Dist. Syst.* (2017), <https://doi.org/10.1080/17445760.17442017.17128726>.
- [193] V. Athanasiou, Z. Konkoli, submitted (2018).
- [194] Z. Konkoli, G. Wendin, *Nanotechnology* 24 (2013) 384007.
- [195] G.S. Kulkarni, K. Reddy, Z. Zhong, X. Fan, *Nat. Commun.* 5 (2014) 4376.
- [196] G.S. Kulkarni, K. Reddy, W. Zang, K. Lee, X. Fan, Z. Zhong, *Nano Lett.* 16 (2015) 695–700.
- [197] G.S. Kulkarni, Z. Zhong, *Nano Lett.* 12 (2012) 719–723.
- [198] V.A. Antohe, A. Radu, S. Mátéfi-Tempfli, L. Piraux, *IEEE Trans. Nanotechnol.* 10 (2011) 1314–1320.
- [199] G.S. Kulkarni, W. Zang, Z. Zhong, *Acc. Chem. Res.* 49 (2016) 2578–2586.
- [200] S. Lee, Z. Zhong, *Nanoscale* 6 (2014) 13283–13300.
- [201] R. Nakane, G. Tanaka, A. Hirose, *IEEE Access* (2018), accepted, manuscript ID 8262616.
- [202] C. Merkel, Q. Saleh, C. Donahue, D. Kudithipudi, *Procedia Comput. Sci.* 41 (2014) 249–254.
- [203] C. Du, F. Cai, M.A. Zidan, W. Ma, S.H. Lee, W.D. Lu, *Nat. Commun.* 8 (2017) 2204.
- [204] J. Li, C. Zhao, K. Hamedani, Y. Yi, in: *IEEE International Joint Conference on Neural Networks 2017*, IEEE, 2017, pp. 3439–3446.
- [205] C. Zhao, B.T. Wysocki, C.D. Thiem, N.R. McDonald, J. Li, L. Liu, Y. Yi, *IEEE Trans. Multi-Scale Comput. Syst.* 2 (2016) 265–276.
- [206] M.L. Alomar, V. Canals, N. Perez-Mora, V. Martínez-Moll, J.L. Rosselló, *Comput. Intell. Neurosci.* 2016 (2016) 1–15.
- [207] Y. Yi, Y. Liao, B. Wang, X. Fu, F. Shen, H. Hou, L. Liu, *Microprocess. Microsyst.* 46 (2016) 175–183.
- [208] S.K. Bose, J.B. Mallinson, R.M. Gazoni, S.A. Brown, *IEEE Trans. Electron. Devices* 64 (2017) 5194–5201.
- [209] P. Antonik, M. Hermans, M. Haelterman, S. Massar, in: *IEEE International Joint Conference on Neural Networks 2017*, IEEE, 2017, pp. 2407–2413.
- [210] L. Larger, A. Baylón-Fuentes, R. Martinenghi, V.S. Udaltsov, Y.K. Chembo, M. Jacquot, *Phys. Rev. X* 7 (2017) 011015–11101.
- [211] G. Van der Sande, R.M. Nguimdo, G. Verschaffelt, in: *Proc. SPIE, International Society for Optics and Photonics*, 2016, p. 98941.
- [212] G. Van der Sande, D. Brunner, M.C. Soriano, *J. Nanophotonics* 6 (2017) 561–576.
- [213] M. Dale, J.F. Miller, S. Stepney, M.A. Trefzer, in: *International Conference on Unconventional Computation and Natural Computation*, Springer, 2016, pp. 49–61.
- [214] N.D. Haynes, M.C. Soriano, D.P. Rosin, I. Fischer, D.J. Gauthier, *Phys. Rev. E* 91 (2015) 020801(R).
- [215] M.C. Soriano, S. Ortín, L. Keuninckx, L. Appellant, *IEEE Trans. Neural Networks* 26 (2015) 388–393.
- [216] A. Aviram, M.A. Ratner, *Chem. Phys. Lett.* 29 (1974) 277–283.
- [217] R.L. McCreery, *Chem. Mater.* 16 (2004) 4477–4496.

Oświadczenia współautorów

Oświadczenie

Jako autor rozprawy doktorskiej niniejszym określam mój wkład w proces przygotowywania publikacji naukowych, które tworzą rozprawę. We wszystkich poniższych pracach brałam udział w dyskusji wyników, pisaniu fragmentów manuskryptów oraz ich korekcie, a w szczególności:

A1. **E. Właźlak**,* A. Blachecki, M. Bisztyga-Szklarz, S. Klejna, T. Mazur, K. Mech,* K. Pilarczyk, D. Przyczyna, M. Suchecki, P. Zawal, K. Szaciłowski* *“Heavy pnictogen chalcogenides: the synthesis, structure and properties of these rediscovered semiconductors”* Chemical Communications, 2018, **54**, 12133-12162

Mój udział polegał na napisaniu części opisującej strukturę krystaliczną chalcogenków i analizie występujących w nich oddziaływań oddziaływań międzycząsteczkowych na podstawie artykułów i struktur krystalicznych obecnych w bazach. Wykonałam też obliczenia z wykorzystaniem programu CRYSTAL EXPLORER 17 i analizę uzyskanych w ten sposób powierzchni Hirshfelda. Brałam też udział w koordynowaniu prac nad manuskrytem, jestem odpowiedzialna za fragment podsumowania, niektórych pomniejszych fragmentów tekstu, redagowaniu jego ostatecznej wersji i odpowiedzi na uwagi recenzentów (wspólnie z prof. Konradem Szaciłowskim).

A2. **E. Właźlak**, W. Macyk, W. Nitek, K. Szaciłowski* *“Influence of π -Iodide Intermolecular Interactions on Electronic Properties of Tin(IV) Iodide Semiconducting Complexes”* Inorganic Chemistry, 2016, **55**, 5935-5945

W powyższym artykule byłam odpowiedzialna za syntezę badanych tetrajodkowych kompleksów cyny(IV), obliczenia teoretyczne, pomiary z wykorzystaniem sondy Kelvina (pomiary prac wyjścia i fotonapięcia powierzchniowego), pomiary oporu

właściwego z wykorzystaniem metody czteropunktowej, wykonanie pomiarów widm UV-vis. Brałam udział w interpretacji wyników uzyskanych z powyższych pomiarów i obliczeń oraz interpretacji oddziaływań obecnych w strukturach krystalicznych badanych kompleksów oraz ich widm $^1\text{HNMR}$. Mój wkład polegał na pisaniu fragmentów manuskryptu i jego korekcie.

A3. **E. Wlazlak,*** J. Kalinowska-Tłuścik, W. Nitek, S. Klejna, K. Mech, W. Macyk, K. Szaciłowski* “*Triiodide Organic Salts: Photoelectrochemistry at the Border between Insulators and Semiconductors*” ChemElectroChem, 2018, **5**, 3486-3497

W powyższej publikacji mój wkład polegał na syntezie badanych soli półprzewodnikowych, wykonaniu pomiarów widm UV-vis i pomiarów prac wyjścia, pomiaru oporności metodą czteropunktową, obliczeniu i wykonaniu analizy powierzchni Hirshfelda oraz rejestrowaniu fotoprądów generowanych przez badane sole trójjodkowe.

Jestem też odpowiedzialna za interpretację wyników otrzymanych z wyżej wymienionych pomiarów oraz analizę oddziaływań obecnych w strukturze, analizę wyników pomiarów impedancyjnych oraz interpretację struktur elektronowych badanych soli (wspólnie z prof. Konradem Szaciłowskim).

Mój wkład polegał na pisaniu fragmentów wstępu, podsumowania, części eksperymentalnej i fragmentów części głównej artykułu.

Odpowiadałam też za koordynację badań i odpowiedzi na uwagi recenzentów (wspólnie z prof. Konrdem Szaciłowskim)

A4. **E. Wlazlak,*** M. Marzec, P. Zawal, K. Szaciłowski* “*Memristor in reservoir system – experimental evidence for high level computing and neuromorphic behaviour of PbI_2* ” ACS Applied Materials & Interfaces, 2019, (DOI:10.1021/acsami.9b01841),

W powyższym artykule byłam odpowiedzialna za przygotowanie warstw PbX_2 , pomiary ich grubości i konstrukcję memrystorów. Mój udział polegał na zaprojektowaniu i wykonaniu pomiarów elektrochemicznych w tym pomiarów charakterystyk prądowo-napięciowych, pomiarów chronoamperometrycznych oraz pomiarów w układzie rezerwurowym. Byłam odpowiedzialna za analizę wyników uzyskanych z powyżej

wymienionych pomiarów elektrycznych, pomiarów STDP i SRDP, pomiarów widm XPS i UPS. Razem z prof. Konradem Szaciłowskim jestem odpowiedzialna za analizę mechanizmu działania zbudowanych memrystorów. W publikacji tej jestem odpowiedzialna za ogólną koncepcję artykułu, napisanie części wstępu, fragmentów opisujących pomiary elektryczne, opis części eksperymentalnej oraz za scalanie całości manuskryptu i korespondencję z recenzentami (wspólnie z Konradem Szaciłowskim).

A5. K. Pilarczyk,* E. **Właźlak**,* D. Przyczyna, A. Blachecki, A. Podborska, V. Anathasiou, Z. Konkoli, K. Szaciłowski* *“Molecules, semiconductors, light and information: Towards future sensing and computing paradigms”* Coordination Chemistry Reviews, 2018, **365**, 23-40

W powyższym artykule jestem odpowiedzialna za rozdział dotyczący fotomemrystorów i urządzeń neuromimetycznych. Jestem też autorem nieopublikowanych wcześniej wyników eksperymentalnych przedstawionych na rysunku 14, pokazujących zachowanie się elektrod o różnych oporach w układzie rezerwuarowym zawierającym pętlę sprzężenia zwrotnego. Byłam też odpowiedzialna za koordynowanie prac nad manuskrytem i jego korektę.

Z poważaniem,

Ewelina Właźlak

Kraków, 17.04.2019

Oświadczenie współautora publikacji wchodzących w skład rozprawy
doktorskiej mgr Eweliny Właźlak

E. Właźlak,* M. Marzec, P. Zawal, K. Szaciłowski* *“Memristor in reservoir system – experimental evidence for high level computing and neuromorphic behaviour of PbI_2 ”*

ACS Applied Materials & Interfaces, 2019, (DOI:10.1021/acsami.9b01841)

Mój udział polegał na napisaniu fragmentów wstępu, pomocy w analizie mechanizmu przełączenia oraz korekcie manuskryptu.

E. Właźlak,* A. Blachecki, M. Bisztyga-Szklarz, S. Klejna, T. Mazur, K. Mech,* K. Pilarczyk, D. Przyczyna, M. Suchecki, P. Zawal, K. Szaciłowski* *“Heavy pnictogen chalcogenides: the synthesis, structure and properties of these rediscovered semiconductors”* Chemical Communications, 2018, **54**, 12133-12162

Mój udział polegał na opracowaniu ogólnej koncepcji artykułu, koordynacji pracy autorów oraz przygotowaniu wstępu oraz odpowiedzi na recenzje (wspólnie z Ewelina Właźlak).

E. Właźlak,* J. Kalinowska-Tłuścik, W. Nitek, S. Klejna, K. Mech, W. Macyk, K. Szaciłowski* *“Triiodide Organic Salts: Photoelectrochemistry at the Border between Insulators and Semiconductors”* ChemElectroChem, 2018, **5**, 3486-3497

Mój wkład polegał na koordynacji badań (wspólnie z Ewelina Właźlak) oraz analizie widm elektronowych.

K. Pilarczyk,* E. Właźlak,* D. Przyczyna, A. Blachecki, A. Podborska, V. Anathasiou, Z. Konkoli, K. Szaciłowski* „*Molecules, semiconductors, light and information: Towards future sensing and computing paradigms*” *Coordination Chemistry Reviews*, 2018, **365**, 23-40

Mój udział polegał na koordynacji pracy zespołu autorów, napisaniu wstępu oraz podsumowania, przygotowaniu niektórych rysunków oraz części dotyczącej efektu fotoelektrochemicznego przełączenia fotoprądu (wspólnie z A. Podborską).

E. Właźlak, W Macyk, W. Nitek, K. Szaciłowski* „*Influence of π -iodide Intermolecular interactions on electronic properties of tin(IV) iodide semiconducting complexes*” *Inorganic Chemistry*, 2016, **55**, 5935–5945

Mój wkład polegał na opracowaniu koncepcji badań, analizie widm elektronowych oraz wykonaniu wstępnych obliczeń kwantowo-mechanicznych.



Prof. dr hab. Wojciech Macyk
Prodziekan ds. badań i współpracy
Kierownik Zakładu Chemii Nieorganicznej
macyk@chemia.uj.edu.pl
tel. 12 686 2494



Kraków, 22 luty 2019

OŚWIADCZENIE

Oświadczam, że mój wkład w powstanie artykułów:

Influence of π -Iodide Intermolecular Interactions on Electronic Properties of Tin(IV) Iodide Semiconducting Complexes

Inorganic Chemistry, 2016, 55 (12), pp 5935–5945

Triiodide Organic Salts: Photoelectrochemistry at the Border between Insulators and Semiconductors,

ChemElectroChem, 2018, 5 (22), 3486-3497

polegał na dyskusji właściwości półprzewodnikowych tytułowych materiałów oraz pomocy w redakcji manuskryptów. Mój wkład w powstanie tych prac oceniam na 5-10%.



Wydział Chemii

Zakład Chemii
Nieorganicznej

Gronostajowa 2
30-387 Kraków, Poland
tel. +48(12) 686 27 00
fax +48(12) 686 27 50
sekretar@chemia.uj.edu.pl
www.chemia.uj.edu.pl

dr inż. Krzysztof Mech
AGH, ACMiN
ul. Kawiory 30
30-055 Kraków
e-mail: kmech@agh.edu.pl

Kraków, 08.01.2019 r.

OŚWIADCZENIE

Oświadczam, że mój wkład w powstanie artykułu:

E. Właźlak, J. Kalinowska-Tłuścik, W. Nitek, S. Klejna, K. Mech, W. Macyk, K. Szaciłowski, Triiodide anion - the source of photocurrent in organic salts, ChemElectroChem, 5, s. 3486 - 3497, 2018.

polegał na wykonaniu pomiarów metodą elektrochemicznej spektroskopii impedancyjnej, mających na celu wyznaczenie wartości potencjału pasma płaskiego oraz opracowaniu i analizie otrzymanych wyników.

Oświadczam, że mój wkład w powstanie artykułu:

E. Właźlak, A. Blachecki, M. Bisztyga-Szklarz, S. Klejna, T. Mazur, K. Mech, Kacper Pilarczyk, D. Przyczyna, M. Suchecki, P. Zawal, K. Szaciłowski, Heavy pnictogen chalcogenides: synthesis, structure and properties of rediscovered semiconductors, Chemical Communications, 54, s. 12133 - 12162, 2018.

polegał na: dokonaniu przeglądu literaturowego oraz opisie właściwości elektrycznych związków MQX, gdzie M = As, Sb, Bi; Q = O, S, Se, Te; oraz X = F, Cl, Br, I.


.....
Podpis współautora



AKADEMIA GÓRNICZO-HUTNICZA
IM. STANISŁAWA STASZICA W KRAKOWIE

Akademickie Centrum Materiałów i Nanotechnologii

AGH

dr inż. Kacper Pilarczyk

Kraków, 08.01.2019

OŚWIADCZENIE

Jako współautor wymienionych poniżej artykułów oświadczam, iż mój wkład w powstanie tychże polegał na:

- P1. E. Właźlak*, A. Blachecki, M. Bisztyga-Szklarz, S. Klejna, T. Mazur, K. Mech*, **K. Pilarczyk**, D. Przyczyna, M. Suchecki, P. Zawał, K. Szaciłowski*
Heavy pnictogen chalcobalides: the synthesis, structure and properties of these rediscovered semiconductors
Chemical Communications, 2018, 54, 12133.

Byłem współodpowiedzialny (wraz z Dawidem Przyczyną) za napisanie części artykułu poświęconej analizie danych spektroskopowych. Brałem także udział w redagowaniu ostatecznej wersji manuskryptu.

- P2. **K. Pilarczyk***, E. Właźlak*, D. Przyczyna, A. Blachecki, A. Podborska, V. Anathasiou, Z. Konkoli, K. Szaciłowski*
Molecules, semiconductors, light and information: Towards future sensing and computing paradigms
Coordination Chemistry Reviews, 2018, 365, 23.

Byłem odpowiedzialny za napisanie części artykułu poświęconej logice wielowartościowej oraz logice rozmytej, a także innych pomniejszych fragmentów publikacji. Brałem udział w koordynowaniu prac nad manuskryptem oraz redagowaniu jego ostatecznej wersji.



Kacper Pilarczyk

Kraków, 09.01.2019

Mgr inż. Dawid Przyczyna

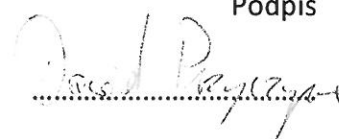
Wydział Fizyki i Informatyki Stosowanej,
Akademickie Centrum Materiałów i Nanotechnologii
Akademia Górniczo-Hutnicza im. Stanisława Staszica w Krakowie
al. A. Mickiewicza 30, 30-059 Kraków

OŚWIADCZENIE

Oświadczam, że w pracy *Molecules, semiconductors, light and information: Towards future sensing and computing paradigms* (Kacper Pilarczyk, Ewelina Właźlak, Dawid Przyczyna, Andrzej Blachecki, Agnieszka Podborska, Vasileios Anathasiou, Zoran Konkoli, Konrad Szaciłowski, *Coordination Chemistry Reviews*, 2018, 365, 23-40) mój udział polegał na opisie i klasyfikacji sensorów fotoelektrochemicznych oraz opisie teorii i przeglądzie zastosowań obliczania rezerwuarowego.

Oświadczam, że w pracy *Heavy pnictogen chalcogenides: the synthesis, structure and properties of these rediscovered semiconductors* (Ewelina Właźlak, , Andrzej Blachecki, Magdalena Bisztyga-Szklarz, Sylwia Klejna, Tomasz Mazur, Krzysztof Mech, Kacper Pilarczyk, Dawid Przyczyna, Maciej Suhecki, Piotr Zawal i Konrad Szaciłowski, *Chemical Communications*, 2018, 54(86), 12133-12162) mój udział polegał na opisie wyników literaturowych spektroskopii optycznej związków potrójnych na bazie pierwiastków z grup 15-16-17 układu okresowego.

Podpis



dr Wojciech Nitek
Wydział Chemii UJ
ul. Gronostajowa 2
30-067 Kraków
Tel. 12 686 2582
Mail: nitek@chemia.uj.edu.pl

Kraków, 22 stycznia 2019

Oświadczenie

Oświadczam, że mój wkład w powstanie artykułu pt. *Triiodide Organic Salts: Photoelectrochemistry at the Border between Insulators and Semiconductors*, ChemElectroChem, 2018, 5 (22), 3486-3497, polegał na wyznaczeniu metodami rentgenowskiej analizy strukturalnej, struktur związków I i III opisanych w artykule.



Wojciech Nitek

dr Wojciech Nitek
Wydział Chemii UJ
ul. Gronostajowa 2
30-067 Kraków
Tel. 12 686 2582
Mail: nitek@chemia.uj.edu.pl

Kraków, 22 stycznia 2019

Oświadczenie

Oświadczam, że mój wkład w powstanie artykułu pt. "*Triiodide Organic Salts: Influence of π -Iodide Intermolecular Interactions on Electronic Properties of Tin(IV) Iodide Semiconducting*", *Complexes Inorg. Chem.*, 2016, 55 (12), pp 5935–5945, polegał na wyznaczeniu metodami rentgenowskiej analizy strukturalnej, struktur związków opisanych w artykule.



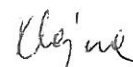
Wojciech Nitek

Sylwia Klejna
Akademia Górniczo-Hutnicza
im. Stanisława Staszica w Krakowie
Akademickie Centrum Materiałów i Nanotechnologii
ul. Kawioro 30, D-16, 30-055 Kraków

Kraków, 08.01.2019 r.

OŚWIADCZENIE

Oświadczam, że mój wkład w powstanie artykułu pt. „Heavy pnictogen chalcogenides: the synthesis, structure and properties of these rediscovered semiconductors” Chemical Communications, 2018, 54, 12133-12162 polegał na opisanu struktury elektronowej i właściwości optycznych chalcogenów antymonu i bizmutu oraz na przygotowaniu manuskryptu.



Podpis współautora

Sylwia Klejna
Akademia Górniczo-Hutnicza
im. Stanisława Staszica w Krakowie
Akademickie Centrum Materiałów i Nanotechnologii
ul. Kawiory 30, D-16, 30-055 Kraków

Kraków, 08.01.2019 r.

OŚWIADCZENIE

Oświadczam, że mój wkład w powstanie artykułu pt. „Triiodide Organic Salts: Photoelectrochemistry at the Border between Insulators and Semiconductors”, ChemElectroChem, 2018, 5 (22), 3486-3497 polegał na zbadaniu i opisanu struktury elektronowej organicznych soli trójjodków oraz na przygotowaniu manuskryptu.



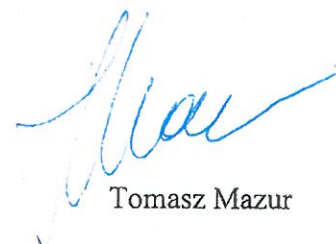
Podpis współautora

Kraków 08.01.2019

Akademia Górniczo-Hutnicza
im. Stanisława Staszica w Krakowie
ACMiN
ul. Kawiory 30 (D-16), 30-055 Kraków
tel. (+48) 12 617 5282

Oświadczenie

Oświadczam, że mój wkład w powstanie artykułu pt. "*Heavy pnictogen chalcogenides: the synthesis, structure and properties of these rediscovered semiconductors*", Chemical Communications, 2018, 54, 12133-12162 polegał na przygotowaniu części manuskryptu dotyczącej opisu struktury elektronowej.



Tomasz Mazur

dr Justyna Kalinowska-Tłuścik
Wydział Chemii UJ
ul. Gronostajowa 2
30-067 Kraków
Tel. 12 686 2467
E-mail: kalinows@chemia.uj.edu.pl

Kraków, 20.02.2019

Oświadczenie

Oświadczam, że mój wkład w powstanie artykułu pt. *Triiodide Organic Salts: Photoelectrochemistry at the Border between Insulators and Semiconductors*, ChemElectroChem, 2018, 5 (22), 3486-3497, polegał na wyznaczeniu metodami rentgenowskiej analizy strukturalnej, struktury związku II i opracowaniu części związanej z opisem prezentowanych struktur krystalicznych.



Piotr Zawal

Kraków, 17.04.2019

Akademickie Centrum Materiałów i Nanotechnologii AGH

ul. Kawiory 30

30-055 Kraków

(dane współautora artykułu)

OŚWIADCZENIE O WSPÓŁAUTORSTWIE

Oświadczam, że mój udział w artykule: "*Memristor in reservoir system – experimental evidence for high level computing and neuromorphic behavior of PbI_2* " ACS Applied Materials & Interfaces, 2019 (doi: 10.1021/acsami.9b01841) polegał na obliczeniu wysokości bariery Schottky'ego, wykonaniu pomiarów efektów neuromimetycznych (*spike-timing dependent plasticity, spike-rate dependent plasticity*) oraz opracowaniu wyników.

..... Piotr Zawal

podpis

Kraków, 10.01.2019 r.

Akademickie Centrum Materiałów i Nanotechnologii AGH
ul. Kawiory 30
30-055 Kraków

OŚWIADCZENIE

Oświadczam, że mój wkład w powstanie artykułu: *Heavy pnictogen chalcogenides: the synthesis, structure and properties of these rediscovered semiconductors*, Chemical Communications, 2018, 54, 12133-12162 polegał na opisanu wymienionych metod otrzymywania i syntezy kryształów związków typu V-VI-VII: krystalizacja z roztopionego materiału, krystalizacja z fazy gazowej, metody chemiczne, synteza solwotermalna, synteza hydrotermalna.

.....Piotr Zawadzki.....

Podpis współautora

dr Magdalena Bisztyga-Szklarz
Akademia Górniczo-Hutnicza
im. St. Staszica w Krakowie
al. A. Mickiewicza 30
30-059 Kraków
adres e-mail: mbs@agh.edu.pl

Kraków, 08.01.2019.

OŚWIADCZENIE

Oświadczam, że mój wkład w powstanie artykułu pt. „Heavy pnictogen chalcogenides: the synthesis, structure and properties of these rediscovered semiconductors”, Chemical Communications, 2018, 54, 12133-12162 polegał na opisanu właściwości fotokatalitycznych i fotoelektrochemicznych chalcogenków metali grup V-VI-VII układu okresowego.



mgr inż. Maciej Suhecki

Kraków, 24.04.2019

Akademia Górniczo-Hutnicza
im. St Staszica w Krakowie
al. A. Mickiewicza
30-059 Kraków
e-mail: suhecki@aghe.edu.pl

Oświadczenie

Oświadczam że mój wkład w powstanie artykułu pt. „Heavy pnictogen chalcogenides: synthesis, structure and properties of rediscovered semiconductors”, Chemical Communications 2018, 54 12133-12162 polegał na opisie syntezy związków materiałów z grup V-VI-VII metodami krystalizacji z roztopionego materiału, krystalizacji z fazy gazowej, chemii mokrej, syntezy solwotermalnej, syntezy hydrotermalnej.

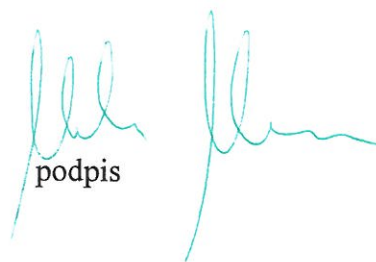
Suhecki Maciej.....

dr inż. Mateusz Marzec
Akademickie Centrum Materiałów
i Nanotechnologii
Akademia Górniczo-Hutnicza im. St.
Staszica w Krakowie

Kraków, 15.05.18

OŚWIADCZENIE O WSPÓŁAUTORSTWIE

Oświadczam, że mój udział w artykule: "*Memristor in reservoir system – experimental evidence for high level computing and neuromorphic behavior of PbI_2* " ACS Applied Materials & Interfaces, 2019 (doi: 10.1021/acsami.9b01841) polegał na wykonaniu pomiarów metodą spektroskopii fotoelektronów (XPS) oraz na analizie wyników wraz z ich opisem.



podpis

Kraków, 08.01.2019

dr Agnieszka Podborska

Akademickie Centrum Materiałów i Nanotechnologii
Akademia Górniczo-Hutnicza im. Stanisława Staszica w Krakowie
al. A. Mickiewicza 30, 30-059 Kraków

OŚWIADCZENIE

Oświadczam, że w pracy *Molecules, semiconductors, light and information: Towards future sensing and computing paradigms* (Kacper Pilarczyk, Ewelina Właźlak, Dawid Przyczyna, Andrzej Blachecki, Agnieszka Podborska, Vasileios Anathasiou, Zoran Konkoli, Konrad Szaciłowski, *Coordination Chemistry Reviews*, 2018, 365, 23-40)

mój udział polegał na opisie materiałów półprzewodnikowych, które posłużyły do budowy molekularnych bramek logicznych w oparciu o logikę dwuwartościową.

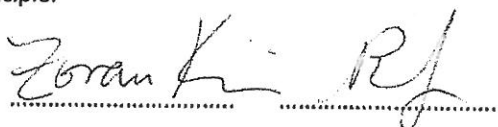
Agnieszka
Podborska

Vasileios Athanasiou
Zoran Konkoli
Tel: +46 31 772 5480
Chalmers University of Technology

Göteborg, Sweden, 2019-01-08

Author contribution statement

In the review paper: *Molecules, semiconductors, light and information: Towards future sensing and computing paradigms*, *Coordination Chemistry Reviews*, 2018, 365, 23-40, we written paragraphs that discussed the use of reservoir computing for sensing applications, and in particular the use of the SWEET sensing principle.

Handwritten signatures of Zoran Konkoli and Vasileios Athanasiou. The signature of Zoran Konkoli is on the left and Vasileios Athanasiou is on the right. Both signatures are written in black ink and are positioned above a horizontal dotted line.

Zoran Konkoli

Vasileios Athanasiou